LATE CRETACEOUS GRAVITATIONAL COLLAPSE OF THE SOUTHERN SIERRA NEVADA BATHOLITH AND ADJACENT AREAS ABOVE UNDERPLATED SCHISTS, SOUTHERN CALIFORNIA

Thesis by

Alan Daniel Chapman

In Partial Fulfillment of the Requirements

for the degree of

Doctor of Philosophy

CALIFORNIA INSTITUTE OF TECHNOLOGY

Pasadena, California

2012

(Defended on July 1, 2011)

Chapter 2 reprinted from *Tectonics*, volume 29,

Alan D. Chapman, Steven Kidder, Jason B. Saleeby, and Mihai N. Ducea, "Role of extrusion of the Rand and Sierra de Salinas schists in Late Cretaceous extension and rotation of the southern Sierra Nevada and vicinity,"
doi:10.1029/ 2009TC002597, © 2010

with kind permission from the American Geophysical Union.

Chapter 3 reprinted from *Journal of Metamorphic Geology*, volume 29,

Alan D. Chapman, Peter I. Luffi, Jason B. Saleeby, and Sierra Petersen, "Metamorphic evolution, partial melting, and rapid exhumation above an ancient flat slab: Insights from the San Emigdio Schist, southern California,"
doi: 10.1111/j.1525-1314.2011.00932.x, © 2011

with kind permission from Wiley-Blackwell Publishing.

ACKNOWLEDGEMENTS

First, I wish to thank my thesis advisor, Jason Saleeby, for his ongoing support and friendship, for sharing his knowledge and infectious geologic gusto, and for introducing me to the greater Sierra Nevada's evil twin: the southern Sierra Nevada-Mojave Desert region. I would also like to thank Zorka Saleeby for her encouragement throughout my Ph.D. research, for discussions ranging from the geology of the Bakersfield Arch to politics, and for teaching me how to make tea from wild stinging nettle. I feel fortunate to have enjoyed excellent working and personal relationships with you both and look forward to continued collaboration and friendship for years to come.

I would like to acknowledge the other members of my thesis advisory committee: Paul Asimow for his mentorship on an electron backscatter diffraction study of Norwegian eclogites, John Eiler for his indispensible feedback on my forays into SIMS and NanoSIMS work and for leading an unforgettable fieldtrip to Santa Catalina Island, John Grotzinger for serving as my academic advisor, and Joann Stock for showing me how to analyze and interpret ASTER data, conduct geologic mapping in volcanic centers, and survive on an uninhabited Mexican island teeming with vicious feral cats. Thanks also to Ken Farley for helping make the Caltech GPS Green Team a reality and for epic trail runs in the San Gabriel Mountains. Brian Wernicke is thanked for teaching an excellent course in Alpine geology. I am also indebted to my Summer Undergraduate Research Fellows (SURFs) Nathaniel Borneman (now at Arizona State University) and Sierra Petersen (now at Harvard University) for their hard work and friendship, Lisa Christiansen, Yunbin Guan and Chi Ma for lab assistance, and Dian Burchess, Jan Haskell, Marcia Hudson, Michelle Medley, and Heather Steele for their open doors.

I owe my gratitude to the following colleagues and collaborators from outside the Caltech bubble: Whitney Behr, Mihai Ducea, Rita Economos, Marty Grove, Carl Jacobson, Seth Kruckenberg, Peter Luffi, Vali Memeti, Elisabeth Nadin, Scott Paterson, John Platt, Daniel Vielzeuf, and D.J. Wood. A special thanks is extended to my undergraduate advisor Jim Stout, whose advice led me to major in geology and apply to Caltech for postgraduate study, and without whom I wouldn't be writing this thesis.

The fieldwork component of my Ph.D. thesis was made possible by the Wind Wolves Preserve of the Wildlands Conservancy. In particular, I express my profound appreciation for the assistance and friendship of Sherryl and David Clendenen, who, despite being faced with the mountainous task of operating the largest non-profit preserve on the west coast, always took the time to help. Dan York, Associate Director at the Wildlands Conservancy and countless rangers and ecologists are also thanked for their ongoing support of, enthusiasm for, and curiosity surrounding this work.

Many thanks are due to my friends and fellow graduate students, especially Steve Chemtob, Steve Kidder, and Andrew Matzen (long live the Cummingtonites!) and Willy Amidon, Dan Bower, Danielle Bower, Robinson Cecil, Natalia Deligne, Kelly Dusinberre, and John Ngo. I have learned more from you all about science and myself than I could ever mention. I am also grateful to my running and musician friends for keeping me balanced.

My love of the outdoors and geology was conceived during family road trips from my relatively rock-barren home state of Minnesota to the southwestern United States. Forrest Gump said it best, "Sometimes I guess there just aren't enough rocks." It is with this anecdote that I thank my parents, Dan and Louaynne Chapman, for cultivating these

interests in me and for their constant love, support, and enthusiasm. To my brothers, Eric and Mark Chapman, current graduate students in wetland ecology at ASU and bioengineering at UCSD, respectively: who knew that sibling rivalry could get us so far?

Finally, I want to express my deepest gratitude to the love of my life: my wife Kelly, for her support, patience, valuable help in the field (sorry about the tick bite!), for pushing me to take an introductory geology course in 2003, and for introducing me to the coolest little guy I know, Gabriel (born September 15, 2010). This thesis is dedicated to you both.

This research was made possible through National Science Foundation grant EAR-0739071 awarded to J. Saleeby and the Gordon and Betty Moore Foundation. Additional financial support came from a Geological Society of America Student Research grant and a Northern California Geological Society Richard Chambers Memorial Scholarship.

ABSTRACT

The greater Sierra Nevada batholith (SNB) is an ~ 600 km long NNW-trending composite arc assemblage consisting of a myriad of plutons exhibiting a distinct transverse zonation in structural, petrologic, geochronologic, and isotopic patterns. However, south of 35.5 °N: 1) the depth of exposure increases markedly; 2) primary zonation patterns swing up to 90˚ westward, taking on an east-west trend; 3) western zone rocks are truncated by eastern zone rocks along the proto-Kern Canyon fault, a Late Cretaceous oblique ductile thrust; and 4) fragments of shallow-level eastern SNB affinity rocks overlie deeper-level western zone rocks and subjacent subduction accretion assemblages (Rand, San Emigdio, and Sierra de Salinas schists) along a major Late Cretaceous detachment system. Integration of these observations with new and existing data reveals a temporal relationship between schist unroofing and upper crustal extension and rotation. I present a model whereby Late Cretaceous shallow subduction and subsequent trench-directed channelized extrusion of the schist triggered gravitational collapse of the overlying crustal column. This overarching model is based on several investigations summarized below.

Thermobarometry, thermodynamic modelling and garnet diffusion modelling are presented that elucidate the tectonics of subduction and eduction of the San Emigdio Schist. I document an upsection increase in peak temperature (i.e. inverted metamorphism), from 590 to 700 °C, peak pressures ranging from 8.5 to 11.1 kbar, limited partial melting, microstructural evidence for large seismic events, rapid cooling (825–380 °C Myr^{-1}) from peak conditions and an "out and back" *P–T* path. Progressive cooling and tectonic underplating beneath an initially hot upper plate following the onset of shallow subduction

provide a working hypothesis explaining high temperatures, inverted metamorphism, partial melting, and the observed *P–T* trajectory calculated from the San Emigdio body.

New geologic mapping and microstructural analysis indicate that the schist was transported to the SSW during structural ascent along a mylonitic contact (the Rand fault and Salinas shear zone) with upper plate assemblages. Crystallographic preferred orientation patterns in deformed quartzites reveal a decreasing simple shear component with increasing structural depth, suggesting a pure shear-dominated westward flow within the subduction channel and localized simple shear along the upper channel boundary. The resulting flow type within the channel is that of general shear extrusion.

Structural, thermobarometric, U-Pb geochronologic, and geochemical data from plutonic and metamorphic framework assemblages in the southern SNB also suggest SSW-directed transport of upper plate(s) along a major Late Cretaceous detachment system. The timing and pattern of regional dispersion of crustal fragments in the southern SNB is most consistent with Late Cretaceous collapse above the underplated schist. These observations imply a high degree of coupling between the shallow and deep crust during high magnitude extension. Zircon (U-Th)/He data presented herein reveal a rapid cooling event at 77 ± 5 Ma, probably reflecting the time of large magnitude detachment faulting. A comparison of this dataset with existing apatite (U-Th)/He thermochronometry suggests that the development of modern landscape and arrangement of tectonic elements in southern California was greatly preconditioned by Late Cretaceous tectonics.

Finally, detrital and metamorphic zircon of the structurally highest and earliest subducted portions of the San Emigdio Schist constrain the depositional age to between

ca. 102 and 98 Ma, respectively. Zircon oxygen isotope data from both lower plate schist and upper plate batholithic assemblages reveal a $\delta^{18}O$ shift of ~ 1.5‰ between igneous (~ 5.5‰) and metamorphic (~ 7‰) domains. These results, taken with previous zircon and whole-rock $\delta^{18}O$ measurements, provide evidence for massive devolatilization of the San Emigdio Schist and fluid traversal of upper plate batholithic assemblages, thereby altering the isotopic composition of overlying material. Furthermore, the timing of fluid-rock interaction in the southwestern SNB is coincident with eastward arc migration and an associated pulse of voluminous magmatism. I posit that during flattening of the Farallon slab the schist was rapidly delivered to the magmatic source, where ensuing devolatilization triggered a magmatic flare-up in the southeastern SNB. This short-lived (< 15 Myr) high-flux event was followed by the termination of arc magmatism as the shallow subduction zone approached thermal equilibrium.

TABLE OF CONTENTS

LIST OF FIGURES

LIST OF TABLES

LIST OF PLATES

CHAPTER 1

Introduction

1. BACKGROUND AND MOTIVATION

Deep-crustal exposures of the southern Sierra Nevada batholith (SNB), subjacent subduction accretion assemblages of the Rand, San Emigdio, and Sierra de Salinas schists, and flanking shallow-level assemblages of the Mojave Desert and Salinian block represent a multi-tiered regional core complex (Figure 1.1) that formed in response to Laramide shallow subduction-driven orogenesis and subsequent gravitational collapse (Malin *et al*., 1995; Wood and Saleeby, 1997; Saleeby, 2003; Chapman *et al*., 2010, 2011). The collapse phase is marked by the structural ascent of presently exposed deep-level (7-11 kbar) rocks of the southwesternmost SNB (Ague and Brimhall, 1988; Pickett and Saleeby, 1993; Fletcher *et al*., 2002; Grove *et al*., 2003; Kidder *et al*., 2003; Saleeby *et al*., 2007; Nadin and Saleeby, 2008; Chapman *et al*., 2010, 2011), the removal of western batholithic and forearc belts south of ~ 35˚ N (Ross *et al*., 1973; James *et al*. 1993; Schott and Johnson, 1998, 2001), and the dispersal of shallow-level (2-4 kbar), southeastern SNB-affinity assemblages across the entire width of the batholith (May, 1989; Malin *et al*, 1995; Wood and Saleeby, 1997; Saleeby, 2003; Chapman *et al*., 2010), thereby disrupting the primary transverse structure of the SNB.

This thesis is motivated by the following first-order questions concerning the tectonopetrologic evolution of the southern SNB and vicinity:

Figure 1.1. Index geologic map of southern and central California basement rocks based on USGS Open-File Report 2005-1305 (Ludington *et al*., 2007). Location of Sr_i = 0.706 isopleth (dotted line) from Kistler (1990). Abbreviations: BL, Ben Lomond Mountain; EF, East Fork (San Gabriel Mountains); GF, Garlock fault; GH, Gavilan Hills; GR, Gabilan Range; GV, Great Valley; KCF, Kern Canyon fault; MD, Mojave Desert; MM, Montara Mountain; NF, Nacimiento fault; O, Orocopia Mountains; PRB, Peninsular Ranges batholith; PQ, Portal Ridge and Quartz Hill; PR, Point Reyes; pKCF, proto-Kern Canyon fault; R, Rand Mountains; RRF, Reliz-Rinconada fault; SAF, San Andreas fault; SE, San Emigdio Mountains; SC, Santa Catalina Island; SNB, Sierra Nevada batholith; SP, Sierra Pelona; SS, Sierra de Salinas; TC, Tehachapi Mountains; WWF, White Wolf fault.

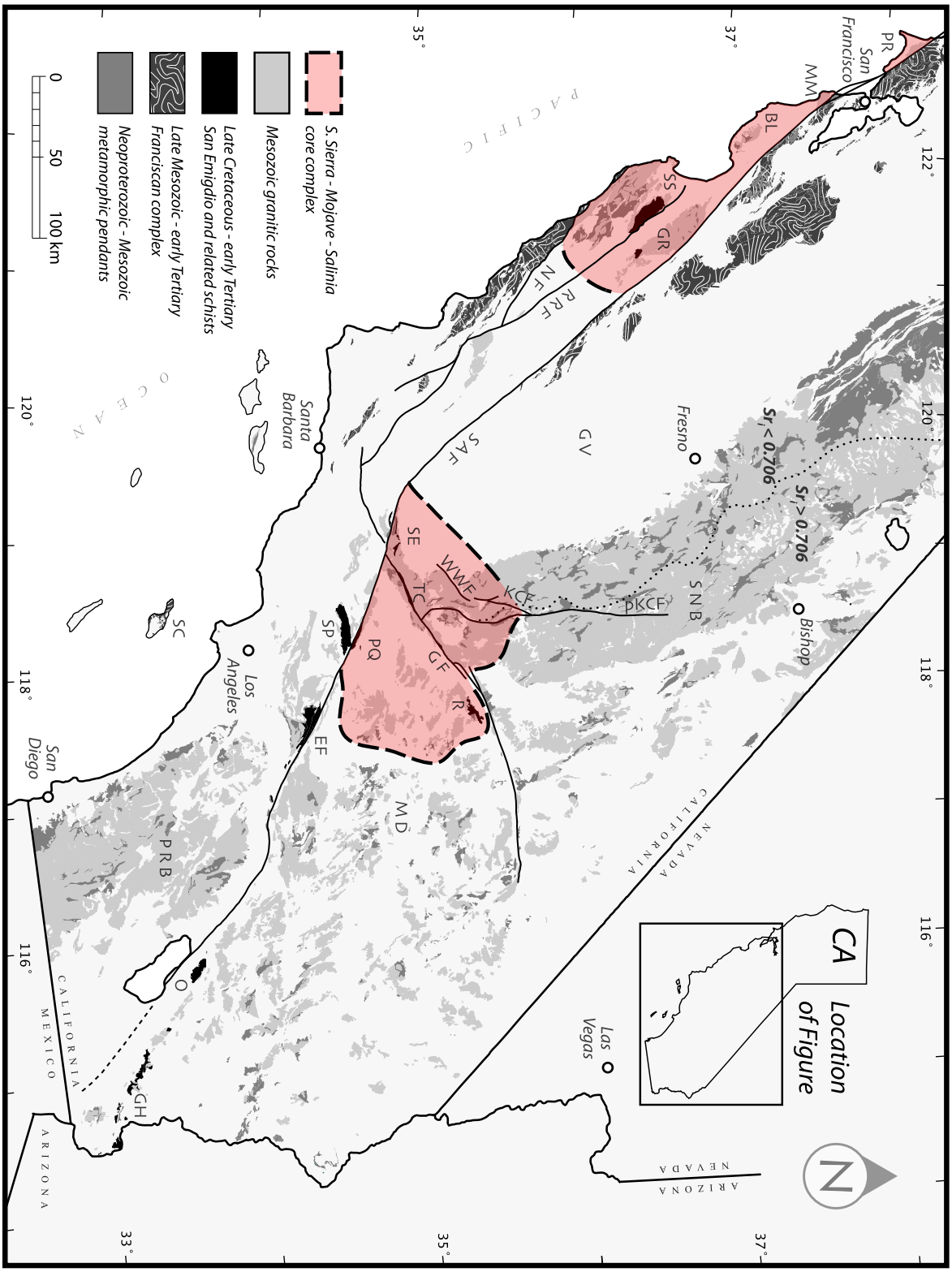
S. Sierra - Mojave - Salinia core complex
Mesozoic granitic rocks
Late Cretaceous - early Tertiary San Emigdio and related schists
Late Mesozoic - early Tertiary Franciscan complex
Neoproterozoic - Mesozoic metamorphic pendants
0 50 100 km
CA
Location of Figure
Sr = 0.706
Sr > 0.706
San Francisco
Fresno
Bishop
Santa Barbara
Los Angeles
San Diego
Las Vegas
PACIFIC OCEAN
NEVADA
CALIFORNIA
ARIZONA
MEXICO
PR
MM
BL
SS
GR
NFRF
SAF
GV
SNB
SE
WWF
TC
KCF
DKCF
SP
PQ
GF
R
EF
MD
PRB
SC
O
GH

1) How does this large (roughly 200 km by 200 km) core complex compare with those of similar size, such as the Shuswap core complex of the Canadian Cordillera?

2) What mechanism(s) drove schist underthrusting and exhumation?

3) How did the thermal structure of Laramide subduction evolve during the slab flattening process?

4) How has schist metamorphism and resultant devolatilization affected the isotopic composition of the overriding plate and are these processes linked to a period of short-lived high-flux magmatism followed by arc shutoff?

5) What was the relationship between schist emplacement and upper plate extension and rotation in the southern Sierra Nevada and adjacent areas? In other words, to what degree were the upper and lower crust coupled during during gravitational collapse?

6) When did gravitational collapse occur, over what scale, and what was the relative importance of strike-slip versus low angle normal faults?

7) Finally, how has Late Cretaceous tectonism influenced the development of the modern southern Sierra Nevada landscape?

These issues are addressed using a combination of fieldwork, petrographic and microstructural analysis, electron microprobe spot analyses and X-ray mapping, scanning electron microscope imaging and electron backscatter diffraction (EBSD) analyses, zircon U-Pb geochronology and (U-Th)/He thermochronometry, zircon $\delta^{18}O$ measurements, whole rock geochemistry, and Sr and Nd isotopic determinations.

2. THESIS OUTLINE

This thesis is organized into five chapters, Section 3 of this introduction included, all originally written for publication in scientific journals. As a result, there is some overlap between chapters. Below is an overview of the main chapters of this thesis.

This thesis begins with the accompanying text to a new 1:24,000 scale geologic map of the San Emigdio Mountains of southern California (Plate 1), submitted to the *Geological Society of America Digital Map and Chart Series* (see Section 1.3). This map was produced through geologic mapping between 2006 and 2010, petrographic examination of collected samples, U-Pb geochronology, and thermobarometry. This chapter establishes the intellectual framework for chapters summarized below, focusing on Cretaceous assemblages belonging to the Sierra Nevada batholith and the Late Cretaceous San Emigdio Schist.

Chapter 2, published in *Tectonics* in 2010, is a compilation of new and published structural data from the principal exposures of southern California schist indicating noncoaxial lower plate transport to the SSW at high structural levels and increasing coaxial component of deformation with structural depth. Integration of these observations with published geochronologic, thermochronometric, thermobarometric, and paleomagnetic studies led my coauthors and I to propose that Late Cretaceous extrusion of underplated schist led to high magnitude extension, deep exhumation, and westward deflection of upper plate rocks of the southern Sierra Nevada and adjacent areas.

Chapter 3, published in the *Journal of Metamorphic Geology* in 2011, presents new field relations, thermobarometry, thermodynamic modelling and garnet diffusion modelling that constrain the *P–T* history and the tectonics of underplating and exhumation of the San Emigdio member of the southern California schist. These observations constrain the

physical conditions once present above the Farallon flat slab segment and further our understanding of the tectonics of slab flattening and schist underthrusting and exhumation in the southern California region. Appendix 1 accompanies this chapter and contains descriptions of garnet diffusion modelling techniques and representative mineral compositions used in thermobarometric calculations.

Chapter 4, submitted to a Sierra Nevada EarthScope Project (SNEP) volume in *Geosphere*, addresses issues pertaining to Late Cretaceous gravitational collapse of the southern Sierra Nevada batholith and vicinity, focusing mainly on the magnitude, direction, and timing of tectonic transport of upper crustal fragments along a regional detachment system. In this effort, new field and structural relations, U-Pb geochronology of plutonic and detrital zircon populations, thermobarometry, major and trace element geochemistry and Sr and Nd isotopic ratios, and zircon (U-Th)/He thermochronometry are presented. These results are integrated with previous geologic studies and thermobarometric, geochronologic, and geochemical databases to clarify: 1) the magnitude of transport between recognized native and displaced terranes, 2) the degree of coupling between the shallow and deep crust during extension, 3) the tectonic context of gravitational collapse, and 4) the development of modern landscape and arrangement of tectonic elements in southern California. Appendix 2 accompanies this chapter and includes analytical techniques, sample petrography, representative mineral compositions, U-Pb and (U-Th)/He zircon data, whole rock and Sr and Nd isotopic data, compilations of all known U-Pb zircon ages, Sr_i ratios, and pressure determinations from the Sierra Nevada batholith, and representative zircon cathodoluminescence (CL) images.

Finally, Chapter 5, to be submitted to *Geology*, integrates new and published *in*

situ zircon U-Pb and oxygen isotope data from lower plate San Emigdio Schist and upper plate batholithic assemblages. These data provide evidence for massive devolatilization of the schist and fluid traversal of upper plate batholithic assemblages, thereby altering the isotopic composition of overlying material and triggering a magmatic flare-up in the southernmost Sierra Nevada batholith. Appendix 3 presents analytical techniques, sample locations and petrography, U-Pb zircon and oxygen isotopic data, and representative zircon cathodoluminescence (CL) images relevant to this chapter.

3. GEOLOGIC MAP OF THE SAN EMIGDIO MOUNTAINS

ABSTRACT

New and existing geologic mapping and geochronology of the San Emigdio Mountains are compiled in a 1:24,000 scale map, establishing the framework for recently published and ongoing studies of Cretaceous assemblages belonging to the Sierra Nevada batholith and the Late Cretaceous San Emigdio Schist. Basement exposures of the San Emigdio Mountains are subdivided into four principal fault-bounded assemblages: 1) mid-to Late Cretaceous shallow-level granitoids and Paleozoic to Mesozoic metamorphic pendant rocks of the Pastoria plate, 2) Early to mid-Cretaceous deep-level intrusive rocks of the Tehachapi-San Emigdio complex, 3) mid- to Late Jurassic gabbro, tonalite, ultramafic rocks, and framework basalts of the western San Emigdio mafic complex, and 4) the Late Cretaceous San Emigdio Schist. The field relations summarized here, when viewed in a regional context, constrain the lateral extent of major Laramide detachment systems (the Pastoria and Rand faults) that were active during Late Cretaceous extensional collapse of the southern

Sierra Nevada batholith and adjacent Mojave Desert area and document a highly dismembered and deeply-exhumed ancient flat slab system.

3.1. Introduction

The San Emigdio and related Pelona, Orocopia, Rand, and Sierra de Salinas schists of Southern California were underplated beneath the southern Sierra Nevada batholith (SNB) along a shallow segment of the subducting Farallon plate in Late Cretaceous - early Tertiary time (e.g., Saleeby, 2003; Chapman *et al*., 2010; 2011; submitted; Jacobson *et al*., 2011). Basement exposures in the San Emigdio Mountains represent a regional, deeply exhumed, shallowly dipping domain from this ancient slab segmentation system and record the complete life cycle of the segmentation process from initial flattening and compression to final extensional collapse. For this study, we remapped the basement rocks in the San Emigdio Mountains at 1:10,000 scale (compiled at 1:24,000 scale in Plate 1), focusing on the structural relations between the San Emigdio Schist and adjacent Cretaceous plutonic and associated framework metamorphic rocks. In addition to the geologic map, three cross sections are provided.

3.2. Field setting

In terms of physiography, the San Emigdio Mountains are part of the Transverse Ranges and include units south of the San Andreas fault. However, the San Emigdio Mountains are distinct from the Transverse Ranges in terms of geology and are better categorized as part of the Sierra Nevada and, in conjunction with the Tehachapi Range to the east, define the "Sierran tail." By this definition, the San Emigdio Mountains extend from Grapevine

Canyon (Interstate 5) in the east to highways 33 and 166 on the west and are bounded by the San Andreas fault to the south and the Pleito thrust to the north, residing within Kern, Los Angeles, and Ventura counties of southern California. The elevation of the San Emigdio Mountains ranges from 7,492 (San Emigdio Mountain) to approximately 1,600 feet, with ridge to valley relief ranging from approximately 1,000 to 3,000 feet. The San Emigdio Mountains lie at the intersection of five geologic provinces: the Sierra Nevada, the Mojave Desert, the Transverse Ranges, the Coast Ranges, and the Great Valley. As such, the climate contains elements of each province, including Mediterranean, xeric, and subalpine zones. Cool, moisture-retaining north-facing slopes are mixed evergreen forest and grasslands, while warmer and drier south-facing slopes are chaparral and woodlands. The combination of high topographic relief and locally thick vegetation render fieldwork in the San Emigdio Mountains difficult, although many areas within the range are accessible year round.

3.3. Previous field and analytical work

Reconnaissance geologic mapping focusing on Eocene to Quaternary sedimentary and volcanic deposits by Dibblee (1973) and Dibblee and Nilsen (1973) and crystalline basement rocks by Ross (1989) represent the bulk of previous work at the regional scale of this investigation. Geologic mapping of sedimentary, volcanic, and crystalline basement rocks adjacent to the San Andreas fault zone has been done by Crowell (1952), Duebendorfer (1979), Davis (1983), Davis and Duebendorfer (1987), Kellogg and Miggins (2002), and Kellogg (2003). A suite of mid- to Late Jurassic layered to isotropic gabbroids and lesser amounts of ultramafic rock, which in turn are intruded by tonalitic assemblages

have received detailed study by Reitz (1986) and James (1986) (the "Northern San Emigdio Plutonic complex"), Ross (1989) (the "Eagle Rest Peak" area), and Chapman *et al*. (2010, in review, and this study) (the "western San Emigdio mafic complex"). Metamorphosed basaltic sheeted dikes and pillows constituting the intruded framework of the western San Emigdio mafic complex are studied by Hammond (1958), and are referred to as the "Schoolhouse Canyon metamorphic complex." A tentative correlation has been drawn between this unit and similar assemblages of the Kings-Kaweah ophiolite on the basis of whole rock geochemistry and Sr and Nd isotopes (Saleeby, in press; Chapman *et al*., in review). A semi-continuous belt of schist constitutes the base of the tectonic section in the San Emigdio and Tehachapi Mountains and is referred to as Pelona Schist by Sharry (1981), Rand Schist by Ross (1989), Grove *et al*. (2003), Saleeby *et al*. (2007), and Chapman *et al*. (2010), and San Emigdio Schist by Jacobson *et al*. (2011) and Chapman *et al*. (2011). Geologic mapping of the San Emigdio Schist has been done in reconnaissance mode by Ross (1989) and at 1:10,000 scale (compiled here at 1:24,000 scale) by Chapman *et al*. (2010, 2011). Continuation of units east of Grapevine Canyon is based on work by Saleeby *et al*. (1987, 2007) and Pickett and Saleeby (1993, 1994). U/Pb zircon igneous emplacement ages (Saleeby *et al*., 1987, 2007; Pickett and Saleeby, 1994; Chapman *et al*., in review) are also shown on the map.

3.4. Geologic setting and summary of key basement field relations

Uplift of basement and sedimentary cover strata in the San Emigdio Mountains is controlled by Pliocene-Quaternary north-south compression between the big bend in the San Andreas fault and the Pleito fault zone (Davis, 1983; Dibblee, 1986). Mesozoic to Paleozoic plutonic

and associated framework metamorphic rocks comprise the bulk of the basement complex in the San Emigdio Mountains (Ross, 1989). These rocks are overlain by a thick (locally > 7,000 m) Cenozoic sequence of largely marine sedimentary and volcanic rocks. A detailed synthesis of sedimentary and volcanic basement cover rocks is provided by Dibblee (1986) and is beyond the scope of this effort. However, in the course of our mapping of basement rocks in the San Emigdio Mountains, we have recognized that Late Pleistocene to Holocene gravels in San Emigdio Canyon (e.g., Keller *et al*., 2000) contain detritus derived exclusively from the Abel Mountain-Frazier Mountain-Mount Pinos area south of the San Andreas fault. This suggests that uplift and exposure of basement rocks north of the San Andreas fault occurred after Late Pleistocene time and that San Emigdio Canyon is an antecedent drainage of the Abel Mountain-Frazier Mountain-Mount Pinos area.

Basement exposures of the San Emigdio Mountains are subdivided into four principal assemblages. First is a collection of shallow-level (3-4 kbar) eastern SNB affinity granitoids and metamorphic pendant rocks referred to as the Pastoria plate (Crowell, 1952; Ross, 1989). The Pastoria fault, a member of the Late Cretaceous-Paleocene southern Sierra detachment system (Wood and Saleeby, 1997; Chapman *et al*., in review), folded and cut in Pliocene-Quaternary time by south-dipping thrust faults, lies at the base of the Pastoria plate. Early to mid-Cretaceous deep-level (7-9 kbar) SNB rocks of the Tehachapi-San Emigdio complex (Pickett and Saleeby, 1993; Chapman *et al*., 2011; in review) lie in the footwall of the Pastoria fault. Contact relations between these units and a third basement assemblage, the western San Emigdio mafic complex, are obscured by Tertiary sedimentary deposits. The Tehachapi-San Emigdio complex sits tectonically above the San Emigdio Schist along the Rand fault, a locally ductile to brittle low-angle detachment fault system

(Ross, 1989; Chapman *et al*., 2010, 2011). During Pliocene to Quaternary compression, the Rand fault in the San Emigdio Mountains was largely folded with a major south-dipping thrust fault cutting across the folded structural section with the San Emigdio Schist in the hanging wall and the Tehachapi-San Emigdio complex in the footwall. The reader is referred to the topics presented in detail in this thesis for additional details regarding these relations and their tectonic significance. In short, our field studies, when viewed in the context of schist windows in the Tehachapi and Rand Mountains, constrain the lateral extent of a major Laramide detachment system that was active during a phase of extensional collapse above the underplated schists and document a highly dismembered and deeply-exhumed ancient flat slab system.

REFERENCES

Ague, J. J., and Brimhall, G. H., 1988, Magmatic arc asymmetry and distribution of anomalous plutonic belts in the batholiths of California; effects of assimilation, crustal thickness, and depth of crystallization: *Geological Society of America Bulletin*, **100**(6), 912-927.

Chapman, A. D., Kidder, S., Saleeby, J. B., and Ducea, M. N., 2010, Role of extrusion of the Rand and Sierra de Salinas schists in Late Cretaceous extension and rotation of the southern Sierra Nevada and vicinity: *Tectonics*, **29(**5), TC5006, doi:10.1029/ 2009TC002597.

Chapman, A. D., Luffi, P., Saleeby, J., and Petersen, S., 2011, Metamorphic evolution, partial melting, and rapid exhumation above an ancient flat slab: Insights from the San

Emigdio Schist, southern California: *Journal of Metamorphic Geology*, **29**, 601-626, doi: 10.1111/j.1525-1314.2011.00932.x.

Chapman, A. D., Saleeby, J. B., Piasecki, A, Farley, K. A., Kidder, S., Ducea, M. N., and Wood, D. J., in review, Late Cretaceous gravitational collapse of the southern Sierra Nevada batholith, California, submitted to *Geosphere*.

Crowell, J. C., 1952, Geology of the Lebec Quadrangle, California: *Special Report - California Division of Mines and Geology*, **24**, 1-24.

Davis, T.L., 1983, Late Cenozoic structure and tectonic history of the western "Big Bend" of the San Andreas fault and adjacent San Emigdio Mountains: Santa Barbara, University of California at Santa Barbara, Ph.D. Dissertation, 563 pp.

Davis, T.L., and Duebendorfer, E.M., 1987, Strip map of San Andreas fault, Western Big Bend segment: *Geological Society of America Map and Chart Series* MC-60, scale 1:31,682.

Dibblee, T.W., 1973. Geologic maps of the Santiago Creek, Eagle Rest Peak, Pleito Hills, Grapevine, and Pastoria Creek quadrangles, Kern County, California: *U.S. Geological Survey Open File Report* 73-57.

Dibblee, T.W., 1986. Geology of the San Emigdio Mountains, California: *Field Trip Guidebook – Pacific Section, Society of Economic Paleontologists and Mineralogists*, **48**, 1-10.

Dibblee T. W., and Nilsen, T. H., 1973, Geologic map of San Emigdio and western Tehachapi Mountains, in Vedder, J. G., chairman: *Sedimentary facies changes in Tertiary rocks, California Transverse and southern Coast Ranges: Society of Economic Paleontologists and Mineralogists annual meeting guidebook 2*, scale 1:62,500.

Duebendorfer, E.M., 1979, Geology of the Frazier Park-Cuddy Valley area, California: Santa Barbara, University of California at Santa Barbara M.A. Thesis, 123 pp.

Fletcher, J. M., Miller, J. S., Martin, M. W., Boettcher, S. S., Glazner, A. F., and Bartley, J. M., 2002, Cretaceous arc tectonism in the Mojave Block; profound crustal modification that controlled subsequent tectonic regimes: *Memoir - Geological Society of America*, **195**, 131-149.

Grove, M., Jacobson, C.E., Barth, A.P. and Vucic, A., 2003. Temporal and spatial trends of Late Cretaceous-early Tertiary underplating Pelona and related schist beneath Southern California and southwestern Arizona: *Geological Society of America Special Paper*, **374**, 381-406.

Hammond, P. E., 1958, Geology of the lower Santiago Creek area, San Emigdio Mountains, Kern County, California. M.S. thesis, University of California, 108 pp.

Jacobson, C. E., Grove, M., Pedrick, J. N., Barth, A. P., Marsaglia, K. M., Gehrels, G. E., and Nourse, J. A., 2011, Late Cretaceous - early Cenozoic tectonic evolution of the southern California margin inferred from provenance of trench and forearc sediments: *Geological Society of America Bulletin*, **123**(3-4), 485-506.

James, E. W., 1986, Geochronology, isotopic characteristics, and paleogeography of parts of the Salinian Block of California. Ph.D. thesis, University of California, 176 pp.

James, E. W., Kimbrough, D. L., and Mattinson, J. M., 1993, Evaluation of displacements of pre-Tertiary rocks on the northern San Andreas Fault using U-Pb zircon dating, initial Sr, and common Pb isotopic ratios: *Memoir - Geological Society of America*, **178**, 257-271.

Keller, E. A., D. B. Seaver, D. L. Laduzinsky, D. L. Johnson, and Ku, T. L., 2000, Tectonic

geomorphology of active folding over buried reverse faults; San Emigdio Mountain front, southern San Joaquin Valley, California: *Geological Society of America Bulletin*, **112**, 86-97.

Kellogg, K. S., 2003, Geologic Map of the Cuddy Valley quadrangle, Kern and Ventura Counties, California: *U.S. Geologic Survey Open-File Report* 03-153, scale 1:24,000.

Kellogg, K.S., and Miggins, D.P., 2002, Geologic Map of the Sawmill Mountain Quadrangle, Kern and Ventura Counties, California: *U.S. Geologic Survey Open-File Report* 02-406, scale 1:24,000.

Kidder, S., Ducea, M., Gehrels, G. E., Patchett, P. J., and Vervoort, J., 2003, Tectonic and magmatic development of the Salinian Coast Ridge Belt, California: *Tectonics*, **22**, doi:10.1029/2002TC001409.

Kistler, R.W., 1990, Two different types of lithosphere in the Sierra Nevada, California, in Anderson, J.L., ed., The Nature and Origin of Cordilleran Magmatism: *Geological Society of America Memoir* **174**, 271-282.

Ludington, S., Moring, B., Miller, R. J., Stone, P. A., Bookstrom, A. A., Bedford, D. R., Evans, J. G., Haxel, G. A., Nutt, C. J., Flyn, K. S., and Hopkins, M. J., 2007. Preliminary integrated geologic map databases for the United States: *U.S. Geological Survey Open File Report* 2005-1305.

Malin, P. E., Goodman, E. D., Henyey, T. L., Li, Y. G., Okaya, D. A., and Saleeby, J. B., 1995, Significance of seismic reflections beneath a tilted exposure of deep continental crust, Tehachapi Mountains, California: *Journal of Geophysical Research*, **100**(B2), 2069-2087, doi: 2010.1029/2094JB02127.

May, D. J., 1989, Late Cretaceous intra-arc thrusting in Southern California: *Tectonics*, **8**(6),

1159-1173.

Nadin, E. S., and Saleeby, J. B., 2008, Disruption of regional primary structure of the Sierra Nevada Batholith by the Kern Canyon fault system, California: *Special Paper - Geological Society of America*, **438**, 429-454.

Pickett, D. A., and Saleeby, J. B., 1993, Thermobarometric constraints on the depth of exposure and conditions of plutonism and metamorphism at deep levels of the Sierra Nevada Batholith, Tehachapi Mountains, California: *Journal of Geophysical Research*, **98**(B1), 609-629.

Pickett, D. A., and Saleeby, J. B., 1994, Nd, Sr, and Pb isotopic characteristics of Cretaceous intrusive rocks from deep levels of the Sierra Nevada Batholith, Tehachapi Mountains, California: *Contributions to Mineralogy and Petrology*, **118**(2), 198-215, doi: 110.1007/BF01052869.

Reitz, A., 1986, The geology and petrology of the northern San Emigdio plutonic complex, San Emigdio Mountains, Southern California. M.A. thesis, University of California, 80 pp.

Ross, D. C., Wentworth, C. M., and McKee, E. H., 1973, Cretaceous mafic conglomerate near Gualala offset 350 miles by San Andreas Fault from oceanic crustal source near Eagle Rest Peak, California: *Journal of Research of the U. S. Geological Survey*, **1**(1), 45-52.

Ross, D. C., 1989, The metamorphic and plutonic rocks of the southernmost Sierra Nevada, California, and their tectonic framework: *U.S. Geological Survey Professional Paper* 1381, 159 pp.

Saleeby, J. B., Sams, D. B., and Kistler, R. W., 1987, U/Pb zircon, strontium, and oxygen isotopic and geochronological study of the southernmost Sierra Nevada Batholith, California: *Journal of Geophysical Research*, **92**(B10), 10,443-410,466.

Saleeby, J., 2003, Segmentation of the Laramide slab; evidence from the southern Sierra Nevada region: *Geological Society of America Bulletin*, **115**, 655-668.

Saleeby, J., Farley, K. A., Kistler, R. W., and Fleck, R. J., 2007, Thermal evolution and exhumation of deep-level batholithic exposures, southernmost Sierra Nevada, California: *Special Paper - Geological Society of America*, **419**, 39-66.

Saleeby, J., 2011, Geochemical mapping of the Kings-Kaweah ophiolite belt, California - evidence for progressive melange formation in a large offset transform-subduction initiation environment: *Special Paper - Geological Society of America* (in press).

Schott, R. C., and Johnson, C. M., 1998, Sedimentary record of the Late Cretaceous thrusting and collapse of the Salinia-Mojave magmatic arc: *Geology*, **26**(4), 327-330.

Schott, R. C., and Johnson, C. M., 2001, Garnet-bearing trondhjemite and other conglomerate clasts from the Gualala Basin, California; sedimentary record of the missing western portion of the Salinian magmatic arc?: *Geological Society of America Bulletin*, **113**(7), 870-880.

Sharry, J., 1981. The Geology of the Western Tehachapi Mountains, California. PhD thesis, Massachusetts Institute of Technology, Cambridge, 215 pp.

Turner, D. L., 1970, Potassium-argon dating of Pacific coast Miocene foraminiferal stages: Boulder, Colorado: *Geological Society of America Special Paper*, **124**, 91-129.

Wood, D. J., and Saleeby, J. B., 1997, Late Cretaceous-Paleocene extensional collapse and disaggregation of the southernmost Sierra Nevada Batholith: *International Geology Review*, **39**(11), 973-1009.

CHAPTER 2

Role of extrusion of the Rand and Sierra de Salinas schists in Late Cretaceous extension and rotation of the southern Sierra Nevada and vicinity

Alan D. Chapman[1], Steven Kidder[1], Jason B. Saleeby[1], and Mihai N. Ducea[2]

[1]*Division of Geological and Planetary Sciences, California Institute of Technology, Pasadena, California, USA*

[2]*Department of Geosciences, University of Arizona, Tucson, Arizona, USA*

Published in *Tectonics*

ABSTRACT

The Rand and Sierra de Salinas schists of southern California were underplated beneath the southern Sierra Nevada batholith and adjacent Mojave-Salinia region along a shallow segment of the subducting Farallon plate in Late Cretaceous time. Various mechanisms including return flow, isostatically driven uplift, upper plate normal faulting, erosion, or some combination thereof, have been proposed for the exhumation of the schist. We supplement existing kinematic data with new vorticity and strain analysis to characterize deformation in the Rand and Sierra de Salinas schists. These data indicate that the schist was transported to the SSW from deep to shallow crustal levels along a mylonitic contact (the Rand fault and Salinas shear zone) with upper plate assemblages. Crystallographic preferred orientation patterns in deformed quartzites reveal a decreasing simple shear component with increasing structural depth, suggesting a pure shear dominated westward flow within the subduction channel and localized simple shear along the upper channel boundary. The

resulting flow type within the channel is that of general shear extrusion. Integration of these observations with published geochronologic, thermochronometric, thermobarometric, and paleomagnetic studies reveals a temporal relationship between schist unroofing and upper crustal extension and rotation. We present a model whereby trench-directed channelized extrusion of the underplated schist triggered gravitational collapse and clockwise rotation of the upper plate.

1. INTRODUCTION

The Rand and Sierra de Salinas schists (referred to here as "the schist") and related Pelona and Orocopia schists have long attracted interest due their underthrust position relative to older Mesozoic batholith over much of southern California (Ehlig, 1958; 1981; Graham and England, 1976; Haxel and Dillon, 1978; Jacobson, 1983; 1995; Jacobson *et al*., 1988; 2007). Most workers agree that the deposition and emplacement of the schist occurred during an episode of shallow subduction related to the Laramide orogeny (Jacobson *et al*., 2007 and references therein). Comparatively less is understood, however, regarding mechanisms underlying schist exhumation. Geochronologic, thermochronometric, and thermobarometric studies indicate a temporal link between schist unroofing and major upper crustal extension (Pickett and Saleeby, 1993; Jacobson, 1995; Kistler and Champion, 2001; Barth *et al*., 2003; Grove *et al*., 2003; Kidder *et al*., 2003; Kidder and Ducea, 2006; Saleeby *et al*., 2007). As discussed below, schist ascent coincided with clockwise rotation of the southern Sierra Nevada batholith (SNB) (Kanter and McWilliams, 1982; McWilliams and Li, 1985; Plescia *et al*., 1994).

Existing models for the exhumation of the northern (i.e., Rand and Sierra de Salinas) and southern (i.e., Pelona and Orocopia) schists invoke return flow (Oyarzabal *et al*., 1997; Jacobson *et al*., 2002; Saleeby, 2003; Saleeby *et al*., 2007), isostatically driven uplift (Jacobson *et al*., 2007), upper plate normal faulting (e.g., Jacobson *et al*., 1996), erosion (Yin, 2002), or some combination thereof. We discuss these models in light of new field and microstructural work and conclude that an alternative exhumation mechanism, channelized extrusion, played an important role in exhumation.

Here we address unresolved issues related to schist emplacement including (1) the mechanisms of schist underthrusting and exhumation; and (2) the relationship between schist emplacement and upper plate extension and rotation in the southern Sierra Nevada and adjacent areas. We compile new and published structural data from the principal exposures of the schist indicating noncoaxial lower plate transport to the SSW at high structural levels and increasing coaxial component of deformation with structural depth. We propose that Late Cretaceous trench-directed channelized extrusion in the underplated schist led to high magnitude extension, deep exhumation, and westward deflection of the upper plate batholith above the flowing channel.

2. GEOLOGIC BACKGROUND

2.1. Rand and Sierra de Salinas schists

The Rand and Sierra de Salinas schists are the northernmost exposures of a high P - intermediate to high T terrane that underlies much of southern California and southwestern Arizona along detachment structures (Cheadle *et al*., 1986; Li *et al*., 1992; Malin *et al*.,

1995; Yan *et al*., 2005). Intensive study of the schist indicates that it formed by deposition of Late Cretaceous arc-derived detritus at the North America - Farallon plate margin and was underplated and metamorposed along a shallow segment of the subducting Farallon slab (Grove *et al*., 2003; Saleeby, 2003). The spatial distribution of the schist (Figure 2.1) was controlled by the geometrical evolution of the Farallon slab. As the slab was underthrust to the east beneath North America in the Late Cretaceous, a south to north inflection from shallow to normal subduction trajectories developed, resembling a regional lateral ramp in the subduction megathrust. This left the lithospheric mantle of the greater SNB intact, while first removing the mantle and subsequently underplating schist directly beneath the southern SNB and the adjacent Salinia terrane (Malin *et al*., 1995; Ducea and Saleeby, 1998; Saleeby, 2003; Nadin and Saleeby, 2008). Intense contractile deformation along the shallow megathrust flat removed virtually the entire forearc and frontal arc plutonic zone by subduction erosion, leading to rapid uplift and denudation of the residual arc to mid-crustal levels (Saleeby, 2003; Saleeby *et al*., 2007; Ducea *et al*., 2009). During the unroofing of the Cretaceous arc, the transport direction in the subduction wedge reversed, and the schist was educted from the subduction zone (Saleeby *et al*., 2007; Ducea *et al*., 2009).

2.2. Kern Canyon-proto-White Wolf fault system

Here we review temporal and kinematic relations between the principal members of the integrated Kern Canyon-White Wolf system (after Nadin and Saleeby, 2008), as they are important for both the contractile and extensional phases of regional deformation related to schist underplating. Continuity between the Kern Canyon fault and the White Wolf fault was first emphasized by Ross (1986), although subsequent workers have not realized the

Figure 2.1. Tectonic map of southern Sierra Nevada basement with related elements of northern Mojave and Sierra de Salinas restored along San Andreas and Garlock faults. For compactness, Sierra de Salinas is shown ~50 km north of its pre-Neogene location. Distribution of Mesozoic and early Tertiary arc plutons in the North American Cordillera (upper left inset) after Miller *et al*. (2000). Primary zonation and structures of the Sierra Nevada batholith (upper right inset) from Nadin and Saleeby (2008) and Saleeby *et al*. (2007). Detachment systems from Wood and Saleeby (1998). Transport directions of Rand schist from Nourse (1989), Wood and Saleeby (1998), and this study. Paleomagnetic data from Kanter and McWilliams (1982), McWilliams and Li (1983), and Wilson and Prothero (1997). Pluton emplacement pressures in California index map (lower inset) from Ague and Brimhall (1988), Pickett and Saleeby (1993), and Nadin and Saleeby (2008). Numbers 1-7 in lower inset refer to locations: 1, San Gabriel Mountains; 2, Orocopia Mountains; 3, Gavilan Hills; 4, Iron Mountains; 5, Old Woman Mountains; 6, Granite Mountains; 7, New York Mountains. Abbreviations: FP, Fremont Peak; GF, Garlock fault; KCF, Kern Canyon fault; KWF, Kern Canyon / proto-White Wolf fault (dashed where concealed); pKCF, proto-Kern Canyon fault; MD, Mojave Desert; PRB, Peninsular Ranges batholith; SAF, San Andreas fault; SNB, Sierra Nevada batholith; TE, Tejon embayment; TM, Tehachapi Mountains.

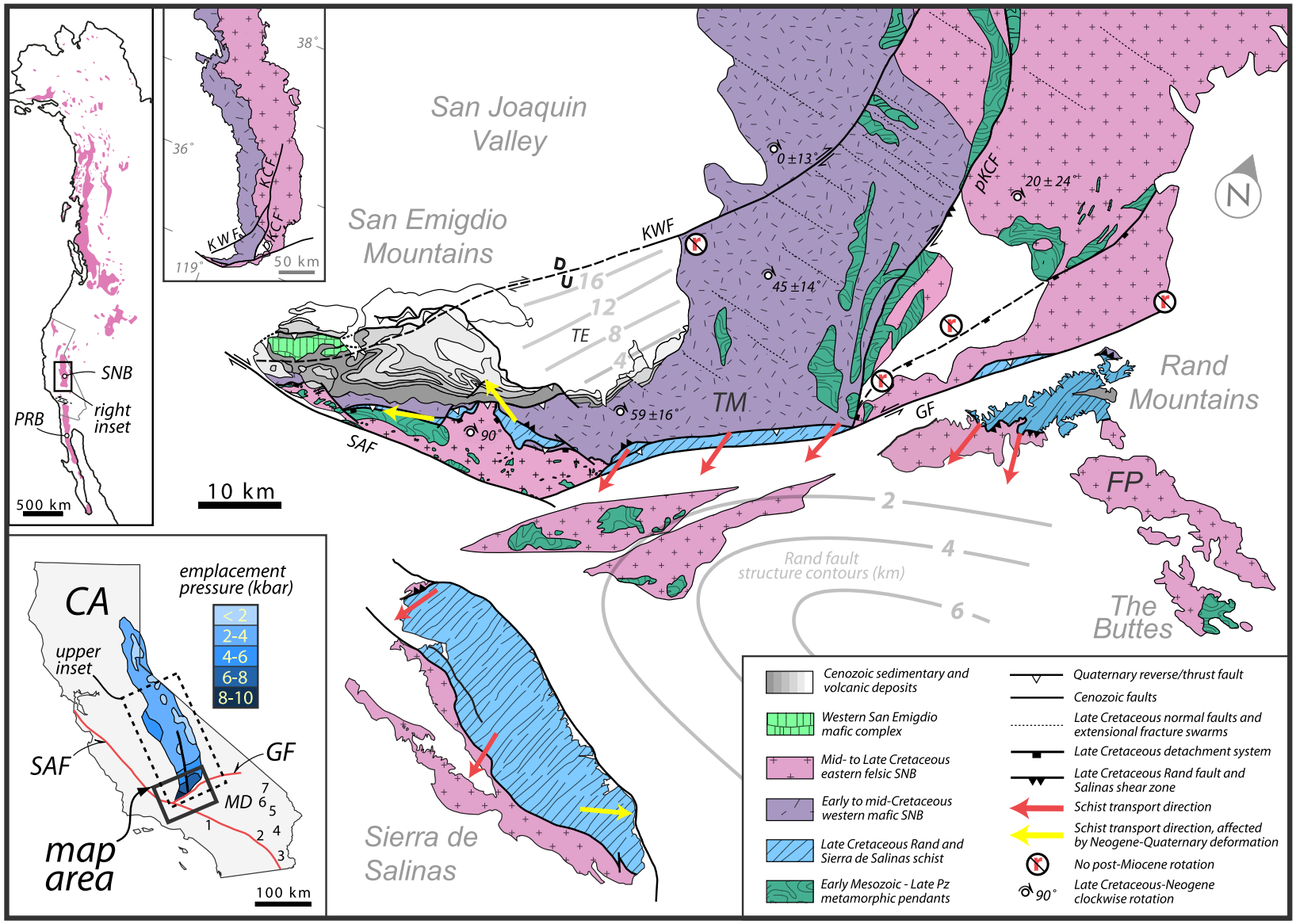
San Joaquin Valley
San Emigdio Mountains
Rand Mountains
Sierra de Salinas
The Buttes
KWF
pKCF
KCF
GF
SAF
TM
TE
FP
D
U
0 ±13°
20 ± 24°
45 ±14°
59 ±16°
90°
16
12
8
4
2
4
6
Rand fault structure contours (km)
N
10 km
38°
36°
119°
50 km
SNB
PRB
right inset
500 km
CA
upper inset
emplacement pressure (kbar)
< 2
2-4
4-6
6-8
8-10
MD
1
2
3
4
5
6
7
map area
100 km
Cenozoic sedimentary and volcanic deposits
Western San Emigdio mafic complex
Mid- to Late Cretaceous eastern felsic SNB
Early to mid-Cretaceous western mafic SNB
Late Cretaceous Rand and Sierra de Salinas schist
Early Mesozoic - Late Pz metamorphic pendants
Quaternary reverse/thrust fault
Cenozoic faults
Late Cretaceous normal faults and extensional fracture swarms
Late Cretaceous detachment system
Late Cretaceous Rand fault and Salinas shear zone
Schist transport direction
Schist transport direction, affected by Neogene-Quaternary deformation
No post-Miocene rotation
90°
Late Cretaceous-Neogene clockwise rotation

significance of this relationship. Dextral slip along the Kern Canyon-White Wolf fault zone (abbreviated as KWF below) increases southward from zero at ~36.7° N to ~40 km near the Tejon embayment. The dip slip component also increases southward to as much as ~15 km near the Tejon embayment. Dextral displacement along the Kern Canyon segment is constrained to ~88-80 Ma, and bracketed to between 98-70 Ma along the White Wolf segment. The KWF acted as a transfer structure between a highly extended and exhumed southeastern block and a significantly less extended and exhumed northwestern block. Northwest-striking extensional fracture swarms are common southeast of, and absent northwest of, the KWF (Figure 2.1).

Following early Cenozoic quiescence the KWF was reactivated as a transfer structure for lower magnitude extension in the early Neogene. In the Quaternary the Kern Canyon segment was again remobilized as a west side up normal fault, while eastern and western segments of the White Wolf fault functioned as a sinistral fault and a north-directed thrust, respectively (Mahéo *et al*., 2009; Saleeby *et al*., 2009; Nadin and Saleeby, 2010).

2.3. Constraints on rotation and tilting

The Sierra Nevada block is a predominantly NNW-trending composite batholith with juvenile batholithic crust extending to ≥ 35 km depth (Ruppert *et al*., 1998; Saleeby *et al*., 2003; 2007). South of 35.5˚ N latitude, the depth of exposure increases markedly while structural and petrologic patterns in the batholith abruptly swing up to 90˚ westward, taking on an east-west trend (Kanter and McWilliams, 1982; McWilliams and Li, 1983; Wood and Saleeby, 1998; Nadin and Saleeby, 2008) (Figure 2.1 insets). This trend continues from the

southernmost SNB into the northwestern Mojave Desert and adjacent Salinia block when restored along the San Andreas fault. A poorly preserved zone of sinistral transcurrent faulting between the San Gabriel Mountains and the Peninsular Ranges (May, 1989) (Figure 2.1 upper left inset) probably represents a "mirror image" of clockwise rotation in the southern SNB. There is no evidence for rotation north of the KWF. Despite concerted efforts to constrain vertical-axis rotation in the southern SNB (e.g., Kanter and McWilliams, 1982; McWilliams and Li, 1985; Plescia *et al*., 1994), the timing of and mechanisms behind the deflection remain poorly understood. Existing explanations for the change in trend include: (1) post-Cretaceous oroclinal bending related to dextral transpression along the North America – Farallon plate margin (Burchfiel and Davis, 1981; McWilliams and Li, 1985); (2) early Miocene transtension in the Mojave Desert (Ross *et al*., 1989; Dokka and Ross, 1995); (3) Late Cretaceous west-directed intra-arc thrusting (May, 1989); and (4) Late Cretaceous coupling between westward displaced underplated Rand and Sierra de Salinas schists and associated upper plate batholithic assemblages (Malin *et al*., 1995; Saleeby, 2003).

In contrast to the rotational history of the southernmost SNB and Salinia, the timing and magnitude of regional northward tilting in the area are well understood (Figure 2.2). Integrated thermochronometric and thermobarometric data from the southwestern SNB track the cooling, ~25˚ northward tilting, and unroofing of deep batholithic rocks from ~9 kbar conditions at ca. 98 Ma to mid-crustal levels (~4 kbar) by ca. 95 Ma (Malin *et al*., 1995; Saleeby *et al*., 2007) (Figure 2.2a). This uplift of the upper plate immediately preceded underplating and cooling of the Rand schist. The cooling path of the Rand schist of the San Emigdio Mountains merges with that of the upper plate beginning at ca. 86 Ma

Figure 2.2. Time-temperature paths for upper plate rocks (solid pattern) and the Sierra de Salinas and Rand schist (dashed pattern) in the Tehachapi and San Emigdio Mountains (a), the Salinian block (b), and the central Mojave metamorphic core complex and Rand Mountains (c). Note that the time-temperature data for the central Mojave metamorphic core complex (upper plate) and the Rand Mountains (lower plate schist) represent a highly oblique section from the upper to the lower plate. Lower plate thermochronologic constraints from Jacobson (1990), Barth *et al*. (2003), and Grove *et al*. (2003). Upper plate thermochronologic constraints from Mattinson (1978), Kistler and Champion (2001), Ducea *et al*. (2003), and Kidder *et al*. (2003) (Salinian block); Henry and Dokka (1992), Fletcher *et al*. (2002), and P. Gans (personal communication, 2010) (central Mojave Desert); and Saleeby *et al*. (1987), Naeser *et al*. (1990), Pickett and Saleeby (1994), and Saleeby *et al*. (2007) (Tehachapi and San Emigdio Mountains). Thermobarometric constraints from: Kidder *et al*. (2003) and Kidder and Ducea (2006) (Salinian block); Henry and Dokka (1992) and Jacobson (1995) (central Mojave Desert); and Pickett and Saleeby (1993) (Tehachapi and San Emigdio Mountains). Mineral abbreviations: Ap, apatite; Bt, biotite; Kfs, K-feldspar; Grt, garnet; Hbl, hornblende; Mnz, monazite; Ms, muscovite; Spn, sphene; Zr, zircon. Other abbreviations: FT, fission track; uncf., unconformity. (d) Summary of kinematic events for the southern SNB, Salinia, and eastern Mojave Desert region. Timing of rotation from Kanter and McWilliams (1982), McWilliams and Li (1983), and Saleeby *et al*. (2007). Schist deposition and cooling age data from Grove *et al*. (2003) and Barth *et al*. (2003). Upper plate tilting/extension from Fletcher *et al*. (2002), Kidder *et al*. (2003), Saleeby *et al*. (2007), and Wells and Hoisch (2008). Intrusion age of asthenospheric magmas from Leventhal *et al*. (1995).

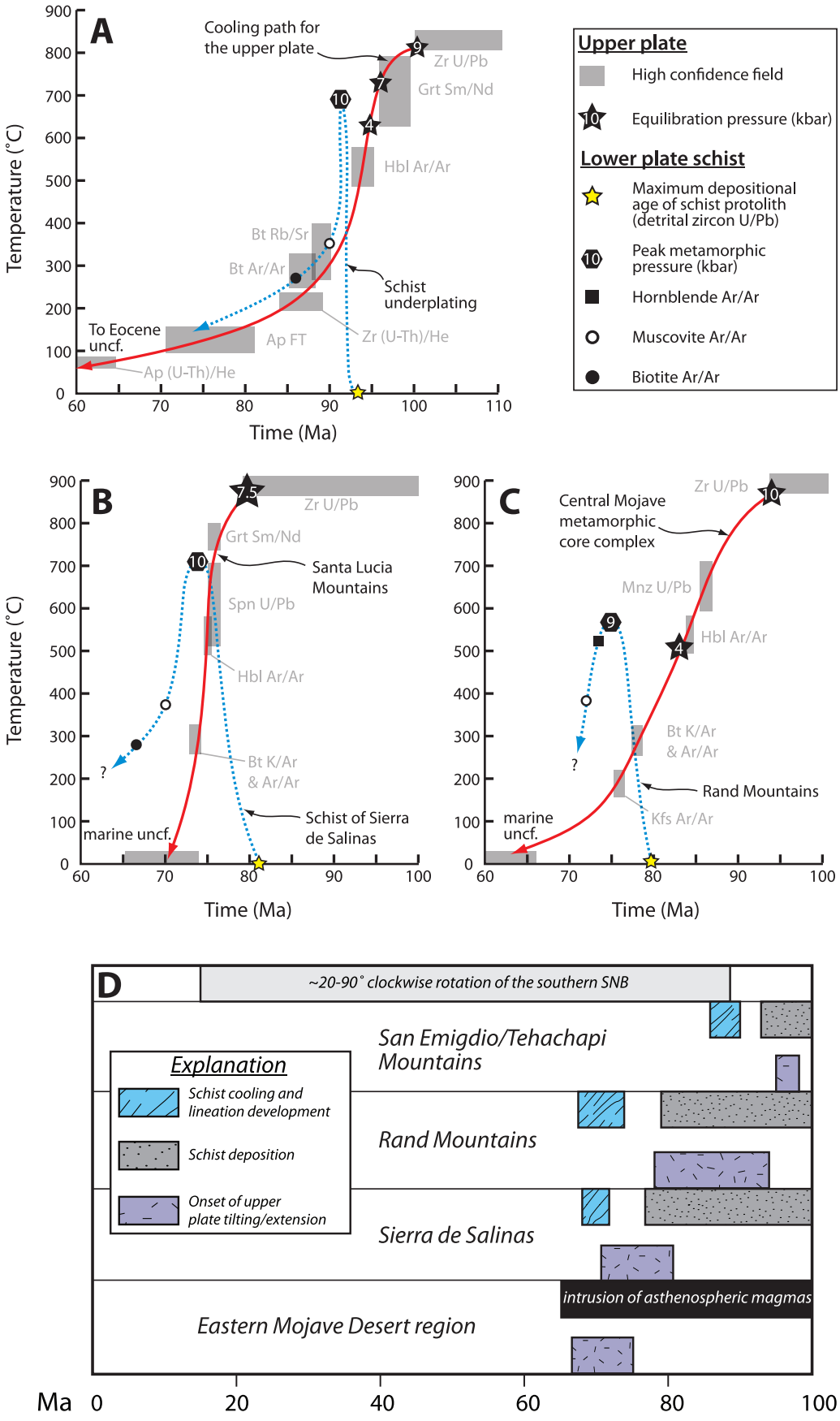
A
Cooling path for the upper plate
Zr U/Pb
Grt Sm/Nd
Hbl Ar/Ar
Bt Rb/Sr
Bt Ar/Ar
Schist underplating
Zr (U-Th)/He
Ap FT
To Eocene uncf.
Ap (U-Th)/He
Temperature (°C)
Time (Ma)
Upper plate
High confidence field
Equilibration pressure (kbar)
Lower plate schist
Maximum depositional age of schist protolith (detrital zircon U/Pb)
Peak metamorphic pressure (kbar)
Hornblende Ar/Ar
Muscovite Ar/Ar
Biotite Ar/Ar
B
Zr U/Pb
Grt Sm/Nd
Santa Lucia Mountains
Spn U/Pb
Hbl Ar/Ar
Bt K/Ar & Ar/Ar
Schist of Sierra de Salinas
marine uncf.
C
Central Mojave metamorphic core complex
Zr U/Pb
Mnz U/Pb
Hbl Ar/Ar
Bt K/Ar & Ar/Ar
Rand Mountains
Kfs Ar/Ar
marine uncf.
D
~20-90° clockwise rotation of the southern SNB
San Emigdio/Tehachapi Mountains
Rand Mountains
Sierra de Salinas
Eastern Mojave Desert region
intrusion of asthenospheric magmas
Explanation
Schist cooling and lineation development
Schist deposition
Onset of upper plate tilting/extension
Ma

(Grove *et al*., 2003). In Salinia, upper plate rocks ascended from ~7.5 kbar to the upper crust between ca. 81-71 Ma, tilting the region ~30˚ to the northeast (Kidder *et al*., 2003) (Figure 2.2b). In the Sierra de Salinas, juxtaposition of lower plate schist with the upper plate also took place in the Late Cretaceous (Barth *et al*., 2003; Kidder and Ducea, 2006). Thermochronologic data from the lower plate schist of the Rand Mountains and adjacent Late Cretaceous plutons in the Fremont Peak region and migmatites in the Buttes indicate a similar relationship between cooling in the upper and lower plates (Fletcher *et al*., 2002; Grove *et al*., 2003) ("Central Mojave metamorphic core complex," Figure 2.2c). One notable feature apparent in Figure 2.2 is that the Salinian block and Rand Mountains vicinity cooled ca. 20 Myr later than the Tehachapi and San Emigdio Mountains.

2.4. Rand fault and Salinas shear zone

In the Rand, Tehachapi, and San Emigdio Mountains, the Rand schist crops out beneath deeply exhumed mafic to intermediate composition SNB assemblages (the "upper plate") along the remains of the Late Cretaceous subduction megathrust flat (the Rand fault) immediately south of the lateral ramp. In Salinia, a correlative structure (the Salinas shear zone) separates middle crustal Cretaceous hornblende-quartz diorites from the underlying Sierra de Salinas schist (Kidder and Ducea, 2006; Ducea *et al*., 2007). The presence of an inverted metamorphic field gradient, i.e., an upward increase in temperature, is a characteristic feature of northern and southern schists (e.g., Ehlig, 1958; Sharry, 1981; Graham and Powell, 1984; Jacobson, 1995; Kidder and Ducea, 2006). In both the southern SNB and Salinia, a narrow (< 10 m) zone of mylonite and cataclasite marks the contact between the schist and upper plate. Shear sense determinations were made within the schist,

at the base of the upper plate, and in intervening mylonites to evaluate the direction of schist transport with respect to the upper plate. The following sections describe the geology and upper plate-lower plate contact relations in the Rand, Tehachapi, Sierra de Salinas, and San Emigdio localities.

3. RESULTS

3.1. Rand Mountains

The Rand fault ("fault I" of Nourse (1989), and the "Rand thrust" of Postlethwaite and Jacobson (1987)) is exposed along the northern and southern margins of the type Rand schist, separating it from upper plate amphibolite grade gneisses in the northeast and the Atolia Quartz Monzonite in the southwest (Figure 2.3). The southern contact between the schist and Atolia Quartz Monzonite is marked by a narrow (< 10 m) zone of mylonite to cataclasite. Mylonitic stretching lineations are generally subhorizontal and oriented oblique to perpendicular to the trace of the Rand fault. Postlethwaite and Jacobson (1987) and Nourse (1989) discern at least two different episodes of shearing in structurally complex noncoaxial fabrics proximal to the Rand fault. Evidence for an early, upper plate to the southwest tectonic event is locally preserved along the shear zone and variably overprinted by top to the northeast structures. Retrograde metamorphic reactions proceeded in concert with mylonitization, suggesting progressive shearing during decreasing temperature.

3.2. Sierra de Salinas

The schist of Sierra de Salinas comprises the largest exposure of the schist. It has been

Figure 2.3. Simplified geologic map of the Rand Mountains. Geology after Dibblee (1967), Vargo (1972), Postlethwaite and Jacobson (1987), and Nourse (1989). Generalized NNE to SSW cross section after Postlethwaite and Jacobson (1987). Rand schist structural data are equal-area lower-hemisphere stereographic projections of the orientation of mineral lineations (Lmin) (contour interval 4σ) and poles to mylonitic foliation (S1) (contour interval 3σ) (Postlethwaite and Jacobson, 1987). Circles show locations of quartz CPO measurements.

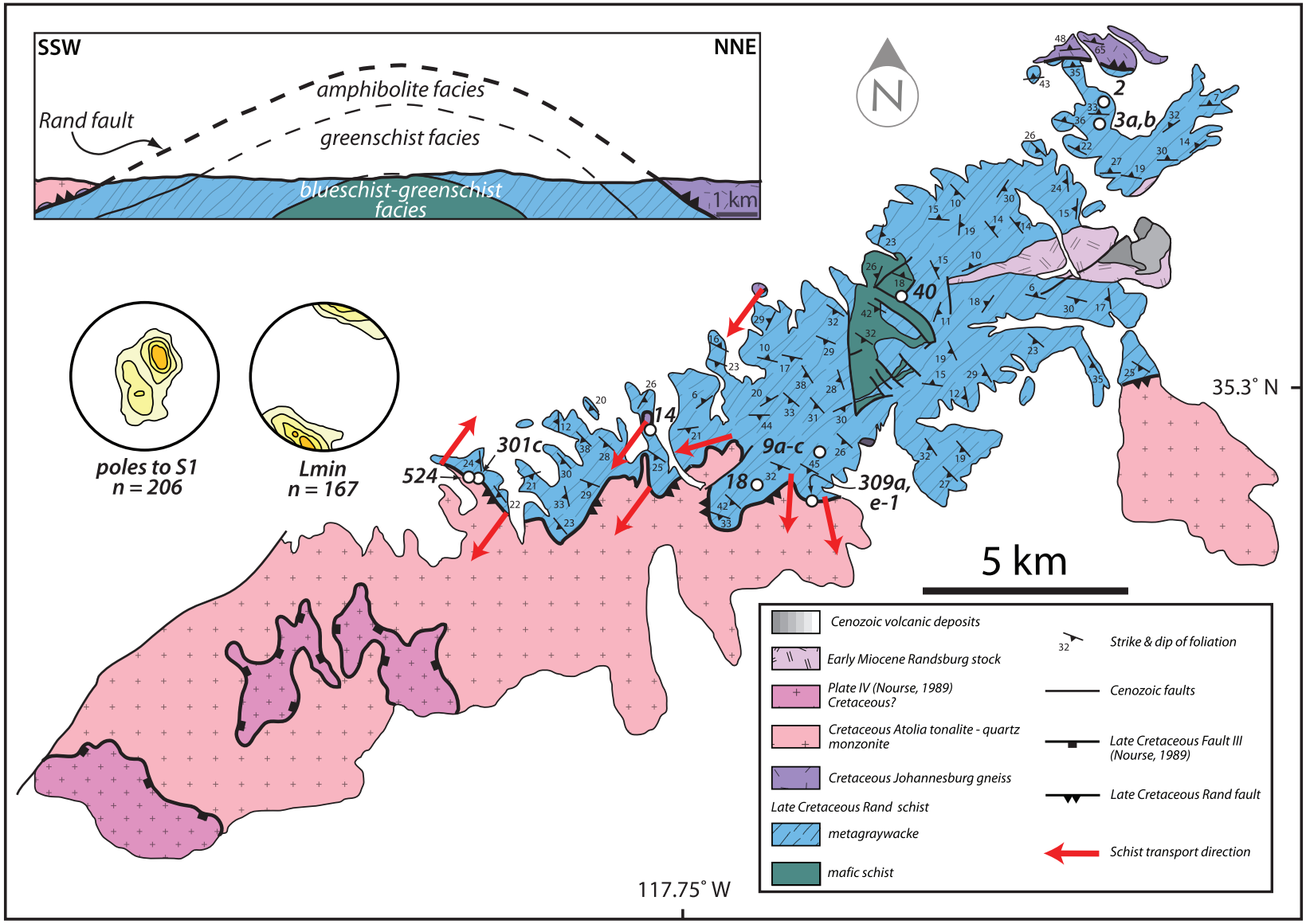
SSW
NNE
amphibolite facies
greenschist facies
Rand fault
blueschist-greenschist facies
1 km
N
poles to S1
n = 206
Lmin
n = 167
524
301c
14
9a-c
18
40
2
3a,b
309a,
e-1
35.3° N
117.75° W
5 km
Cenozoic volcanic deposits
Early Miocene Randsburg stock
Plate IV (Nourse, 1989)
Cretaceous?
Cretaceous Atolia tonalite - quartz monzonite
Cretaceous Johannesburg gneiss
Late Cretaceous Rand schist
metagraywacke
mafic schist
Strike & dip of foliation
Cenozoic faults
Late Cretaceous Fault III
(Nourse, 1989)
Late Cretaceous Rand fault
Schist transport direction

translated ~330 km from a location ~75 km south of the San Emigdio mountains along the San Andreas fault (Powell, 1993) and tilted such that it exposes a ~2.5 km thick structural section of predominantly metasandstone.

Measurements of the strike and dip of foliation and rake of mineral stretching lineations in the schist and upper plate are shown in Figure 2.4. Lineations in the schist dominantly trend northeast - southwest, but show some scatter. The schist is notably less lineated at deeper levels in terms of the abundance of lineated outcrops (Figure 2.4a) and, where present, the strength of lineations. The decrease in lineation abundance may not simply be attributed to a decrease in strain with depth, as highly transposed quartz veins are observed at all structural levels, and may instead signify a change in the shape of the finite strain ellipsoid with depth. Differences in foliation between the central and northern area are interpreted as a late rotation roughly about the lineation direction. A single shear sense determination made in the southern area is considered dubious due to recent faulting.

Outcrop scale shear sense indicators are rare in the Sierra de Salinas, but were found in thin sections of both the schist and upper plate. The most common shear sense indicators are biotite fish, although feldspar, sphene, clinopyroxene, hornblende, and muscovite fish are also present. Mineral fish are considered here to be any isolated grains of reduced size showing morphologic similarity to the fish described by Lister and Snoke (1984), Pennacchioni *et al*. (2001) or ten Grotenhius *et al*. (2003). In most cases, fish are included in or between fairly equant or amoeboid quartz grains in foliation-parallel quartz bands (e.g., Figures 2.5a and 2.5b). Mineral fish develop during mylonitic deformation (Lister and Snoke, 1984), thus substantial annealing grain growth or high temperature grain boundary migration recrystallization occurred in quartz in nearly all observed samples following an

Figure 2.4. (a) Geologic map of the Sierra de Salinas based on Ross (1976), Dibblee (1974), Kidder and Ducea (2006) and this study. All plotted attitudes were made by the authors. (b) schematic cross section across the Sierra de Salinas. (c) Equal-area lower-hemisphere stereonets from northern, central and southern portions of the map area showing foliation (S1) and lineation (Lmin) measurements. Upper plate lineation shown as filled dots, schist lineations as unfilled dots.

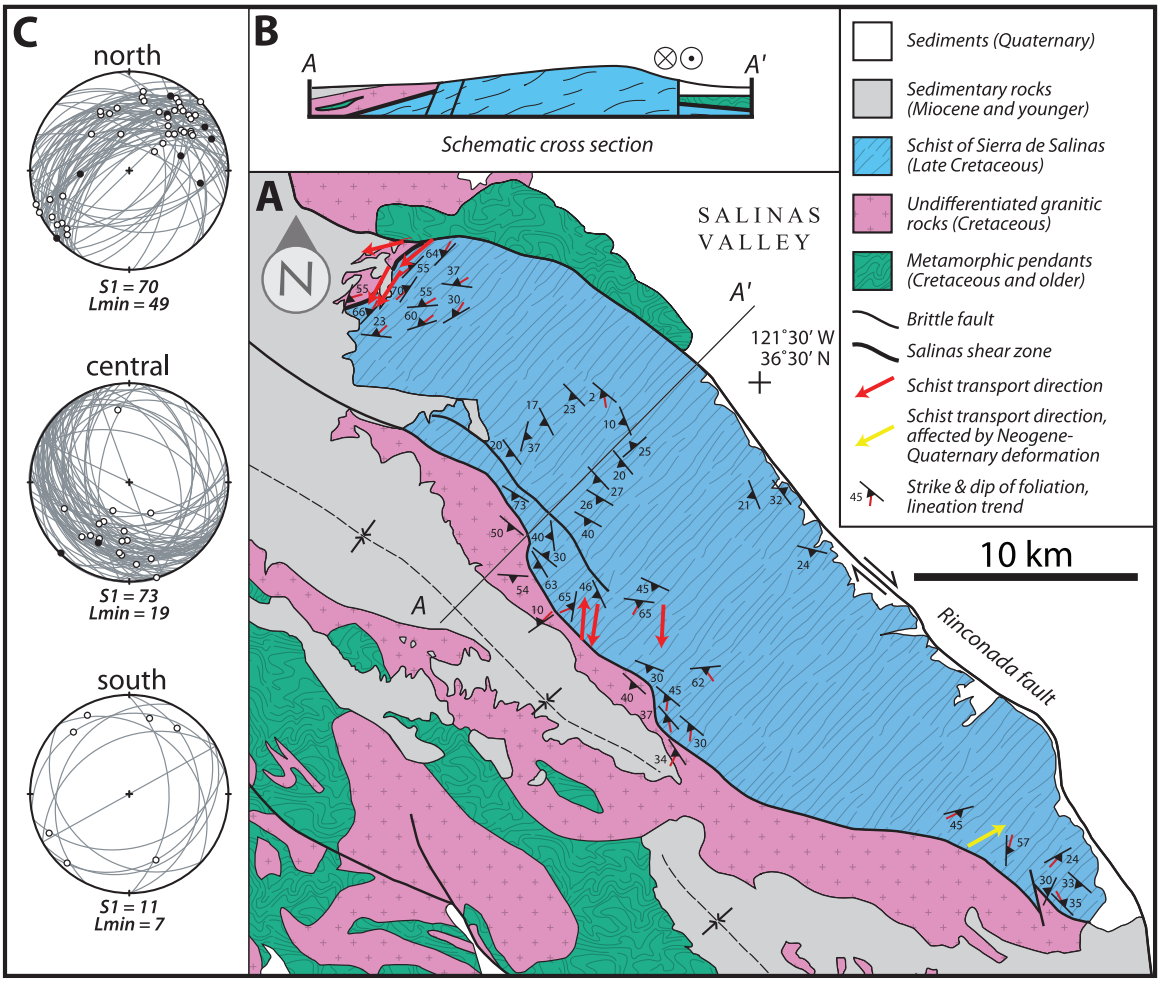
C
north
S1 = 70
Lmin = 49
central
S1 = 73
Lmin = 19
south
S1 = 11
Lmin = 7
B
A
A′
Schematic cross section
A
N
SALINAS
VALLEY
A′
121°30′ W
36°30′ N
A
Rinconada fault
10 km
Sediments (Quaternary)
Sedimentary rocks (Miocene and younger)
Schist of Sierra de Salinas (Late Cretaceous)
Undifferentiated granitic rocks (Cretaceous)
Metamorphic pendants (Cretaceous and older)
Brittle fault
Salinas shear zone
Schist transport direction
Schist transport direction, affected by Neogene-Quaternary deformation
Strike & dip of foliation, lineation trend

Figure 2.5. Photographs of microstructural features in the Sierra de Salinas (a-d) and the Rand schist of the San Emigdio Mountains (e-h). Photographs are upright and lineation azimuth is inscribed in each figure. (a) Typical biotite fish in a quartz band in the schist; xpl. (b) Two biotite fish in a quartz band and a plagioclase grain showing undulose extinction in the schist; xpl. (c) Quartz ribbons in a late upper plate mylonite showing sphene fish (outlined) and inclined recrystallized quartz grains (TTN); xpl. (d) Shear band from top left to lower right in the schist. Quartz and partially chloritized biotite grains are deflected into the shear band (TTN); ppl. (e) Top to the east (TTE) S-C fabrics and garnet porphyroblasts surrounded by asymmetric pressure shadows of quartz; ppl. (f) Plagioclase sigma porphyroclast and S-C fabrics (TTE); ppl. (g) Sample 06SE66. Elongate quartz grains with sweeping undulatory extinction and recrystallization by subgrain rotation. Note S-C fabrics and biotite fish (TTE); xpl. (h) Sample 08SE473. Quartz with sutured grain boundaries and recrystallization by subgrain rotation and grain boundary migration; xpl. Mineral Abbreviations: Bt, biotite; Grt, garnet; Plag, plagioclase; Qtz, quartz; Spn, sphene. Other abbreviations: ppl, plane-polarized light; xpl, cross-polarized light.

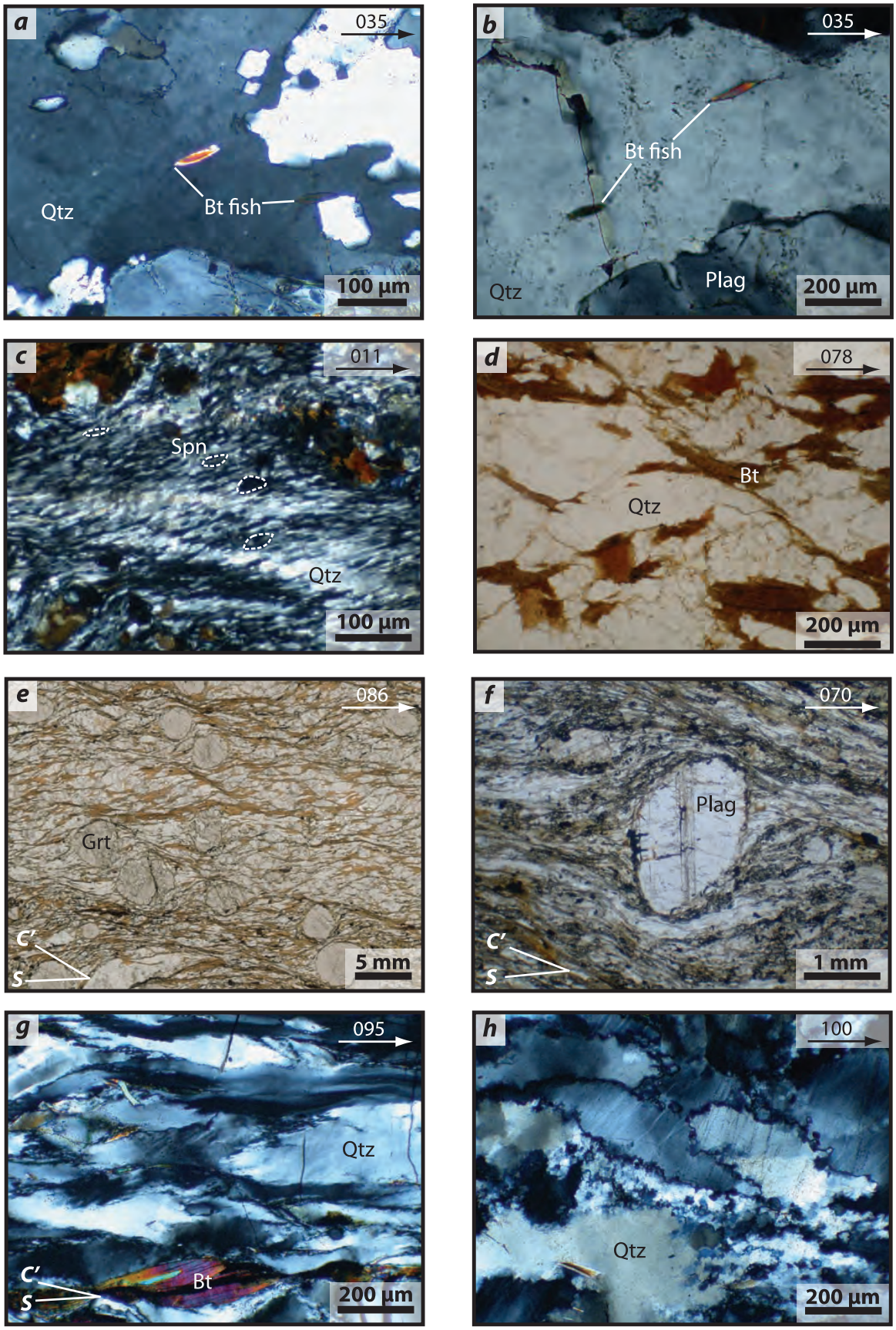
a
035
Qtz
Bt fish
100 µm
b
035
Bt fish
Qtz
Plag
200 µm
c
011
Spn
Qtz
100 µm
d
078
Bt
Qtz
200 µm
e
086
Grt
C′
S
5 mm
f
070
Plag
C′
S
1 mm
g
095
Qtz
C′
S
Bt
200 µm
h
100
Qtz
200 µm

early phase of mylonitization. Only fish inclined in the same direction to both the overall foliation and local boundaries of quartz bands were used as shear sense indicators (e.g., Figure 2.5b). Near the schist-upper plate contact, highly deformed fine-grained asymmetric quartz (Figure 2.5c) and C' shear bands (Passchier and Trouw, 2005) associated with retrograde chlorite (Figure 2.5d) are also observed. Shear sense indicators were tallied without knowledge of sample orientation during petrographic analysis to avoid bias. Ten of 44 samples contain a sufficiently large population and uneven distribution of top to the northeast (TTN) and top to the southwest (TTS) shear sense indicators such that there is high probability of noncoaxial flow (Figure 2.6). "High probability" indicates a greater than 95% likelihood that a given distribution was not sampled from an evenly distributed population.

Shear sense in greenschist facies (i.e., late) mylonites near the schist-upper plate contact are unambiguously TTN (Figures 2.5 and 2.6). Late shear sense indicators are far less abundant than amphibolite facies (i.e., early) fabrics at deep structural levels in the schist. Away from the shear zone in the schist, TTS shear indicators are slightly more abundant than TTN features (130 vs. 116). Two samples of the schist show a TTS shear sense and two are TTN.

3.3. San Emigdio Mountains

Uplift of basement and sedimentary cover strata in the San Emigdio Mountains is controlled by Pliocene-Quaternary north-south compression between the big bend in the San Andreas fault and the Pleito fault zone (Davis, 1983; Dibblee, 1986) (Figures 2.1 and 2.7). Cretaceous plutonic and associated framework metamorphic rocks comprise the bulk of the

Figure 2.6. Graphical representation of shear sense indicators in the Sierra de Salinas. Top to the northeast (TTN) and top to the southwest (TTS) indicators are tallied versus structural depth. Each point (n=402) represents a single indicator. Filled symbols represent indicators associated with retrograde metamorphism or overprinting relationships, mainly C' shear bands or asymmetric quartz (49 TTN, 5 TTS). Open symbols represent shear sense indicators associated with early deformation. Arrows indicate the position of individual samples showing a consistent sense of shear and the associated direction of upper plate motion.

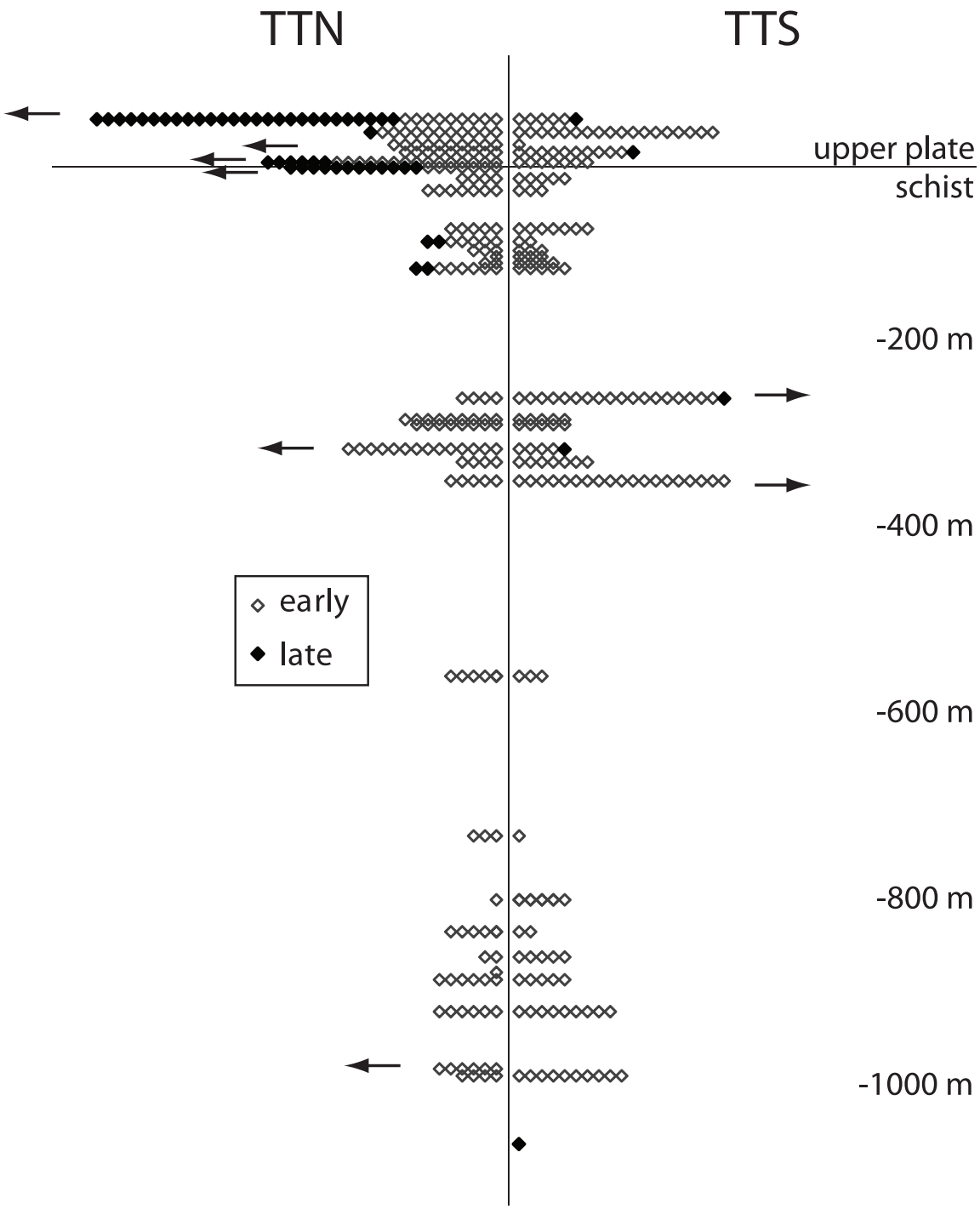
TTN
TTS
upper plate
schist
-200 m
-400 m
-600 m
-800 m
-1000 m
early
late

Figure 2.7. Simplified geologic map of the San Emigdio Mountains. Geology from Ross (1989), Dibblee (1973), and this study. Equal-area lower-hemisphere stereographic projections (Kamb contours at 2σ, 4σ, 6σ, 10σ, 14σ, and 20σ) of the orientation of mineral lineations (Lmin) and poles to mylonitic foliation (S1) are shown along western, central, and eastern domains of the Rand fault. Circles show locations of EBSD measurements. Abbreviations as in Figure 2.1.

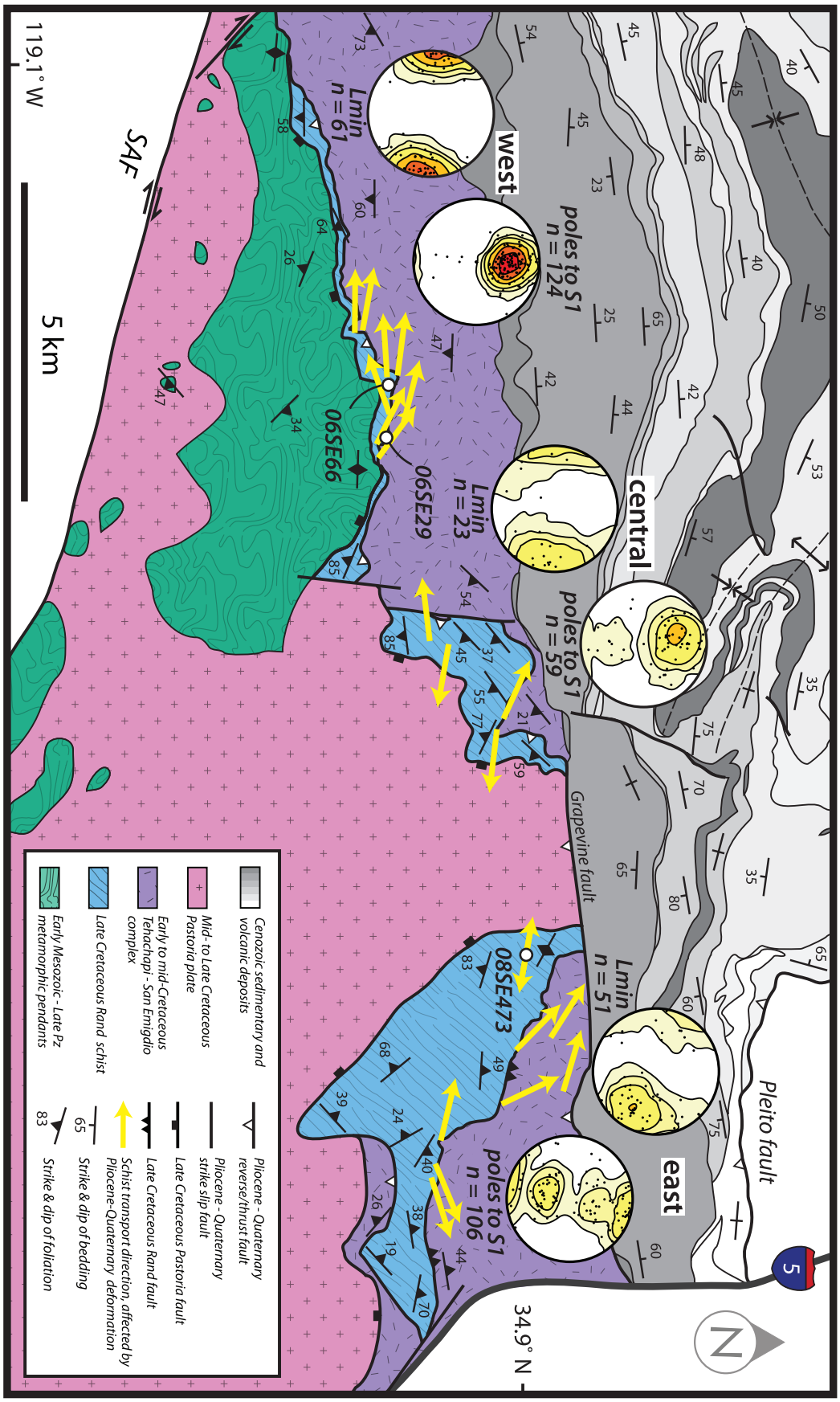
Pleito fault
Grapevine fault
SAF
5 km
119.1° W
34.9° N
N
5
west
central
east
poles to S1
n = 124
poles to S1
n = 59
poles to S1
n = 106
Lmin
n = 61
Lmin
n = 23
Lmin
n = 51
06SE66
06SE29
08SE473
Cenozoic sedimentary and volcanic deposits
Mid- to Late Cretaceous Pastoria plate
Early to mid-Cretaceous Tehachapi - San Emigdio complex
Late Cretaceous Rand schist
Early Mesozoic - Late Pz metamorphic pendants
Pliocene - Quaternary reverse/thrust fault
Pliocene - Quaternary strike slip fault
Late Cretaceous Pastoria fault
Late Cretaceous Rand fault
Schist transport direction, affected by Pliocene-Quaternary deformation
Strike & dip of bedding
Strike & dip of foliation

basement complex in the San Emigdio Mountains (Ross, 1989). This basement complex is subdivided into four principal assemblages. First is a collection of shallow-level (3-4 kbar) eastern SNB affinity granitoids and metamorphic pendant rocks referred to as the Pastoria plate (modified after Crowell, 1952). The Pastoria fault, a member of the Late Cretaceous-Paleocene southern Sierra detachment system of Wood and Saleeby (1998) reactivated in Pliocene-Quaternary time as a south-dipping thrust, lies at the base of the Pastoria plate. Beneath the Pastoria fault lies the western continuation of Early to mid-Cretaceous deep-level SNB rocks defined in the Tehachapi Mountains as the Tehachapi complex (Saleeby *et al*., 2007). Continuity of the Tehachapi complex into the San Emigdio Range leads us to rename the entire deep batholithic complex as the Tehachapi-San Emigdio complex. A third basement assemblage consisting of shallow level (< 3 kbar) western Sierra Nevada Foothills belt rocks (James *et al*., 1993; Reitz, 1986) crops out in the westernmost San Emigdio Mountains, and is named here the western San Emigdio mafic complex.

The Tehachapi-San Emigdio complex sits tectonically above the Rand schist along the polyphase Rand fault. The Rand schist is juxtaposed against the Tehachapi-San Emigdio complex along the remains of a locally ductile to brittle low-angle detachment fault system that likely correlates with the type Rand fault (Postlethwaite and Jacobson, 1987; Nourse, 1989). This fault is largely remobilized as a south-dipping thrust fault with the Rand schist in the hanging wall and the Tehachapi-San Emigdio complex in the footwall.

The Pastoria plate overlies the contact between the Tehachapi-San Emigdio complex and the Rand schist in two locations in the San Emigdio Mountains, partitioning the schist into western, central, and eastern domains. In each domain, both the schist and the Tehachapi-San Emigdio complex contain gently plunging, E-W trending stretching

lineations and fold hinges that are most penetrative within ~100 m of the Rand fault. Compositional layering in the schist is generally parallel to that of the Tehachapi-San Emigdio complex and dips ~45˚ to the south.

In each domain, lineations are recorded first in amphibolite facies assemblages, and are overprinted by parallel greenschist facies fabrics and subsequent brittle deformation. We interpret these overprinting relationships to represent progressive shearing during exhumation of the schist and upper plate through the ductile-brittle transition. In 19 of 25 locations where shear-sense determinations were possible (Table 2.1), microstructures are indicative of schist transport to the west (top to the east) (Figure 2.7). Evidence for west-directed transport of the schist is best expressed in type II S-C mylonites (Lister and Snoke, 1984), asymmetric garnet and plagioclase porphyroclasts, and mica fish (e.g., Figures 2.5e, 2.5f, and 2.5g). The extensional fabric is fairly homogeneous within the lower ~500 m of the upper plate, the upper ~10 m of the Rand schist, and intervening Rand fault mylonites; however, with increased structural depth in the schist (> 10 m from the Rand fault), lineations are less penetrative, shear sense indicators commonly conflict at the outcrop scale, quartz veins are more symmetrically transposed parallel to the foliation, and boudinaged quartz + plagioclase layers within less competent metasandstone are more symmetric, indicating dominantly coaxial flattening within the schist > 10 m from the Rand fault. Both coaxial and noncoaxial fabrics are associated with retrograde paragenesis, indicating roughly coeval development of fabrics near the contact (noncoaxial) and > 10 m from the contact (coaxial).

Table 2.1. Sample information and shear sense determinations from the San Emigdio Mountains.

Field location	Lithology	UTM easting†	UTM northing†	Distance to Rand fault (m)#	Shear sense	Schist transport azimuth	Criteria§
08SE194	Rand fault mylonite	231760	3864257	667	top E	286	AP
08SE156	Rand fault mylonite	321144	3864254	530	top E	302	AP
08SE198	sheared upper plate paragneiss	321810	3863870	376	top SE	334	AP
08SE172	Rand fault mylonite	321547	3863586	88	top E	314	AP
06SE24	Rand fault ultramylonite	310535	3862054	65	top E	287	SC'
06SE25	sheared upper plate diorite	310551	3862034	46	top E	288	AP
06SE77	Rand fault mylonite	311141	3861938	40	top E	284	AP, SC'
06SE16	sheared upper plate paragneiss	310569	3861996	17	top E	266	AP, SC'
06SE63	Rand fault mylonite	310684	3861986	8	top E	266	SC'
06SE31	Rand fault mylonite	311250	3861882	0	top E	250	AP, SC'
07SE112	Rand fault mylonite	315081	3863988	0	top E	294	AP, SC'
07SE114	Rand fault mylonite	315144	3863864	0	top E	283	SC'
07SE135	sheared upper plate paragneiss	315748	3863559	0	top W	97	AP, SC'
08SE270	sheared upper plate diorite	309137	3861143	0	top E	275	AP
08SE303	Rand fault mylonite	309822	3861321	0	top E	280	SC', AP
08SE347	Rand fault mylonite	309987	3861486	0	top E	270	SC'
08SE236	Rand schist quartzite	322478	3862567	0	top W	67	SC'
08SE340	Rand schist metagraywacke	309912	3861283	0	coaxial	N/A	2SB
08SE631	Rand schist metagraywacke	311720	3861700	-3	top E	306	SC'
08SE241	Rand schist deformed quartz vein	322715	3862533	-14	top W	72	SC'
08SE651	Rand schist metagraywacke	311542	3861851	-21	top E	296	SC'
06SE29	Rand schist quartzite	311187	3861844	-31	top E	315	QF, MF, SC'
08SE210	Rand schist quartzite	322130	3862568	-31	top E	283	SC'
06SE66	Rand schist quartzite mylonite	310749	3861869	-37	top E	275	QF, SC', MF
06SE37	Rand schist quartzite	314535	3862739	-247	top W	100	SC', AP
06SE35	Rand schist metagraywacke	314607	3862477	-283	top E	263	SC', AP
08SE473	Rand schist quartzite mylonite	319423	3862435	-623	coaxial	N/A	QF, 2SB

† UTM coordinates are WGS datum, zone 11N
# Distance to Rand fault: positive and negative values indicate position above and below the Rand fault, respectively.
§ Shear sense criteria: AP, asymmetric porphyroclasts; SC, S-C fabric; 2SB, 2 sets of shear bands; MF, mica fish; QF, quartz fabrics (CPO).

3.4. Tehachapi Mountains

Tehachapi Range basement rocks south of the Garlock fault consist of relatively shallow-level (< 3.5 kbar) eastern SNB assemblages that resemble the Pastoria plate. North of the Garlock fault, basement rocks of the Tehachapi Mountains consist primarily of deep-level (8-11 kbar) SNB tonalites, diorites and gabbros that extend to the north in overall structural continuity with shallower level rocks of the southern SNB autochthon (Pickett and Saleeby, 1993; Saleeby *et al*., 2003; 2007). The deep-level SNB rocks of this region constitute a relatively thin tectonic layer above the Rand schist, thickening to the north above the lateral ramp in the Rand fault (Malin *et al*., 1995; Yan *et al*., 2005) (Figure 2.8). The Rand schist of this area crops out primarily as an ENE-WSW-striking fault-bounded sliver that has emerged through overlying plates to exposure levels by oblique sinistral motion along the main branch of the Garlock fault and north-directed reverse motion along the north branch of the Garlock fault. A small half window through the Rand fault is preserved near the western end of the Garlock fault. The basal domain of the Tehachapi-San Emigdio complex in the Tehachapi range is comprised mainly of the White Oak diorite gneiss, a tectonic mixture of amphibolite to locally retrograde greenschist facies dioritic and subordinate tonalitic, gabbroic, and mylonitic gneisses and cataclasites.

Structural and thermochronometric data suggest that the White Oak diorite gneiss constitutes the structural base of the Tehachapi-San Emigdio complex throughout much of the Tehachapi range (Saleeby *et al*., 2007). The dominant structural fabric of the White Oak unit is that of strong attenuation along moderately north dipping anastomosing ductile to brittle shear bands (Figure 2.9). In most locations the shear bands assume a conjugate form suggesting a strong coaxial component of shear strain. In a critical area (~20 x 30 m) in the

Figure 2.8. Simplified geologic map of the Tehachapi Mountains. Geology after Sharry (1981), Saleeby *et al*. (1987; 2007), Ross (1989), Wood (1997), and this study. Generalized NNW-SSE cross section after Malin *et al*. (1995). Schist foliation data are presented as an equal-area lower-hemisphere stereographic projection of the orientation of poles to mylonitic foliation (S1) (Kamb contours at 2σ, 4σ, 6σ, 10σ, and 14σ) (Sharry, 1981). All shear sense determinations from White Oak diorite gneiss. Abbreviations as in Figure 2.1.

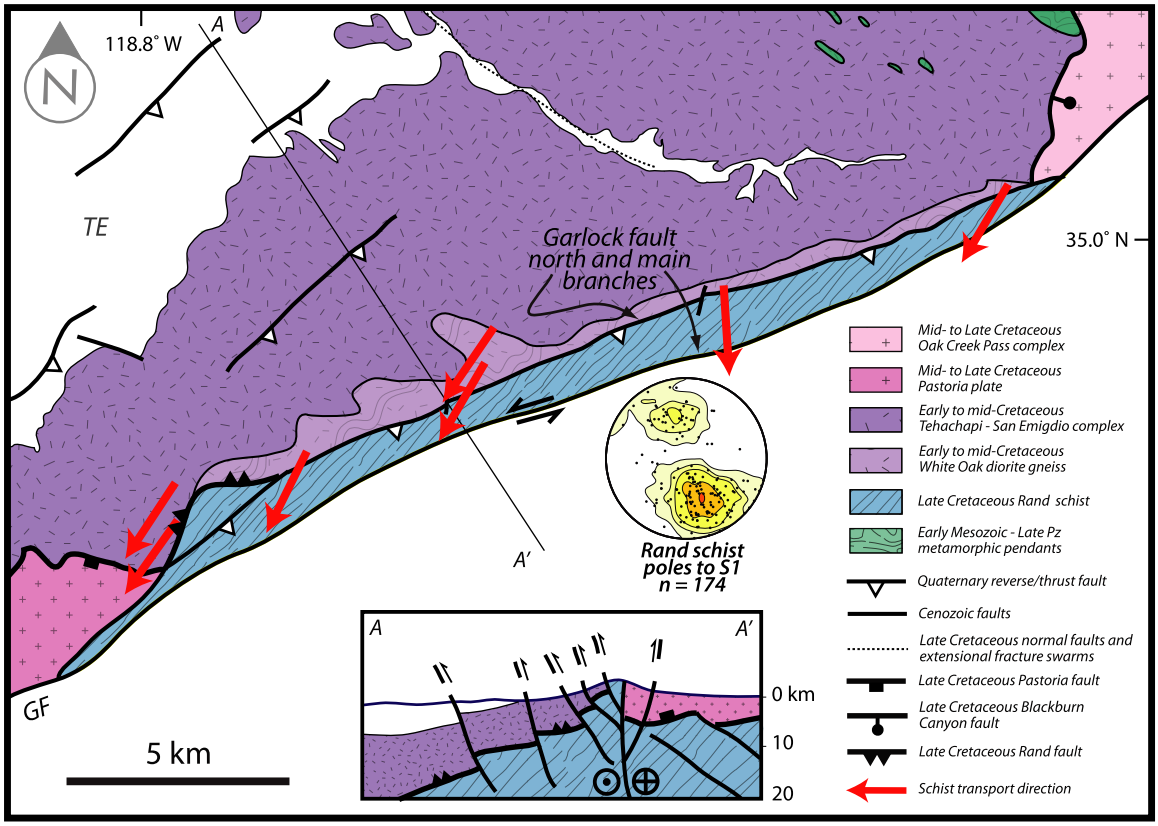
118.8° W
A
N
TE
Garlock fault
north and main
branches
35.0° N
A′
Rand schist
poles to S1
n = 174
GF
5 km
A
A′
0 km
10
20
Mid- to Late Cretaceous
Oak Creek Pass complex
Mid- to Late Cretaceous
Pastoria plate
Early to mid-Cretaceous
Tehachapi - San Emigdio complex
Early to mid-Cretaceous
White Oak diorite gneiss
Late Cretaceous Rand schist
Early Mesozoic - Late Pz
metamorphic pendants
Quaternary reverse/thrust fault
Cenozoic faults
Late Cretaceous normal faults and
extensional fracture swarms
Late Cretaceous Pastoria fault
Late Cretaceous Blackburn
Canyon fault
Late Cretaceous Rand fault
Schist transport direction

Figure 2.9. Photograph of highly attenuated White Oak diorite gneiss in the Tehachapi Mountains. Note anastomosing ductile to brittle shear bands between boudinaged dikes. Field of view 20 m long. Abbreviations: ag, amphibolite gneiss; br, breccia; myl, mylonite; tg, tonalite gneiss.

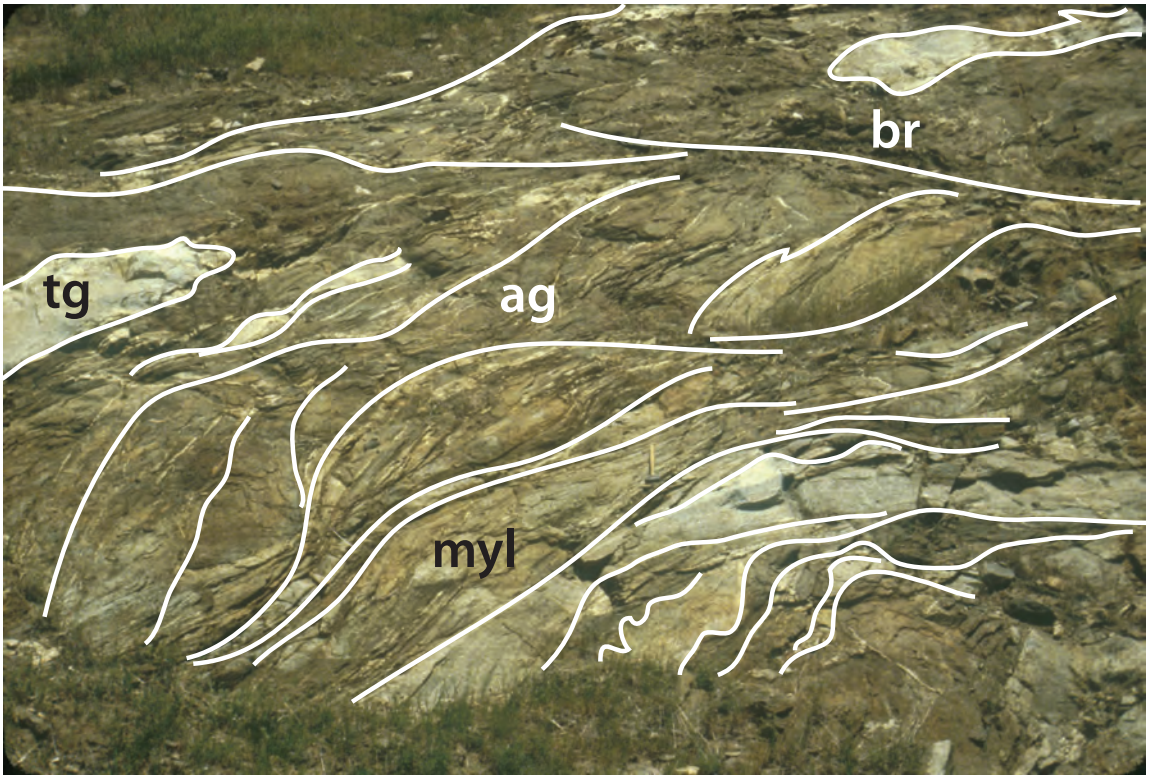
br
tg
ag
myl

proximal hanging wall of the schist half window, a top to the northeast shear sense is apparent in asymmetric leucotonalite boudins and associated lineation patterns. This shear sense is consistent with that of S-C fabrics, mica fish, asymmetric hornblende porphyroclasts, and asymmetric boudins in White Oak unit mylonites east of the half window (Wood, 1997) (Figure 2.8).

3.5. Deformation temperature, strain, and flow vorticity analysis using quartz fabrics

For the case of homogeneous flow, the relative proportions of pure shear and simple shear can be derived by means of the kinematic vorticity number W_k. For steady state deformation, i.e., no spatial gradients in velocity, $W_k = \cos \theta$, where θ is the minimum angle between the two directions of zero angular velocity (the flow apophyses) (Hanmer and Passchier, 1991; Wallis, 1992; 1995). In cases of non-steady state flow, the finite deformation is more appropriately characterized by the space and time integrated mean vorticity number W_m (Passchier, 1988). The likelihood of non-steady state flow during progressive deformation is problematic for flow vorticity analysis; specifically, for a given analytical procedure, uncertainties exist as to whether the technique records time-integrated flow or the last few increments of deformation. However, recent vorticity studies indicate that differences in W_m from sample to sample can be detected with the use of the quartz c-axis fabric and strain ratio method (abbreviated here as the R_{xz}/β - method) (Wallis, 1992; 1995; Grasemann *et al*., 1999; Law *et al*., 2004; Xypolias, 2009). In our vorticity analysis of the Rand schist, we apply this method to estimate the relative contributions of pure shear and simple shear at different structural levels.

The R_{xz}/β - method assumes steady-state monoclinic flow symmetry and that the angle between the foliation (flattening plane of finite strain) and the normal to the central segment of the c-axis girdle (shear plane), β, is dependent on finite strain and flow vorticity. Therefore, if β and the strain ratio in the XZ plane of finite strain (R_{xz}) are known, W_m can be calculated by the following equation:

$$W_m = \sin\left[\tan^{-1}\left\{\frac{\sin 2\beta}{\frac{(R_{xz}+1)}{(R_{xz}-1)} - \cos 2\beta}\right\}\right] \times \frac{(R_{xz}+1)}{(R_{xz}-1)} \quad (1)$$

(Wallis, 1992; 1995). To estimate R_{xz}, we used the R_f/ϕ method (Ramsay, 1967; Dunnet and Siddans, 1971; Lisle, 1985) by approximating detrital quartz grain shapes as ellipses and measuring the axial ratio (R_f) and orientation of the long axis with respect to the foliation (ϕ). Care was taken to avoid grains that were recrystallized, although it is possible that some small new grains were mistaken for larger original detrital grains. This is especially true for sample 06SE66, which has likely been significantly recrystallized and we interpret the calculated R_{xz} value of 8.2 as a lower bound. In contrast, quartz grains in sample 08SE473 are commonly pinned by mica, inhibiting the migration of quartz grain boundaries. R_{xz} values were calculated using the Excel spreadsheet of Chew (2003). Mean vorticity number values, R_f/ϕ method-derived strain ratios in the XZ plane of the finite strain ellipsoid, and measured angles between poles to foliation and the central segment of the c-axis girdle are

reported in Table 2.2. The range of W_m values reported for sample 08SE473 results from uncertainty in the measurement of β.

We measured quartz CPO from three oriented mylonitic quartzites collected from the San Emigdio schist locality by means of manual Electron Backscatter Diffraction (EBSD) analyses (Figure 2.10). The locations of these samples are indicated on Figure 2.7. Samples 06SE66 and 06SE29 show strong fabrics with c-axes populating type I girdles (Lister, 1977; Schmid and Casey, 1986). The girdles are asymmetric in a top to the east sense and are oriented perpendicular to macroscopic shear bands with <a> directions aligned with the inferred shear direction. This implies crystallographic slip along the basal plane in the <a> direction, a characteristic of noncoaxial greenschist facies deformation (Schmid and Casey, 1986). Samples 06SE66 and 06SE29 contain elongate quartz ribbons that exhibit sweeping undulose extinction with recrystallized subgrain mantles (Figure 2.5g). These features are indicative of regime 2 (i.e., roughly greenschist facies conditions) quartz recrystallization (Hirth and Tullis, 1992).

Upper greenschist to amphibolite facies mylonites commonly show quartz c-axis maxima oriented parallel with the foliation and normal to the lineation (i.e., the Y-direction of the finite strain ellipsoid) (Schmid and Casey, 1986). Quartz CPO from sample 08SE473 is transitional between girdle-type and Y-maximum-type c-axis fabrics, suggesting slightly higher deformation temperatures than 06SE66 (Figure 2.10). Conjugate sets of mica rich shear bands are locally developed, indicating a significant component of coaxial deformation. As in 06SE66, the <a> direction is aligned with the inferred shear direction; however, in addition to slip on the basal plane, slip is also accommodated on first order

Figure 2.10. EBSD results showing quartz crystallographic preferred orientations. Pole figures are equal-area lower-hemisphere stereographic projections (contours at 1, 2, 3, 4 times mean uniform distribution with maximum density shown under each figure) of c-axes (0001) and second order prisms $[11\bar{2}0]$; foliation shown by horizontal line, down-plunge lineation trend shown by white circle, average shear band orientation indicated by dashed line, skeletal outlines showing β of c-axis fabric are overlain, and c-axis fabric opening angles (OA) are shown for each sample. Inverse pole figures are for the inferred shear plane normal and the inferred direction of shear; c: basal plane, m: prism planes, a: second order prism planes, r and z: positive and negative rhomb planes. Sample locations shown in Figure 2.7.

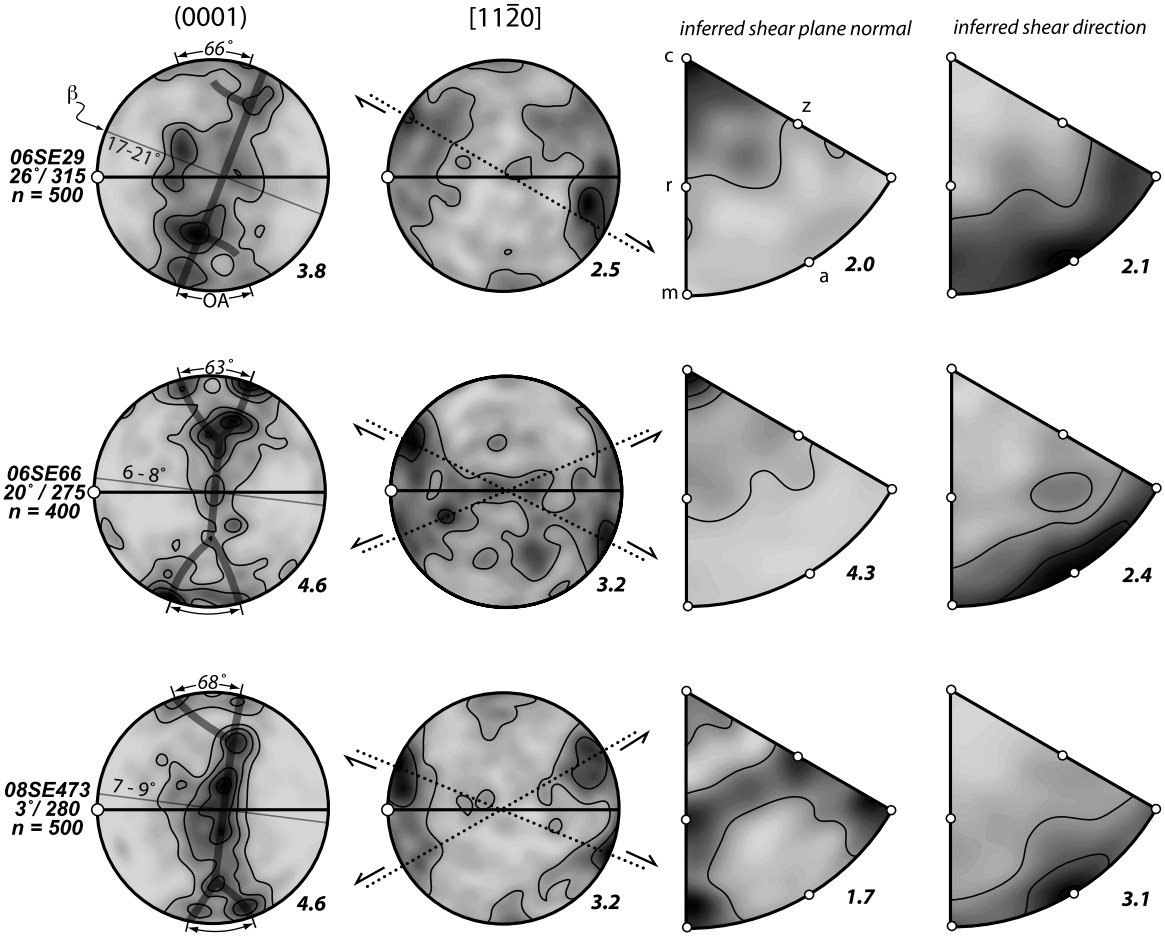
(0001)
[11$\bar{2}$0]
inferred shear plane normal
inferred shear direction
66°
β
17-21°
06SE29
26°/ 315
n = 500
OA
3.8
2.5
c
z
r
a
m
2.0
2.1
63°
06SE66
20° / 275
n = 400
6 - 8°
4.6
3.2
4.3
2.4
68°
08SE473
3°/ 280
n = 500
7 - 9°
4.6
3.2
1.7
3.1

Table 2.2. Summary of quartz fabric, strain, and vorticity data from the San Emigdio and Rand Mountains.

Sample	Locality†	Distance from Rand fault (m)	Quartz c-axis opening angle	Deformation temperature (˚C)	Quartz c-axis β angle	XZ Strain ratio R_s	Wm#
06SE29	SE	31	66˚	520 ± 50	17 - 21˚	> 5	A
06SE66	SE	37	63˚	500 ± 50	6 - 8˚	8.2	0.73 - 0.84
08SE473	SE	623	68˚	540 ± 50	7 - 9˚	3.2	0.48 - 0.59
309A	R	<100	65˚	515 ± 50	15 - 22˚	> 5	A
309E-1	R	<100	67˚	535 ± 50	9 - 11˚	> 5	A
301C	R	<100	65˚	515 ± 50	11 - 12˚	> 5	A
524	R	<100	61˚	480 ± 50	4 - 7˚	> 5	B
18	R	<100	-	-	13 - 19˚	> 5	A
14	R	<100	-	-	14 - 19˚	> 5	A
2	R	~500-700	73˚	590 ± 50	7 - 9˚	> 5	B
9a	R	~750-1000	67˚	535 ± 50	2 - 4˚	> 5	B
9b	R	~750-1000	60˚	470 ± 50	3 - 7˚	> 5	B
9c	R	~750-1000	63˚	500 ± 50	0 - 1˚	> 5	C
3b	R	~800-1000	-	-	0 - 1˚	> 5	C
40	R	~2500-4000	70˚	550 ± 50	7 - 10˚	> 5	B

† SE, San Emigdio Mountains; R, Rand Mountains
# Deformation settings (Grasemann et al., 1999): A, simple shear with $\beta > 10˚$; B, general shear with intermediate β ($0˚ < \beta < 10˚$); C, pure shear with $\beta \approx 0˚$.

prism and both positive and negative rhomb planes. Evidence for both grain boundary migration and subgrain rotation in quartz implies transitional regime 2 to regime 3 recrystallization conditions (Hirth and Tullis, 1992) (Figure 2.5h). Quartz c-axis fabric opening angles of 63˚, 66˚, and 68˚ (samples 06SE66, 06SE29, and 08SE473, respectively) indicate deformation temperatures of ~500 ˚C (Kruhl, 1998; Law *et al*., 2004) (Table 2.2). Similar opening angles (60˚ - 73˚) were observed in samples from the Rand Mountains, discussed below, indicating similar conditions of deformation. Systematic variations in opening angle with structural depth were not observed in either San Emigdio or Rand localities, implying that the entire structural section of schist was deformed at ~500 ˚C.

Quartz CPO for 12 samples of Rand schist quartzite mylonite from different structural levels in the Rand Mountains are compiled from Postlethwaite and Jacobson (1987) and Nourse (1989) and shown in Figure 2.11. For samples collected from the upper ~100 m of the schist, a systematic obliquity exists between the central portion of c-axis fabrics and the foliation, consistent with TTN shear. At deeper structural levels (> 100 m from the Rand fault), c-axis fabrics are more symmetric about the foliation, indicating a stronger influence of coaxial flow.

Near the schist – upper plate contact, quartz ribbon microstructures are well preserved in strongly lineated and foliated tectonites with individual ribbon aspect ratios > 20:1 (Nourse, 1989). Estimates of finite strain near the base of the schist section from deformed volcanic “clasts” indicate highly flattening strain with strain ellipsoid axial ratios of 1.5 : 1.0 : 0.1 and R_{xz}= 16.3 ± 1.4 (Postlethwaite, 1983). At this level of exposure, lineations are poorly developed and boudinage of quartzite layers is common (Postlethwaite, 1983). Strain estimates were not possible for the samples presented in Figure 2.11 or for

Figure 2.11. Quartz c-axis fabrics for 12 samples of Rand schist quartzite mylonite from the Rand Mountains. Pole figures are equal-area lower-hemisphere stereographic projections with foliation shown by horizontal line and lineation parallel to the projection plane (oriented NNE - SSW), skeletal outlines showing β of c-axis fabric are overlain. Note higher β values and more systematic asymmetry of the central portion of c-axis fabrics proximal to Rand fault (RF). Samples 309A, 309E-1, 301C, and 524 from Nourse (1989), contouring at 1, 3, 5, 7, 9, 11, and 13 times mean uniform distribution. Samples 14, 18, 2, 9a-c, 3b, and 40 from Postlethwaite and Jacobson (1987), Kamb contours at 2σ, 4σ, 6σ, 8σ, 10σ, and 12σ. Sample locations shown in Figure 2.3.

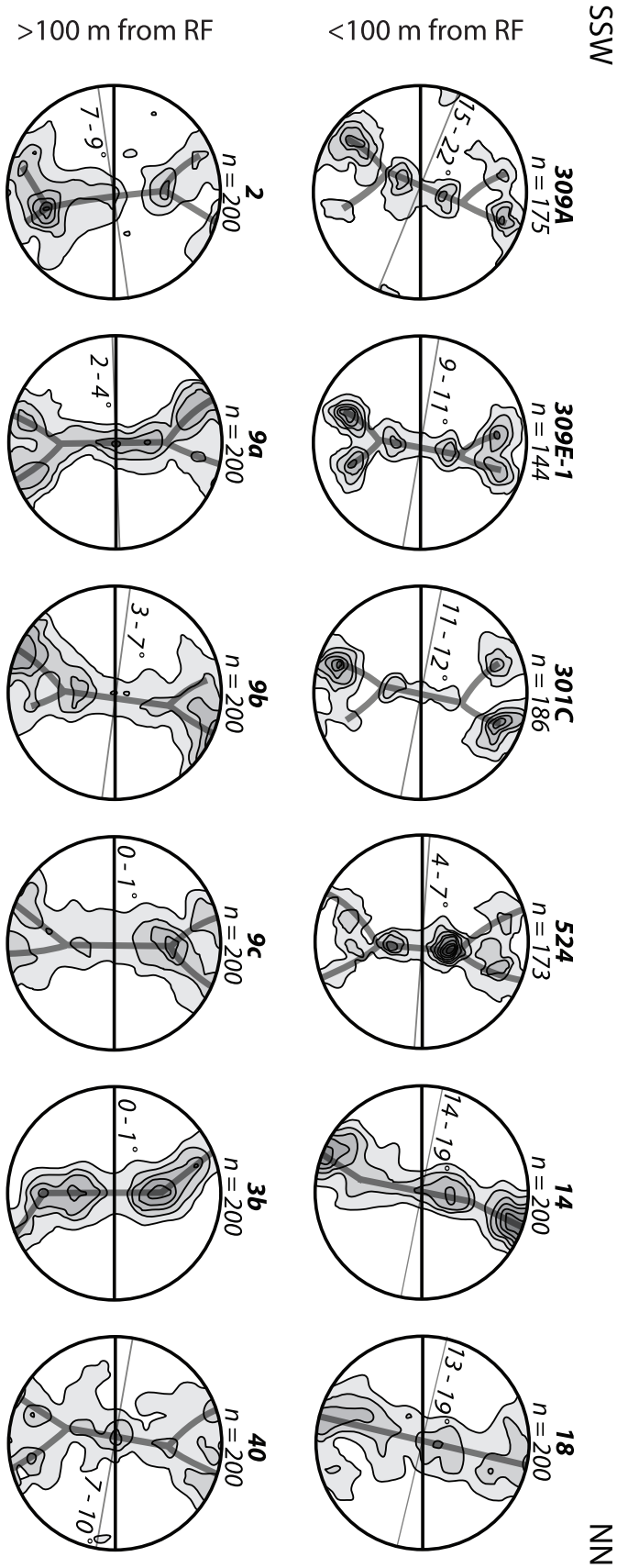
SSW
<100 m from RF
>100 m from RF
309A
n = 175
15 - 22°
2
n = 200
7 - 9°
309E-1
n = 144
9 - 11°
9a
n = 200
2 - 4°
301C
n = 186
11 - 12°
9b
n = 200
3 - 7°
524
n = 173
4 - 7°
9c
n = 200
0 - 1°
14
n = 200
14 - 19°
3b
n = 200
0 - 1°
18
n = 200
13 - 19°
40
n = 200
7 - 10°
NNE

sample 06SE29 due to difficulties in recognizing and tracing outlines of detrital quartz grains. However, given the high strains ($R_{xz} > 16$) observed at different structural levels by Postlethwaite (1983) and Nourse (1989) and the large displacement along the Rand fault (100s of km), we assume large finite strains ($R_{xz} > 5$) for these samples. At high finite strain, vorticity number estimates are quite sensitive to small changes in β (Figure 2.12) and only three deformation settings can be distinguished: (1) pure shear with $\beta \approx 0^{\circ}$; (2) general shear with intermediate β ($0^{\circ} < \beta < 10^{\circ}$); and (3) simple shear with $\beta > 10^{\circ}$ (Grasemann *et al*., 1999). Measured β angles are summarized in Table 2.2. The highest values of β, averaging ~13˚ for samples 309A, 309E-1, 301C, 524, 18, and 14, are found within ~100 m of the Rand fault, indicating predominantly simple shear at high structural levels. In contrast, at deeper structural levels β averages ~4˚ (samples 2, 9a-c, 3b, and 40), implying a decrease in W_m (i.e., an increase in pure shear component) away from the Rand fault (Figure 2.12). Although we assume $R_{xz} > 5$ for the entire structural thickness of schist in the Rand Mountains, we consider it likely, based on larger strain estimates near the Rand fault (Nourse, 1989) than from deep in the section (Postlethwaite, 1983) and from strain analysis in the San Emigdio window ($R_{xz} > 8.2$ in 06SE66 and $R_{xz} \sim 3.2$ in 08SE473), that finite strain decreases with structural depth in the schist. A decrease in R_{xz} from the top of the schist downward would still require a decrease in W_m away from the Rand fault, although this scenario would involve a larger decrease than for the case of constant R_{xz} (Figure 2.12).

Figure 2.12. Relationship between R_{xz} and β for different values of W_m. Vorticity constraints from the San Emigdio schist locality are shown as boxes (06SE66 and 06SE29) and a circle (08SE473) with hatchured lines and distance from the Rand fault (in meters) inscribed. For the Rand locality, average β (dashed dark gray lines) and standard deviation envelopes (pink boxes) are shown for $R_{xz} > 5$ for < 100 m and > 100 m from the Rand fault (see text for discussion).

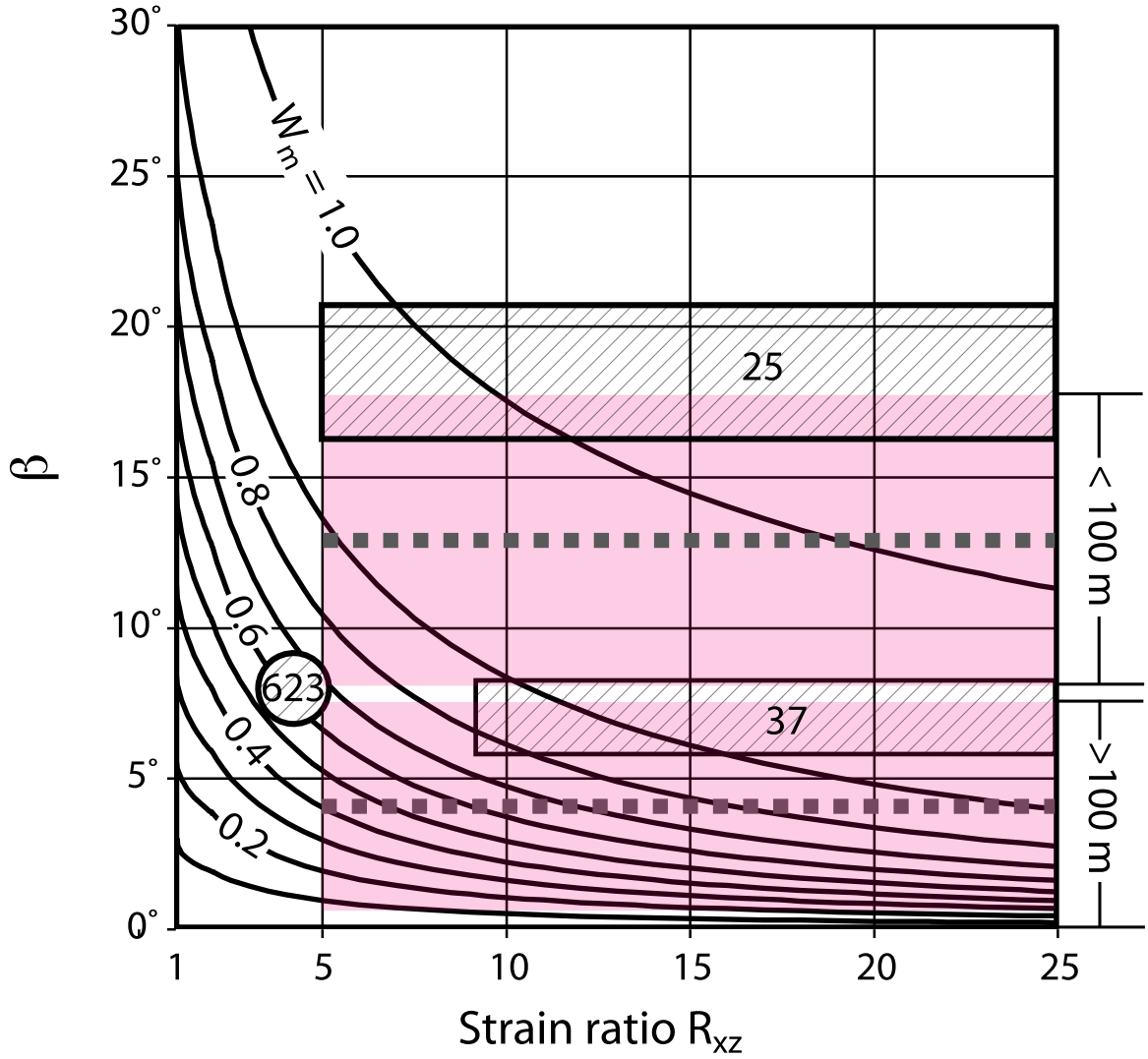
30°
25°
20°
15°
10°
5°
0°
β
$W_m = 1.0$
0.8
0.6
0.4
0.2
623
25
37
< 100 m
< 100 m
1
5
10
15
20
25
Strain ratio R_{xz}

4. DISCUSSION

4.1. Tectonic model

The deposition, subduction, and structural ascent of the schist is temporally and spatially associated in plate reconstructions with the subduction of a conjugate massif to the Shatsky Rise, a large igneous province (LIP) ~2,000 km southeast of Japan (Saleeby, 2003; Liu *et al*., 2008; 2010). Subduction of the LIP is hypothesized to have driven slab flattening and upper plate extension (Figure 2.13) somewhat analogous to the ongoing subduction of the Nazca Ridge and trench-directed detachment faulting above the Peruvian flat slab segment (Gutscher *et al*., 2000; McNulty and Farber, 2002). To explain northwest - southeast younging patterns in protolith and cooling age of the schist (Grove *et al*., 2003), we view this conjugate LIP as an elongate body that first collided with North America at the latitude of the San Emigdio Mountains and propagated to the southeast (Barth and Schneiderman, 1996). As a result of this time-transgressive collision the events described below for the Tehachapi and San Emigdio windows occurred ca. 20 Myr prior to analogous events in the Sierra de Salinas and the Rand Mountains. At ca. 95 Ma (Figure 2.13b), the LIP entered the trench with a high normal component of convergence (~100 km/Myr) (Engebretson *et al*., 1985) and the angle of subduction shallowed, driving the tectonic removal of sub-batholithic mantle lithosphere and the cessation of arc magmatism. Increased coupling between the LIP and the upper plate led to abrupt crustal thickening (House *et al*., 2001; Saleeby, 2003). Decompression and partial exhumation of batholithic assemblages from ~9 kbar to ~4 kbar levels occurred during this phase of rapid uplift. Erosion of the high-elevation mountain belt shed the schist protolith into the trench, which was immediately underplated and

Figure 2.13. Block diagrams of the southern SNB showing the tectonic context of northward tilting and westward deflection of the upper plate and the development of lower plate transport directions. (a) Ca. 100 Ma. Immediately prior to collision of the LIP. (b) Ca. 95 Ma. Segmentation of the Farallon slab into shallow and more deeply subducting portions, with intervening lateral ramp. To the north, the sub-batholith mantle lithosphere is preserved, while to the south, the mantle wedge is sheared off by the subducting LIP. Schist protolith is shed into trench and begins to subduct while upper plate uplift and extensional collapse occur above the shallow segment. (c) Ca. 85 Ma. Gravitational collapse of the upper plate drives trench-directed channelized extrusion of the schist. Strain coupling between the schist and upper plate leads to continued extension and exhumation in the upper plate, and clockwise rotation in the upper plate. Schist flow is dominated by simple shear near the boundaries of the channel and by pure shear at the center of the wedge. Abbreviations: KWF, Late Cretaceous Kern Canyon – White Wolf fault system; LIP, large igneous province; MSL, mean sea level; pKCF, proto-Kern Canyon fault; SBML, sub-batholith mantle lithosphere; SOML, sub-oceanic mantle lithosphere.

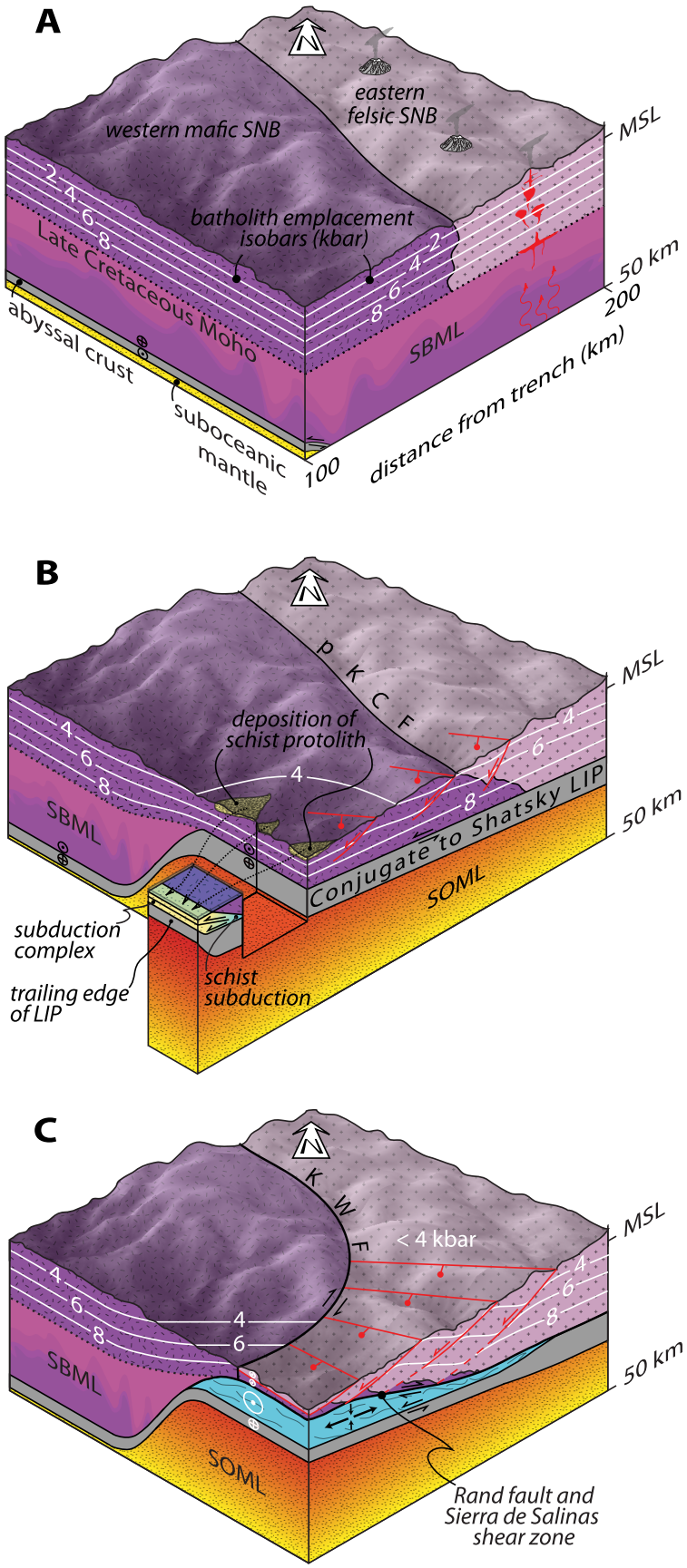
A
N
western mafic SNB
eastern
felsic SNB
MSL
batholith emplacement
isobars (kbar)
2
4
6
8
Late Cretaceous Moho
abyssal crust
suboceanic
mantle
SBML
50 km
200
100
distance from trench (km)
B
N
P
K
C
F
deposition of
schist protolith
4
6
8
SBML
MSL
Conjugate to Shatsky LIP
SOML
50 km
subduction
complex
trailing edge
of LIP
schist
subduction
C
N
K
W
F
< 4 kbar
T
L
4
6
8
SBML
MSL
50 km
SOML
Rand fault and
Sierra de Salinas
shear zone

subjected to high-temperature metamorphism at least 150 km inboard beneath the extinguished arc (Kidder and Ducea, 2006). Replacement of sub-batholith mantle lithosphere with relatively weak schist led to gravitational collapse of the thickened upper plate and regionally extensive trench-directed flow in the schist (Saleeby, 2003). During this exhumation phase, (1) the KWF functioned as a crustal-scale transfer structure, the southeastern side of which underwent high-magnitude extension and clockwise rotation above the trenchward-moving schist (Figure 2.13c) and (2) northwest-striking extensional fracture swarms southeast of the KWF (Figures 2.1 and 2.13c) developed perpendicular to the principal transport direction in the underplated schist.

4.2. Rotation of the southern Sierra Nevada batholith

The structural and kinematic relations presented here provide strong evidence that the schist moved from deep to shallow crustal levels along the Rand fault and Salinas shear zone with a top to the NNE sense of shear. With the exception of the San Emigdio Mountains, which experienced significant Pliocene-Quaternary contractile deformation (Davis, 1983), lower plate transport directions are uniform at S30W ±10˚ within a ~10,000 km^2 region (Figure 2.1). The consistency in schist transport direction stands in marked contrast to apparent vertical-axis rotations of 45 - 90° (Kanter and McWilliams, 1982; McWilliams and Li, 1983; 1985) observed in the batholithic rocks from the same region, and suggests that the schist escaped major systematic rotation. It could be argued that the Garlock fault may be a transrotation boundary (e.g., Dickinson, 1996) and that any rotation in the southern Sierra Nevada (e.g., in the Tehachapi schist body) would not be expected in the Sierra de Salinas or Rand windows. However, the geometry and kinematics of Neogene-Quaternary faulting

in the southern Sierra Nevada are inconsistent with the proposed boundary (Mahéo *et al*., 2009).

In the SNB, ca. 86 Ma $^{40}Ar/^{39}Ar$ cooling ages indicate that the schist reached its present position relative to the upper plate at about the same time that the upper plate cooled sufficiently to lock in a magnetic orientation (ca. 88-80 Ma). These observations leave little time for rotation prior to schist arrival, and rule out major crustal block rotation following ca. 86 Ma. We assume that following schist emplacement and cooling, any upper plate rotation that occurred would also involve rotation of the underlying schist. We conclude that a significant fraction of upper plate rotation of the southern SNB occurred in the Late Cretaceous coincident with schist ascent and cooling at ca. 88-86 Ma. It is important to reiterate here that fabrics at the base of the upper plate and in the schist are generally parallel. We suggest that the trenchward flowing schist exerted traction at the base of the upper plate, driving upper plate extension and rotation. We further speculate that this coupling increased toward the Rand fault (i.e., from high to low structural levels in the upper plate), leading to the observed upper plate clockwise deflection into parallelism with the schist. This interpretation is at odds with models linking clockwise rotation in the southern SNB to post-Cretaceous dextral transpression (Burchfiel and Davis, 1981; McWilliams and Li, 1985) or Miocene transtension (Ross *et al*., 1989; Dokka and Ross, 1995). Although the west-directed thrusting model of May (1989) attributes displacement of upper crustal fragments in the southern SNB, Salinia, Mojave Desert, Transverse Ranges, and Peninsular Ranges to Late Cretaceous deformation, the tectonic setting of the deformation is demonstrably extensional (Wood and Saleeby, 1998; Saleeby *et al*., 2007).

4.3. Schist Exhumation Mechanisms

Previous workers have proposed a number of scenarios for exhumation of the schist, both for the northern schist that we focus on here and for related Pelona and Orocopia schists to the south (e.g., Grove *et al*., 2003): return flow (Malin *et al*., 1995; Oyarzabal *et al*., 1997; Jacobson *et al*., 2002; Saleeby, 2003; Saleeby *et al*., 2007), isostatically driven uplift (Jacobson *et al*., 2007), upper plate normal faulting (e.g., Jacobson *et al*., 1996) and erosion (Yin, 2002). Upper plate ductile thinning (e.g., Ring *et al*., 1999) was apparently not a major schist exhumation mechanism since the upper plate is rather heterogeneously deformed. As the distinction between return flow and extrusion may not be clear, we first define these terms as end-member possibilities in what we recognize in nature may be a continuum of scenarios.

We consider "return flow" in the sense of Cloos (1982): forced convection of low viscosity material above a down-going plate with zero- or low-slip boundary conditions. In return flow, subducted material returns to the surface along roughly the same route as it descended (Platt, 1986). Return flow involves concurrent downward and upward flow resulting in a distributed, strongly noncoaxial flow. Return flow is extended from the steady state scenario of Cloos (1982) in the numerical models of Gerya *et al*. (2002), which illustrate the growth of a return flow channel over time.

In the context of subducted material, extrusion, like return flow, involves the channelized structural ascent of material along roughly the same path as it descended. In the case of extrusion, exhumation occurs by localization of noncoaxial flow along coeval upper and lower shear zones with opposing senses of shear. Unlike the return flow "two-way street," the extrusion end-member brings the entire subduction assemblage toward the trench

en masse. The resulting flow pattern is predominantly coaxial except near the boundaries of the channel. Strain compatibility is maintained during extrusion by discontinuous deformation along channel boundaries and elongation at the center of the wedge.

Retrograde deformation features in the schist are more consistent with channelized extrusion than return flow. Microstructural observations from the Sierra de Salinas also suggest generally coaxial deformation in lower levels of the schist (Figure 2.6). These observations are inconsistent with distributed TTN noncoaxial flow as predicted within a return flow channel. We assert that the predominant exhumation mechanism of the schist was extrusion, i.e., deformation in the interior of the schist was predominantly coaxial with coeval noncoaxial shear displacement limited to the remobilized subduction megathrust and an unexposed structure with opposing shear sense at depth (Figure 2.13c). This general shear extrusion involves more rapid lower plate schist ascent than would be expected for the case of strictly noncoaxial deformation (Grasemann, *et al*., 1999; Law *et al*., 2004) and is consistent with high decompression rates of > 0.5 kbar/Myr (> 1.5 mm/yr) in the schist (Saleeby *et al*., 2007). Comparable decompression rates of ~2 – 4 mm/yr are calculated from the High Himalayan Crystalline Series (Ganguly *et al*., 2000; Searle *et al*., 2003; Harris *et al*., 2004), which is suggested to have been exhumed by extrusion from beneath the Tibetan Plateau (e.g., Burchfiel and Royden, 1985; Grujic *et al*., 1996; Grasemann *et al*., 1999; Hodges *et al*., 2001; Law *et al*., 2004).

Extrusion and return flow, acting alone or in combination, return subducted material to the surface at the trench rather than substantially inboard beneath the magmatic arc where the schists are found. Some combination of upper plate normal faulting and erosion thus played an important role in schist exhumation (Postlethwaite and Jacobson, 1987; Jacobson

et al., 1988; 1996; Simpson, 1990; Malin *et al*., 1995; Wood and Saleeby, 1998; Jacobson *et al*., 2007; Saleeby *et al*., 2007). Extensive upper plate normal faulting is evident from the regional displacement pattern of the extended southern SNB and the outboard position of Salinia. We speculate that the dominant exhumation mechanism evolved from extrusion in the middle and lower crust to extensional faulting and erosion in the upper crust.

A critical assumption, supported by the following arguments, of the interpretation that the schist ascended by channelized extrusion is that coaxial and noncoaxial fabrics developed at the same time. (1) Deep and shallow fabrics in the Rand, San Emigdio, and Tehachapi bodies are commonly associated with retrograde mineral assemblages. (2) Amphibolite facies mylonites from the Sierra de Salinas indicate a high probability of noncoaxial flow at the top of the schist and the base of the upper plate, while at deeper levels (>200 m) TTN and TTS shear indicators are roughly evenly distributed (Figure 2.6). These "early" features, while commonly overprinted by demonstrably retrograde "late" fabrics, probably record exhumation-related deformation since the TTN sense of shear at the top of the schist is opposite the subduction direction. This is not the case, however, in the Orocopia schist, in which two generations of deformation are attributed to subduction and exhumation (Jacobson and Dawson, 1995; Jacobson *et al*., 2007). (3) In the Rand and San Emigdio Mountains, quartz CPO indicate that plastic deformation occurred by localized simple shear-dominated deformation proximal to the upper plate at the same temperature conditions (~500 ˚C) as more coaxial deformation in deeper parts of the schist. Inverted gradients preserved in the schist likely formed during prograde metamorphism (e.g., Kidder and Ducea, 2006); therefore, since the entire schist section was deformed at ~500 ˚C, this deformation must have occurred following peak metamorphism. (4) While peak

metamorphic temperatures in the Rand Mountains window of 525 – 556 ˚C (Graham and Powell, 1984) are similar to deformation temperatures of 470 – 590 ˚C inferred from quartz fabrics (Table 2.2), peak temperatures in the Tehachapi and San Emigdio Mountains of 590 – 680 ˚C (Pickett and Saleeby, 1993) are significantly higher, indicating that these fabrics could not have formed prior to peak metamorphism (i.e., during underthrusting).

4.4. A comparison with Cordilleran metamorphic core complexes

Like the schist - upper plate system, middle-Tertiary metamorphic core complexes of the North American Cordillera formed as predominantly brittle upper crust extended by normal faulting above a weak substrate (Coney, 1980). A detailed comparison of the schist and Cordilleran metamorphic core complexes has been made previously (Jacobson *et al*., 2007) and is beyond the scope of this paper. We note, however, one key difference between the schist and core complexes. Schist exhumation involved lower plate transport to the SSW in at least Sierra de Salinas, Tehachapi, Rand, Orocopia, and Gavilan Hills localities (Simpson, 1990; Jacobson *et al*., 1996; Oyarzabal *et al*., 1997) (Figure 2.1, lower inset), i.e., in each locality where a sense of shear has been established. In contrast, Cordilleran core complexes show no systematic sense of shear (Wernicke, 1992, Plate 8). For example, the Shuswap core complex of the Canadian Cordillera crops out over an area comparable to that of the schist and exhibits opposing shear sense along its western (top to the west) and eastern (top to the east) margins (Vanderhaeghe *et al*., 1999). The consistency of schist transport to the SSW highlights the role of the schist as an active agent of tectonic rotation and large magnitude extension in the upper plate. In core complexes, the middle crust flows

more passively in response to the local asymmetries of breakaway zones, forming domes beneath brittlely thinned upper crust (Wernicke, 1992).

4.5. Do the schist localities preserve a subduction interface?

Metamorphic convergence between an upper and lower plate of a subduction zone may result through either prograde metamorphism in the lower plate and retrograde metamorphism in the upper plate or retrograde metamorphism in both plates. The former type of metamorphic convergence along the schist - upper plate contact is cited as evidence for localized preservation of the original subduction interface (Jacobson *et al*., 1996; Jacobson, 1997). While we do not dispute this claim for the case of the Pelona schist of the San Gabriel Mountains, where no consistent direction of transport has been established (Jacobson, 1983; Dillon *et al*., 1990), metamorphic convergence in the northern schists is at odds with the observed top to the NNE transport direction. We suggest that the contact was indeed proximal to the original subduction megathrust, but was later remobilized as a normal fault during exhumation. The current upper - lower plate configuration may have resulted from upper plate decompression to ~4 kbar conditions at the time of schist subduction to ~9 kbar conditions (Saleeby *et al*., 2007). Subsequent schist extrusion would have placed the schist against an upper plate that had already been exhumed from deep levels. In other words, metamorphic convergence along the Rand fault and Salinas shear zone may be a structural accident. Further thermochronologic work is needed to verify this hypothesis since it is based on upper plate and schist cooling ages from Tehachapi and San Emigdio localities, respectively (Saleeby *et al*., 2007). It is also possible that the schist-upper plate contact fused at peak conditions resulting in a low-slip boundary that is still

preserved. In either case, while the shear zones involving Pelona, Orocopia, Rand, and Sierra de Salinas schists preserve metamorphic and structural evidence for deformation along the Late Cretaceous subduction megathrust, they subsequently experienced a significant penetrative, exhumation-related deformation. Deciphering prograde deformation through retrograde overprints remains a significant challenge for studies relating metamorphic and microstructural observations to subduction megathrust processes (e.g., Peacock, 1987; England and Molnar, 1993; Ducea *et al*., 2007).

4.6. Dynamics of schist exhumation

One outstanding geodynamic problem not resolved here is whether schist unroofing and associated collapse of the overthickened upper plate were purely driven by excess potential energy or if extension was facilitated by slab rollback. Saleeby (2003) argues that following passage of the conjugate to the Shatsky rise, the slab became negatively buoyant and reverted to a steeper trajectory (i.e., slab rollback), inducing regionally extensive trench-directed flow in the underplated schist and coupled extensional collapse of the upper plate. Our studies do not elucidate the role of slab rollback in crustal structures. Further iterative studies between observational geophysics, geologic data, and dynamic modeling are needed to resolve this issue. Future generation three-dimensional modeling is required to investigate the slab rollback hypothesis by allowing lateral inflow of asthenosphere into steepening flat segments from regions above adjacent steeply-dipping segments.

4.7. Late Cretaceous Regional Cooling

Late Cretaceous extension in the western U.S. was not restricted to the southern Sierra Nevada region. Widespread Late Cretaceous cooling in the Mojave Desert region has long been recognized (e.g., Dumitru *et al*., 1991). Wells *et al*. (2005) link this cooling to extension by detailing the geometry, kinematics, deformation temperature, and thermal history of the Pinto shear zone in the New York Mountains (Figure 2.1, lower inset). Similarly, synextensional emplacement of Late Cretaceous granites and pegmatites from the Iron, Old Woman, and Granite Mountains (Figure 2.1, lower inset) indicates widespread Late Cretaceous ~northeast - southwest extension in the eastern Mojave Desert region (Wells and Hoisch, 2008). Late Cretaceous-early Tertiary extension in the western Mojave, Salinia, and the southern SNB is clearly linked to emplacement of Rand and related schists. However, Wells and Hoisch (2008) suggest that synconvergent extension and magmatism in the eastern Mojave Desert region resulted from delamination of mantle lithosphere in the backarc region, causing asthenospheric upwelling and partial melting in the lower crust. Recent work by Luffi *et al*. (2009) shows that the cratonic basement of the Mojave Desert region is underlain by a section of North American lithospheric mantle above tectonically imbricated Farallon oceanic lithosphere. The presence of North American lithospheric mantle beneath the Mojave Desert region precludes complete removal of Mojavian lithospheric mantle in the backarc region due to delamination. Instead, we suggest that schist extrusion and arc collapse to the west enabled extension, asthenospheric upwelling, and anatexis in the eastern Mojave by changing plate boundary conditions. In other words, following passage of the LIP, gravitational collapse of the rootless SNB to the west pulled the more rigid crust of the eastern Mojave with it, allowing for asthenospheric upwelling

and synextensional magmatism. This localized phenomenon may explain focused Late Cretaceous extension in the Mojave with considerably less extension at this time in other parts of the Cordillera (Wells and Hoisch, 2008).

5. CONCLUSIONS

Through consideration of new and published structural data, recent geochronologic studies, and available paleomagnetic constraints, we have developed a model for roughly coeval high magnitude extension, clockwise rotation, and schist extrusion in Salinia and the southern SNB. We suggest the following sequence of Late Cretaceous events in the southern SNB and Salinia: (1) low angle subduction of the conjugate to the Shatsky Rise, resulting in uplift of the upper plate and schist underplating; (2) trench-directed channelized extrusion in the subducted schist with lower plate to the SSW kinematics, leading to collapse of the upper plate; and (3) high magnitude extension and westward deflection of the upper plate batholith above the flowing channel. We argue that a significant fraction of observed clockwise rotation in the southern SNB is the direct result of schist return flow; this argument does not preclude localized, basement structure-controlled, increments of Neogene rotation.

REFERENCES

Ague, J. J., and Brimhall, G. H., 1988, Magmatic arc asymmetry and distribution of anomalous plutonic belts in the batholiths of California; effects of assimilation, crustal thickness, and depth of crystallization: *Geological Society of America Bulletin*, **100**, 912-927.

Barth, A. P., and Schneiderman, J. S., 1996, A comparison of structures in the Andean Orogen of northern Chile and exhumed midcrustal structures in Southern California, USA; an analogy in tectonic style?: *International Geology Review*., **38**, 1075-1085.

Barth, A. P., Wooden, J. L., Grove, M., Jacobson, C. E., and Pedrick, J. N., 2003, U-Pb zircon geochronology of rocks in the Salinas Valley region of California; a reevaluation of the crustal structure and origin of the Salinian Block: *Geology*, **31**, 517-520.

Burchfiel, B. C., and Davis, G. A., 1981, Mojave Desert and environs, in: *The geotectonic development of California, Rubey Volume I: Englewood Cliffs*, edited by W. G. Ernst, 217-252, Prentice-Hall, New Jersey.

Burchfiel, B. C., and Royden, L. H., 1985, North-south extension within the convergent Himalayan region: *Geology*, **13**, 679-682.

Cheadle, M. J., Czuchra, B. L., Byrne, T., Ando, C. J., Oliver, J. E., Brown, L. D., Kaufman, S., Malin, P. E., and Phinney, R. A., 1986, The deep crustal structure of the Mojave Desert, California, from COCORP seismic reflection data: *Tectonics*, **5**, 293-320.

Chew, D. M., 2003, An Excel spreadsheet for finite strain analysis using the Rf/phi technique: *Computational Geosciences*, **29**, 795-799.

Cloos, M., 1982, Flow melanges; numerical modeling and geologic constraints on their origin in the Franciscan subduction complex, California: *Geological Society of America*

Bulletin, **93**, 330-344.

Coney, P. J., 1980, Cordilleran metamorphic core complexes; an overview: *Memoir - Geological Society of America*, **153**, 7-31.

Crowell, J. C., 1952, Geology of the Lebec Quadrangle, California: *Special Report - California Division of Mines and Geology*, **24**, p. 1-24.

Davis, T. L., 1983, Late Cenozoic structure and tectonic history of the western "Big Bend" of the San Andreas Fault and adjacent San Emigdio Mountains, Ph.D. thesis, University of California, Santa Barbara, 563 pp.

Dibblee, T. W., Jr., 1967, Areal geology of the western Mojave Desert, California: *U.S. Geological Survey Professional Paper* 522, 153 pp.

Dibblee, T. W., Jr., 1973, Geologic maps of the Santiago Creek, Eagle Rest Peak, Pleito Hills, Grapevine, and Pastoria Creek quadrangles, Kern County, California: *U.S. Geological Survey Open File Report* 73-57.

Dibblee, T. W., Jr., 1974, Geologic maps of the Monterey, Salinas, Gonzales, Point Sur, Jamesburg, Soledad and Junipero Serra 15' quadrangles, Monterey County, California: *U.S. Geological Survey Open File Report* 74-1021.

Dibblee, T. W., Jr., 1986, Geology of the San Emigdio Mountains, California: *Field Trip Guidebook - Pacific Section, Society of Economic Paleontologists and Mineralogists*, **48**, 1-10.

Dickinson, W. R., 1996, Kinematics of transrotational tectonism in the California Transverse Ranges and its contribution to cumulative slip along the San Andreas transform fault system: *Geological Society of America Special Paper*, **305**, 46 pp.

Dillon, J. T., Haxel, G. B., and Tosdal, R. M., 1990, Structural evidence for northeastward

movement on the Chocolate Mountains Thrust, southeasternmost California: *Journal of Geophysical Research*, **95**, 19,953-19,971.

Dokka, R. K., and Ross, T. M., 1995, Collapse of southwestern North America and the evolution of early Miocene detachment faults, metamorphic core complexes, the Sierra Nevada orocline, and the San Andreas fault system: *Geology*, **23**, 1075-1078.

Ducea, M. N., and Saleeby, J. B., 1998, The age and origin of a thick mafic-ultramafic keel from beneath the Sierra Nevada Batholith: *Contributions to Mineralogy and Petrology*, **133**, 169-185, doi: 110.1007/s004100050445.

Ducea, M. N., Ganguly, J., Rosenberg, E. J., Patchett, P. J., Cheng, W., and Isachsen, C., 2003, Sm-Nd dating of spatially controlled domains of garnet single crystals; a new method of high-temperature thermochronology: *Earth and Planetary Science Letters*, **213**, 31-42.

Ducea, M. N., Kidder, S., and Chesley, J. T., 2007, A geologic window into a subduction megathrust: *Eos, Transactions, American Geophysical Union*, **88**, 277.

Ducea, M. N., Kidder, S., Chesley, J. T., and Saleeby, J. B., 2009, Tectonic underplating of trench sediments beneath magmatic arcs; the Central California example: *International Geology Review*, **51**, 1-26.

Dumitru, T. A., Gans, P. B., Foster, D. A., and Miller, E. L., 1991, Refrigeration of the western Cordilleran lithosphere during Laramide shallow-angle subduction: *Geology*, **19**, 1145-1148.

Dunnet, D., and Siddans, A. W. B., 1971, Non-random sedimentary fabrics and their modification by strain: *Tectonophysics*, **12**, 307-325.

Ehlig, P. L., 1958, The geology of the Mount Baldy region of the San Gabriel Mountains,

California, Ph.D. thesis, University of California, Los Angeles, 195 pp.

Ehlig, P. L., 1981, Origin and tectonic history of the basement terrane of the San Gabriel Mountains, central Transverse Ranges, in: *The geotectonic development of California, Rubey Volume I*, edited by W. G. Ernst, 253-283, Prentice-Hall, New Jersey.

England, P., and Molnar, P., 1993, The interpretation of inverted metamorphic isograds using simple physical calculations: *Tectonics*, **12**, 145-158.

Fletcher, J. M., Miller, J. S., Martin, M. W., Boettcher, S. S., Glazner, A. F., and Bartley, J. M., 2002, Cretaceous arc tectonism in the Mojave Block; profound crustal modification that controlled subsequent tectonic regimes: *Memoir - Geological Society of America*, **195**, 131-149.

Ganguly, J., Dasgupta, S., Cheng, W., and Neogi, S., 2000, Exhumation history of a section of the Sikkim Himalayas, India; records in the metamorphic mineral equilibria and compositional zoning of garnet: *Earth and Planetary Science Letters*, **183**, 471-486.

Gerya, T. V., Stöckhert, B., and Perchuk, A. L., 2002, Exhumation of high-pressure metamorphic rocks in a subduction channel; a numerical simulation: *Tectonics*, **21**, doi:10.1029/2002TC001406.

Graham, C. M., and England, P. C., 1976, Thermal regimes and regional metamorphism in the vicinity of overthrust faults; an example of shear heating and inverted metamorphic zonation from southern California: *Earth and Planetary Science Letters*, **31**, 142-152.

Graham, C. M., and Powell, R., 1984, A garnet-hornblende geothermometer; calibration, testing, and application to the Pelona schist, Southern California: *Journal of Metamorphic Geology*, **2**, 13-31.

Grasemann, B., Fritz, H., and Vannay, J.-C., 1999, Quantitative kinematic flow analysis

from the Main Central Thrust Zone (northwest-Himalaya, India); implications for a decelerating strain path and the extrusion of orogenic wedges: *Journal of Structural Geology*, **21**, 837-853.

Grove, M., Jacobson, C. E., Barth, A. P., and Vucic, A., 2003, Temporal and spatial trends of Late Cretaceous-early Tertiary underplating Pelona and related schist beneath Southern California and southwestern Arizona: *Geological Society of America Special Paper*, **374**, 381-406.

Grujic, D., Casey, M., Davidson, C., Hollister, L. S., Kuendig, R., Pavlis, T. L., and Schmid, S. M., 1996, Ductile extrusion of the Higher Himalayan Crystalline in Bhutan; evidence from quartz microfabrics: *Tectonophysics*, **260**, 21-43.

Gutscher, M.-A., Spakman, W., Bijwaard, H., and Engdahl, E. R., 2000, Geodynamics of flat subduction; seismicity and tomographic constraints from the Andean margin: *Tectonics*, **19**, 814-833, doi: 810.1029/1999TC001152.

Hanmer, S., and Passchier, C., 1991, Shear-sense indicators; a review: *Paper - Geological Survey of Canada*, 90-17.

Harris, N. B. W., Caddick, M., Kosler, J., Goswami, S., Vance, D., and Tindle, A. G., 2004, The pressure-temperature-time path of migmatites from the Sikkim Himalaya: *Journal of Metamorphic Geology*, **22**, 249-264.

Haxel, G., and Dillon, J., 1978, The Pelona-Orocopia schist and Vincent-Chocolate Mountain thrust system, southern California, in: *Mesozoic paleogeography of the western United States: Pacific Section, Society of Economic Paleontologists and Mineralogists Pacific Coast Paleogeography Symposium 2*, edited by D. G. Howell and K. A. McDougall, 453-469.

Henry, D. J., and Dokka, R. K., 1992, Metamorphic evolution of exhumed middle to lower crustal rocks in the Mojave extensional belt, Southern California, USA: *Journal of Metamorphic Geology*, **10**, 347-364.

Hirth, G., and Tullis, J., 1992, Dislocation creep regimes in quartz aggregates: *Journal of Structural Geology*, **14**, 145-159.

Hodges, K. V., Hurtado, J. M., and Whipple, K. X., 2001, Southward extrusion of Tibetan crust and its effect on Himalayan tectonics: *Tectonics*, **20**, 799-809.

House, M. A., Wernicke, B. P., and Farley, K. A., 2001, Paleo-geomorphology of the Sierra Nevada, California, from (U-Th)/He ages in apatite: *American Journal of Science*, **301**, 77-102.

Jacobson, C. E., 1983, Structural geology of the Pelona schist and Vincent Thrust, San Gabriel Mountains, California: *Geological Society of America Bulletin*, **94**, 753-767.

Jacobson, C. E., 1990, The 40Ar/39Ar geochronology of the Pelona schist and related rocks, Southern California: *Journal of Geophysical Research*, **95**, 509-528.

Jacobson, C. E., 1995, Qualitative thermobarometry of inverted metamorphism in the Pelona and Rand schists, Southern California, using calciferous amphibole in mafic schist: *Journal of Metamorphic Geology*, **13**, 79-92.

Jacobson, C. E., 1997, Metamorphic convergence of the upper and lower plates of the Vincent Thrust, San Gabriel Mountains, Southern California, USA: *Journal of Metamorphic Geology*, **15**, 155-165.

Jacobson, C. E., and Dawson, M. R., 1995, Structural and metamorphic evolution of the Orocopia schist and related rocks, southern California: Evidence for late movement on the Orocopia fault: *Tectonics*, **14**, 933-944.

Jacobson, C. E., Dawson, M. R., and Postlethwaite, C. E., 1988, Structure, metamorphism, and tectonic significance of the Pelona, Orocopia, and Rand schists, Southern California, in: *Metamorphism and crustal evolution of the Western United States, Rubey Volume*, edited by W. G. Ernst, 976-997, Prentice-Hall, New Jersey.

Jacobson, C. E., Oyarzabal, F. R., and Haxel, G. B., 1996, Subduction and exhumation of the Pelona-Orocopia-Rand schists, Southern California: *Geology*, **24**, 547-550.

Jacobson, C. E., Grove, M., Stamp, M. M., Vucic, A., Oyarzabal, F. R., Haxel, G. B., Tosdal, R. M., and Sherrod, D. R., 2002, Exhumation history of the Orocopia schist and related rocks in the Gavilan Hills area of southeasternmost California: *Geological Society of America Special Paper*, **365**, 129-154.

Jacobson, C. E., Grove, M., Vucic, A., Pedrick, J. N., and Ebert, K. A., 2007, Exhumation of the Orocopia schist and associated rocks of southeastern California; relative roles of erosion, synsubduction tectonic denudation, and middle Cenozoic extension: *Geological Society of America Special Paper*, **419**, 1-37.

James, E. W., Kimbrough, D. L., and Mattinson, J. M., 1993, Evaluation of displacements of pre-Tertiary rocks on the northern San Andreas Fault using U-Pb zircon dating, initial Sr, and common Pb isotopic ratios: *Memoir - Geological Society of America*, **178**, 257-271.

Kanter, L. R., and McWilliams, M. O., 1982, Rotation of the southernmost Sierra Nevada, California: *Journal of Geophysical Research*, **87**, 3819-3830.

Kidder, S., Ducea, M., Gehrels, G. E., Patchett, P. J., and Vervoort, J., 2003, Tectonic and magmatic development of the Salinian Coast Ridge Belt, California: *Tectonics*, **22**, doi:10.1029/2002TC001409.

Kidder, S., and Ducea, M. N., 2006, High temperatures and inverted metamorphism in the schist of Sierra de Salinas, California: *Earth and Planetary Science Letters*, **241**, 422-437.

Kistler, R. W., and Champion, D. E., 2001, Rb-Sr whole-rock and mineral ages, K-Ar, 40Ar/39Ar, and U-Pb mineral ages, and strontium, lead, neodymium, and oxygen isotopic compositions for granitic rocks from the Salinian Composite Terrane, California: *U.S. Geological Survey Open File Report* 01-453, 84 pp.

Kruhl, J. H., 1998, Prism- and basal-plane parallel subgrain boundaries in quartz: a microstructural geothermobarometer: Reply, *Journal of Metamorphic Geology*, **16**, 142-146.

Law, R. D., Searle, M. P., and Simpson, R. L., 2004, Strain, deformation temperatures and vorticity of flow at the top of the Greater Himalayan Slab, Everest Massif, Tibet: *Journal of the Geological Society, London*, **161**, 305-320.

Leventhal, J. A., Reid, M. R., Montana, A., and Holden, P., 1995, Mesozoic invasion of crust by MORB-source asthenospheric magmas, U.S. Cordilleran interior: *Geology*, **23**, 399-402.

Li, Y.-G., Henyey, T. L., and Silver, L. T., 1992, Aspects of the crustal structure of the western Mojave Desert, California, from seismic reflection and gravity data: *Journal of Geophysical Research*, **97**, 8805-8816.

Lisle, R. J., 1985, *Geological strain analysis; a manual for the Rf/phi technique*, 99 pp., Pergamon, New York.

Lister, G. S., 1977, Discussion; crossed-girdle c-axis fabrics in quartzites plastically deformed by plane strain and progressive simple shear: *Tectonophysics*, **39**, 51-54.

Lister, G. S., and Snoke, A. W., 1984, S-C mylonites: *Journal of Structural Geology*, **6**, 617-638.

Liu, L., Spasojevic, S., and Gurnis, M., 2008, Reconstructing Farallon Plate subduction beneath North America back to the Late Cretaceous: *Science*, **322**, 934-938, doi: 910.1126/science.1162921.

Liu, L., Gurnis, M., Seton, M., Saleeby, J., Müller, R. D., and Jackson, J. M., 2010, The role of oceanic plateau subduction in the Laramide orogeny: *Nature Geoscience*, doi: 10.1038/NGEO829.

Luffi, P., Saleeby, J. B., Lee, C. A., and Ducea, M. N., 2009, Lithospheric mantle duplex beneath the central Mojave Desert revealed by xenoliths from Dish Hill, California: *Journal of Geophysical Research,* **114**, doi:10.1029/2008JB005906.

Mahéo, G., Saleeby, J., Saleeby, Z., and Farley, K.A., 2009, Tectonic control on southern Sierra Nevada topography, California: *Tectonics*, **28**, doi:10.1029/2008TC002340.

Malin, P. E., Goodman, E. D., Henyey, T. L., Li, Y. G., Okaya, D. A., and Saleeby, J. B., 1995, Significance of seismic reflections beneath a tilted exposure of deep continental crust, Tehachapi Mountains, California: *Journal of Geophysical Research*, **100**, 2069-2087, doi: 2010.1029/2094JB02127.

Mattinson, J. M., 1978, Age, origin, and thermal histories of some plutonic rocks from the Salinian Block of California, *Contributions to Mineralogy and Petrology*, **67**, 233-245.

May, D. J., 1989, Late Cretaceous intra-arc thrusting in Southern California: *Tectonics*, **8**, 1159-1173.

McNulty, B., and Farber, D., 2002, Active detachment faulting above the Peruvian flat slab: *Geology*, **30**, 567-570.

McWilliams, M., and Li, Y., 1983, A paleomagnetic test of the Sierran Orocline hypothesis: *Eos, Transactions, American Geophysical Union*, **64**, 686.

McWilliams, M., and Li, Y., 1985, Oroclinal bending of the southern Sierra Nevada Batholith: *Science*, **230**, 172-175.

Miller, R. B., Paterson, S. R., DeBari, S. M., and Whitney, D. L., 2000, North Cascades Cretaceous crustal section: Changing kinematics, rheology, metamorphism, pluton emplacement and petrogenesis from 0 to 40 km depth, in *Guidebook for geological field trips in southwestern British Columbia and northern Washington*, edited by G.J. Woodsworth *et al*., 229–278, Geological Association of Canada, Vancouver.

Nadin, E. S., and Saleeby, J. B., 2008, Disruption of regional primary structure of the Sierra Nevada Batholith by the Kern Canyon fault system, California: *Geological Society of America Special Paper*, **438**, 429-454.

Nadin, E.S., and Saleeby, J., 2010, Quaternary Scarps of the Kern Canyon Fault System, Sierra Nevada, CA: *Geological Society of America Bulletin*, **122**, 1671-1685.

Naeser, N. D., Naeser, C. W., and McCulloh, T. H., 1990, Thermal history of rocks in southern San Joaquin Valley, California; evidence from fission-track analysis: *AAPG Bulletin*, **74**, 13-29.

Nourse, J. A., 1989, Geological evolution of two crustal scale shear zones; Part I, The Rand thrust complex, northwestern Mojave Desert, California; Part II, The Magdalena metamorphic core complex, north central Sonora, Mexico, Ph.D. thesis, California Institute of Technology, Pasadena, 394 pp.

Oyarzabal, F. R., Jacobson, C. E., and Haxel, G. B., 1997, Extensional reactivation of the Chocolate Mountains subduction thrust in the Gavilan Hills of southeastern California:

Tectonics, **16**, 650-661.

Passchier, C. W., 1988, Analysis of deformation paths in shear zones: *Geologische Rundschau*, **77**, 309-318.

Passchier, C. W., and Trouw, R. A. J., 2005, *Microtectonics*, 2 ed., 366 pp., Springer, Berlin.

Peacock, S. M., 1987, Thermal effects of metamorphic fluids in subduction zones: *Geology*, **15**, 1057-1060.

Pennacchioni, G., Di Toro, G., and Mancktelow, N. S., 2001, Strain-insensitive preferred orientation of porphyroclasts in Mont Mary mylonites: *Journal of Structural Geology*, **23**, 1281-1298.

Pickett, D. A., and Saleeby, J. B., 1993, Thermobarometric constraints on the depth of exposure and conditions of plutonism and metamorphism at deep levels of the Sierra Nevada Batholith, Tehachapi Mountains, California: *Journal of Geophysical Research*, **98**, 609-629.

Pickett, D. A., and Saleeby, J. B., 1994, Nd, Sr, and Pb isotopic characteristics of Cretaceous intrusive rocks from deep levels of the Sierra Nevada Batholith, Tehachapi Mountains, California: *Contributions to Mineralogy and Petrology*, **118**, 198-215, doi: 110.1007/BF01052869.

Platt, J. P., 1986, Dynamics of orogenic wedges and the uplift of high-pressure metamorphic rocks: *Geological Society of America Bulletin*, **97**, 1037-1053.

Plescia, J. B., Calderone, G. J., and Snee, L. W., 1994, Paleomagnetic analysis of Miocene basalt flows in the Tehachapi Mountains, California: *U.S. Geological Survey Bulletin*, *2100*, 11 pp.

Postlethwaite, C. E., 1983, The structural geology of the western Rand Mountains, northwestern Mojave Desert, California, M.S. thesis, Iowa State University, Ames, 91 pp.

Postlethwaite, C. E., and Jacobson, C. E., 1987, Early history and reactivation of the Rand Thrust, Southern California: *Journal of Structural Geology*, **9**, 195-205, doi: 110.1016/0191-8141(1087)90025-90023.

Powell, R. E., 1993, Balanced palinspastic reconstruction of pre-late Cenozoic paleogeology, Southern California; geologic and kinematic constraints on evolution of the San Andreas fault system: *Memoir - Geological Society of America*, **178**, 1-106.

Ramsay, J. G., 1967, *Folding and fracturing of rocks*, 568 pp., McGraw-Hill, New York.

Reitz, A., 1986, The geology and petrology of the northern San Emigdio plutonic complex, San Emigdio Mountains, Southern California, M.A. thesis, University of California, Santa Barbara, 80 pp.

Ring, U., Brandon, M. T., Willett, S. D., and Lister, G. S., 1999, Exhumation processes: *Geological Society [London] Special Publications*, **154**, 1-27.

Ross, D. C., 1976, Reconnaissance geologic map of pre-Cenozoic basement rocks, northern Santa Lucia Range, Monterey County, California: *U.S. Geological Survey Miscellaneous Field Studies Map* MF-750, 7 pp.

Ross, D. C., 1986, Basement-rock correlations across the White Wolf-Breckenridge-southern Kern Canyon fault zone, southern Sierra Nevada, California: *U.S. Geological Survey Bulletin* 1651, 25 pp.

Ross, D. C., 1989, The metamorphic and plutonic rocks of the southernmost Sierra Nevada, California, and their tectonic framework: *U.S. Geological Survey Professional Paper*

1381, 159 pp.

Ross, T. M., Luyendyk, B. P., and Haston, R. B., 1989, Paleomagnetic evidence for Neogene clockwise tectonic rotations in the central Mojave Desert, California: *Geology*, **17**, 470-473.

Ruppert, S., Fliedner, M. M., and Zandt, G., 1998, Thin crust and active upper mantle beneath the southern Sierra Nevada in the Western United States: *Tectonophysics*, **286**, 237-252, doi: 210.1016/S0040-1951(1097)00268-00260.

Saleeby, J., 2003, Segmentation of the Laramide slab; evidence from the southern Sierra Nevada region: *Geological Society of America Bulletin*, **115**, 655-668.

Saleeby, J. B., Sams, D. B., and Kistler, R. W., 1987, U/Pb zircon, strontium, and oxygen isotopic and geochronological study of the southernmost Sierra Nevada Batholith, California: *Journal of Geophysical Research*, **92**, 10,443-10,466.

Saleeby, J. B., Ducea, M. N., and Clemens-Knott, D., 2003, Production and loss of high-density batholithic root, southern Sierra Nevada, California: *Tectonics*, **22**, doi: 10.1029/2002TC001374.

Saleeby, J., Farley, K. A., Kistler, R. W., and Fleck, R. J., 2007, Thermal evolution and exhumation of deep-level batholithic exposures, southernmost Sierra Nevada, California: *Geological Society of America Special Paper*, **419**, 39-66.

Saleeby, J., Saleeby, Z., Nadin, E., and Mahéo, G., 2009, Step-over in the structure controlling the regional west tilt of the Sierra Nevada microplate: eastern escarpment system to Kern Canyon system: *International Geology Review*, **51**, 634-669, doi: 10.1080/00206810902867773.

Schmid, S. M., and Casey, M., 1986, Complete fabric analysis of some commonly observed

quartz c-axis patterns: *Geophysical Monograph*, **36**, 263-286.

Searle, M. P., Simpson, R. L., Law, R. D., Parrish, R. R., and Waters, D. J., 2003, The structural geometry, metamorphic and magmatic evolution of the Everest Massif, High Himalaya of Nepal-South Tibet: *Journal of the Geological Society, London*, **160**, 345-366.

Sharry, J., 1981, The geology of the western Tehachapi Mountains, California, Ph.D. thesis, Massachusetts Institute of Technology, Cambridge, 215 pp.

Simpson, C., 1990, Microstructural evidence for northeastward movement on the Chocolate Mountains fault zone, southeastern California: *Journal of Geophysical Research*, **95**, 529-537.

ten Grotenhuis, S. M., Trouw, R. A. J., and Passchier, C. W., 2003, Evolution of mica fish in mylonitic rocks: *Tectonophysics*, **372**, 1-21.

Vanderhaeghe, O., Teyssier, C., and Wysoczanski, R., 1999, Structural and geochronological constraints on the role of partial melting during the formation of the Shuswap metamorphic core complex at the latitude of the Thor-Odin dome, British Columbia: *Canadian Journal of Earth Sciences*, **36**, 917–943, doi: 10.1139/cjes-36-6-917.

Vargo, J. M., 1972, Structural geology of a portion of the eastern Rand Mountains, Kern and San Bernardino counties, California, M.A. thesis, University of Southern California, Los Angeles, 117 pp.

Wallis, S., 1992, Vorticity analysis in a metachert from the Sanbagawa Belt, SW Japan: *Journal of Structural Geology*, **14**, 271-280.

Wallis, S., 1995, Vorticity analysis and recognition of ductile extension in the Sanbagawa

Belt, SW Japan: *Journal of Structural Geology*, **17**, 1077-1093.

Wells, M. L., Beyene, M. A., Spell, T. L., Kula, J. L., Miller, D. M., and Zanetti, K. A., 2005, The Pinto shear zone; a Laramide synconvergent extensional shear zone in the Mojave Desert region of the Southwestern United States: *Journal of Structural Geology*, **27**, 1697-1720.

Wells, M. L., and Hoisch, T. D., 2008, The role of mantle delamination in widespread Late Cretaceous extension and magmatism in the Cordilleran Orogen, western United States: *Geological Society of America Bulletin*, **120**, 515-530, doi: 510.1130/B26006.26001.

Wernicke, B., 1992, Cenozoic extensional tectonics of the U.S. Cordillera, in: *The Cordilleran Orogen: Conterminous U.S., The Geology of North America, G-3: Geological Society of America*, edited by B. C. Burchfiel, *et al*., 553-582, Boulder, Colorado.

Wilson, E. L., and Prothero, D. R., 1997, Magnetic stratigraphy and tectonic rotations of the middle-upper Miocene "Santa Margarita" and Chanac formations, north-central Transverse Ranges, California: *Book - Pacific Section, Society of Economic Paleontologists and Mineralogists*, **82**, 35-48.

Wood, D. J., 1997, Geology of the eastern Tehachapi Mountains and Late Cretaceous-early Cenozoic tectonics of the southern Sierra Nevada region, Kern County, California, Ph.D. thesis, California Institute of Technology, Pasadena, 287 pp.

Wood, D. J., and Saleeby, J. B., 1998, Late Cretaceous-Paleocene extensional collapse and disaggregation of the southernmost Sierra Nevada Batholith: *International Geology Review*, **39**, 973-1009.

Xypolias, P., 2009, Some new aspects of kinematic vorticity analysis in naturally deformed

quartzites: *Journal of Structural Geology*, **31**, 3-10.

Yan, Z., Clayton, R. W., and Saleeby, J., 2005, Seismic refraction evidence for steep faults cutting highly attenuated continental basement in the central Transverse Ranges, California: *Geophysical Journal International*, **160**, 651-666.

Yin, A., 2002, Passive-roof thrust model for the emplacement of the Pelona-Orocopia schist in Southern California, United States: *Geology*, **30**, 183-186.

CHAPTER 3

Metamorphic evolution, partial melting, and rapid exhumation above an ancient flat slab: Insights from the San Emigdio Schist, southern California

Alan D. Chapman,[1] Peter Luffi,[2] Jason B. Saleeby[1] and Sierra Petersen[3]

[1]*Division of Geological and Planetary Sciences, California Institute of Technology, Pasadena, California, USA*

[2]*Department of Earth Science, Rice University, Houston, Texas, USA*

[3]*Department of Earth and Planetary Sciences, Harvard University, Cambridge, Massachusetts, USA*

Published in *Journal of Metamorphic Geology*

MINERAL ABBREVIATIONS

Act, actinolite; alm, almandine; And, andalusite; Bt, biotite; Chl, chlorite; Cpx, clinopyroxene; Crd, cordierite; Cum, cummingtonite; Ep, epidote; Fsp, feldspar; Grt, garnet; Gln, glaucophane; Gr, graphite; grs, grossular; Hbl, hornblende; Ilm, Ilmenite; Kfs, K-feldspar; Ky, kyanite; Lws, lawsonite; Ms, muscovite; Omp, omphacite; Opx, orthopyroxene; Pg, paragonite; Pl, plagioclase; prp, pyrope; Qz, quartz; Rt, rutile; Sil, sillimanite; sps, spessartine; Spn, sphene; St, staurolite; Zo, zoisite.

ABSTRACT

The San Emigdio and related Pelona, Orocopia, Rand, and Sierra de Salinas schists of southern California were underplated beneath the southern Sierra Nevada batholith and adjacent southern California batholith along a shallow segment of the subducting Farallon

plate in Late Cretaceous to early Tertiary time. These subduction accretion assemblages represent a regional, deeply exhumed, shallowly dipping domain from an ancient slab segmentation system and record the complete life cycle of the segmentation process from initial flattening and compression to final extensional collapse. An important unresolved question regarding shallow subduction zones concerns how the thermal structure evolves during the slab flattening process. We present new field relations, thermobarometry, thermodynamic modelling, and garnet diffusion modelling that speak to this issue and elucidate the tectonics of underplating and exhumation of the San Emigdio Schist. We document an upsection increase in peak temperature (i.e., inverted metamorphism), from 590 to 700 ˚C, peak pressures ranging from 8.5 to 11.1 kbar, limited partial melting, microstructural evidence for large seismic events, rapid cooling (825 to 380 ˚C / Myr) from peak conditions, and an "out and back" *P-T* path. While inverted metamorphism is a characteristic feature of southern California schists, the presence of partial melt and high temperatures (> 650 ˚C) are restricted to exposures with maximum depositional ages between 80 to 90 Ma. Progressive cooling and tectonic underplating beneath an initially hot upper plate following the onset of shallow subduction provides a working hypothesis explaining high temperatures and partial melting in San Emigdio and Sierra de Salinas schists, inverted metamorphism in the schist as a whole, and the observed *P-T* trajectory calculated from the San Emigdio body. Lower temperatures in Pelona, Orocopia, and Rand schists are likewise explained in the context of this overarching model. These results are consistent with an inferred tectonic evolution from shallow subduction beneath the then recently active Late Cretaceous arc to exhumation by rapid trench-directed channelized extrusion in the subducted schist.

1. INTRODUCTION

Crustal rocks are subducted along a variety of trajectories into the mantle. For instance, along-strike variations in slab dip have resulted in the concomitant formation of the high-pressure/low-temperature Franciscan complex and the high-pressure/moderate- to high-temperature Pelona, Orocopia, Rand, San Emigdio, and Sierra de Salinas schist (collectively referred to as "the southern California schist") terrane in California (Grove *et al*., 2003; Wakabayashi and Dumitru, 2007) (Figure 3.1). While the Middle Mesozoic to early Tertiary Franciscan complex is thought to be the product of moderately dipping subduction, the Late Cretaceous to early Tertiary southern California schist was underplated directly beneath the southern Sierra Nevada batholith (SNB) and the once contiguous southern California batholith (granitoids of the Mojave-Salinia region) along a comparatively shallowly dipping segment of the subducting Farallon plate (Jacobson *et al*., 2007 and references therein). The deposition, subduction, and structural ascent of the schist is temporally and spatially associated in plate reconstructions with the subduction of the eastern conjugate massif to the Shatsky Rise, a large igneous province (LIP) approximately 2,000 km southeast of Japan (Saleeby, 2003; Liu *et al*., 2008; 2010). Subduction of the LIP is hypothesized to have driven slab flattening and upper plate extension (Saleeby *et al*., 2007; Chapman *et al*., 2010) somewhat analogous to the ongoing subduction of the Nazca Ridge and trench-directed detachment faulting above the Peruvian flat slab segment (Gutscher *et al*., 2000; McNulty and Farber, 2002).

An along strike inflection zone varying from shallower to steeper slab dips northwestward, approximately centered along the trace of the superimposed Garlock fault (Saleeby, 2003), separates the schist and Franciscan subduction accretion assemblages,

Figure 3.1. Geologic map of southern California basement rocks based on USGS Open-File Report 2005-1305 (Ludington *et al*., 2007). Abbreviations: EF, East Fork (San Gabriel Mountains); GF, Garlock fault; GH, Gavilan Hills; GV, Great Valley; KCF, Kern Canyon fault; MD, Mojave Desert; O, Orocopia Mountains; PRB, Peninsular Ranges batholith; PR, Portal Ridge; pKCF, proto-Kern Canyon fault; R, Rand Mountains; RRF, Reliz-Rinconada fault; SAF, San Andreas fault; SE, San Emigdio Mountains; SC, Santa Catalina Island; SNB, Sierra Nevada batholith; SP, Sierra Pelona; SS, Sierra de Salinas; TC, Tehachapi Mountains; WWF, White Wolf fault.

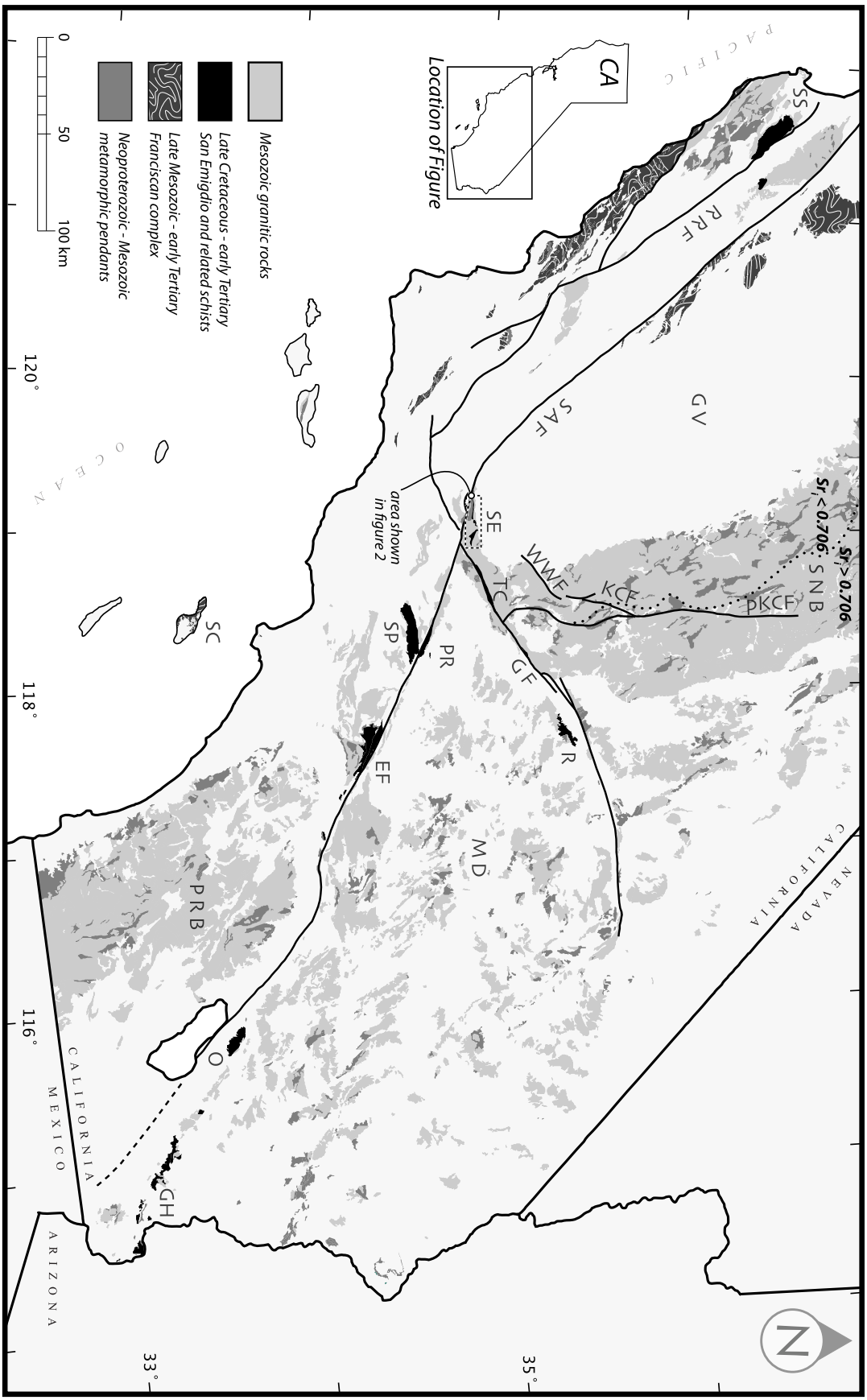
Mesozoic granitic rocks
Late Cretaceous - early Tertiary San Emigdio and related schists
Late Mesozoic - early Tertiary Franciscan complex
Neoproterozoic - Mesozoic metamorphic pendants
0
50
100 km
CA
Location of Figure
PACIFIC
OCEAN
SS
RRF
SAF
GV
SE
area shown in figure 2
WWF
KCF
PKCF
TC
SNB
Sr=0.706
Sr=0.706
SP
PR
GF
R
EF
MD
PRB
SC
O
GH
CALIFORNIA
MEXICO
NEVADA
CALIFORNIA
ARIZONA
120°
118°
116°
35°
33°
N

respectively (Figure 3.1). Deep-crustal batholithic exposures, subjacent schist, and an intervening shear zone (the Rand fault and Salinas shear zone) of the southern Sierra Nevada, the adjacent northwest Mojave Desert, and the northern Salinia terrane (prior to Neogene northward translation) offer a unique opportunity to observe the inflection zone above a segmented slab. Furthermore, this package records a complete life cycle of the segmentation process with initial flattening resulting in the upper plate mantle lithosphere removal coincident with compressional deformation, rock uplift and denudation, followed abruptly by extensional collapse, all occurring in series as subduction progressed (Saleeby *et al*., 2007). An important unresolved question regarding shallow subduction zones concerns how the thermal structure evolves during the slab flattening process (English *et al*., 2003; Kidder and Ducea, 2006). We address this issue through petrogenetic characterization of the earliest formed schist in the San Emigdio Mountains (Grove *et al*., 2003), and comparison of this schist with later formed Pelona, Orocopia, Rand, and Sierra de Salinas members.

Metasandstone and metabasaltic rocks of the San Emigdio Schist are distinguished from exposures of related Pelona, Orocopia, Rand, and Sierra de Salinas schists by the nearly ubiquitous presence of garnet porphyroblasts. Growth zonation in these garnets is well-preserved, allowing for straightforward recovery of a portion of the pressure-temperature (*P*-*T*) history of the shallowly subducted schist (e.g. Spear and Selverstone, 1983; Vance and Mahar, 1998; Escuder-Viruete *et al*., 2000). In addition, some garnets experienced cataclastic deformation. Subsequent overgrowth along broken margins resulted in natural diffusion couples from which the duration of metamorphic processes may be derived (e.g. Chakraborty and Ganguly, 1991; Ganguly *et al*., 1996; Dachs and Proyer, 2002; Ganguly, 2002; Vielzeuf *et al*., 2007). We present here new field relations,

thermobarometry, thermodynamic modelling, and garnet diffusion modelling that constrain the *P-T* history and the tectonics of underplating and exhumation of the San Emigdio Schist. These observations constrain the physical conditions once present above the Farallon flat slab segment and further our understanding of the tectonics of slab flattening and schist underthrusting and exhumation in the southern California region.

2. GEOLOGIC BACKGROUND

The southern California schist has long attracted interest due to its position structurally beneath older Mesozoic batholithic rocks throughout southern California (Ehlig, 1981; Graham and England, 1976; Haxel and Dillon, 1978; Jacobson, 1983; 1995; Jacobson *et al*., 1988; 2007; in press). Most workers agree that the deposition and emplacement of the schist occurred during an episode of shallow subduction related to the Laramide orogeny (Jacobson *et al*., 2007 and references therein). Geochronologic, thermochronometric, and thermobarometric studies indicate a temporal link between schist unroofing and major upper crustal extension (Pickett and Saleeby, 1993; Jacobson, 1995; Kistler and Champion, 2001; Barth *et al*., 2003; Grove *et al*., 2003; Kidder *et al*., 2003; Kidder and Ducea, 2006; Saleeby *et al*., 2007). Existing models for the exhumation of the northern (i.e., Rand and Sierra de Salinas) and southern (i.e., Pelona and Orocopia) schists invoke return flow (Oyarzabal *et al*., 1997; Jacobson *et al*., 2002; Saleeby, 2003; Saleeby *et al*., 2007; Chapman *et al*., 2010), isostatically driven uplift (Jacobson *et al*., 2007), upper plate normal faulting (e.g. Jacobson *et al*., 1996), erosion (Yin, 2002), or some combination thereof. In the San Emigdio and Tehachapi Mountains, trench-directed channelized extrusion in the subducted schist is

hypothesized to have led to collapse of the upper plate between ca. 98 and 86 Ma (Saleeby *et al*., 2007; Chapman *et al*., 2010).

Uplift and folding of basement rocks and sedimentary cover strata in the San Emigdio Mountains was controlled by Pliocene-Quaternary north-south compression between the big bend in the San Andreas fault and the Pleito fault zone (Dibblee, 1986) (Figure 3.2). A semi-continuous belt of southern California schist constitutes the base of the tectonic section in the San Emigdio and Tehachapi Mountains (referred to as "Pelona Schist" by Sharry, 1981; "Rand Schist" by Grove *et al*., 2003; Saleeby *et al*., 2007; Chapman *et al*., 2010; and "San Emigdio Schist" by Jacobson *et al*., in press). We follow the usage of Jacobson *et al*. (2011) and present evidence here that the San Emigdio Schist is distinct from other southern California members on the basis of geography, petrology, and detrital zircon age distribution.

The Tehachapi-San Emigdio (TSE) complex structurally overlies the San Emigdio Schist and consists of a series of Early to mid-Cretaceous deep level plutonic rocks and associated pre-Cretaceous framework metamorphic rocks (Saleeby *et al*., 2007; Chapman *et al*., 2010). The San Emigdio Schist is juxtaposed against the TSE complex along the remains of a locally ductile to brittle low-angle detachment fault system that likely correlates with the type Rand fault exposed in the Rand Mountains (Postlethwaite and Jacobson, 1987). During Pliocene-Quaternary compression, the Rand fault in the San Emigdio Mountains was largely folded with a major south-dipping thrust fault cutting across the folded structural section. As a result, the tectonostratigraphy is inverted with the San Emigdio Schist in the hanging wall and the TSE complex in the footwall. Decompression of the San Emigdio Schist from deep- to mid-crustal levels is well constrained at 91 to 86 Ma

Figure 3.2. (a) Simplified geologic map of the San Emigdio Mountains. Geology from Ross (1989), Dibblee (1973), Chapman *et al*. (2010), and this study. Mafic schist shown in black. Black and white circles show locations of thermobarometric determinations from upper plate and San Emigdio Schist, respectively. Metamorphic pendant abbreviations: GC, Grapevine Canyon (north of Rand fault); SC, Salt Creek (south of Pastoria fault). Other abbreviations as in Figure 3.1. (b) Graphical representation of thermometric data along western, central, and eastern transects.

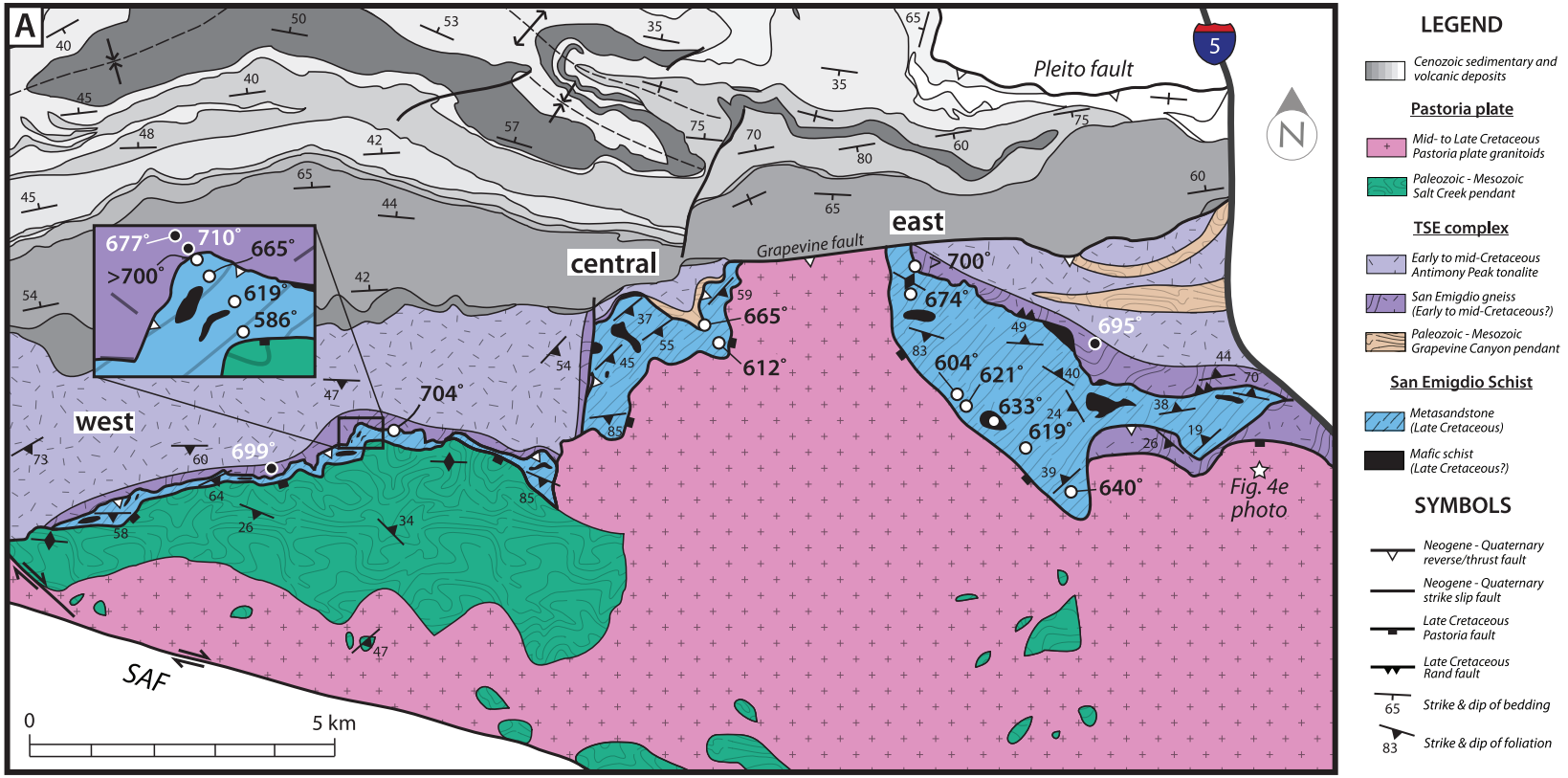
A
Pleito fault
Grapevine fault
central
east
west
677°
710°
665°
>700°
619°
586°
704°
699°
665°
612°
700°
674°
695°
604°
621°
633°
619°
640°
Fig. 4e photo
SAF
0
5 km
N
5
LEGEND
Cenozoic sedimentary and volcanic deposits
Pastoria plate
Mid- to Late Cretaceous Pastoria plate granitoids
Paleozoic - Mesozoic Salt Creek pendant
TSE complex
Early to mid-Cretaceous Antimony Peak tonalite
San Emigdio gneiss (Early to mid-Cretaceous?)
Paleozoic - Mesozoic Grapevine Canyon pendant
San Emigdio Schist
Metasandstone (Late Cretaceous)
Mafic schist (Late Cretaceous?)
SYMBOLS
Neogene - Quaternary reverse/thrust fault
Neogene - Quaternary strike slip fault
Late Cretaceous Pastoria fault
Late Cretaceous Rand fault
Strike & dip of bedding
Strike & dip of foliation

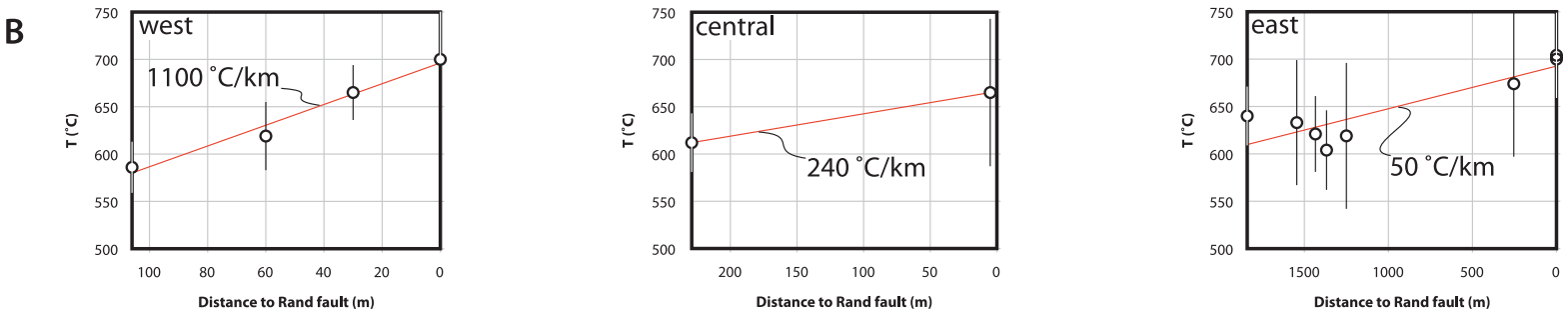
B
west
1100 °C/km
central
240 °C/km
east
50 °C/km
T (°C)
Distance to Rand fault (m)

(Grove *et al*., 2003) and is linked to extensional deformation along the Rand fault (Saleeby *et al*., 2007). The TSE complex structurally overlies the Pastoria plate along the Late Cretaceous to Eocene (?) (Wood and Saleeby, 1997) south-dipping Pastoria detachment. The Pastoria plate is composed of relatively shallow level (3 to 4 kbar) eastern SNB affinity granitoids and metamorphic pendant rocks (modified after Crowell, 1952).

3. RESULTS

3.1. Metamorphic petrology

3.1.1. Tehachapi-San Emigdio complex

The TSE complex in the upper plate of the Rand fault in San Emigdio Mountains consists of at least two distinct upper amphibolite facies orthogneiss units (Figure 3.2) and one paragneiss unit. These include 1) the 131 Ma Antimony Peak tonalite (James, 1986), 2) an undated hornblende quartz diorite gneiss that likely correlates with hornblende gabbroids of the 99 to 105 Ma intrusive suite of Bear Valley (Saleeby *et al*., 1987; Pickett and Saleeby, 1993; Saleeby *et al*., 2007), and 3) the western continuation of the Grapevine Canyon paragneiss (Pickett and Saleeby, 1993; 1994).

The Antimony Peak body is a medium- to coarse-grained massive to penetratively foliated tonalite that contains mainly plagioclase, quartz, hornblende, and K-feldspar, with minor amounts of garnet, biotite, epidote, apatite, sphene, and ilmenite (Figure 3.3a). Where hypidiomorphic granular (igneous) textures are not overprinted by metamorphic foliation, the epidote occurs as subhedral replacement products of embayed hornblende and retains distinct core and rim regions, consistent with a magmatic origin. Original petrographic

Figure 3.3. Photographs of petrologic features in the TSE complex. (a) Magmatic epidote in Antimony Peak tonalite; ppl. (b) Field photograph showing textural relations of garnet formation in San Emigdio gneiss. Abbreviations: ppl, plane-polarized light.

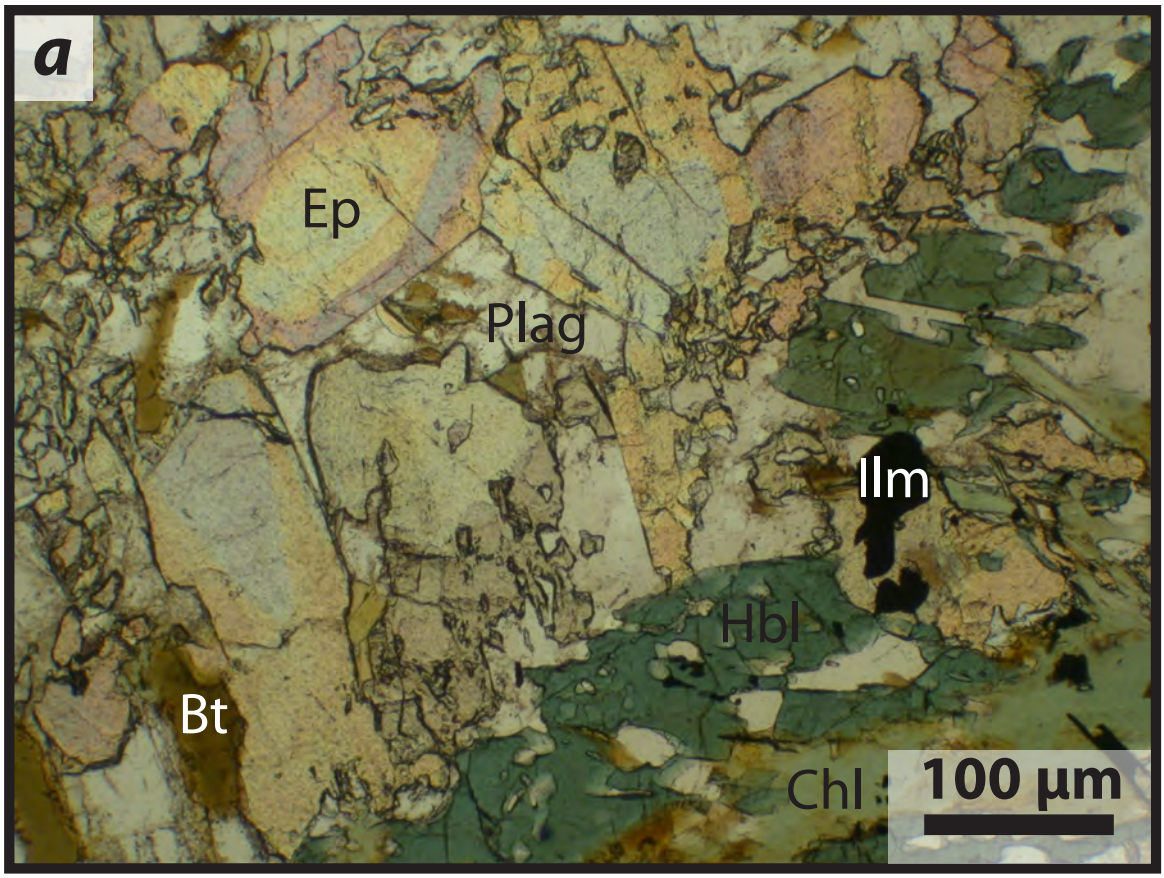
a
Ep
Plag
Ilm
Hbl
Bt
Chl
100 µm

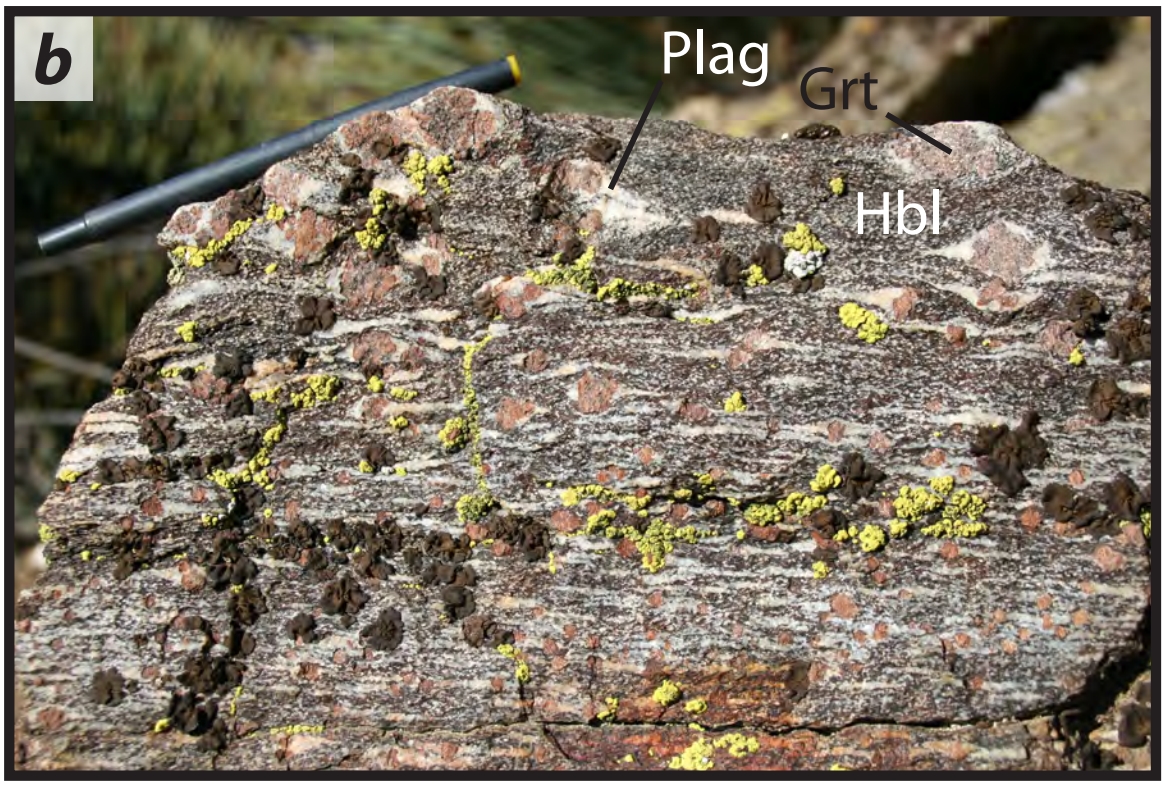
b
Plag
Grt
Hbl

relationships are locally obscured by extensive seritization and chloritization. The second unit is informally named the San Emigdio quartz diorite orthogneiss and abbreviated the San Emigdio gneiss (Figure 3.3b). The San Emigdio gneiss lies structurally above the Rand fault, and consequently exhibits a strongly attenuated structural fabric characterized by anastomosing ductile to brittle shear zones. We consider the San Emigdio gneiss a tectonic unit that consists mainly of strongly sheared quartz diorite: hornblende + plagioclase + quartz + ilmenite ± coarse subsolidus garnet ± sphene ± K-feldspar, with lesser amounts of deformed tonalite and trondhjemite. We focus upper plate thermobarometric work primarily on the San Emigdio gneiss, as this unit lies in structural contact with the San Emigdio Schist.

3.1.2. San Emigdio Schist

The San Emigdio Schist consists of roughly 80% interlayered metapsammite and quartzite ("metasandstone") commingled with 15% metabasalt and 5% ultramafic (talc-actinolite) schist (Figure 3.4). The metasandstone member of the schist is characterized by the well-preserved peak mineral paragenesis garnet + plagioclase + biotite + quartz ± muscovite ± kyanite, which defines the D1 foliation, a weakly crenulated fabric with lesser amounts of rutile, ilmenite, and graphite. In addition, mineral assemblages and textures vary with structural depth. Highly altered kyanite grains and chloritized kyanite pseudomorphs prevalent at low structural levels of the schist are absent at higher structural levels (Figure 3.4). Also, as the Rand fault is approached from low structural levels, 1) garnet size and abundance increases, 2) plagioclase changes from untwinned, graphitic poikiloblasts to

Figure 3.4. Photographs of structural and petrologic features in metasandstone (a, b, f, and g) and mafic (c, d, and h) San Emigdio schist. (a) Altered kyanite porphyroblast surrounded by graphitic plagioclase poikiloblasts; xpl. (b) Broken garnet porphyroblast exhibiting two sets of fractures corresponding to D1 (F1) and D2 (F2) episodes. Note D2 minerals between garnet fragments; ppl. (c) Coexisting diopsidic clinopyroxene and hornblende at high structural levels; ppl. (d) Epidote relic; ppl. (e) View north from Digier Canyon (star in Figure 3.2) of commingled metasandstone (not labeled), quartzite (q), mafic (mb), and ultramafic (um) schist. Kses, San Emigdio Schist; Kseg, San Emigdio gneiss; Qls, landslide deposit. Field of view approximately 1 km long. (f) Quartzofeldspathic veins transposed into D1 foliation. (g) Coarse quartz + feldspar melt vein. (h) Talc-actinolite lens within mafic schist. Abbreviations: ppl, plane-polarized light; xpl, cross-polarized light.

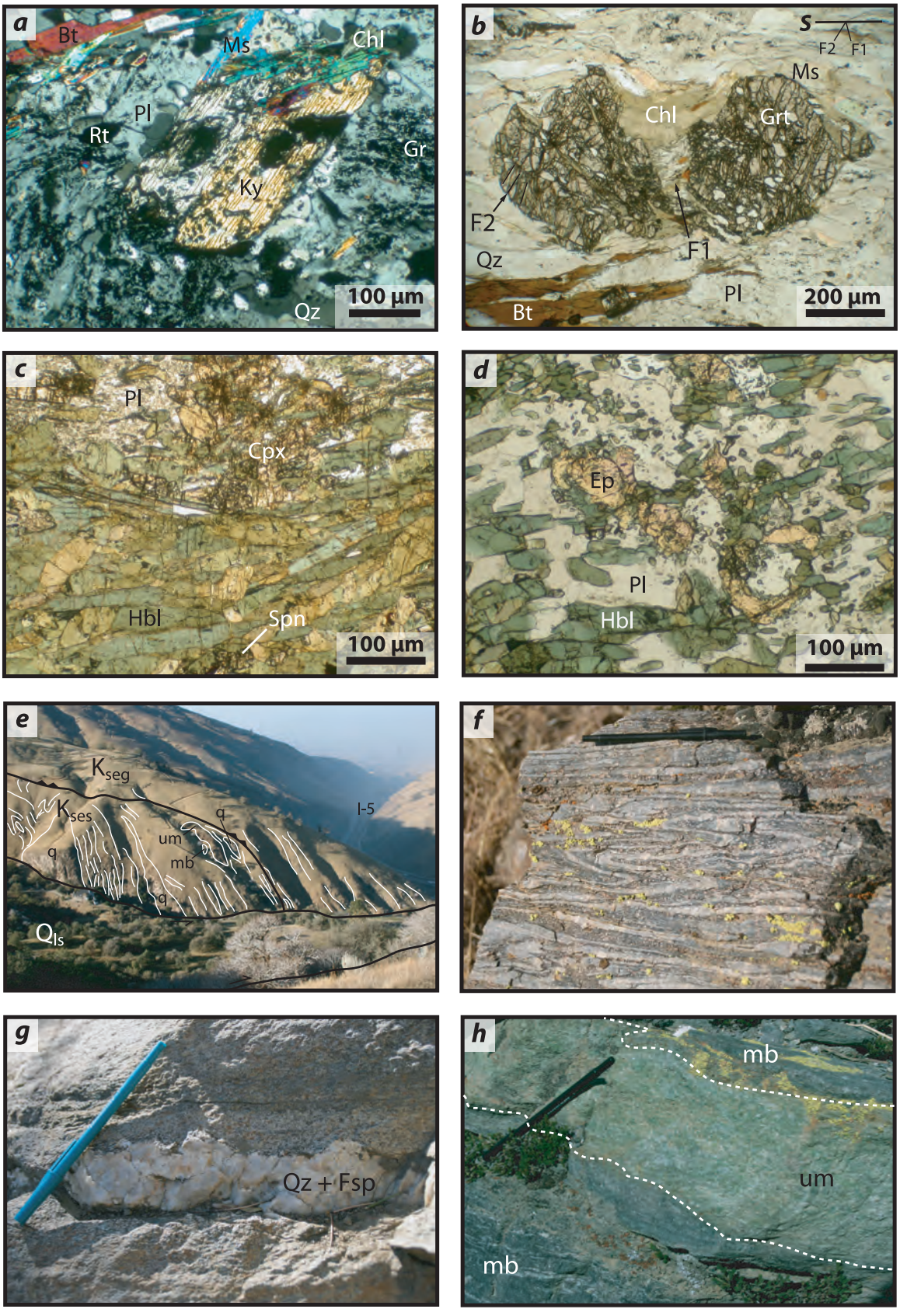
a
Bt
Ms
Chl
Pl
Rt
Gr
Ky
Qz
100 µm
b
S
F2
F1
Ms
Chl
Grt
F2
F1
Qz
Pl
Bt
200 µm
c
Pl
Cpx
Hbl
Spn
100 µm
d
Ep
Pl
Hbl
100 µm
e
Kseg
Kses
q
I-5
um
mb
Qls
f
g
Qz + Fsp
h
mb
um
mb

twinned, graphite-free and inclusion-poor porphyroblasts, 3) primary muscovite disappears, 4) the overall grain size increases, 5) macroscopic stromatic leucosomes and melanosomes develop within the D1 foliation, and 6) ductilely deformed quartzofeldspathic (milky quartz + plagioclase ± garnet ± muscovite) veins become more common and more strongly transposed along the D1 foliation (Figure 3.4). Observations 5 and 6 suggest that fluid-saturated partial melting occurred during the D1 episode. A less pervasive fabric, D2, is localized within mm-scale noncoaxial shear zones that truncate D1 mineral assemblages and anatectic textures and contain retrograde clinozoisite, chlorite, celadonitic muscovite, tourmaline, and highly sheared minerals belonging to the D1 assemblage. Finally, clinozoisite, while only associated with the D2 assemblage at moderate to high structural levels, is a rare D1 phase at deep levels (> 1000 m). Therefore, in contrast to high structural levels where amphibolite facies conditions were reached and limited partial melting may have occurred, peak conditions probably did not exceed epidote amphibolite facies at low structural levels. These observations support thermobarometric work (detailed below) indicating the presence of an inverted metamorphic field gradient.

The metabasalt member, referred to here as “mafic schist,” also records multiple distinct phases of deformation and metamorphism. Epidote relics characterize the earliest preserved phase, occurring as isolated, 2 to 5 mm long optically continuous inclusions in plagioclase, commonly exhibiting concentric birefringence zonation (Figure 3.4). Narrow rims of opaque minerals and small (25 to 50 μm) ovoid quartz blebs commonly intervene between epidote and host plagioclase. We interpret the textural relations between plagioclase and epidote to result from epidote breakdown by a reaction such as epidote +

quartz ⇒ anorthite + opaque + H_2O (Spear, 1993). A D1 fabric is wrapped about epidote porphyroblasts, and is defined by well-preserved elongate tschermakitic to pargasitic hornblende + plagioclase ± quartz and subordinate Ti-oxides ± garnet ± biotite. Plagioclase porphyroblasts are typically homogeneous and range in composition from An_{17} to An_{35} (oligoclase to andesine) from sample to sample. At high structural levels (< 100 m from the Rand fault), diopsidic to augitic clinopyroxene enters the stable D1 assemblage (Figure 3.4). The D1 fabric is locally overprinted by retrograde D2 minerals clinozoisite, tremolite, and calcite. Retrograde chlorite is rare. Retrograde conversion of hornblende to actinolite, as seen along the Vincent fault in the San Gabriel Mountains (Jacobson, 1997), is not observed. Lenses of ultramafic material typically crop out within or adjacent to mafic schist (Figure 3.4).

In contrast to other exposures of the southern California schist (e.g. Sharry, 1981; Postlethwaite and Jacobson, 1987; Jacobson 1997; Kidder and Ducea, 2006; Jacobson *et al*., 2007), the San Emigdio Schist has abundant garnet except at the lowest structural levels. The majority of garnets from both metasandstone and mafic schist are 1 to 5 mm idioblastic grains with blebby quartz inclusions. In contrast, within the upper approximately150 m of the schist, garnet is locally cataclastically deformed along two sets of fractures, F1 and F2, potentially corresponding to D1 and D2 episodes (Figure 3.4). While we cannot conclusively link F1 and F2 fractures to D1 and D2 fabric development, there exists a clear temporal relationship between the fracture sets. Garnets exhibiting F2 fractures are characterized by pervasive, linear, near foliation-normal, dilatant cracks that overprint F1 fractures. Similar features reported from the Morin shear zone of the Canadian Grenville

Province are interpreted as evidence of structural ascent in the upper crust (Ji *et al*., 1997). We focus here on garnets exhibiting F1 fractures. Such garnets are hereafter referred to as "broken garnets." These garnets are either torn completely apart or frictionally displaced along fractured surfaces with no systematic orientation and are partially replaced by D2 minerals. The displacement along fractured surfaces is typically between 50 μm and 2 mm. However, large portions of several broken garnets are entirely missing and cannot be recognized in the same thin section. This implies large displacements (> 2 mm; comparable to or exceeding the grain size) along fractures regardless of whether missing garnet fragments were dispersed into the third dimension or translated entirely from the thin section.

3.2. Mineral zonation

3.2.1. Analytical methods

Electron microprobe analyses were performed using a JEOL8200 system (California Institute of Technology) equipped with 5 LiF, PET, and TAP crystal spectrometers. Major element concentrations were measured in point and line analyses at 15 kV accelerating voltage and a 25 nA beam current with 60 s count times, using natural and synthetic standards, and the CITZAF correction algorithm. Garnet analyses were done in spot mode, while plagioclase, muscovite, and biotite grains were measured using a 5 μm beam width. Individual points along some analytical traverses in garnet were spaced as little as 1 μm apart. At this spacing interval, given the length of our diffusion profile, the effect of spatial averaging in microprobe analysis is negligible compared to the uncertainties in available

self-diffusion and interdiffusion data (Ganguly *et al*., 1988). X-ray imaging of Fe, Mg, Ca, Mn, P, and Ti distribution in garnet was done with the same instrument at 15 kV accelerating voltage and 400 nA beam current with a pixel size of 5 μm and dwell times of 300 ms/pixel. Maps were processed to enhance zonation features using the imagesc function in Matlab.

3.2.2. Schist

X-ray mapping and analytical traverses of broken and intact garnets from both metasandstone and mafic schist members (Figure 3.5) show well-preserved bell-shaped Mn-profiles with Mn-rich core regions and Mn-poor rims, plus monotonically increasing Mg# (Mg/Mg+Fe) from core to rim, features indicative of typical prograde garnet growth (Spear, 1993). However, sharp and pronounced compositional gradients, particularly in Mn and Ca, corresponding to inclusion-rich rims and relatively inclusion-poor cores suggest a two-stage growth history. While a detailed analysis of the growth history of San Emigdio Schist garnets is beyond the scope of this paper, we argue below that core-overgrowth textures probably developed during a single metamorphic event as opposed to two discrete events because: 1) steep compositional gradients may be explained by fractional crystallization and 2) the time interval between deposition, deep subduction (approximately 30 km), and structural ascent to midcrustal levels was extremely short (< 3 Myr) (Grove *et al*., 2003). At high structural levels (< 150 m from the Rand fault) in the extreme easternmost and westernmost exposures of the schist in the San Emigdio Mountains, garnet resorption features and diffusive relaxation of major and trace element growth zonation are common (Figures 3.5 and 3.6). Except at high structural levels, garnets lack “Mn kick-ups” (Kohn

Figure 3.5. (a) X-ray maps and (b) zonation profiles in schist garnets. Location of profiles shown in Ca maps of samples 06SE23 and 08SE479B. Hot colors in X-ray images represent relatively high concentration with red for the highest and bluish purple for the lowest.

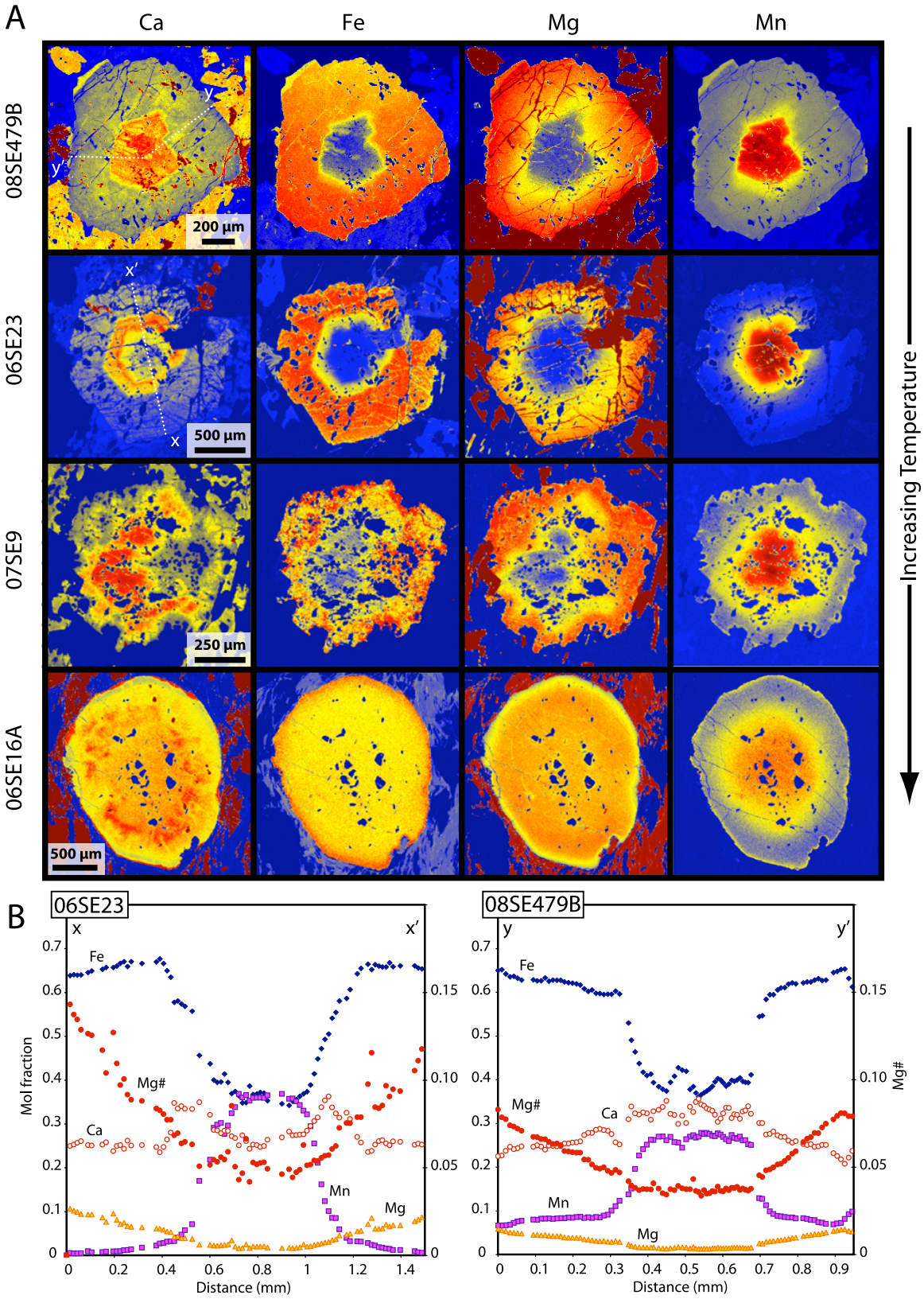
A
Ca
Fe
Mg
Mn
08SE479B
06SE23
07SE9
06SE16A
y
y′
x
x′
200 µm
500 µm
250 µm
500 µm
Increasing Temperature
B
06SE23
08SE479B
Fe
Mg#
Ca
Mn
Mg
Mol fraction
Distance (mm)
Mg#

Figure 3.6. X-ray map of garnet from schist sample 06SE16A for phosphorus. Note partially resorbed idioblastic core (arrows) mantled by rounded rim. Bright areas denote relatively high P.

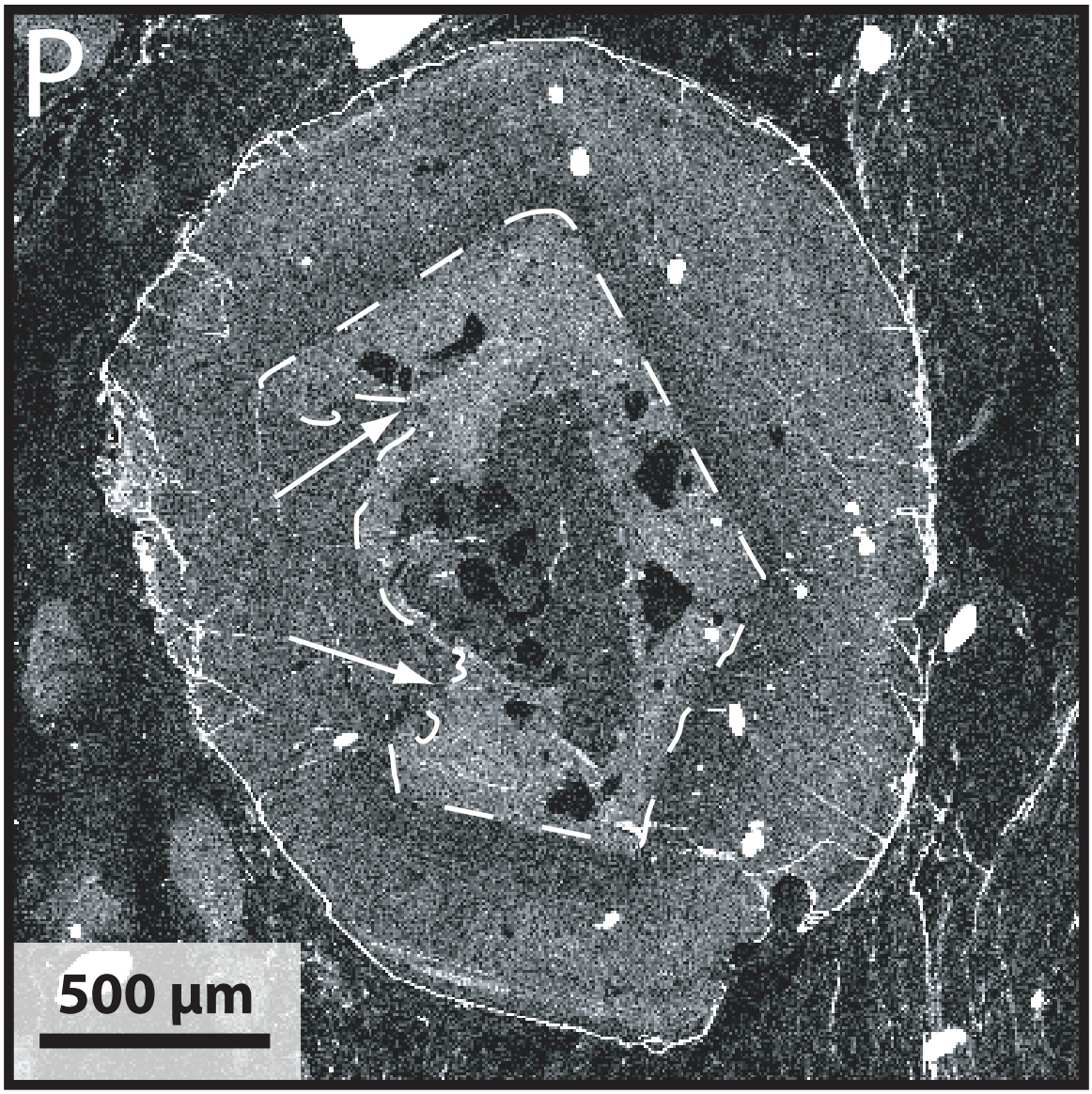
P
500 µm

and Spear, 2000), indicating that Fe-Mg exchange between garnet and biotite has not been disrupted by retrograde net transfer reactions. Whereas zonation is concentric in idioblastic garnets, there is an obvious truncation, most evident in Ti X-ray maps, in the zonation pattern of broken garnets approximately 25 μm inward from the rims (Figure 3.7). This truncation is interpreted as the original location of the broken margin. Broken garnet rims are compositionally identical to idioblastic garnet rims (Figures 3.5 and 3.7) and are interpreted, based on the sharpness of the interface between juxtaposed compositions, to represent growth zonation. By this logic, overgrowth along broken margins resulted in natural diffusion couples.

Biotite, muscovite, and plagioclase in metasandstone and hornblende and plagioclase in mafic schist were analyzed in line traverses and X-ray maps across each section in regions lacking D2 minerals to evaluate the extent of retrogression of the D1 assemblage. Biotite, muscovite, and hornblende exhibit negligible core to rim variation in composition, while plagioclase interiors in both metasandstone and mafic varieties show patchy zonation, ranging in composition from An_{16} to An_{39} (oligoclase to andesine). Plagioclase rims are more uniform than cores, and are in apparent textural equilibrium with garnet, muscovite, biotite, and quartz in metasandstones, and with garnet, hornblende, and quartz in mafic schists. We infer from these chemical and textural relationships that these assemblages were in equilibrium during peak metamorphism and are therefore suitable for thermobarometric work.

Figure 3.7. (a) X-ray map of broken garnet from schist sample 06SE23 for Ti; referred to as "grain 1" in text. (b and c) Results of diffusion modelling for grains 1 and 2, respectively. Location of profile in grain 1 shown in (a); grain 2 not shown.

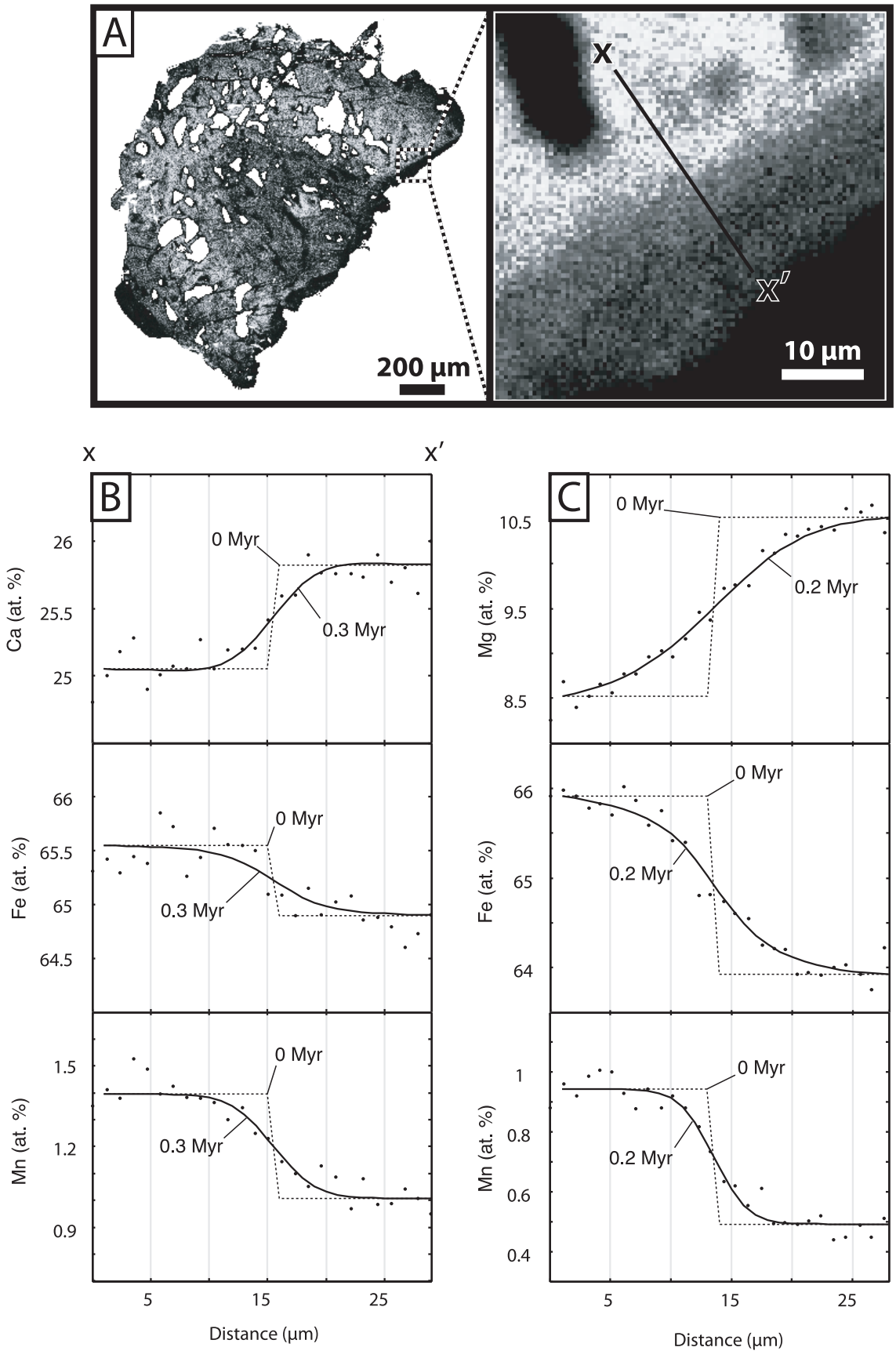
A
200 µm
X
X′
10 µm
B
C
0 Myr
0.3 Myr
0.2 Myr
Ca (at. %)
Fe (at. %)
Mn (at. %)
Mg (at. %)
Distance (µm)

Figure 3.8. (a) X-ray maps and (b) zonation profiles in garnet from upper plate sample 06SE14A. Location of profile shown in Ca map. Bright colors in X-ray images represent relatively high concentration. Garnet is approximately 1 cm in diameter. See text for discussion.

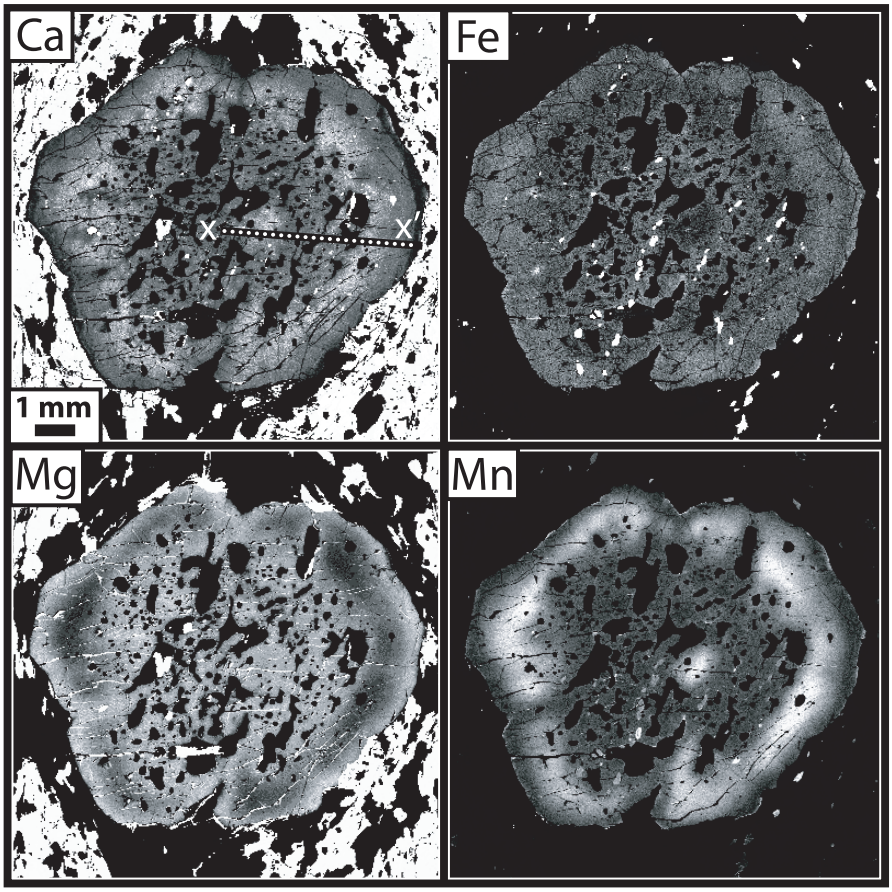
Ca
Fe
Mg
Mn
x
x′
1 mm

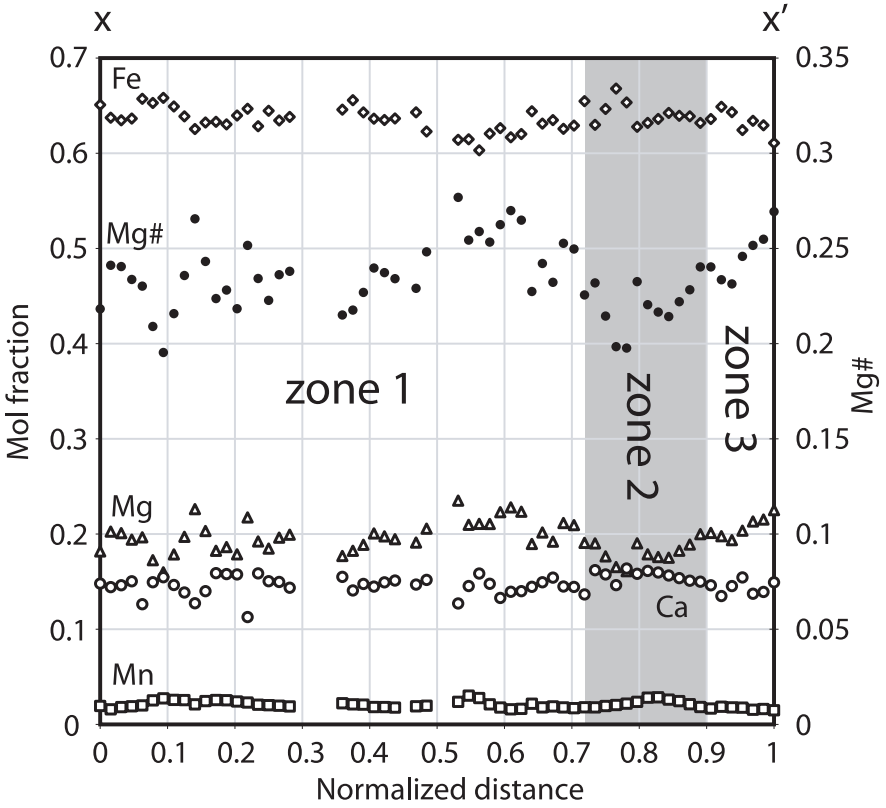
x
x′
Fe
Mg#
Mg
Ca
Mn
zone 1
zone 2
zone 3
Mol fraction
Mg#
Normalized distance
0
0.1
0.2
0.3
0.4
0.5
0.6
0.7
0.8
0.9
1
0.05
0.15
0.25
0.35

3.2.3. Upper plate

Garnets from the San Emigdio gneiss are almandine-rich with lesser amounts of pyrope, grossular, and spessartine components (X_{alm} = 0.73 – 0.60, X_{prp} = 0.25 – 0.16, X_{grs} = 0.17 – 0.09, and X_{sps} = 0.04 – 0.01) (Figure 3.8; Table A1.1). Representative garnet mole fractions and precision (1σ) calculated from counting statistics from sample 06SE14A are: X_{alm}, 0.627 ± 0.012; X_{grs}, 0.150 ± 0.003; X_{prp}, 0.206 ± 0.008; X_{sps}, 0.017 ± 0.002. At the scale of Figure 3.8, this uncertainty is smaller than the size of the symbols representing each data point. While considerable scatter is apparent in conventional microprobe traverses, subtle variations in garnet composition are detectable within analytical uncertainty. Moreover, X-ray maps clearly resolve three distinct compositional domains in garnets from the San Emigdio gneiss. These garnets are generally compositionally homogeneous with flat interior profiles (zone 1) except for weak annuli in a second zone between 300 to 1500 μm from the rims (normalized distances of 0.7 to 0.9 from core regions). These annuli first change to relatively high concentrations of Ca, Fe, and Mn, and low Mg# values, and then along the outer approximately 300 μm (zone 3) the trends reverse back toward interior compositions. The zone 1 mantled by zone 2 pattern is typical for garnets throughout the deep-level batholithic plate (Pickett and Saleeby, 1993), but the outermost compositional reversal is restricted to proximity to the Rand fault.

Line traverses and X-ray maps of plagioclase and hornblende porphyroblasts show little internal variation in composition, suggesting that they are not significantly modified by retrograde metamorphism. Textural relationships between garnet, hornblende, plagioclase,

and quartz grains in direct contact corroborate chemical evidence, outlined above, that this is an equilibrium assemblage suitable for thermobarometry.

3.3. Thermobarometry and inverted metamorphic field gradient

Equilibrium *P-T* conditions were calculated using the internally consistent average *P-T* mode in THERMOCALC, version 3.26 (Powell and Holland, 1994; Holland and Powell, 1998). Thermobarometry was done on garnet-bearing schist and upper plate samples (Figure 3.9). *P-T* conditions for metasandstone schist were calculated from garnet + plagioclase + muscovite + biotite + quartz assemblages interpreted, based on chemical and textural evidence outlined above, to have equilibrated during peak metamorphism. Garnet – hornblende thermometry and garnet – hornblende – plagioclase – quartz barometry were applied to mafic schist and upper plate lithologies. For all samples, we use garnet rim compositions where Mg# is highest suggesting garnet growth at peak temperatures (Spear, 1993). All calculations were done assuming a water activity of unity, due to the abundance of hydrous phases. Calculated temperatures and pressures for the schist range from 590 to 700 ˚C and 8.5 to 11.1 kbar. Temperatures calculated from the San Emigdio gneiss (675 to 710 ˚C) are identical within error to those from the uppermost levels of the schist, whereas calculated pressures are approximately 1 kbar lower (7.1 to 8.4 kbar). Results from thermobarometric work and representative mineral compositions are summarized in Tables 3.1 and A1.1 to A1.5.

Three thermobarometric transects were done from high to low structural levels of the schist (Figure 3.2). In each transect, temperature determinations from samples in close proximity to the Rand fault were approximately 90 to 120 ˚C higher than those from

Figure 3.9. Calculated pressures and temperatures for the San Emigdio Schist and upper plate San Emigdio gneiss, using THERMOCALC v. 3.26. 1σ uncertainty ellipses based on propagation of uncertainties on thermodynamic data and activity-composition relationships through thermobarometric calculations.

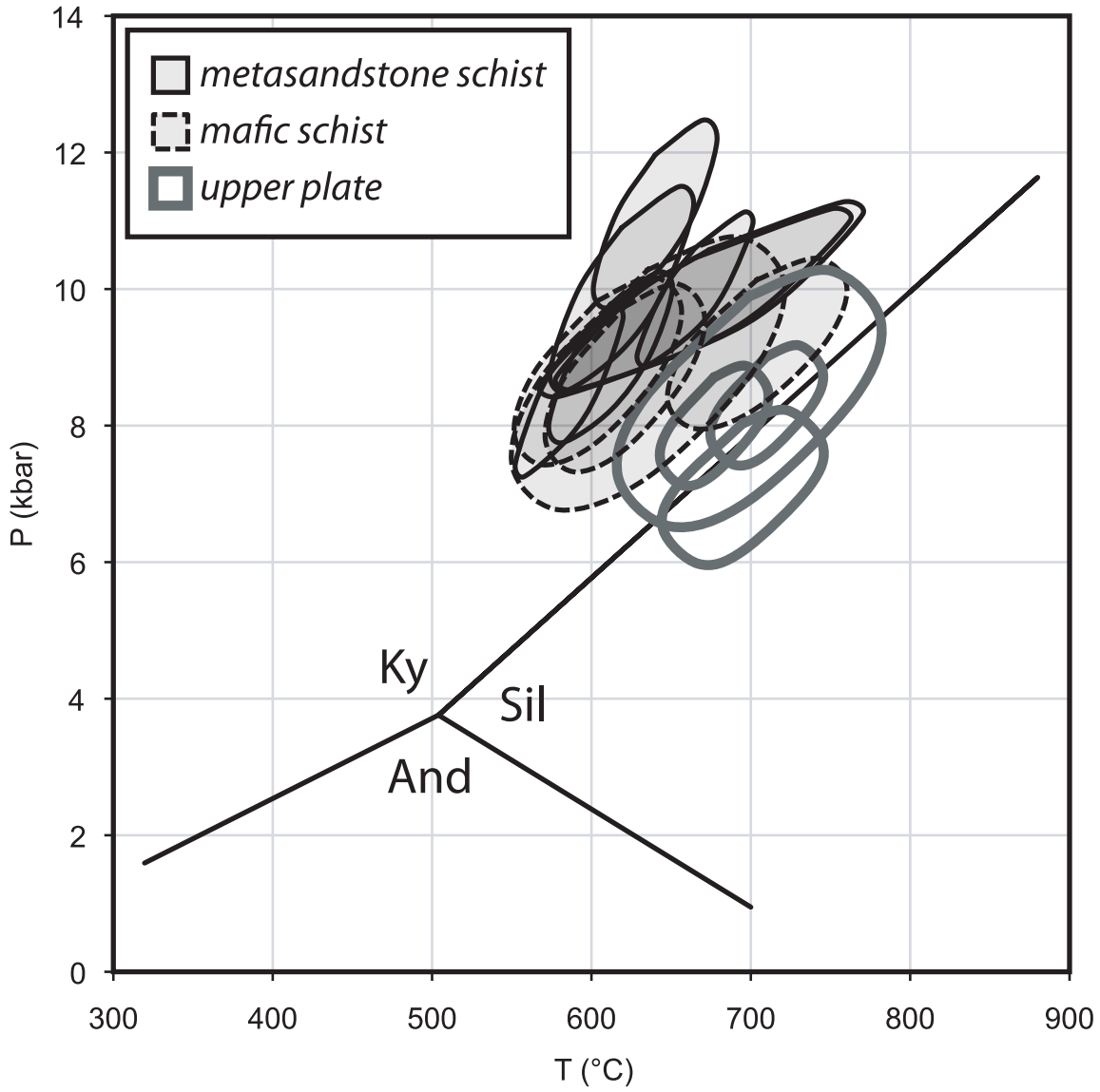
metasandstone schist
mafic schist
upper plate
Ky
Sil
And
P (kbar)
T (°C)
0
2
4
6
8
10
12
14
300
400
500
600
700
800
900

samples collected 106 to 1840 m below the fault. This equates to thermal gradients from 50 to 1100 ˚C / km. Calculated thermal gradients increase with decreasing exposed structural thickness from east to west (Figure 3.2), suggesting that structural attenuation is at least partly responsible for the 1100 ˚C / km value. Thermal gradients of 50 to 240 ˚C / km (calculated from eastern and central transects, respectively) are similar to those reported in the schist of Sierra de Salinas (50 to 70 ˚C; Kidder and Ducea, 2006) and in the Pelona Schist (240 ˚C / km; Graham and Powell, 1984).

3.4. Thermodynamic modelling and *P-T* paths

Prograde garnet zonation features in the schist are remarkably well-preserved, allowing for straightforward recovery of a large portion of the early *P-T* history of the schist. The *P-T* paths for metasandstone and mafic schist samples were constrained using petrography, garnet zonation patterns, and *P-T* pseudosection calculations. A description of the thermodynamic modelling routine is given in Appendix 1. Figure 3.10a shows a *P-T* pseudosection for the bulk composition of sample 06SE23. The peak mineral assemblage of garnet + plagioclase + muscovite + biotite + quartz present in 06SE23 is quite common in other metasandstones from intermediate to high structural levels of the schist and is consistent with those predicted from the pseudosection. *P-T* results from THERMOCALC plot within the field of the peak assemblage and are in close proximity to the H_2O-saturated solidus.

Figure 3.11 shows the pseudosection of Figure 3.10a superimposed with volume percent H_2O in solids, garnet abundance contours, and almandine, spessartine, grossular, and pyrope isopleths. In general, X_{alm} and X_{prp} are strongly temperature-dependent, X_{sps} is

Figure 3.10. Calculated "prograde" *P-T* pseudosections for samples (a) 06SE23 and (b) 08SE479B. THERMOCALC results overlain for comparison. Numbered fields listed in Appendix 1. Bulk compositions listed in A1.6.

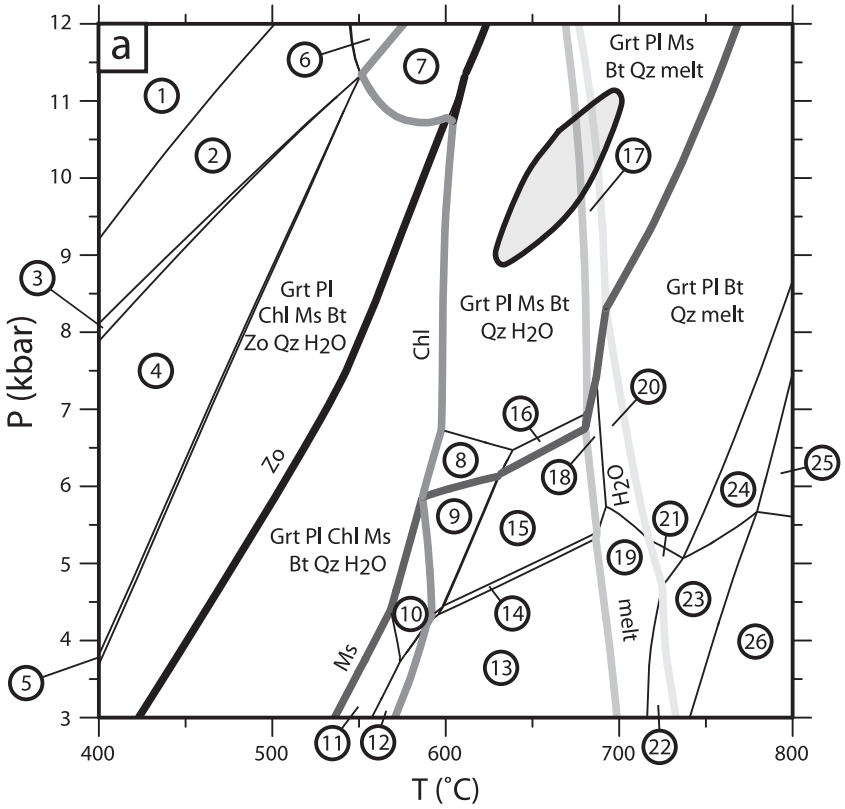
a
Grt Pl Ms
Bt Qz melt
Grt Pl
Chl Ms Bt
Zo Qz H2O
Chl
Grt Pl Ms Bt
Qz H2O
Grt Pl Bt
Qz melt
Zo
H2O
Grt Pl Chl Ms
Bt Qz H2O
melt
Ms
P (kbar)
T (°C)

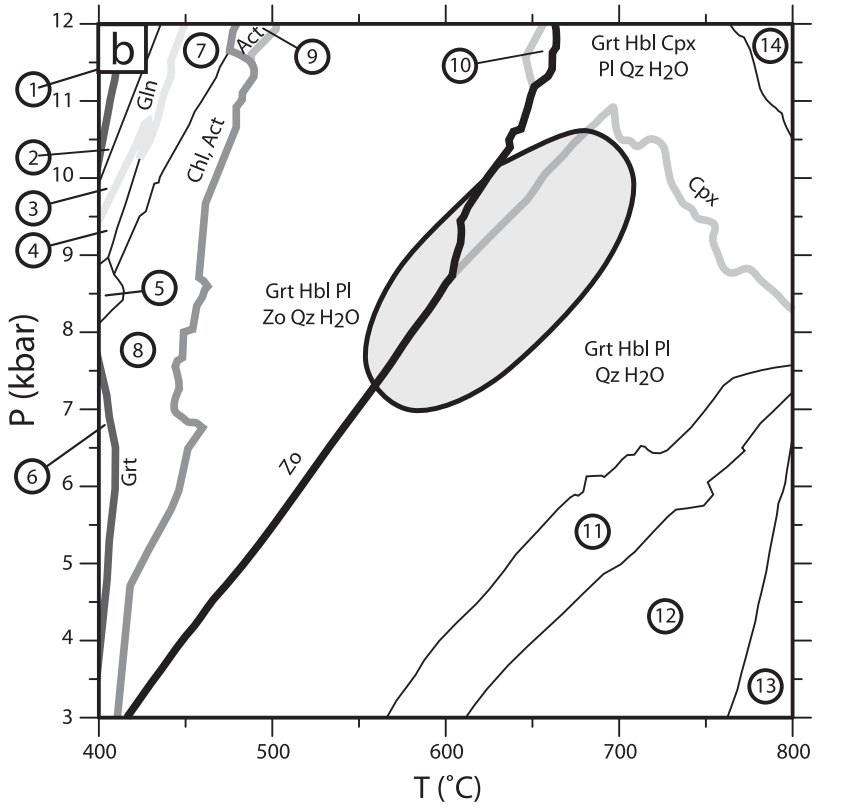
b
Gln
Act
Chl, Act
Grt Hbl Cpx
Pl Qz H2O
Cpx
Grt Hbl Pl
Zo Qz H2O
Grt Hbl Pl
Qz H2O
Grt
Zo
P (kbar)
T (°C)

Figure 3.11. Pseudosection shown in Figure 3.10a with contours of (a) volume percent H_2O in solids, (b) volume fraction garnet and (c-f) garnet composition expressed as mol fractions overlain. Arrow represents inferred prograde *P-T* trajectory.

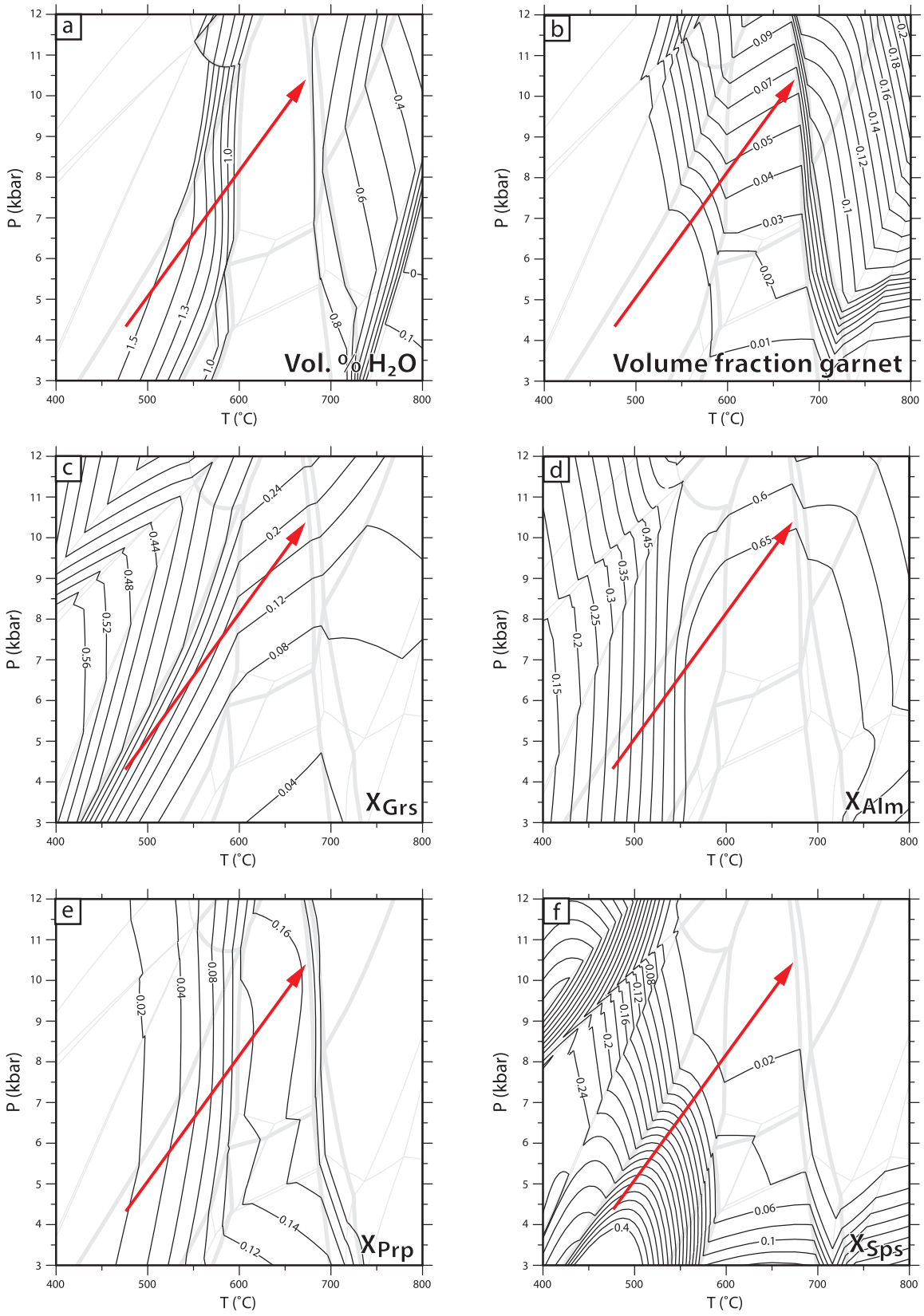
a
Vol. % H2O
b
Volume fraction garnet
c
XGrs
d
XAlm
e
XPrp
f
XSps
P (kbar)
T (°C)

strongly pressure-dependent, and at high temperatures X_{grs} is as pressure-dependent as X_{sps}. We calculate conditions of garnet nucleation from the intersection of end member isopleths that correspond to garnet core compositions (e.g. Vance and Mahar, 1998). The intersection of the garnet core composition isopleths (X_{alm} = 0.35, X_{sps}= 0.37, X_{grs}= 0.26, and X_{prp}= 0.02) indicates the temperature and pressure conditions at the onset of growth. Although garnet contains no inclusions useful for thermobarometry, which prohibits an independent check of the conditions of garnet core formation, the tight intersection of the compositional contours at the point 4.3 kbar, 475 ˚C strongly suggests that the pseudosection accurately reproduces the physical conditions of garnet nucleation.

Mafic sample 08SE479b contains the peak assemblage garnet + plagioclase + hornblende + quartz and is representative of mafic schist outcrops > 100 m from the Rand fault. The pseudosection of Figure 3.10b is overlain by garnet isopleths in Figure 3.12. Garnet core composition isopleths (X_{alm} = 0.36, X_{grs}=0.35, X_{sps}=0.28, and X_{prp}=0.02) intersect at approximately 6.5 kbar, 575 ˚C. Mineral isopleth-based constraints of garnet nucleation in both metasandstone and mafic schist lie well inside the stability field of garnet as predicted by equilibrium growth (Figures 3.10, 3.11, and 3.12). This is most likely due to the effect of missing Mn end-members in the solution models of competing phases. The presence of Mn-bearing chlorite, biotite, and ilmenite during prograde metamorphism would hinder garnet nucleation and growth at low metamorphic grades, restricting its stability field to higher pressures and temperatures. Additional explanations for this observation include: 1) late metastable nucleation of garnet (i.e., overstepping of the garnet isograd), 2) limited local equilibrium due to slow reaction kinetics at low temperatures, and 3) diffusional modification of the core.

Figure 3.12. Pseudosection shown in Figure 3.10b with contours of (a) volume percent H_2O in solids, (b) volume fraction garnet and (c-f) garnet composition expressed as mol fractions overlain. Arrow represents inferred prograde *P-T* trajectory.

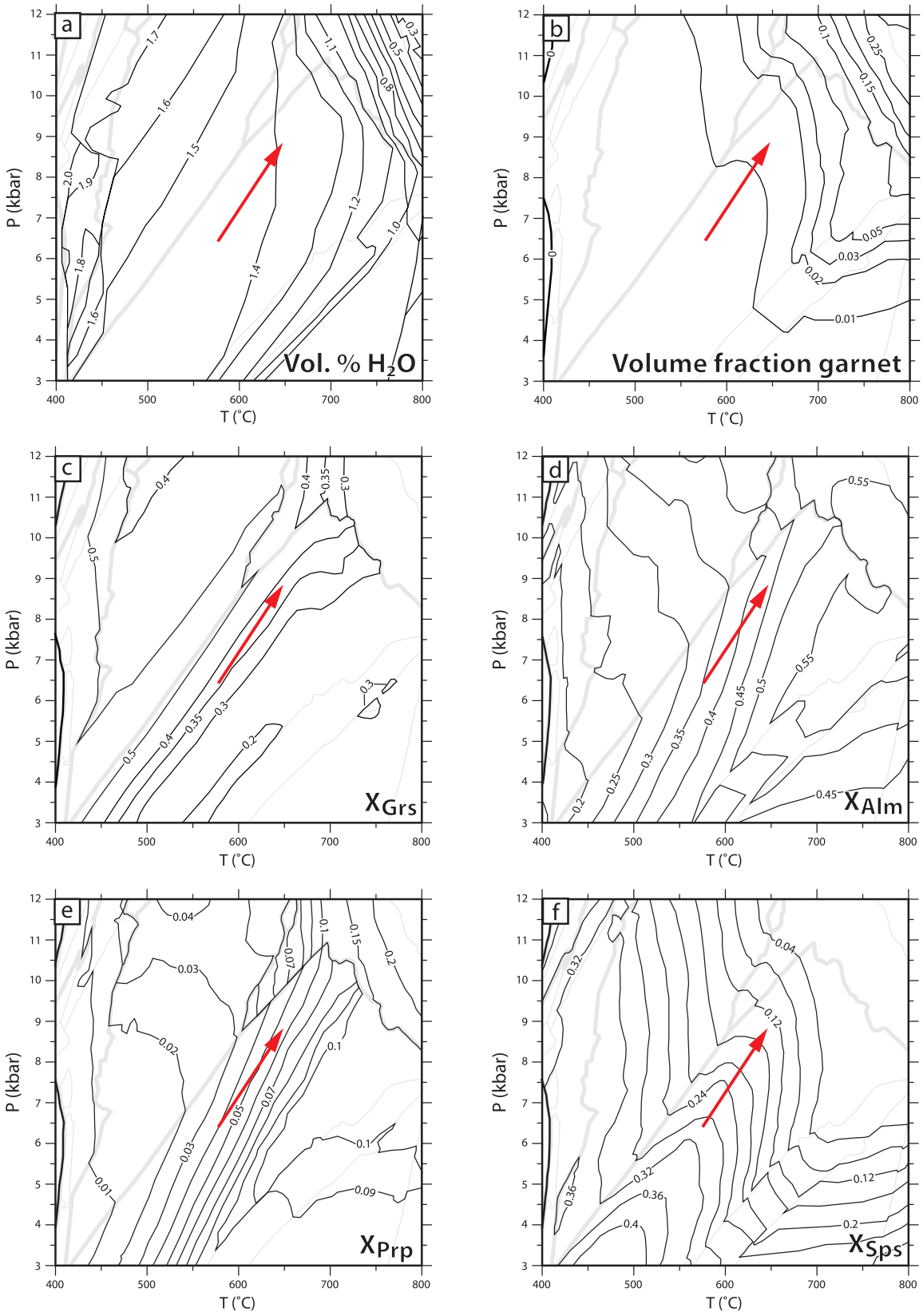
a
Vol. % H2O
b
Volume fraction garnet
c
XGrs
d
XAlm
e
XPrp
f
XSps
P (kbar)
T (°C)

Prograde paths for garnets in samples 06SE23 and 08SE479b are approximated by interpolating the conditions of garnet core formation with peak metamorphic conditions. The preferred prograde paths outlined in Figures 3.11 and 3.12 incorporate these constraints and take into consideration 1) the lack of prograde clinozoisite in sample 06SE23 and the presence of prograde epidote in sample 08SE479b; 2) the preservation of primary muscovite in sample 06SE23; and 3) the lack of evidence for partial melting in these samples, although such evidence is present at higher structural levels in the schist. Therefore, the likely prograde path for sample 06SE23 involves burial from approximately 4.3 to 10 kbar and contemporaneous heating from 475 to 665 ˚C. Along this path, the only net transfer reaction encountered in sample 06SE23 during garnet growth is the chlorite-out reaction. The lack of primary chlorite as inclusions within garnet probably resulted from garnet scavenging Fe, Mg, Al, and Si from the mineral, which was likely present during garnet core growth. The prograde trajectory of sample 08SE479b overlaps that of 06SE23, with conditions increasing from 7 kbar, 575 ˚C to 8.4 kbar, 636 ˚C. It is important to note that although the preferred prograde *P-T* paths shown in Figures 3.11 and 3.12 explain many core-to-rim garnet zonation trends in samples 06SE23 and 08SE479b (e.g. monotonically increasing X_{prp}, monotonically decreasing X_{sps}, approximately constant X_{grs}, and increasing X_{alm} prior to reaching a compositional plateau in the outer 400 μm), modelled garnet isopleths do not match the composition of garnet beyond the cores at any point in *P-T* space. In other words, the garnet core compositions are the only regions that can be successfully modelled. This is because the assumption of equilibrium garnet growth is no longer valid outside the cores. Isopleth intersection thermobarometry breaks down following garnet core growth because the bulk rock composition is changed as garnet sequesters material, particularly Mn, forever

Figure 3.13. Comparison of modelled garnet zonation patterns (a-c) and observed garnet compositional profiles (d). Modelled profiles for the prograde *P-T* trajectory shown in Figure 3.11 (sample 06SE23) for (a) homogeneous equilibrium crystallization, (b) 10% fractional crystallization, and (c) 25% fractional crystallization.

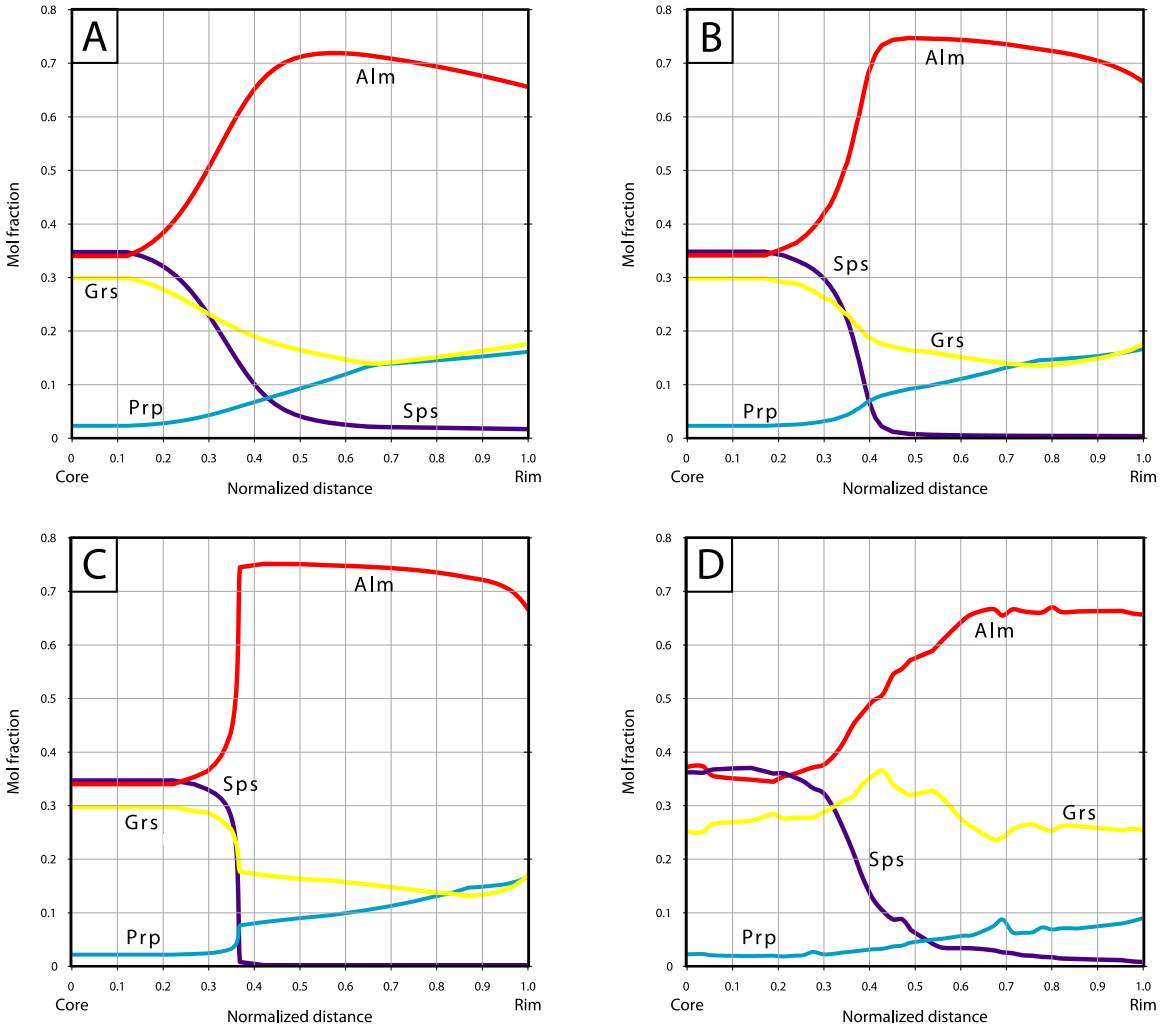
A
Alm
Grs
Prp
Sps
Mol fraction
Core
Rim
Normalized distance
B
Alm
Sps
Grs
Prp
Mol fraction
Core
Rim
Normalized distance
C
Alm
Sps
Grs
Prp
Mol fraction
Core
Rim
Normalized distance
D
Alm
Grs
Sps
Prp
Mol fraction
Core
Rim
Normalized distance

removing it from the system unless the temperature becomes sufficiently high that diffusion and/or resorption reintroduces it to the system (Spear, 1993; Vance and Mahar, 1998). Figure 3.13 compares modelled and observed garnet zonation patterns and illustrates the effect of fractional crystallization for the preferred prograde path of sample 06SE23 (see Appendix 1 for a description of the calculation routine). This effect is to deplete the bulk rock composition, leading to a decrease in nutrient availability at the garnet surface and a corresponding decrease in growth rate. While the observed garnet zonation is fit quite well by the equilibrium growth model, some proportion of fractional crystallization may explain sharp compositional gradients in San Emigdio Schist garnets, particularly in Mn. While we do not consider the effect of volume diffusion in garnet, some amount of diffusional relaxation of these steep compositional variations has likely occurred. High-Ca annuli in garnets from metasandstone schist (Figures 3.5 and 3.13) cannot be explained by fractional crystallization alone and likely reflect chemical disequilibrium during prograde metamorphism (Chernoff and Carlson, 1999; Konrad-Schmolke *et al*., 2005; Chapman *et al*., 2006).

Zonation preserved in garnets from samples 06SE23 and 08SE479b indicates that growth did not occur under decreasing pressure and/or temperature conditions (i.e., following peak conditions). Contours of garnet volume % are generally nearly isothermal with slightly negative slopes, indicating that it is impossible to grow garnet during decompression in these bulk compositions. Furthermore, garnet rims are characterized by decreasing X_{alm} and X_{sps} and increasing X_{prp}, which is only possible under conditions of increasing temperature (Figures 3.11 and 3.12).

The prograde path described above involves dehydration reactions, fluid loss (Figures 3.11a and 3.12a), and sequestration of Al, Ca, Fe, Mg, Mn, and Si associated with garnet fractionation. In addition, peak assemblages are well preserved, indicating that the necessary H_2O was not available to promote extensive retrogression. However, free water must have been locally present in order to stabilize the D2 assemblage. Therefore, in order to reconstruct the retrograde path of the schist, separate pseudosections were drawn for the bulk compositions of samples 06SE23 and 08SE479B with sufficient free water (i.e., water saturated) to stabilize chlorite and clinozoisite along the retrograde path (Figure 3.14). For simplicity, we assume that the bulk composition effectively equilibrating during retrogression is similar to the original bulk composition from which garnet was subtracted (garnet rims preserve peak *P-T* composition and show no retrogressive modification). We estimated the modal proportion of garnet, approximated the composition of garnet grains by subdividing them into constituent zones and adding together the contribution of each zone, and finally calculated and subtracted the contribution of garnet to the bulk compositions.

The retrograde paths outlined in Figure 3.15 are based on the stabilization of D2 assemblages. As garnet growth ceased and metasandstone schist (06SE23) entered the retrograde portion of the *P-T* path, chlorite and clinozoisite were stabilized. According to the retrograde pseudosection for sample 06SE23, this sample must have followed a trajectory with similar *P-T* slope during decompression than during burial in order to pass through the stability fields of chlorite and clinozoisite. Although epidote entered the stable mineral assemblage in mafic schist (08SE479b) varieties following peak metamorphism, chlorite and actinolite stability fields were not traversed along the retrograde path. The pseudosection for sample 08SE479b indicates that this is possible if the retrograde *P-T*

Figure 3.14. Calculated "retrograde" *P-T* pseudosections for samples (a) 06SE23 and (b) 08SE479B with (c and d) contours of volume percent H_2O in solids overlain. Numbered fields listed in Appendix 1. Bulk compositions listed in Table A1.6.

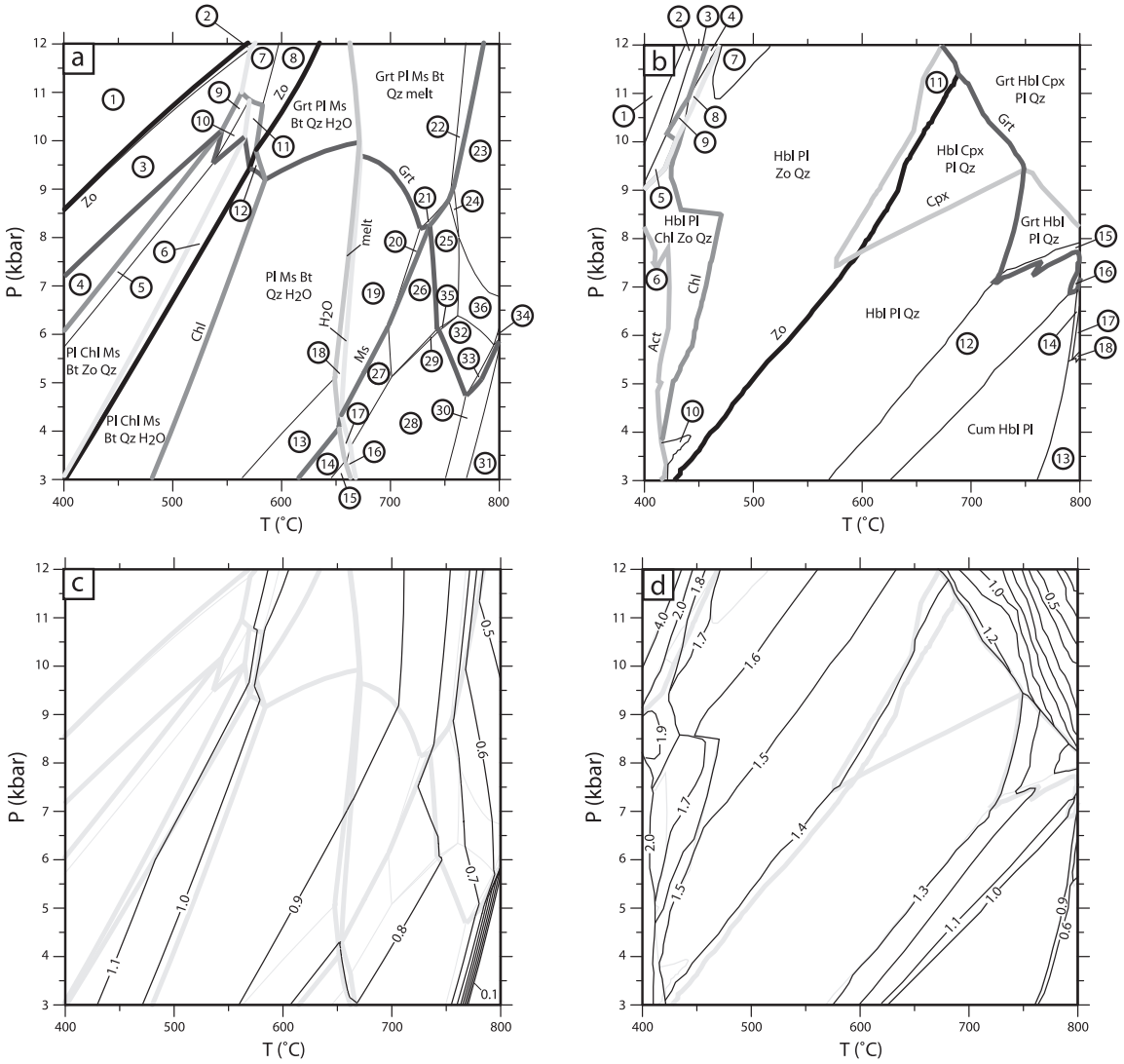
a
Grt Pl Ms Bt
Qz melt
Grt Pl Ms
Bt Qz H2O
Zo
Grt
melt
Pl Ms Bt
Qz H2O
H2O
Ms
Chl
Pl Chl Ms
Bt Zo Qz
Pl Chl Ms
Bt Qz H2O
P (kbar)
T (°C)
b
Grt Hbl Cpx
Pl Qz
Hbl Pl
Zo Qz
Hbl Cpx
Pl Qz
Cpx
Hbl Pl
Chl Zo Qz
Grt Hbl
Pl Qz
Chl
Act
Zo
Hbl Pl Qz
Cum Hbl Pl
P (kbar)
T (°C)
c
P (kbar)
T (°C)
d
P (kbar)
T (°C)

Figure 3.15. *P-T* evolution for samples (a) 06SE23 and (b) 08SE479B. Prograde paths shown as solid lines. (a) "Core" conditions from intersection of garnet isopleths in Figure 3.11, "rim" conditions from Figure 3.9, end-member retrograde paths (dashed lines) constrained by the stability of chlorite and clinozoisite (fields from Figure 3.14a). (b) "Core" conditions from intersection of garnet isopleths in Figure 3.12, "rim" conditions from Figure 3.9, end-member retrograde paths (dashed lines) constrained by the stability of clinozoisite and the lack of retrograde chlorite (fields from Figure 3.14b).

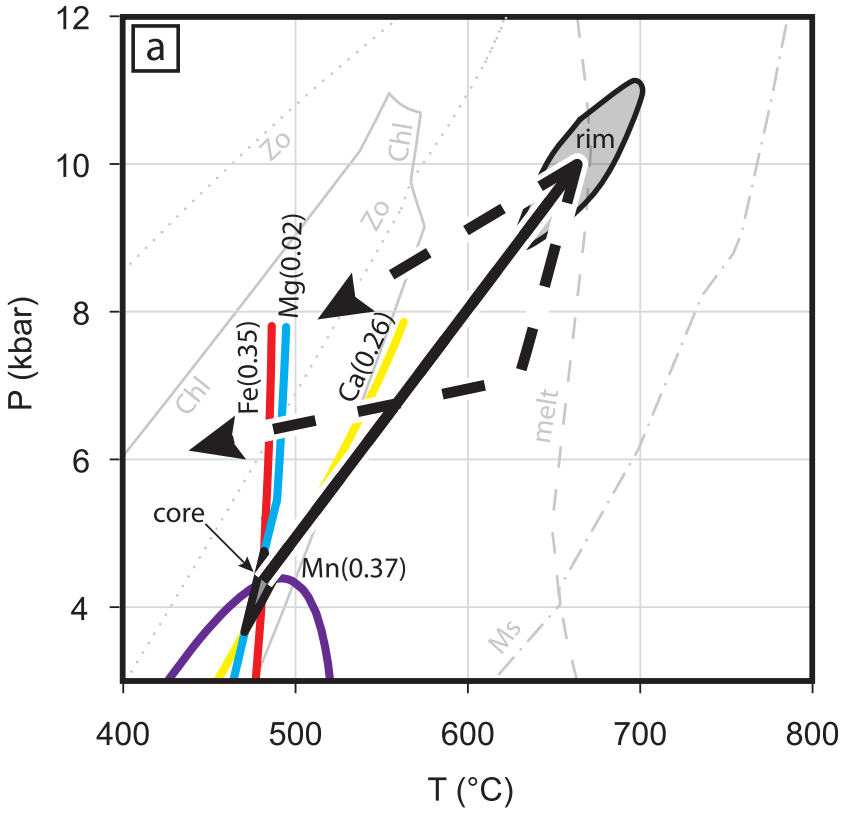
a
12
10
8
6
4
P (kbar)
400
500
600
700
800
T (°C)
rim
core
Mn(0.37)
Fe(0.35)
Mg(0.02)
Ca(0.26)
Zo
Chl
melt
Ms

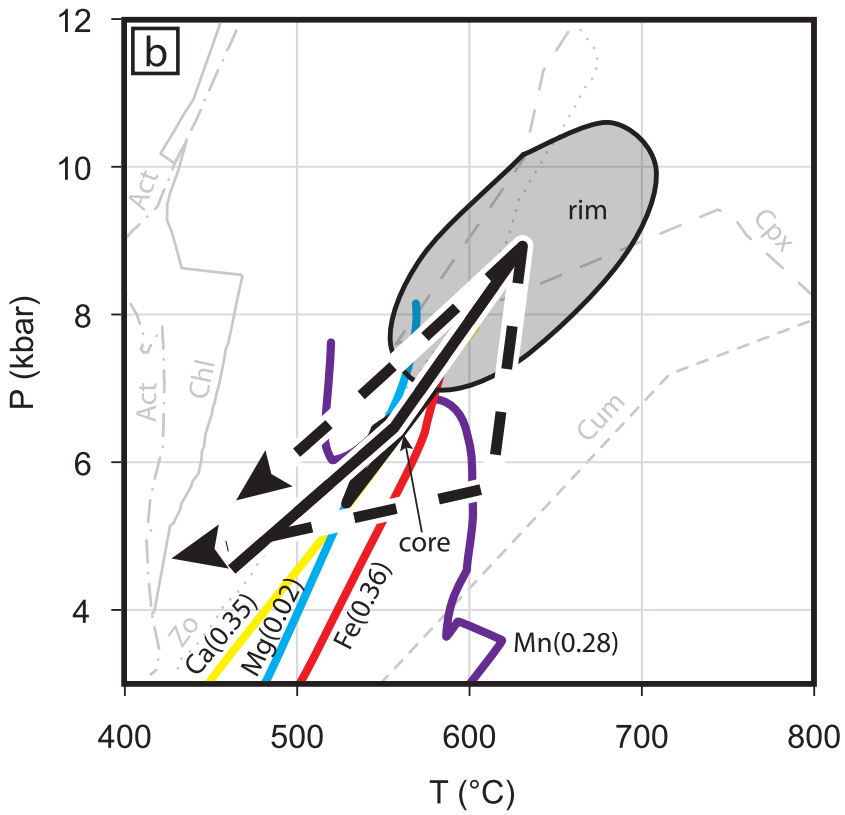
b
12
10
8
6
4
P (kbar)
400
500
600
700
800
T (°C)
rim
core
Mn(0.28)
Fe(0.36)
Mg(0.02)
Ca(0.35)
Act
Chl
Cpx
Cum
Zo

trajectory passed between chlorite/actinolite-out and clinozoisite/epidote-out reaction boundaries. Figure 3.15 shows, for both metasandstone and mafic schist, two end-member retrograde paths that satisfy the constraints outlined above: 1) one with a shallower *P-T* slope than the prograde path (i.e., a counterclockwise *P-T* loop) and 2) one with a steeper slope (i.e., a clockwise *P-T* loop). While the retrograde path cannot be further constrained, we consider it likely that the geometry of the *P-T* loop for the schist lies between the end-member possibilities with roughly overlapping prograde and retrograde *P-T* trajectories (i.e., "Franciscan-type" or "out and back" *P-T* path; Ernst, 1988).

The retrograde paths shown in Figure 3.15 involve the formation of clinozoisite/epidote and/or chlorite, which require the presence of H_2O in order to take place. Along these retrograde paths, each sample encounters contours of increasing H_2O content, implying that the assemblage becomes fluid-absent unless fluid is available along grain boundaries or is externally derived (Guiraud *et al*., 2001) (Figure 3.14). Therefore, overprinting of peak assemblages by D2 minerals is evidence for open system behavior involving H_2O influx.

3.5. Diffusion modelling of broken garnet

Sample 06SE23 contains two garnet grains that ruptured and subsequently overgrew their broken margins, creating sharp compositional discontinuities. When a mineral overgrows itself in this fashion, the resulting interface between juxtaposed compositions in the composite grain is a natural diffusion couple. The degree of relaxation of the originally steep compositional step is dependent chiefly on temperature and the time interval over which diffusion was possible.

We exploit the diffusional annealing of the hypothetically originally sharp compositional steps in broken garnets from sample 06SE23 to estimate the amount of time required for their relaxation. We assume that the amount of time required for overgrowth of broken garnet margins is infinitesimally small compared to rates of diffusion (Ganguly *et al*., 1996; Dachs and Proyer, 2002). We model the diffusive timescales for two grains in sample 06SE23. For grain 1, we model Ca, Fe, and Mn profiles and for grain 2, Fe, Mg, and Mn profiles were used. We did not attempt to model Mg and Ca in grains 1 and 2, respectively, due to the erratic nature of the measured profiles.

We use the analytical program *Profiler* (available in Glicksman, 2000) to calculate interdiffusion coefficients and time scales of diffusion from measured compositional profiles. *Profiler* solves Fick's second law for multicomponent diffusion couples based on user specified end member compositions, distance, temperature, pressure, diffusion timescale, and self-diffusion data. The solutions calculated from *Profiler* are only valid if diffusion coefficients do not vary with time. Since diffusion coefficients are not constant during non-isothermal processes, such as during progressive metamorphism, Chakraborty and Ganguly (1991, 1992) developed the concept of a "characteristic temperature," T_{ch}, which yields identical diffusive relaxation profiles when compared to those of metamorphic *T-t* paths. The San Emigdio Schist certainly experienced non-isothermal metamorphism during underplating and exhumation, and as such, we use the relation $T_{ch} \approx 0.97\ T_{peak}$ to calculate characteristic temperatures based on peak metamorphic temperature estimates from thermobarometry. A discussion of model parameters and the theory behind garnet diffusion modelling is given in Appendix 1.

Table 3.1. Summary of thermobarometric calculations from the San Emigdio Mountains.

Sample	Lithology	UTM easting[a]	UTM northing[a]	Distance to Rand fault (m)[b]	Mineralogy	T (˚C)[c]	P (kbar)[c]	Corr[d]
08SE202	Upper plate	322237	3863252	357	Grt Hbl Pl Qz	695 ± 40	7.1 ± 0.9	0.555
08SE270	Upper plate	309137	3861143	3	Grt Hbl Pl Qz	699 ± 66	8.4 ± 1.5	0.604
04SE1a	Upper plate	310571	3861983	0	Grt Hbl Pl Qz	710 ± 28	8.3 ± 0.7	0.577
06SE14a	Upper plate	310573	3861982	0	Grt Hbl Pl Qz	677 ± 27	8.0 ± 0.7	0.586
08SE467[f]	metasandstone	319332	3864641	0	Grt Bt[g]	> 700	nd	NA
06SE16a[f]	metasandstone	310569	3861996	0	Grt Bt[g]	> 700	nd	NA
06SE74a	metabasalt	311043	3861862	0	Grt Hbl Pl Qz	704 ± 45	9.2 ± 1.0	0.661
07SE17	metasandstone	316031	3863579	-5	Grt Ms Bt Pl Qz	665 ± 78	9.8 ± 1.1	0.879
06SE23	metasandstone	310593	3861943	-30	Grt Ms Bt Pl Qz	665 ± 29	10.0 ± 0.9	0.845
06SE54	metasandstone	310682	3861857	-60	Grt Ms Bt Pl Qz	619 ± 36	10.0 ± 1.2	0.800
06SE9	metasandstone	310713	3861775	-106	Grt Hbl Ms Bt Pl Qz	586 ± 27	8.5 ± 1.0	0.844
07SE19	metasandstone	316248	3863358	-229	Grt Ms Bt Pl Qz	612 ± 31	9.0 ± 1.0	0.783
08SE469	metasandstone	319291	3864057	-254	Grt Ms Bt Pl Qz	674 ± 77	9.9 ± 1.1	0.870
08SE478[e]	metasandstone	321131	3861596	-1250	Grt Bt Pl Qz	619 ± 77	10.0	NA
08SE474	metabasalt	320041	3862435	-1368	Grt Hbl Pl Qz	604 ± 42	8.8 ± 1.1	0.661
08SE475	metabasalt	320182	3862264	-1434	Grt Hbl Pl Qz	621 ± 40	8.7 ± 1.1	0.650
08SE479b	metabasalt	320620	3862026	-1545	Grt Hbl Pl Qz	633 ± 66	8.7 ± 1.6	0.662
08SE476	metasandstone	321804	3860814	-1840	Grt Ms Bt Pl Qz	640 ± 31	11.1 ± 1.1	0.776

[a] UTM coordinates are WGS datum, zone 11N.

[b] Distance to Rand fault: positive and negative values indicate position above and below the Rand fault, respectively.

[c] 1σ uncertainties based on propagation of uncertainties on thermodynamic data and activity-composition relationships through thermobarometric calculations.

[d] Correlation coefficient between pressure and temperature from THERMOCALC.

[e] Garnet-biotite temperatures; calculated at 10 kbar.

[f] Sample shows evidence of partial melt.

[g] Phases not touching; lack of primary muscovite and presence of partial melt suggests $T > 700$ ˚C at 10 kbar (Figure 3.10a), assuming similar bulk composition to 06SE23.

Garnet end member compositions achieve plateau values adjacent to the diffusion zone in both grains (Figure 3.7). Interdiffusion coefficients were calculated for each profile using thermobarometric constraints on sample 06SE23 (Table 3.1) at P = 10 kbar and $T_{ch} \approx 0.97$ T_{peak} = 645 ˚C. In each case, the relaxation time was adjusted until modelled results could be visually fit to analytical profiles. Diffusion timescales of 0.3 and 0.2 Myr were calculated from grains 1 and 2, respectively (Figure 3.7). These values represent the amount of time required to cool garnet from peak temperatures to approximately 500 to 550 ˚C, below which garnet compositions become locked in due to sluggish diffusion kinetics (Ganguly, 2002). Therefore, garnets from sample 06SE23 cooled from peak conditions at rates between 825 and 380 ˚C / Myr.

Deformation proceeded following the cessation of garnet growth into the stability field of D2 minerals. Morphologically similar broken garnets from deeper structural levels did not overgrow their broken margins and therefore, may have broken following peak conditions (Figure 3.4).

4. DISCUSSION

4.1. Inverted metamorphism

The presence of an inverted metamorphic field gradient in the San Emigdio Schist, i.e., an upsection increase in peak temperature, is a characteristic feature of this and the majority of other southern California Schist exposures (e.g. Ehlig, 1981; Sharry, 1981; Graham and Powell, 1984; Jacobson, 1995; Kidder and Ducea, 2006). Our petrologic and

thermobarometric work indicate that the San Emigdio Schist exhibits a gradation from upper amphibolite facies (approximately 700 ˚C) to epidote amphibolite facies (approximately 600 ˚C) with increasing structural depth. We resolve no clear relationship between calculated metamorphic pressures and structural depth. Inverted temperature gradients preserved in other exposures of the southern California Schist have been explained by 1) shear heating along the subduction interface (Graham and England, 1976; England and Molnar, 1993; Ducea *et al*., 2009), 2) rapid *en masse* underthrusting of cold schist beneath a hot upper plate (i.e., the 'hot iron effect'; Peacock, 1992), and 3) tectonic underplating and progressive cooling beneath an initially hot upper plate following the onset of shallow subduction (Peacock, 1992; Kidder and Ducea, 2006). Each scenario requires rapid cooling to preserve the inverted gradient. Explanations 1 and 2 require that the metamorphic gradient preserved in the schist records a geothermal gradient that existed during subduction, while scenario 3 does not. Although our results do not cast new light on this long-standing debate, we believe scenario 3 provides the most satisfactory explanation of inverted metamorphism in the schist for the following reasons:

1) To preserve the inverted gradient in scenario 1, the effect of shear heating must become less significant following schist accretion to the upper plate. This may be accomplished through cessation or slowing of subduction, for which there is no evidence, or by re-localization of the megathrust beneath the schist - upper plate contact.

2) The schist was too weak to have experienced any significant shear heating. Kidder and Ducea (2006) argue, based primarily on evidence of partial melting and ductile deformation of quartz, that the schist is incapable of supporting shear stresses of 50 to 90 MPa required by the shear heating hypothesis.

3) The upper plate was hot, with peak temperatures of 680 to 790 ˚C in the TSE complex (Pickett and Saleeby, 1993; this study). Kidder and Ducea (2006) argue, based on a 1D thermal model, that high temperatures exhibited in upper levels of the schist (approximately 700 ˚C) can be reached in approximately 0.3 Myr when exposed to an upper plate at 800 ˚C.

4) Scenario 2 requires subduction of the entire schist section as a single tectonic slice. While no major internal structural breaks have been identified in the schist, synchronous formation of the entire schist section is an unlikely scenario given that inverted metamorphic gradients rarely represent fossilized thermal gradients (e.g. Jamieson *et al*., 1996).

4.2. Metamorphic convergence between upper and lower plates

In the San Emigdio Mountains, the schist and upper plate share similar structural relations and mineral parageneses. For instance, temperature estimates from the top of the schist and the base of the upper plate are identical within error (665 to 710 ˚C) and foliations and lineations in the schist are parallel to those in the upper plate and intervening mylonites (Chapman *et al*., 2010). Similar criteria were used by Ehlig (1981) and later by Jacobson (1997) to identify the Vincent fault, an approximately 1 km thick shear zone separating the Pelona Schist from superjacent upper plate rocks, as an intact remnant of the Cretaceous megathrust. However, Rand fault mylonites in the San Emigdio Mountains are clearly associated with retrograde metamorphism and indicate top to the east (i.e., trench-directed) shear (Chapman *et al*., 2010). Therefore, we view metamorphic convergence between upper and lower plates in the San Emigdio Mountains as a structural coincidence. During shallow subduction, the schist must have been carried approximately 150 km inboard in order to reach a depth of 30 km (9 kbar) (Kidder and Ducea, 2006). We suggest that the schist came

in contact with a hot (approximately 800 ˚C) upper plate at these conditions, while the upper plate rocks that the schist would later come in contact with had already decompressed from 9 kbar to 4 kbar conditions (Saleeby *et al*., 2007). In other words, we view the schist-upper plate contact preserved in the San Emigdio Mountains as being proximal to the original subduction megathrust, but subsequent schist ascent would have placed the hot schist against an upper plate that had already experienced significant cooling during uplift from deep levels (Figure 3.16).

Thermochronometric studies of the upper plate indicate that within approximately 100 m of the Rand fault, biotite Ar/Ar and Rb/Sr as well as (U-Th)/He zircon systems were reset as a consequence of schist ascent (Saleeby *et al*., 2007). Hornblende Ar/Ar systems were only affected in pervasively mylonitized rocks along the basal aureole of the upper plate. Such reheating by the schist is also recorded in proximal upper plate garnet compositional profiles. Compositionally flat garnet interiors (zone 1) with increasing X_{grs}, X_{alm}, and X_{sps} and decreasing X_{prp} and Mg# at the rim (zone 2) are typical of garnets throughout the TSE complex (Pickett and Saleeby, 1993). In the San Emigdio gneiss, however, an additional zone (zone 3) overgrows zone 2 with compositions similar to those found in zone 1. In aggregate we interpret the San Emigdio gneiss garnet patterns to indicate deep-crustal residence at elevated temperatures (zone 1), followed by cooling (zone 2), and reheating (zone 3) of the base of the upper plate adjacent to the ascending schist along the Rand fault.

Figure 3.16. Generalized cross section model for the southern SNB. Black and white stars show depositional site of the San Emigdio Schist and native site of the TSE complex, respectively. No vertical exaggeration. (a) Ca. 100 Ma onset of shallow subduction. (b) Ca. 95 Ma upward migration of slab interface to within batholithic crust (base of crust and mantle lithosphere sheared off) and shutoff of arc magmatism. Uplift, contractile deformation, and erosional denudation of the upper plate is followed by deposition and subduction of San Emigdio Schist protolith. (c) Ca. 90 Ma schist underplated beneath recently active arc rocks (approximately 800 ˚C). Upper plate rocks exposed in San Emigdio and Tehachapi Mountains decompressed from 9 kbar (panel a) to 4 kbar conditions. (d) Ca. 85 Ma. Gravitational collapse of the upper plate drives trench-directed channelized extrusion of the schist (Chapman *et al*., 2010). Schist flow is dominated by simple shear near the boundaries of the channel and by pure shear at the center of the wedge. Hot schist juxtaposed with TSE complex, reheating upper plate rocks.

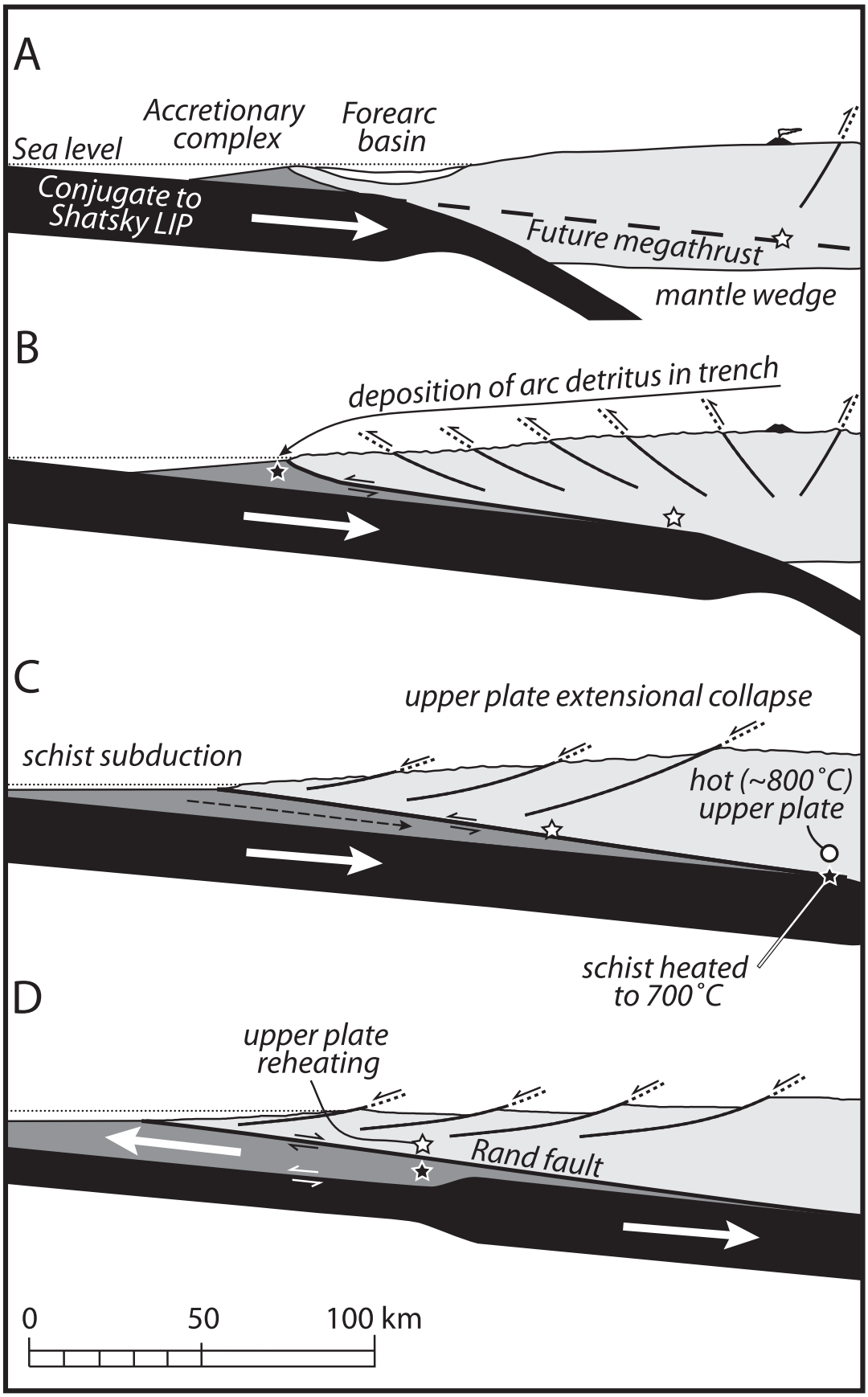
A
Accretionary complex
Forearc basin
Sea level
Conjugate to Shatsky LIP
Future megathrust
mantle wedge
B
deposition of arc detritus in trench
C
upper plate extensional collapse
schist subduction
hot (~800˚C) upper plate
schist heated to 700˚C
D
upper plate reheating
Rand fault
0
50
100 km

4.3. *P-T* path

The schist of the San Emigdio Mountains has likely undergone a "Franciscan-type" *P-T* path. Thermal models of subduction initiation (Cloos, 1982; 1985; Peacock, 1987; Kincaid and Sacks, 1997; Gerya *et al*., 2002) demonstrate high geothermal gradients (between a hot upper plate and cool lower plate) that relax with continued subduction as the upper plate cools. A possible explanation for our calculated *P-T* trajectories is in a newly initiated subduction zone with a decreasing geothermal gradient. Subduction of a conjugate massif to the Shatsky Rise is hypothesized to have driven slab flattening, thereby removing the mantle wedge and lowermost crust and repositioning the subduction zone along mid-to lower crustal levels of the recently active Late Cretaceous arc (Saleeby, 2003; Ducea *et al*., 2009). Later schist underplating led to refrigeration of the upper plate and relaxation of the initially high geothermal gradient. Similar scenarios are envisioned to explain *P-T* trajectories calculated from high-grade blocks in the Franciscan Complex (e.g. Wakabayashi, 1990; Krogh *et al*., 1994), eclogites in the Yukon-Tanana terrane (Perchuk *et al*., 1999), and in the subduction-related migmatitic Sierra del Convento mélange (García-Casco *et al*., 2008). Following peak conditions, the subducted schist ascended by trench-directed channelized extrusion (Chapman *et al*., 2010). This stage is recorded by the stabilization of D2 minerals in metasandstone and mafic schist samples as the schist cooled rapidly (between 825 and 380 ˚C / Myr) from peak conditions. Since prograde and retrograde portions of the *P-T* path shown in Figure 3.15 follow similar trajectories, retrograde alteration of peak assemblages is limited. As a result, D1 assemblages are remarkably well preserved, as is commonly the case for the Franciscan Complex (Spear, 1993). Rapid cooling during decompression may

also explain well-preserved garnet zonation features and the lack of "Mn kick-ups" except at high structural levels (Kohn and Spear, 2000).

4.4. Prograde elevated stresses and strain rates and rapid cooling following peak conditions

Garnet is a high strength mineral, with high yield stress (approximately 7 GPa; Pardavi-Horváth, 1984), Peierls stress (resistance to dislocation glide) (Karato *et al*., 1995), and toughness (resistance to fracture) (Whitney *et al*., 2007). Therefore, brittle deformation of natural garnet during metamorphism, while incompletely understood (Whitney, 1996), is probably restricted to very high stresses and strain rates. Broken garnets from the San Emigdio Schist exhibit similar microstructures to brittlely deformed garnets from the Sesia Zone of the Western Alps, which are attributed to major paleoseismic events (Trepmann and Stöckhert, 2002). Microstructural characteristics of broken garnets (outlined above) and the highly strained texture of host metasandstones are most consistent with deformation-induced garnet fracture, and cannot be explained by alternative mechanisms (e.g. Prior, 1993; Whitney, 1996; Ji *et al*., 1997). High-stress cataclastic deformation of garnet is in conflict with earlier arguments that the schist is not capable of supporting shear stresses in excess of 90 MPa. While the mechanics of brittle failure of rigid inclusions in a ductile matrix are poorly understood, with explanations favoring sequential fracture by high shear stresses at the garnet-matrix interface, the "modified shear-lag theory" of Ji *et al*. (1997), the phenomenon has long been recognized (e.g. Ramberg, 1955; Boullier, 1980; Mandal *et al*., 2001; Trepmann and Stöckhert, 2002). We suggest a similar mechanism of stress transfer from the weak quartzofeldspathic matrix to the stiff garnet inclusions of the schist.

Fracturing of and deformation twinning in clinopyroxene along the Salinas shear zone is cited as evidence for large (140 to 1000 MPa), quasi-instantaneous, localized stresses accompanying seismic events (Ducea *et al*., 2007). Deformation twinning in clinopyroxene proceeded in concert with the prograde metamorphic replacement of amphibole by clinopyroxene (Kidder and Ducea, 2006), indicating that seismic events occurred during burial of the schist of Sierra de Salinas to approximately 10 kbar. Moreover, in the San Emigdio Schist, broken garnet overgrowths are compositionally identical to unbroken garnet rims (Figures 3.5 and 3.7), which must have grown during the waning stages of prograde metamorphism at 10 kbar. Therefore, in both Sierra de Salinas and San Emigdio Schist localities, there exists microstructural evidence for large paleoseismic events, possibly along the subduction megathrust, at approximately 30 km depth.

If large paleoseismic events are responsible for cataclastic deformation of San Emigdio Schist garnets, these events must have occurred near peak conditions, i.e., during the reversal from subduction to eduction (Chapman *et al*., 2010). We speculate that stress buildups associated with the reversal in transport polarity resulted in large paleoseismic events. Numerical simulations indicate that the closure of subduction channels at depth may be characterized by large gradients in stress state (Gerya *et al*., 2002).

Modelling of diffusive relaxation of juxtaposed garnet compositions suggests that garnets from the schist cooled from peak conditions at several 100s ˚C / Myr. These cooling rates are consistent with geochronologic and thermochronometric studies of the schist (Grove *et al*., 2003; 2008; Saleeby *et al*., 2007; Jacobson *et al*., in press). In the San Emigdio Schist, the time interval between the youngest detrital zircon U-Pb ages (i.e., the maximum possible depositional age) and muscovite $^{40}Ar/^{39}Ar$ cooling ages is < 3 Myr (Grove *et al*.,

2003). Therefore, the schist was subducted to a depth of approximately 30 km at 700 ˚C and cooled through the 400 ˚C closure isotherm for $^{40}Ar/^{39}Ar$ muscovite (McDougall and Harrison, 1999) in < 3 Myr, corresponding to cooling rates of > 100 ˚C/Myr. Similar cooling rates (100s ˚C/Myr) are fit through high-temperature range garnet and medial range hornblende thermochronometric data from upper plate rocks in the Tehachapi Mountains (Saleeby *et al*., 2007) and are linked to gravitational collapse of the upper plate above the underplated schist (Chapman *et al*., 2010).

4.5. Evolution of the thermal structure of a newly initiated flat subduction zone

Field relations, mineral assemblages, thermobarometry, and thermodynamic modelling suggest partial melting of metasandstone San Emigdio Schist under water-saturated conditions. The development of quartzofeldspathic leucosomes and veins took place during ductile deformation associated with the D1 episode and are locally overprinted by the D2 fabric. These features indicate that anatexis coincided with ductile deformation near peak conditions, implying that partial melting of metasandstone occurred as the schist reached a maximum depth of subduction (30 km) approximately 150 km inboard of the trench. We provide here a comparison with subduction complexes in adjacent areas that exhibit evidence for partial melting: the schist of Sierra de Salinas and the Catalina Schist of the California borderland.

Although partial melting probably did not occur in lower grade Pelona, Orocopia, and/or Rand schists, thermobarometric determinations (approximately 700 ˚C, 10 kbar) and quartzofeldspathic veins and dikes from the schist of Sierra de Salinas suggest that anatexis proceeded under similar pressure, temperature, and fluid activity conditions as in the San

Figure 3.17. Palinspastic map showing pre-Neogene positions of San Emigdio and related schist after Grove *et al*. (2003) with 50 km of sinistral slip along the Garlock fault restored (Ross, 1989). Detrital zircon (dz) ages after Grove *et al*. (2003; 2008). Temperatures shown are the highest reported values from individual schist exposures. Temperatures from Sharry (1981) and Pickett and Saleeby (1993) (Tehachapi Mountains); Kidder and Ducea (2006) (Sierra de Salinas); Grove *et al*. (2008) (Santa Catalina Island); Graham and Powell (1984) (Rand Mountains and Sierra Pelona); Oyarzabal (1996) and Jacobson *et al*. (2007) (Orocopia and Gabilan Hills); and this study (San Emigdio Mountains). Abbreviations: pm, partial melting; SGF, San Gabriel fault. Other abbreviations as in Figure 3.1.

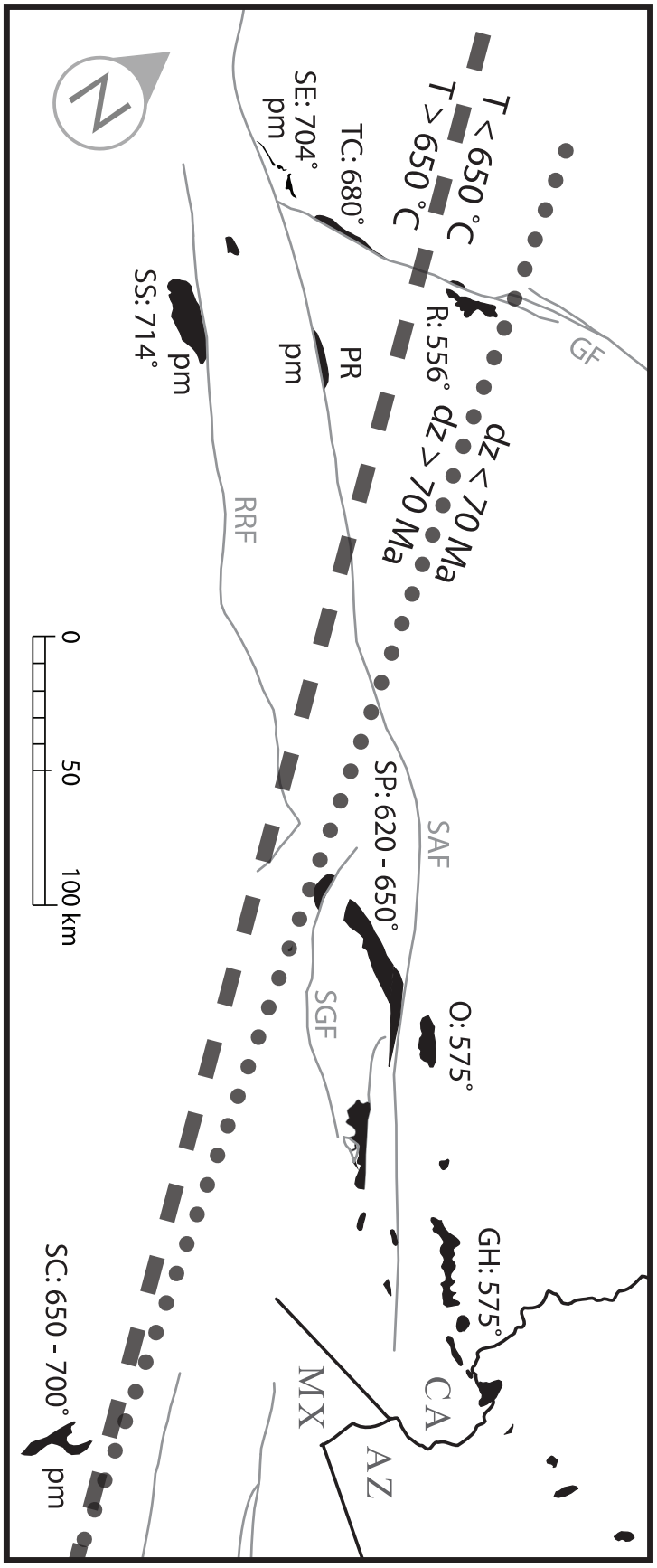
T < 650 °C
T > 650 °C
dz < 70 Ma
dz > 70 Ma
N
GF
RRF
SAF
SGF
SE: 704°
pm
TC: 680°
R: 556°
PR
pm
SS: 714°
pm
SP: 620 - 650°
O: 575°
GH: 575°
SC: 650 - 700°
pm
CA
AZ
MX
0
50
100 km

Emigdio Schist (Kidder and Ducea, 2006; Ducea *et al*., 2009). The timing of schist deposition and metamorphism decreases systematically from northwestern (San Emigdio Schist, schists of Sierra de Salinas and Portal Ridge, and Rand Schist) to central and southeastern exposures (Pelona and Orocopia schists) (Grove *et al*., 2003; Jacobson *et al*., in press) (Figure 3.17). Another distinctive trend not yet recognized is that high reported peak temperatures (590 to 714 ˚C) and partial melting are restricted to exposures of the schist with maximum depositional ages between 80 to 90 Ma (Sharry, 1981; Pickett and Saleeby, 1993; Kidder and Ducea, 2006; this study), while moderate temperatures (480 to 575 ˚C) typify 55 to 80 Ma schists (Graham and England, 1976; Graham and Powell, 1984; Jacobson, 1995; 1997; Jacobson *et al*., 2007) (Figure 3.17). Tectonic underplating and progressive cooling beneath an initially hot upper plate following the onset of shallow subduction may explain this trend. This model also explains partial melting and/or high temperatures in San Emigdio, Tehachapi, and Sierra de Salinas schists, lower temperatures in Pelona, Orocopia, and Rand schists, inverted metamorphism in the schist as a whole, and the observed *P-T* paths calculated from the San Emigdio body. It could be argued that 55 to 80 Ma schists sit beneath the arc in an inboard position where the upper plate contains younger plutonic rocks than does the upper plate of 80 to 90 Ma schists, and was therefore hotter later. However, Cretaceous to Tertiary plutons are volumetrically minor compared to pre-Cretaceous bodies in the upper plate of 55 to 80 Ma schists (e.g. Jacobson, 1997; Haxel *et al*., 2002; Jacobson *et al*., 2007) and we posit that the arc geotherm in the southern Sierra Nevada was higher than that of the Mojave region.

Based on overlapping age and provenance between the San Emigdio Schist and the youngest (ca. 97 to 95 Ma), structurally deepest, and lowest grade (blueschist and lower-

grade facies) portions of the Catalina Schist, a tentative correlation has been assigned (Grove *et al*., 2008; Jacobson *et al*., in press). No correlation is drawn, however, between the San Emigdio Schist and older (ca. 120 to 115 Ma), structurally shallow, and high-grade (upper amphibolite facies) levels of the Catalina Schist (Grove *et al*., 2008 and references therein; Jacobson *et al*., in press). The top of this inverted metamorphic sequence is characterized by variably migmatized and metasomatized mafic blocks set in a matrix of ultramafic material (Sorensen, 1988). Partial melting in the Catalina Schist is explained by underthrusting of a portion of the Cretaceous forearc beneath the northwestern Peninsular Ranges batholith (Grove *et al*., 2008). Thrusting within the forearc region proceeded as blueschist and lower-grade varieties were accreted along a comparably long-lived, outboard subduction megathrust. Therefore, similar to the San Emigdio Schist, the Catalina Schist preserves a record of juxtaposing of hot upper plate with relatively cold material and continued underplating of lower grade units, although accretion of the Catalina Schist occurred over a longer time interval and conceivably along paired subduction megathrusts.

The Catalina Schist, Sierra de Salinas and San Emigdio schists, and subduction-related migmatitic complexes in other areas (e.g. Swakane Gneiss; Matzel *et al*., 2004, Sierra del Convento mélange; García-Casco *et al*., 2008) preserve high-pressure/temperature metamorphic parageneses that are inconsistent with those predicted from the thermal structure of steady state subduction (e.g. Peacock, 1987; 2003). These aberrantly high temperatures may be achieved during subduction by some combination of 1) shear heating (Graham and England, 1976; England and Molnar, 1993); 2) subduction of hot oceanic lithosphere; 3) subduction of a spreading center (e.g. DeLong *et al*., 1979); 4) initiation of a new subduction zone (e.g. Platt, 1975; Cloos, 1985; Grove and Bebout, 1995); 5) subduction

erosion (e.g. Grove *et al*., 2008); and 6) upward migration of the subduction interface (i.e., slab shallowing; Kidder and Ducea, 2006; Ducea *et al*., 2009). While mechanisms 1, 2, and 3 were probably not significant in the aforementioned terranes (e.g. Kidder and Ducea, 2006), 4, 5, and 6 are favored for the cases of the Sierra del Convento mélange (García-Casco *et al*., 2008), Catalina Schist (Grove *et al*., 2008) and Swakane Gneiss (Matzel *et al*., 2004), and Sierra de Salinas (Kidder and Ducea, 2006) and San Emigdio schists (Saleeby *et al*., 2007; Chapman *et al*., 2010; this study), respectively. A common thread shared by scenarios 4, 5, and 6 is that each places a hot upper plate above a relatively cold lower plate, temporarily raising the geothermal gradient along the interface before steady state subduction is achieved.

5. SUMMARY AND CONCLUSIONS

(1) Field and petrologic relations for the San Emigdio Schist reveal two episodes of fabric development corresponding to peak (D1) and post-peak (D2) conditions. D1 mineral assemblages and degree of partial melting vary with proximity to the Rand fault, indicating the presence of an inverted metamorphic field gradient. Localized cataclastic deformation of schist garnets and subsequent formation of natural garnet diffusion couples occurred during the D1 episode.

(2) Thermobarometric work corroborates petrologic evidence for inverted metamorphism in the schist, with peak temperatures increasing from 590 to 700 ˚C from low to high structural levels, corresponding to thermal gradients of 50 to 240 ˚C / km. Peak pressures range from 8.5 to 11.1 kbar and do not vary with structural depth. Temperatures calculated from the San Emigdio gneiss (675 to 710 ˚C) are

identical within error to those from the uppermost levels of the schist, whereas calculated pressures are approximately 1 kbar lower (7.1 to 8.4 kbar).

(3) Thermodynamic modelling constrains the *P-T* history of the schist, which probably involved retrogression along a similar trajectory as the prograde path, resulting in a "Franciscan-type" *P-T* path.

(4) Diffusion modelling of natural garnet couples indicates rapid (825 to 380 ˚C / Myr) cooling from peak conditions to approximately 500 ˚C.

These data constrain the *P-T* history and the tectonics of underplating and exhumation of the San Emigdio Schist. This involved 1) subduction and progressive underplating of the primarily turbiditic and basaltic schist protolith and the development of an inverted metamorphic gradient, 2) low volume partial melting in the schist at peak conditions, 3) localized fracture of garnet at high stresses and strain rates immediately prior to peak conditions, possibly related to large subduction zone seismic events, and 4) reheating of upper plate batholithic assemblages during rapid structural ascent of the schist. While these results are consistent with an inferred tectonic evolution from shallow subduction beneath the recently active Late Cretaceous arc to exhumation by rapid trench-directed channelized extrusion in the subducted schist (Chapman *et al*., 2010), we cannot preclude alternative models solely based on this study.

We document the physical conditions fossilized in a deeply-exhumed subduction channel in an ancient flat slab system. This research should facilitate future recognition of analogous ancient systems in other orogenic belts. Continued understanding of the dynamics

of flat subduction requires a highly interactive approach between observational geophysics, dynamic modelling and geologic observation of both active and ancient systems.

REFERENCES

Barth, A. P., Wooden, J. L., Grove, M., Jacobson, C. E. and Pedrick, J. N., 2003, U-Pb zircon geochronology of rocks in the Salinas Valley region of California; a reevaluation of the crustal structure and origin of the Salinian Block: *Geology*, **31**(6), 517-520.

Boullier, A. M., 1980, A preliminary study on the behaviour of brittle minerals in a ductile matrix: example of zircons and feldspars: *Journal of Structural Geology*, **2**(1-2), 211-217.

Chakraborty, S. and Ganguly, J., 1991, Compositional zoning and cation diffusion in garnets: *Advances in Physical Geochemistry*, **8**, 120-175.

Chakraborty, S. and Ganguly, J., 1992, Cation diffusion in aluminosilicate garnets; experimental determination in spessartine-almandine diffusion couples, evaluation of effective binary, diffusion coefficients, and applications: *Contributions to Mineralogy and Petrology*, **111**(1), 74-86.

Chapman, A. D., Luffi, P. and Saleeby, J. B., 2006, The origin of high-Ca annuli in garnets from the Rand Schist of the San Emigdio Mountains, Southern California: *Eos, Transactions, American Geophysical Union*, **87**(52), Fall Meet. Suppl., Abstract V31B-0588.

Chapman, A. D., Kidder, S., Saleeby, J., and Ducea, M., 2010, Role of extrusion of the Rand and Sierra de Salinas schists in Late Cretaceous extension and rotation of the southern Sierra Nevada and vicinity: *Tectonics*, **29**, TC5006,

doi:10.1029/2009TC002597.

Chernoff, C. B. and Carlson, W. D., 1999, Trace element zoning as a record of chemical disequilibrium during garnet growth: *Geology*, **27**(6), 555-558.

Cloos, M., 1982, Flow melanges; numerical modeling and geologic constraints on their origin in the Franciscan subduction complex, California: *Geological Society of America Bulletin*, **93**(4), 330-344.

Cloos, M., 1985, Thermal evolution of convergent plate margins; thermal modeling and reevaluation of isotopic Ar-ages for blueschists in the Franciscan Complex of California: *Tectonics*, **4**(5), 421-433.

Crowell, J. C., 1952, Geology of the Lebec Quadrangle, California: *Special Report - California Division of Mines and Geology*, **24**, 1-24.

Dachs, E. and Proyer, A., 2002, Constraints on the duration of high-pressure metamorphism in the Tauern Window from diffusion modelling of discontinuous growth zones in eclogite garnet: *Journal of Metamorphic Geology*, **20**(8), 769-780.

DeLong, S. E., Schwarz, W. M. and Anderson, R. N., 1979, Thermal effects of ridge subduction: *Earth and Planetary Science Letters*, **44**(2), 239-246.

Dibblee, T. W., Jr., 1973, Geologic maps of the Santiago Creek, Eagle Rest Peak, Pleito Hills, Grapevine, and Pastoria Creek quadrangles, Kern County, California: *U.S. Geological Survey Open File Report*, 73-57.

Dibblee, T. W., Jr., 1986, Geology of the San Emigdio Mountains, California: *Field Trip Guidebook - Pacific Section, Society of Economic Paleontologists and Mineralogists*, **48**, 1-10.

Ducea, M. N., Kidder, S. and Chesley, J. T., 2007, A geologic window into a subduction

megathrust: *Eos, Transactions, American Geophysical Union*, **88**(27), 277.

Ducea, M. N., Kidder, S., Chesley, J. T. and Saleeby, J. B., 2009, Tectonic underplating of trench sediments beneath magmatic arcs; the Central California example: *International Geology Review*, **51**(1), 1-26.

Ehlig, P. L., 1981, Origin and tectonic history of the basement terrane of the San Gabriel Mountains, central Transverse Ranges. In: *The geotectonic development of California, Rubey Volume I* (ed Ernst, W. G.), 253-283, Prentice-Hall, New Jersey.

England, P. and Molnar, P., 1993, The interpretation of inverted metamorphic isograds using simple physical calculations: *Tectonics*, **12**(1), 145-158.

English, J. M., Johnston, S. T. and Wang, K., 2003, Thermal modelling of the Laramide Orogeny; testing the flat-slab subduction hypothesis: *Earth and Planetary Science Letters*, **214**(3-4), 619-632.

Ernst, W. G., 1988, Tectonic history of subduction zones inferred from retrograde blueschist *P-T* paths: *Geology*, **16**(12), 1081-1084.

Escuder Viruete, J., Indares, A. and Arenas, R., 2000, *P-T* paths derived from garnet growth zoning in an extensional setting; an example from the Tormes gneiss dome (Iberian Massif, Spain): *Journal of Petrology*, **41**(10), 78.

Ganguly, J., 2002, Diffusion kinetics in minerals: Principles and applications to tectono-metamorphic processes. In: *Energy modelling in minerals*, pp. 271-309.

Ganguly, J., Bhattacharya, R. N. and Chakraborty, S., 1988, Convolution effect in the determination of composition profiles and diffusion coefficients by microprobe step scans: *American Mineralogist*, **73**(7-8), 901-909.

Ganguly, J., Cheng, W. and Tirone, M., 1996, Thermodynamics of aluminosilicate garnet

solid solution; new experimental data, an optimized model, and thermometry applications: *Contributions to Mineralogy and Petrology*, **126**(1-2), 137-151.

Garcia-Casco, A., Lazaro, C., Rojas-Agramonte, Y., Kroener, A., Torres-Roldan, R. L., Nunez, K., Neubauer, F., Millan, G. and Blanco-Quintero, I., 2008, Partial melting and counterclockwise *P-T* path of subducted oceanic crust (Sierra del Convento Melange, Cuba): *Journal of Petrology*, **49**(1), 129-161.

Gerya, T. V., Stöckhert, B. and Perchuk, A. L., 2002, Exhumation of high-pressure metamorphic rocks in a subduction channel; a numerical simulation: *Tectonics*, **21**(6), 19.

Glicksman, M. E., 2000, *Diffusion in solids: field theory, solid-state principles, and applications*. Wiley, New York.

Graham, C. M. and England, P. C., 1976, Thermal regimes and regional metamorphism in the vicinity of overthrust faults; an example of shear heating and inverted metamorphic zonation from southern California: *Earth and Planetary Science Letters*, **31**(1), 142-152.

Graham, C. M. and Powell, R., 1984, A garnet-hornblende geothermometer; calibration, testing, and application to the Pelona Schist, Southern California: *Journal of Metamorphic Geology*, **2**(1), 13-31.

Grove, M. and Bebout, G. E., 1995, Cretaceous tectonic evolution of coastal Southern California; insights from the Catalina Schist: *Tectonics*, **14**(6), 1290-1308.

Grove, M., Jacobson, C. E., Barth, A. P. and Vucic, A., 2003, Temporal and spatial trends of Late Cretaceous-early Tertiary underplating Pelona and related schist beneath Southern California and southwestern Arizona: *Geological Society of America Special Paper*, **374**, 381-406.

Grove, M., Bebout, G. E., Jacobson, C. E., Barth, A. P., Kimbrough, D. L., King, R. L., Zou, H., Lovera, O. M., Mahoney, B. J. and Gehrels, G. E., 2008, The Catalina Schist; evidence for Middle Cretaceous subduction erosion of southwestern North America: *Geological Society of America Special Paper*, **436**, 335-361.

Guiraud, M., Powell, R., and Rebay, G., 2001, H_2O in metamorphism and unexpected behaviour in the preservation of metamorphic mineral assemblages: *Journal of Metamorphic Geology*, **19**, 445-454.

Gutscher, M.-A., Spakman, W., Bijwaard, H. and Engdahl, E. R., 2000, Geodynamics of flat subduction; seismicity and tomographic constraints from the Andean margin: *Tectonics*, **19**(5), 814-833, doi: 10.1029/1999TC001152.

Haxel, G. and Dillon, J., 1978, The Pelona-Orocopia Schist and Vincent-Chocolate Mountain thrust system, southern California. In: *Mesozoic paleogeography of the western United States: Pacific Section, Society of Economic Paleontologists and Mineralogists Pacific Coast Paleogeography Symposium 2* (eds Howell, D. G. and McDougall, K. A.), 453-469.

Haxel, G.B., Jacobson, C.E., Richard, S.M., Tosdal, R.M., and Grubensky, M.J., 2002, The Orocopia Schist in southwest Arizona: Early Tertiary oceanic rocks trapped or transported far inland, *in* Barth, A., ed., Contributions to crustal evolution of the southwestern United States: *Geological Society of America Special Paper*, **365**, 99-128.

Holland, T. J. B. and Powell, R., 1998, An internally consistent thermodynamic data set for phases of petrological interest: *Journal of Metamorphic Geology*, **16**(3), 309-343.

Jacobson, C. E., 1983, Structural geology of the Pelona Schist and Vincent Thrust, San Gabriel Mountains, California: *Geological Society of America Bulletin*, **94**(6), 753-767.

Jacobson, C. E., 1995, Qualitative thermobarometry of inverted metamorphism in the Pelona and Rand schists, Southern California, using calciferous amphibole in mafic schist: *Journal of Metamorphic Geology*, **13**(1), 79-92.

Jacobson, C. E., 1997, Metamorphic convergence of the upper and lower plates of the Vincent Thrust, San Gabriel Mountains, Southern California, USA: *Journal of Metamorphic Geology*, **15**(1), 155-165.

Jacobson, C. E., Dawson, M. R. and Postlethwaite, C. E., 1988, Structure, metamorphism, and tectonic significance of the Pelona, Orocopia, and Rand schists, Southern California. In: *Metamorphism and crustal evolution of the Western United States, Rubey Volume* (ed Ernst, W. G.), 976-997, Prentice-Hall, New Jersey.

Jacobson, C. E., Oyarzabal, F. R. and Haxel, G. B., 1996, Subduction and exhumation of the Pelona-Orocopia-Rand schists, Southern California: *Geology*, **24**(6), 547-550.

Jacobson, C. E., Grove, M., Stamp, M. M., Vucic, A., Oyarzabal, F. R., Haxel, G. B., Tosdal, R. M. and Sherrod, D. R., 2002, Exhumation history of the Orocopia Schist and related rocks in the Gavilan Hills area of southeasternmost California: *Geological Society of America Special Paper*, **365**, 129-154.

Jacobson, C. E., Grove, M., Vucic, A., Pedrick, J. N. and Ebert, K. A., 2007, Exhumation of the Orocopia Schist and associated rocks of southeastern California; relative roles of erosion, synsubduction tectonic denudation, and middle Cenozoic extension: *Geological Society of America Special Paper*, **419**, 1-37.

Jacobson, C. E., Grove, M., Pedrick, J. N., Barth, A. P., Marsaglia, K. M., Gehrels, G. E., Nourse, J. A., 2011, Late Cretaceous-early Cenozoic tectonic evolution of the southern

California margin inferred from provenance of trench and forearc sediments: *Geological Society of America Bulletin*, **123**(3-4), 485-506.

James, E. W., 1986, Geochronology, isotopic characteristics, and paleogeography of parts of the Salinian Block of California. Ph.D. Thesis, University of California, Santa Barbara, 176 pp.

Jamieson, R. A., Beaumont, C., Hamilton, J., Fullsack, P., 1996, Tectonic assembly of inverted metamorphic sequences: *Geology*, **24**(9), 839-842.

Ji, S., Zhao, P. and Saruwatari, K., 1997, Fracturing of garnet crystals in anisotropic metamorphic rocks during uplift: *Journal of Structural Geology*, **19**(5), 603-620.

Karato, S., Wang, Z., Liu, B., and Fujino, K., 1995, Plastic deformation of garnets: systematics and implications for the rheology of the mantle transition zone: *Earth and Planetary Science Letters*, **130**(3-4), 13-30.

Kidder, S., Ducea, M., Gehrels, G. E., Patchett, P. J. and Vervoort, J., 2003, Tectonic and magmatic development of the Salinian Coast Ridge Belt, California: *Tectonics*, **22**, doi:10.1029/2002TC001409.

Kidder, S. and Ducea, M. N., 2006, High temperatures and inverted metamorphism in the schist of Sierra de Salinas, California: *Earth and Planetary Science Letters*, **241**(3-4), 422-437.

Kincaid, C. and Sacks, I. S., 1997, Thermal and dynamical evolution of the upper mantle in subduction zones: *Journal of Geophysical Research*, **102**(B6), 12,295-12,315.

Kistler, R. W. and Champion, D. E., 2001, Rb-Sr whole-rock and mineral ages, K-Ar, 40Ar/39Ar, and U-Pb mineral ages, and strontium, lead, neodymium, and oxygen isotopic compositions for granitic rocks from the Salinian Composite Terrane,

California: *U.S. Geological Survey Open File Report*, **01-453**, 84.

Kohn, M. J. and Spear, F., 2000, Retrograde net transfer reaction insurance for pressure-temperature estimates: *Geology*, **28**(12), 1127-1130.

Konrad-Schmolke, M., Handy, M. R., Babist, J. and O'Brien, P. J., 2005, Thermodynamic modeling of diffusion-controlled garnet growth: *Contributions to Mineralogy and Petrology*, **149**(2), 181-195.

Krogh, E. J., Oh, C. W. and Liou, J. G., 1994, Polyphase and anticlockwise *P-T* evolution for Franciscan eclogites and blueschists from Jenner, California, USA: *Journal of Metamorphic Geology*, **12**(2), 121-134.

Liu, L., Spasojevic, S. and Gurnis, M., 2008, Reconstructing Farallon Plate subduction beneath North America back to the Late Cretaceous: *Science*, **322**(5903), 934-938, doi: 10.1126/science.1162921.

Liu, L., Gurnis, M., Seton M., Saleeby J., Müller R. D., and Jackson, J. M., 2010, The role of oceanic plateau subduction in the Laramide orogeny: *Nature Geoscience*, doi: 10.1038/NGEO829.

Ludington, S., Moring, B., Miller, R. J., Stone, P. A., Bookstrom, A. A., Bedford, D. R., Evans, J. G., Haxel, G. A., Nutt, C. J., Flyn, K. S., and Hopkins, M. J., 2007, Preliminary integrated geologic map databases for the United States: *U.S. Geological Survey Open File Report*, 2005-1305.

Mandal, N., Chakraborty, C., and Samanta, S. K., 2001, Controls on the failure mode of brittle inclusions hosted in a ductile matrix: *Journal of Structural Geology*, **23**(1), 51-66, doi: 10.1016/S0191-8141(00)00127-9.

Matzel, J. E. P., Bowring, S. A. and Miller, R. B., 2004, Protolith age of the Swakane

Gneiss, north Cascades, Washington; evidence of rapid underthrusting of sediments beneath an arc: *Tectonics*, **23**, no.6, 18.

McDougall, I. and Harrison, T. M., 1999, *Geochronology and thermochronology by the $^{40}Ar/^{39}Ar$ method*, Oxford University Press, New York, 269 pp.

McNulty, B. and Farber, D., 2002, Active detachment faulting above the Peruvian flat slab: *Geology*, **30**(6), 567-570.

Oyarzabal, F.R., 1996, Metamorphic history and structural evolution of the Orocopia Schist in the Gavilan Hills, S.E. Ph.D. Thesis, Iowa State University, Ames, 103 pp.

Oyarzabal, F. R., Jacobson, C. E. and Haxel, G. B., 1997, Extensional reactivation of the Chocolate Mountains subduction thrust in the Gavilan Hills of southeastern California: *Tectonics*, **16**(4), 650-661.

Pardavi-Horváth, 1984, Microhardness and brittle fracture of garnet single crystals: *Journal of Materials Science*, **19**, 1159-1170.

Peacock, S. M., 1987, Thermal effects of metamorphic fluids in subduction zones: *Geology*, **15**(11), 1057-1060.

Peacock, S. M., 1992, Blueschist-facies metamorphism, shear heating, and *P-T-t* paths in subduction shear zones: *Journal of Geophysical Research*, **97**(B12), 17,693-17,707.

Peacock, S. M., 2003, Thermal structure and metamorphic evolution of subducting slabs. In: *Geophysical Monograph* (ed Eiler, J. M.), 7-22.

Perchuk, A., Philippot, P., Erdmer, P. and Fialin, M., 1999, Rates of thermal equilibration at the onset of subduction deduced from diffusion modeling of eclogitic garnets, Yukon-Tanana Terrane, Canada: *Geology*, **27**(6), 531-534.

Pickett, D. A. and Saleeby, J. B., 1993, Thermobarometric constraints on the depth of

exposure and conditions of plutonism and metamorphism at deep levels of the Sierra Nevada Batholith, Tehachapi Mountains, California: *Journal of Geophysical Research*, **98**(B1), 609-629.

Pickett, D. A. and Saleeby, J. B., 1994, Nd, Sr, and Pb isotopic characteristics of Cretaceous intrusive rocks from deep levels of the Sierra Nevada Batholith, Tehachapi Mountains, California: *Contributions to Mineralogy and Petrology*, **118**(2), 198-215, doi: 10.1007/BF01052869.

Platt, J. P., 1975, Metamorphic and deformational processes in the Franciscan Complex, California; some insights from the Catalina Schist terrane: *Geological Society of America Bulletin*, **86**(10), 1337-1347.

Postlethwaite, C. E. and Jacobson, C. E., 1987, Early history and reactivation of the Rand Thrust, Southern California: *Journal of Structural Geology*, **9**(2), 195-205, doi: 10.1016/0191-8141(87)90025-3.

Powell, R. and Holland, T., 1994, Optimal geothermometry and geobarometry: *American Mineralogist*, **79**(1-2), 120-133.

Prior, D. J., 1993, Sub-critical fracture and associated retrogression of garnet during mylonitic deformation: *Contributions to Mineralogy and Petrology*, **113**(4), 545-556.

Ramberg, H., 1955, Natural and experimental boudinage and pinch-and-swell structures: *Journal of Geology*, **63**(6), 512-526.

Ross, D. C., 1989, The metamorphic and plutonic rocks of the southernmost Sierra Nevada, California, and their tectonic framework: *U.S. Geological Survey Professional Paper*, *1381*, 159 pp.

Saleeby, J., 2003, Segmentation of the Laramide slab; evidence from the southern Sierra

Nevada region: *Geological Society of America Bulletin*, **115**(6), 655-668.

Saleeby, J. B., Sams, D. B. and Kistler, R. W., 1987, U/Pb zircon, strontium, and oxygen isotopic and geochronological study of the southernmost Sierra Nevada Batholith, California: *Journal of Geophysical Research*, **92**(B10), 10,443-10,466.

Saleeby, J., Farley, K. A., Kistler, R. W. and Fleck, R. J., 2007, Thermal evolution and exhumation of deep-level batholithic exposures, southernmost Sierra Nevada, California: *Geological Society of America Special Paper*, **419**, 39-66.

Sharry, J., 1981, The geology of the western Tehachapi Mountains, California. Ph.D. Thesis, Massachusetts Institute of Technology, Cambridge, 215 pp.

Sorensen, S. S., 1988, Petrology of amphibolite-facies mafic and ultramafic rocks from the Catalina Schist, Southern California; metasomatism and migmatization in a subduction zone metamorphic setting: *Journal of Metamorphic Geology*, **6**(4), 405-435.

Spear, F. S. and Selverstone, J., 1983, Quantitative *P-T* path from zoned minerals; theory and tectonic applications: *Contributions to Mineralogy and Petrology*, **83**(3-4), 348-357.

Spear, F. S., 1993, *Metamorphic phase equilibria and pressure-temperature-time paths*. Mineralogical Society of America, Washington, D.C., 799 pp.

Trepmann, C. A. and Stöckhert, B., 2002, Cataclastic deformation of garnet; a record of synseismic loading and postseismic creep: *Journal of Structural Geology*, **24**(11), 1845-1856.

Vance, D. and Mahar, E., 1998, Pressure-temperature paths from *P-T* pseudosections and zoned garnets; potential, limitations and examples from the Zanskar Himalaya, NW India: *Contributions to Mineralogy and Petrology*, **132**(3), 225-245.

Vielzeuf, D., Baronnet, A., Perchuk, A. L., Laporte, D. and Baker, M. B., 2007, Calcium

diffusivity in alumino-silicate garnets; an experimental and ATEM study: *Contributions to Mineralogy and Petrology*, **154**(2), 153-170.

Wakabayashi, J., 1990, Counterclockwise *P-T-t* paths from amphibolites, Franciscan Complex, California; relics from the early stages of subduction zone metamorphism: *Journal of Geology*, **98**(5), 657-680.

Wakabayashi, J. and Dumitru, T.A., 2007, $^{40}Ar/^{39}Ar$ Ages from Coherent, High-Pressure Metamorphic Rocks of the Franciscan Complex, California: Revisiting the Timing of Metamorphism of the World's Type Subduction Complex: *International Geology Review*, **49**, 873-906.

Whitney, D. L., 1996, Garnets as open systems during regional metamorphism: *Geology*, **24**(2), 147-150.

Whitney, D. L., Broz, M., and Cook, R. F., 2007, Hardness, toughness, and modulus of some common metamorphic minerals: *American Mineralogist*, **92**(2-3), 281-288, doi: 10.2138/am.2007.2212.

Wood, D.J. and Saleeby, J.B., 1997, Late Cretaceous - Paleocene extensional collapse and disaggregation of the southernmost Sierra Nevada Batholith: *International Geology Review*, **39**, 973-1009, doi:10.1080/ 00206819709465314.

Yin, A., 2002, Passive-roof thrust model for the emplacement of the Pelona-Orocopia Schist in Southern California, United States: *Geology*, **30**(2), 183-186.

CHAPTER 4

Late Cretaceous gravitational collapse of the southern Sierra Nevada batholith, California

Alan D. Chapman[1], Jason B. Saleeby[1], David J. Wood[1,2], Alison Piasecki[1], Kenneth A. Farley[1], Steven Kidder[1], and Mihai N. Ducea[3]

[1]*Division of Geological and Planetary Sciences, California Institute of Technology, Pasadena, California, USA*

[2]*Now at 3423 Broadmead Dr. Houston, Texas, USA*

[3]*Department of Geosciences, University of Arizona, Tucson, Arizona, USA.*

Submitted to *Geosphere*

ABSTRACT

The Sierra Nevada batholith (SNB) is an ~ 600 km long NNW-trending composite arc assemblage consisting of a myriad of plutons exhibiting a distinct transverse zonation in structural, petrologic, geochronologic, and isotopic patterns. This zonation is most clearly expressed in terms of bulk composition with west to east variation from mainly mafic to felsic plutonic assemblages. South of 35.5 °N, the depth of exposure increases markedly and the aforementioned trends are disrupted such that: 1) the primary zonation pattern takes on an east-west trend; 2) western zone rocks are truncated by eastern zone rocks along the proto-Kern Canyon fault, a Late Cretaceous oblique ductile thrust; and 3) fragments of shallow-level eastern SNB affinity rocks overlie deeper-level western zone rocks and subjacent subduction accretion assemblages along a major Late Cretaceous detachment

system. The magnitude of displacement along this detachment system is constrained here by palinspastic reconstruction of vertical piercing points provided by primary batholithic and metamorphic pendant structure and stratigraphy. Integration of new and published U-Pb zircon geochronologic, thermobarometric, (U-Th)/He thermochronometric, and geochemical data from plutonic and metamorphic framework assemblages in the southern SNB reveal seven potential correlations between dispersed crustal fragments and the SNB autochthon. Each correlation suggests at least 50 km of south to southwest-directed transport and tectonic excision of approximately 5 to 10 km of crust along the Late Cretaceous detachment system. The timing and pattern of regional dispersion of crustal fragments in the southern SNB is most consistent with Late Cretaceous collapse above the underplated accretionary complex. Collectively, data reported and compiled herein have implications for the degree of coupling between the shallow and deep crust during high magnitude extension, the tectonic context of gravitational collapse, and the development of modern landscape and the arrangement of tectonic elements in southern California.

1. INTRODUCTION

In zones of convergence, regional gradients in gravitational potential energy can be relaxed through lateral spreading and vertical thinning of orogenic crust (e.g., Dewey, 1988; Rey *et al*., 2001). Deep-crustal exposures of the southern Sierra Nevada batholith (SNB), subjacent subduction accretion assemblages of the Rand, San Emigdio, and Sierra de Salinas schists (referred to in aggregate as “the schist”), and flanking shallow-level assemblages of the Mojave Desert and Salinian block represent a multi-tiered regional core complex that formed in response to Laramide shallow subduction-driven orogenesis and subsequent

gravitational collapse (Malin *et al*., 1995; Wood and Saleeby, 1997; Saleeby, 2003; Chapman *et al*., 2010, 2011). The collapse phase is marked by the structural ascent of presently exposed deep-level (7-11 kbar) rocks of the southernmost SNB (Ague and Brimhall, 1988; Pickett and Saleeby, 1993; Fletcher *et al*., 2002; Grove *et al*., 2003; Kidder *et al*., 2003; Saleeby *et al*., 2007; Nadin and Saleeby, 2008; Chapman *et al*., 2010, 2011), the removal of western batholithic and forearc belts south of ~ 35˚ N (Ross *et al*., 1973; Ross, 1988; James *et al*. 1993; Schott and Johnson, 1998, 2001), and the dispersal of shallow-level (2-4 kbar), southeastern SNB affinity assemblages across the entire width of the batholith (May, 1989; Malin *et al*, 1995; Wood and Saleeby, 1997; Saleeby, 2003; Chapman *et al*., 2010), thereby disrupting the primary transverse structure of the SNB. This effort focuses on specific and elusive issues pertaining to Late Cretaceous disruption and dispersion of the southern SNB and vicinity, including: 1) the magnitude and timing of tectonic transport of upper crustal fragments along a regional detachment system; 2) the degree of strain coupling between differentially exhuming levels of the crust; 3) the importance of strike-slip faulting during collapse; and 4) the extent to which the development of the southern Sierra Nevada landscape was influenced by tectonism reaching back into the Late Cretaceous.

Major plutonic units and metamorphic pendants of the southern SNB are fairly well-characterized in terms of geologic, U-Pb zircon, $^{87}Sr/^{86}Sr$ (Sr_i), thermobarometric, paleontologic, and bulk compositional data (Kistler and Peterman, 1978; Chen and Moore, 1982; Saleeby *et al*., 1987; 2007; 2008; Ross, 1989; Kistler and Ross, 1990; Pickett and Saleeby, 1993; 1994; Saleeby and Busby, 1993; Nadin and Saleeby, 2008; Memeti *et al*., 2010). These datasets clearly reveal a regional primary zonation pattern to the batholith

and distinct longitudinal belts of Neoproterozoic to lower Mesozoic metamorphic pendant sequences. In aggregate the pendants and hosting plutons of the southern SNB are characterized well enough to readily recognize allochthonous equivalents. South of 35.5 °N, the depth of exposure increases markedly and aforementioned trends are disrupted along two major Late Cretaceous systems of parallel low-angle normal faults that juxtapose: 1) the schist and deep crustal levels of the SNB (the Rand fault and Salinas shear zone; Postlethwaite and Jacobson, 1987; Nourse, 1989; Kidder and Ducea, 2006; Chapman *et al*., 2010, 2011) and 2) eastern and western SNB assemblages (the southern Sierra detachment; Wood and Saleeby, 1997). The resulting generalized tectonostratigraphy of the southern SNB, from top to bottom, is that of a multi-tiered core complex consisting of three packages: allochthonous shallow-level eastern SNB affinity rocks, (par)autochthonous deep-level western SNB assemblages, and the schist.

In this study, we present new: 1) field and structural relations to provide the basis for recognizing potential correlations; 2) U-Pb geochronology of plutonic and detrital zircon populations to identify the age and provenance of displaced plutonic and metamorphic assemblages; 3) thermobarometric work to assess pressure differentials between native and displaced assemblages; 4) major and trace element geochemistry and Sr and Nd isotopic ratios to determine the sources of allochthonous metavolcanic rocks; and 5) zircon (U-Th)/He thermochronometry to constrain the timing of exhumation during extension. These results are integrated with previous geologic studies and thermobarometric, geochronologic, and geochemical databases in order to recognize allochthon-autochthon pairs and to estimate the magnitude of transport that they imply. Our zircon (U-Th)/He data reveal a rapid cooling event in the SNB autochthon at 77 ± 5

Ma, which we interpret as the principal time of large magnitude detachment faulting. We also recognize seven allochthon-autochthon pairs, each implying 50 to 70 km of lateral transport and the removal of approximately 5 to 10 km of crust along the southern Sierra detachment system. An important finding of this work is that the timing and kinematics of dispersal of upper crustal fragments and ascent of deep-level batholithic and subduction accretion assemblages coincide, suggesting that the shallow and deep crust were highly coupled during extension.

2. GEOLOGIC BACKGROUND

2.1. "Autochthonous" Sierra Nevada batholith

The Sierra Nevada block is a predominantly NNW-trending composite batholith with juvenile batholithic crust extending to ≥ 35 km depth (Ruppert *et al*., 1998; Saleeby *et al*., 2003, 2007). Gradients in pluton ages, integrated bulk compositions, amounts of recycled crustal components, and the paleogeographic affinities of metamorphic pendants define a distinct west to east zonation to the SNB (Figure 4.1). These batholithic zones, along with outboard forearc basin segments, may be used to recognize and reconstruct superimposed tectonic disruptions. For much of the SNB up to five distinct longitudinal belts of Paleozoic metamorphic pendant sequences can be mapped at regional scales (Figure 4.2). For the purpose of assessing the magnitude of Late Cretaceous disruption of the southern SNB and adjacent southern California batholith (SCB) of the Mojave Desert and Salinia, we refer to the pre-Late Cretaceous architecture of the SNB-SCB as "autochthonous." Of course, a number of the pre-batholithic architectural elements experienced significant tectonic

Figure 4.1. (a) Tectonic map of southern Sierra Nevada basement with related elements of northern Mojave and Salinia restored along San Andreas and Garlock faults. Primary zonation and structures of the SNB from Saleeby *et al*. (2007) and Nadin and Saleeby (2008). Pressure determinations from Wiebe (1966, 1970), DeCrisoforo and Cameron (1977), John (1981), Ague and Brimhall (1988), Pickett and Saleeby (1993), Kidder *et al*. (2003), Nadin and Saleeby (2008), and this study. Extent of the Independence dike swarm from Carl and Glazner (2002), Glazner *et al*. (2002), Bartley *et al*. (2007), and Hopson *et al*. (2008). Rand fault structure contours from Cheadle *et al*. (1986), Li *et al*. (1992), Malin *et al*. (1995), Yan *et al*. (2005), and Luffi *et al*. (2009). Subsurface sources from Ross (1989), Monastero *et al*. (2002), and T. Nilsen, personal communication, 2005. Upper Cretaceous isopachs from Reid (1988). (b) Map showing locations of metamorphic pendants and faults discussed in text. Calaveras complex shown in dark gray; Neoproterozoic to Early Mesozoic pendants including Kings sequence shown in gray. Cretaceous and Tertiary faults shown in black and red, respectively.

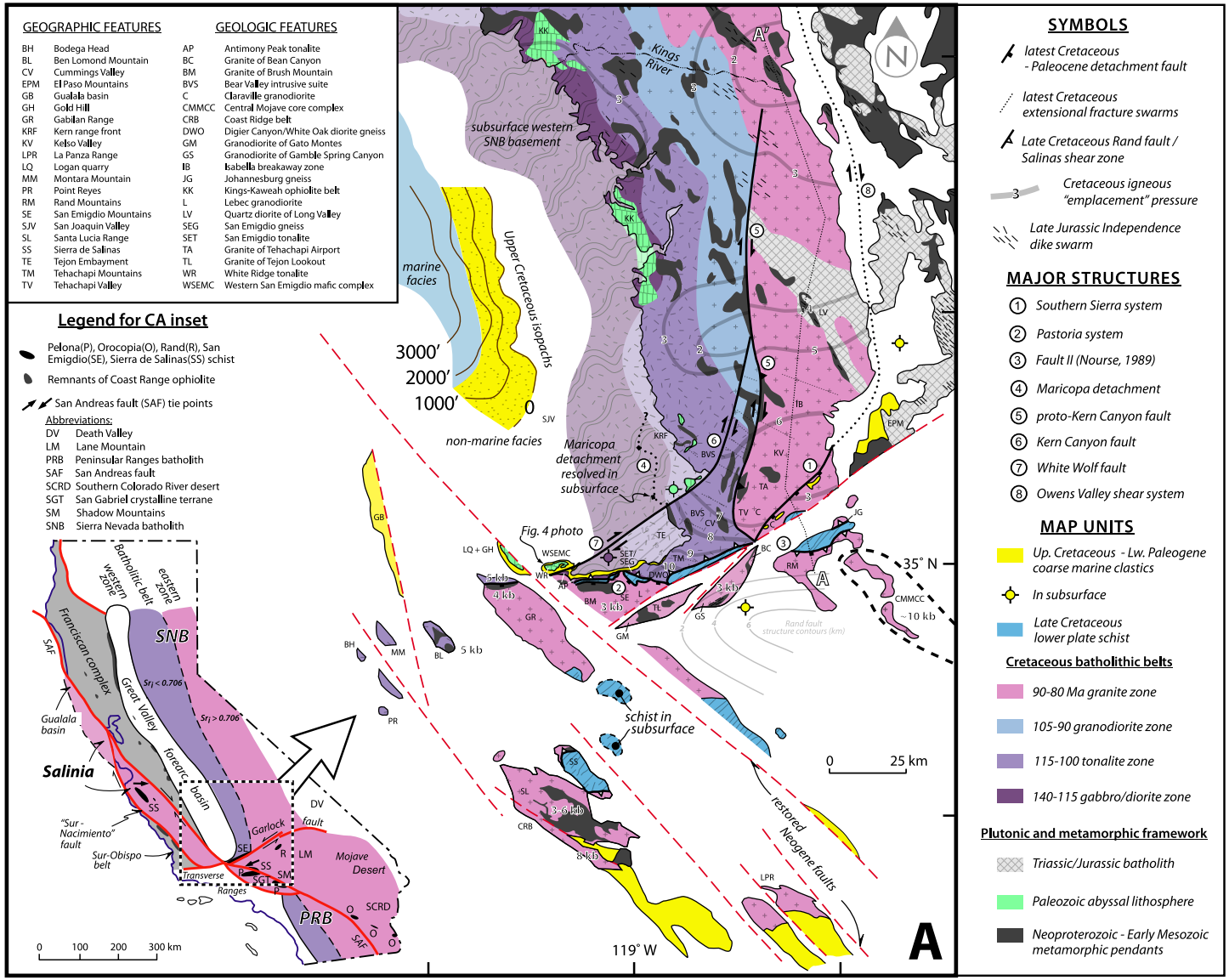
GEOGRAPHIC FEATURES
BH Bodega Head
BL Ben Lomond Mountain
CV Cummings Valley
EPM El Paso Mountains
GB Gualala basin
GH Gold Hill
GR Gabilan Range
KRF Kern range front
KV Kelso Valley
LPR La Panza Range
LQ Logan quarry
MM Montara Mountain
PR Point Reyes
RM Rand Mountains
SE San Emigdio Mountains
SJV San Joaquin Valley
SL Santa Lucia Range
SS Sierra de Salinas
TE Tejon Embayment
TM Tehachapi Mountains
TV Tehachapi Valley
GEOLOGIC FEATURES
AP Antimony Peak tonalite
BC Granite of Bean Canyon
BM Granite of Brush Mountain
BVS Bear Valley intrusive suite
C Claraville granodiorite
CMMCC Central Mojave core complex
CRB Coast Ridge belt
DWO Digier Canyon/White Oak diorite gneiss
GM Granodiorite of Gato Montes
GS Granodiorite of Gamble Spring Canyon
IB Isabella breakaway zone
JG Johannesburg gneiss
KK Kings-Kaweah ophiolite belt
L Lebec granodiorite
LV Quartz diorite of Long Valley
SEG San Emigdio gneiss
SET San Emigdio tonalite
TA Granite of Tehachapi Airport
TL Granite of Tejon Lookout
WR White Ridge tonalite
WSEMC Western San Emigdio mafic complex
Legend for CA inset
Pelona(P), Orocopia(O), Rand(R), San Emigdio(SE), Sierra de Salinas(SS) schist
Remnants of Coast Range ophiolite
San Andreas fault (SAF) tie points
Abbreviations:
DV Death Valley
LM Lane Mountain
PRB Peninsular Ranges batholith
SAF San Andreas fault
SCRD Southern Colorado River desert
SGT San Gabriel crystalline terrane
SM Shadow Mountains
SNB Sierra Nevada batholith
Batholithic belt
western zone
eastern zone
Franciscan complex
SAF
SNB
Sri < 0.706
Sri > 0.706
Great Valley
forearc basin
Gualala basin
Salinia
"Sur - Nacimiento" fault
Sur-Obispo belt
Garlock fault
Transverse Ranges
Mojave Desert
PRB
DV
LM
SCRD
0 100 200 300 km
subsurface western SNB basement
Kings River
marine facies
Upper Cretaceous isopachs
3000'
2000'
1000'
0
SJV
non-marine facies
Maricopa detachment resolved in subsurface
Fig. 4 photo
schist in subsurface
restored Neogene faults
Rand fault structure contours (km)
5 kb
4 kb
3 kb
~10 kb
3-6 kb
8 kb
35° N
119° W
0 25 km
A
A'
SYMBOLS
latest Cretaceous - Paleocene detachment fault
latest Cretaceous extensional fracture swarms
Late Cretaceous Rand fault / Salinas shear zone
Cretaceous igneous "emplacement" pressure
Late Jurassic Independence dike swarm
MAJOR STRUCTURES
1 Southern Sierra system
2 Pastoria system
3 Fault II (Nourse, 1989)
4 Maricopa detachment
5 proto-Kern Canyon fault
6 Kern Canyon fault
7 White Wolf fault
8 Owens Valley shear system
MAP UNITS
Up. Cretaceous - Lw. Paleogene coarse marine clastics
In subsurface
Late Cretaceous lower plate schist
Cretaceous batholithic belts
90-80 Ma granite zone
105-90 granodiorite zone
115-100 tonalite zone
140-115 gabbro/diorite zone
Plutonic and metamorphic framework
Triassic/Jurassic batholith
Paleozoic abyssal lithosphere
Neoproterozoic - Early Mesozoic metamorphic pendants

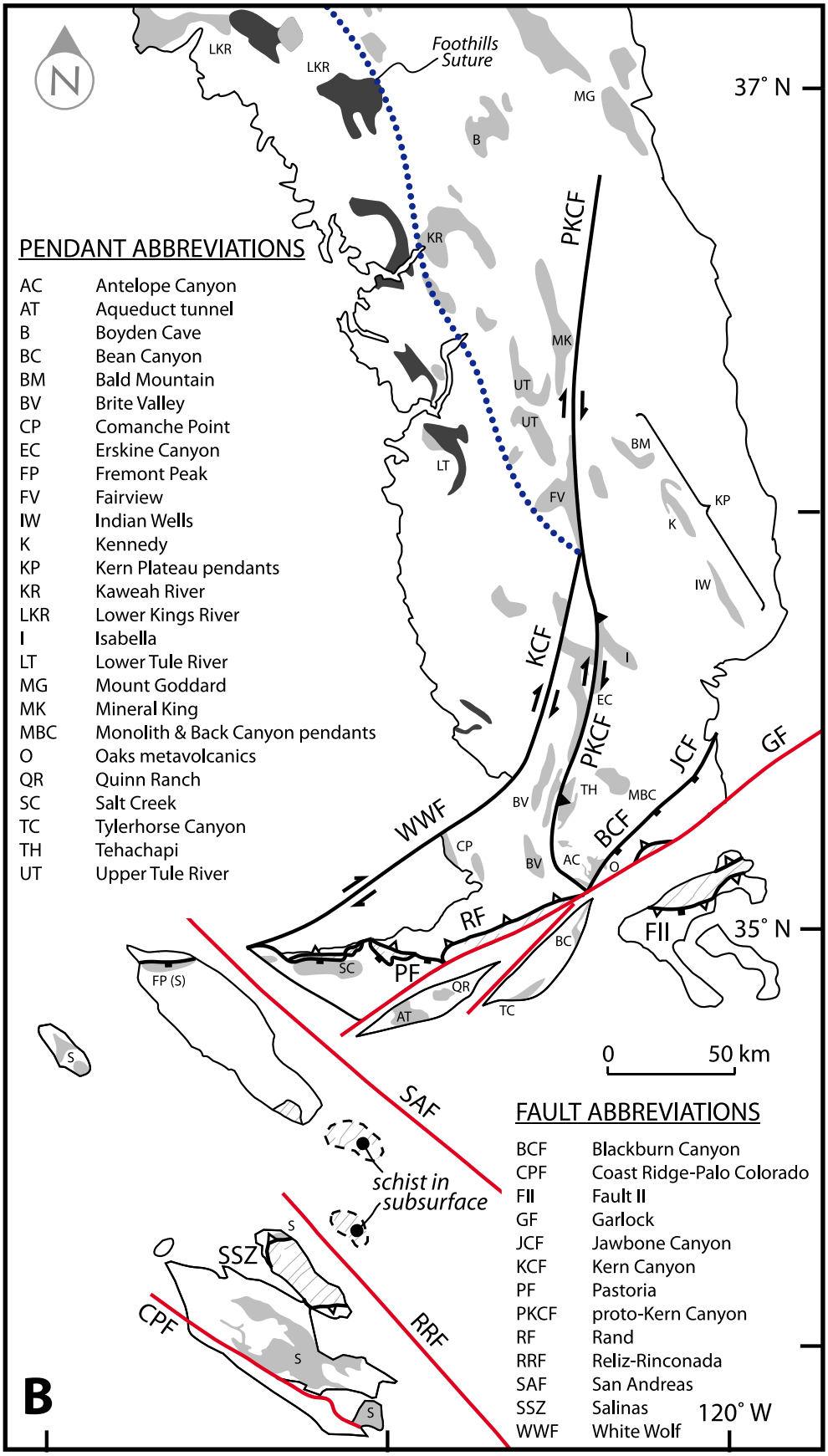
N
LKR
LKR
Foothills Suture
MG
37° N
B
PKCF
KR
MK
UT
UT
LT
BM
FV
KP
K
IW
I
EC
KCF
PKCF
JCF
GF
TH
MBC
BV
WWF
CP
BV
AC
O
BCF
RF
BC
FII
35° N
SC
PF
QR
AT
TC
FP (S)
S
0
50 km
SAF
schist in subsurface
S
O
SSZ
CPF
S
RRF
S
B
120° W
PENDANT ABBREVIATIONS
AC Antelope Canyon
AT Aqueduct tunnel
B Boyden Cave
BC Bean Canyon
BM Bald Mountain
BV Brite Valley
CP Comanche Point
EC Erskine Canyon
FP Fremont Peak
FV Fairview
IW Indian Wells
K Kennedy
KP Kern Plateau pendants
KR Kaweah River
LKR Lower Kings River
I Isabella
LT Lower Tule River
MG Mount Goddard
MK Mineral King
MBC Monolith & Back Canyon pendants
O Oaks metavolcanics
QR Quinn Ranch
SC Salt Creek
TC Tylerhorse Canyon
TH Tehachapi
UT Upper Tule River
FAULT ABBREVIATIONS
BCF Blackburn Canyon
CPF Coast Ridge-Palo Colorado
FII Fault II
GF Garlock
JCF Jawbone Canyon
KCF Kern Canyon
PF Pastoria
PKCF proto-Kern Canyon
RF Rand
RRF Reliz-Rinconada
SAF San Andreas
SSZ Salinas
WWF White Wolf

Figure 4.2. Tectonic map showing paleogeographic affinities of metamorphic pendant belts in the SNB. Major Paleozoic and Mesozoic strike slip faults shown in heavy black and red, respectively. Eugeoclinal assemblages of the El Paso terrane and Roberts Mountains allochthon both shown in orange, despite differences in tectonic setting. Abbreviations: KCF, Kern Canyon fault; LCT, Last Chance thrust; MSLF, Mojave-Snow Lake fault; RMT, Roberts Mountains thrust; WWF, White Wolf fault.

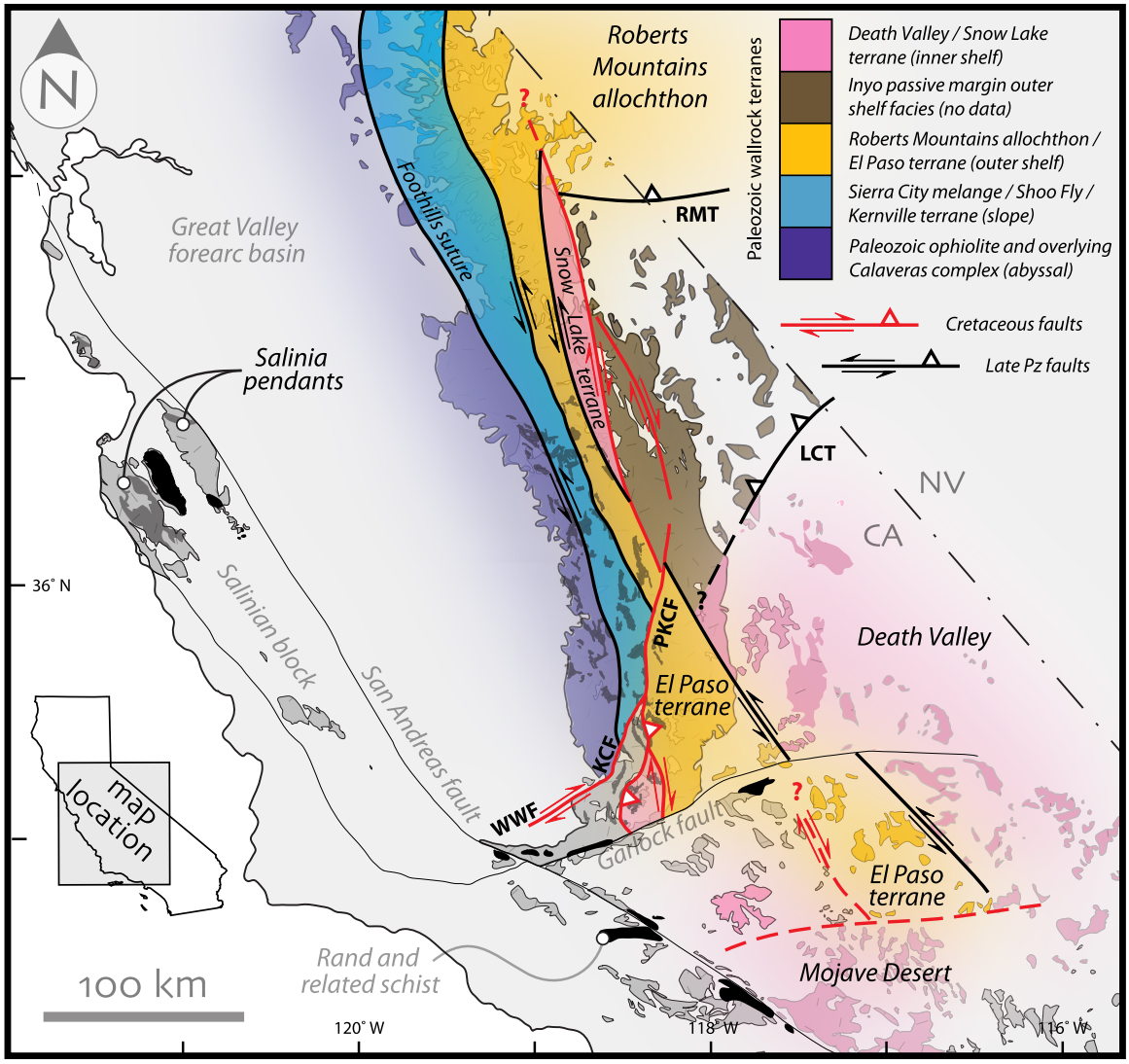
N
Roberts Mountains allochthon
Paleozoic wallrock terranes
Death Valley / Snow Lake terrane (inner shelf)
Inyo passive margin outer shelf facies (no data)
Roberts Mountains allochthon / El Paso terrane (outer shelf)
Sierra City melange / Shoo Fly / Kernville terrane (slope)
Paleozoic ophiolite and overlying Calaveras complex (abyssal)
Cretaceous faults
Late Pz faults
RMT
LCT
Foothills suture
Snow Lake terrane
Great Valley forearc basin
Salinia pendants
Salinian block
San Andreas fault
PKCF
KCF
WWF
El Paso terrane
Garlock fault
Death Valley
Mojave Desert
Rand and related schist
NV
CA
map location
100 km
36° N
120° W
118° W
116° W

rearrangement prior to and during emplacement of the SNB (Kistler, 1990; Dunne and Suczek, 1991; Saleeby and Busby, 1993; Stevens and Stone, 2005; Nadin and Saleeby, 2008; Saleeby, 2011) (Figure 4.2). The following is a summary of key compositional, geochemical, geochronological, and structural relations between "autochthonous" longitudinal zones of the SNB and its framework.

2.1.1. Cretaceous batholithic belts

Across strike variations in composition, pluton emplacement ages, and geochemistry delineate four distinct zones to the SNB (Nadin and Saleeby, 2008 and references therein). From west to east, we define the following zones: 1) the ~ 140 – 115 Ma dioritic zone, a collection of mafic assemblages dominated by quartz diorite, gabbro, and tonalite, with limited outcrop along the westernmost Sierra Nevada and extensive subcrop beneath the San Joaquin Basin (May and Hewitt, 1948; Williams and Curtis, 1976; Ross, 1989; Saleeby, 2009a, 2011 and unpub. data); 2) the ~ 115 – 100 Ma tonalitic zone with domains of tonalite and lesser amounts of quartz diorite and gabbro; 3) the ~105 – 90 Ma granodioritic zone rich in mainly tonalite and granodiorite; and 4) ~ 90 – 80 Ma granitic zone granodioritic and granitic rocks (Figures 4.1 and Figure 4.3). Initial $^{87}Sr/^{86}Sr$ (Sr_i) increases systematically eastward across the Cretaceous zones from ~0.703 to ~0.709, reflecting an increasing continental crustal component progressing from the dioritic to the granitic zone. The boundary between tonalitic and granodioritic zones is generally defined by the $Sr_i = 0.706$ isopleth (Nadin and Saleeby, 2008).

Figure 4.3. Block diagram illustrating petrologic, isotopic, and age zonation of the SNB and the distribution of Paleozoic wallrock terranes and infolds of lower Mesozoic sedimentary and volcanic protolith sequences ("Kings sequence") immediately prior to Late Cretaceous extensional collapse and activity of the SSD.

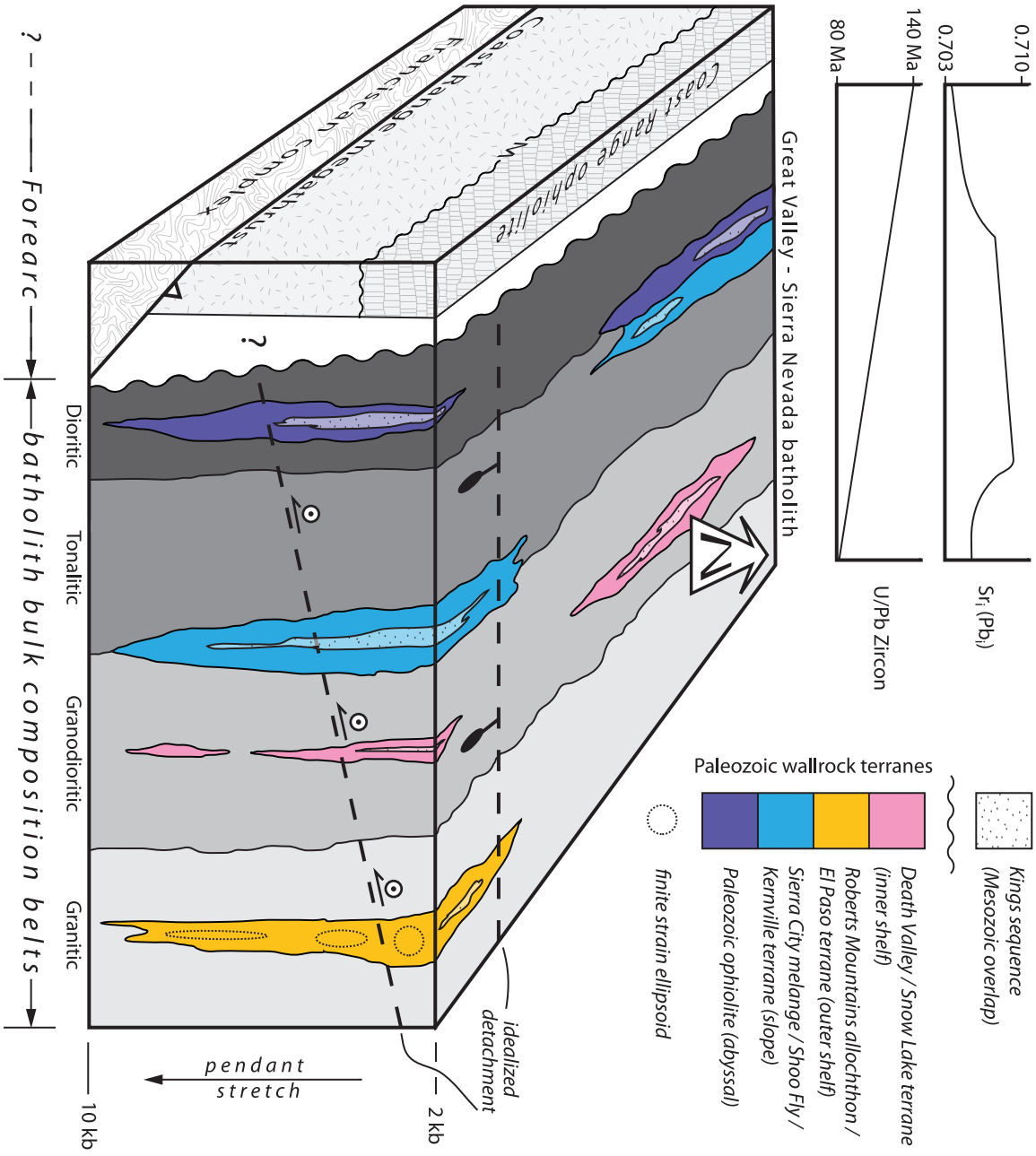
0.710
0.703
Sr_i (Pb_i)
140 Ma
80 Ma
U/Pb Zircon
Kings sequence (Mesozoic overlap)
Paleozoic wallrock terranes
Death Valley / Snow Lake terrane (inner shelf)
Roberts Mountains allochthon / El Paso terrane (outer shelf)
Sierra City melange / Shoo Fly / Kernville terrane (slope)
Paleozoic ophiolite (abyssal)
finite strain ellipsoid
Great Valley - Sierra Nevada batholith
Coast Range ophiolite
Coast Range megathrust
Franciscan Complex
?
Dioritic
Tonalitic
Granodioritic
Granitic
idealized detachment
2 kb
10 kb
pendant stretch
? – – – Forearc
batholith bulk composition belts

2.1.2. Pre-Cretaceous plutons and metamorphic framework

The bulk of the SNB was constructed during a magmatic flare-up event in Cretaceous time (Ducea, 2001) and intruded a framework of Triassic to Jurassic plutons, Neoproterozoic to Mesozoic continental shelf, slope, and rise strata, and a belt of accreted abyssal lithosphere, now all exposed as metamorphic pendants (Figures 4.1, 4.2, and 4.3) (Saleeby *et al*., 2008). Co-variation of pendant stratigraphy, age, and provenance track with plutonic zonation patterns discussed above (Figures 4.2 and 4.3). West to east longitudinal zones include: (1) the Paleozoic Foothills ophiolite belt with overlying Permian to Triassic (?) Calaveras complex hemipelagic deposits, and unconformable infolds of supra-subduction mafic volcanic rocks and siliciclastic turbidites (Saleeby, 2011) ("Paleozoic ophiolite," Figure 4.2). The concealed Foothills Suture (e.g., Saleeby, 2011) marks the eastern boundary of this lithotectonic domain (Figure 4.1b). (2) A belt, spanning western to eastern SNB zones, of Cambrian to Ordivician eugeoclinal (i.e., deep marine sediments of the outer continental margin) quartzite, phyllite, and chert named the Sierra City mélange and Shoo Fly Complex (e.g., Harding *et al*., 2000) in the north and the remnants of similar strata preserved in pendants of the Kernville terrane (e.g., Saleeby and Busby, 1993) in the south. Distinct nonconformable infolds of mid-Cretaceous silicic metavolcanic rocks and consanguineous hypabyssal intrusive rocks are diagnostic of this belt in the southern SNB. (3) Neoproterozoic to Cambrian inner shelf facies of miogeoclinal (i.e., shallow marine sedimentary rocks of the inner continental margin) strata of the Death Valley and Mojave Desert regions, and correlative exposures in the Snow Lake terrane, an allochthonous slice that may have been shuffled ~ 400 km northward along the cryptic Mesozoic Mojave-Snow Lake fault (Memeti *et al*., 2010; Saleeby, 2011). Strata of the Death Valley facies are

characterized by abundant, thick, shallow marine sandstone and carbonate beds (Grasse *et al*., 2001). (4) Neoproterozoic to Cambrian outer shelf miogeoclinal strata of the Inyo facies (Grasse *et al*., 2001). (5) Cambrian to Devonian eugeoclinal deposits of chert, siliceous argillite, limestone, shale, meta-serpentinites, and volcanics belonging to the El Paso terrane (Miller and Sutter, 1982; Carr *et al*., 1984; Walker, 1988; Martin and Walker, 1995; Gehrels *et al*., 2000b). The Roberts Mountains allochthon, a similar package of eugeoclinal rocks in Nevada, differs from the El Paso terrane in that the Roberts Mountains allochthon has been thrust over belts 3 and 4 during the Late Devonian to Early Mississippian Antler Orogeny (e.g., Stevens and Greene, 1999; Gehrels *et al*., 2000a).

The lower Mesozoic Kings sequence, consisting of sparsely fossiliferous quartzite, carbonate, psammite, pelite and generally westward-younging Triassic to Cretaceous silicic metavolcanic sequences that unconformably overlie Paleozoic strata from the western to eastern zones of the SNB (Saleeby *et al*., 1978; 1987; Saleeby and Busby, 1993; Memeti *et al*., 2010). The Early Jurassic or younger Snow Lake cover sequence of Memeti *et al*. (2010), a similar series of pelite, calcsilicate, and carbonate, overlaps Paleozoic strata of the Snow Lake terrane. Cover strata in the eastern Sierra Nevada, the Lane Mountain area, and the El Paso Mountains (referred to here as the "El Paso cover sequence") include Triassic deep marine siliciclastics and carbonates and subaerial volcanic rocks (Walker, 1988; Manuszak *et al*., 2000).

Steeply dipping foliations and steeply plunging lineations are characteristic of Neoproterozoic to Proterozoic framework rocks and unconformably overlying Kings sequence assemblages that typically lie in steep infolds (e.g., Saleeby and Busby, 1993). The steeply dipping structure and shape fabrics of the pendants may be used to resolve

piercing points between autochthon-allochthon pairs when disrupted by low-angle normal faults. These may, in turn, be used to derive displacement vectors.

2.2. Tectonostratigraphy of the southern Sierra Nevada region

South of 35.5˚ N, the depth of exposure increases markedly while structural and petrologic patterns in the batholith abruptly swing up to 90˚ westward, taking on an east-west trend (Kanter and McWilliams, 1982; McWilliams and Li, 1983; Malin *et al*., 1995; Wood and Saleeby, 1997; Nadin and Saleeby, 2008; Chapman *et al*., 2010) (Figure 4.1). The resulting tectonostratigraphy of the southern Sierra Nevada, the adjacent northwest Mojave Desert region, and the northern Salinia terrane (pre-Neogene restored), from shallow to deep crustal levels, consists of: 1) mafic and ultramafic assemblages of the Western San Emigdio Mafic complex, Gold Hill, and Logan Quarry; 2) shallow-level (2-4 kbar) Late Cretaceous eastern SNB affinity granitoids and associated Paleozoic to Mesozoic metamorphic pendant rocks; 3) deep-level (7-11 kbar) Early to mid-Cretaceous western SNB affinity assemblages and associated Paleozoic to Mesozoic framework assemblages; 4) Late Cretaceous subduction accretion assemblages (Rand, San Emigdio, and Sierra de Salinas schist); and 5) an imbricated section of oceanic mantle lithosphere (not exposed) (Luffi *et al*., 2009). Characteristic features of exposed tectonostratigraphic units and bounding structures in the southern SNB and Salinia are discussed below.

2.2.1. Mafic complexes

The western San Emigdio mafic complex (WSEMC) consists of hornblende-hornfels facies basaltic sheeted dikes and pillows intruded by a suite of mid- to Late Jurassic layered to

isotropic gabbroids and lesser amounts of ultramafic cumulates, which in turn are intruded by tonalitic assemblages (Hammond, 1958; James, 1986a; Reitz, 1986; Ross, 1989; Chapman *et al*., 2010). Correlative rocks of Logan Quarry and Gold Hill continue from the southwesternmost SNB into adjacent Salinia (Ross, 1970; Ross *et al*., 1973; James, 1986a; James *et al*., 1993).

The contact between the WSEMC and western SNB assemblages is concealed beneath a veneer of Tertiary sedimentary rocks that form the southern margin of the San Joaquin basin. Subcrop mapping using basement core and geophysical data indicates that rocks similar to those found in the WSEMC extend to the vicinity of the Kern range front, approximately 70 km northeast of the San Emigdio Mountains (Saleeby *et al*., 2009a). From the Kern range front, the basal Tertiary unconformity dips west and the underlying basement surface consists of northeast-southwest striated mylonitic and cataclastic assemblages derived from dioritic and tonalitic zones of the SNB and the WSEMC (Saleeby *et al*., 2009a). This surface represents a corrugated detachment fault, informally named here as the Maricopa detachment. Thermochronologic data along the Kern range front and the White Wolf fault indicate that the Maricopa detachment was active in the Late Cretaceous (Mahéo *et al*., 2009). The Uvas Member of the Eocene Tejon Formation (e.g., Critelli and Nilsen, 2000) unconformably overlies the WSEMC and contains meter-scale subrounded boulders of WSEMC material (Figure 4.4). Extreme brecciation and disaggregation are typical of *in situ* WSEMC and blocks within the Uvas Member, presumably reflecting upper plate extension during transport along the Maricopa detachment surface. The proximity of the Uvas Member to this recently recognized detachment structure and the presence of large boulders within the unit are consistent with inferred deposition in a supradetachment basin

Figure 4.4. Photographs of Uvas member of the Tejon formation in the San Emigdio Mountains. Note pervasive fracturing of and intrusion of clastic dikes into meter-scale blocks of WSEMC-derived gabbro. (a) Field of view 50 m long. (b) Field of view 7 m long.

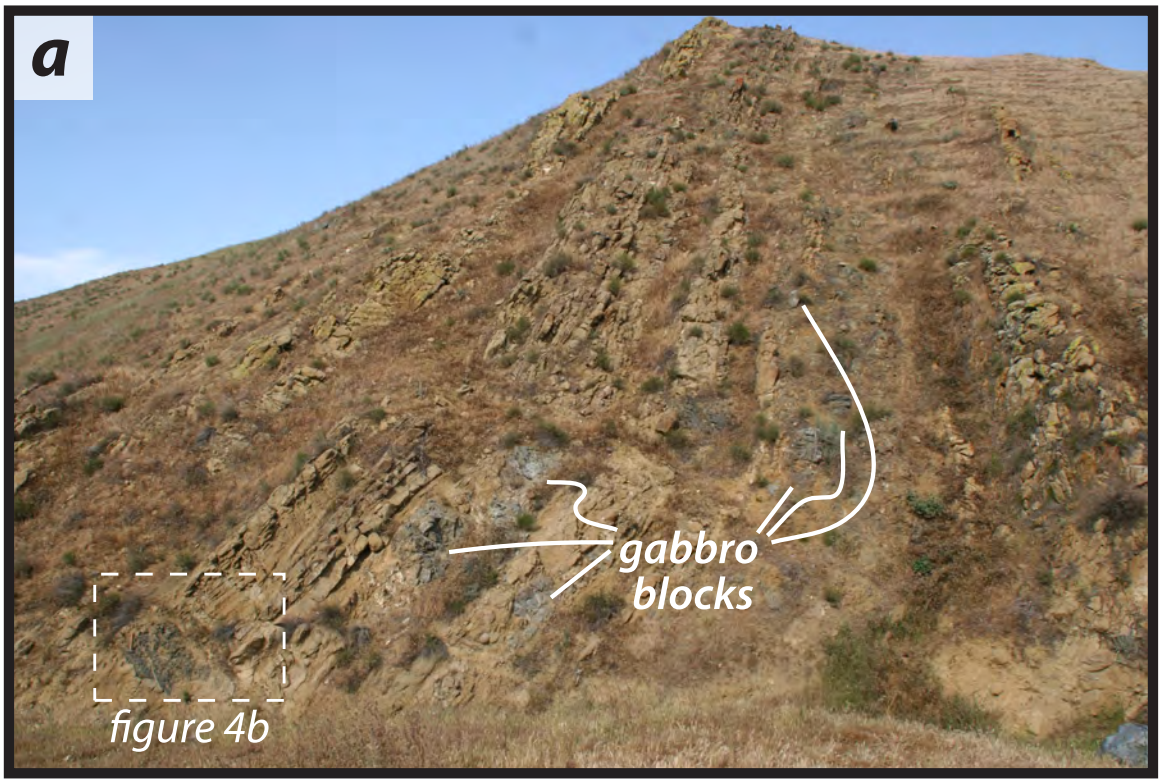
a
gabbro
blocks
figure 4b


b

(Wood and Saleeby, 1997).

Eastern SNB affinity shallow-level granitoids and metamorphic framework rocks

A profound feature of the southern SNB and vicinity is a tectonostratigraphy topped by crustal fragments of shallow-level granitoids and amphibolite to hornblende hornfels facies metamorphic pendant rocks, referred to by various authors as "Plate III," Blackburn, southern Tehachapi, Gabilan, central Santa Lucia, and Pastoria plates (Nourse, 1989; Wood and Saleeby, 1997). These crustal fragments lie in the hanging wall of a regional detachment system consisting of "fault II" of Nourse (1989), the Blackburn Canyon, Jawbone Canyon, and Pastoria faults (Wood and Saleeby, 1997), and the cryptic westward continuation of the Pastoria fault into the Gabilan range, where it separates footwall midcrustal tonalites from hanging wall upper crustal granitoids (Figure 4.1b) (e.g., Kistler and Champion, 2001). These faults are referred to in aggregate as the southern Sierra detachment system (SSD). Here we review key temporal, kinematic, and structural relations of the SSD critical to the palinspastic restoration of allochthonous crustal fragments in the southern SNB and vicinity.

The SSD is a complex ductile to mainly brittle low-angle structure that has been differentially remobilized, truncated, and folded by Transverse Ranges contractile deformation. Locally preserved ductile fabrics along eastern elements of the SSD indicate a top to the south or southeast transport direction (Nourse, 1989; Wood and Saleeby, 1997). Kinematic analysis of the Pastoria fault is prohibited as original ductile fabrics are severely overprinted in the brittle regime, as is the case for many exposures of the SSD system. Upper – lower plate juxtapositions across the SSD are profound. These consist

of: 2 to 4 kbar versus 7 to 11 kbar for pluton emplacement pressures, 87 to 105 Ma versus 102 to 138 Ma for pluton emplacement ages, and ~ 0.708 versus ~ 0.705 for Sr_i (Saleeby *et al*., 1987; Kistler and Ross, 1990; Pickett and Saleeby, 1994; Wood and Saleeby, 1997).

2.2.2. Deep-level exposures of the western SNB

Deep-crustal exposures of the Cretaceous batholithic belt and underlying schist (discussed below) in the southern SNB, the Santa Lucia Range of Salinia and the central Mojave metamorphic core complex together form an integrated core complex that underlies an area with map dimensions of roughly 200 km by 200 km (Figure 4.1). These deep-level exposures decrease in thickness and abundance westward from the southern SNB into Salinia, where ultimately only small remnants of western zone rocks are preserved as basement inliers in northernmost Salinia (Kistler and Champion, 2001) and conglomerate clasts from the Late Cretaceous-Paleogene Gualala basin (James *et al*. 1993; Schott and Johnson, 1998, 2001), suggesting that a westward-increasing component of tectonic and/or surficial erosion is responsible for the removal of western zone assemblages (Figure 4.1). Crustal thinning of the southern Sierra-Salinia core complex was accompanied by Late Cretaceous to Paleocene subsidence to marine conditions, and the deposition of coarse proximally derived clastic strata. Scattered remnants of these strata in surface exposures and in the subsurface (Figure 4.1) define a marine embayment that formed across the highly extended southernmost SNB (Cox, 1987; Lucas and Reynolds, 1991; Seiders and Cox, 1992; Grove, 1993; Wood and Saleeby, 1997; Critelli and Nilsen, 2000; Calif. Div. of Oil and Gas Well Repository Data).

Basement exhumation within the core complex is clearly linked to the transport of

upper crustal fragments in the hanging wall of the SSD. Mated thermochronometric and barometric data for the southern SNB, northern Salinia, and the northwestern Mojave Desert show an abrupt Late Cretaceous decompression event coincident with rapid cooling in the deep-level batholithic upper plate, indicating profound tectonic denudation (Saleeby *et al*., 2007; Chapman *et al*., 2010 and references therein).

2.2.3. Subduction accretion assemblages

The schist and similar early Tertiary Pelona and Orocopia schists of more southerly California have long attracted interest due to their position beneath older crystalline rocks of the southwest Cordilleran batholithic belt, typically along detachment structures (e.g., the Rand fault, Salinas shear zone, Vincent fault, Chocolate Mountains fault) (Ehlig, 1981; Graham and England, 1976; Haxel and Dillon, 1978; Jacobson, 1983; 1995; Jacobson *et al*., 1988; 2007; 2011; Simpson, 1990; Kidder and Ducea, 2006; Chapman *et al*., 2010; 2011). Most workers agree that the deposition and emplacement of the schist occurred during an episode of shallow subduction related to the Laramide orogeny (Jacobson *et al*., 2007 and references therein).

The deposition, subduction, and structural ascent of the schist is temporally and spatially associated in plate reconstructions with the subduction of a hypothesized conjugate massif to the Shatsky Rise, a large igneous province (LIP) in the northwest Pacific Ocean (Saleeby, 2003; Liu *et al*., 2008, 2010). Subduction of the LIP beneath the southernmost SNB and adjacent SCB is hypothesized to have driven slab flattening, leading to the tectonic removal of subbatholithic mantle lithosphere, the cessation of arc magmatism, abrupt crustal thickening in the overriding batholithic plate (Malin *et al*., 1995; Ducea and Saleeby, 1998;

House *et al*., 2001; Saleeby, 2003; Nadin and Saleeby, 2008) and decompression of batholithic assemblages from deep- to midcrustal levels (Saleeby *et al*., 2007; Chapman *et al*., 2010). Erosion of the resultant high-elevation mountain belt segment shed detritus as the schist protolith into the trench, which was immediately underthrust at least 150 km inboard beneath the recently extinguished arc (Kidder and Ducea, 2006). Replacement of subbatholith mantle lithosphere with relatively weak schist is thought to have led to disruption and dispersion of the thickened upper plate and regionally extensive trench-directed flow in the schist (Saleeby, 2003; Saleeby *et al*., 2007; Chapman *et al*., 2010, 2011).

2.2.4. Late Cretaceous tectonic shuffling

Here we review temporal and kinematic relations between the principal members of the integrated proto-Kern Canyon – Kern Canyon – White Wolf fault system (Nadin and Saleeby, 2008) and the Owens Valley shear system (Bartley *et al*., 2007), as they are important for both the contractile and extensional phases of regional deformation related to schist underplating. Beginning at ca. 95 Ma, the proto-Kern Canyon fault (PKCF) functioned as a west-directed deep crustal reverse fault with southward increasing throw of 10 to 25 km and a northward increasing component of dextral shear (Nadin and Saleeby, 2008). This resulted in granodioritic zone batholithic exposures and the $Sr_i = 0.706$ isopleth being overthrust by granitic zone rocks along the PKCF with progressively greater structural overlap southwards. The southern end of the PKCF flattened and merged with the Rand fault, behaving as a lateral ramp in the upper plate of the subduction megathrust.

At ca. 88 Ma and at a latitude of ~ 35.7 ˚N, the Kern Canyon fault branched from the

PKCF to the southwest and merged with the proto-White Wolf fault (abbreviated in aggregate as KWF below) at ~ 35.3 ˚N. Displacement along the KWF increases southward from zero at 36.7° N to 40 km of dextral slip and 15 km of dip slip near the Tejon embayment (Nadin and Saleeby, 2008). Dextral displacement along the Kern Canyon segment is constrained to 88–80 Ma, and bracketed to between 98 and 70 Ma along the proto-White Wolf segment.

Bartley *et al*. (2007) show that ~ 65 km of dextral slip along the Owens Valley shear system occurred between Late Cretaceous and Paleogene time. Coeval shear along the Owens Valley shear system, KWF, and SSD suggests that these structures may have been cogenetic, with the Owens Valley shear system and KWF representing transfer faults flanking the southern Sierra-Salinia core complex. The Owens Valley shear system probably flattens and merges with the SSD west of the El Paso Mountains (Figure 4.1), as implied by Bartley *et al*. (2007).

Upper plate rocks of the SSD were derived wholly from the area between the KWF and the Owens Valley shear system, reflecting large magnitude extension within that corridor. The WSEMC is, as of yet, the only recognized allochthonous fragment in the less extended northwest wall of the KWF. In other words, the KWF separates deep-level exposures and upper crustal fragments in the south from significantly less extended and exhumed rocks of the WSEMC and western SNB in the north (Nadin and Saleeby, 2008; Chapman *et al*., 2010) (Figure 4.1). Similarly, the Owens Valley shear system separates footwall rocks of the southern Sierra-Salinia core complex in the west from shallow-level assemblages in the east. Northwest-striking extensional fracture swarms are common in the extensional corridor between the KWF and the Owens Valley shear system (Figure 4.1).

3. U-PB ZIRCON GEOCHRONOLOGY

3.1. Plutonic rocks

This geochronologic investigation focuses on batholithic suites adjacent to the SSD and Maricopa detachment: hanging wall granitoids of the Pastoria and southern Tehachapi plates, footwall deep level plutonic assemblages of the San Emigdio Mountains (Tehachapi-San Emigdio complex of Chapman *et al*., 2010; 2011; Chapman and Saleeby, in review), and the White Ridge tonalite of the WSEMC. One sample from the Guadalupe complex of the southern Foothills belt was analyzed for inter-laboratory calibration purposes (G11; Saleeby *et al*., 1989; Ernst *et al*., 2009).

Deep level rocks from the San Emigdio Mountains include: 1) the Antimony Peak tonalite, dated at 131 Ma in reconnaissance U-Pb zircon studies by James (1986a, 1986b); 2) the San Emigdio tonalite, a more felsic phase of the Antimony Peak body; 3) the San Emigdio gneiss (Chapman *et al*., 2011), an undated hornblende quartz diorite orthogneiss that crops out north of the San Emigdio schist and likely correlates with similar rocks of the 99 to 105 Ma intrusive suite of Bear Valley (Saleeby *et al*., 1987; Pickett and Saleeby, 1993; Saleeby *et al*., 2007); 4) the Digier Canyon diorite gneiss, the western continuation of the White Oak diorite gneiss (Saleeby *et al*., 2007), a tectonic mixture of amphibolite to locally retrograde greenschist facies dioritic and subordinate tonalitic, gabbroic, and mylonitic gneisses and cataclasites at the base of the Tehachapi–San Emigdio complex, and 5) the western continuation of the Grapevine Canyon paragneiss (Pickett and Saleeby, 1993; 1994).

Hanging wall granitoids include: 1) the Lebec granodiorite of Crowell (1952), which hosts the Salt Creek pendant, 2) the Claraville granodiorite of the Blackburn plate, which yields U-Pb zircon ages of 91 ± 1 Ma ~50 km north of our sample site (Saleeby *et al*., 1987; 2008) 3) the granite of Brush Mountain, assigned a 98 Ma U-Pb zircon age by James (1986b), 4) the granodiorite of Gato Montes, which yields a Rb-Sr isochron age of 96.3 ± 8.7 Ma (Kistler and Ross, 1990), and 5) a hornblende granodiorite in contact with the Tylerhorse Canyon pendant, informally named here the granodiorite of Gamble Spring Canyon. Sample locations and interpreted U-Pb ages of plutonic as well as metavolcanic rocks are given in Table 4.1 and shown in Plate 2. Graphical representations of U-Pb age determinations are shown in Figure 4.5. U-Pb geochronology of zircons from samples 91TH181, 93TH417, and 91TH140 was conducted by TIMS-isotope dilution analysis. All remaining samples were analyzed by laser ablation multicollector inductively coupled plasma mass spectrometry (LA-MC-ICPMS). Analytical techniques, sample petrography, isotopic data, and representative cathodoluminescence (CL) images are available in Appendix 2.

3.1.1. Antimony Peak tonalite and San Emigdio tonalite

Zircons in samples 08SE46, 08SE262, 08SE451, 08SE582, and 08SE675 are generally subhedral, ~ 50 – 350 μm in length, inclusion-poor, and exhibit simple oscillatory zoning patterns in CL images that we interpret as magmatic features. CL-dark cores are commonly overgrown by CL-bright rims up to ~35 μm wide in samples 08SE46 and 08SE675. While conventional zircon fractions yielded highly discordant U-Pb ages (James, 1986a, 1986b), *in*

Figure 4.5. (a) U-Pb age-frequency spectra (after Ludwig, 2003) from LA-ICPMS data on 18 samples from the SNB. Errors are 2s. Abbreviations for rejected grains: HE, high $^{206}Pb/^{238}U$ error; I/E, source inheritance and/or entrainment; IN, inclusion(s) overlapped during ablation; LL, lead loss; OL, analysis of overlapping age domains. (b) Tera-Wasserburg diagrams and concordia intercept ages (after Ludwig, 2003) from ID-TIMS data on 3 samples from the southern SNB. Errors are 2s. Isotopic data in Tables A2.1 and A2.2.

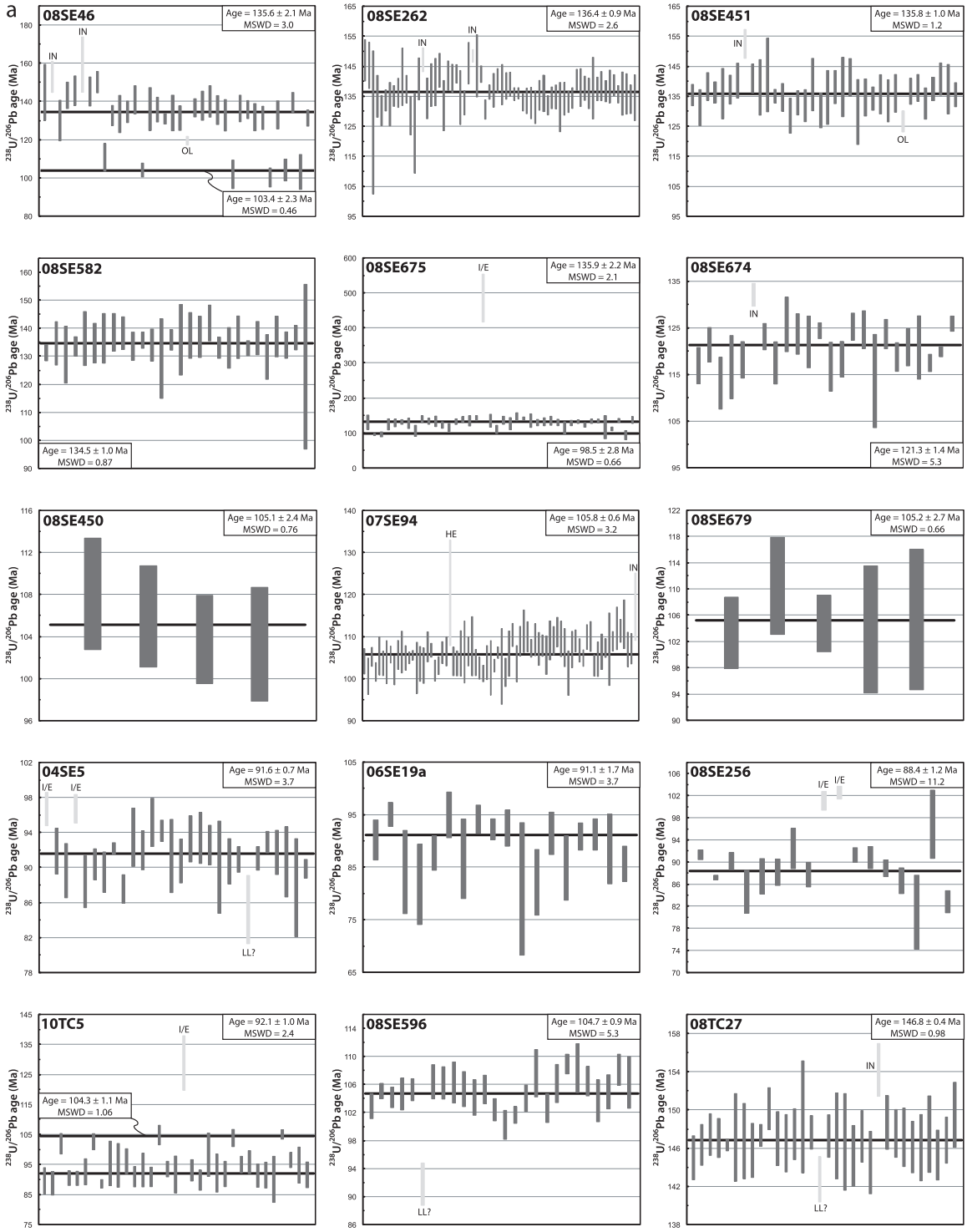
a
08SE46
Age = 135.6 ± 2.1 Ma
MSWD = 3.0
IN
IN
OL
Age = 103.4 ± 2.3 Ma
MSWD = 0.46
08SE262
Age = 136.4 ± 0.9 Ma
MSWD = 2.6
IN
IN
08SE451
Age = 135.8 ± 1.0 Ma
MSWD = 1.2
IN
OL
08SE582
Age = 134.5 ± 1.0 Ma
MSWD = 0.87
08SE675
Age = 135.9 ± 2.2 Ma
MSWD = 2.1
I/E
Age = 98.5 ± 2.8 Ma
MSWD = 0.66
08SE674
IN
Age = 121.3 ± 1.4 Ma
MSWD = 5.3
08SE450
Age = 105.1 ± 2.4 Ma
MSWD = 0.76
07SE94
Age = 105.8 ± 0.6 Ma
MSWD = 3.2
HE
IN
08SE679
Age = 105.2 ± 2.7 Ma
MSWD = 0.66
04SE5
Age = 91.6 ± 0.7 Ma
MSWD = 3.7
I/E
I/E
LL?
06SE19a
Age = 91.1 ± 1.7 Ma
MSWD = 3.7
08SE256
Age = 88.4 ± 1.2 Ma
MSWD = 11.2
I/E
I/E
10TC5
Age = 92.1 ± 1.0 Ma
MSWD = 2.4
I/E
Age = 104.3 ± 1.1 Ma
MSWD = 1.06
08SE596
Age = 104.7 ± 0.9 Ma
MSWD = 5.3
LL?
08TC27
Age = 146.8 ± 0.4 Ma
MSWD = 0.98
IN
LL?
238U/206Pb age (Ma)

a (*continued*)

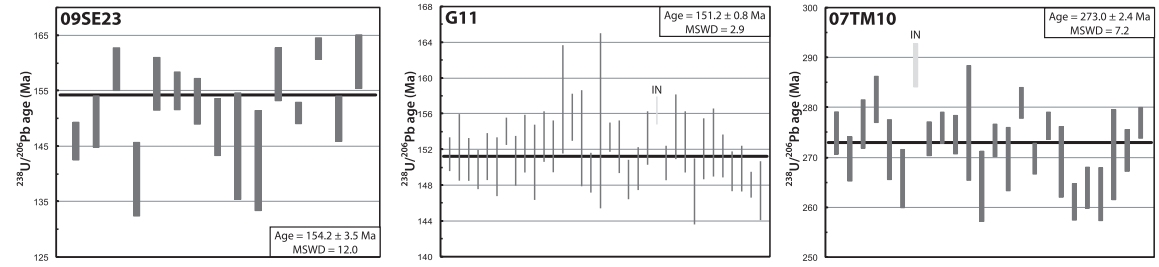

b

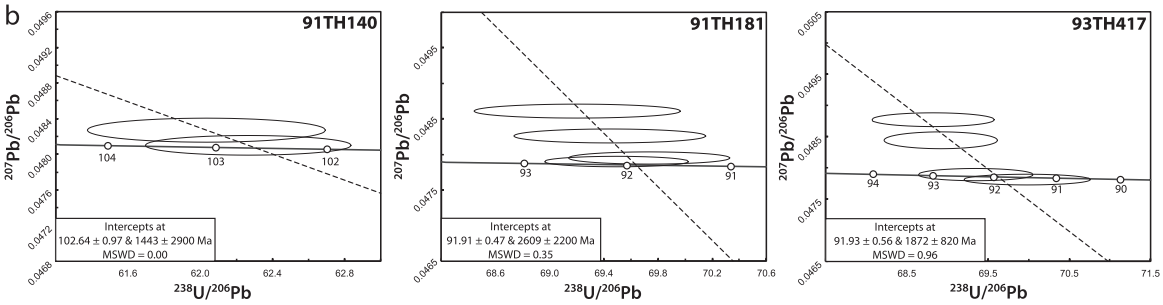

Table 4.1. Summary of sample locations, rock units, and U-Pb zircon ages. Isotopic data in Tables A2.1 and A2.2. Sample petrography in Appendix 2.

Sample	Lithology	Zone	UTM easting[a]	UTM northing[a]	U-Pb zircon age (Ma)
08SE46	Antimony Peak tonalite	11	319551	3864823	Cores: 135.6 ± 2.1 Rims: 103.4 ± 2.3
08SE262	Antimony Peak tonalite	11	308858	3863886	136.4 ± 0.9
08SE451	Antimony Peak tonalite	11	307028	3861038	135.8 ± 1.0
08SE582	Antimony Peak tonalite	11	305678	3860356	134.5 ± 1.0
08SE675	Antimony Peak tonalite	11	324340	3863296	Cores: 136.4 ± 2.1 Rims: 98.5 ± 2.8
07SE94	San Emigdio gneiss	11	314647	3863872	105.8 ± 0.6
08SE450	San Emigdio gneiss	11	307107	3860929	105.1 ± 2.4
08SE674	Digier Canyon/White Oak diorite gneiss	11	324461	3861916	121.3 ± 1.4
08SE679	Digier Canyon/White Oak diorite gneiss	11	325421	3861840	105.2 ± 2.7
04SE5	Lebec granodiorite	11	311257	3858324	91.6 ± 0.7
06SE19a	Lebec granodiorite	11	316199	3864484	91.1 ± 1.7
08SE256	Lebec granodiorite	11	312736	3860408	88.4 ± 1.2
91TH181	Claraville granodiorite	11	371313	3879868	91.91 ± 0.47
93TH417	Claraville granodiorite	11	368657	3878458	91.93 ± 0.56
10TC5	Granodiorite of Gato Montes	11	294640	3863171	92.1 ± 1.0
08TC27a	Granodiorite of Gamble Spring Canyon	11	367862	3870810	146.8 ± 0.4
08SE596	Granite of Brush Mountain	11	297219	3861811	104.5 ± 0.8
09SE23	White Ridge tonalite	11	291420	3867183	155.2 ± 3.4
G11	Guadalupe pluton	10	754858	4147150	151.2 ± 0.8
91TH140	Oaks metavolcanic	11	368664	3881115	102.64 ± 0.97
07TM10	Bean Canyon metavolcanic	11	374359	3872499	273.0 ± 2.4

[a] UTM coordinates are WGS datum.

situ LA-MC-ICPMS analyses of core and rim regions are concordant with weighted mean ages of ca. 135 and 100 Ma, respectively. These ages are interpreted to reflect the timing of crystallization (cores) and deep crustal overgrowth (rims). A single aberrant grain in sample 08SE675, yielding an age of 485.0 ± 34.0 Ma, is interpreted here as related to source inheritance and/or entrainment of a Paleozoic or older zircon.

3.1.2. San Emigdio gneiss

Zircons in samples 07SE94 and 08SE450 are rounded to subrounded, ~100 – 200 μm in length, inclusion-poor, and preserve a faint and broad zoning texture. Weighted mean ages for the San Emigdio gneiss range from ca. 105-106 Ma.

3.1.3. Digier Canyon/White Oak diorite gneiss

Zircon grains in sample 08SE674 (quartz diorite) and 08SE679 (gabbro) are generally subhedral, ~100 – 300 μm in length, inclusion-poor, and exhibit broad zoning in ~95% of grains; the remainder contain convolute zoning domains that truncate the oscillatory zoning. Weighted mean ages of 120.6 ± 1.4 and 104.4 ± 4.2 for samples 08SE674 and 08SE679, respectively reflect the lithologic and structural variability of the White Oak tectonic unit. Earlier U-Pb zircon geochronologic studies (Saleeby *et al*., 1987, 2007) specifically avoided this unit owing to structural complexities and metamorphic overprinting adjacent to the Rand fault in the Tehachapi Mountains.

3.1.4. Lebec granodiorite

Zircon morphology and zoning vary widely in the Lebec body, depending mainly on the proximity of Salt Creek pendant rocks. Sample 04SE5 was collected over 200 m from the nearest exposure of pendant rocks, and contains 100 – 300 μm, subhedral zircon grains that exhibit oscillatory zoning. Samples 06SE19A and 08SE256 were collected adjacent to pendant assemblages and contain large (up to 1 cm) skeletal garnets in textural disequilibrium with the surrounding matrix and zircon grains that are subhedral, ~25 – 150 μm in length, and inclusion-poor with core regions exhibiting oscillatory zoning with local convolute zoning at the rims. Four grains of the 04SE5 and 08SE256 spectra, yielding aberrant ages of 97-102 Ma, are interpreted as a source inheritance and/or entrainment feature. Weighted mean ages for the Lebec granodiorite range from 88 – 92 Ma.

3.1.5. Claraville granodiorite

Samples 91TH181 and 93TH417 were collected from the Whiterock facies of the Claraville granodiorite (Ross, 1989; Wood, 1997), a medium grained porphyritic hornblende biotite granodiorite. The Tera-Wasserburg diagrams (Figure 4.5b) show concordant fractions at ca. 92 Ma, and slightly discordant fractions probably reflecting minor inheritance and/or entrainment of Proterozoic grains.

3.1.6. Granodiorite of Gato Montes

Zircons in sample 10TC5 are euhedral to subhedral, ~150 – 200 μm in length, inclusion poor, and exhibit oscillatory zoning. The weighted mean age of this sample is 92. 1 ± 1.0

Ma. The five grains that yield ages of ca. 104 Ma resemble the principal inherited component observed from Lebec granodiorite samples. The grain that yields an anomalous age of ca. 129 Ma is also attributed to source inheritance or entrainment.

3.1.7. Granodiorite of Gamble Spring Canyon

Large lensoidal bodies of this unit separate rocks of the Tylerhorse Canyon pendant from the more felsic granodiorite of Gato Montes (Ross, 1989) and lie within the metasedimentary sequence, possibly as dikes (Rindosh, 1977). Sample 08TC27 was collected from the northern margin of the Tylerhorse Canyon pendant. The interpreted age of this sample is 146.8 ± 0.4 Ma.

3.1.8. Granite of Brush Mountain

Zircons in sample 08SE596 are euhedral to subhedral, ~ 50 – 200 μm in length, inclusion poor, and exhibit faint CL-dark oscillatory zoning. The interpreted age of this sample is 104.7 ± 0.9 Ma. A single aberrant age of 91.9 ± 3.0 Ma is probably due to isotopic disturbance of a labile grain. However, the U concentration (3141 ppm) and U/Th (4.7) for the aberrant grain are similar to those of other grains, suggesting that significant isotopic disturbance has not occurred. Dikelet contamination from the 1 km distant Lebec granodiorite is precluded, as the contact between the two bodies is clearly a fault (Chapman and Saleeby, in review) and microscale intrusions are not visible in thin section.

3.1.9. White Ridge tonalite

Zircons in sample 09SE23 are subhedral to subrounded, ~50 – 250 μm in length, inclusion-poor, and exhibit oscillatory and sector zoning. The weighted mean age of this sample is 154.2 ± 3.5 Ma.

3.1.10. Inter-laboratory calibration and geochronological data syntheses

Sample G11 is from the Guadalupe pluton of the central Sierra Nevada Foothills. Zircons in sample G11 are euhedral to subhedral, ~50 – 150 μm in length, inclusion-poor, and exhibit oscillatory and sector zoning. Sample G11 is dated by TIMS at 151 ± 2 Ma (Saleeby *et al*., 1989) and by SHRIMP at 153 ± 2 Ma (Ernst *et al*., 2009). We report a weighted mean age of 151.2 ± 0.8 Ma for this sample. Grain morphology, texture, and color, a highly concordant population, and good agreement between SHRIMP, TIMS, and ICPMS ages suggest that zircon from the Guadalupe pluton may be a suitable inter-laboratory standard for Mesozoic U-Pb geochronology.

Results from our geochronologic work are combined with all known U-Pb zircon ages from the southern Sierra Nevada and Salinia to produce a color contour map (Plate 2), showing regional variations in pluton emplacement age, using the spatial analyst extension of Arcmap 9 and employing "barriers" such as the PKCF, KWF, and other faults shown on Figure 4.1. Sr_i (Plate 3) and pluton emplacement and metamorphic equilibration pressure (Plate 4) compilation maps were also produced in an identical manner. The purpose of our U-Pb zircon, Sr_i, and igneous and metamorphic pressure (discussed below) syntheses is to

emphasize the disruption of longitudinal batholithic zonation patterns south of 35.5 °N. Complete databases are presented in Appendix 2.

3.2. Metamorphic pendant rocks

Samples of metamorphosed siliciclastic rock from the Salt Creek (08SE258), Tylerhorse (08TC44), and Bean Canyon (07BC60) pendants yielded a total of 286 concordant grains suitable for provenance analysis. Zircons in these samples generally contain detrital cores characterized by igneous oscillatory zoning truncated by zones of metamorphic recrystallization and local development of patchy and convolute zoning along rims (Figure A2.1). Metamorphic domains were avoided during analysis. Sample 08SE258 has major age peaks at ca. 1100 Ma, 1400 Ma, and 1700 Ma. Sample 07BC60 has a major age peak at ca. 1800 Ma, with scattered ages between 1000 – 1700 Ma and 2300 – 2900 Ma. Sample 08TC44 contains scattered ages between ca. 200 – 600 Ma, 1000 – 1800 Ma, and 2000 – 2900 Ma. A single sample of dacitic metatuff from the Bean Canyon pendant (07TM10) yields a total of 24 concordant analyses with an interpreted age of 273.0 ± 2.4 Ma (Figure 4.5). The Complete LA-MC-ICPMS dataset is included in Appendix 2. A TIMS concordia age of ca. 102.6 ± 1 Ma was determined using two multigrain zircon fractions from a metamorphosed pumice lapilli silicic tuff (sample 91TH140) from the Oak Creek Pass complex.

Figure 4.6 is a normalized probability plot illustrating detrital zircon age spectra for samples analyzed here and combined curves from Paleozoic strata of Death Valley and the Snow Lake terrane (Memeti *et al*., 2010), the Salinian block (Barbeau *et al*., 2005), the

Kernville terrane (Saleeby, 2011), the El Paso terrane (Paterson *et al*., in preparation), the Roberts Mountains allochthon (Smith and Gehrels, 1994; Gehrels *et al*., 2000a), Fairview pendant (Saleeby, 2011), and the Sierra City mélange and Shoo Fly complex (Harding *et al*., 2000) shown for comparison.

Figure 4.7 compares the age spectra of samples from this study with those of a suite of samples from the terranes listed above using multidimensional scaling (MDS). MDS offers an advantage over traditionally used Kolmogorov-Smirnov (K-S) statistical tests in that they can be used to produce visual representations of statistical distances between arrays of age data. In other words, MDS calculates a matrix of statistical distances between samples of detrital zircon ages and plots the samples on a map such that the samples that contain similar age spectra are placed close to each other on the map. MDS mapping of data from the El Paso terrane / Roberts Mountains allochthon, Death Valley /Snow Lake terrane, and northern and southern Sierra produces clusters (Figure 4.7) that can be exploited to test provenance hypotheses for unknown samples. Details of the MDS algorithm are outlined in Appendix 2.

3.3. Tylerhorse Canyon Pendant Fossils

During our mapping of the Tylerhorse Canyon pendant, Caltech undergraduate field assistant S. Peek discovered broken bivalve remains in a hornfelsic calcareous sandstone (Figure 4.8). The remains are too fragmented to identify in detail, but they strongly resemble Early Jurassic bivalves of the Genera Weyla that were recovered from two locations in the Isabella pendant, the first identified by J.W. Durham and the second by D.L. Jones. The two Isabella pendant fossil locations were from the same stratigraphic horizon, but separated by

Figure 4.6. Normalized probability plots comparing LA-MC-ICPMS zircon ages from this study with spectra from: Paleozoic slope, inner shelf, and outer shelf strata of the Shoo Fly complex and Sierra City Mélange (SF+SCM); eugeoclinal strata of the Roberts Mountains allochthon (RMA); Kern Plateau pendants of the El Paso terrane (EP); miogeoclinal strata of Death Valley and the Snow Lake terrane (DV+SL); the Fairview pendant of the Kernville terrane (KT); and Santa Lucia ("Seco") and Gabilan ("Fremont") ranges, showing the number of grains analyzed. Composite curves consist of (in parentheses): Shoo Fly complex (Lang sequence and Duncan Peak and Culbertson Lake allochthons); Roberts Mountains allochthon (Harmony, Vinini, Valmy, Snow Canyon, McAfee, Elder, and Slaven formations); Kern Plateau pendants (Bald Mountain, Indian Wells, and Kennedy pendants); Death Valley (Wood Canyon Formation and Zabriskie and Stirling quartzites); and Snow Lake terrane (Snow Lake pendant "Carrara Quartzite," "Zabriskie," "Upper Wood Canyon Formation," and "Stirling"). Colors correspond to Figure 4.2. Samples of unknown paleogeographic affinity shown in gray. Plots constructed with isoplot (Ludwig, 2003) using $^{206}Pb/^{238}U$ ages for grains younger than 800 Ma and $^{207}Pb/^{206}Pb$ ages for grains older than 800 Ma. Analyses with greater than 10% uncertainty, 30% discordance, and/or 5% reverse discordance excluded. Isotopic data in Table A2.3.

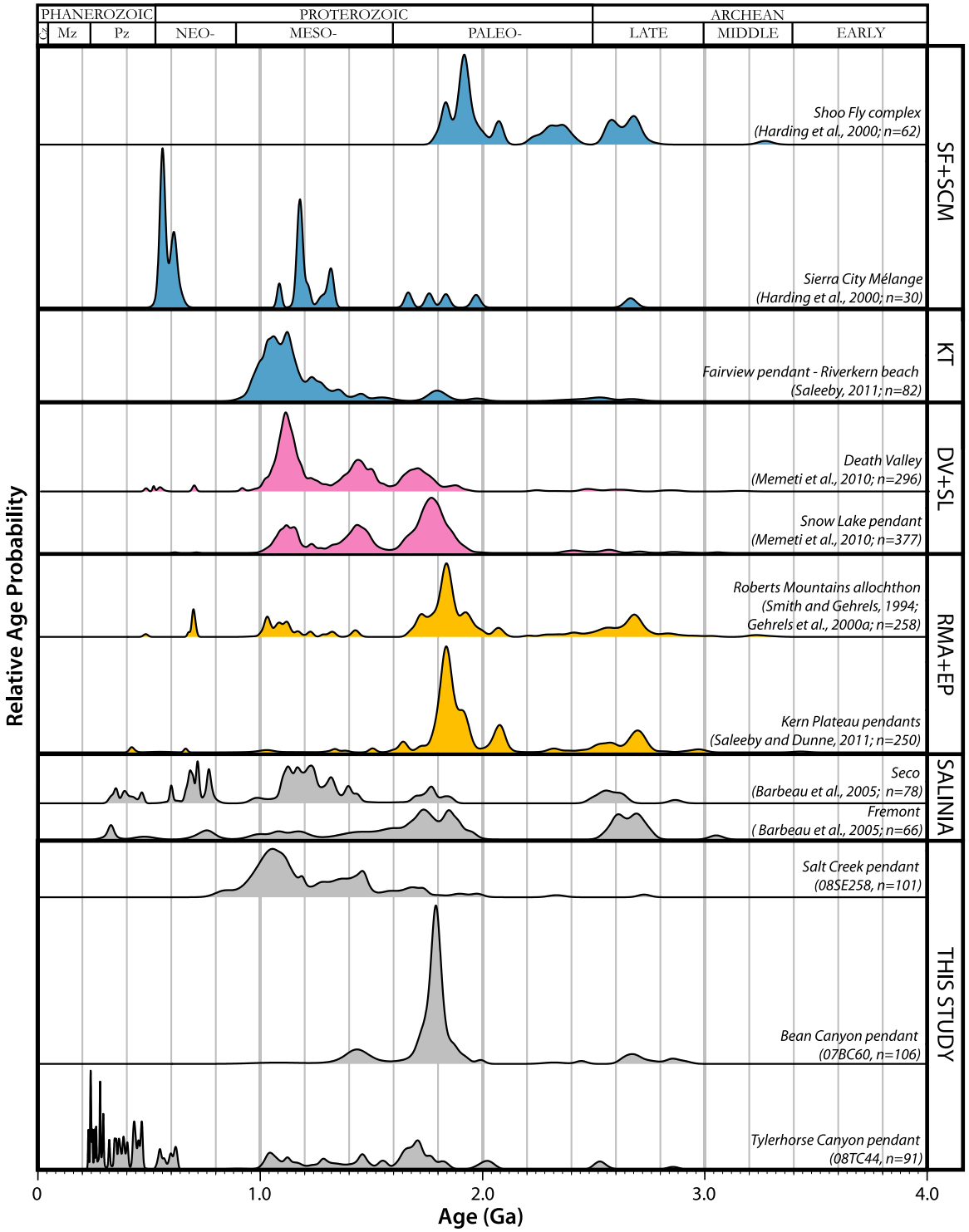
PHANEROZOIC
Mz
Pz
PROTEROZOIC
NEO-
MESO-
PALEO-
ARCHEAN
LATE
MIDDLE
EARLY
Shoo Fly complex
(Harding et al., 2000; n=62)
Sierra City Mélange
(Harding et al., 2000; n=30)
SF+SCM
Fairview pendant - Riverkern beach
(Saleeby, 2011; n=82)
KT
Death Valley
(Memeti et al., 2010; n=296)
Snow Lake pendant
(Memeti et al., 2010; n=377)
DV+SL
Roberts Mountains allochthon
(Smith and Gehrels, 1994;
Gehrels et al., 2000a; n=258)
Kern Plateau pendants
(Saleeby and Dunne, 2011; n=250)
RMA+EP
Seco
(Barbeau et al., 2005; n=78)
Fremont
(Barbeau et al., 2005; n=66)
SALINIA
Salt Creek pendant
(08SE258, n=101)
Bean Canyon pendant
(07BC60, n=106)
Tylerhorse Canyon pendant
(08TC44, n=91)
THIS STUDY
Relative Age Probability
0
1.0
2.0
3.0
4.0
Age (Ga)

Figure 4.7. Multidimensional scaling map showing dimensionless K-S distances between arrays of detrital zircon age data. Symbol colors correspond to Figure 4.6. Note clustering of samples of known paleogeographic affinity. Abbreviations in key as in Figure 4.6. Other Abbreviations: N and S Sierra - CL, Culbertson Lake allochthon; DP, Duncan Peak allochthon; FP, Fairview pendant; LS, Lang sequence; SCM, Sierra City mélange (Harding *et al*., 2000; Saleeby, 2011). Roberts Mountains allochthon - EQ, Eureka Quartzite; HA, Harmony A; HB, Harmony B; LV, Lower Vinini; ML1, May Lake pendant (sample ML369); ML2, May Lake pendant (sample ML459); VVSMES, Upper Vinini-Valmy-Snow Canyon-McAfee-Elder-Slaven (Smith and Gehrels, 1994; Gehrels *et al*., 2000a; Memeti *et al*., 2010). El Paso terrane - KPB, Bald Mountain pendant; KPI, Indian Wells pendant; KPK, Kennedy pendant (Paterson *et al*., in preparation). Death Valley - WC1, Wood Canyon #1; WC2, Wood Canyon #2; ZQ, Zabriskie Quartzite (Memeti *et al*., 2010). Snow Lake terrane - BL1, Benson Lake pendant (sample BPM-314), BL2, Benson Lake pendant (sample RE242); QP, Quartzite Peak; SLC, Snow Lake pendant "Carrara Quartzite;" SLS, Snow Lake pendant "Stirling Quartzite;" SLW, Snow Lake pendant "Wood Canyon #2;" SLZ, Snow Lake pendant "Zabriskie" (Memeti *et al*., 2010). Allochthons - BC, Bean Canyon pendant; F, Fremont; S, Seco; SC, Salt Creek pendant; TC, Tylerhorse Canyon pendant (Barbeau *et al*., 2005; this study).

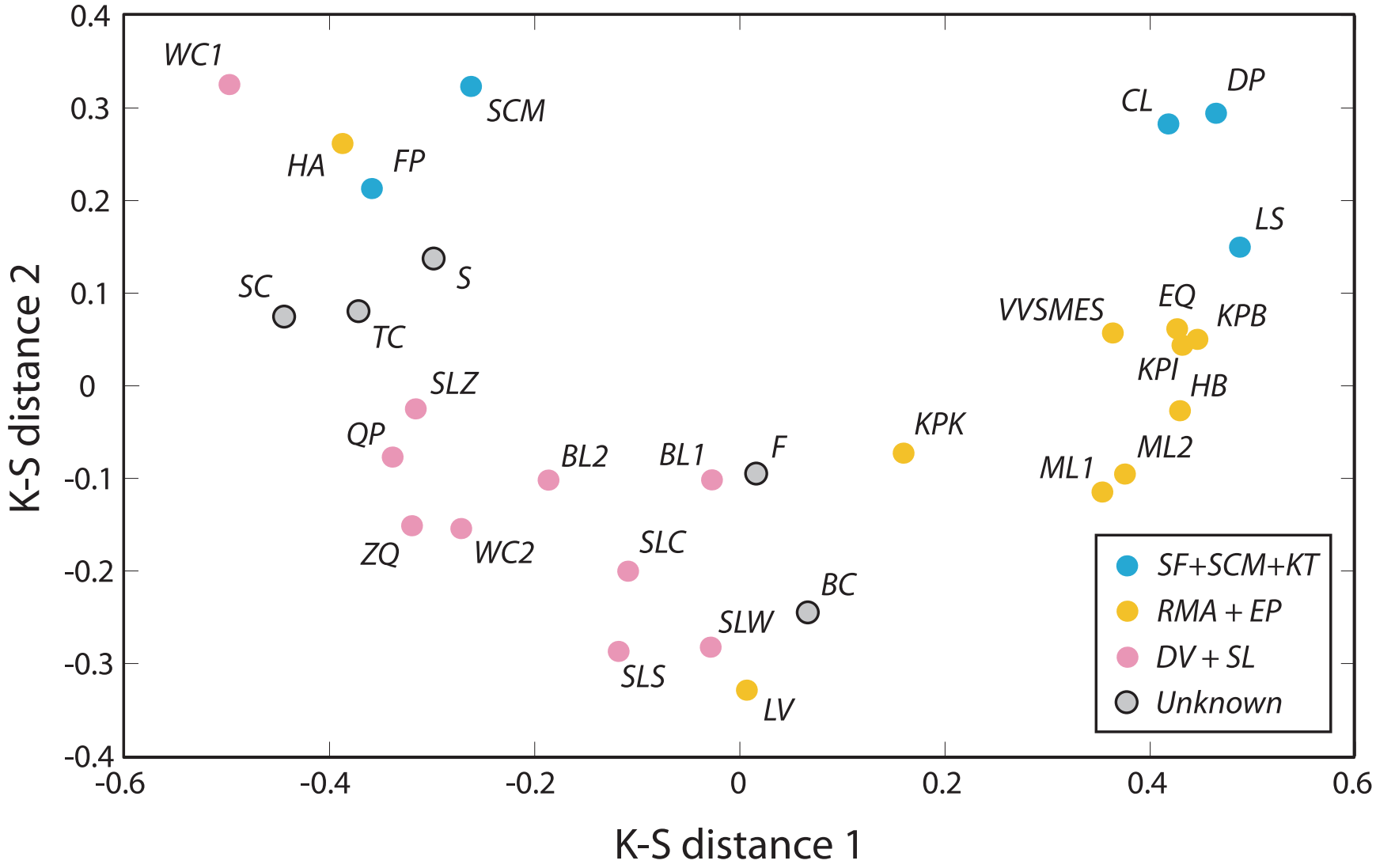
K-S distance 2
K-S distance 1
0.4
0.3
0.2
0.1
0
-0.1
-0.2
-0.3
-0.4
-0.6
-0.4
-0.2
0
0.2
0.4
0.6
WC1
SCM
HA
FP
S
SC
TC
SLZ
QP
BL2
BL1
F
KPK
ZQ
WC2
SLC
BC
SLW
SLS
LV
CL
DP
LS
VVSMES
EQ
KPB
KPI
HB
ML2
ML1
SF+SCM+KT
RMA + EP
DV + SL
Unknown

several map-scale folds (Saleeby and Busby, 1993). The stratigraphic position of bivalve fragments in the Tylerhorse Canyon pendant is virtually the same as those in the Isabella pendant. All three locations are located in a centimeter-to meter-scale layered quartzite unit characterized by thin calc-silicate and psammitic interbeds that sits stratigraphically above a thick highly recrystallized gray marble. The Isabella pendant fossils are from ~10 and ~50 meters above the marble, and the Tylerhorse Canyon fossils are from ~40 m above the marble. Furthermore, the host rock is identical in each of the three locations, being a fine-grained texturally and compositionally mature quartz arenite with calcareous and calc-silicate cement. We provisionally consider the marble-layered quartzite units of these two pendants stratigraphically equivalent to one another based on these relations.

4. (U-TH)/HE THERMOCHRONOMETRY

(U-Th)/He zircon ages were determined along a strategic traverse in the tectonically exhumed autochthon for the detachment plates of the Oak Creek Pass complex. Analytical techniques and details of replicate analyses are available in Appendix 2. The He zircon system is ideal for this application because Claraville plutonic rocks of the autochthon were tectonically denuded along the traverse to ~6 kb levels (Nadin and Saleeby, 2008) shortly after igneous construction (93-85 Ma, Saleeby *et al*., 1987, 2008), making the ~200°C closure temperature for the zircon He system (Reiners, 2005) ideal for resolving the timing of the rapid removal of upper crustal plates. Zircon He ages were determined from a subset of samples studied by apatite He (see Mahéo *et al*., 2009 for details and sample locations) collected from the medial area of the autochthon which lacks the potential complications of

Figure 4.8. Photograph of probable Early Jurassic pectinid bivalve Weyla from the Tylerhorse Canyon pendant.

Neogene-Quaternary faulting and burial by Miocene volcanogenic strata. Equal elevation and vertical transect sampling traverses are included in the data (Table 4.2). Figure 4.9a shows apatite He ages plotted against sample elevation and zircon He ages adjusted to a "pseudo-elevation," assuming, as shown by Clark *et al*. (2005), Cecil *et al*. (2006), and Mahéo *et al*. (2009), that following the termination of magmatism at ca. 84 Ma (Nadin and Saleeby, 2008), the topographic surface of the arc underwent slow regional erosion at a rate of 0.05 ± 0.01 mm/yr throughout much of Cenozoic time. These age-elevation relationships show that the area cooled through ~200°C rapidly at 77 ± 5 Ma. K/Ar and Ar/Ar ages on biotite and hornblende scattered across the autochthon are in the 89-75 Ma range (Kistler and Peterman, 1978; Dixon, 1995), when coupled to the zircon U-Pb igneous and He cooling ages further indicate rapid cooling from Claraville solidus to He zircon closure conditions at ~100° C/m.y. scale (Figure 4.9b). We interpret this ca. 77 Ma rapid cooling event as the principal time of large magnitude detachment faulting in the southeastern SNB. It also corresponds in time with the rapid eduction of the schist from beneath the autochthon (Saleeby *et al*., 2007; Chapman *et al*., 2010), and strike-slip transfer motion along the Kern Canyon-proto-White Wolf fault and Owens Valley shear system (Bartley *et al*., 2007; Nadin and Saleeby, 2008).

5. THERMOBAROMETRY

The rationale behind our thermobarometric work is that correlative native and displaced sites should show pressure differentials that reflect the relative upper and lower plate positions. To investigate igneous emplacement pressures as well as peak metamorphic

Figure 4.9. (a) Age pseudo-elevation relationship for southern Sierra Nevada apatite (Mahéo *et al*., 2009) and zircon He (this study) thermochronologic data. See text for discussion. (b) Time-temperature path for the autochthonous southern SNB. Geochronologic and thermochronometric data from Kistler and Peterman (1978), Dixon (1995), Saleeby *et al*. (2008), Mahéo *et al*. (2009), and this study.

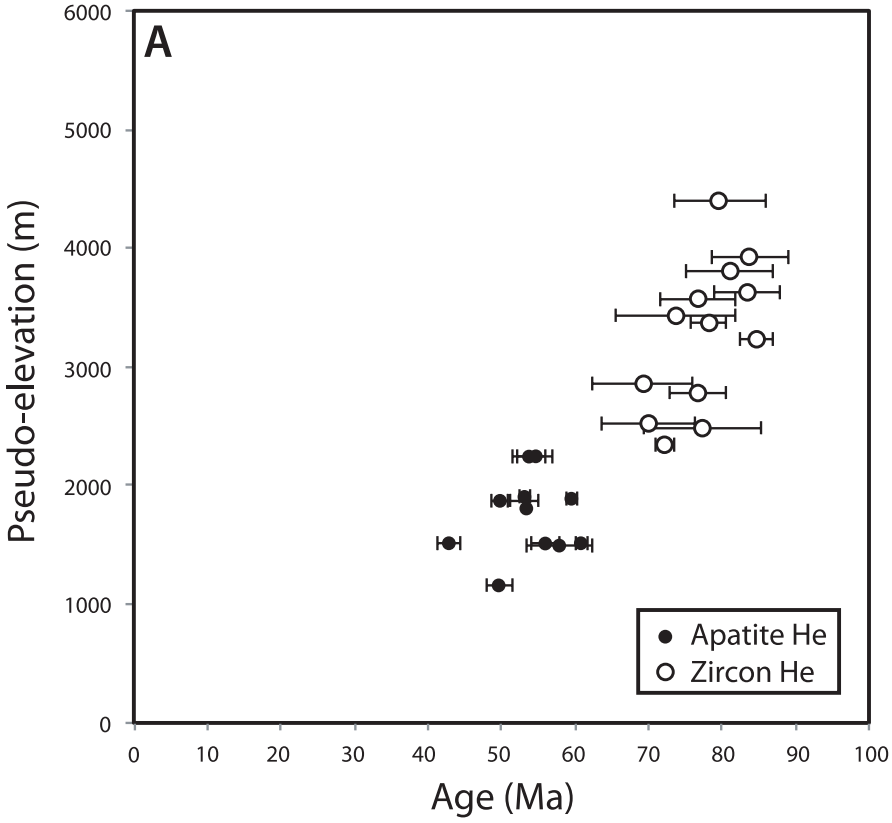
A
Pseudo-elevation (m)
Age (Ma)
Apatite He
Zircon He
0
1000
2000
3000
4000
5000
6000
0
10
20
30
40
50
60
70
80
90
100

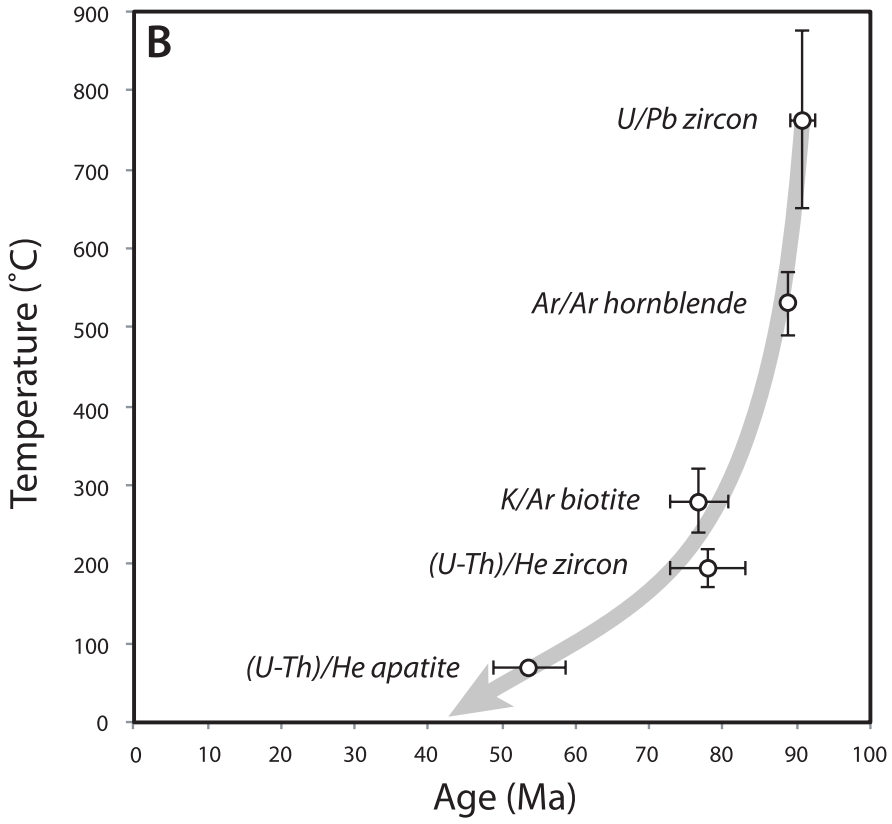
B
Temperature (°C)
Age (Ma)
U/Pb zircon
Ar/Ar hornblende
K/Ar biotite
(U-Th)/He zircon
(U-Th)/He apatite
0
100
200
300
400
500
600
700
800
900
0
10
20
30
40
50
60
70
80
90
100

Table 4.2. Summary of sample locations and zircon (U-Th)/He ages. Replicate data in Table A2.7.

Sample	UTM easting[a]	UTM northing[a]	Elevation (m)	Pseudo-elevation[b] (m)	Mean age (Ma)	Error[c] (Ma)	Number of replicates
04SS32	350708	3940938	1506	2327	77.3	8.0	4
04SS27	350384	3899048	1485	2193	72.2	4.5	4
04SS28	349061	3897426	1818	3319	83.5	6.3	4
04SS30	396529	3933080	1891	2416	70.0	3.9	3
04SS33	391015	3932556	1164	2518	76.8	2.3	4
04SS35	388629	3925972	1515	2949	84.7	6.7	6
04SS36	384771	3924533	1900	2701	69.2	2.4	4
04SS38	380280	3923122	1879	3129	78.2	8.1	5
04SS39	376370	3924106	2242	3239	73.7	5.2	4
04SS40	373067	3921963	2242	3347	76.7	5.2	4
04SS41	371086	3920961	1874	3576	83.8	5.9	5
04SS43	371523	3918853	1515	3424	81.1	8.3	7

[a] UTM coordinates are WGS datum, zone 11N.

[b] calculated assuming apparent exhumation rate of 0.05 mm/yr, see text for discussion.

[c] Errors (1s) are taken as the standard deviation divided by the square root of the number of replicates minus one.

conditions within pendant rocks, a suite of samples was collected from the southern Tehachapi Mountains, San Emigdio Mountains, and the Santa Lucia Range. Analytical techniques and representative mineral compositions are available in Appendix 2. *P-T* conditions for metapelitic pendant rock were calculated from garnet + biotite + plagioclase + quartz ± sillimanite/andalusite ± cordierite ± K-feldspar (Table 4.3) assemblages interpreted to have equilibrated during peak metamorphism. For these samples, we use garnet compositions where Mg# is highest suggesting garnet growth at peak temperatures (Spear, 1993) and avoid "Mn kick-ups" (Kohn and Spear, 2000) that indicate retrograde Fe-Mg exchange between garnet and biotite. All calculations were done assuming a water activity of unity, due to the abundance of hydrous phases in all samples. Equilibrium *P-T* conditions were calculated using the internally consistent average *P-T* mode in THERMOCALC, version 3.26 (Powell and Holland, 1994; Holland and Powell, 1998). Calculated temperatures and pressures for metapelitic pendant rock range from approximately 550 to 700 ˚C and 2.5 to 4 kbar.

Host plutons containing the equilibrium assemblage of hornblende + plagioclase + K-feldspar + quartz + sphene were collected for aluminum-in-hornblende (Al-in-hbl) igneous barometry (Hammarstrom and Zen, 1986; Hollister *et al*., 1987; Johnson and Rutherford, 1989; Schmidt, 1992; Anderson and Smith, 1995; Ague, 1997). We determine Al-in-hbl emplacement pressures and calculate temperatures from coexisting hornblende and plagioclase from analyses of at least 3 hornblende-plagioclase pairs per sample. We report hornblende-plagioclase temperatures as well as Al-in-hbl pressures for Hammarstrom and Zen (1986), Hollister *et al*. (1987), Johnson and Rutherford (1989), Schmidt (1992), and

Table 4.3. Summary of thermobarometric calculations from metamorphic pendant rocks. Representative mineral compositions in Table A2.8. Sample petrography in Appendix 2.

Sample	Location	Zone	UTM easting[a]	UTM northing[a]	Mineralogy[b]	T (°C)[c]	P (kbar)[c]	Corr[d]
31001-5	Santa Lucia Mountains adjacent to the Pine Ridge ultramafic body (Bush, 1981)	10	621473	4015561	Garnet + cordierite + sillimanite + quartz	695 ± 59	3.4 ± 0.5	0.835
08TC29	Southern Tehachapi Mountains: Tylerhorse Canyon pendant	11	366844	3870569	Garnet + cordierite + andalusite + quartz + plagioclase + biotite	557 ± 40	2.4 ± 0.5	0.851
10SE41	San Emigdio Mountains: Salt Creek pendant	11	322430	3860201	Garnet + sillimanite + plagioclase + quartz	649 ± 102	3.7 ± 1.7	0.620

[a] UTM coordinates are WGS datum.

[b] Peak equilibrium assemblages used in thermobarometric determinations.

[c] 1σ uncertainties based on propagation of uncertainties on thermodynamic data and activity-composition relationships through thermobarometric calculations.

[d] Correlation coefficient between pressure and temperature from THERMOCALC.

Anderson and Smith (1995) calibrations in Table 4.4. Thermobarometric results are appended to a recent compilation by Nadin and Saleeby (2008) to produce a color contour map (Plate 4), showing regional variations in igneous and metamorphic pressure for the southern SNB and Salinia. We refer below to the Schmidt (1992) determinations to remain consistent with the Nadin and Saleeby (2008) compilation.

6. GEOCHEMISTRY

6.1. Western San Emigdio Mafic Complex

Major and trace element geochemistry and Sr and Nd isotopic ratios were determined from allochthonous metavolcanic rocks to evaluate the most likely native sites of these rocks. Analytical techniques, whole-rock compositions, and isotopic data are available in Appendix 2. Major and trace element data indicate that sheeted dikes and pillow basalts from the WSEMC are of normal MORB (N-MORB) affinity (Sun and McDonough, 1989), with SiO_2 of approximately 49 wt. %. Trace element data for these rocks are normalized to N-MORB on Figure 4.10 and shown with the compositional trend of enriched MORB (E-MORB) as well as the range of data from the Paleozoic Kings-Kaweah ophiolite of the Foothills belt (Saleeby, 2011) abundances underlain for comparison. Compositional trends of WSEMC basalts lie between N-MORB and E-MORB with positive compositional spikes in Cs, Ba, U, K, Pb, and Sr. While similar spikes are commonly observed in supra-subduction zone volcanic rocks (e.g., Hofmann, 2003), these spikes are more likely related to mobilization during sea floor metamorphism and/or SNB contact metamorphism.

The relationship between $^{143}Nd/^{144}Nd$ and $^{87}Sr/^{86}Sr$ support a MORB association for

Table 4.4. Summary of thermobarometric calculations from plutonic rocks. Representative mineral compositions in Tables A2.9 and A2.10.

Sample	Unit	Zone	UTM easting[a]	UTM northing[a]	Hbl-Plag T[b] (°C)	Error[c]	AS95 P[d] (kbar)	Error[c]	HZ86 P[e] (kbar)	Error[c]	H87 P[f] (kbar)	Error[c]	JR89 P[g] (kbar)	Error[c]	S92 P[h] (kbar)	Error[c]
94KK27	Granodiorite of Jacobsen Meadow	11	355753	4010210	712	13	3.8	0.4	3.7	0.5	3.8	0.6	2.9	0.5	4.2	0.5
10SE1	Granite of Brush Mountain	11	296912	3862460	731	24	3.2	0.7	3.5	1.2	3.5	1.4	2.7	1.0	4.0	1.2
K16b-87	South tonalite of Vergeles	10	634652	4073302	710	8	4.7	0.3	4.8	0.3	5.0	0.4	3.9	0.3	5.2	0.3
04SE5	Lebec granodiorite	11	311257	3858324	636	13	3.3	0.9	2.6	0.9	2.5	1.0	2.0	0.7	3.1	0.8
93TH417	Claraville granodiorite	11	368657	3878458	679	15	3.8	0.3	3.3	0.3	3.3	0.3	2.6	0.3	3.8	0.3
91TH181	Claraville granodiorite	11	371313	3879868	732	9	3.6	0.3	3.9	0.2	4.0	0.3	3.1	0.2	4.4	0.2
08SE463	Tonalite of San Emigdio Creek	11	307763	3860816	711	15	5.2	0.6	5.2	0.5	5.5	0.5	4.2	0.4	5.7	0.4
08SE429	Tonalite of San Emigdio Creek	11	305382	3860121	687	25	5.6	0.3	5.4	0.3	5.7	0.3	4.4	0.2	5.8	0.3
08SE451	Antimony Peak tonalite	11	307028	3861038	675	78	9.7	1.5	10.0	0.4	10.9	0.4	8.2	0.3	10.2	0.3
08SE674	White Oak diorite gneiss	11	324461	3861916	657	17	11.0	0.3	10.6	0.1	11.5	0.1	8.8	0.1	10.7	0.1
08TC27a	Granodiorite of Gamble Spring Canyon	11	367862	3870810	626	28	3.0	0.6	2.2	0.5	2.1	0.6	1.7	0.5	2.8	0.5

[a] UTM coordinates are WGS datum.

[b] Hornblende-plagioclase temperatures based on Holland and Blundy (1994).

[c] 1σ uncertainties based on counting statistics from multiple analyses.

[d] Anderson and Smith (1995) pressures calculated by iteration using Holland and Blundy (1994) temperatures.

[e] Hammarstrom and Zen (1986) Al-in-hbl pressures.

[f] Hollister *et al*. (1987) Al-in-hbl pressures.

[g] Johnson and Rutherford (1989) Al-in-hbl pressures.

[h] Schmidt (1992) Al-in-hbl pressures.

the WSEMC basalts. Initial εNd and $^{87}Sr/^{86}Sr$ (Sr_i) values, age corrected for 160 Ma (the intrusion age of tonalite and gabbro of the WSEMC) and 484 Ma (the age of basalt-gabbro blocks of the Kings-Kaweah ophiolite belt), range from: εNd_{160} = +9.3 to +13.7, εNd_{484} = +11.3 to +15.9, Sr_{160} = 0.7033 to 0.7035, and Sr_{484} = 0.7032 to 0.7033 (Table A2.11), indicating that WSEMC basalts were derived from a source with long-term large ion lithophile element depletion, like that of convecting mantle beneath the Pacific Ocean basin (Hofmann, 2003). This is consistent with the trace element patterns of Figure 4.10, and with primitive mantle normalized La/Sm values of 0.67 to 0.72 at high initial εNd, which also plot within the field of modern Pacific MORB (Hofmann, 2003) and reflect long-term large-ion lithophile element depletion of the mantle source. The remarkable similarity between WSEMC and Kings-Kaweah ophiolite basalt isotopic systematics and elemental abundance relationships suggests that the WSEMC and ophiolitic assemblages of the Foothills belt are likely correlative. Details of this correlation are further discussed below.

6.2. Bean Canyon metavolcanic rocks

Approximately 150 m of Permian silicic metavolcanic rock crops out near the top of the Bean Canyon pendant section. These metatuffs display similar age, geochemical, and stratigraphic relations with metavolcanic rocks of the Kern Plateau, the El Paso Mountains, and the western Mojave Desert (Walker, 1988; Dunne and Suczek, 1991). Geochemical analysis of Bean Canyon metavolcanic rocks indicates that they are medium- to high-K dacite with approximately 66 wt. % SiO_2. Figure 4.11 is an N-MORB normalized spidergram comparing the trace element patterns of Bean Canyon pendant metatuffs and

Figure 4.10. N-MORB-normalized trace element diagram comparing basaltic rocks of the western San Emigdio mafic complex to E-MORB and the range of Kings-Kaweah ophiolite abundances (shaded area) (Saleeby, 2011). Idealized N-MORB and E-MORB from Sun and McDonough (1989). Data in Table A2.11.

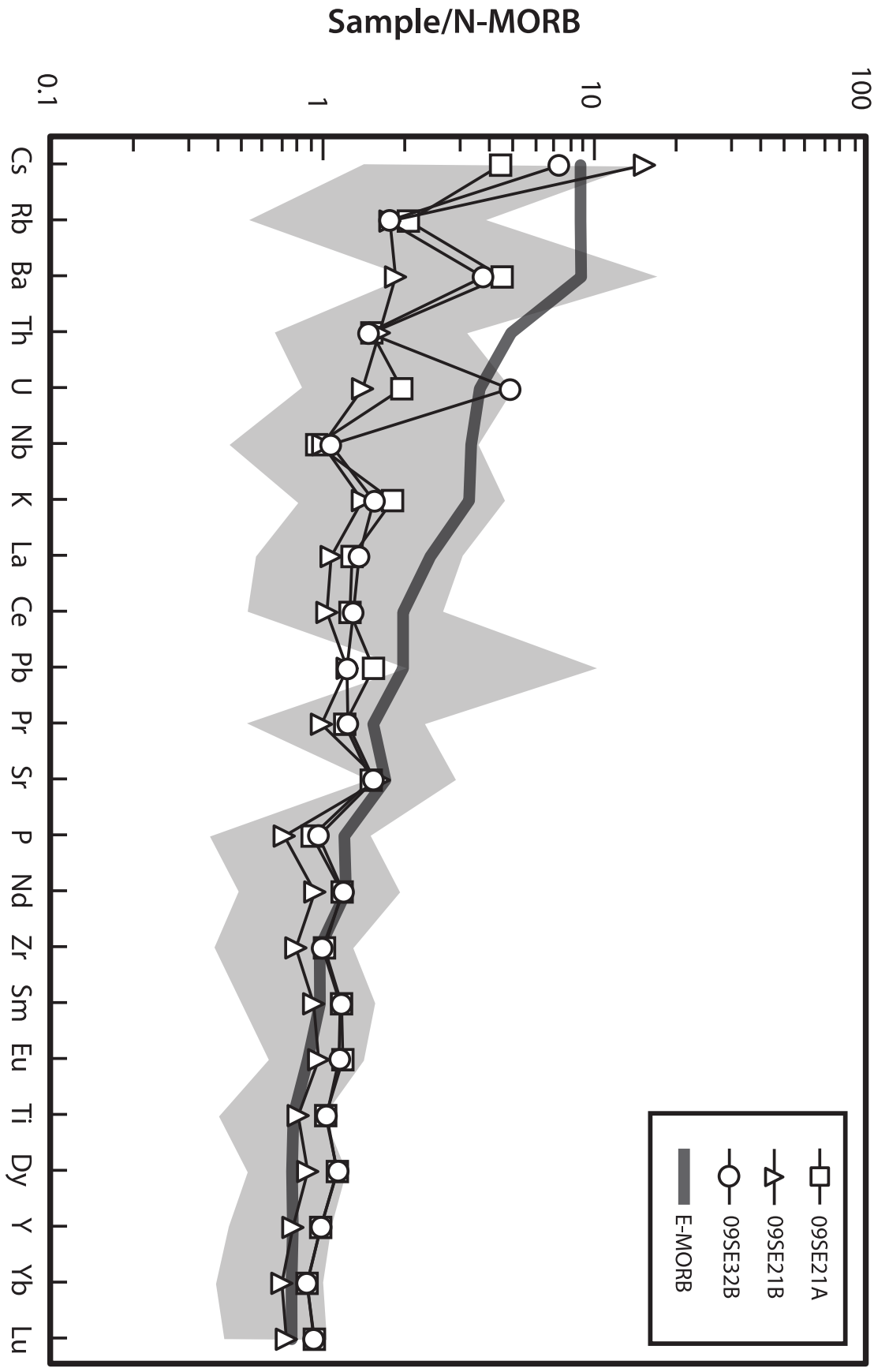
Sample/N-MORB
100
10
1
0.1
Cs Rb Ba Th U Nb K La Ce Pb Pr Sr P Nd Zr Sm Eu Ti Dy Y Yb Lu
09SE21A
09SE21B
09SE32B
E-MORB

dacitic to rhyolitic metatuffs of the Kennedy pendant (Dunne and Suczek, 1991). Compositional trends of both metatuff suites are remarkably similar, with prominent troughs in Nb, P, Ti and a peak in K. An additional peak in Pb is detected in Bean Canyon metavolcanic rocks. Subduction-related volcanic rocks commonly exhibit similar Nb and Pb spikes, as well as spikes in mobile elements such as K (e.g., Hofmann, 2003). Troughs in P and Ti are probably related to prior extraction of phases such as apatite and ilmenite, respectively. AFM and Ti vs. Zr diagrams (Pearce *et al*., 1981) support the view that Bean Canyon and Kennedy pendant metavolcanic rocks resulted from supra-subduction zone magmatism, with data plotting within calc-alkaline (Figure 4.12a) and arc volcanic (Figure 4.12b) fields.

7. DISCUSSION

7.1. Palinspastic restoration of vertical piercing points

Detailed field mapping, petrography, geochronology, and geochemistry of mafic complexes and pendants and hosting plutons reveal seven distinctive allochthonous assemblages that may correlate with similar autochthonous rocks of the southern Sierra Nevada and vicinity. Wood and Saleeby (1997) argued on the basis of geologic evidence for an additional nine correlations, two of which are supported by this study (correlations 2 and 3, described below), two are modified slightly (correlations 1 and 5), and the remainder are shown on Figure 4.13 as h-h' through m-m'. In aggregate, these are shown as a-a' through m-m' on Figure 4.13, a palinspastic base map with ~ 310 km of dextral slip along the San

Figure 4.11. N-MORB-normalized trace element diagram comparing silicic metavolcanic rocks of the Bean Canyon pendant (this study; open symbols) and the Kennedy pendant of the Kern Plateau (Dunne and Suzcek, 1991; filled symbols). Idealized N-MORB from Sun and McDonough (1989). Data in Table A2.11.

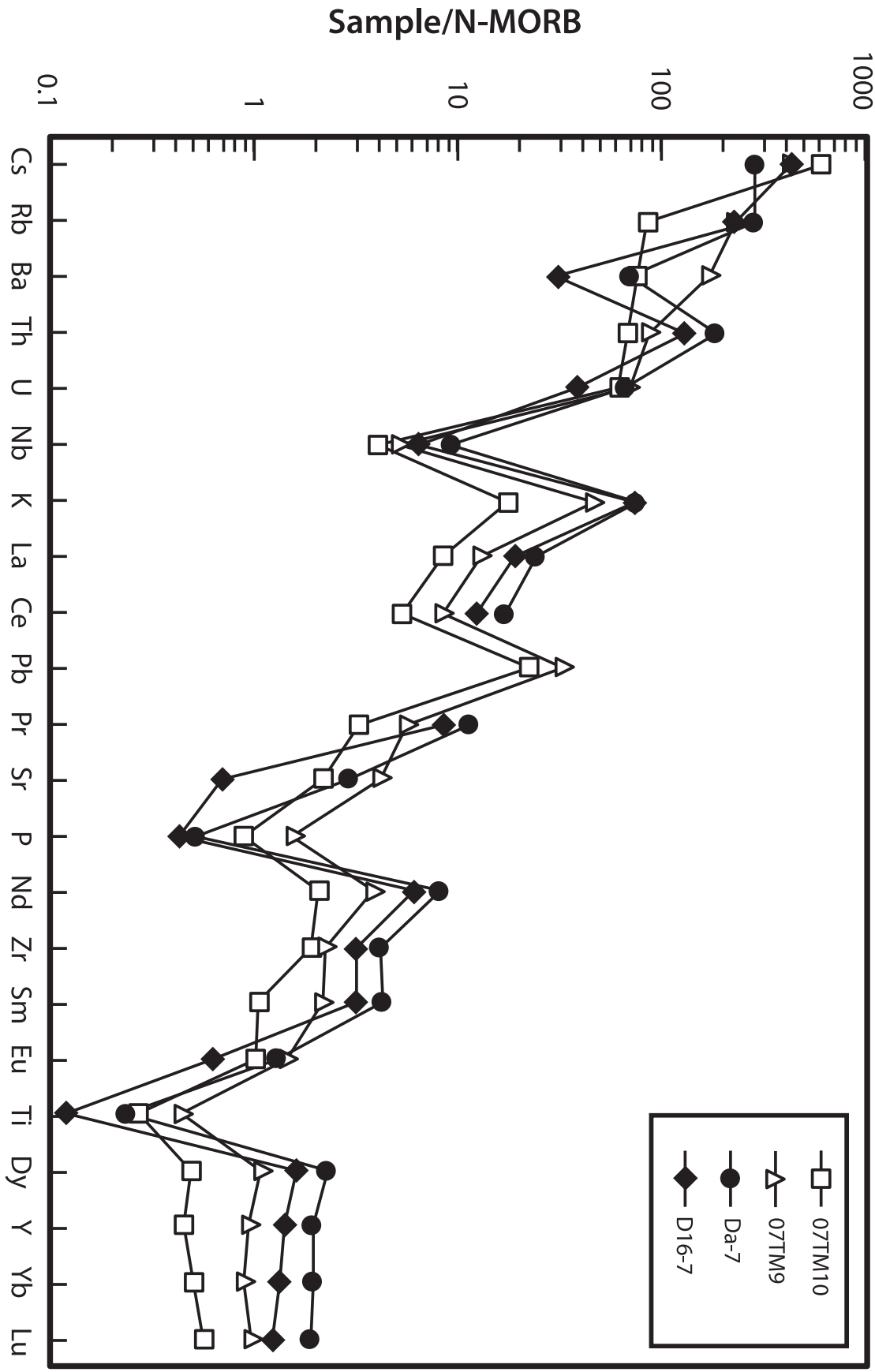
Sample/N-MORB
1000
100
10
1
0.1
Cs Rb Ba Th U Nb K La Ce Pb Pr Sr P Nd Zr Sm Eu Ti Dy Y Yb Lu
07TM10
07TM9
Da-7
D16-7

Figure 4.12. (a) AFM diagram showing that silicic metavolcanic rocks of the Bean Canyon pendant (open symbols) and the Kennedy pendant of the Kern Plateau (filled symbols) belong to a calc-alkaline trend. FeO* denotes total Fe as FeO. (b) Trace element discrimination diagram showing that silicic metavolcanic rocks plot within the field of arc lavas of Pearce *et al*. (1981). Symbols as in (a).

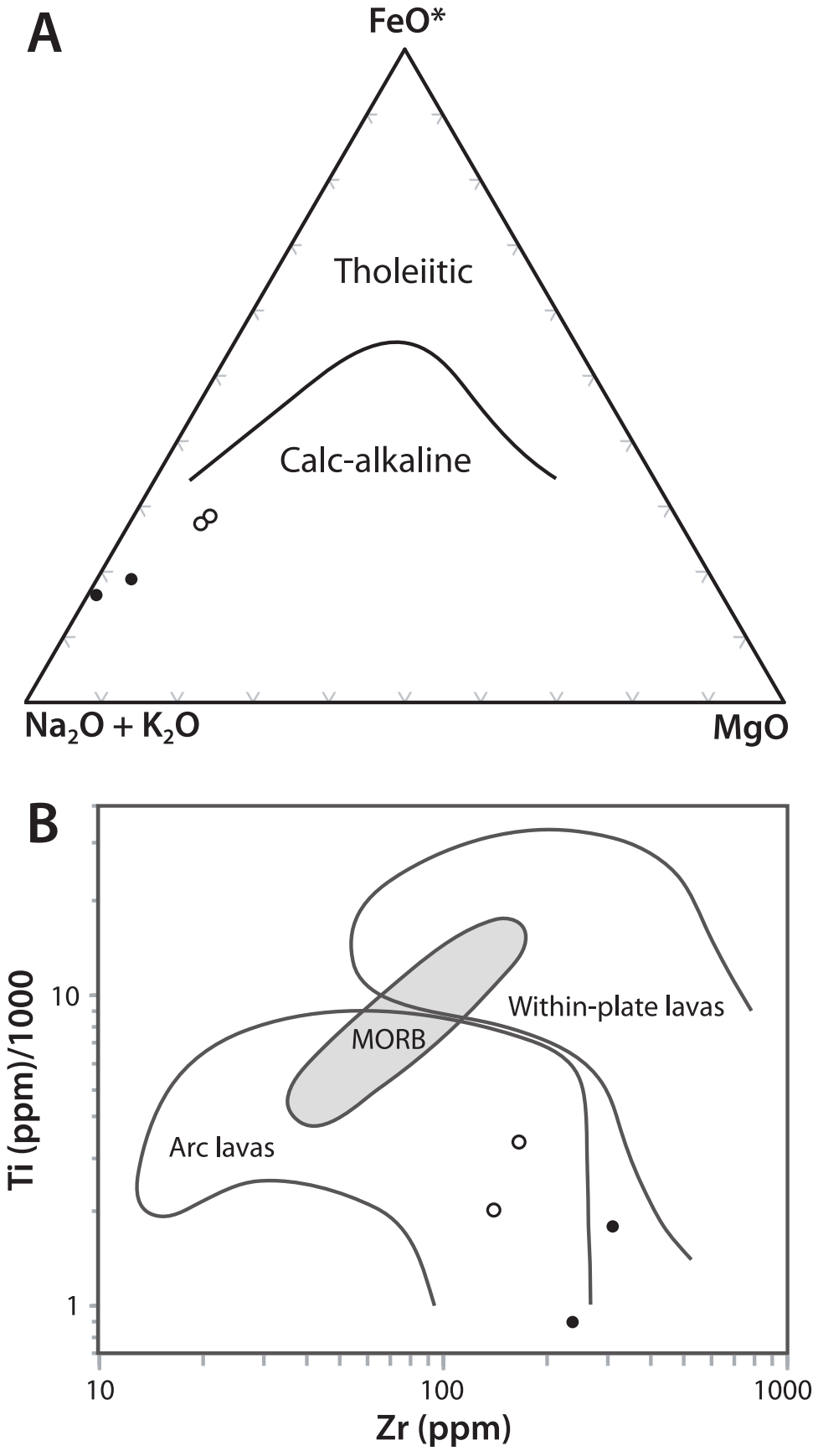
A
FeO*
Tholeiitic
Calc-alkaline
Na2O + K2O
MgO
B
Ti (ppm)/1000
10
1
Within-plate lavas
MORB
Arc lavas
10
100
1000
Zr (ppm)

Andreas fault (Huffman, 1972; Matthews, 1976) and ~ 50 km of sinistral slip along the Garlock fault (Ross, 1989) removed, with prime letters denoting the respective displaced piercing points and summarized in Table 4.5. The proposed correlations are further tested by relative barometric relations with the idea that pressure determinations from detachment plates should be lower that those of respective autochthonous sites.

7.1.1. Correlative granitoids

The granodiorites of Claraville, Gato Montes, Lebec, and the granites of Tejon Lookout, Brush Mountain, Tehachapi Airport, and Bean Canyon (Figure 4.1) constitute the vast majority of plutonic rocks exposed in the area surrounding correlations 1-4, discussed below (Ross, 1989). The granodiorites are nearly identical in field appearance, petrography, major and trace element geochemistry, and Sr_i, which led Ross (1989) and Kistler and Ross (1990) to assign a tentative correlation between the units. U-Pb geochronology yields identical emplacement ages of 91 ± 1 (Saleeby *et al*., 1987; 2008), 92 ± 1, and 90 ± 2 for Claraville, Gato Montes, and Lebec bodies, respectively. Exposures of biotite hornblende granodiorite and biotite granite in the Rand Mountains, plates III and IV of Nourse (1989), are quite similar to aforementioned granodiorite and granite units, and are probably correlative, yet are not studied in sufficient detail to permit correlation. Ross (1989) mapped the granites of Brush Mountain and Tejon Lookout as intruding the granodiorites of Lebec and Gato Montes, respectively. However, new field mapping (Chapman and Saleeby, in review) indicates that the contact, where exposed, is a shallowly dipping fault characterized by narrow (< 10 m) zones of cataclasis and hydrothermal alteration. In contrast to the intrusion

Figure 4.13. (a) Tectonic map of Figure 4.1 with Pliocene-Quaternary north-south shortening in the San Emigdio Mountains (Davis, 1983) removed and inferred allochthon (primed letters)-autochthon (corresponding letters) correlations and kinematic relations overlain. Correlations of Wood and Saleeby (1997) shown as black circles. Correlations of this study shown as white circles. Schist and allochthonous plate shear sense determinations from Nourse (1989), Wood and Saleeby (1997), and Chapman *et al*. (2010). Equal-area lower hemisphere stereonets show lineation measurements from the Rand Schist (Postlethwaite and Jacobson, 1987), schist of Sierra de Salinas (Chapman *et al*., 2010), the SSD (Wood, unpublished data), and inferred transport directions of upper crustal fragments (Kamb contour interval 4σ) (Table 4.5). (b) Map showing allochthonous regions of similar inferred paleogeographic affinity (shaded), correlative autochthonous areas (outlined with corresponding colors) and $^{40}Ar/^{39}Ar$ and K-Ar cooling ages (Evernden and Kistler, 1970; Huffman, 1972; Ross, 1989; Kistler and Champion, 2001; Saleeby *et al*., 2007). Abbreviations, symbols, and map units as in Figures 4.1 and 4.2.

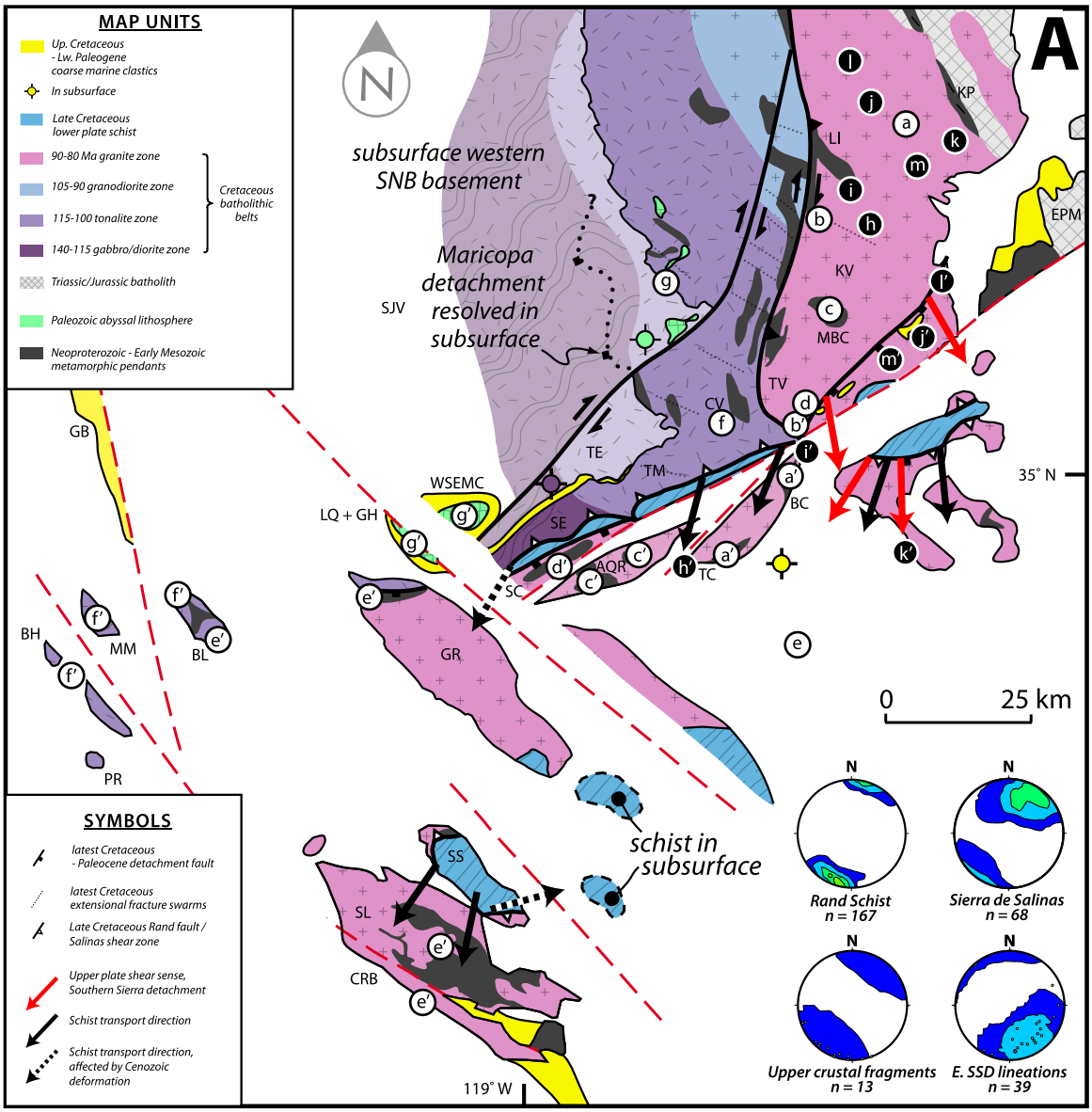
MAP UNITS
Up. Cretaceous - Lw. Paleogene coarse marine clastics
In subsurface
Late Cretaceous lower plate schist
90-80 Ma granite zone
105-90 granodiorite zone
115-100 tonalite zone
140-115 gabbro/diorite zone
Cretaceous batholithic belts
Triassic/Jurassic batholith
Paleozoic abyssal lithosphere
Neoproterozoic - Early Mesozoic metamorphic pendants
SYMBOLS
latest Cretaceous - Paleocene detachment fault
latest Cretaceous extensional fracture swarms
Late Cretaceous Rand fault / Salinas shear zone
Upper plate shear sense, Southern Sierra detachment
Schist transport direction
Schist transport direction, affected by Cenozoic deformation
A
N
subsurface western SNB basement
Maricopa detachment resolved in subsurface
SJV
schist in subsurface
KP
LI
EPM
KV
MBC
TV
CV
TE
TM
WSEMC
LQ + GH
SE
AQR
SC
TC
BC
GB
BH
MM
BL
PR
GR
SS
SL
CRB
35° N
119° W
0
25 km
Rand Schist n = 167
Sierra de Salinas n = 68
Upper crustal fragments n = 13
E. SSD lineations n = 39

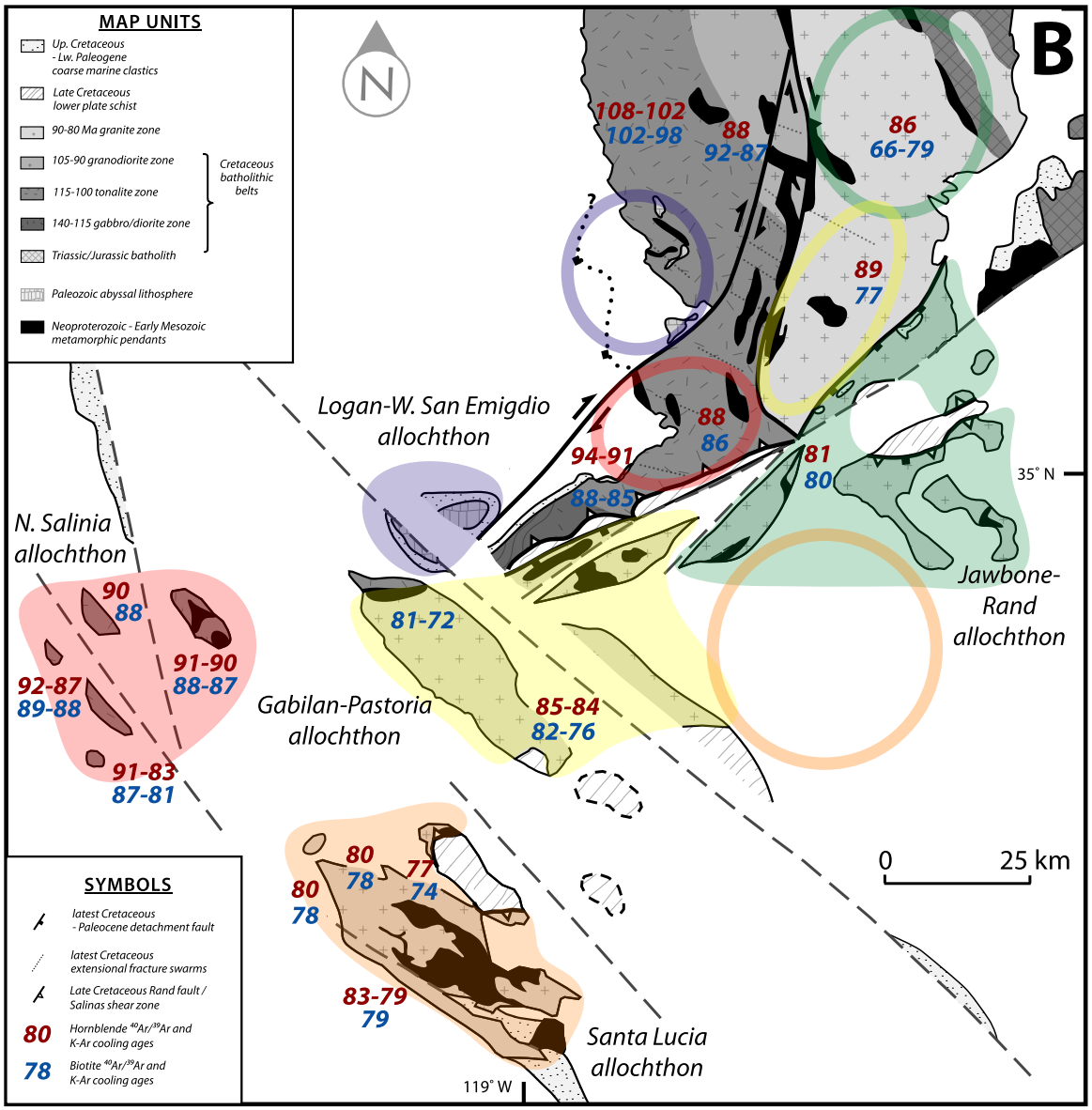
MAP UNITS
Up. Cretaceous - Lw. Paleogene coarse marine clastics
Late Cretaceous lower plate schist
90-80 Ma granite zone
105-90 granodiorite zone
115-100 tonalite zone
140-115 gabbro/diorite zone
Cretaceous batholithic belts
Triassic/Jurassic batholith
Paleozoic abyssal lithosphere
Neoproterozoic - Early Mesozoic metamorphic pendants
SYMBOLS
latest Cretaceous - Paleocene detachment fault
latest Cretaceous extensional fracture swarms
Late Cretaceous Rand fault / Salinas shear zone
80 Hornblende 40Ar/39Ar and K-Ar cooling ages
78 Biotite 40Ar/39Ar and K-Ar cooling ages
N
B
108-102
102-98
88
92-87
86
66-79
89
77
Logan-W. San Emigdio allochthon
88
86
94-91
88-85
81
80
35° N
N. Salinia allochthon
90
88
91-90
88-87
92-87
89-88
91-83
87-81
81-72
Jawbone-Rand allochthon
Gabilan-Pastoria allochthon
85-84
82-76
80
78
77
74
80
78
83-79
79
Santa Lucia allochthon
0
25 km
119° W

Table 4.5. Summary of correlated features. See text for discussion.

Correlation	Native site	Displaced site	Features[a]	Distance (km)[b]	Azimuth[c]	ΔP (kbar)[d]	Plunge[e]	Source[f]
a-a'	Area between Kern Plateau pendants and Isabella pendant	Bean Canyon and Tylerhorse Canyon pendants	S, UM, MV, DZ, IA, F, ID, Sri	100	200˚	1.3 - 3.1	4˚	this study, WS97 (b-b')
b-b'	Erskine Canyon sequence	Oak Creek Pass complex	S, MV, IA, Sri	45	185˚	0.1 - 3.3	7˚	this study, WS97 (e-e')
c-c'	Monolith and Back Canyon pendants	Quinn Ranch and Aqueduct Tunnel pendants	S, IA, Sri	75	220˚	> 1.7	4˚	this study, WS97 (a-a')
d-d'	Antelope Canyon group	Salt Creek pendant	S, DZ, IA, Sri	60	250˚	2.8 - 3.4	10˚	this study
e-e'	Area southwest of Rand Mountains	Gabilan Range, Santa Lucia Range, and southern Ben Lomond Mountain	S, UM, DZ, IA, Sri	75	225˚	~2.5 (CRB)	6˚	this study
f-f'	Cummings Valley	Montara Mountain, northern Ben Lomond Mountain, and Bodega Head	IA, Sri	150	250˚	~ 3	4˚	this study. WS97 (j-j')
g-g'	Southwestern Sierra Nevada foothills	Western San Emigdio mafic complex	MV, IA, Sri	60	220˚	> 2.5	8˚	this study
h-h'	Area between Tylerhorse Canyon and Quinn Ranch pendants	Area north of Kelso Valley	I, IA, Sri	60	210˚	2.9 - 3.7	10˚	WS97 (c-c')
i-i'	Granite of Bob Rabbit Canyon	Granite of Tejon Lookout	I, IA, Sri	70	195˚	~ 3	8˚	WS97 (d-d')
j-j'	Granite of Onyx	Granite of Lone Tree Canyon	I	50	170˚	ND	ND	WS97 (f-f')
k-k'	Summit gabbro of Walker Pass	mafic plutons in the southern Rand Mountains	I	70	200˚	ND	ND	WS97 (g-g')
l-l'	Granite of Long Meadow	Granite of Bishop Ranch	I	55	160˚	ND	ND	WS97 (h-h')
m-m'	Granite of Onyx	Bishop Ranch leucogranite	I	50	185˚	ND	ND	WS97 (i-l')
Average[g]				71 ± 28	205 ± 28˚	2.5 ± 0.6˚	6.5 ± 3.1˚	

[a] Correlated features. DZ, detrital zircon spectra of quartzofeldspathic intervals; F, fossils; I, igneous relations; IA, igneous ages of pendant hosting plutons; ID independence dikes present; MV, presence of metavolcanics of similar geochemistry and age; S, stratigraphic relations; Sri, Sr_i of pendant hosting plutons; UM, presence of geochemically enriched ultramafic rock.

[b] Approximate lateral distance between sites calculated by measuring the map view distance between native and displaced sites after restoring slip along San Andreas and Garlock faults.

[c] Approximate transport azimuth calculated by measuring the map view heading of the displaced site from the native site after restoring slip along San Andreas and Garlock faults.

[d] Pressure differential between sites. CRB, Coast Ridge Belt; ND, not determined.

[e] Calculated by multiplying the pressure differential between sites by 3.3 km/kbar, dividing this value by the lateral distance between sites, and taking the arc tangent of this quotient

[f] WS97, letters in parentheses correspond to correlations inferred by Wood and Saleeby (1997).

[g] 1σ uncertainties based on counting statistics from multiple measurements.

model explaining the current position of the granites, our reinterpretation is compatible with older U-Pb zircon ages in the granites, ranging from 105 to 98 Ma (James, 1986b, and this study), than in the granodiorites. Similar low angle fault contact relations are documented between "Plate III" granodiorite and "Plate IV" granite in the Rand Mountains (Nourse, 1989).

7.1.2. Correlation #1: Area between Lake Isabella and Kern Plateau pendants (a) and Bean Canyon and Tylerhorse Canyon pendants (a')

The Bean Canyon pendant is characterized by a succession of marble, quartzite, calc-silicate hornfels, pelitic schist, and silicic metatuff, unconformably underlain by amphibolite and associated ultramafic rock (Rindosh, 1977; Wood and Saleeby, 1997; Ross, 1989, and this study) with vertical to sub-vertical foliation and steeply plunging lineation. The correlation of metamorphosed ultramafic bodies in Bean Canyon and Salinia with similar rocks at the apparent base of the Kennedy pendant section in the El Paso terrane is discussed below in "*correlation #5*." Detrital zircon geochronologic data reported herein indicates that quartzite (sample 07BC60) from the Bean Canyon pendant contains an age distribution similar to that of eugeoclinal deposits of the El Paso terrane (Paterson *et al*., in preparation) and Roberts Mountains allochthon (Gehrels *et al*., 2000a) and miogeoclinal rocks of the Snow Lake pendant (Figures 4.6 and 4.7). U-Pb zircon ages of 273.0 ± 2.4 Ma for dacitic metatuff from near the top of the Bean Canyon section overlap in age with andesitic flows and breccias from the El Paso Mountains (Walker, 1988; Martin and Walker, 1995) and indicate that the Bean Canyon pendant is entirely Paleozoic. Trace element abundances of

undated silicic metavolcanic rocks from the Kern Plateau are quite similar to those of the Bean Canyon pendant (Figure 4.11). Age, geochemical, petrographic, and stratigraphic relations lead us to suggest that volcanic and metavolcanic rocks exposed in the El Paso Mountains, and Bean and Kern Plateau pendants are consanguineous.

The Tylerhorse Canyon pendant lies stratigraphically above the Bean Canyon pendant and consists of thick intervals of pelitic and psammitic schist, calc-silicates, and marble with steeply dipping foliation and down-dip lineation. The thickness of individual layers, with some marble intervals reaching ~300 m in thickness, is likely an artifact of east-trending (now rotated) isoclinal folding (Rindosh, 1977). The U-Pb detrital zircon age spectrum from metapsammitic sample 08TC44 partially overlaps that of sample 07BC60 from the Bean Canyon pendant for grains older than ca. 1400 Ma (Figure 4.6), but abundant late Paleozoic to early Mesozoic grains indicate that strata of the Tylerhorse Canyon pendant were deposited into Jurassic time. The Tylerhorse Canyon section is, therefore, interpreted as a Mesozoic overlap sequence deposited across Bean Canyon pendant protoliths. Scattered 1000 – 1400 Ma grains, also present in the Sur Series of Salinia (Barbeau *et al*., 2005), were probably sourced from proximal inner shelf and slope deposits. A similar El Paso terrane-overlapping setting is envisaged for the Isabella pendant, based on the presence of Paleozoic amphibolite overlain by Triassic metavolcanic rocks and detrital zircon age spectra indicating deposition of Kings sequence assemblages into Jurassic time (J. Saleeby, unpublished data). Fossils resembling Early Jurassic pectinid bivalve Weyla (Figure 4.8) corroborate a Mesozoic depositional age for Tylerhorse Canyon strata and permit correlation of equivalent strata found in the Lake Isabella pendant.

Two distinct igneous suites intrude the Bean Canyon - Tylerhorse Canyon package. First is a series of east-striking tonalitic, gabbroic, and granodioritic dikes and lenticular masses distributed throughout and along the margins of the pendants. The granodiorite of Gamble Spring Canyon represents one phase of the suite and with an inferred emplacement age of 146.8 ± 0.4 Ma, is similar in age to the quartz diorite of Long Valley (Saleeby and Dunne, in review) and to the Late Jurassic Independence dike swarm of the eastern Sierra Nevada-Owens Valley-Mojave Desert region (Chen and Moore, 1979; Carl and Glazner, 2002; Glazner *et al*., 2002; Bartley *et al*., 2007; Hopson *et al*., 2008) (Figure 4.1). In the light of our new U-Pb geochronology, Rb-Sr ages of ca. 150 Ma (R. A. Fleck, written communication in Ross, 1977; 1989) from Bean Canyon metavolcanic rocks, originally thought to represent the age of volcanism, probably instead reflect isotopic disturbance owing to intrusion of the granodiorite of Gamble Spring Canyon. The granodiorite of Gato Montes and granite of Bean Canyon, both Late Cretaceous in age (Evernden and Kistler, 1970; Kistler and Ross, 1990) comprise a second plutonic suite that intrudes Bean Canyon and Tylerhorse Canyon pendants and the Jurassic granodiorite of Gamble Spring Canyon. High Sr_i ratios (> 0.707) characterize these plutons and native equivalents, and a pressure differential of ~ 2.4 – 2.8 kbar (samples 08TC27a and 08TC29) for the upper plate (a') versus 4.1 – 5.5 kbar for the lower plate (Nadin and Saleeby, 2008, samples 03SS1, 04SS31, and 51) (a), suggest the removal of 5-10 km of crust along the SSD during faulting.

7.1.3. Correlation #2: Silicic metavolcanic rocks of the Erskine Canyon sequence (b) and the Oak Creek Pass complex (b')

Small screens of finely recrystallized laminated tuffs with remnants of quartz phenocrysts and pumice lapilli recrystallized to biotite + quartz and set in a faintly schistose groundmass consisting of quartz, feldspar, biotite and sericite, crop out in the Oak Creek Pass complex (Wood, 1997; Wood and Saleeby, 1997). The Oaks metatuffs are similar in petrography, texture, and field setting to the 102 – 105 Ma Erskine Canyon rhyolitic to andesitic metavolcanic sequence, which has been partly transposed over an ~ 40 km stretch along the PKCF adjacent to Lake Isabella (Nadin and Saleeby, 2008; Saleeby *et al*., 2008). The Erskine Canyon sequence crops out to the west of and within the PKCF and dextrally displaced equivalents have not been recognized east of the structure. We hypothesize that Oaks metavolcanic rocks represent Erskine Canyon assemblages formerly situated east of the PKCF that were subsequently displaced by detachment faulting. U-Pb zircon geochronology reported here supports this view, with an interpreted eruption age of 102.6 ± 1.0 Ma for Oaks metavolcanic rocks. While it is implicit that Erskine Canyon and Oaks metavolcanic assemblages must have been emplaced at or near surface level conditions at ca. 102 – 105 Ma, they are now exposed adjacent to plutonic rocks of slightly younger age, implying that considerable post-eruptive downward flow has occurred. Pressure determinations from plutons and Kings sequence assemblages in contact with Erskine Canyon metavolcanic rocks range from 6.6 to 4.5 kbar (Nadin and Saleeby, 2008, Plate 4), in contrast to 3 to 4.4 kbar determinations from the Claraville granodiorite (Nadin and

Saleeby, 2008, sample RB020601, and samples 93TH417 and 91TH181) which intrudes Oaks metavolcanic rocks, corresponding to ~5 ± 5 km of missing crust.

7.1.4. Correlation #3: Monolith and Back Canyon pendants (c) and Quinn Ranch and Aqueduct Tunnel pendants (c')

West of the Tylerhorse Canyon pendant, pendant-pluton contacts and metamorphic foliation abruptly change from vertical to moderately dipping and subhorizontal (Crowell, 1952; Ross, 1989). The Quinn Ranch and Aqueduct Tunnel pendants are characterized by thick sequences of chiefly marble interleaved with calc-silicate and minor quartzite and siliceous meta-argillite (Ross, 1989). The granodiorite of Gato Montes intrudes these pendants and yields a U-Pb zircon age of 92. 1 ± 1.0 Ma. The Aqueduct Tunnel and Quinn Ranch pendants, neighboring small marble septa, and host plutons share similar pendant-pluton relations with Monolith and Back Canyon pendants and intrusive Claraville granodiorite of the south-central SNB. A similar range of lithologies to that of Aqueduct Tunnel and Quinn Ranch pendants are seen in Monolith and Back Canyon pendants, which are likewise characterized by shallowly dipping contacts and foliation (Wood and Saleeby, 1997). We suggest, on the basis of distinctive thick marble successions found in pendants at c and c', that these pendants belong to the Death Valley facies of the passive margin as exposed in the Shadow Mountains of the western Mojave Desert (Martin and Walker, 1995) (Figure 4.1). A single Al-in-hbl pressure of 5.7 kbar is calculated from a mafic phase of the Claraville granodiorite southwest of Kelso Valley, adjacent to the Back Canyon pendant (Ague and Brimhall, 1988, sample 420). The presence of prograde andalusite as the only

stable aluminosilicate phase in pelitic assemblages of the Quinn Ranch pendant (Ross, 1989) suggests that these rocks were intruded and contact metamorphosed at pressures no greater than ~ 4 kbar (Spear, 1993). These relations suggest the excision of at least 5.5 km of crust along the SSD.

7.1.5. Correlation #4: Antelope Canyon group (d) and Salt Creek pendant (d')

The Salt Creek pendant of the San Emigdio Mountains is composed principally of thick layers of marble, quartzite, and quartzofeldspathic gneiss, with lesser amounts (< 5%) of pelitic to psammitic schist. Quartzofeldspathic gneisses and pelitic and psammitic assemblages are commonly segregated into quartz + two feldspar leucosomes and biotite ± fibrolite/sillimanite ± cordierite ± garnet melanosomes and injected with veins of Lebec granodiorite. These lithologies suggest that the protoliths of the Salt Creek pendant were deposited in a slope to inner shelf environment and potentially correlate to similar assemblages found in the Sierra City mélange - Shoo Fly – Kernville terrane (Figure 4.2). Our detrital zircon geochronologic data from quartzite sample 08SE258 support this view, with major age peaks corresponding to those of slope strata from the Kernville terrane of the Fairview pendant (Saleeby, 2011) (Figures 4.6 and 4.7).

The Salt Creek pendant is intruded by the ca. 90 Ma Lebec granodiorite. Ross (1989) notes lithologic similarities between the Salt Creek pendant and pendants north of Tehachapi Valley, including the Brite Valley, Tehachapi, Monolith and Back Canyon pendants. However, the Lebec granodiorite-hosted Salt Creek pendant does not likely correlate with Brite Valley and Tehachapi pendants as they are intruded by 99 – 105 Ma

tonalites, diorites, and gabbroids of the intrusive suite of Bear Valley (Saleeby *et al*., 2007; 2008). In contrast, similar siliciclastic and carbonate rocks of the Antelope Canyon group are intruded by a border phase of the Claraville granodiorite (Wood, 1997), representing the most likely native site for similar assemblages of the Salt Creek pendant and adjacent rocks. A pressure differential of 6.5 (Dixon, 1995, sample Th275) versus 3.1 (sample 04SE5) and 3.7 (sample 10SE41) kbar for autochthonous versus allochthonous assemblages, corresponding to 9 to 11 km of missing crust, is implied by this correlation. Samples 08SE463 and 08SE429, yielding Al-in-hbl pressures of 5.7 and 5.8 kbar, were collected from an ~100 m wide fault horse of an unnamed hornblende-clinopyroxene quartz monzonite that crops out along the Pastoria fault system between the Pastoria plate and lower plate San Emigdio schist. This fault sliver is interpreted to represent a tectonic fragment calved off the lower plate as the Pastoria plate descended structurally. We exclude these pressure determinations from autochthon-allochthon pressure differential calculations based on the structural setting of these samples.

7.1.6. Correlation #5: Area southwest of the Rand Mountains (e) and Salinian framework of the Gabilan Range, Santa Lucia Range, and southern Ben Lomond Mountain (e')

The Sur Series (Trask, 1926) of the Santa Lucia and Gabilan Ranges, and smaller exposures in the Ben Lomond and Point Reyes areas contains abundant thinly interbedded marble and calc-silicate, leading several workers to suggest that metasedimentary rocks of the Salinian block correlate with strata of the Paleozoic Cordilleran miogeocline (e.g., Ross *et al*., 1973; Ross, 1977; Kidder *et al*., 2003). However, thick, pure quartzite and marble units, that

resemble the Stirling and Zabriskie quartzites and the Bonanza King Formation of the Death Valley-Mojave Desert region, are conspicuously absent from the Salinian block, calling into question such a correlation. Metasedimentary assemblages of the Salinian terrane also share several similarities with eugeoclinal strata of the El Paso terrane. First, thinly-bedded Sur Series assemblages are lithologically similar to strata of the Kern Plateau pendants and the Bean Canyon pendant (Rindosh, 1977; Ross, 1977; Dunne and Suczek, 1991). Second, Sur Series assemblages exhibit broad Late Archean and Proterozoic U-Pb detrital zircon age peaks that roughly correspond to those of the El Paso terrane, including the Bean Canyon pendant (Barbeau *et al*., 2005; Paterson *et al*., in preparation) (Figure 4.6). While Sur Series age peaks are too broad to discern between miogeoclinal and eugeoclinal sources within the Mojave Desert, potentially due to zircon isotopic disturbance during high-grade metamorphism (amphibolite to granulite facies) and dike injection, the presence of Permian zircons in Upper Cretaceous cover strata suggests derivation from, or at least proximity to, the El Paso terrane (Barbeau *et al*., 2005). Finally, small mafic to ultramafic bodies crop out entirely within, and are elongated parallel to the foliation of, Sur Series metasedimentary rocks (Wiebe, 1966, 1970; Nutt, 1977; Bush, 1981), the Lake Isabella pendant (Saleeby and Busby, 1993), the Bean Canyon pendant (Rindosh, 1977; this study), and the Kern Plateau pendants (Dunne and Suczek, 1991). REE diagrams with negative slopes and rock/chondrite ratios of up to 40 from the Kern Plateau (G. Dunne, written communication, 2011) and $Sr_i > 0.7075$ from clinopyroxene separates from the Santa Lucia Range (Kidder and Ducea, unpublished data) indicate that they are geochemically enriched and suggest that they are fragments of continental mantle lithosphere. Such unique geochemical and field relations make these bodies useful for correlation purposes.

The central Santa Lucia and Gabilan Ranges and southern Ben Lomond Mountain contain plutons with high Sr_i (typically > 0.708) and young emplacement ages from 93 to 76 Ma (Kistler and Champion, 2001; Kidder *et al*., 2003; Dickinson *et al*., 2005) that intruded the Sur Series at pressures of 3.4 to 4 kbar (John, 1981, and this study). A zone of platformal sequences characterized by quartzite, marble, and psammitic schist (Miller *et al*., 1995) and high Sr_i and young plutons (Plates 2 and 3) southwest of the Rand Mountains appears to be the most likely native site for the central Santa Lucia and Gabilan Ranges. However, Permian metavolcanic rocks and Independence dikes, two striking yet volumetrically minor constituents of the El Paso terrane, are not reported from the Salinian block. These rock types may be absent from the Salinian block or obscured due to poor exposure.

The Coast Ridge Belt, an ~7.5 kbar exposure of orthogneiss and subordinate marble and quartzite (Kidder *et al*., 2003), probably represents the midcrustal equivalent of the central Santa Lucia Range and crops out ~ 5 km to the west of our 3.4 kbar determination and 4 to 6 kbar estimates of peak metamorphic pressures in the Sur Series by Wiebe (1966, 1970). The pressure gradient between the Coast Ridge Belt and the central Santa Lucia Mountains is explained by Kidder *et al*. (2003) as the result of regional ~30˚ to the NE tilt. However, this tilt can only account for an ~ 3 km (i.e., ~ 1 kbar) difference over 5 km. Therefore, the pressure difference between the Coast Ridge Belt and the central Santa Lucia Range must have resulted either from structural attenuation or faulting, potentially along the Coast Ridge and/or Palo Colorado faults (Ross, 1976). We suggest that the Coast Ridge Belt restores to a position along the west flank of the central Mojave metamorphic core complex, possibly correlating with the Johannesburg gneiss in the hanging wall of the Rand fault, with shallow

exposures of the central Santa Lucia Range, Gabilan Range, and southern Ben Lomond Mountain lying in fault contact above the belt. Pressure determinations from footwall assemblages southwest of the Rand Mountains are sparse, yet values of ~ 10 kbar are reported from the central Mojave metamorphic core complex (Henry and Dokka, 1992). A pressure differential of ~ 2.5 kbar between the Coast Ridge Belt and the central Mojave metamorphic core complex implies the removal of ~ 8 km of crust along a structure that has not yet been recognized.

7.1.7. Correlation #6: Cummings Valley (f) and Salinian framework of Montara Mountain, northern Ben Lomond, and Bodega Head (f')

Tonalitic plutonic rocks of Montara Mountain, northern Ben Lomond Mountain, and Bodega Head range in age from 99 to 104 Ma (James and Mattinson, 1985; James, 1992; Kistler and Champion, 2001) and have similar Sr_i (0.707 – 0.705) to the 99 to 105 Ma intrusive suite of Bear Valley (Saleeby *et al*., 1987; Pickett and Saleeby, 1993; Saleeby *et al*., 2007). Moreover, the lack of ultramafic bodies and similarities between Sur Series metasedimentary rocks of northern Salinia and the Brite Valley and Tehachapi pendants in the southern SNB (Wood, 1997) suggest an origin for these basement fragments near Cummings Valley, where pressure determinations of up to 8.3 kbar are reported (Pickett and Saleeby, 1993, sample GC-16). These plutons and their framework rocks have not received detailed thermobarometric study, although pressures of ~ 5 kbar are reported from metapelitic assemblages from Ben Lomond Mountain (Leo, 1965; DeCrisoforo and Cameron, 1977).

7.1.8. Correlation #7: Southwestern Sierra Nevada foothills (g) and Western San Emigdio mafic complex (g')

Reitz (1986) suggests that the WSEMC is a unique exposure of a primitive intra-oceanic arc and that it does not correlate with 1) the Coast Range Ophiolite because the mafic complex lacks ophiolite stratigraphy, or 2) Sierran Foothills belt peridotitic to dioritic intrusive complexes (Snoke *et al*., 1982) and associated ophiolitic wall rocks due to slight differences in crystallization sequence, geochemistry, and the presence of minor orthopyroxene in the WSEMC, which is incorrectly stated to be rare in peridotitic to dioritic complexes. New geochemical data and field relations call this interpretation into question. Major and trace element geochemistry and $^{143}Nd/^{144}Nd$ versus $^{87}Sr/^{86}Sr$ systematics indicate that sheeted dikes and pillow basalts from the WSEMC were generated through MORB magmatism (Figure 4.10). The remarkable geochemical similarity between basaltic rocks of the WSEMC and the Kings-Kaweah segment of the Foothills ophiolite belt suggests that the two bodies are correlative. Sheeted dikes and pillow basalts of the WSEMC are intruded by a mid- to Late Jurassic suite of ultramafic, gabbroic, and tonalitic assemblages (Hammond, 1958; Ross, 1970; 1989; Dibblee and Nilsen, 1973; James, 1986a; Reitz, 1986) that resemble 170 to 150 Ma intrusive complexes of the western Sierra Nevada and Klamath Mountains (Snoke *et al*., 1982). Zircons from tonalitic segregations in gabbros yield concordant U-Pb ages of ca. 161 Ma (James, 1986a). These gabbros are intruded by the White Ridge tonalite, which yielded a U-Pb age of 154.2 ± 3.5 Ma. Similar U-Pb zircon ages of 170 to 156 Ma are reported from gabbroic to tonalitic assemblages of the Mill Creek complex, which intrudes the Kings-Kaweah ophiolite belt segment (Saleeby and Sharp,

1980; Snoke *et al*., 1982; Wolf and Saleeby, 1995; Saleeby, 2011; Saleeby and Dunne, in review), and from previously correlated exposures at Logan Quarry and Gold Hill that were offset from the western San Emigdio Mountains area along the San Andreas fault (Ross, 1970; Ross *et al*., 1973; James, 1986a; James *et al*., 1993).

Exposures and basement cores of variably mylonitized and highly altered mafic to ultramafic rocks occur in the vicinity of locality g on Figure 4.13 (e.g., Dibblee and Chesterman, 1953; Ross, 1989; Saleeby *et al*., 2009a). As noted previously, the basement surface between g and g' is the corrugated Maricopa detachment fault with the WSEMC in the hanging wall, similar assemblages near g in the footwall, and supradetachment basin deposits of the Uvas Member of the Tejon Formation unconformably overlying the WSEMC (Figures 4.1 and 4.4). Constraining the amount of crust that was removed by this structure is difficult, as the WSEMC does not contain Cretaceous assemblages conducive to thermobarometry. However, the preservation of albite-epidote and hornblende hornfels facies assemblages in pillow basalts and sheeted dikes of the WSEMC (Hammond, 1958; this study) suggest that metamorphic pressures of equilibration did not exceed ~ 2 kbar (Spear, 1993). Al-in-hbl pressure determinations of 4.5 to 5.8 kbar from footwall assemblages (Nadin and Saleeby, 2008, samples 48 and 49) suggest that restoration of g' to g implies the removal of at least 8 km of formerly intervening crust.

7.1.9. Magnitude and direction of displacement

The correlations discussed above each imply the removal of approximately 5 to 10 km of crust along detachment faults with a north bounding breakaway zone in the Isabella basin area. This corresponds to the "Isabella breakaway" of Mahéo *et al*. (2009), in the southern

SNB. The KWF bounds the western margin of the Isabella breakaway and transfers the zone ~ 50 km to the southwest to the Kern range front, the headwall for the Maricopa detachment (Figure 4.13). The average magnitude of transport is 71 ± 28 km (Table 4.5), calculated by measuring the map view distance between native and displaced assemblages. The distances between recognized allochthon-autochthon pairs are great enough that transport directions may be approximated through palinspastic reconstruction of these vertical piercing points. Transport azimuths, with an average of 205 ± 28˚, were determined by measuring the map view heading of the displaced site from the native site after restoring slip along San Andreas and Garlock faults. Plunge angles, with an average of 2.5 ± 6˚, were calculated by multiplying the pressure differential between sites by 3.3 km/kbar, dividing this value by the lateral distance between sites, and taking the arc tangent of this quotient.

The determination of these values critically depends on recognizing superimposed increments of post-Cretaceous deformation that may have contributed to the transport of allochthonous fragments. The biggest challenge in "seeing through" post-Cretaceous deformation in the southern SNB and vicinity, after restoring slip along the San Andreas and Garlock faults, is accounting for apparent clockwise vertical axis rotations of up to 90˚ in the region (Kanter and McWilliams, 1982; McWilliams and Li, 1983; Wood and Saleeby, 1997; Nadin and Saleeby, 2008; Hopson *et al*., 2008). In short, a significant fraction of observed clockwise rotation in the southern SNB is thought to have taken place during Late Cretaceous extension (Malin *et al*, 1995; Saleeby, 2003; Chapman *et al*., 2010) and post-Cretaceous vertical axis rotation probably did not result in significant additional dispersion of upper crustal fragments in the southern SNB, with the exception of the San Emigdio Mountains, which accomodated ~ 7 km of north-south shortening since late Pliocene time

(Davis, 1983). The reader is referred to Chapman *et al*. (2010), reproduced here as Chapter 2 of this thesis, for a thorough review of rotations in the Sierran "tail."

7.2. Time-transgressive detachment faulting

The calculated average transport azimuth of 205 ± 28˚ is oblique to SSE trending and moderately plunging lineations along the Blackburn Canyon and Jawbone Canyon faults (Wood, 1997; Wood and Saleeby, 1997) and fault II of the Rand fault complex (Nourse, 1989) (Figure 4.13). Two potential explanations for this difference are that Cretaceous to recent deformation has led either to remobilization of the eastern SSD with a top to the SSE sense of shear, or systematic clockwise rotation of allochthonous fragments without concurrent rotation of lineations along the eastern SSD. Small increments of post-Cretaceous tectonism may account for some of the discrepancy between the lineation orientation and the actual transport direction along the SSD. Alternatively, the orientation of lineations along the SSD may not reflect the tectonic transport direction and instead may record a three dimensional deformation field with components of horizontal extension and vertical strike slip, as is common along transtensional shear zones (e.g., Fossen *et al*., 1994; Tikoff and Greene, 1997; Dewey *et al*., 1998). Furthermore, the wide dispersion of lineation orientations (Figure 4.13) may reflect local variations in strain partitioning between extensional and strike slip components, possibly related to interactions between the southern end of the dextral Owens Valley shear system and the SSD (Bartley *et al*., 2007).

Our preferred explanation for the discrepancy between the lineation orientation and inferred transport direction along the SSD, however, is that extension began in the southwestern SNB and propagated eastward with time. To better articulate this model, we

define the following allochthonous regions of similar inferred paleogeographic affinity and timing of transport: the Logan-western San Emigdio allochthon, the northern Salinia allochthon, the Gabilan-Pastoria allochthon, the Santa Lucia allochthon, and the Jawbone-Rand allochthon (Figure 4.13b). Hornblende and biotite $^{40}Ar/^{39}Ar$ and K-Ar cooling ages from the northern Salinia allochthon cluster around 90 Ma (Kistler and Champion, 2001), reflecting the timing of tectonic transport and upper plate attenuation from above the Cummings Valley area. The Logan-western San Emigdio allochthon was derived from a nearby area and has a similar dispersal pattern to the northern Salinia allochthon, suggesting a similar timing of transport. In contrast, K-Ar hornblende and biotite ages from the Gabilan-Pastoria, Santa Lucia, and Jawbone-Rand allochthons lie in the 85-75 Ma range (Evernden and Kistler, 1970; Huffman, 1972), in good agreement with He zircon results indicating ca. 77 Ma rapid cooling in the autochthonous southeastern SNB. We suggest that detachment and transport of these plates occurred at roughly 80 Ma with a more southerly transport direction than Logan-western San Emigdio and northern Salinia allochthons. A similar outboard to inboard time-transgressive model invoking oblique collision of an aseismic ridge with North America is envisioned by Barth and Schneiderman (1996) and Chapman *et al*. (2010) to explain an ~20 Myr time lag in schist cooling ages between the southwestern SNB, northwestern Mojave Desert, and Salinia. We speculate that south- and south-southeast-directed transport of upper crustal fragments in the Jawbone-Rand allochthon resulted as schist eduction created a void at the lateral ramp in the subduction megathrust, approximately centered along the trace of the superimposed Garlock fault, causing superjacent batholithic crust to breach southward across the inflection zone (Figure 4.14).

Figure 4.14. Tectonic model for Late Cretaceous free boundary gravitational collapse and transport of upper crustal fragments in the southern SNB. Strain coupling between the schist (shown in blue) and upper plates accompanies high magnitude extension and lateral spreading toward the unconfined continental margin. Displaced pendant with vertical piercing point (a-a') shown in brown. Abbreviations KWF, Late Cretaceous Kern Canyon–White Wolf fault system; LIP, large igneous province; MSL, mean sea level; OVSS, Owens Valley shear system; SBML, subbatholith mantle lithosphere; SOML, suboceanic mantle lithosphere.

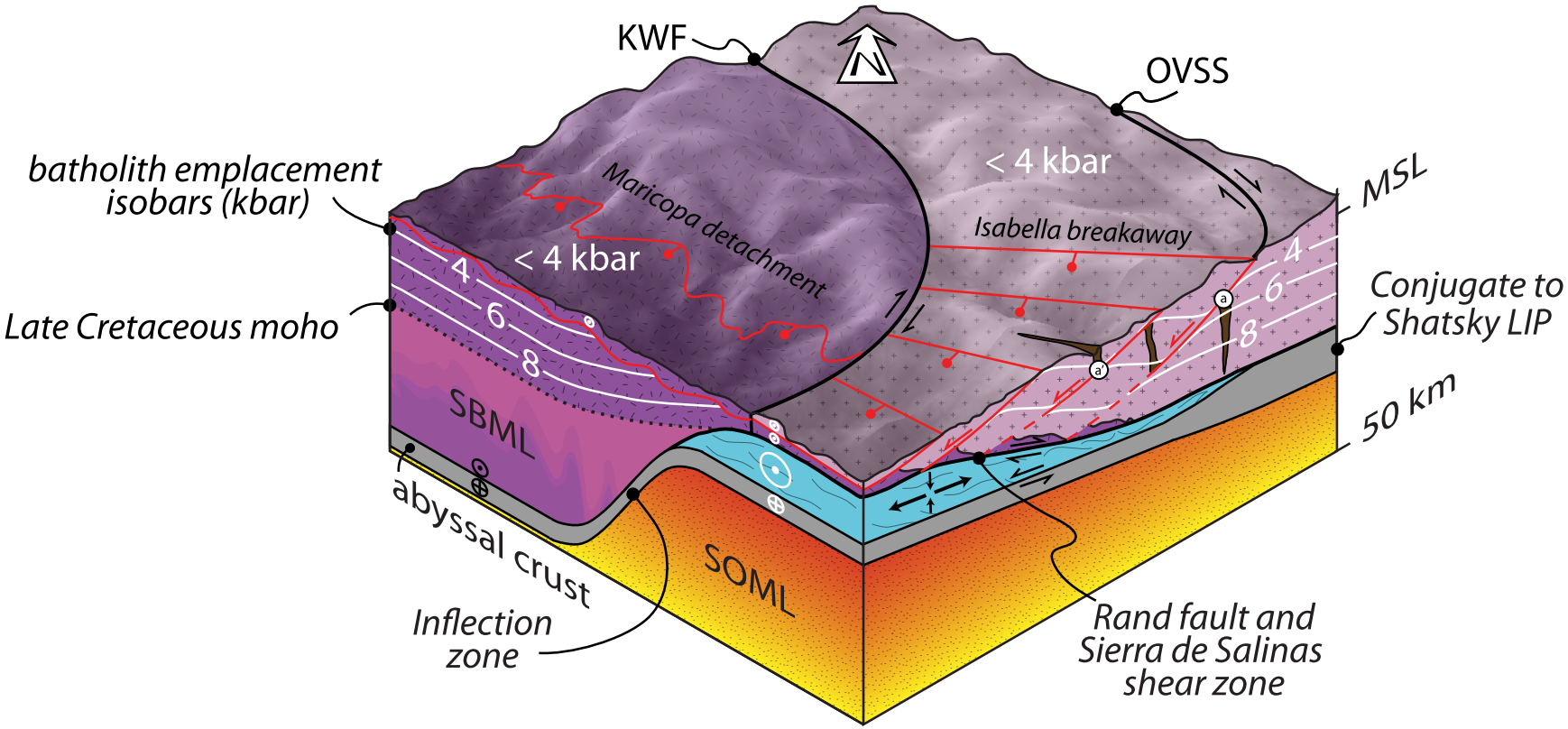
KWF
OVSS
batholith emplacement isobars (kbar)
Maricopa detachment
< 4 kbar
< 4 kbar
Isabella breakaway
MSL
Late Cretaceous moho
4
6
8
4
6
8
Conjugate to Shatsky LIP
SBML
50 km
abyssal crust
SOML
Inflection zone
Rand fault and Sierra de Salinas shear zone

7.3. Late Cretaceous gravitational collapse of the southern Sierra Nevada batholith

A thorough review of crosscutting relationships between dated plutons, detachment faults, and Late Cretaceous to Eocene nonconformities by Wood and Saleeby (1997) loosely constrains tectonic unroofing along the SSD and the transport of upper crustal fragments to between ca. 90 and 50 Ma, suggesting that extension may have taken place over as much as 40 Myr. However, thermochronometric work presented here and a recent review of available geochronologic, thermochronometric, and thermobarometric data (Chapman *et al*., 2010) indicate that the majority of extension, while diachronous across the southern Sierra Nevada, occurred entirely within the Late Cretaceous. As discussed above, age elevation relationships for autochthonous rocks south of the Isabella breakaway indicate that the area cooled through ~200°C rapidly at 77 ± 5 Ma (Figure 4.9), interpreted as the principal time of tectonic denudation related to large magnitude detachment faulting.

The transport of upper crustal fragments from above the southern SNB at 77 ± 5 Ma coincides with: 1) structural ascent of deep batholithic rocks in the Tehachapi, San Emigdio, Santa Lucia, and Rand Mountains from ca. 95 to 70 Ma (Malin *et al*., 1995; Fletcher *et al*., 2002; Kidder *et al*., 2003; Saleeby *et al*., 2007); 2) rapid eduction of the schist from beneath the autochthon from ca. 90 to 70 Ma (Barth *et al*., 2003; Grove *et al*., 2003; Kidder and Ducea, 2006; Chapman *et al*., 2010); 3) dextral strike-slip transfer motion along the KWF (Nadin and Saleeby, 2008); 4) dextral shear across Owens Valley (Bartley *et al*., 2007); and 5) marine transgression and deposition of supradetachment basin deposits across the highly attenuated crust of the southern SNB and adjacent areas (Grove, 1993; Wood and Saleeby, 1997; Saleeby, 2003). Furthermore, structural and kinematic relations from the Rand fault

and Salinas shear zone suggest that the schist moved from deep to shallow crustal levels with a lower plate to the SSW (210 ± 10˚) sense of shear (Chapman *et al*., 2010), overlapping with the 205 ± 28˚ transport direction of allochthonous upper crustal assemblages (Figure 4.13). These relations indicate that coeval SSW-directed transport of the entire crustal column, from upper plate shallow-level assemblages of the southern SNB, Mojave Desert, and Salinian block, through middle plate deep-crustal exposures of the southern SNB, and into the lower plate schist, occurred in Late Cretaceous time. Late Cretaceous trenchward flow of Rand and related schists (Malin *et al*., 1995; Saleeby, 2003; Chapman *et al*., 2010) and strain coupling between the educting schist and upper plate(s) provides an explanation for the overlapping transport directions along the SSD, Rand fault, and Salinas shear zone. We speculate that strain coupling between the schist and deep batholithic plate along the Rand fault and Salinas shear zone and, in turn, between the deep batholithic plate and upper crustal fragments along the SSD reflect gravitational collapse of the southern SNB and adjacent northwest Mojave and Salinia.

Mass transfer associated with lateral spreading and vertical thinning of the Sierran crust leads to a space problem. Rey *et al*. (2001) address this space problem by defining two end-member modes of gravitational collapse in which gravitational potential energy is ("fixed-boundary collapse") and is not ("free-boundary collapse") transferred from hinterland to foreland regions. South- to southwestward-directed extension of the entire crustal column of the southern SNB without synchronous shortening in the foreland best fit the criteria for free-boundary gravitational collapse. However, Late Cretaceous transcurrent faulting along the KWF and Owens Valley shear system has partitioned the highly extended and exhumed core of the southern SNB from less extended and exhumed adjacent regions. These

relations imply that SSW-directed extrusion toward the unconfined continental margin probably accompanied crustal attenuation in the southern SNB (Figure 4.14). Subduction of the conjugate massif to the Shatsky Rise beneath the southern SNB and adjacent areas (Liu *et al*., 2010) and associated transient horizontal compressional stresses, basal shear stresses, and lithospheric strength (i.e., the replacement of mantle wedge material with underplated schist) is posited to have preconditioned the southern SNB for lateral extrusion-modified free-boundary collapse.

7.4. Dynamics of gravitational collapse

An outstanding geodynamic problem not resolved here is whether structural ascent of the underplated schists and extensional collapse of the upper plate(s) were purely driven by excess potential energy in the orogenic plateau, or if extension was facilitated by focused slab rollback that operated in the wake of the subducted LIP. Saleeby (2003) argues that following the passage of the conjugate to the Shatsky rise, an increase in negative buoyancy forces arising from the resumption of subduction of normal abyssal lithosphere deformed the slab into a steeper subduction trajectory (i.e., slab rollback). This induced regionally extensive trench-directed channel flow in the underplated schists that coupled trench-directed extensional collapse into the upper plate. The return flow channel envisaged is similar to that proposed by Cloos (1982) for the Franciscan Complex, a fluid model for accretionary wedges by Emerman and Turcotte (1983), and to numerical simulations by Gerya *et al*. (2002). However, Saleeby (2003) envisions a non-steady state forced return flow event that developed specifically in response to the passing of the trailing edge of the

LIP down the subduction zone. This effect would be diminished and ultimately reversed as eclogitization in the subducting slab led to a difference in the relative buoyancy of the slab proximal to the subducted LIP (Liu *et al*., 2010). Our studies do not elucidate the role of slab rollback in the eduction of the underplated schist and the attenuation of the overlying crustal column. We offer the scenario depicted in Figure 14, which is similar to that offered in Malin *et al*., (1995), as a viable alternative to the focused slab rollback model of Saleeby (2003). The observations presented and compiled here can be adequately explained without invoking slab rollback, and we defer to future generation three-dimensional numerical modeling procedures that may adequately test the focused slab rollback hypothesis and the potential role lateral inflow of lower crust and asthenosphere from regions above adjacent steeply-dipping slab segments.

7.5. Southern Sierra landscape development

The published apatite He data (Mahéo *et al*., 2009) on the zircon He sample suite can be further utilized to constrain the approximate position of the principal detachment surface relative to the modern topographic surface and to relate the topography of the detachment surface to the early landscape development of the greater Sierra Nevada. Following the termination of large volume arc magmatism in the SNB at ca. 84 Ma (Nadin and Saleeby, 2008), the topographic surface of the arc underwent slow regional erosion at a rate of 0.05 ± 0.01 mm/yr throughout much of Cenozoic time (Clark *et al*., 2005; Cecil *et al*., 2006; Mahéo *et al*., 2009). Thus the constructional topographic surface of the greater Sierran arc, commonly interpreted to have constituted the western margin of a Cordilleran-wide

orogenic plateau locally termed the Nevadaplano (e.g., Saleeby *et al*., 2009b), began to slowly erode at virtually the same time as the tectonically denuded lower plate regime of the southern Sierra detachment system. In Figure 4.15, the apatite He age-elevation relations are used to adjust each data point of our zircon He suite to a position that would correspond to the freshly denuded detachment surface. The reconstructed detachment surface is subhorizontal and projects at about 2 ± 1 km above the modern landscape. We have also calculated "virtual-pressures" of igneous equilibration for the reconstructed surface above each location where Al-in-hbl determinations are available in order to compare to typical igneous pressures of the removed upper plates. Figure 4.15 shows that the detachment surface in the area of the sample traverse sat at ~ 4 ± 1 kb levels of the crust, which corresponds well to the typical 3 ± 1 kb crustal levels determined for the detachment sheets. These features are synthesized in Figure 4.16, a regional N-S cross section crossing the restored Rand Mountains, extending the schist under the southern SNB, and passing north of footwall assemblages of the SSD, with the SSD continuing northward as the reconstructed detachment surface up to the Isabella breakaway zone. The breakaway zone ramps up to the Kern plateau and continues to the Nevadaplano margin with the Late Cretaceous-early Tertiary paleo-drainage of the Kings River region shown at the northern end of the section (House *et al*., 2001; Saleeby *et al*., 2009b). This cross section represents a snapshot of southern Sierra paleo-landscape and large-scale crustal structure immediately following large magnitude detachment faulting.

Figure 4.15. Plot showing "virtual distance," the calculated distance above the modern landscape of the reconstructed detachment surface, versus northing. Secondary axis shows "virtual pressure" of igneous equilibration, calculated along the reconstructed detachment fault, for locations where Al-in-hbl determinations are available (samples 04SS27, 04SS28, 04SS39, and 04SS43 of Nadin and Saleeby, 2008). See text for discussion.

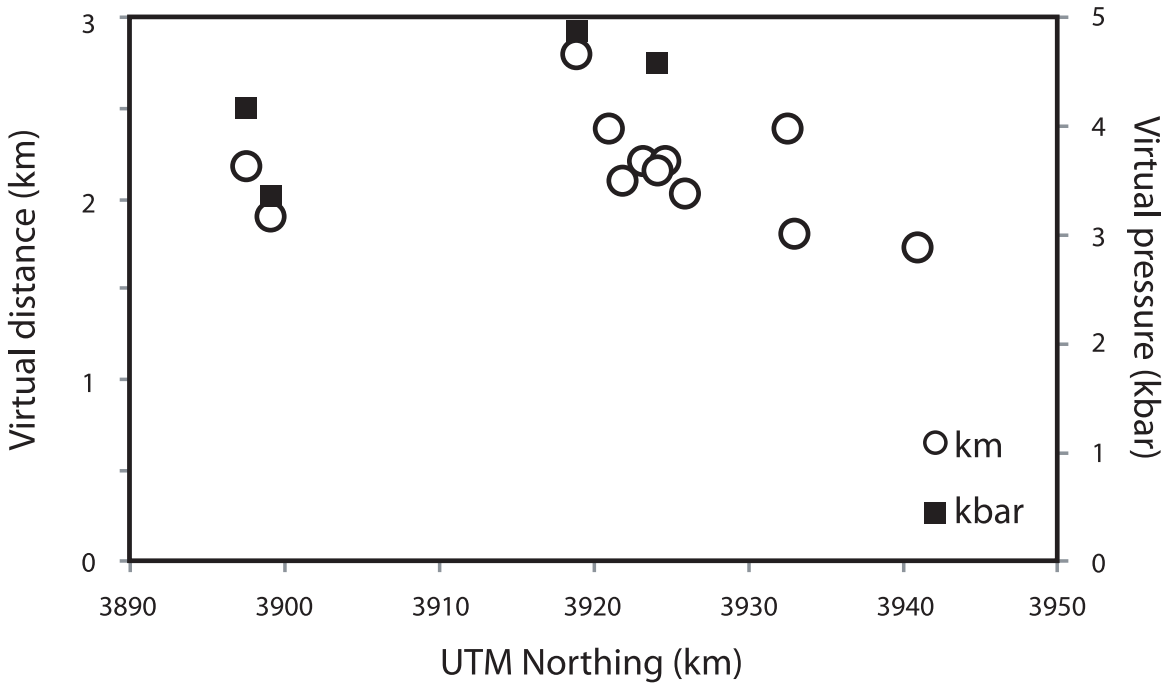
Virtual distance (km)
Virtual pressure (kbar)
UTM Northing (km)
km
kbar
0
1
2
3
4
5
3890
3900
3910
3920
3930
3940
3950

Figure 4.16. Regional geologic cross section from the Rand Mountains to the Nevadaplano margin. Cross section trace shown in Figure 4.1. Abbreviations, symbols, and map units as in Figure 4.1. Other abbreviations: LIP, Large igneous province; MSL, mean sea level; SSD, southern Sierra detachment.

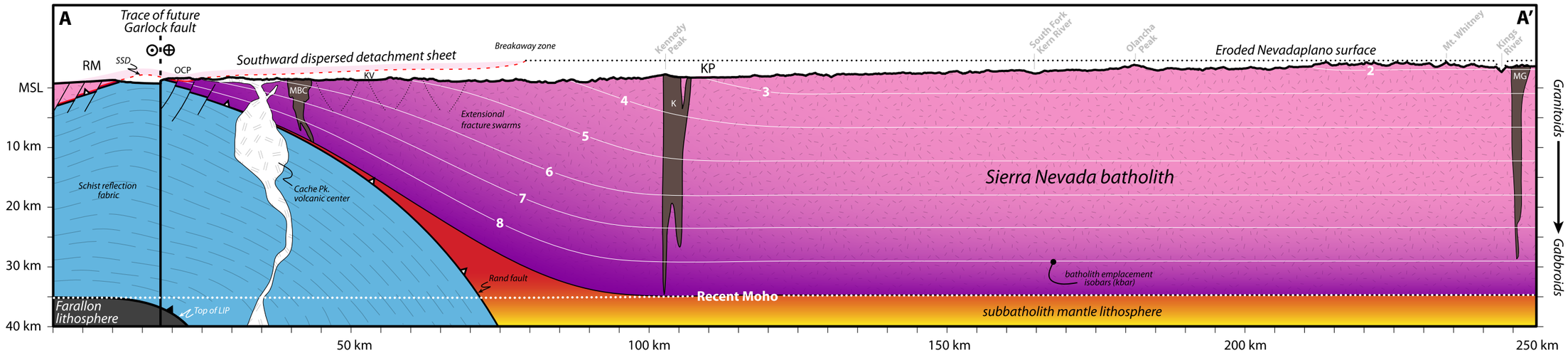
A
A'
Trace of future
Garlock fault
RM
SSD
OCP
Southward dispersed detachment sheet
Breakaway zone
Kennedy
Peak
KP
South Fork
Kern River
Olancha
Peak
Eroded Nevadaplano surface
Mt. Whitney
Kings
River
MG
MBC
KV
K
Extensional
fracture swarms
Schist reflection
fabric
Cache Pk.
volcanic center
Sierra Nevada batholith
Granitoids
Gabbroids
Rand fault
batholith emplacement
isobars (kbar)
Recent Moho
Farallon
lithosphere
Top of LIP
subbatholith mantle lithosphere
MSL
10 km
20 km
30 km
40 km
50 km
100 km
150 km
200 km
250 km
2
3
4
5
6
7
8

8. Conclusions

In summary, integration of new field and structural relations, U-Pb zircon geochronology, thermobarometry, major and trace element chemistry, Sr and Nd isotopic ratios, and zircon (U-Th)/He thermochronometry with existing databases reveal temporal and spatial relationships between the tectonic transport of allochthonous fragments of shallow-level eastern SNB affinity rocks, structural attenuation and ascent of deep-level western SNB assemblages, and trench-directed flow in the schist, suggesting that the entire crustal column of the southern SNB and vicinity collapsed in Late Cretaceous time due to excess gravitational potential energy. This work places several significant constraints on the timing and magnitude of extension attending gravitational collapse of the southern SNB. First, zircon (U-Th)/He data presented herein reveal a rapid cooling event at 77 ± 5 Ma, probably reflecting the time of large magnitude detachment faulting. A comparison of this dataset with existing apatite (U-Th)/He thermochronometry from the same sample suite (Mahéo *et al*., 2009) suggests that the development of modern landscape and arrangement of tectonic elements in southern California was greatly preconditioned by Late Cretaceous tectonics. Most notably is the strong southward sloping topographic gradient off the modern southern Sierra, which reflects profound elevation loss in that region due to large magnitude extension and detachment faulting. Second, palinspastic restoration of seven presumably correlative allochthon-autochthon pairs imply 50 to 70 km of lateral transport and the removal of approximately 5 to 10 km of crust along the southern Sierra detachment. Finally, the timing and the kinematics of dispersal of upper crustal fragments and ascent of deep-level batholithic and subduction accretion assemblages coincide, suggesting that the shallow and deep crust were highly coupled during gravitational

collapse. The observations presented here clarify several issues pertaining to Late Cretaceous orogenesis and subsequent collapse of the southern SNB and vicinity, and are consistent with the free-boundary gravitational collapse mode of Rey *et al*. (2001).

REFERENCES

Ague, J. J., 1997, Thermodynamic calculation of emplacement pressures for batholithic rocks, California: Implications for the aluminum-in-hornblende barometer: *Geology*, **25**(6), 563-566.

Ague, J. J., and Brimhall, G. H., 1988, Magmatic arc asymmetry and distribution of anomalous plutonic belts in the batholiths of California; effects of assimilation, crustal thickness, and depth of crystallization: *Geological Society of America Bulletin*, **100**(6), 912-927.

Anderson, J. L., and Smith, D. R., 1995, The effects of temperature and fO2 on the Al-in-hornblende barometer: *American Mineralogist*, **80**(5-6), 549-559.

Barbeau, D. L., Ducea, M. N., Gehrels, G. E., Kidder, S., Wetmore, P. H., and Saleeby, J. B., 2005, U-Pb detrital-zircon geochronology of northern Salinian basement and cover rocks: *Geological Society of America Bulletin*, **117**(3), 466-481.

Barth, A. P., and Schneiderman, J. S., 1996, A comparison of structures in the Andean Orogen of northern Chile and exhumed midcrustal structures in Southern California, USA; an analogy in tectonic style?: *International Geology Review*, **38**(12), 1075-1085.

Barth, A. P., Wooden, J. L., Coleman, D. S., and Vogel, M. B., 2009, Assembling and disassembling California; a zircon and monazite geochronologic framework for Proterozoic crustal evolution in Southern California: *Journal of Geology*, **117**(3), 221-

239.

Barth, A. P., Wooden, J. L., Grove, M., Jacobson, C. E., and Pedrick, J. N., 2003, U-Pb zircon geochronology of rocks in the Salinas Valley region of California; a reevaluation of the crustal structure and origin of the Salinian Block: *Geology*, **31**(6), 517-520.

Bartley, J.M., Glazner, A. F., Coleman, D. S., Kylander-Clark, A.R.C., and Friedrich, A.M., 2007, Large Laramide dextral offset across Owens Valley, California, and its possible relation to tectonic unroofing of the southern Sierra Nevada, in Till, A. B., Roeske, S. M., Foster, D. A. and Sample, J. C., eds., Exhumation Processes Along Major Continental Strike-slip Fault Systems: *Geological Society of America Special Paper*, **434**, 129-148.

Bush, R. N., 1981, Small Salinian ultramafic bodies near Jamesburg, California, M.S. thesis, Stanford University, 123 pp.

Carl, B.S., and Glazner, A.F., 2002, Extent and significance of the Independence dike swarm, eastern California, in Glazner, A.F., Walker, J.D., and Bartley, J.M., eds., Geologic evolution of the Mojave Desert and southwestern Basin and Range: *Memoir - Geological Society of America*, **195**, 117-130.

Carr, M. D., Christiansen, R. L., and Poole, F. G., 1984, Pre-Cenozoic geology of the El Paso Mountains, southwestern Great Basin, California - a summary, *in* Lintz, J. J., ed., *Western geological excursions*, **4**: Reno, Nevada, 84-93.

Cecil, M. R., Ducea, M. N., Reiners, P. W., and Chase, C. G., 2006, Cenozoic exhumation of the northern Sierra Nevada, California, from (U-Th)/He thermochronology: *Geological Society of America Bulletin*, **118**(11-12), 1481-1488.

Chapman, A. D., Kidder, S., Saleeby, J. B., and Ducea, M. N., 2010, Role of extrusion of

the Rand and Sierra de Salinas schists in Late Cretaceous extension and rotation of the southern Sierra Nevada and vicinity: *Tectonics*, **29(**5), TC5006, doi:10.1029/ 2009TC002597.

Chapman, A. D., Luffi, P., Saleeby, J., and Petersen, S., 2011, Metamorphic evolution, partial melting, and rapid exhumation above an ancient flat slab: Insights from the San Emigdio Schist, southern California: *Journal of Metamorphic Geology*, **29**, 601-626, doi: 10.1111/j.1525-1314.2011.00932.x.

Chapman, A. D. and Saleeby, J., in review, Geologic map of the San Emigdio Mountains: *Geological Society of America digital map and chart series*.

Cheadle, M. J., Czuchra, B. L., Byrne, T., Ando, C. J., Oliver, J. E., Brown, L. D., Kaufman, S., Malin, P. E., and Phinney, R. A., 1986, The deep crustal structure of the Mojave Desert, California, from COCORP seismic reflection data: *Tectonics*, **5**, 293-320.

Chen, J. H., and Moore, J. G., 1979, Late Jurassic Independence dike swarm in eastern California: *Geology*, **7**(3), 129-133.

Clark, M. K., Mahéo, G., Saleeby, J., and Farley, K. A., 2005, The non-equilibrium landscape of the southern Sierra Nevada, California: *GSA Today*, **15**(9), 4-10.

Cloos, M., 1982, Flow melanges; numerical modeling and geologic constraints on their origin in the Franciscan subduction complex, California: *Geological Society of America Bulletin*, **93**, 330-344.

Cox, B. F., 1987, Stratigraphy, depositional environments, and paleotectonics of the Paleocene and Eocene Goler Formation, El Paso Mountains, California; geologic summary and roadlog: *Field Trip Guidebook - Pacific Section, Society of Economic Paleontologists and Mineralogists*, **57**, 1-29.

Critelli, S., and Nilsen, T. H., 2000, Provenance and stratigraphy of the Eocene Tejon Formation, Western Tehachapi Mountains, San Emigdio Mountains, and southern San Joaquin Basin, California: *Sedimentary Geology*, **136**(1-2), 7-27.

Crowell, J. C., 1952, Geology of the Lebec Quadrangle, California: *Special Report - California Division of Mines and Geology*, **24**, 1-24.

Davis, T. L., 1983, Late Cenozoic structure and tectonic history of the western "Big Bend" of the San Andreas Fault and adjacent San Emigdio Mountains, Ph.D. thesis, University of California, Santa Barbara, 563 pp.

DeCrisoforo, D. T., and Cameron, K. L., 1977, Petrology of sillimanite-K-spar zone metapelites from Ben Lomond Mountain, central Coast Ranges, California: *Abstracts with Programs Geological Society of America*, **9**, 411.

Dewey, J. F., 1988, Extensional collapse of orogens: *Tectonics*, **7**, 1123-1139.

Dewey, J. F., Holdsworth, R. E., and Strachan, R. A., 1998, Transpression and transtension zones: *Geological Society, London, Special Publications*, **135**(1), 1-14.

Dibblee, T. W., Jr., and Chesterman, C. W., 1953, Geology of the Breckenridge Mountain Quadrangle, California: *Bulletin - California, Division of Mines and Geology*, **168**, 1-56.

Dibblee, T. W., Jr., and Nilsen, T. H., 1973, Geologic map of San Emigdio and western Tehachapi Mountains, *in* Vedder, J. G., ed., *Sedimentary facies changes in Tertiary rocks-California Transverse and southern Coast Ranges, Society of Economic Paleontologists and Mineralogists guidebook to field trip 2*: Anaheim, California.

Dickinson, W.R., Ducea, M., Rosenberg, L.I., Greene, H.G., Graham, S.A., Clark, J.C., Weber, G.E., Kidder, S., Ernst, G.W., and Brabb, E.E., 2005, Net dextral slip, Neogene San Gregorio-Hosgri fault zone, coastal California; geologic evidence and tectonic

implications: *Geological Society of America Special Paper*, **391**, 43 pp.

Dixon, E. T., 1995, $^{40}Ar/^{39}Ar$ Hornblende Geochronology and Evaluation of Garnet and Hornblende Barometry, Lake Isabella, the Tehachapi Area, Southern Sierra Nevada, California, M.S. thesis, University of Michigan, 63 pp.

Dokka, R. K., 1989, The Mojave extensional belt of Southern California: *Tectonics*, **8**(2), 363-390.

Dokka, R. K., and Ross, T. M., 1995, Collapse of southwestern North America and the evolution of early Miocene detachment faults, metamorphic core complexes, the Sierra Nevada orocline, and the San Andreas fault system: *Geology*, **23**(12), 1075-1078.

Ducea, M., 2001, The California Arc; thick granitic batholiths, eclogitic residues, lithospheric-scale thrusting, and magmatic flare-ups: *GSA Today*, **11**, 4-10.

Ducea, M. N., and Saleeby, J. B., 1998, The age and origin of a thick mafic-ultramafic keel from beneath the Sierra Nevada Batholith: *Contributions to Mineralogy and Petrology*, **133**(1-2), 169-185, doi: 110.1007/s004100050445.

Dunne, G. C., and Suczek, C. A., 1991, Early Paleozoic eugeoclinal strata in the Kern Plateau pendants, southern Sierra Nevada, California, *in* Cooper, J. D., and Stevens, C. H., eds., *Paleozoic paleogeography of the western United States: Pacific Section, Society of Economic Paleontologists and Mineralogists,* **2**, 677-692.

Ehlig, P. L., 1981, Origin and tectonic history of the basement terrane of the San Gabriel Mountains, central Transverse Ranges, *in* Ernst, W. G., ed., The geotectonic development of California, Rubey Volume I: New Jersey, Prentice-Hall, 253-283.

Emerman, S. H., and D. L. Turcotte, 1983, A fluid model for the shape of accretionary wedges: *Earth and Planetary Science Letters*, **63**, 379-384.

Ernst, W. G., Saleeby, J. B., and Snow, C. A., 2009, Guadalupe pluton - Mariposa Formation age relationships in the southern Sierran Foothills: Onset of Mesozoic subduction in northern California?: *Journal of Geophysical Research*, **114**(B11), B11204.

Evernden, J. F., and Kistler, R. W., 1970, Chronology of emplacement of Mesozoic batholithic complexes in California and western Nevada: *U. S. Geological Survey Professional Paper* 623, 42 pp.

Fletcher, J. M., Miller, J. S., Martin, M. W., Boettcher, S. S., Glazner, A. F., and Bartley, J. M., 2002, Cretaceous arc tectonism in the Mojave Block; profound crustal modification that controlled subsequent tectonic regimes: *Memoir - Geological Society of America*, **195**, 131-149.

Fossen, H., Tikoff, B., and Teyssier, C., 1994, Strain modeling of transpressional and transtensional deformation: *Norsk Geologisk Tidsskrift*, **74**, 134-145.

Gehrels, G. E., Dickinson, W. R., Riley, B. C. D., Finney, S. C., and Smith, M. T., 2000a, Detrital zircon geochronology of the Roberts Mountains Allochthon, Nevada: *Geological Society of America Special Paper*, **347**, 19-42.

Gehrels, G. E., Dickinson, W. R., Darby, B. J., Harding, J. P., Manuszak, J. D., Riley, B. C. D., Spurlin, M. S., Finney, S. C., Girty, G. H., Harwood, D. S., Miller, M. M., Satterfield, J. I., Smith, M. T., Snyder, W. S., Wallin, E. T., and Wyld, S. J., 2000b, Tectonic implications of detrital zircon data from Paleozoic and Triassic strata in western Nevada and Northern California: *Geological Society of America Special Paper*, **347**, 133-150.

Gerya, T. V., Stoeckhert, B., and Perchuk, A. L., 2002, Exhumation of high-pressure

metamorphic rocks in a subduction channel; a numerical simulation: *Tectonics*, **21**, doi:10.1029/2002TC001406.

Glazner, A. F., Walker, J. D., Bartley, J. M., and Fletcher, J. M., 2002, Cenozoic evolution of the Mojave block and environs, in Glazner, A.F., Walker, J.D., and Bartley, J.M., eds., Geologic evolution of the Mojave Desert and southwestern Basin and Range: *Memoir - Geological Society of America*, **195**, 19-41.

Graham, C. M., and England, P. C., 1976, Thermal regimes and regional metamorphism in the vicinity of overthrust faults; an example of shear heating and inverted metamorphic zonation from southern California: *Earth and Planetary Science Letters*, **31**(1), 142-152.

Grasse, S. W., Gehrels, G. E., Lahren, M. M., Schweickert, R. A., and Barth, A. P., 2001, U-Pb geochronology of detrital zircons from the Snow Lake Pendant, central Sierra Nevada; implications for Late Jurassic-Early Cretaceous dextral strike-slip faulting: *Geology*, **29**(4), 307-310.

Grove, K., 1993, Latest Cretaceous basin formation within the Salinian Terrane of west-central California: *Geological Society of America Bulletin*, **105**(4), 447-463.

Grove, M., Jacobson, C. E., Barth, A. P., and Vucic, A., 2003, Temporal and spatial trends of Late Cretaceous-early Tertiary underplating Pelona and related schist beneath Southern California and southwestern Arizona: *Geological Society of America Special Paper*, **374**, 381-406.

Hall, C. A., Jr., 1991, Geology of the Point Sur-Lopez Point region, Coast Ranges, California; a part of the Southern California Allochthon: *Geological Society of America Special Paper*, **266**, 40 pp.

Hammarstrom, J. M., and Zen, E. a., 1986, Aluminum in hornblende; an empirical igneous

geobarometer: *American Mineralogist*, **71**(11-12), 1297-1313.

Hammond, P. E., 1958, Geology of the lower Santiago Creek area, San Emigdio Mountains, Kern County, California. M.S. thesis, University of California, 108 pp.

Harding, J.P., Gehrels, G.E., Harwood, D.S., and Girty, G.H., 2000, Detrital zircon geochronology of the Shoo Fly complex, northern Sierra terrane, northeastern California, in Soreghan, M.J., and Gehrels, G.E., eds., Paleozoic and Triassic Paleogeography and tectonics of western Nevada and northern California: *Geological Society of America Special Paper*, **347**, 43-55.

Haxel, G., and Dillon, J., 1978, The Pelona-Orocopia Schist and Vincent-Chocolate Mountain thrust system, southern California, *in* Howell, D. G., and McDougall, K. A., eds., *Mesozoic paleogeography of the western United States: Pacific Section, Society of Economic Paleontologists and Mineralogists Pacific Coast Paleogeography Symposium*, **2**, 453-469.

Henry, D. J., and Dokka, R. K., 1992, Metamorphic evolution of exhumed middle to lower crustal rocks in the Mojave extensional belt, Southern California, USA: *Journal of Metamorphic Geology*, 10, 347-364.

Hofmann, A. W., 2003, Sampling Mantle Heterogeneity through Oceanic Basalts: Isotopes and Trace Elements, *in* Heinrich, D. H., and Karl, K. T., eds., *Treatise on Geochemistry*, **2**: Oxford, Pergamon, 61-101.

Holland, T., and Blundy, J., 1994, Non-ideal interactions in calcite amphiboles and their bearing on amphibole-plagioclase thermometry: *Contributions to Mineralogy and Petrology*, **116**(4), 433-447.

Holland, T. J. B., and Powell, R., 1998, An internally consistent thermodynamic data set for

phases of petrological interest: *Journal of Metamorphic Geology*, **16**(3), 309-343.

Hollister, L. S., Grissom, G. C., Peters, E. K., Stowell, H. H., and Sisson, V. B., 1987, Confirmation of the empirical correlation of Al in hornblende with pressure of solidification of calc-alkaline plutons: *American Mineralogist*, **72**(3-4), 231-239.

Hopson, R. F., Hillhouse, J. W., and Howard, K. A., 2008, Dike orientations in the Late Jurassic Independence dike swarm and implications for vertical axis tectonic rotations in eastern California: *Geological Society of America Special Paper*, **438**, 481-498.

House, M. A., Wernicke, B. P., and Farley, K. A., 2001, Paleo-geomorphology of the Sierra Nevada, California, from (U-Th)/He ages in apatite: *American Journal of Science*, **301**(2), 77-102.

Huffman, O.F., 1972, Lateral displacement of upper Miocene rocks and the Neogene history of offs*et al*ong the San Andreas fault in central California: *Geological Society of America Bulletin*, **83**, 2913–2946.

Jacobson, C. E., 1983, Structural geology of the Pelona Schist and Vincent Thrust, San Gabriel Mountains, California: *Geological Society of America Bulletin*, **94**(6), 753-767.

Jacobson, C. E., 1995, Qualitative thermobarometry of inverted metamorphism in the Pelona and Rand schists, Southern California, using calciferous amphibole in mafic schist: *Journal of Metamorphic Geology*, **13**(1), 79-92.

Jacobson, C. E., Dawson, M. R., and Postlethwaite, C. E., 1988, Structure, metamorphism, and tectonic significance of the Pelona, Orocopia, and Rand schists, Southern California, *in* Ernst, W. G., ed., *Metamorphism and crustal evolution of the Western United States, Rubey Volume*, **7**: New Jersey, Prentice-Hall, 976-997.

Jacobson, C. E., Grove, M., Pedrick, J. N., Barth, A. P., Marsaglia, K. M., Gehrels, G. E.,

and Nourse, J. A., 2011, Late Cretaceous - early Cenozoic tectonic evolution of the southern California margin inferred from provenance of trench and forearc sediments: *Geological Society of America Bulletin*, **123**(3-4), 485-506.

Jacobson, C. E., Grove, M., Vucic, A., Pedrick, J. N., and Ebert, K. A., 2007, Exhumation of the Orocopia Schist and associated rocks of southeastern California; relative roles of erosion, synsubduction tectonic denudation, and middle Cenozoic extension: *Geological Society of America Special Paper*, **419**, 1-37.

Jacobson, C. E., Oyarzabal, F. R., and Haxel, G. B., 1996, Subduction and exhumation of the Pelona-Orocopia-Rand schists, Southern California: *Geology*, **24**(6), 547-550.

James, E. W., 1986a, Geochronology, isotopic characteristics, and paleogeography of parts of the Salinian Block of California. Ph.D. thesis, University of California, 176 pp.

James, E. W., 1986b, U/Pb age of the Antimony Peak tonalite and its relation to Rand Schist in the San Emigdio Mountains, California: *Geological Society of America Abstracts with Programs*, **18**(2), 121.

James, E. W., 1992, Cretaceous metamorphism and plutonism in the Santa Cruz Mountains, Salinian Block, California, and correlation with the southernmost Sierra Nevada: *Geological Society of America Bulletin*, **104**, 1326-1339.

James, E. W., Kimbrough, D. L., and Mattinson, J. M., 1993, Evaluation of displacements of pre-Tertiary rocks on the northern San Andreas Fault using U-Pb zircon dating, initial Sr, and common Pb isotopic ratios: *Memoir - Geological Society of America*, **178**, 257-271.

James, E. W., and Mattinson, J. M., 1985, Evidence for 160 km post-Mid Cretaceous slip on the San Gregorio Fault, coastal California: *Eos, Transactions, American Geophysical*

Union, **66**(46), 1093.

John, D., 1981, Structure and petrology of pelitic schist in the Fremont Peak Pendant, northern Gabilan Range, California: *Geological Society of America Bulletin*, **92**(5), 237-246.

Johnson, M. C., and Rutherford, M. J., 1989, Experimental calibration of the aluminum-in-hornblende geobarometer with application to Long Valley Caldera (California) volcanic rocks: *Geology*, **17**(9), 837-841.

Kanter, L. R. and McWilliams, M. O., 1982, Rotation of the southernmost Sierra Nevada, California: *Journal of Geophysical Research*, **87**(B5), 3819-3830.

Kidder, S., and Ducea, M. N., 2006, High temperatures and inverted metamorphism in the schist of Sierra de Salinas, California: *Earth and Planetary Science Letters*, **241**(3-4), 422-437.

Kidder, S., Ducea, M., Gehrels, G. E., Patchett, P. J., and Vervoort, J., 2003, Tectonic and magmatic development of the Salinian Coast Ridge Belt, California: *Tectonics*, **22**, doi:10.1029/2002TC001409.

Kistler, R.W., 1990, Two different types of lithosphere in the Sierra Nevada, California, in Anderson, J.L., ed., The Nature and Origin of Cordilleran Magmatism: *Geological Society of America Memoir*, **174**, 271-282.

Kistler, R. W., and Champion, D. E., 2001, Rb-Sr whole-rock and mineral ages, K-Ar, 40Ar/39Ar, and U-Pb mineral ages, and strontium, lead, neodymium, and oxygen isotopic compositions for granitic rocks from the Salinian Composite Terrane, California: *U.S. Geological Survey Open-File Report* 01-453, 84 pp.

Kistler, R. W., and Ross, D. C., 1990, A strontium isotopic study of plutons and associated

rocks of the southern Sierra Nevada and vicinity, California: *U. S. Geological Survey Bulletin* 1920, 20 pp.

Kohn, M. J., and Spear, F., 2000, Retrograde net transfer reaction insurance for pressure-temperature estimates: *Geology*, **28**(12), 1127-1130.

Lackey, J. S., Valley, J. W., Chen, J. H., and Stockli, D. F., 2008, Dynamic Magma Systems, Crustal Recycling, and Alteration in the Central Sierra Nevada Batholith: the Oxygen Isotope Record: *Journal of Petrology*, **49**(7), 1397-1426.

Leo, G. W., 1967, The plutonic and metamorphic rocks of the Ben Lomond Mountain area, Santa Cruz County, California: *Special Report California Division of Mines and Geology* 91, 27-43.

Li, Y. G., Henyey, T. L., and Silver, L. T., 1992, Aspects of the crustal structure of the western Mojave Desert, California, from seismic reflection and gravity data: *Journal of Geophysical Research*, **97**, 8805-8816, doi:10.1029/ 91JB02119.

Liu, L., and Gurnis, M., 2010, Dynamic subsidence and uplift of the Colorado Plateau: *Geology*, **38**(7), 663-666.

Liu, L., Spasojevic, S., and Gurnis, M., 2008, Reconstructing Farallon Plate subduction beneath North America back to the Late Cretaceous: *Science*, **322**(5903), 934-938, doi: 910.1126/science.1162921.

Liu, L., Gurnis, M., Seton, M., Saleeby, J., Muller, R.D., and Jackson, J., 2010, The role of oceanic plateau subduction in the Laramide Orogeny: *Nature Geoscience*, **3**, 353-357, doi: 10.1038/NGEO829.

Lucas, S.G., and Reynolds, R.E., 1991, Late Cretaceous (?) Plesiosaurs from Cajon Pass,

California: *San Bernardino County Museum Association Quarterly*, **38**, 53–54.

Ludwig, K. R., 2003, Mathematical-statistical treatment of data and errors for (super 230) Th/U geochronology: *Reviews in Mineralogy and Geochemistry*, **52**, 631-656.

Luffi, P., Saleeby, J. B., Lee, C. A., and Ducea, M. N., 2009, Lithospheric mantle duplex beneath the central Mojave Desert revealed by xenoliths from Dish Hill, California: *Journal of Geophysical Research*, **114**(B03202), doi:10.1029/2008JB005906.

Mahéo, G., Saleeby, J., Saleeby, Z., and Farley, K. A., 2009, Tectonic control on southern Sierra Nevada topography, California: *Tectonics*, **28**(6), TC6006.

Malin, P. E., Goodman, E. D., Henyey, T. L., Li, Y. G., Okaya, D. A., and Saleeby, J. B., 1995, Significance of seismic reflections beneath a tilted exposure of deep continental crust, Tehachapi Mountains, California: *Journal of Geophysical Research*, **100**(B2), 2069-2087, doi: 2010.1029/2094JB02127.

Manuszak, J. D., Satterfield, J. I., and Gehrels, G. E., 2000, Detrital zircon geochronology of Upper Triassic strata in western Nevada: *Geological Society of America Special Paper*, **347**, 109-118.

Martin, M. W., and Walker, J., 1995, Stratigraphy and paleogeographic significance of metamorphic rocks in the Shadow Mountains, western Mojave Desert, California: *Geological Society of America Bulletin*, **107**(3), 354-366.

Matthews, V., III, 1976, Correlation of Pinnacles and Neenach volcanic fields and their bearing on San Andreas fault problem: *The American Association of Petroleum Geologists Bulletin*, **60**, 2128–2141.

Mattinson, J. M., 1978, Age, origin, and thermal histories of some plutonic rocks from the Salinian Block of California: *Contributions to Mineralogy and Petrology*, **67**(3), 233-

245.

May, D. J., 1989, Late Cretaceous intra-arc thrusting in Southern California: *Tectonics*, **8**(6), 1159-1173.

May, J.C., and Hewitt, R.L., 1948, The basement complex in well samples from Sacramento and San Joaquin Valleys, California: *California Division of Mines and Geology Journal*, **44**, 129-158.

McWilliams, M. O., and Li, Y., 1983, A paleomagnetic test of the Sierran Orocline hypothesis: *Eos, Transactions, American Geophysical Union*, **64**(45), 686.

Memeti, V., Gehrels, G. E., Paterson, S. R., Thompson, J. M., Mueller, R. M., and Pignotta, G. S., 2010, Evaluating the Mojave-Snow Lake Fault hypothesis and origins of central Sierran metasedimentary pendant strata using detrital zircon provenance analyses: *Lithosphere*, **2**(5), 341-360.

Miller, E. L., and Sutter, J. F., 1982, Structural geology and 40Ar-39Ar geochronology of the Goldstone-Lane Mountain area, Mojave Desert, California: *Geological Society of America Bulletin*, **93**(12), 1191-1207.

Miller, J.S., Glazner, A.F., Walker, J.D., and Martin, M.W., 1995, Geochronologic and isotopic evidence for Triassic-Jurassic emplacement of the eugeoclinal allochthon in the Mojave Desert region, California: *Geological Society of America Bulletin*, **107**, 1441–1457, doi: 10.1130/0016–7606(1995)1072.3.CO;2.

Monastero, F. C., Walker, J. D., Katzenstein, A. M., and Sabin, A. E., 2002, Neogene evolution of the Indian Wells Valley, east-central California: *Geological Society of America Memoirs*, 195, 199-228.

Nadin, E. S., and Saleeby, J. B., 2008, Disruption of regional primary structure of the Sierra

Nevada Batholith by the Kern Canyon fault system, California: *Geological Society of America Special Paper*, **438**, 429-454.

Nadin, E. S., and Saleeby, J. B., 2010, Quaternary reactivation of the Kern Canyon fault system, southern Sierra Nevada, California: *Geological Society of America Bulletin*, **122**(9-10), 1671-1685.

Nourse, J. A., 1989, Geological evolution of two crustal scale shear zones; Part I, The Rand thrust complex, northwestern Mojave Desert, California; Part II, The Magdalena metamorphic core complex, north central Sonora, Mexico. Ph.D. thesis, California Institute of Technology, 394 pp.

Nutt, C. J., 1977, The Escondido mafic-ultramafic complex; a concentrically zoned body in the Santa Lucia Range, California. M.S. thesis, Stanford University, 90 pp.

Pearce, J.A., Alabaster, T., Scheton, A. W. and Searle, M. P., 1981, The Oman ophiolite as a Cretaceous arc-basin complex: evidence and implications: *Philosophical Transactions Royal Society of London*, **A300**, 299-317.

Pickett, D. A., and Saleeby, J. B., 1993, Thermobarometric constraints on the depth of exposure and conditions of plutonism and metamorphism at deep levels of the Sierra Nevada Batholith, Tehachapi Mountains, California: *Journal of Geophysical Research*, **98**(B1), 609-629.

Pickett, D. A., and Saleeby, J. B., 1994, Nd, Sr, and Pb isotopic characteristics of Cretaceous intrusive rocks from deep levels of the Sierra Nevada Batholith, Tehachapi Mountains, California: *Contributions to Mineralogy and Petrology*, **118**(2), 198-215, doi: 110.1007/BF01052869.

Postlethwaite, C. E., and Jacobson, C. E., 1987, Early history and reactivation of the Rand

Thrust, Southern California: *Journal of Structural Geology*, **9**(2), 195-205, doi: 110.1016/0191-8141(1087)90025-90023.

Powell, R., and Holland, T., 1994, Optimal geothermometry and geobarometry: *American Mineralogist*, **79**(1-2), 120-133.

Reid, S.A., 1988, Late Cretaceous and Paleogene sedimentation along the east side of the San Joaquin Basin: in Graham, S.A., ed., *Studies of the Geology of the San Joaquin Basin. Pacific Section, Society of Economic Paleontologists and Mineralogists*. **60**, 157–171.

Reiners, P. W., 2005, Zircon (U-Th)/He thermochronometry: *Reviews in Mineralogy and Geochemistry*, **58**(1), 151-179.

Reitz, A., 1986, The geology and petrology of the northern San Emigdio plutonic complex, San Emigdio Mountains, Southern California. M.A. thesis, University of California, 80 pp.

Rey, P., Vanderhaeghe, O., and Teyssier, C., 2001, Gravitational collapse of the continental crust; definition, regimes and modes: *Tectonophysics*, **342**, 435-449.

Rindosh, M. C., 1977, Geology of the Tylerhorse Canyon pendant southern Tehachapi Mountains Kern County, California. M.S. thesis, University of Southern California, 80 pp.

Ross, D. C., 1970, Quartz gabbro and anorthositic gabbro; markers of offs*et al*ong the San Andreas fault in the California Coast Ranges: *Geological Society of America Bulletin*, **81**(12), 3647-3661.

Ross, D. C., 1976, Reconnaissance geologic map of pre-Cenozoic basement rocks, northern Santa Lucia Range, Monterey County, California: *U.S. Geological Survey*

Miscellaneous Field Studies Map MF-750, 7 pp.

Ross, D. C., 1977, Pre-intrusive metasedimentary rocks of the Salinian block, California; a paleotectonic dilemma, *in* Stewart, J. H., Stevens, C. H., and Fritsche, A. E., eds., *Paleozoic paleogeography of the western United States: Pacific Section, Society of Economic Paleontologists and Mineralogists Pacific Coast Paleogeography Symposium* **1**, 371-380.

Ross, D. C., 1988, Chemical traits and trends of the granitic rocks of the southern Sierra Nevada, California: *U.S. Geological Survey Open-File Report* 88-374, 119 pp.

Ross, D. C., 1989, The metamorphic and plutonic rocks of the southernmost Sierra Nevada, California, and their tectonic framework: *U.S. Geological Survey Professional Paper* 1381, 159 pp.

Ross, D. C., Wentworth, C. M., and McKee, E. H., 1973, Cretaceous mafic conglomerate near Gualala offset 350 miles by San Andreas Fault from oceanic crustal source near Eagle Rest Peak, California: *Journal of Research of the U. S. Geological Survey*, **1**(1), 45-52.

Ruppert, S., Fliedner, M. M., and Zandt, G., 1998, Thin crust and active upper mantle beneath the southern Sierra Nevada in the Western United States: *Tectonophysics*, **286**(1-4), 237-252, doi: 210.1016/S0040-1951(1097)00268-00260.

Saleeby, J., 1978, Kings River Ophiolite, Southwest Sierra Nevada foothills, California: *Geological Society of America Bulletin*, **89**(4), 617-636.

Saleeby, J., 2003, Segmentation of the Laramide slab; evidence from the southern Sierra Nevada region: *Geological Society of America Bulletin*, **115**(6), 655-668.

Saleeby, J., 2011, Geochemical mapping of the Kings-Kaweah ophiolite belt, California -

evidence for progressive melange formation in a large offset transform-subduction initiation environment: *Geological Society of America Special Paper* (in press).

Saleeby, J., and Dunne, G. C., in review, Temporal and Structural Relations of Early Mesozoic Arc Plutonism, southern Sierra Nevada, California: *Geological Society of America Bulletin*.

Saleeby, J., Farley, K. A., Kistler, R. W., and Fleck, R. J., 2007, Thermal evolution and exhumation of deep-level batholithic exposures, southernmost Sierra Nevada, California: *Geological Society of America Special Paper*, **419**, 39-66.

Saleeby, J., and Sharp, W., 1980, Chronology of the structural and petrologic development of the Southwest Sierra Nevada foothills, California: *Geological Society of America Bulletin*, **91**(6), 317-320.

Saleeby, J. B., and Busby, C., 1993, Paleogeographic and tectonic setting of axial and western metamorphic framework rocks of the southern Sierra Nevada, California: *Field Trip Guidebook - Pacific Section, Society of Economic Paleontologists and Mineralogists*, **71**, 197-225.

Saleeby, J. B., Sams, D. B., and Kistler, R. W., 1987, U/Pb zircon, strontium, and oxygen isotopic and geochronological study of the southernmost Sierra Nevada Batholith, California: *Journal of Geophysical Research*, **92**(B10), 10,443-10,466.

Saleeby, J. B., Geary, E. E., Paterson, S. R., and Tobisch, O. T., 1989, Isotopic systematics of Pb/U (zircon) and $^{40}Ar/^{39}Ar$ (biotite-hornblende) from rocks of the central Foothills terrane, Sierra Nevada, California: *Geological Society of America Bulletin*, **101**(11), 1481-1492.

Saleeby, J. B., Ducea, M. N., and Clemens-Knott, D., 2003, Production and loss of high-

density batholithic root, southern Sierra Nevada, California: *Tectonics*, **22**, doi: 10.1029/2002TC001374.

Saleeby, J. B., Ducea, M. N., Busby, C. J., Nadin, E. S., and Wetmore, P. H., 2008, Chronology of pluton emplacement and regional deformation in the southern Sierra Nevada Batholith, California: *Geological Society of America Special Paper*, **438**, 397-427.

Saleeby, J. B., Saleeby, Z., Chapman, A. D., and Nadin, E. S., 2009a, Origin and evolution of the White Wolf Fault and the Maricopa Basin (MB), southernmost Great Valley (GV), California: *Geological Society of America Abstracts with Programs*, **41**(7), 180.

Saleeby, J. B., Saleeby, Z., Nadin, E., and Mahéo, G., 2009b, Step-over in the structure controlling the regional west tilt of the Sierra Nevada Microplate; eastern escarpment system to Kern Canyon system: *International Geology Review*, **51**(7-8), 634-669.

Schmidt, M. W., 1992, Amphibole composition in tonalite as a function of pressure; an experimental calibration of the Al-in-hornblende barometer: *Contributions to Mineralogy and Petrology*, **110**(2-3), 304-310.

Schott, R. C., and Johnson, C. M., 1998, Sedimentary record of the Late Cretaceous thrusting and collapse of the Salinia-Mojave magmatic arc: *Geology*, **26**(4), 327-330.

Schott, R. C., and Johnson, C. M., 2001, Garnet-bearing trondhjemite and other conglomerate clasts from the Gualala Basin, California; sedimentary record of the missing western portion of the Salinian magmatic arc?: *Geological Society of America Bulletin*, **113**(7), 870-880.

Seiders, V. M., and Cox, B. F., 1992, Place of origin of the Salinian Block, California, as based on clast compositions of Upper Cretaceous and lower Tertiary conglomerates:

U.S. Geological Survey Professional Paper 1526, 80 pp.

Simpson, C., 1990, Microstructural evidence for northeastward movement on the Chocolate Mountains fault zone, southeastern California: *Journal of Geophysical Research*, **95**(B1), 529-537.

Smith, M., and Gehrels, G., 1994, Detrital zircon geochronology and the provenance of the Harmony and Valmy Formations, Roberts Mountains allochthon, Nevada: *Geological Society of America Bulletin*, **106**(7), 968-979.

Snoke, A. W., Sharp, W. D., Wright, J. E., and Saleeby, J. B., 1982, Significance of mid-Mesozoic peridotitic to dioritic intrusive complexes, Klamath Mountains-western Sierra Nevada, California: *Geology*, **10**(3), 162-166.

Spear, F. S., 1993, Metamorphic phase equilibria and pressure-temperature-time paths, Washington, D.C., Mineralogical Society of America, 799 p.

Stevens, C. H., and Greene, D. C., 1999, Stratigraphy, depositional history, and tectonic evolution of Paleozoic continental-margin rocks in roof pendants of the eastern Sierra Nevada, California: *Geological Society of America Bulletin*, **111**(6), 919-933.

Stevens, C. H., and Stone, P., 2005, Interpretation of the Last Chance Thrust, Death Valley region, California, as an Early Permian decollement in a previously undeformed shale basin: *Earth-Science Reviews*, **73**(1-4), 79-101.

Sun, S., McDonough, W.F., 1989, Chemical and isotopic systematics of oceanic basalts: implications for mantle composition and processes: in Saunders., A.D. and Norry, M.J., eds. Magmatism in the Ocean Basins: *Geological Society of London Special Publication* **42**, 313-345.

Tikoff, B., and Greene, D., 1997, Stretching lineations in transpressional shear zones: an

example from the Sierra Nevada Batholith, California: *Journal of Structural Geology*, **19**(1), 29-39.

Trask, P. D., 1926, Geology of Point Sur Quadrangle, California: *University of California Publications in Geological Sciences*, **16**(6), 119-186.

Walker, J. D., 1988, Permian and Triassic rocks of the Mojave Desert and their implications for timing and mechanisms of continental truncation: *Tectonics*, **7**(3), 685-709.

Wiebe, R. A., 1966, Structure and petrology of Ventana Cones area, California. Ph.D. thesis, Stanford University, 95 pp.

Wiebe, R. A., 1970, Pre-Cenozoic tectonic history of the Salinian Block, western California: *Geological Society of America Bulletin*, **81**, 1837-1842.

Williams, H., and Curtis, G.H., 1976, The Sutter Buttes, a study of Plio-Pleistocene volcanism: University of California Publications In Geological Sciences: *University of California Press*, **116**, 1-56.

Wolf, M. B., and Saleeby, J. B., 1995, Late Jurassic dike swarms in the southwestern Sierra Nevada Foothills Terrane, California; implications for the Nevadan Orogeny and North American Plate motion: *Geological Society of America Special Paper*, **299**, 203-228.

Wood, D. J., 1997, Geology of the eastern Tehachapi Mountains and Late Cretaceous-early Cenozoic tectonics of the southern Sierra Nevada region, Kern County, California. Ph.D. thesis, California Institute of Technology, 287 pp.

Wood, D. J., and Saleeby, J. B., 1997, Late Cretaceous-Paleocene extensional collapse and disaggregation of the southernmost Sierra Nevada Batholith: *International Geology Review*, **39**(11), 973-1009.

Yan, Z., Clayton, R. W., and Saleeby, J., 2005, Seismic refraction evidence for steep faults

cutting highly attenuated continental basement in the central Transverse Ranges, California: *Geophysical Journal International*, **160**, 651-666.

CHAPTER 5

Slab flattening trigger for isotopic disturbance and magmatic flare-up in the southernmost Sierra Nevada batholith, California

Alan D. Chapman, Jason B. Saleeby, and John Eiler

Division of Geological and Planetary Sciences, California Institute of Technology, Pasadena, California, USA

To be submitted to *Geology*

ABSTRACT

The San Emigdio Schist of the southwestern Sierra Nevada batholith (SNB) permits examination of partial melting and devolatilization processes along a Late Cretaceous shallow subduction zone. Detrital and metamorphic zircon of the structurally highest and earliest subducted portions of the San Emigdio Schist constrain the depositional age to between ca. 102 and 98 Ma, respectively. Zircon oxygen isotope data from both lower plate schist and upper plate batholithic assemblages reveal a $\delta^{18}O$ shift of ~ 1.5‰ between igneous (~ 5.5‰) and metamorphic (~ 7‰) domains. These results, taken with previous zircon and whole-rock $\delta^{18}O$ measurements, provide evidence for massive devolatilization of the San Emigdio Schist and fluid traversal of upper plate batholithic assemblages, thereby altering the isotopic composition of overlying material. Furthermore, the timing of fluid-rock interaction in the southwestern SNB is coincident with eastward arc migration and an associated pulse of voluminous magmatism. We posit that during flattening of the Farallon slab the schist was rapidly delivered to the magmatic source, where ensuing devolatilization

triggered a magmatic flare-up in the southeastern SNB. This short-lived (< 15 Myr) high-flux event was followed by the termination of arc magmatism as the shallow subduction zone approached thermal equilibrium.

1. INTRODUCTION

Continental arc magmatism is widely regarded to reflect melting of the mantle wedge by addition of fluids produced through progressive metamorphism of trench sediments and oceanic crust in moderately to steeply dipping subduction zones (e.g., Tatsumi *et al*., 1986; Davies and Bickle, 1991; Bebout, 1991). In contrast, shallow to flat subduction is a commonly invoked mechanism for the termination and/or migration of arc magmatism due to tectonic erosion of the mantle wedge and subduction refrigeration (e.g., Coney and Reynolds, 1977; Dumitru *et al*., 1991; Saleeby, 2003). However, the onset of shallow subduction is marked by high geothermal gradients at the slab interface that relax with continued subduction as the upper plate cools (Cloos, 1985, Peacock, 1992; Gutscher *et al*., 2000; Gerya *et al*., 2002; Chapman *et al*., 2011). Therefore, during slab flattening it is conceivable that rapid delivery of subduction accretion assemblages to the magmatic source region of an active arc may trigger a brief episode of high-flux magmatism prior to thermal equilibration of upper and lower plates.

This scenario for slab flattening-induced magmatic flare-up events predicts: 1) contamination of upper plate isotopic signatures by fluids derived from subducted immature clastic sedimentary material with limited modification by tectonically eroded/removed mantle wedge material, and 2) the timing of fluid-rock interaction should broadly coincide with upper plate magmatism and/or isotopic contamination. In this study, we compile new

and published *in situ* zircon U-Pb and oxygen isotope data to better understand fluid-rock interaction attending Late Cretaceous shallow subduction of the Farallon plate beneath North America. Data presented herein lead us to suggest that devolatilization of underplated subduction accretion assemblages triggered a magmatic flare-up in the southernmost Sierra Nevada batholith (SNB).

2. SOUTHWESTERN SIERRA NEVADA BATHOLITH

Late Cretaceous – early Tertiary shallow subduction beneath the southern SNB and adjacent areas resulted in major lithospheric reorganization, associated with tectonic removal of subcontinental mantle and replacement with accretionary wedge and/or forearc basin material (e.g., Saleeby, 2003; Jacobson *et al*., 2007, 2011; Luffi *et al*., 2009; Chapman *et al*., 2010). These subduction accretion assemblages, referred to as the "southern California schist" by Chapman *et al*. (2011), crop out beneath older crystalline rocks of the southwest Cordilleran batholithic belt, typically along detachment structures (Figure 5.1). Exposures of the southern California schist in the San Emigdio and Tehachapi Mountains (the "San Emigdio Schist") are juxtaposed beneath deeply exhumed Cretaceous batholithic rocks along the Rand fault, a Late Cretaceous locally ductile to brittle low-angle detachment fault system. Upper plate-lower plate contact relations are locally obscured by Pliocene–Quaternary contractile structures.

The presence of an inverted metamorphic field gradient in the San Emigdio Schist, i.e. an upsection increase in metamorphic grade, is a characteristic feature of this and the majority of other southern California schist exposures (Ehlig, 1981; Graham and Powell, 1984; Jacobson, 1995; Kidder and Ducea, 2006; Chapman *et al*., 2011). Inverted

Figure 5.1. Geologic map of southern California basement rocks after Chapman *et al*. (2011). Shaded areas show extent of isotopically anomalous granitoids. EF, Pelona Schist (East Fork); GF, Garlock fault; GR, Gabilan Range; JM, Josephine Mountain intrusion; KCF, Kern Canyon fault; LP, La Posta suite; MD, Mojave Desert; PRB, Peninsular Ranges batholith; pKCF, proto-Kern Canyon fault; SAF, San Andreas fault; SE, San Emigdio Mountains; SC, Santa Catalina Island; SL, Santa Lucia Mountains; SNB, Sierra Nevada batholith; SP, Pelona Schist (Sierra Pelona); TC, Tehachapi Mountains; WWF, White Wolf fault.

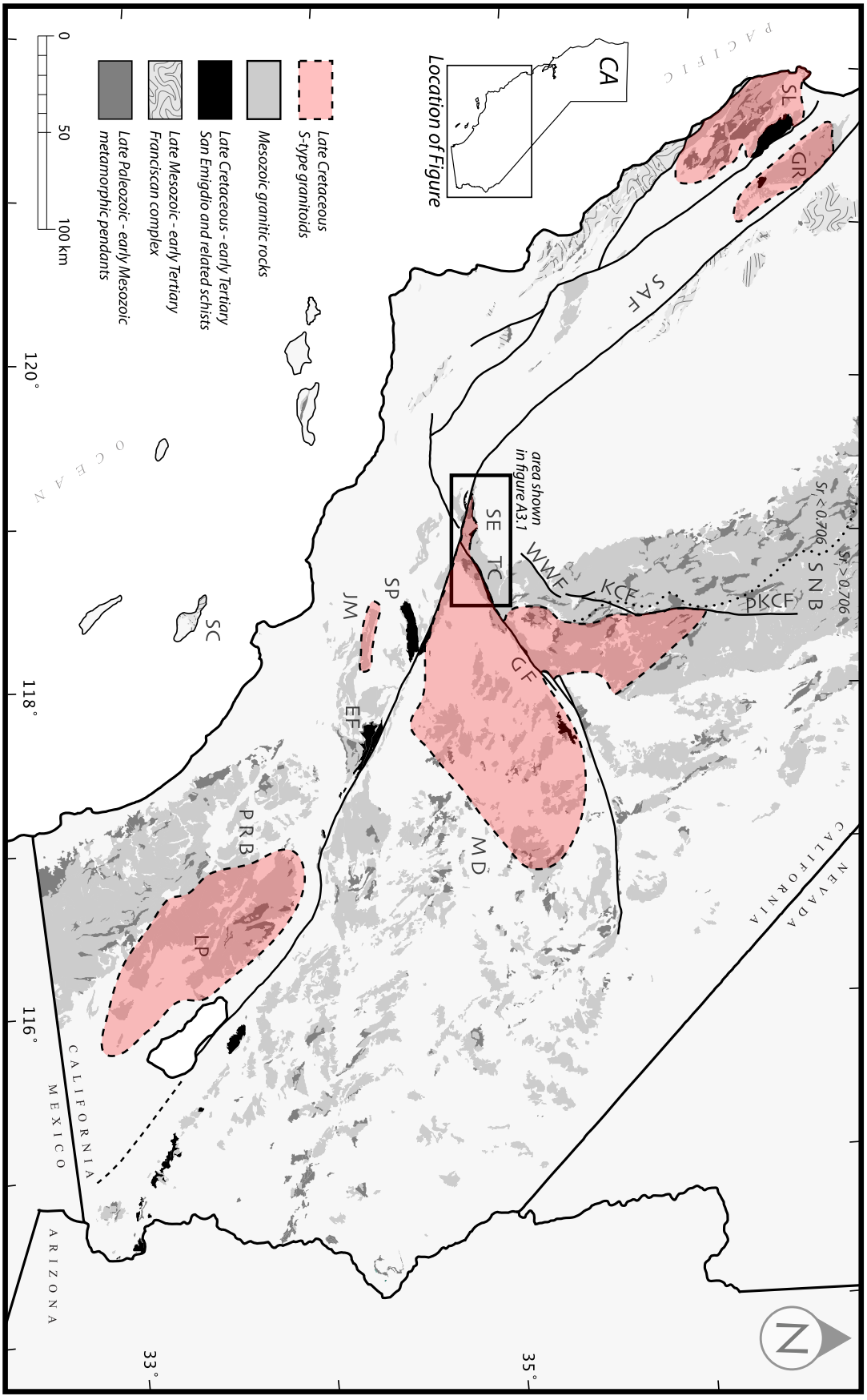
Late Cretaceous S-type granitoids
Mesozoic granitic rocks
Late Cretaceous - early Tertiary San Emigdio and related schists
Late Mesozoic - early Tertiary Franciscan complex
Late Paleozoic - early Mesozoic metamorphic pendants
0
50
100 km
Location of Figure
CA
area shown in figure A3.1
Sr < 0.706
Sr > 0.706
SNB
PKCF
KCF
WWF
SAF
SL
GR
SE
TC
SP
JM
SC
GF
EF
MD
PRB
LP
PACIFIC
OCEAN
NEVADA
CALIFORNIA
MEXICO
ARIZONA
120°
118°
116°
35°
33°
N

metamorphism of the southern California schist has been explained by a combination of shear heating along the subduction interface (Graham and England, 1976; England and Molnar, 1993; Ducea *et al*., 2009) and tectonic underplating and progressive cooling beneath an initially hot upper plate following the onset of shallow subduction (Peacock, 1992; Kidder and Ducea, 2006; Chapman *et al*., 2011). The San Emigdio Schist exhibits a gradation from upper amphibolite facies (~700 °C) to epidote–amphibolite facies (~600 °C) with increasing structural depth. Quartzofeldspathic veins and migmatitic textures are also abundant within ~100 m of the Rand fault, suggesting that fluid-saturated partial melting and extensive fluid flow were restricted to shallow structural levels of the schist body.

3. RESULTS

U-Pb detrital zircon geochronology of four metasandstone samples collected from different structural levels of the San Emigdio Schist was conducted at the University of Arizona LaserChron Center. Analytical techniques, sample locations and petrography, isotopic data, and representative cathodoluminescence (CL) images are available in Appendix 3.

Two key features are apparent in Figure 5.2, a normalized probability plot comparing detrital zircon age spectra for samples analyzed here and by Grove *et al*. (2003) and Jacobson *et al*. (2011). First, all samples exhibit a major mid- to Late Cretaceous age peak with scattered Early Cretaceous, Jurassic and Triassic ages, and rare pre-Mesozoic grains. Second, a shift in youngest U-Pb zircon ages from 87.8 ± 1.5 to 101.6 ± 3.8 Ma is observed from deep (~500 m) to intermediate (~100 m) structural levels, while samples from intermediate to shallow structural levels exhibit an opposite shift from 101.6 ± 3.8 to 91.2 ± 2.7 Ma. The former shift is clearly a primary feature resulting from the analysis of detrital

Figure 5.2. U-Pb detrital zircon age spectra from the San Emigdio Schist arranged by structural depth, shown on left. Filled and open circles (2σ error bars) denote youngest analyzed grain and youngest detrital grain in the sample, respectively. Samples 9957 from Grove *et al*. (2003), SE1b and SE03 from Jacobson *et al*. (2011), and the remainder from this study. A composite curve is shown for samples SE23 and SE1b as they are from the same outcrop. Isotopic data in Table A3.1.

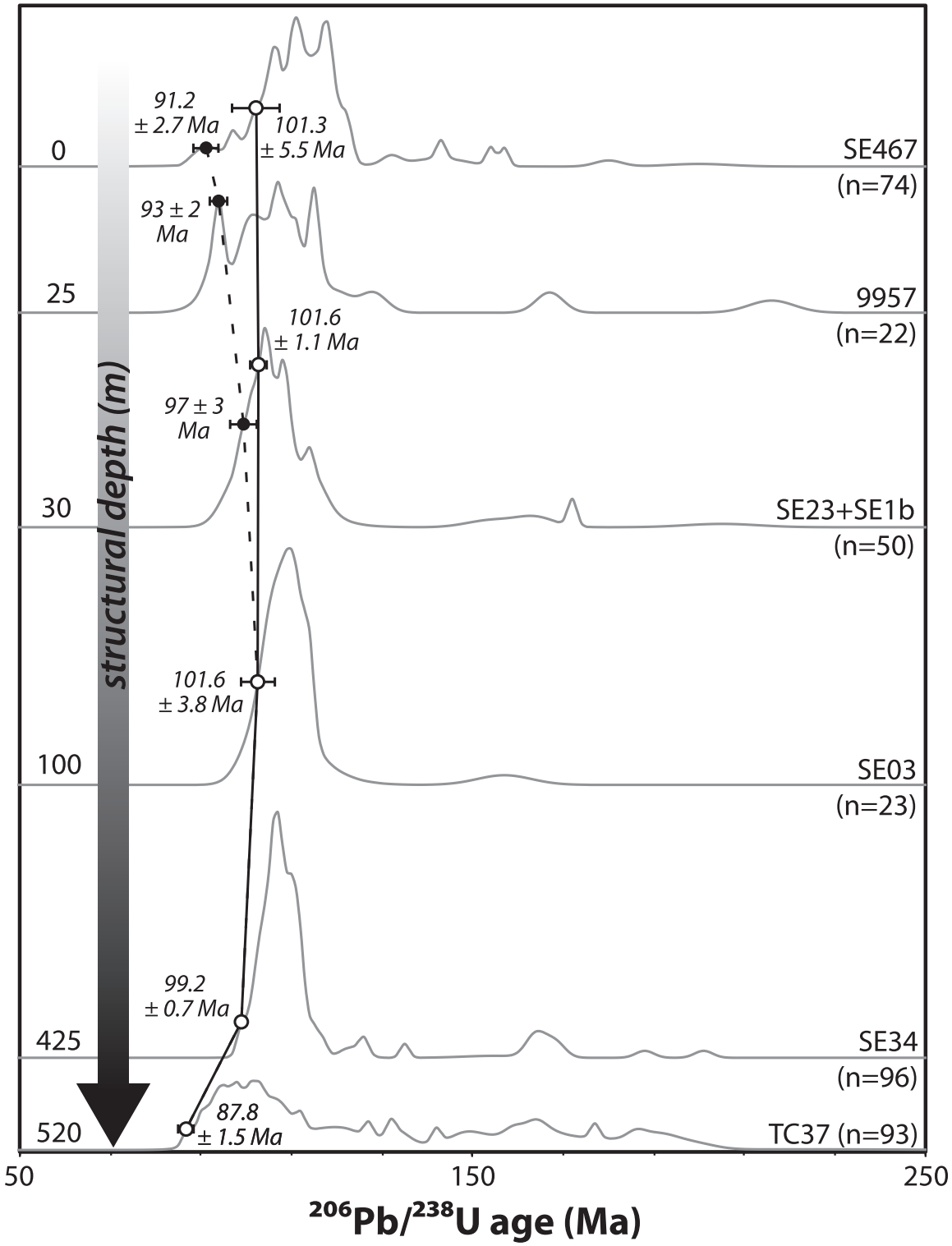
structural depth (m)
0
25
30
100
425
520
91.2 ± 2.7 Ma
101.3 ± 5.5 Ma
93 ± 2 Ma
101.6 ± 1.1 Ma
97 ± 3 Ma
101.6 ± 3.8 Ma
99.2 ± 0.7 Ma
87.8 ± 1.5 Ma
SE467 (n=74)
9957 (n=22)
SE23+SE1b (n=50)
SE03 (n=23)
SE34 (n=96)
TC37 (n=93)
50
150
250
206Pb/238U age (Ma)

zircon grains characterized by simple oscillatory zoning. However, the latter shift was produced through targeted analysis of grains exhibiting 1-50 μm thick, CL-bright rims and complex metamorphic zonation features, found in abundance within ~100 m of the Rand fault. Relative to less disturbed grains, such domains are younger (~ 91 to 100 Ma), with higher (~2400 to 3200 ppm) U concentration and lower (generally < 0.1) Th-U ratios, features commonly interpreted as characteristic of metamorphic zircon (e.g., Williams *et al*., 1996). Assuming a cogenetic origin, these metamorphic zircon domains yield a weighted mean age of 97.9 ± 3.2 Ma, probably reflecting the timing of peak metamorphism of the schist. Similar overgrowths are reported by Barth *et al*. (2003) from deep (> 2 km), relatively low grade (< 600 ˚C; Kidder and Ducea, 2006) levels of the related schist of Sierra de Salinas.

Zircon grains from upper plate plutonic assemblages within 100 m of the Rand fault exhibit oscillatory zoned, ca. 135 Ma cores mantled by CL-homogenous, ca. 100 Ma metamorphic rims with elevated U concentrations and low Th-U ratios (Chapman *et al*., in review). To assess the isotopic composition of metamorphic fluids responsible for zircon recrystallization, $\delta^{18}O$ values were determined at the Caltech Center for Microanalysis (see Appendix 3 for details) from a subset of schist and upper plate zircons studied by U-Pb geochronology (Figure 5.3). Measured $\delta^{18}O$ from schist and upper plate zircon cores average 5.61 ± 0.33‰ and 5.37 ± 0.20‰, respectively. Values of $\delta^{18}O$ from metamorphic domains in the same grains yield a weighted mean of 7.20 ± 0.46‰ (schist) and 6.96 ± 0.63‰ (upper plate).

Figure 5.3. Generalized cross-section model for the southern SNB. No vertical exaggeration. (a) Ca. 105 Ma subduction of Farallon plate beneath North America prior to shallow subduction. (b) Ca. 100 Ma slab flattening, eastward migration of arc magmatism, and schist deposition and subduction. (c) Ca. 90 Ma flat subduction, arc shutoff, and continued schist underplating. (d) Detailed view of tectonic schist assembly.

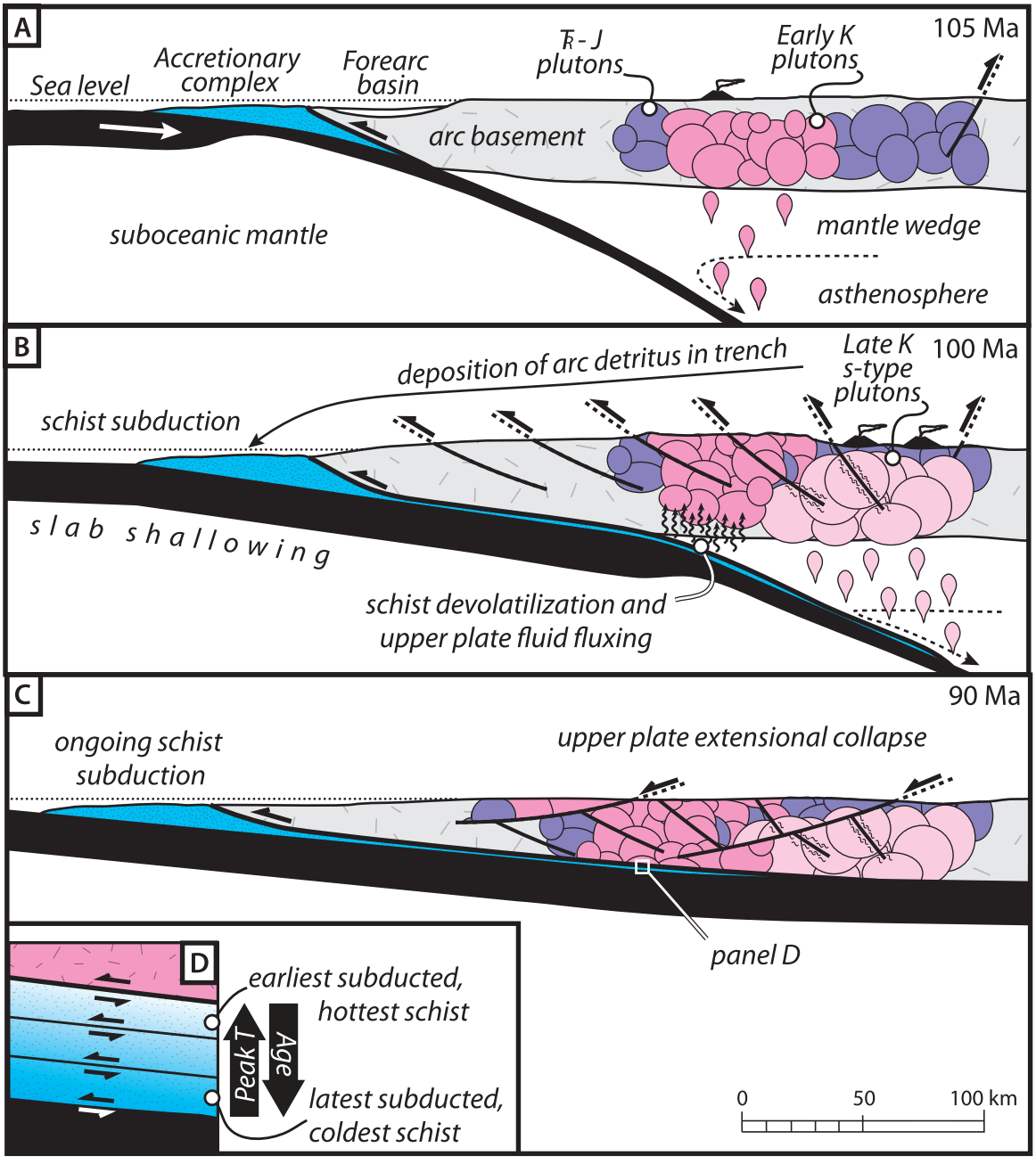
A
105 Ma
Sea level
Accretionary complex
Forearc basin
Tr - J plutons
Early K plutons
arc basement
suboceanic mantle
mantle wedge
asthenosphere
B
100 Ma
deposition of arc detritus in trench
Late K s-type plutons
schist subduction
slab shallowing
schist devolatilization and upper plate fluid fluxing
C
90 Ma
ongoing schist subduction
upper plate extensional collapse
panel D
D
earliest subducted, hottest schist
Peak T
Age
latest subducted, coldest schist
0
50
100 km

4. DISCUSSION

4.1. Growth of metasomatic zircon and upper plate fluid fluxing

The abundance of mid- to Late Cretaceous detrital zircon grains reported here is consistent with previous interpretations (Grove *et al*., 2003; Jacobson *et al*., 2011) that the sedimentary protoliths of the San Emigdio Schist were first cycle clastic deposits sourced from the western to central SNB. The reasons behind variations in youngest U-Pb zircon ages with structural depth are less clear and warrant special attention. At depths > 100 m from the Rand fault, youngest grains and grain clusters are clearly detrital and exhibit downsection younging from ca. 102 to 88 Ma. This downsection younging trend is explained by tectonic underplating of progressively younger material during subduction. We posit that this trend originally continued upsection from ~100 m depth to the Rand fault (the youngest truly detrital zircon age from the top of the section is 101.3 ± 5.5 Ma [Figure 5.2]), but emplacement of this earliest subducted material beneath hot (680 – 790 ˚C; Pickett and Saleeby, 1993; Chapman *et al*., 2011) upper plate rocks led to the growth of metamorphic zircon at 97.9 ± 3.2 Ma. By this interpretation, a conservative estimate of the depositional age of the structurally highest and earliest subducted portions of the San Emigdio Schist is constrained to the time interval between the youngest truly detrital U-Pb zircon ages (ca. 102 Ma) and the age of peak metamorphism (ca. 98 Ma). Alternatively, it could be argued, based on upsection younging of schist within ~100 m of the contact, that this portion of the section represents a subducted slice of intact stratigraphy. However, zircon domains that yield the youngest U-Pb ages in this interval are clearly metamorphic.

Zircon core $\delta^{18}O$ values in both the San Emigdio schist and upper plate plutonic assemblages are similar to the mantle value of 5.3 ± 0.3‰ (Valley *et al*., 1998), suggesting limited input of supracrustal material during igneous crystallization. Values of $\delta^{18}O$ measured from metamorphic domains in upper plate and schist zircon are ~1.5‰ higher than those of oscillatory zoned regions in the same grains, suggesting that the growth of metamorphic zircon occurred in the presence of isotopically heavy aqueous fluids. Such fluids in the schist were likely internally derived based on whole rock $\delta^{18}O$ values of +9.9 to +19.5 (Ross, 1989; Miller *et al*., 1996) and evidence for *in situ* veining, partial melting, and devolitalization associated with (clino)zoisite, chlorite, and/or muscovite breakdown (Chapman *et al*., 2011).

In contrast, growth of upper plate zircon rims with elevated $\delta^{18}O$ values indicates significant supracrustal contamination due to allochemical processes such as fluid infiltration. Lackey *et al*. (2005) report high zircon $\delta^{18}O$ values of 7.8 ± 0.7‰ from deeply exhumed plutonic rocks of the southernmost SNB and lower values of 6.1 ± 0.9‰ from less exhumed assemblages of the central and northern SNB. Furthermore, Lackey *et al*. (2005) note increasing zircon $\delta^{18}O$ values in younger (< ca. 100 Ma) assemblages in the southernmost SNB, consistent with our observation of young (89 to 105 Ma) overgrowths with elevated $\delta^{18}O$ on old (ca. 135 Ma) upper plate zircon cores, and attribute this change to a greater supracrustal input with time. Assimilation of high-$\delta^{18}O$ metamorphic framework rocks may account for some contamination of plutons in the southernmost SNB, but cannot explain the observed shift toward higher zircon $\delta^{18}O$ at ca. 100 Ma. We propose an alternative explanation that subduction, metamorphism, and devolatilization of the earliest

formed San Emigdio Schist between ca. 102 and 98 Ma led to fluid fluxing and isotopic contamination of upper plate plutonic assemblages (Figure 5.3).

Schist devolatilization beneath the upper plate may explain the presence of large garnet porphyroblasts in the hanging wall of the Rand fault. These garnet grains have been interpreted previously to have grown during an episode of fluid-fluxed partial melting (Luffi *et al*., 2005) and have Sm/Nd ages ranging from 102 to 95 Ma (Saleeby *et al*., 2007), coincident with the inferred timing of schist subduction and metamorphism.

Similar scenarios are envisioned to explain isotopic data from: 1) the Catalina Schist of the California borderland, a mid- to Late Cretaceous subduction complex formed by tectonic underplating, exhibiting evidence for upward migration of fluids and isotopic contamination of structurally high units (e.g., Bebout, 1991; Grove *et al*., 2008), and 2) the northeastern Peninsular Ranges batholith (PRB) of southern California, where isotopically enriched granitoids are attributed to influx of high-$\delta^{18}O$ and high-δD fluids derived from subducted oceanic crust and/or underplated sediments (Holk *et al*., 2006).

4.2. Relation of schist underplating to voluminous last gasp of arc magmatism

Our age constraints indicate that the earliest formed member of the southern California schist, exposed in the San Emigdio and Tehachapi Mountains, was subducted to 30 to 35 km depth between 100 and 90 Ma, somewhat earlier than previous estimates (Grove *et al*., 2003; Jacobson *et al*., 2011). Therefore, it is likely that the earliest schist was present beneath the Mojave Desert-southernmost SNB region during large volume magmatism and emplacement of a belt of ca. 92 to 85 Ma S-type granitoids (Ross, 1989; Miller *et al*., 1996; Saleeby *et al*., 2008; Chapman *et al*., in preparation) (Figure 5.1). Plutons within this belt

are characterized by elevated $\delta^{18}O$ whole-rock and zircon values (Masi *et al*., 1981; Saleeby *et al*., 1987; Lackey *et al*., 2005), $^{87}Sr/^{86}Sr$ (Kistler and Ross, 1990) and negative ε_{Nd} (DePaolo, 1981; Pickett and Saleeby, 1994), indicative of derivation from a magmatic source regime rich in immature clastic sediments. These isotopic relations and the paucity of wallrock exposures and xenoliths in these plutons preclude regional scale assimilation of metamorphic framework assemblages and/or the availability of these materials in the magmatic source regime as first order processes influencing magmagenesis in these plutons.

Instead, we suggest, as did Miller *et al*. (1996), that the schist was delivered to the magmatic source via shallow subduction and fluxed a transient layer of mantle wedge (e.g., Gutscher *et al*., 2000) with fluid to produce these S-type granitoids. The emplacement of S-type granitoids in the southernmost SNB and adjacent areas occurred during eastward arc migration and at the peak of a high magmatic flux event in the Late Cretaceous (100-85 Ma; Ducea, 2001). Magmatic flare-ups are thought to be triggered by lithospheric thickening, either by subduction erosion from the trench side or retroarc trusting from the foreland (Ducea, 2001; Ducea and Barton, 2007). Ducea (2001) invokes west-vergent thrusting of North America beneath the arc to explain magmatic flare-ups for the entire length of the SNB. However, in 100 to 85 Ma plutons north of ~36 ˚N, whole-rock and zircon $\delta^{18}O$ values are significantly lower than in the southern SNB, with similarly high $^{87}Sr/^{86}Sr$, reflecting a higher proportion of Paleozoic and older crystalline lower crust to sedimentary material (Saleeby *et al*., 1987; Kistler, 1990; Pickett and Saleeby, 1994; Lackey *et al*., 2005; 2008). Furthermore, there is no evidence for major Late Cretaceous deformation along the Cordilleran retroarc thrust belt south of ~36 ˚N (e.g., Walker *et al*., 1995; DeCelles, 2004; Dunne and Walker, 2004). Therefore, 100 to 85 Ma high flux magmatism must be related

to fundamentally different processes north (retroarc thrusting) and south (shallow subduction and schist melting) of ~ 36 ˚N.

The isotopic and structural relations exhibited by Late Cretaceous granitoids in the southern SNB are strikingly similar to those of: 1) the La Posta plutonic suite in the northernmost PRB (e.g., Kistler *et al*., 2003; Holk *et al*., 2006; Grove *et al*., 2008) and 2) the Josephine Mountain intrusion of the San Gabriel Mountains. The La Posta suite was emplaced during a ca. 98 to 92 Ma high magmatic flux event and exhibits elevated $\delta^{18}O$ values in plutons along the northern PRB, where it is underlain by Catalina Schist. These relations led Grove *et al*. (2008) to hypothesize that subduction erosion delivered the Catalina Schist to the magmatic source, causing partial melting and devolatilization in the schist and igniting a magmatic flare-up in the northernmost PRB. Likewise, granitoids with Sri > 0.708, $\delta^{18}O$ (whole-rock) > 8.6‰, and ε_{Nd} <-10 of the ca. 72 to 86 Ma Josephine Mountain intrusion (Barth *et al*., 1995) overlap in age with the youngest zircons (ca. 79 to 82 Ma) at high structural levels of the underlying Pelona schist (Grove *et al*., 2003), suggesting a possible schist source for the intrusion.

4.3. Termination of arc magmatism

The termination of arc magmatism occurred throughout the SNB between ca. 80 and 85 Ma (e.g., Chen and Moore, 1982). Shallow subduction and the removal of mantle lithosphere from beneath the southern SNB - Mojave Desert region is commonly called upon to explain the end of arc magmatism (Dumitru *et al*., 1991; Saleeby, 2003), but cannot account for simultaneous shutoff in the greater SNB and northward to the Idaho batholith, where the subbatholithic column was left intact. Ducea (2001) suggests that the mantle lithosphere

and lower crust of the central and northern SNB became melt-drained and infertile following Late Cretaceous retroarc thrusting and associated voluminous arc magmatism. A hybrid model of subduction refrigeration related to progressive schist underplating and shallow subduction in the southern SNB and concomitant melt depletion of the retroarc source region in the central and northern SNB provides one explanation for the cessation of arc magmatism throughout the greater SNB between ca. 80 and 85 Ma. Alternatively, arc shutoff may be related to large-scale disruption of asthenospheric circulation patterns by shallow subduction in the southern SNB and adjacent areas (Saleeby, 2003).

REFERENCES

Barth, A. P., Wooden, J. L., Tosdal, R. M., and Morrison, J., 1995, Crustal contamination in the petrogenesis of a calc-alkalic rock series: Josephine Mountain intrusion, California: *Geological Society of America Bulletin*, **107**(2), 201-212.

Barth, A. P., Wooden, J. L., Grove, M., Jacobson, C. E., and Pedrick, J. N., 2003, U-Pb zircon geochronology of rocks in the Salinas Valley region of California; a reevaluation of the crustal structure and origin of the Salinian Block: *Geology*, **31**(6), 517-520.

Bebout, G. E., 1991, Field-based evidence for devolatization in subduction zones; implications for arc magmatism: *Science*, **251**(4992), 413-416.

Chapman, A. D., Kidder, S., Saleeby, J. B., and Ducea, M. N., 2010, Role of extrusion of the Rand and Sierra de Salinas schists in Late Cretaceous extension and rotation of the southern Sierra Nevada and vicinity: *Tectonics*, **29(**5), TC5006, doi:10.1029/ 2009TC002597.

Chapman, A. D., Luffi, P., Saleeby, J., and Petersen, S., 2011, Metamorphic evolution, partial melting, and rapid exhumation above an ancient flat slab: Insights from the San Emigdio Schist, southern California: *Journal of Metamorphic Geology*, **29**, 601-626, doi: 10.1111/j.1525-1314.2011.00932.x.

Chapman, A. D., Saleeby, J. B., Wood, D. J., , Piasecki, A, Farley, K. A., Kidder, S., and Ducea, M. N., in review, Late Cretaceous gravitational collapse of the southern Sierra Nevada batholith, California, submitted to *Geosphere*.

Chen, J. H., and Moore, J. G., 1982, Uranium-lead isotopic ages from the Sierra Nevada Batholith, California: *Journal of Geophysical Research*, **87**(B6), 4761-4784.

Cloos, M., 1985, Thermal evolution of convergent plate margins; thermal modeling and reevaluation of isotopic Ar-ages for blueschists in the Franciscan Complex of California: *Tectonics*, **4**(5), 421-433.

Coney, P. J., and Reynolds, S. J., 1977, Cordilleran Benioff zones: *Nature*, **270**(5636), 403-406.

Davies, J. H., and Bickle, M. J., 1991, A physical model for the volume and composition of melt produced by hydrous fluxing above subduction zones: *Philosophical Transactions of the Royal Society of London, Series A: Mathematical and Physical Sciences*, **335**(1638), 355-364.

DeCelles, P. G., 2004, Late Jurassic to Eocene evolution of the Cordilleran thrust belt and foreland basin system, western U.S.A: *American Journal of Science*, **304**(2), 105-168.

DePaolo, D. J., 1981, A neodymium and strontium isotopic study of the Mesozoic calc-alkaline granitic batholiths of the Sierra Nevada and Peninsular Ranges, California: *Journal of Geophysical Research*, **86**(B11), 10470-10488.

Ducea, M., 2001, The California Arc; thick granitic batholiths, eclogitic residues, lithospheric-scale thrusting, and magmatic flare-ups: *GSA Today*, **11**(11), 4-10.

Ducea, M. N., and Barton, M. D., 2007, Igniting flare-up events in Cordilleran arcs: *Geology*, **35**(11), 1047-1050.

Ducea, M. N., Kidder, S., Chesley, J. T., and Saleeby, J. B., 2009, Tectonic underplating of trench sediments beneath magmatic arcs; the Central California example: *International Geology Review*, **51**(1), 1-26.

Dumitru, T. A., Gans, P. B., Foster, D. A., and Miller, E. L., 1991, Refrigeration of the western Cordilleran lithosphere during Laramide shallow-angle subduction: *Geology*, **19**(11), 1145-1148.

Dunne, G. C., and Walker, J. D., 2004, Structure and evolution of the East Sierran thrust system, east central California: *Tectonics*, **23**(4).

Ehlig, P. L., 1981, Origin and tectonic history of the basement terrane of the San Gabriel Mountains, central Transverse Ranges, *in* Ernst, W. G., ed., *The geotectonic development of California, Rubey Volume I*: New Jersey, Prentice-Hall, 253-283.

England, P., and Molnar, P., 1993, The interpretation of inverted metamorphic isograds using simple physical calculations: *Tectonics*, **12**(1), 145-158.

Gerya, T. V., Stoeckhert, B., and Perchuk, A. L., 2002, Exhumation of high-pressure metamorphic rocks in a subduction channel; a numerical simulation: *Tectonics*, **21**, doi:10.1029/2002TC001406.

Graham, C. M., and England, P. C., 1976, Thermal regimes and regional metamorphism in the vicinity of overthrust faults; an example of shear heating and inverted metamorphic zonation from southern California: *Earth and Planetary Science Letters*, **31**(1), 142-152.

Graham, C. M., and Powell, R., 1984, A garnet-hornblende geothermometer; calibration, testing, and application to the Pelona Schist, Southern California: *Journal of Metamorphic Geology*, **2**(1), 13-31.

Grove, M., Bebout, G. E., Jacobson, C. E., Barth, A. P., Kimbrough, D. L., King, R. L., Zou, H., Lovera, O. M., Mahoney, B. J., and Gehrels, G. E., 2008, The Catalina Schist; evidence for Middle Cretaceous subduction erosion of southwestern North America: *Geological Society of America Special Paper*, **436**, 335-361.

Grove, M., Jacobson, C. E., Barth, A. P., and Vucic, A., 2003, Temporal and spatial trends of Late Cretaceous-early Tertiary underplating Pelona and related schist beneath Southern California and southwestern Arizona: *Geological Society of America Special Paper*, **374**, 381-406.

Gutscher, M.-A., Maury, R., Eissen, J.-P., and Bourdon, E., 2000, Can slab melting be caused by flat subduction?: *Geology*, **28**(6), 535-538.

Holk, G. J., Taylor, H. P., Jr., and Gromet, L. P., 2006, Stable isotope evidence for large-scale infiltration of metamorphic fluids generated during shallow subduction into the Eastern Peninsular Ranges mylonite zone (EPRMZ), Southern California: *International Geology Review*, **48**(3), 209-222.

Jacobson, C. E., 1995, Qualitative thermobarometry of inverted metamorphism in the Pelona and Rand schists, Southern California, using calciferous amphibole in mafic schist: *Journal of Metamorphic Geology*, **13**(1), 79-92.

Jacobson, C. E., Grove, M., Pedrick, J. N., Barth, A. P., Marsaglia, K. M., Gehrels, G. E., and Nourse, J. A., 2011, Late Cretaceous - early Cenozoic tectonic evolution of the southern California margin inferred from provenance of trench and forearc sediments:

Geological Society of America Bulletin, **123**(3-4), 485-506.

Jacobson, C. E., Grove, M., Vucic, A., Pedrick, J. N., and Ebert, K. A., 2007, Exhumation of the Orocopia Schist and associated rocks of southeastern California; relative roles of erosion, synsubduction tectonic denudation, and middle Cenozoic extension: *Geological Society of America Special Paper*, **419**, 1-37.

Kidder, S., and Ducea, M. N., 2006, High temperatures and inverted metamorphism in the schist of Sierra de Salinas, California: *Earth and Planetary Science Letters*, **241**(3-4), 422-437.

Kistler, R. W., and Ross, D. C., 1990, A strontium isotopic study of plutons and associated rocks of the southern Sierra Nevada and vicinity, California: *U. S. Geological Survey Bulletin* 1920, 20 pp.

Kistler, R. W., 1990, Two different lithosphere types in the Sierra Nevada, California: *Memoir Geological Society of America*, **174**, 271-281.

Lackey, J. S., Valley, J. W., and Saleeby, J. B., 2005, Supracrustal input to magmas in the deep crust of Sierra Nevada Batholith; evidence from high-$\delta^{18}O$ zircon: *Earth and Planetary Science Letters*, **235**(1-2), 315-330.

Lackey, J. S., Valley, J. W., Chen, J. H., and Stockli, D. F., 2008, Dynamic Magma Systems, Crustal Recycling, and Alteration in the Central Sierra Nevada Batholith: the Oxygen Isotope Record: *Journal of Petrology*, **49**(7), 1397-1426.

Luffi, P. I., Saleeby, J. B., and Asimow, P. D., 2005, Water-fluxed fractional melting; a new, efficient mechanism of garnet enrichment during mid- and lower-crustal anatexis: *Eos, Transactions, American Geophysical Union*, **86**(52).

Luffi, P., Saleeby, J. B., Lee, C. A., and Ducea, M. N., 2009, Lithospheric mantle duplex

beneath the central Mojave Desert revealed by xenoliths from Dish Hill, California: *Journal of Geophysical Research*, **114**(B03202), doi:10.1029/2008JB005906.

Masi, U., O'Neil, J. R., and Kistler, R. W., 1981, Stable isotopes in Mesozoic granites of central and northern California and southwestern Oregon: *Contributions to Mineralogy and Petrology*, **76**, 116–126.

Miller, J. S., Glazner, A. F., and Crowe, D. E., 1996, Muscovite-garnet granites in the Mojave Desert; relation to crustal structure of the Cretaceous arc: *Geology*, **24**(4), 335-338.

Peacock, S. M., 1992, Blueschist-facies metamorphism, shear heating, and *P-T-t* paths in subduction shear zones: *Journal of Geophysical Research*, **97**(B12), 17,693-617,707.

Pickett, D. A., and Saleeby, J. B., 1993, Thermobarometric constraints on the depth of exposure and conditions of plutonism and metamorphism at deep levels of the Sierra Nevada Batholith, Tehachapi Mountains, California: *Journal of Geophysical Research*, **98**(B1), 609-629.

Pickett, D. A., and Saleeby, J. B., 1994, Nd, Sr, and Pb isotopic characteristics of Cretaceous intrusive rocks from deep levels of the Sierra Nevada Batholith, Tehachapi Mountains, California: *Contributions to Mineralogy and Petrology*, **118**(2), 198-215, doi: 110.1007/BF01052869.

Ross, D. C., 1989, The metamorphic and plutonic rocks of the southernmost Sierra Nevada, California, and their tectonic framework: *U.S. Geological Survey Professional Paper* 1381, 159 pp.

Saleeby, J., 2003, Segmentation of the Laramide slab; evidence from the southern Sierra Nevada region: *Geological Society of America Bulletin*, **115**(6), 655-668.

Saleeby, J., Farley, K. A., Kistler, R. W., and Fleck, R. J., 2007, Thermal evolution and exhumation of deep-level batholithic exposures, southernmost Sierra Nevada, California: *Geological Society of America Special Paper*, **419**, 39-66.

Saleeby, J. B., Ducea, M. N., Busby, C. J., Nadin, E. S., and Wetmore, P. H., 2008, Chronology of pluton emplacement and regional deformation in the southern Sierra Nevada Batholith, California: *Geological Society of America Special Paper*, **438**, 397-427.

Saleeby, J. B., Sams, D. B., and Kistler, R. W., 1987, U/Pb zircon, strontium, and oxygen isotopic and geochronological study of the southernmost Sierra Nevada Batholith, California: *Journal of Geophysical Research*, **92**(B10), 10,443-410,466.

Tatsumi, Y., Hamilton, D. L., and Nesbitt, R. W., 1986, Chemical characteristics of fluid phase released from a subducted lithosphere and origin of arc magmas; evidence from high-pressure experiments and natural rocks: *Journal of Volcanology and Geothermal Research*, **29**, 1-4.

Valley, J. W., Kinny, P. D., Schulze, D. J., and Spicuzza, M. J., 1998, Zircon megacrysts from kimberlite; oxygen isotope variability among mantle melts: *Contributions to Mineralogy and Petrology*, **133**, 1-11.

Walker, J. D., Burchfiel, B. C., and Davis, G. A., 1995, New age controls on initiation and timing of foreland belt thrusting in the Clark Mountains, Southern California: *Geological Society of America Bulletin*, **107**(6), 742-750.

Williams, I. S., Buick, I. S., and Cartwright, I., 1996, An extended episode of early Mesoproterozoic metamorphic fluid flow in the Reynolds Range, central Australia: *Journal of Metamorphic Geology*, **14**(1), 29-47.

APPENDIX 1

Supporting information and data repository for:

Metamorphic evolution, partial melting, and rapid exhumation above an ancient flat slab: Insights from the San Emigdio Schist, southern California

1. THERMODYNAMIC MODELLING

We use the Gibbs free energy minimization software package THERIAK-DOMINO (de Capitani and Brown, 1987) and the thermodynamic end-member and solution models of the accompanying 'tc321p2.txt' database (THERMOCALC database as distributed in version 3.21) to construct *P-T* pseudosections, mole fraction isopleth plots, and garnet volume fraction contour plots, for 1) the water-saturated (i.e. "prograde") and 2) the water-saturated and garnet-subtracted (i.e. "retrograde") bulk composition of metasandstone sample 06SE23 (Figures 3.10a, 3.11, 3.13, 3.14a, and 3.14c). Complementary plots were constructed for mafic schist sample 08SE479b using Perple_X 07 (Connolly, 2009) with the amphibole model of Dienier *et al*. (2007) (Figures 3.10b, 3.12, 3.14b, and 3.14d). Perple_X calculations for sample 08SE479b were necessary since the Holland and Powell (1998) and related amphibole models cannot be imported into DOMINO properly. Thermodynamic calculations were made in the MnNCKFMASH (prograde 06SE23), MnNCFMASH (prograde 08SE479b), NCKFMASH (retrograde 06SE23), and NCFMASH (retrograde 08SE479b) chemical systems. We assume that quartz is in excess, that Fe^{3+} is negligible in comparison to Fe^{2+}, and that the fluid phase is pure H_2O. Pressures and temperatures in Figures 3.10, 3.11, 3.12, and 3.14 should be viewed as approximate values due to large

uncertainties in solution models and standard state data. Modelled garnet zonation patterns (Figure 3.13) were obtained with the THERIAK algorithm for the water-saturated bulk composition of sample 06SE23. We model fractional garnet crystallization by removing a fraction of garnet from the bulk composition after each calculation along the *P-T* path shown in Figure 3.12a.

Major element compositions for metasandstone and mafic schist samples, expressed in atomic percents, are presented in Table A1.6. Whole rock X-ray fluorescence (XRF) measurements were done at the GeoAnalytical Laboratory of Washington State University following the methods of Johnson *et al*. (1999). Weathering rinds, quartz veins, and retrograde shear zones were removed to avoid contamination. We assume that XRF-determined bulk compositions represent, except for H_2O, the rock chemistry of samples 06SE23 and 08SE479b throughout metamorphism, i.e. metamorphism occurred in an isochemical system.

2. MULTICOMPONENT DIFFUSION MODELLING

2.1. Theory

When a mineral overgrows itself with a different composition than the core segment, the resulting interface between juxtaposed compositions in the composite grain is a natural diffusion couple. The degree of relaxation of the originally steep compositional step is dependent chiefly on temperature and the time interval over which diffusion was possible. Assuming that the activation volume of diffusion ΔV^+ is independent of pressure in garnet up to 85 kbar (Chakraborty and Rubie, 1996), the activation energy (at P = 1 bar)

$$Q(P) = Q(1) + \Delta V^{+}(P-1).$$

The Arrhenius relationship between diffusion coefficients for Ca, Fe, Mg, and Mn and temperature is then given by:

$$D_i^* = D_0 e^{\frac{-\Delta Q + \Delta V^{+}(P-1)}{RT}} \tag{1}$$

where D_i^* is the tracer diffusion coefficient of species i and D_0 is the empirically determined self diffusion coefficient. We used the diffusion data of Ganguly *et al*. (1998) for multicomponent modelling. Solutions were only calculated from analytical traverses in which the gradients in end member compositions approach zero (i.e. compositions become plateau-like at each end of the diffusion couple).

2.2. Multicomponent Diffusion Modelling

Fick's first law states that the diffusion flux of species i (J_i) in a system is related to the magnitude of the concentration gradient of all j species (C_j) by the interdiffusion coefficients between i and j (D_{ij}):

$$J_i = -[D_{ij}]\nabla C_j \,. \tag{2}$$

For example, the diffusion flux of Mn in the garnet system depends on the concentration gradient of Mn and the concentration gradients of all other diffusing species, i.e. Ca, Fe, and Mg:

$$J_{Mn} = -D_{MnMn}\left(\frac{\partial C_{Mn}}{\partial x}\right) - D_{MnCa}\left(\frac{\partial C_{Ca}}{\partial x}\right) - D_{MnFe}\left(\frac{\partial C_{Fe}}{\partial x}\right) - D_{MnMg}\left(\frac{\partial C_{Mg}}{\partial x}\right) \quad (3)$$

where J_i and $\frac{\partial C_i}{\partial x}$ are the flux and concentration gradient of species i, respectively, and D_{ij} is the interdiffusion coefficient between species i and j. Assuming that mass is conserved during diffusion, Fick's second law can be derived from equation 2:

$$\frac{\partial^2}{\partial x^2}([D_{ij}]\cdot C_j) = \frac{\partial}{\partial t}(C_i).$$

2.3. Diffusion Coefficients

Garnet diffusion data are available from a number of sources and are summarized by Vielzeuf *et al*. (2007); Table 5. We used the data of Ganguly *et al*. (1998) derived from a pyrope-almandine diffusion couple for our multicomponent modelling as opposed to Chakraborty and Ganguly (1992) from a spessartine-almandine diffusion couple since garnet compositions from grains 1 and 2 (Figure 3.9) are quite Mn – poor (Xsps ≈ 0.01). Results from the dataset of Chakraborty and Ganguly (1992) give significantly shorter diffusion timescales (approximately 10 Kyr for both grains 1 and 2). Cooling rates of 14500

– 9500 ˚C/Myr calculated from these shorter times are geologically unfeasible and comparable values have not been reported aside from in the lowermost portions of ophiolites (Hacker and Mosenfelder, 1996). Regardless of the dataset, the diffusivity of Ca in garnet is less understood than Fe, Mg, and Mn. To address this issue, we used a wide range of Ca diffusivities, e.g. $D_{Ca} = D_{Fe} = 3.5\times10^{-9}$ m^2/s (Ganguly *et al*., 1998) and $D_{Ca} = 7.2\times10^{-16}$ m^2/s (Schwandt *et al*., 1996), and find that the calculated relaxation profiles do not change when different diffusivities are used. For this reason, we conclude that Ca has little effect on the outcome of our modelling.

2.4. Sample sectioning

Accurate electron microprobe-determined garnet zonation profiles are critically dependent on the geometry with which the sample is sectioned. Any garnet that is sectioned at an angle to the grain center will display attenuated zonation. To avoid this sectioning effect, we analyzed the largest garnets in the populations of samples 06SE23 and 08SE479b. Therefore, the results of garnet core analyses are a close approximation to the true core values, which, according to observed zonation trends is probably marginally lower in almandine and pyrope, and higher in spessartine content. In addition, oblique traverses across diffusion couples yield artificially broad profiles. As a result, the differing calculated diffusion timescales of 0.2 and 0.3 Myr may have resulted from sectioning and both represent constraints on the maximum amount of time required for diffusive relaxation.

3. Listing of numbered fields

Numbers in Figures 3.10 and 3.14 refer to mineral stability fields listed below.

Figure 3.10a:

1. Grt + Cpx + Chl + Ms + Pg + Qz + H_20

2. Grt + Cpx + Pl + Chl + Ms + Pg + Qz + H_2O

3. Grt + Cpx + Pl + Chl + Ms + Pg + Zo + Qz + H_2O

4. Grt + Cpx + Pl + Chl + Ms + Zo + Qz + H_2O

5. Grt + Cpx + Pl + Chl + Ms + Bt + Zo + Qz + H_2O

6. Grt + Cpx + Pl + Chl + Ms + Pg + Qz + H_2O

7. Grt + Pl + Ms + Bt + Zo + Qz + H_2O

8. Grt + Pl + Ms + Bt + St + Qz + H_2O

9. Grt + Pl + Bt + St + Qz + H_2O

10. Grt + Pl + Chl + Bt + St + Qz + H_2O

11. Grt + Pl + Chl + Bt + Qz + H_2O

12. Grt + Pl + Chl + Bt + Crd + Qz + H_2O

13. Grt + Pl + Bt + Crd + Qz + H_2O

14. Grt + Pl + Bt + Crd + Sil + Qz + H_2O

15. Grt + Pl + Bt + Sil + Qz + H_2O

16. Grt + Pl + Ms + Bt + Sil + Qz + H_2O

17. Grt + Pl + Ms + Bt + Qz + H_2O + melt

18. Grt + Pl + Bt + Sil + Qz + H_2O + melt

19. Grt + Pl + Bt + Crd + Qz + H_2O + melt

20. Grt + Pl + Bt + Qz + H_2O + melt

21. Grt + Pl + Bt + Crd + Qz + melt

22. Grt + Opx + Pl + Bt + Crd + Qz + H_2O + melt

23. Grt + Opx + Pl + Bt + Crd + Qz + melt

24. Grt + Opx + Pl + Bt + Qz + melt

25. Grt + Opx + Pl + Qz + melt

26. Grt + Opx + Pl + Crd + Qz + melt

Figure 3.10b:

1. Act + Gln + Omp + Chl + Lws + Qz

2. Grt + Act + Gln+ Omp + Chl + Lws + Qz

3. Grt + Act + Gln + Chl + Zo + Qz

4. Grt + Act + Omp + Chl + Zo + Qz

5. Grt + Act + Omp + Pl + Chl + Zo + Qz

6. Act + Pl + Chl + Zo + Qz

7. Grt + Act + Chl + Zo + Qz

8. Grt + Act + Pl + Chl + Zo + Qz

9. Grt + Act + Zo + Qz

10. Grt + Hbl + Cpx + Pl + Zo + Qz

11. Grt + Cum + Hbl + Pl + Qz

12. Grt + Cum + Hbl + Pl

13. Grt + Cum + Opx + Pl

14. Grt + Cpx + Pl + Qz

Figure 3.14a:

1. Grt + Cpx + Pl + Ms + Bt + Pg + Qz
2. Grt + Cpx + Pl + Ms + Bt + Zo + Pg + Qz
3. Grt + Pl + Ms + Bt + Zo + Pg + Qz
4. Pl + Ms + Bt + Zo + Pg + Qz
5. Pl + Chl + Ms + Bt + Zo + Pg + Qz
6. Pl + Chl + Ms + Bt + Zo + Qz + H_2O
7. Grt + Pl + Ms + Bt + Zo + Pg + Qz + H_2O
8. Grt + Pl + Ms + Bt + Zo + Qz + H_2O
9. Grt + Pl + Chl + Ms + Bt + Zo + Pg + Qz
10. Grt + Pl + Chl + Ms + Bt + Zo + Qz
11. Grt + Pl + Chl + Ms + Bt + Zo + Qz + H_2O
12. Grt + Pl + Chl + Ms + Bt + Qz + H_2O
13. Pl + Kfs + Ms + Bt + Qz + H_2O
14. Pl + Kfs + Bt + Qz + H_2O
15. Pl + Kfs + Bt + Crd + Qz + H_2O
16. Kfs + Bt + Crd + Qz + H_2O + melt
17. Kfs + Bt + Qz + H_2O + melt
18. Pl + Ms + Bt + Qz + H_2O + melt
19. Pl + Ms + Bt + Qz + melt
20. Pl + Ms + Bt + Sil + Qz + melt
21. Grt + Pl + Ms + Bt + Sil + Qz + melt

22. Pl + Kfs + Grt + Ms + Bt + Qz + melt

23. Pl + Kfs + Grt + Bt + Qz + melt

24. Pl + Kfs + Grt + Bt + Sil + Qz + melt

25. Kfs + Grt + Bt + Sil + Qz + melt

26. Kfs + Bt + Sil + Qz + melt

27. Kfs + Bt + Qz + melt

28. Kfs + Bt + Crd + Qz + melt

29. Kfs + Bt + Sil + Qz + melt

30. Kfs + Opx + Bt + Crd + Qz + melt

31. Kfs + Opx + Crd + Qz + melt

32. Kfs + Grt + Bt + Crd + Qz + melt

33. Kfs + Grt + Opx + Bt + Crd + Qz + melt

34. Kfs + Grt + Opx + Bt + Qz + melt

35. Kfs + Grt + Bt + Crd + Sil + Qz + melt

36. Kfs + Grt + Bt + Qz + melt

Figure 3.14b:

1. Act + Gln + Omp + Chl + Lws + Qz

2. Act + Gln + Omp + Chl + Zo + Qz

3. Act + Gln + Chl + Zo + Qz

4. Act + Gln + Zo + Qz

5. Act + Omp + Chl + Pl + Zo + Qz

6. Act + Hbl + Chl + Pl + Zo + Qz

7. Hbl + Omp + Pl + Zo + Qz

8. Act + Gln + Pl + Zo + Qz

9. Act + Gln + Chl + Pl + Zo + Qz

10. Act + Hbl + Pl + Zo + Qz

11. Hbl + Cpx + Pl + Zo + Qz

12. Cum + Hbl + Pl + Qz

13. Cum + Hbl + Opx + Pl

14. Cum + Hbl + Opx + Pl + Qz

15. Grt + Cum + Hbl + Pl + Qz

16. Grt + Cum + Hbl + Pl

17. Cum + Opx + Pl + Qz

18. Cum + Opx + Pl

Table A1.1. Representative garnet analyses used in thermobarometric calculations (normalized to 12 O). Ferric iron calculated using the program AX (Holland and Powell, 1998). Abbreviations: m, mafic schist; s, metasandstone schist; seg, San Emigdio gneiss.

Sample	07SE17	06SE23	07SE19	06SE54	08SE476	08SE469	06SE9	08SE478	08SE467
Lithology	s	s	s	s	s	s	s	s	s
SiO_2	37.71	38.09	38.44	37.99	38.05	38.23	38.03	37.21	37.67
TiO_2	0.01	0.06	0.02	0.03	0.06	0.01	0.02	0.04	0.00
Al_2O_3	20.57	20.93	20.77	20.77	20.55	20.86	21.17	20.41	20.70
Cr_2O_3	0.01	0.01	0.01	0.01	0.01	0.02	0.00	0.02	0.01
Fe_2O_3	1.37	0.83	0.16	1.39	0.97	0.46	0.13	2.04	1.72
FeO	29.16	29.52	31.87	28.80	29.70	29.78	28.62	28.31	30.26
MnO	0.91	0.23	0.50	0.73	1.38	0.77	3.35	2.15	2.75
MgO	3.98	2.47	3.75	3.34	2.93	4.01	3.03	3.02	4.43
CaO	6.18	8.92	5.40	7.77	7.20	6.25	6.30	6.75	3.20
Total	99.77	101.05	100.92	100.84	100.85	100.40	100.65	99.95	100.73
Si	3.00	3.00	3.03	2.99	3.01	3.02	3.01	2.98	2.98
Al	1.93	1.94	1.93	1.93	1.92	1.94	1.97	1.92	1.93
Fe^{3+}	0.08	0.05	0.01	0.08	0.06	0.03	0.01	0.12	0.10
ΣM2	2.01	1.99	1.94	2.01	1.98	1.97	1.98	2.05	2.03
Fe^{2+}	1.94	1.95	2.10	1.90	1.97	1.96	1.89	1.89	2.00
Mn	0.06	0.02	0.03	0.05	0.09	0.05	0.22	0.15	0.18
Mg	0.47	0.29	0.44	0.39	0.35	0.47	0.36	0.36	0.52
Ca	0.53	0.75	0.46	0.66	0.61	0.53	0.53	0.58	0.27
ΣM1	3.00	3.00	3.03	3.00	3.01	3.02	3.01	2.98	2.98
Total	8.00	8.00	8.00	8.00	8.00	8.00	8.00	8.00	8.00
X_{alm}	0.65	0.65	0.69	0.63	0.65	0.65	0.63	0.64	0.67
X_{grs}	0.18	0.25	0.15	0.22	0.20	0.18	0.18	0.19	0.09
X_{prp}	0.16	0.10	0.15	0.13	0.11	0.16	0.12	0.12	0.18
X_{sps}	0.02	0.01	0.01	0.02	0.03	0.02	0.07	0.05	0.06

Table A1.1 (Continued). Representative garnet analyses used in thermobarometric calculations (normalized to 12 O). Ferric iron calculated using the program AX (Holland and Powell, 1998). Abbreviations: m, mafic schist; s, metasandstone schist; seg, San Emigdio gneiss.

Sample	06SE16a	06SE74a	08SE479b	08SE475	08SE474	04SE1a	06SE14a	08SE270	08SE202
Lithology	s	m	m	m	m	seg	seg	seg	seg
SiO_2	38.95	37.95	37.77	37.87	37.96	37.81	39.11	37.81	37.76
TiO_2	0.00	0.01	0.04	0.02	0.01	0.01	0.02	0.01	0.00
Al_2O_3	20.97	20.29	20.28	20.53	20.57	21.45	20.58	20.64	21.23
Cr_2O_3	0.02	0.04	0.06	0.00	0.02	0.01	0.02	0.00	0.00
Fe_2O_3	0.00	1.34	1.03	0.00	0.40	1.85	0.00	1.50	1.43
FeO	32.51	25.42	27.50	30.73	27.43	28.09	28.59	28.87	28.39
MnO	0.99	5.80	2.94	0.96	3.48	1.06	0.76	1.86	1.28
MgO	5.46	2.40	2.45	3.40	3.19	5.18	5.28	4.00	5.06
CaO	1.94	7.65	8.07	5.79	6.83	5.32	5.34	5.72	5.03
Total	100.85	100.90	100.14	99.29	99.88	100.78	99.70	100.42	100.18
Si	3.05	3.01	3.01	3.03	3.02	2.96	3.07	2.99	2.97
Al	1.94	1.90	1.91	1.94	1.93	1.98	1.91	1.93	1.97
Fe^{3+}	0.00	0.08	0.06	0.00	0.02	0.11	0.00	0.09	0.08
ΣM2	1.94	1.98	1.97	1.94	1.95	2.09	1.91	2.01	2.06
Fe^{2+}	2.13	1.69	1.84	2.06	1.83	1.84	1.88	1.91	1.87
Mn	0.07	0.39	0.20	0.06	0.23	0.07	0.05	0.12	0.09
Mg	0.64	0.28	0.29	0.41	0.38	0.60	0.62	0.47	0.59
Ca	0.16	0.65	0.69	0.50	0.58	0.45	0.45	0.49	0.42
ΣM1	3.00	3.01	3.02	3.03	3.02	2.96	3.00	2.99	2.97
Total	7.98	8.00	8.00	8.00	8.00	8.00	7.97	8.00	8.00
X_{alm}	0.71	0.56	0.61	0.68	0.60	0.62	0.63	0.64	0.63
X_{grs}	0.05	0.22	0.23	0.16	0.19	0.15	0.15	0.16	0.14
X_{prp}	0.21	0.09	0.10	0.13	0.13	0.20	0.21	0.16	0.20
X_{sps}	0.02	0.13	0.07	0.02	0.08	0.02	0.02	0.04	0.03

Table A1.2. Representative biotite analyses used in thermobarometric calculations (normalized to 8 cations). Ferric iron calculated using the program AX (Holland and Powell, 1998). Abbreviations as in Table A1.1.

Sample	07SE17	06SE23	07SE19	06SE54	08SE476	08SE469	06SE9	08SE478	08SE467
Lithology	s	s	s	s	s	s	s	s	s
SiO_2	36.58	36.40	36.34	36.16	35.64	37.24	37.46	36.12	35.80
TiO_2	1.50	2.02	1.94	1.56	1.83	1.48	1.52	1.43	1.81
Al_2O_3	18.18	18.35	17.69	17.59	17.29	18.67	18.00	17.04	17.68
Cr_2O_3	0.05	0.05	0.04	0.06	0.09	0.10	0.06	0.07	0.01
Fe_2O_3	0.00	0.00	0.00	0.00	0.00	0.00	0.00	0.00	0.00
FeO	15.27	19.02	17.87	19.18	18.59	15.36	15.75	18.80	19.14
MnO	0.04	0.06	0.04	0.21	0.17	0.03	0.12	0.31	0.14
MgO	12.58	10.00	11.20	10.25	10.48	12.10	12.58	10.38	9.73
CaO	0.00	0.13	0.02	0.01	0.03	0.03	0.03	0.02	0.02
Na_2O	0.25	0.04	0.07	0.07	0.02	0.21	0.14	0.04	0.13
K_2O	8.63	8.73	9.25	9.20	9.26	8.73	8.72	9.34	9.39
Si	2.86	3.05	3.06	3.05	3.04	3.13	3.15	3.07	3.03
Al^{iv}	1.14	0.95	0.94	0.95	0.96	0.87	0.85	0.93	0.97
ΣT	4.00	4.00	4.00	4.00	4.00	4.00	4.00	4.00	4.00
Al^{vi}	0.54	0.87	0.81	0.80	0.77	0.99	0.93	0.78	0.79
Ti	0.09	0.13	0.12	0.10	0.12	0.09	0.10	0.09	0.12
Mg	1.47	0.71	0.80	0.73	0.76	0.86	0.90	0.75	0.70
Fe^{3+}	0.00	0.00	0.00	0.00	0.00	0.00	0.00	0.00	0.00
Fe^{2+}	1.00	1.33	1.26	1.35	1.33	1.08	1.11	1.34	1.35
Mn	0.00	0.00	0.00	0.02	0.01	0.00	0.01	0.02	0.01
Ca	0.00	0.01	0.00	0.00	0.00	0.00	0.00	0.00	0.00
Al	1.68	1.81	1.75	1.75	1.74	1.85	1.78	1.71	1.76
Na	0.04	0.01	0.01	0.01	0.00	0.03	0.02	0.01	0.02
K	0.86	0.93	0.99	0.99	1.01	0.94	0.94	1.01	1.01
ΣA	0.90	0.94	1.00	1.00	1.01	0.97	0.96	1.02	1.03
Total	8.00	8.00	8.00	8.00	8.00	8.00	8.00	8.00	8.00

Table A1.3. Representative muscovite analyses used in thermobarometric calculations (normalized to 7 cations). Ferric iron calculated using the program AX (Holland and Powell, 1998). Abbreviations as in Table A1.1.

Sample	07SE17	06SE23	07SE19	06SE54	08SE476	08SE469	06SE9
Lithology	s	s	s	s	s	s	s
SiO_2	45.92	47.17	46.50	46.43	46.33	46.66	46.85
TiO_2	0.56	0.76	0.50	0.58	0.83	0.61	0.48
Al_2O_3	34.54	33.16	33.72	33.77	34.29	34.11	32.53
Cr_2O_3	0.04	0.03	0.04	0.04	0.06	0.05	0.02
Fe_2O_3	0.00	0.00	0.00	0.00	0.71	0.00	0.00
FeO	0.91	1.57	1.52	1.17	0.76	1.11	1.14
MnO	0.00	0.00	0.00	0.01	0.00	0.00	0.01
MgO	1.02	1.52	1.33	1.54	1.32	1.09	1.53
CaO	0.01	0.03	0.00	0.00	0.01	0.01	0.00
Na_2O	1.37	0.76	0.92	0.81	0.72	1.34	1.08
K_2O	8.82	9.75	9.65	9.62	9.29	8.68	9.46
Si	3.11	3.16	3.13	3.13	3.14	3.15	3.19
Al^{iv}	0.89	0.84	0.87	0.87	0.86	0.85	0.81
ΣT	4.00	4.00	4.00	4.00	4.00	4.00	4.00
Al^{vi}	1.87	1.79	1.81	1.82	1.88	1.87	1.79
Ti	0.03	0.04	0.03	0.03	0.04	0.03	0.02
Mg	0.10	0.15	0.13	0.15	0.13	0.11	0.16
Fe^{3+}	0.00	0.00	0.00	0.00	0.04	0.00	0.00
Fe^{2+}	0.05	0.09	0.09	0.07	0.04	0.06	0.06
Mn	0.00	0.00	0.00	0.00	0.00	0.00	0.00
Ca	0.00	0.00	0.00	0.00	0.00	0.00	0.00
ΣM	2.06	2.07	2.05	2.07	2.10	2.08	2.04
Na	0.18	0.10	0.12	0.11	0.09	0.18	0.14
K	0.76	0.83	0.83	0.83	0.80	0.75	0.82
ΣA	0.94	0.93	0.95	0.93	0.90	0.92	0.96
Total	7.00	7.00	7.00	7.00	7.00	7.00	7.00

Table A1.4. Representative plagioclase analyses used in thermobarometric calculations (normalized to 8 O). Ferric iron calculated using the program AX (Holland and Powell, 1998). Abbreviations as in Table A1.1.

Sample	07SE17	06SE23	07SE19	06SE54	08SE476	08SE469	06SE9	08SE478	08SE467
Lithology	s	s	s	s	s	s	s	s	s
SiO_2	58.31	58.28	59.21	61.27	63.21	59.62	60.29	62.63	58.70
Al_2O_3	26.36	26.93	25.51	24.98	22.58	25.89	26.15	23.15	25.67
Fe_2O_3	0.06	0.38	0.48	0.16	0.54	0.18	0.18	0.22	0.24
FeO	0.00	0.00	0.00	0.00	0.00	0.00	0.00	0.00	0.00
CaO	8.16	8.34	7.26	5.82	3.19	7.43	6.74	4.54	7.50
Na_2O	7.05	7.06	7.88	8.13	9.26	7.55	6.70	9.46	7.57
K_2O	0.06	0.06	0.06	0.22	0.65	0.09	0.31	0.07	0.85
Total	100.00	101.04	100.41	100.58	99.43	100.76	100.37	100.08	100.53
Si	2.61	2.59	2.65	2.71	2.82	2.64	2.67	2.78	2.63
Al	1.39	1.41	1.34	1.30	1.19	1.35	1.36	1.21	1.35
Fe^{3+}	0.00	0.01	0.02	0.01	0.02	0.01	0.01	0.01	0.01
ΣT	4.00	4.01	4.01	4.02	4.03	4.00	4.04	4.00	3.99
Ca	0.39	0.40	0.35	0.28	0.15	0.35	0.32	0.22	0.36
Na	0.61	0.61	0.68	0.70	0.80	0.65	0.58	0.81	0.66
K	0.00	0.00	0.00	0.01	0.04	0.00	0.02	0.00	0.05
ΣM	1.01	1.01	1.03	0.99	0.99	1.01	0.91	1.03	1.07
Total	5.00	5.02	5.04	5.00	5.02	5.01	4.95	5.03	5.06
X_{an}	0.39	0.40	0.34	0.28	0.16	0.35	0.36	0.21	0.35
X_{ab}	0.61	0.60	0.66	0.72	0.84	0.65	0.64	0.79	0.65

Table A1.4 (Continued). Representative plagioclase analyses used in thermobarometric calculations (normalized to 8 O). Ferric iron calculated using the program AX (Holland and Powell, 1998). Abbreviations as in Table A1.1.

Sample	06SE16a	06SE74a	08SE479b	08SE475	08SE474	04SE1a	06SE14a	08SE270	08SE202
Lithology	s	m	m	m	m	seg	seg	seg	seg
SiO_2	60.87	63.62	61.31	60.70	59.38	58.22	59.02	60.07	54.86
Al_2O_3	24.78	23.28	23.67	24.13	24.52	26.15	26.67	25.07	29.00
Fe_2O_3	0.01	0.28	0.38	0.32	0.19	0.11	0.01	0.24	0.11
FeO	0.00	0.00	0.00	0.00	0.00	0.00	0.00	0.00	0.00
CaO	6.53	4.13	5.26	5.78	6.66	8.38	8.47	6.49	11.29
Na_2O	8.07	9.44	8.68	8.50	8.22	6.97	6.78	7.91	5.17
K_2O	0.07	0.06	0.07	0.08	0.08	0.06	0.15	0.16	0.06
Total	100.33	100.81	99.37	99.50	99.06	99.89	101.10	99.94	100.49
Si	2.70	2.80	2.75	2.72	2.68	2.61	2.61	2.68	2.46
Al	1.30	1.21	1.25	1.27	1.30	1.38	1.39	1.32	1.54
Fe^{3+}	0.00	0.01	0.01	0.01	0.01	0.00	0.00	0.01	0.00
ΣT	3.99	4.01	4.01	4.00	3.99	4.00	4.00	4.01	4.00
Ca	0.31	0.19	0.25	0.28	0.32	0.40	0.40	0.31	0.54
Na	0.69	0.80	0.75	0.74	0.72	0.61	0.58	0.68	0.45
K	0.00	0.00	0.00	0.00	0.00	0.00	0.01	0.01	0.00
ΣM	1.01	1.00	1.01	1.02	1.05	1.01	0.99	1.00	1.00
Total	5.00	5.01	5.02	5.03	5.04	5.01	4.99	5.01	5.00
X_{an}	0.31	0.19	0.25	0.27	0.31	0.40	0.41	0.31	0.55
X_{ab}	0.69	0.81	0.75	0.73	0.69	0.60	0.59	0.69	0.45

Table A1.5. Representative amphibole analyses used in thermobarometric calculations (normalized to 23 O). Ferric iron calculated using the program AX (Holland and Powell, 1998). Abbreviations as in Table A1.1.

Sample	06SE74a	08SE479b	08SE475	08SE474	04SE1a	06SE14a	08SE270	08SE202
Lithology	m	m	m	m	seg	seg	seg	seg
SiO_2	40.78	43.50	42.65	42.12	44.39	45.75	44.02	43.80
TiO_2	0.60	0.40	0.35	0.43	0.96	0.74	1.00	0.64
Al_2O_3	14.21	14.48	16.62	17.46	12.51	14.55	13.70	14.76
Fe_2O_3	3.03	1.14	1.47	1.30	2.68	2.41	1.32	0.87
FeO	16.53	14.32	14.20	12.75	11.06	11.47	13.68	14.46
MnO	0.43	0.28	0.11	0.26	0.08	0.09	0.19	0.14
MgO	7.65	9.25	8.15	8.83	11.70	10.84	9.79	9.05
CaO	11.23	11.48	10.83	11.20	11.29	10.35	11.37	11.69
Na_2O	1.88	1.81	1.86	1.80	1.35	1.24	1.48	1.26
K_2O	0.83	0.36	0.40	0.42	0.40	0.44	0.49	0.52
Total	97.17	97.03	96.64	96.57	96.42	97.88	97.03	97.10
Si	6.18	6.45	6.32	6.22	6.51	6.53	6.50	6.47
Al^{iv}	1.82	1.55	1.68	1.78	1.49	1.47	1.50	1.53
ΣT	8.00	8.00	8.00	8.00	8.00	8.00	8.00	8.00
Al^{vi}	0.71	0.97	1.22	1.26	0.67	0.98	0.88	1.04
Ti	0.07	0.05	0.04	0.05	0.11	0.08	0.11	0.07
Fe^{3+}	0.35	0.13	0.16	0.15	0.30	0.26	0.15	0.10
Fe^{2+}	2.11	1.78	1.77	1.58	1.37	1.38	1.69	1.79
Mn	0.06	0.04	0.01	0.03	0.01	0.01	0.02	0.02
Mg	1.73	2.04	1.80	1.94	2.56	2.31	2.15	1.99
ΣM1-M3	5.02	5.01	5.01	5.01	5.01	5.02	5.01	5.00
Ca	1.82	1.82	1.72	1.77	1.77	1.58	1.80	1.85
Na^{M4}	0.18	0.18	0.28	0.23	0.23	0.42	0.20	0.15
ΣM4	2.00	2.00	2.00	2.00	2.00	2.00	2.00	2.00
Na^{A}	0.37	0.34	0.25	0.29	0.16	0.00	0.22	0.21
K	0.16	0.07	0.08	0.08	0.08	0.08	0.09	0.10
ΣA	0.53	0.41	0.33	0.37	0.23	0.08	0.31	0.31
Total	15.55	15.42	15.34	15.37	15.24	15.10	15.32	15.31

Table A1.6. Bulk compositions of San Emigdio Schist from XRF analyses. "Prograde" compositions are H_2O-saturated. "Retrograde" compositions are H_2O-saturated and modified by subtracting garnet from "prograde" compositions. Abbreviations as in Table A1.1.

Sample	06SE23 prograde	06SE23 retrograde	08SE479b prograde	08SE479b retrograde
Lithology	s	s	m	m
Si	61.07	63.13	48.96	49.44
Al	15.20	13.90	15.50	15.35
Fe	4.00	2.69	12.00	10.87
Mn	0.04	-	0.10	-
Mg	3.28	3.20	4.58	4.76
Ca	2.63	1.89	9.10	9.13
Na	4.63	5.30	2.78	2.92
K	2.54	2.92	-	-
H	20.00	7.00	20.00	7.00

REFERENCES

de Capitani, C. and Brown, T. H., 1987, The computation of chemical equilibrium in complex systems containing non-ideal solutions: *Geochimica et Cosmochimica Acta*, **51**(10), 2639-2652.

Chakraborty, S. and Ganguly, J., 1992, Cation diffusion in aluminosilicate garnets; experimental determination in spessartine-almandine diffusion couples, evaluation of effective binary, diffusion coefficients, and applications: *Contributions to Mineralogy and Petrology*, **111**(1), 74-86.

Chakraborty, S. and Rubie, D. C., 1996, Mg tracer diffusion in aluminosilicate garnets at 750-850 degrees C, 1 atm. and 1300 degrees C, 8.5 GPa: *Contributions to Mineralogy and Petrology*, **122**(4), 406-414.

Connolly, J. A. D., 2009, The geodynamic equation of state: what and how: *Geochemistry, Geophysics, Geosystems*, **10:** Q10014, doi:10.1029/2009GC002540.

Diener, J. F. A., Powell, R., White, R. W. and Holland, T. J. B., 2007, A new thermodynamic model for clino- and orthoamphiboles in the system Na (sub 2) O-CaO-FeO-MgO-Al_2O_3 -SiO_2 -H_2O-O: *Journal of Metamorphic Geology*, **25**(6), 631-656.

Ganguly, J., Cheng, W. and Chakraborty, S., 1998, Cation diffusion in aluminosilicate garnets; experimental determination in pyrope-almandine diffusion couples: *Contributions to Mineralogy and Petrology*, **131**(2-3), 171-180.

Hacker, B. R. and Mosenfelder, J. L., 1996, Metamorphism and deformation along the emplacement thrust of the Samail Ophiolite, Oman: *Earth and Planetary Science Letters*, **144**(3-4), 435-451.

Holland, T. J. B. and Powell, R., 1998, An internally consistent thermodynamic data set for

phases of petrological interest: *Journal of Metamorphic Geology*, **16**(3), 309-343.

Johnson, D. M., Hooper, P. R. and Conrey, R. M., 1999, XRF Analysis of Rocks and Minerals for Major and Trace Elements on a Single Low Dilution Li-tetraborate Fused Bead: *Advances in X-Ray Analysis*, **41**, 843-867.

Schwandt, C. S., Cygan, R. T. and Westrich, H. R., 1996, Ca self-diffusion in grossular garnet: *American Mineralogist*, **81**(3-4), 448-451.

Vielzeuf, D., Baronnet, A., Perchuk, A. L., Laporte, D. and Baker, M. B., 2007, Calcium diffusivity in alumino-silicate garnets; an experimental and ATEM study: *Contributions to Mineralogy and Petrology*, **154**(2), 153-170.

APPENDIX 2

Supporting information and data repository for:

Late Cretaceous gravitational collapse of the southern Sierra Nevada batholith, California

1. ANALYTICAL METHODS

1.1. LA-MC-ICPMS

With the exception of samples 91TH181, 93TH417, and 91TH140, U-Pb geochronology of igneous and detrital zircons was conducted by laser ablation multicollector inductively coupled mass spectrometry (LA-MC-ICPMS) at the Arizona LaserChron Center (ALC) following the methods outlined in Gehrels *et al*. (2006). Zircon grains were extracted from plutonic and metamorphic samples using standard mineral separation techniques of crushing, sieveing, magnetic separation, processing through heavy liquids, and hand picking. Separates were then mounted in epoxy, polished, and imaged on the Caltech Zeiss 1550 VP field emission scanning electron microscope before analysis. Representative cathodoluminescence images are shown in Figure A2.1. Zircons were ablated using a 193 nm ArF laser with a pit depth of ~12 μm and spot diameters of 25-30 μm depending on grain size. Data reduction was done using in-house ALC Microsoft Excel programs and ISOPLOT/Ex Version 3 (Ludwig, 2003).

Figure A2.1 Representative cathodoluminescence images of selected zircon grains from samples 08SE46 (a and b), 08SE451 (c), 08SE675 (d), 08SE450 (e), 08SE674 (f), 04SE5 (g), 10TC5 (h), 06SE19a (i), 08SE596 (j), 09SE23 (k), G11 (l), 08SE258 (m), and 07BC60 (n and o).

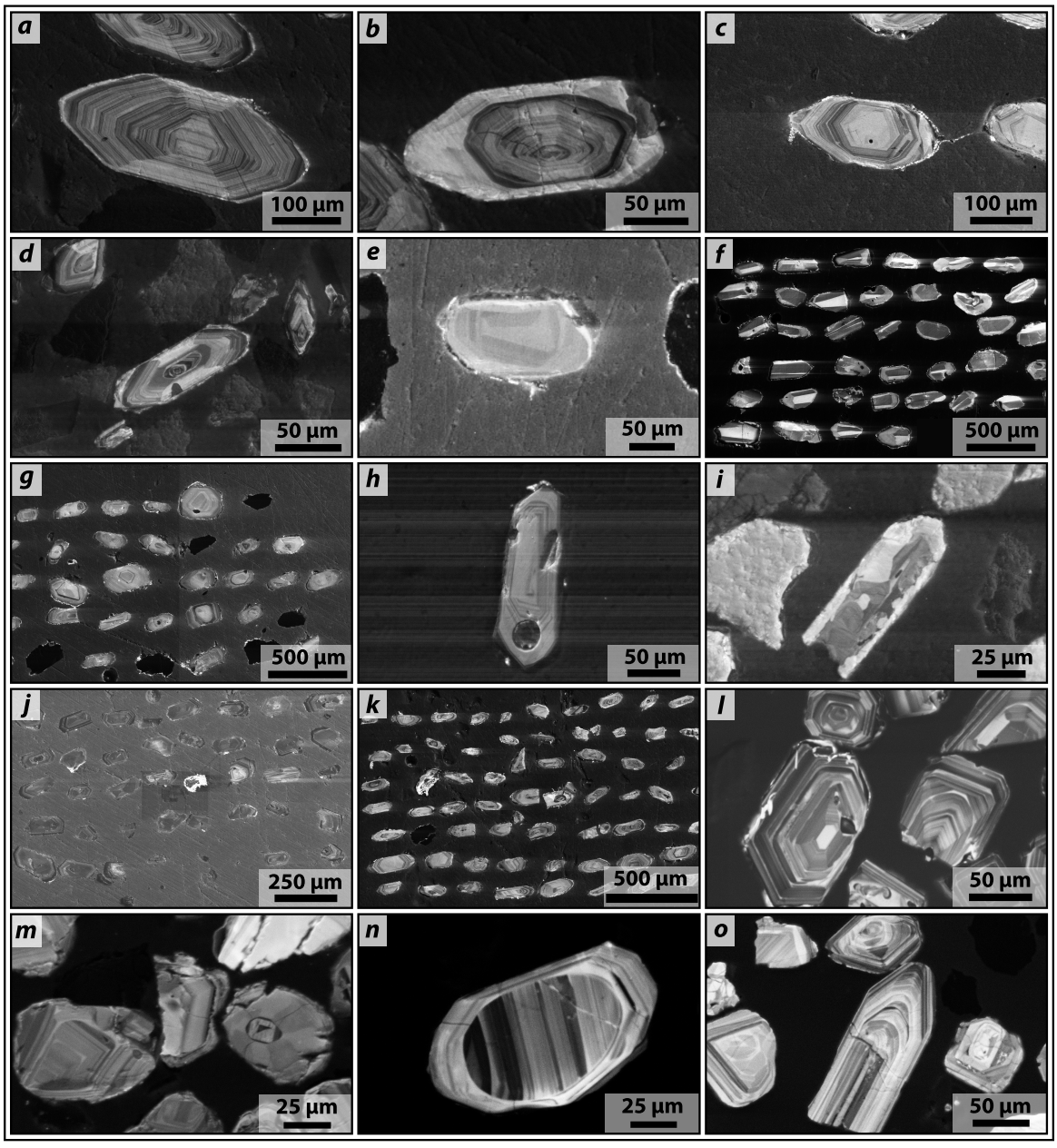
a
100 µm
b
50 µm
c
100 µm
d
50 µm
e
50 µm
f
500 µm
g
500 µm
h
50 µm
i
25 µm
j
250 µm
k
500 µm
l
50 µm
m
25 µm
n
25 µm
o
50 µm

1.2. Isotope dilution analyses

Zircons from samples 91TH181, 93TH417, and 91TH140 were separated from 2-10 kg rock samples for TIMS-isotopic dilution analysis. Magnetic separation procedures were aimed towards maximum sample purity and selection of highest integrity grains. Non- or paramagnetic zircon was taken from Franz Isodynamic Separator runs with a front slope of 20° and a side slope of either 0° or -1°. After initial washing in 8N, and sieving in expendable nylon sieves, the fractions to be analyzed were picked to 100 percent purity by inspection of each grain. Only well-faceted clear euhedral grains lacking visible inclusions or cores were accepted.

Zircon separates were weighed into a TFE bomb capsule and then given an additional 15-minute warm wash with ultrapure concentrated HNO_3. Dissolution was performed in concentrated ultrapure HF with a drop of ultrapure concentrated HNO_3 at 235°C for 3 days. Following dissolution, the samples were evaporated and re-bombed overnight in ultrapure 6N HC1 prior to spiking. Samples were then spiked with a mixed $^{205}Pb/^{235}U$ tracer, and equilibration was obtained in hot 6N HCL within a sealed PFA container overnight on a hotplate.

Dissolution and chemical extraction techniques for zircon entailed cycles of 2N, 3N and 6N HCl, similar to those described in Krogh (1973). Mass spectrometry was performed on a VG Sector multicollector instrument. Pb and U were run on outgassed Re single filaments with silica gel and graphite loads, respectively. Pb was ionized at ~1400°C and U at ~2000°C, yielding typical ion beam currents of 1 to 5 x 10^{-11} A. Regular inter-calibrations of the multiple detector system yielded stabilities at the 10-ppm level for time periods

typically in excess of several hours, and thus Pb and U were run in a static multicollector mode. $^{206}Pb/^{204}Pb$ ratios were measured with the ^{204}Pb beam directed into a Daly deflection knob-photomultiplier system. The gain factor was stable within 5 per mil over the course of the Pb runs. A 0.13±0.05/amu mass fractionation correction was applied to both U and Pb runs based on replicate analyses of NBS 982, 983 and U500 standards. Uncertainties in radiogenic $^{206}Pb/^{238}U$ and radiogenic $^{207}Pb/^{206}Pb$ were calculated as in technique described in Saleeby *et al*. (2008).

1.3. (U-Th)/He zircon analyses

(U-Th)/He zircon ages were determined for a subset of samples studied by apatite He (Mahéo *et al*., 2009). Three to seven grains were analyzed per sample and the results were averaged. Following the methods outlined in Farley (2002), molybdenum crucibles with two depressions were used to hold the sample while heated. Individual zircon grains were placed in one depression with a ruby ball on top to prevent the zircon from leaving the capsule, and the other depression was heated with a laser to a temperature of approximately 1400°C to extract helium. The extracted gas was spiked with a known aliquot of ^{3}He, and the $^{4}He/^{3}He$ ratio was measured.

The grain was then dissolved in HF within a pressurized bomb for approximately 48 hours. The sample was spiked with a known thorium and uranium content. Then the HF was evaporated, the sample was re-dissolved with HCl to break up any salts that could have formed between Th or U and F. Finally, the sample was dried down and heated slightly on a hot plate with HNO_3 to run through the mass spectrometer. The Th and U isotopes were then

measured on an inductively coupled mass spectrometer. The results were compared to a normal and a spike blank, and an age is calculated using a corrected mass that helps to account for helium ejection and diffusion from the grain (Farley 2002).

1.4. Thermobarometry

Electron microprobe analyses were performed using a JEOL8200 system (California Institute of Technology) except for sample 31001-5, which was analyzed with a Cameca SX50 microprobe (University of Arizona). Each system is equipped with 5 LiF, PET, and TAP crystal spectrometers. Major element concentrations were measured in point analyses at 15 kV accelerating voltage and a 25 nA beam current with 60 s count times, using natural and synthetic standards, and the CITZAF correction algorithm. Garnet analyses were done in spot mode, while plagioclase, hornblende, and biotite grains were measured using a 5 μm beam width.

Equilibrium *P-T* conditions were calculated from metamorphic pendant rocks using the internally consistent average *P-T* mode in THERMOCALC, version 3.26 (Powell and Holland, 1994; Holland and Powell, 1998). Thermobarometry was done on garnet-bearing metapelitic assemblages. *P-T* conditions for pendant rocks were calculated from garnet + cordierite + sillimanite + quartz (sample 31001-5), garnet + cordierite + andalusite + quartz + plagioclase + biotite (sample 08TC29), and garnet + sillimanite + plagioclase + quartz (sample 10SE41) assemblages interpreted, based on chemical and textural evidence, to have equilibrated during peak metamorphism. For metamorphic pendant samples, we use garnet rim compositions where Mg# is highest suggesting garnet growth at peak temperatures (Spear, 1993). All calculations were done assuming a water activity of unity, due to the

abundance of hydrous phases. Hornblende-plagioclase thermometry (Holland and Blundy, 1994) and aluminum-in-hornblende barometry (Hammarstrom and Zen, 1986; Hollister *et al*., 1987; Johnson and Rutherford, 1989; Schmidt, 1992; Anderson and Smith, 1995) were applied to plutonic assemblages interpreted, based on chemical and textural evidence, to have equilibrated during crystallization attending emplacement. Anderson and Smith (1995) pressures were calculated by iteration using Holland and Blundy (1994) temperatures. Results from thermobarometric work and representative mineral compositions are summarized in Tables 4.3, 4.4, A2.8, A2.9, and A2.10.

1.5. Geochemistry

Two samples of basaltic sheeted dikes and one sample of pillow basalt from the WSEMC as well as two samples of dacitic metatuff from the Bean Canyon pendant were analyzed for major, minor, and trace elements by X-ray fluorescence (XRF) and inductively coupled plasma-mass spectrometry (ICP-MS). Weathering rinds and mineralized veins were removed to avoid contamination. Whole-rock compositions for WSEMC and Bean Canyon samples are presented in Table A2.11. XRF measurements were done at the GeoAnalytical Laboratory of Washington State University following the methods of Johnson *et al*. (1999). ICP-MS analyses were done at the same facility using a combination fusion-dissolution method that effectively decomposes refractory mineral phases and removes the bulk of unwanted matrix elements. Of the WSEMC samples, 2 were analyzed for Sr and Nd isotopes by thermal ionization mass spectrometry (TIMS) at the University of Arizona (Table A2.11).

2. MULTIDIMENSIONAL SCALING OF U-PB DETRITAL ZIRCON DATA

The Multidimensional scaling (MDS) method used in this study was inspired by Dr. Pieter Vermeesch, who provided a Matlab script for MDS of U-Pb zircon ages. To my knowledge, this is the first application of MDS to U-Pb detrital zircon age data, aside from unpublished work by P. Vermeesch. The MDS mapping algorithm used to compare U-Pb detrital zircon spectra is as follows: 1) input square, symmetric matrix of K-S distances between samples; 2) assign points to arbitrary coordinates in 2-dimensional space; 3) Compute K-S distances among all pairs of points, to form a new matrix; 4) Compare the new matrix with the input matrix by evaluating the stress function, a measure of the degree of correspondence between the observed and reproduced distances; 5) perturb the coordinates of each data point; and 6) repeat steps 2 through 5 until stress is minimized. The resuting 2-dimensional map (Figure 4.7) should be interpreted as follows. The degree of similarity in U-Pb detrital zircon age spectra is higher for samples that plot close to each other than for samples that are positioned farther apart. The reader is referred to Borg and Groenen (1997) for a comprehensive treatment of MDS.

3. SAMPLE PETROGRAPHY

3.1. Plutonic rocks

G11

Guadalupe two-pyroxene gabbro. See Saleeby *et al*. (1989) for petrographic description.

K16b-87

South tonalite of Vergeles. Light gray, medium-grained hypidiomorphic-granular quartz monzodiorite. Biotite and hornblende are the dominant mafic minerals. Accessory minerals: sphene, apatite, epidote, and zircon. Local alteration of hornblende and biotite to chlorite.

91TH181

Claraville granodiorite, Mendiburu Canyon phase. Light gray, medium- to coarse-grained porphyritic hornblende biotite granodiorite. 1-2 cm K-feldspar phenocrysts in subhedral granular matrix. Accessory minerals: apatite, allanite, and zircon. Minor alteration of plagioclase to sericite and biotite to chlorite.

93TH417

Claraville granodiorite, Bootleg Canyon phase. Light gray, medium-grained, equigranular sphene hornblende biotite granodiorite. Cataclasis and hydrothermal alteration common. Quartz is commonly fractured, biotite are crinkled and chloritized, and plagioclase is saussuritized.

94KK27

Unnamed granodiorite. Light gray, medium-grained hornblende biotite granodiorite. Accessory sphene is euhedral with well-developed concentric zoning. Other accessory minerals: magnetite and zircon.

04SE5

Lebec granodiorite. Medium- to coarse-grained, light orange granular hornblende biotite granodiorite. Quartz, K-feldspar, and plagioclase have consertal texture. Interstitial hornblende is closely associated with biotite. Hornblende and biotite are variably chloritized. Plagioclase is sericitized. Minor zircon, sphene, and opaques.

06SE19a

Lebec granodiorite. Escapula Peak phase. Medium- to coarse-grained, light gray granular biotite granodiorite with skeletal garnet porphyroblasts. Quartz, K-feldspar, and plagioclase display consertal texture with interstitial biotite. Alteration is minor, with local chloritization of biotite and sericitation of plagioclase.

07SE94

San Emigdio gneiss. Brown, medium-grained, foliated, hornblende-bearing quartz diorite gneiss. 1 cm skeletal garnet porphyroblasts with trondhjemitic halos and blebby quartz inclusions. Minor biotite, ilmenite, rutile, zircon, K-feldspar, and apatite. Minor alteration of hornblende and garnet to chlorite. Quartz is undulose.

08TC27a

Granodiorite of Gamble Spring Canyon. Dark gray, medium- to coarse-grained, porphyritic granular, hornblende biotite granodiorite. Hornblende is closely associated with biotite. Accessory ilmenite, sphene, zircon, and apatite. Plagioclase is variably sericitized.

08SE46

San Emigdio tonalite. Gray, medium- to coarse-grained, weakly foliated biotite tonalite. Alteration is minor.

08SE256

Lebec granodiorite, Escapula Peak phase. Strongly sheared garnetiferous leuco-granodiorite collected adjacent to the Salt Creek pendant. K-feldspar and plagioclase phenocrysts and skeletal garnet porphyroblasts are set within a deformed quartz matrix. Quartz is characterized by grain boundary migration and strong crystallographic preferred orientation. Secondary chlorite and sericite are abundant. Minor biotite, opaques, and zircon.

08SE262

San Emigdio tonalite. Light pink, medium-grained, weakly foliated leucotonalite. Biotite makes up about 5 percent of this rock. Alteration is minor. The sampled outcrop is unconformably overlain (depositional contact) by the Uvas formation.

08SE429

Unnamed quartz monzonite. Light gray to green, medium-grained, equigranular monzonite. Mafic minerals include hornblende and clinopyroxene. Alteration of hornblende by chlorite and plagioclase by sericite is common. Minor apatite and opaques.

08SE450

San Emigdio gneiss. Brown, medium-grained, foliated, hornblende-bearing quartz diorite gneiss. Strong shape preferred orientation in hornblende. Minor biotite, ilmenite, K-feldspar, zircon, and epidote. Minor alteration of hornblende to chlorite and plagioclase to sericite. Biotite-rich shear bands anastomose through sample and outcrop.

08SE451

Antomony Peak tonalite. Light gray, medium- to coarse-grained, porphyritic, massive to penetratively foliated, hornblende-biotite tonalite containing mainly plagioclase, quartz, hornblende, and K-feldspar, with minor amounts of garnet, biotite, epidote, apatite, sphene, and ilmenite. Where hypidiomorphic granular (igneous) textures are not overprinted by metamorphic foliation, the epidote occurs as subhedral replacement products of embayed hornblende and retains distinct core and rim regions, consistent with a magmatic origin. Original petrographic relationships are locally obscured by extensive seritization and chloritization. Hornblende-rich mafic schlieren are found in the same outcrop as 08SE451.

08SE463

Unnamed quartz monzonite. Gray, coarse-grained, equigranular hornblende clinopyroxene quartz monzonite. Mafic minerals, plagioclase, and K-feldspar are highly altered to sericite, chlorite, and secondary epidote. Minor apatite, calcite, and opaques.

08SE582

Antomony Peak tonalite. Light gray, medium-grained, porphyritic, foliated, hornblende

tonalite. Epidote phenocrysts embayed in hornblende. Minor K-feldspar, apatite, zircon, and ilmenite. Plagioclase, epidote, and hornblende are altered to chlorite, sericite, and opaques. Approximately 5μm-wide cross-cutting veins filled with secondary epidote, apparently injecting the host rock, may represent devitrified pseudotachylyte.

08SE596

Granite of Brush Mountain. Light pink, coarse-grained, granular biotite granite. Porphyritic K-feldspar is microperthitic. Accessory zircon. Biotite is somewhat chloritized and plagioclase is sericitized.

08SE674

Digier Canyon quartz diorite gneiss. Foliated, dark green to black, hornblende-bearing quartz diorite. Minor rutile, ilmenite, apatite, zircon, K-feldspar, and secondary chlorite and sericite.

08SE675

San Emigdio tonalite. Foliated garnet-biotite leucotonalite. Similar in appearance to the 101 Ma "Garnet-biotite tonalite of Grapevine" of Pickett and Saleeby (1993, 1994). Epidote phenocrysts embayed in biotite. Garnet is 0.5-1 mm in diameter with blebby quartz inclusions. Accessory minerals include zircon, apatite, and opaques. Very little alteration. Radiation-damage halos surrounding zircon inclusions in biotite are common.

08SE679

Digier Canyon quartz diorite gneiss. Brownish-green, medium-grained, hornblende-clinopyroxene gabbro. Weakly developed solid state foliation. Clinopyroxene are altered to epidote, sericite, and chlorite and are found within hornblende cores. Secondary sphene, opaques, and zircon.

10SE1

Granite of Brush Mountain. Dark brown, fine- to medium-grained hornblende gabbro enclave. Rock is essentially bimineralic (hornblende + plagioclase) with minor K-feldspar, quartz, and ilmenite. Alteration of K-feldspar to sericite and hornblende to chlorite are common.

10TC5

Granodiorite of Gato Montes. Light orange-brown medium-grained biotite granodiorite. Dark brown biotite cores locally stained red due to chlorite alteration. Minor alteration of plagioclase to sericite. Accessory minerals: ilmenite, apatite, zircon, and monazite.

3.2. Metamorphic pendant rocks

91TH140

Oaks metavolcanics. Metamorphosed pumice lapilli silicic tuff: finely recrystallized laminated tuff with remnants of fine quartz phenocrysts, pumice lapilli recrystallized to biotite+quartz, and faintly schistose groundmass consisting of quartz, feldspar, biotite and sericite.

31001-5

Sur series metapelitic schist. Garnet + cordierite + sillimanite + quartz + K-feldspar + biotite metapelitic schist with secondary plagioclase and muscovite. Cordierite is locally altered to pinite, K-feldspar is microperthitic, and garnet is homogeneous with Mn "kick-ups" at rims. Accessory minerals: zircon and ilmenite.

07BC60

Bean Canyon pendant quartzite. Nearly pure quartzite with minor biotite, muscovite, plagioclase, and andalusite. Biotite define a faint foliation surrounded by polygonal aggregates of quartz.

07TM10

Bean Canyon pendant metavolcanics. Metamorphosed porphyritic silicic tuff. 1-5 mm plagioclase porphyroblasts are set in a fine-grained and annealed (120˚ grain boundaries in quartz) quartz+biotite schistose matrix. Relict pumice lapilli recrystallized to biotite+quartz. Plagioclase is mildly sericitized. Accessory zircon and opaques.

08TC29

Tylerhorse Canyon pendant metapelitic schist. Garnet + cordierite + andalusite + quartz + plagioclase + biotite metapelitic schist. Foliation is characterized by alternating garnet-rich and garnet-poor bands. Garnet is homogeneous. Alteration is minor.

08TC44

Tylerhorse Canyon pendant impure quartzite. Quartz + muscovite + biotite + cordierite + andalusite + tourmaline metasandstone. Polygonal aggregates of quartz define an annealed texture. Accessory tourmaline, zircon, and graphite are especially prevalent in veins.

08SE258

Salt Creek pendant metaturbidite. Sillimanite + cordierite + biotite + muscovite + plagioclase + quartz metapsammite. The foliation consists of alternating sillimanite + biotite and quartz + plagioclase layers. Plagioclase is highly sericitized. Blocky pods of fibrolitic sillimanite probably represent pseudomorphs after andalusite. Adjacent sample 08SE259 contains garnet porphyroblasts.

10SE41

Salt Creek pendant migmatitic gneiss. Garnet + sillimanite + plagioclase + quartz + biotite migmatitic gneiss with accessory hornblende, ilmenite, and zircon. The rock contains ~1 cm garnet and sillimanite porphyroblasts in a granular matrix. Dikelets of host Lebec granodiorite truncate gneissose foliation. Garnet is homogeneous. Alteration is minor.

3.3. Western San Emigdio mafic complex

09SE21A

Metamorphosed sheeted dike. Hornfelsic groundmass consists mainly of hornblende and recrystallized plagioclase laths. Epidote + calcite veins truncate sample. The equilibrium

assemblage of hornblende + plagioclase + epidote suggests metamorphism at albite-epidote hornfels to hornblende hornfels facies.

09SE21B

Metamorphosed sheeted dike. Sample is coarser grained than 09SE21A, yet still exhibits hornfelsic texture. Groudmass consists mainly of hornblende and diopsidic clinopyroxene. Plagioclase lath relics (up to 0.5 mm) are better-preserved than 09SE21A. Epidote-, garnet-, and calcite-filled endoskarn veins truncate the sample. The equilibrium assemblage of hornblende + clinopyroxene + plagioclase suggests metamorphism at hornblende hornfels facies.

09SE23

White Ridge tonalite. Gray, coarse-grained, granular hornblende tonalite. Plagioclase is sericitized.

09SE32B

Metamorphosed pillow basalt with hornfelsic texture. Groudmass consists mainly of hornblende and plagioclase lath relics with scattered epidote. The equilibrium assemblage of hornblende + plagioclase + epidote suggests metamorphism at albite-epidote hornfels to hornblende hornfels facies.

Table A2.1 LA-MC-ICPMS U-Pb zircon data for plutonic and metavolcanic rocks of the southern Sierra Nevada batholith.

Analysis	U	^{206}Pb	U/Th	Isotope ratios							Isotopic ages (Ma)[§]					
				$^{206}Pb^*$	±	$^{207}Pb^*$	±	$^{206}Pb^*$	±	Error	$^{206}Pb^*$	±	$^{207}Pb^*$	±	$^{206}Pb^*$	±
	(ppm)	^{204}Pb		$^{207}Pb^*$	(%)	$^{235}U^*$	(%)	^{238}U	(%)	correlation	^{238}U	(Ma)	$^{235}U^*$	(Ma)	$^{207}Pb^*$	(Ma)
Sample 08SE46		*Antimony Peak tonalite*														
08SE46-01	333	8700	2.5	19.7945	11.0	0.1582	12.1	0.0227	5.1	0.42	144.8	7.3	149.2	16.8	218.9	255.2
08SE46-02	913	28962	1.7	20.5577	2.1	0.1611	3.4	0.0240	2.7	0.78	153.0	4.1	151.6	4.8	130.7	49.8
08SE46-03	521	12118	1.6	21.1743	7.7	0.1329	8.7	0.0204	4.1	0.47	130.3	5.3	126.7	10.4	60.7	184.1
08SE46-04	273	10039	2.9	21.6953	9.2	0.1428	9.5	0.0225	2.4	0.25	143.3	3.4	135.6	12.0	2.5	221.5
08SE46-05	304	9232	2.2	21.0099	8.0	0.1501	8.5	0.0229	2.7	0.32	145.8	3.9	142.0	11.2	79.2	190.7
08SE46-06	492	23280	3.6	20.4454	5.8	0.1689	7.4	0.0250	4.6	0.62	159.4	7.2	158.4	10.9	143.6	137.3
08SE46-07	358	8913	2.3	22.4983	8.1	0.1397	8.5	0.0228	2.6	0.31	145.3	3.8	132.8	10.6	-85.8	199.4
08SE46-08	383	14231	2.8	21.3560	9.0	0.1522	9.2	0.0236	1.9	0.20	150.2	2.8	143.8	12.4	40.3	216.8
08SE46-09	117	2273	5.0	27.3892	40.0	0.0875	40.1	0.0174	3.3	0.08	111.1	3.6	85.2	32.8	-592.5	1121.8
08SE46-10	277	5889	3.2	22.4633	14.1	0.1278	14.2	0.0208	2.0	0.14	132.8	2.6	122.1	16.4	-82.0	346.7
08SE46-11	181	7662	5.7	20.5153	16.7	0.1407	17.1	0.0209	3.7	0.22	133.6	4.9	133.7	21.4	135.6	394.1
08SE46-12	344	12886	4.7	20.7827	5.2	0.1399	5.6	0.0211	2.1	0.38	134.5	2.8	133.0	7.0	105.0	122.1
08SE46-13	449	13492	5.3	20.5222	8.0	0.1484	8.4	0.0221	2.7	0.32	140.8	3.7	140.5	11.0	134.7	187.5
08SE46-14	1120	33274	71.9	20.9767	5.5	0.1075	5.8	0.0163	1.8	0.31	104.5	1.8	103.6	5.7	83.0	130.0
08SE46-15	319	9836	4.3	21.5082	12.0	0.1368	12.7	0.0213	4.2	0.33	136.1	5.6	130.2	15.5	23.3	288.6
08SE46-16	656	24051	4.6	21.0751	4.9	0.1394	5.5	0.0213	2.4	0.44	135.9	3.2	132.5	6.8	71.9	116.4
08SE46-17	551	23234	3.4	19.5260	5.9	0.1451	6.0	0.0205	1.1	0.18	131.1	1.4	137.6	7.7	250.4	135.2
08SE46-18	352	13418	3.7	19.9698	10.2	0.1451	10.8	0.0210	3.5	0.33	134.1	4.7	137.6	13.8	198.5	236.7
08SE46-20	350	13234	10.3	21.2977	8.7	0.1334	9.1	0.0206	2.4	0.27	131.5	3.2	127.2	10.8	46.8	209.1
08SE46-21	500	19829	8.0	20.9730	6.1	0.1233	6.2	0.0188	1.0	0.15	119.8	1.1	118.1	6.9	83.4	145.3
08SE46-22	301	9709	4.1	20.6188	10.2	0.1434	10.3	0.0214	1.7	0.17	136.8	2.3	136.1	13.1	123.7	240.2
08SE46-23	357	7026	4.1	20.4494	6.2	0.1456	6.8	0.0216	2.8	0.41	137.7	3.8	138.0	8.7	143.1	145.0
08SE46-24	373	13490	6.6	20.6791	11.6	0.1464	12.0	0.0220	3.0	0.25	140.0	4.1	138.7	15.6	116.8	274.9
08SE46-25	352	14764	4.6	22.9303	8.4	0.1277	8.9	0.0212	2.8	0.32	135.5	3.7	122.0	10.2	-132.6	208.5
08SE46-26	282	9508	5.5	21.2653	12.7	0.1351	13.1	0.0208	3.1	0.24	132.9	4.1	128.6	15.9	50.5	305.4
08SE46-27	994	30420	47.9	20.4952	2.6	0.1076	4.4	0.0160	3.6	0.82	102.3	3.7	103.8	4.4	137.8	60.3
08SE46-28	307	16435	6.7	21.8456	17.9	0.1350	18.0	0.0214	2.6	0.14	136.5	3.5	128.6	21.8	-14.2	434.5
08SE46-29	428	22154	5.1	20.5983	9.9	0.1426	10.1	0.0213	1.7	0.17	135.9	2.3	135.4	12.8	126.1	234.2
08SE46-30	458	19846	4.5	20.3831	7.2	0.1397	7.7	0.0207	2.7	0.36	131.8	3.6	132.8	9.5	150.7	168.0
08SE46-31	183	5674	4.8	20.0201	14.2	0.1419	14.4	0.0206	2.3	0.16	131.4	3.0	134.7	18.1	192.7	330.8
08SE46-32	611	12580	40.1	22.3028	14.1	0.0973	14.3	0.0157	2.5	0.17	100.7	2.5	94.3	12.9	-64.5	346.3
08SE46-33	244	4539	4.5	22.9651	21.5	0.1252	21.7	0.0209	2.8	0.13	133.1	3.6	119.8	24.5	-136.4	537.1
08SE46-34	1536	46267	99.7	20.5866	2.5	0.1095	3.7	0.0163	2.7	0.73	104.5	2.8	105.5	3.7	127.4	59.5
08SE46-35	423	15662	3.4	21.5791	10.0	0.1399	10.2	0.0219	1.9	0.18	139.7	2.6	133.0	12.7	15.4	241.2
08SE46-36	199	7019	9.2	22.7278	34.0	0.0982	34.3	0.0162	4.5	0.13	103.5	4.6	95.1	31.1	-110.7	858.3
08SE46-37	377	12501	4.2	22.2706	10.1	0.1275	10.3	0.0206	1.6	0.16	131.4	2.1	121.9	11.8	-60.9	247.8
Sample 08SE262		*Antimony Peak tonalite*														
265-1	320	8740	2.6	19.4672	7.1	0.1633	7.5	0.0231	2.4	0.32	146.9	3.5	153.6	10.7	257.4	163.3
265-2	93	3780	4.0	22.5515	13.6	0.1394	13.9	0.0228	2.7	0.19	145.3	3.9	132.5	17.3	-91.6	335.8
265-3	70	1788	4.4	12.7913	55.8	0.2135	56.6	0.0198	9.5	0.17	126.5	11.8	196.5	101.5	1151.4	1211.2
265-4	269	6612	3.0	20.3937	12.9	0.1431	13.1	0.0212	2.6	0.20	135.0	3.5	135.8	16.7	149.5	302.4
265-5	359	8604	8.7	20.3347	8.8	0.1385	9.0	0.0204	2.0	0.22	130.3	2.5	131.7	11.1	156.3	206.0
265-6	252	5524	2.4	18.3094	15.4	0.1578	15.4	0.0210	1.3	0.08	133.7	1.7	148.8	21.4	396.5	346.5
265-9	139	3396	6.9	18.2264	22.5	0.1571	22.7	0.0208	2.8	0.12	132.5	3.6	148.1	31.2	406.7	509.1
265-10	173	4000	3.1	21.9991	16.8	0.1328	16.9	0.0212	1.3	0.08	135.2	1.7	126.6	20.1	-31.1	410.0
265-11	279	6272	3.0	19.6795	8.0	0.1495	8.2	0.0213	1.8	0.22	136.1	2.4	141.5	10.8	232.4	184.0
265-12	148	3504	4.0	21.5168	20.7	0.1422	21.0	0.0222	3.4	0.16	141.5	4.8	135.0	26.6	22.3	502.1
265-13	138	3320	3.1	19.0678	15.5	0.1558	15.6	0.0215	1.7	0.11	137.4	2.3	147.0	21.4	304.8	355.6
265-14	277	3120	3.0	19.6913	12.0	0.1412	12.3	0.0202	2.5	0.20	128.7	3.2	134.1	15.4	231.0	278.6
265-16	61	1468	10.6	12.7433	54.6	0.2084	54.9	0.0193	5.5	0.10	123.0	6.7	192.2	96.3	1158.8	1177.4
265-17	215	4884	3.7	19.4645	7.2	0.1565	7.7	0.0221	2.5	0.33	140.9	3.5	147.6	10.5	257.7	166.5
265-18	146	4528	3.1	21.3312	17.3	0.1492	17.4	0.0231	1.4	0.08	147.1	2.0	141.2	22.9	43.1	417.1
265-19	173	4476	2.4	21.1448	13.7	0.1373	13.9	0.0211	2.5	0.18	134.3	3.3	130.7	17.0	64.0	326.4
265-20	280	6648	2.4	20.7088	7.3	0.1449	7.7	0.0218	2.6	0.34	138.8	3.6	137.4	9.9	113.4	171.6

Table A2.1 (Continued).

Analysis	U (ppm)	$^{206}Pb/^{204}Pb$	U/Th	Isotope ratios							Isotopic ages (Ma)[§]					
				$^{206}Pb^*/^{207}Pb^*$	± (%)	$^{207}Pb^*/^{235}U^*$	± (%)	$^{206}Pb^*/^{238}U$	± (%)	Error correlation	$^{206}Pb^*$ ^{238}U	± (Ma)	$^{207}Pb^*$ $^{235}U^*$	± (Ma)	$^{206}Pb^*$ $^{207}Pb^*$	± (Ma)
265-21	101	3868	5.4	25.6979	105.4	0.1176	105.4	0.0219	2.8	0.03	139.8	3.9	112.9	113.1	-422.6	1440.5
265-22	129	4576	3.7	23.5078	39.1	0.1323	39.1	0.0226	2.0	0.05	143.8	2.8	126.1	46.4	-194.5	1011.7
265-23	204	4312	3.3	22.0076	9.2	0.1296	9.8	0.0207	3.2	0.32	132.0	4.1	123.7	11.4	-32.1	224.6
265-24	150	5032	3.2	22.2718	16.7	0.1378	16.8	0.0223	1.7	0.10	141.9	2.4	131.1	20.7	-61.1	410.6
265-25	99	728	4.7	11.0307	23.2	0.2765	23.3	0.0221	1.7	0.07	141.1	2.3	247.9	51.2	1439.4	448.3
265-26	131	4608	3.6	17.4608	9.1	0.1764	9.2	0.0223	1.1	0.12	142.4	1.5	165.0	14.0	502.0	200.7
265-27	116	2400	3.4	18.2013	32.9	0.1598	33.1	0.0211	3.4	0.10	134.6	4.5	150.6	46.4	409.8	755.3
265-28	320	3452	10.1	19.5443	7.7	0.1469	7.8	0.0208	1.5	0.20	132.9	2.0	139.2	10.2	248.3	176.6
265-29	141	4028	4.4	22.8028	22.9	0.1386	23.0	0.0229	2.4	0.10	146.1	3.4	131.8	28.4	-118.8	570.6
265-30	120	3680	3.8	21.1243	14.5	0.1521	14.6	0.0233	0.7	0.05	148.5	1.1	143.7	19.5	66.3	347.6
265-31	204	4976	3.6	21.0582	12.0	0.1491	12.6	0.0228	3.6	0.29	145.1	5.2	141.1	16.5	73.8	286.8
265-33	286	4040	3.0	17.5321	21.2	0.1757	21.2	0.0223	1.0	0.05	142.4	1.4	164.3	32.2	493.0	472.3
265-34	187	2564	4.1	21.4039	8.9	0.1319	9.0	0.0205	1.2	0.14	130.7	1.6	125.8	10.7	34.9	214.3
265-35	170	3108	4.3	19.8121	15.2	0.1488	15.3	0.0214	0.9	0.06	136.4	1.2	140.9	20.1	216.9	354.7
265-36	187	3736	3.8	22.5558	12.4	0.1313	12.6	0.0215	2.1	0.16	137.0	2.8	125.3	14.8	-92.1	305.3
945-1	142	4416	3.0	21.8668	6.1	0.1388	6.3	0.0220	1.4	0.22	140.4	1.9	132.0	7.7	-16.5	147.4
945-2	98	2898	4.5	22.3352	10.1	0.1344	10.4	0.0218	2.4	0.23	138.8	3.3	128.0	12.5	-68.0	247.3
945-6-3	108	4102	4.0	22.2551	8.2	0.1345	8.3	0.0217	1.6	0.19	138.4	2.2	128.1	10.0	-59.2	199.0
945-6-4	95	3199	4.2	22.1618	9.2	0.1357	9.3	0.0218	1.4	0.16	139.1	2.0	129.2	11.3	-49.0	223.4
945-6-5	105	2936	3.8	24.2696	10.5	0.1210	10.6	0.0213	0.8	0.07	135.9	1.0	116.0	11.6	-274.9	268.2
945-6-6	114	1911	3.7	24.4925	11.9	0.1201	12.0	0.0213	0.7	0.06	136.1	0.9	115.2	13.0	-298.3	306.1
945-6-7	101	1094	4.1	27.5359	13.4	0.1043	13.5	0.0208	1.1	0.08	132.9	1.4	100.7	12.9	-607.0	367.0
945-6-8	80	1756	4.7	25.9671	15.2	0.1112	15.3	0.0209	1.6	0.10	133.6	2.1	107.0	15.6	-449.9	403.5
945-6-9	112	4457	4.1	23.0002	6.1	0.1248	6.4	0.0208	2.0	0.31	132.8	2.6	119.4	7.2	-140.1	151.1
945-6-10	114	3746	3.3	23.0062	9.6	0.1234	9.8	0.0206	2.1	0.21	131.4	2.7	118.2	11.0	-140.8	238.3
945-6-11	95	2680	5.0	21.6939	11.2	0.1349	11.3	0.0212	1.8	0.16	135.4	2.4	128.5	13.7	2.6	269.9
945-6-12	262	6192	2.6	21.4036	4.2	0.1373	4.8	0.0213	2.2	0.47	135.9	3.0	130.6	5.8	35.0	100.6
945-6-13	141	3792	3.9	23.7315	10.0	0.1202	10.0	0.0207	1.2	0.12	132.0	1.6	115.2	10.9	-218.2	250.9
945-6-14	212	3756	3.3	22.9093	4.7	0.1270	4.9	0.0211	1.4	0.28	134.6	1.8	121.4	5.6	-130.3	116.7
945-6-15	121	3574	3.7	24.9505	11.4	0.1168	11.5	0.0211	1.5	0.13	134.9	2.0	112.2	12.2	-345.8	293.8
945-6-16	99	1964	4.4	24.3594	15.4	0.1167	15.7	0.0206	3.2	0.20	131.5	4.1	112.1	16.6	-284.4	393.1
945-6-17	126	2041	4.2	25.4403	9.0	0.1139	9.2	0.0210	2.0	0.22	134.1	2.7	109.5	9.5	-396.2	233.9
945-6-18	93	1428	4.7	29.4792	14.4	0.0976	14.4	0.0209	1.3	0.09	133.1	1.7	94.6	13.0	-796.5	408.9
945-6-19	171	1993	3.1	23.9143	5.8	0.1216	6.0	0.0211	1.3	0.21	134.5	1.7	116.5	6.6	-237.6	147.4
945-6-20	192	3509	3.2	23.4958	8.1	0.1292	8.2	0.0220	1.3	0.15	140.4	1.8	123.4	9.5	-193.2	202.7
945-6-21	109	2385	4.3	22.4279	10.1	0.1330	10.3	0.0216	2.3	0.22	137.9	3.2	126.8	12.3	-78.1	247.1
945-6-22	125	3481	4.3	21.9445	9.2	0.1357	9.3	0.0216	1.5	0.16	137.7	2.0	129.2	11.3	-25.1	222.6
945-6-23	169	4973	4.4	20.9214	12.9	0.1405	13.0	0.0213	1.8	0.14	136.0	2.5	133.5	16.3	89.3	305.9
945-6-24	72	2666	5.9	26.3305	31.5	0.1131	31.7	0.0216	3.7	0.12	137.8	5.1	108.8	32.7	-486.7	853.9
945-6-25	131	3989	4.4	22.9039	7.6	0.1297	7.7	0.0215	1.4	0.18	137.4	1.9	123.8	9.0	-129.8	188.1
945-6-26	385	16642	2.6	21.0138	2.0	0.1425	2.7	0.0217	1.8	0.66	138.5	2.4	135.2	3.4	78.8	48.1
945-6-27	147	3223	4.1	22.0650	6.0	0.1338	6.1	0.0214	1.3	0.21	136.6	1.7	127.5	7.3	-38.4	144.8
945-6-28	122	4824	4.7	22.9727	7.2	0.1302	7.5	0.0217	2.0	0.26	138.3	2.7	124.3	8.7	-137.2	178.4
945-6-29	156	7030	4.1	22.2611	9.9	0.1347	10.0	0.0218	1.3	0.13	138.7	1.7	128.3	12.1	-59.9	242.4
945-6-30	146	3169	4.3	23.5175	9.5	0.1247	9.6	0.0213	1.1	0.11	135.7	1.4	119.3	10.8	-195.5	238.7
945-6-32	179	938	4.2	28.3856	17.7	0.1034	17.9	0.0213	2.7	0.15	135.8	3.6	100.0	17.0	-690.5	493.8
945-6-33	195	5503	3.0	20.4561	5.6	0.1436	6.1	0.0213	2.5	0.41	135.9	3.3	136.2	7.8	142.3	131.1
945-6-33	195	4013	3.0	21.8269	4.3	0.1328	4.7	0.0210	1.8	0.38	134.1	2.4	126.6	5.6	-12.1	104.6
945-6-35	98	3077	4.8	21.6829	17.1	0.1341	17.3	0.0211	2.9	0.17	134.5	3.8	127.8	20.8	3.8	413.6
Sample 08SE451		*Antimony Peak tonalite*														
08SE451-1	287	4224	4.5	23.9326	12.7	0.1224	12.8	0.0212	1.3	0.10	135.5	1.8	117.3	14.2	-239.5	322.1
08SE451-2	491	6710	3.6	21.1605	11.0	0.1341	11.3	0.0206	2.3	0.21	131.3	3.0	127.8	13.5	62.3	263.5
08SE451-3	517	9843	3.6	21.1900	7.6	0.1411	7.8	0.0217	1.7	0.21	138.3	2.3	134.0	9.7	59.0	181.0
08SE451-4	349	5360	3.8	20.3378	10.5	0.1450	10.6	0.0214	1.3	0.12	136.4	1.7	137.5	13.6	155.9	246.6
08SE451-5	635	10713	3.2	20.7972	5.1	0.1414	6.0	0.0213	3.1	0.52	136.0	4.2	134.3	7.5	103.4	120.8
08SE451-6	272	4433	4.0	20.9007	16.6	0.1419	16.7	0.0215	1.8	0.11	137.2	2.4	134.8	21.1	91.7	395.3
08SE451-7	158	2358	5.5	26.7413	34.4	0.1134	34.4	0.0220	2.1	0.06	140.3	2.9	109.1	35.6	-528.0	942.9

Table A2.1 (Continued).

Analysis	U	^{206}Pb	U/Th	Isotope ratios							Isotopic ages (Ma)[§]					
		^{204}Pb		$^{206}Pb^*$	±	$^{207}Pb^*$	±	$^{206}Pb^*$	±	Error	$^{206}Pb^*$	±	$^{207}Pb^*$	±	$^{206}Pb^*$	±
	(ppm)			$^{207}Pb^*$	(%)	$^{235}U^*$	(%)	^{238}U	(%)	correlation	^{238}U	(Ma)	$^{235}U^*$	(Ma)	$^{207}Pb^*$	(Ma)
08SE451-8	388	8042	3.4	22.6383	8.3	0.1458	8.4	0.0239	1.6	0.19	152.5	2.4	138.2	10.9	-101.0	204.2
08SE451-9	317	7880	4.0	21.6431	11.8	0.1409	12.0	0.0221	1.7	0.14	141.0	2.4	133.8	15.0	8.3	285.5
08SE451-10	338	5326	4.6	22.2482	14.7	0.1341	15.0	0.0216	3.4	0.22	138.0	4.6	127.8	18.1	-58.5	358.7
08SE451-11	321	5057	2.9	19.6284	6.8	0.1566	8.1	0.0223	4.3	0.54	142.1	6.1	147.7	11.1	238.4	156.6
08SE451-12	591	7680	7.0	19.8833	6.4	0.1469	6.4	0.0212	0.8	0.13	135.2	1.1	139.2	8.3	208.6	147.5
08SE451-13	474	8343	3.3	21.5265	12.5	0.1353	12.6	0.0211	1.7	0.14	134.7	2.3	128.8	15.2	21.3	300.5
08SE451-14	277	3592	3.8	21.1706	19.8	0.1313	20.0	0.0202	2.3	0.11	128.6	2.9	125.2	23.5	61.2	476.9
08SE451-15	692	11763	3.1	21.1520	8.4	0.1358	8.6	0.0208	1.5	0.18	132.9	2.0	129.3	10.4	63.2	201.0
08SE451-16	350	5724	2.5	21.1318	15.6	0.1350	15.7	0.0207	2.0	0.13	132.0	2.7	128.6	19.0	65.5	373.3
08SE451-17	217	6670	4.3	25.0428	8.8	0.1200	9.4	0.0218	3.1	0.34	139.0	4.3	115.1	10.2	-355.4	228.7
08SE451-18	275	4753	3.1	21.0576	20.5	0.1337	20.7	0.0204	2.2	0.11	130.3	2.9	127.4	24.7	73.9	492.7
08SE451-19	466	8829	2.6	21.5786	7.0	0.1349	7.7	0.0211	3.3	0.43	134.7	4.4	128.5	9.3	15.4	168.2
08SE451-20	697	12155	2.4	20.5625	8.1	0.1452	8.3	0.0217	2.0	0.24	138.1	2.7	137.7	10.7	130.2	189.7
08SE451-21	258	4439	4.3	22.9916	7.6	0.1299	8.4	0.0217	3.6	0.43	138.1	4.9	124.0	9.8	-139.2	189.2
08SE451-22	316	6211	3.2	21.9086	13.1	0.1395	13.3	0.0222	2.2	0.17	141.3	3.1	132.6	16.5	-21.1	318.5
08SE451-23	338	5325	3.6	23.0531	10.8	0.1217	11.6	0.0204	4.2	0.36	129.9	5.4	116.6	12.7	-145.8	268.2
08SE451-24	507	11095	2.6	21.8755	12.6	0.1331	12.8	0.0211	2.3	0.18	134.7	3.1	126.9	15.2	-17.5	304.6
08SE451-25	474	6309	2.9	21.5480	12.4	0.1348	12.5	0.0211	1.5	0.12	134.4	2.0	128.4	15.1	18.9	299.3
08SE451-26	604	10879	3.1	22.0907	7.1	0.1328	7.5	0.0213	2.4	0.32	135.7	3.2	126.6	8.9	-41.2	173.0
08SE451-26	724	12925	2.5	20.8522	6.6	0.1384	7.1	0.0209	2.6	0.37	133.5	3.5	131.6	8.8	97.1	155.9
08SE451-27	257	7397	3.5	22.2740	26.9	0.1320	27.0	0.0213	2.3	0.09	136.0	3.1	125.9	32.0	-61.3	666.3
08SE451-28	431	7986	3.9	21.6136	14.5	0.1266	14.5	0.0198	1.4	0.09	126.6	1.7	121.0	16.6	11.5	349.5
08SE451-28	498	11486	3.7	23.1188	8.5	0.1277	8.6	0.0214	1.6	0.19	136.6	2.2	122.0	9.9	-152.9	210.4
08SE451-29	261	6519	4.5	21.8373	17.0	0.1365	17.1	0.0216	1.6	0.10	137.8	2.2	129.9	20.8	-13.2	412.8
08SE451-30	575	9383	3.3	21.5012	6.6	0.1334	6.9	0.0208	2.0	0.29	132.7	2.6	127.1	8.3	24.1	159.7
08SE451-31	433	8825	2.6	21.6586	15.6	0.1373	15.7	0.0216	1.4	0.09	137.5	2.0	130.6	19.2	6.6	377.9
08SE451-32	1484	1327	0.9	19.4461	14.6	0.0982	14.7	0.0139	1.8	0.12	88.7	1.6	95.1	13.3	259.9	335.9
08SE451-33	675	14417	2.8	21.5193	3.6	0.1415	4.1	0.0221	1.9	0.47	140.8	2.7	134.4	5.2	22.1	86.8
08SE451-34	596	12003	2.3	21.2439	9.8	0.1398	10.3	0.0215	3.0	0.29	137.3	4.1	132.8	12.8	52.9	235.5
08SE451-35	634	10568	4.2	21.3705	6.8	0.1371	7.0	0.0212	1.5	0.22	135.5	2.0	130.5	8.5	38.7	163.3
Sample 08SE582		*Antimony Peak tonalite*														
09SE23-1	477	5858	3.4	20.6384	11.0	0.1375	11.1	0.0206	1.1	0.10	131.3	1.5	130.8	13.6	121.5	260.1
09SE23-2	284	4831	4.5	29.2471	25.1	0.0995	25.3	0.0211	2.9	0.11	134.7	3.8	96.3	23.2	-774.1	717.7
09SE23-3	239	3389	4.3	23.2084	18.6	0.1216	19.0	0.0205	3.9	0.21	130.6	5.1	116.5	20.9	-162.5	466.3
09SE23-4	613	11961	3.9	21.2813	6.9	0.1357	7.0	0.0209	1.3	0.19	133.6	1.7	129.2	8.6	48.7	165.5
09SE23-5	236	1761	3.8	19.5127	19.8	0.1511	20.1	0.0214	3.5	0.18	136.4	4.8	142.9	26.8	252.0	458.8
09SE23-6	368	4937	3.9	21.7185	6.6	0.1342	7.1	0.0211	2.6	0.37	134.8	3.5	127.8	8.5	-0.1	158.9
09SE23-7	355	4614	2.8	22.4992	9.6	0.1312	10.1	0.0214	3.3	0.32	136.6	4.4	125.2	11.9	-85.9	234.9
09SE23-8	422	6222	3.8	20.4645	6.8	0.1463	7.2	0.0217	2.4	0.34	138.5	3.3	138.6	9.4	141.4	159.9
09SE23-9	412	5835	4.2	20.9166	10.9	0.1429	11.1	0.0217	2.1	0.19	138.3	2.9	135.7	14.1	89.8	259.2
09SE23-11	512	7044	3.6	20.9289	6.8	0.1380	7.0	0.0209	1.9	0.27	133.6	2.5	131.3	8.7	88.5	160.7
09SE23-12	290	6783	3.7	20.6244	10.8	0.1421	10.8	0.0213	1.1	0.10	135.6	1.4	134.9	13.7	123.0	254.3
09SE23-13	393	5378	4.2	20.7321	9.5	0.1397	9.7	0.0210	2.2	0.22	134.0	2.9	132.8	12.1	110.8	224.0
09SE23-14	1009	15045	3.0	20.3668	3.0	0.1371	6.3	0.0203	5.5	0.88	129.3	7.1	130.5	7.7	152.6	70.9
09SE23-15	538	8836	2.8	20.5878	6.4	0.1425	6.6	0.0213	1.4	0.21	135.8	1.8	135.3	8.3	127.3	151.0
09SE23-16	406	8124	2.6	21.8724	6.0	0.1343	7.6	0.0213	4.7	0.61	135.9	6.3	127.9	9.1	-17.1	145.4
09SE23-17	246	3083	3.4	23.2999	8.2	0.1275	8.8	0.0216	3.0	0.34	137.5	4.1	121.9	10.1	-172.3	205.6
09SE23-18	539	8803	2.6	21.0838	10.0	0.1405	10.4	0.0215	2.7	0.26	137.0	3.7	133.5	13.0	70.9	239.5
09SE23-20	699	10022	3.3	21.4368	6.3	0.1431	6.7	0.0223	2.3	0.34	141.9	3.2	135.8	8.6	31.3	151.9
09SE23-21	299	7164	3.8	26.4298	33.7	0.1088	33.7	0.0209	1.4	0.04	133.1	1.9	104.9	33.6	-496.7	917.8
09SE23-22	678	11932	4.1	21.4311	4.8	0.1342	5.5	0.0209	2.7	0.49	133.1	3.6	127.9	6.6	31.9	114.9
09SE23-23	377	7262	4.2	21.3651	11.2	0.1383	11.5	0.0214	2.8	0.24	136.7	3.8	131.5	14.2	39.3	268.2
09SE23-24	342	6015	4.1	20.1156	11.6	0.1428	11.7	0.0208	1.0	0.09	132.9	1.3	135.6	14.8	181.6	271.2
09SE23-25	449	5297	4.2	20.8881	10.2	0.1413	10.4	0.0214	2.2	0.21	136.6	2.9	134.2	13.1	93.0	241.7
09SE23-26	323	4731	3.3	22.1631	8.8	0.1266	9.3	0.0203	3.1	0.33	129.8	4.0	121.0	10.7	-49.2	214.9
09SE23-27	303	5829	3.5	20.8509	10.8	0.1421	11.2	0.0215	2.7	0.24	137.1	3.6	134.9	14.1	97.3	256.9
09SE23-28	432	6643	3.1	21.3463	6.1	0.1357	6.4	0.0210	1.8	0.28	134.0	2.3	129.2	7.7	41.4	146.3

Table A2.1 (Continued).

Analysis	U (ppm)	$^{206}Pb/^{204}Pb$	U/Th	Isotope ratios							Isotopic ages (Ma)[§]					
				$^{206}Pb^*/^{207}Pb^*$	± (%)	$^{207}Pb^*/^{235}U^*$	± (%)	$^{206}Pb^*/^{238}U$	± (%)	Error correlation	$^{206}Pb^*/^{238}U$	± (Ma)	$^{207}Pb^*/^{235}U^*$	± (Ma)	$^{206}Pb^*/^{207}Pb^*$	± (Ma)
09SE23-29	759	13683	3.2	20.7479	5.0	0.1424	5.3	0.0214	1.6	0.30	136.7	2.2	135.2	6.7	109.0	118.2
09SE23-30	229	3095	5.0	23.9894	19.8	0.1138	22.9	0.0198	11.7	0.51	126.4	14.6	109.4	23.8	-245.5	503.7
Sample 08SE675		*Antimony Peak tonalite*														
08SE675-2	310	7046	4.1	20.7890	17.0	0.1381	18.7	0.0208	7.8	0.42	132.9	10.3	131.4	23.1	104.3	405.1
08SE675-4	533	3185	3.0	23.4689	14.8	0.0902	14.9	0.0153	1.8	0.12	98.2	1.7	87.7	12.5	-190.3	371.5
08SE675-5	1051	13002	21.4	21.2341	5.5	0.1002	6.4	0.0154	3.4	0.53	98.7	3.3	97.0	5.9	54.0	130.3
08SE675-7	673	16159	4.5	21.1073	8.5	0.1296	10.6	0.0198	6.3	0.60	126.6	7.9	123.7	12.3	68.3	202.5
08SE675-8	402	6837	2.4	19.2682	14.7	0.1463	15.3	0.0204	4.3	0.28	130.4	5.6	138.6	19.9	281.0	338.3
08SE675-10	381	4385	2.4	22.1222	8.7	0.1306	9.1	0.0209	2.6	0.29	133.6	3.4	124.6	10.7	-44.7	212.1
08SE675-11	368	8037	3.0	23.8635	19.9	0.1174	20.6	0.0203	5.5	0.27	129.6	7.1	112.7	22.0	-232.2	504.9
08SE675-12	312	5277	9.3	23.1084	30.7	0.1016	31.5	0.0170	7.2	0.23	108.8	7.8	98.2	29.5	-151.8	777.6
08SE675-13	1650	35821	3.4	20.2107	2.3	0.1514	4.2	0.0222	3.5	0.83	141.5	4.8	143.2	5.6	170.6	54.0
08SE675-14	749	15762	5.1	21.6960	10.9	0.1349	11.4	0.0212	3.2	0.28	135.5	4.3	128.5	13.7	2.4	263.0
08SE675-15	895	7671	9.3	20.1339	8.2	0.1459	9.9	0.0213	5.6	0.57	135.9	7.5	138.3	12.8	179.4	190.7
08SE675-16	299	3974	3.6	19.0766	18.8	0.1416	19.2	0.0196	3.8	0.20	125.1	4.7	134.5	24.2	303.8	432.3
08SE675-17	1274	20557	16.5	21.2008	5.0	0.1201	7.1	0.0185	5.0	0.71	118.0	5.9	115.2	7.7	57.7	118.1
08SE675-19	819	10870	2.5	21.3538	7.7	0.1360	8.4	0.0211	3.2	0.38	134.4	4.2	129.5	10.2	40.6	185.5
08SE675-20	436	11268	3.0	19.2403	11.6	0.1578	12.0	0.0220	3.0	0.25	140.4	4.2	148.8	16.6	284.3	266.9
08SE675-21	594	6157	4.0	22.5718	11.3	0.1315	12.5	0.0215	5.4	0.43	137.3	7.4	125.4	14.8	-93.8	278.1
08SE675-22	1113	22556	7.5	21.0778	4.4	0.1481	5.2	0.0226	2.7	0.52	144.3	3.8	140.2	6.8	71.6	104.8
08SE675-23	1801	30920	160.5	21.1268	9.2	0.0977	11.4	0.0150	6.6	0.58	95.8	6.3	94.7	10.3	66.1	220.1
08SE675-24	401	7755	2.7	20.4201	8.1	0.1441	10.6	0.0213	6.9	0.65	136.1	9.3	136.7	13.6	146.5	190.3
08SE675-25	489	5128	3.7	20.3677	15.1	0.1196	15.9	0.0177	5.2	0.32	112.9	5.8	114.7	17.3	152.5	354.9
08SE675-26	515	23121	3.6	22.1123	9.5	0.1352	10.5	0.0217	4.4	0.42	138.3	6.0	128.8	12.7	-43.6	232.1
08SE675-27	409	6936	3.1	21.5611	10.9	0.1295	12.8	0.0203	6.8	0.53	129.3	8.7	123.7	14.9	17.4	262.2
08SE675-28	494	46545	3.0	21.2332	9.8	0.1517	10.6	0.0234	4.0	0.38	148.9	5.9	143.4	14.1	54.1	233.7
08SE675-30	1027	27804	3.7	21.1113	5.3	0.1471	5.4	0.0225	1.3	0.25	143.5	1.9	139.3	7.1	67.8	125.0
08SE675-31	645	12925	5.4	19.7998	6.8	0.1493	9.9	0.0214	7.2	0.73	136.8	9.7	141.3	13.1	218.3	157.6
08SE675-32	253	4935	3.3	22.2958	19.6	0.1282	19.9	0.0207	3.4	0.17	132.3	4.5	122.5	23.0	-63.7	483.1
08SE675-33	273	3566	3.7	26.2611	32.8	0.1105	33.0	0.0210	4.2	0.13	134.2	5.6	106.4	33.4	-479.7	888.3
08SE675-34	338	9288	3.6	23.7283	10.2	0.1250	11.3	0.0215	4.9	0.43	137.2	6.6	119.6	12.7	-217.9	257.0
08SE675-35	518	6897	6.2	22.5017	12.4	0.1274	12.8	0.0208	3.5	0.27	132.6	4.6	121.7	14.7	-86.2	303.7
08SE675-36	836	13539	11.6	21.4516	15.1	0.1168	17.0	0.0182	7.9	0.46	116.1	9.1	112.2	18.1	29.6	363.2
08SE675-37	657	13713	8.2	19.9618	12.3	0.1419	12.6	0.0205	2.7	0.22	131.1	3.6	134.7	15.9	199.4	286.1
08SE675-39	495	8459	7.9	19.6270	13.9	0.1480	14.0	0.0211	2.0	0.14	134.4	2.7	140.2	18.4	238.6	321.7
08SE675-40	380	4519	4.1	17.0878	15.6	0.1583	15.8	0.0196	2.8	0.18	125.2	3.4	149.2	22.0	549.4	342.3
08SE675-43	463	7201	3.0	22.5705	20.2	0.1294	20.3	0.0212	2.4	0.12	135.1	3.2	123.6	23.7	-93.7	499.8
08SE675-44	622	18023	2.0	21.4831	16.9	0.1375	17.0	0.0214	2.0	0.11	136.7	2.6	130.8	20.9	26.1	407.3
08SE675-45	696	12763	2.5	19.8305	8.7	0.1296	16.4	0.0186	13.9	0.85	119.1	16.4	123.7	19.1	214.7	202.3
08SE675-46	1142	7593	18.6	21.1630	6.2	0.1150	6.6	0.0176	2.3	0.35	112.8	2.6	110.5	6.9	62.0	147.5
08SE675-47	939	18859	3.0	20.2311	6.4	0.1477	6.8	0.0217	2.2	0.32	138.2	3.0	139.8	8.8	168.2	150.0
08SE675-49	335	18324	1.3	16.1509	5.3	0.6671	9.0	0.0781	7.3	0.81	485.0	34.0	518.9	36.6	671.2	113.8
08SE675-50	578	12599	4.7	21.2336	7.3	0.1422	8.1	0.0219	3.6	0.45	139.6	5.0	135.0	10.3	54.1	174.0
Sample 07SE94		*San Emigdio gneiss*														
27-1	433	8838	16.3	21.0208	2.3	0.1069	2.7	0.0163	1.4	0.53	104.2	1.5	103.2	2.7	78.0	55.3
27-2	277	2952	2.1	21.6998	4.9	0.1001	5.4	0.0157	2.2	0.40	100.7	2.1	96.8	5.0	2.0	118.5
27-3	285	4476	4.5	22.0675	8.2	0.1029	8.3	0.0165	1.1	0.13	105.3	1.1	99.5	7.8	-38.6	199.2
27-4	279	4308	5.5	21.5098	5.9	0.1020	6.0	0.0159	1.1	0.18	101.8	1.1	98.6	5.6	23.1	141.7
27-5	239	2682	1.9	21.5648	5.7	0.1055	6.1	0.0165	2.2	0.36	105.5	2.3	101.9	5.9	17.0	136.2
27-6	178	2610	2.4	21.8854	9.5	0.1023	9.6	0.0162	1.4	0.14	103.8	1.4	98.9	9.1	-18.6	231.1
27-7	160	2469	3.1	22.7410	11.8	0.0987	12.1	0.0163	2.5	0.20	104.1	2.5	95.6	11.0	-112.2	291.4
27-8	243	2916	2.0	21.7643	6.3	0.1049	6.4	0.0166	1.0	0.15	105.9	1.0	101.3	6.2	-5.2	152.4
27-9	234	3267	2.7	21.9974	7.3	0.1001	7.5	0.0160	1.7	0.22	102.1	1.7	96.8	6.9	-30.9	178.0
27-10	195	2544	2.3	23.6344	12.5	0.0965	12.6	0.0165	1.6	0.13	105.8	1.7	93.6	11.3	-208.0	315.1
27-11	190	2886	2.5	20.6468	7.6	0.1112	7.9	0.0167	2.3	0.29	106.5	2.5	107.1	8.0	120.5	178.1
27-12	257	4539	3.1	21.5127	6.9	0.1053	7.1	0.0164	1.4	0.19	105.1	1.4	101.7	6.9	22.8	166.9

Table A2.1 (Continued).

Analysis	U	^{206}Pb	U/Th	Isotope ratios							Isotopic ages (Ma)[§]					
				$^{206}Pb^*$	±	$^{207}Pb^*$	±	$^{206}Pb^*$	±	Error	$^{206}Pb^*$	±	$^{207}Pb^*$	±	$^{206}Pb^*$	±
	(ppm)	^{204}Pb		$^{207}Pb^*$	(%)	$^{235}U^*$	(%)	^{238}U	(%)	correlation	^{238}U	(Ma)	$^{235}U^*$	(Ma)	$^{207}Pb^*$	(Ma)
27-13	175	3276	6.0	21.5512	10.1	0.1051	10.2	0.0164	0.7	0.07	105.1	0.7	101.5	9.8	18.5	243.8
27-14	239	3315	2.6	22.0071	7.6	0.1035	7.6	0.0165	0.5	0.07	105.7	0.6	100.0	7.3	-32.0	185.0
27-15	360	5952	15.1	19.9602	4.9	0.1108	5.7	0.0160	3.0	0.52	102.6	3.0	106.7	5.8	199.6	113.4
27-16	307	4839	12.6	20.7770	5.3	0.1076	5.6	0.0162	2.0	0.36	103.7	2.1	103.8	5.5	105.7	124.2
27-17	259	3480	2.8	22.6867	9.1	0.0981	9.4	0.0161	2.1	0.22	103.2	2.1	95.0	8.5	-106.3	224.8
27-18	286	3840	2.4	20.9770	6.2	0.1107	6.4	0.0168	1.7	0.26	107.7	1.8	106.6	6.5	83.0	147.9
27-19	252	2733	2.0	22.7085	9.2	0.1015	9.2	0.0167	0.8	0.08	106.9	0.8	98.2	8.6	-108.7	226.5
27-20	331	6015	31.3	21.0752	3.6	0.1044	3.8	0.0160	1.2	0.32	102.1	1.2	100.8	3.6	71.9	84.7
27-21	322	3240	2.0	21.9231	6.8	0.1015	6.9	0.0161	1.0	0.15	103.2	1.0	98.2	6.5	-22.7	165.5
27-22	337	5661	5.1	21.7005	5.4	0.1057	5.5	0.0166	1.2	0.23	106.4	1.3	102.0	5.3	1.9	129.4
27-23	245	3213	2.8	22.3326	8.1	0.1028	8.3	0.0167	1.6	0.20	106.5	1.7	99.4	7.8	-67.7	198.4
27-24	103	2169	6.8	22.7181	11.4	0.1144	12.5	0.0188	5.2	0.42	120.4	6.2	110.0	13.1	-109.7	281.3
27-25	181	2475	2.8	21.9956	8.5	0.1022	8.7	0.0163	1.6	0.19	104.2	1.7	98.8	8.2	-30.7	207.6
27-26	408	6591	3.0	21.3932	4.7	0.1046	4.9	0.0162	1.4	0.29	103.8	1.5	101.0	4.7	36.1	112.4
27-27	119	2229	9.7	22.6483	10.5	0.1011	10.8	0.0166	2.5	0.24	106.1	2.7	97.8	10.0	-102.1	258.1
27-28	228	3435	2.9	21.7162	9.5	0.1057	10.1	0.0166	3.5	0.35	106.4	3.7	102.0	9.8	0.1	228.6
27-29	129	2556	5.6	22.6098	20.3	0.1016	20.4	0.0167	1.6	0.08	106.6	1.7	98.3	19.1	-98.0	503.5
27-30	1484	20493	2.4	20.5760	1.9	0.1130	3.8	0.0169	3.3	0.87	107.8	3.5	108.7	3.9	128.6	44.0
27-31	734	6510	3.3	21.0501	4.2	0.1065	4.5	0.0163	1.5	0.34	104.0	1.6	102.8	4.4	74.7	99.6
27-32	419	5151	2.3	21.1652	2.4	0.1046	2.7	0.0161	1.3	0.47	102.7	1.3	101.0	2.6	61.7	56.7
27-33	126	1845	107.9	25.2037	18.5	0.0867	18.6	0.0159	1.0	0.05	101.4	1.0	84.5	15.1	-372.0	484.3
27-34	228	4095	128.5	21.9015	8.4	0.1023	8.6	0.0162	2.0	0.23	103.9	2.0	98.9	8.1	-20.4	204.1
27-35	594	8811	11.2	20.9911	5.0	0.1055	5.9	0.0161	3.1	0.53	102.7	3.2	101.8	5.7	81.4	119.5
27-36	156	2448	4.8	22.5830	8.9	0.0986	8.9	0.0161	0.7	0.08	103.2	0.7	95.5	8.1	-95.1	217.7
27-37	283	2937	2.1	21.7050	7.6	0.1056	7.6	0.0166	0.7	0.09	106.3	0.7	101.9	7.4	1.4	182.5
27-38	119	1698	4.9	24.3041	15.2	0.0914	15.8	0.0161	4.4	0.28	103.1	4.5	88.8	13.5	-278.6	389.0
27-39	134	2538	11.4	23.9548	15.7	0.0914	15.7	0.0159	1.7	0.11	101.6	1.7	88.8	13.4	-241.9	397.4
27-40	183	2460	2.2	23.2374	11.8	0.0984	12.1	0.0166	2.6	0.21	106.1	2.7	95.3	11.0	-165.6	294.3
94TEHA-1	293	4935	1.3	21.8237	7.9	0.1093	8.0	0.0173	1.3	0.16	110.5	1.4	105.3	8.0	-11.7	191.0
94TEHA-2	633	9811	8.5	21.3445	1.9	0.1047	2.8	0.0162	2.1	0.73	103.7	2.1	101.1	2.7	41.6	45.9
94TEHA-3	888	14049	1.3	21.0014	1.7	0.1119	2.4	0.0170	1.6	0.69	108.9	1.8	107.7	2.4	80.2	40.8
94TEHA-4	542	9033	2.5	20.8477	2.5	0.1152	3.4	0.0174	2.3	0.68	111.3	2.5	110.7	3.5	97.7	58.3
94TEHA-5	111	2073	9.3	28.2391	14.9	0.0841	15.0	0.0172	1.6	0.11	110.1	1.8	82.0	11.8	-676.2	413.9
94TEHA-6	246	3857	1.7	22.8293	8.2	0.1014	8.3	0.0168	1.0	0.11	107.3	1.0	98.0	7.8	-121.7	203.7
94TEHA-7	269	5031	1.7	22.7540	5.6	0.1036	5.9	0.0171	1.7	0.30	109.3	1.9	100.1	5.6	-113.6	138.2
94TEHA-8	143	2673	3.4	23.9071	9.2	0.0967	9.4	0.0168	1.8	0.19	107.2	1.9	93.7	8.4	-236.8	232.1
94TEHA-9	103	1450	3.8	23.5290	13.6	0.0989	13.7	0.0169	1.2	0.09	107.9	1.3	95.7	12.5	-196.7	342.7
94TEHA-10	197	3466	32.7	23.3617	6.4	0.0976	6.8	0.0165	2.1	0.32	105.7	2.3	94.6	6.1	-178.9	160.9
94TEHA-11	141	2199	2.4	23.0436	15.2	0.1022	15.4	0.0171	2.1	0.14	109.2	2.3	98.8	14.5	-144.8	379.7
94TEHA-12	275	3333	1.4	22.0336	4.7	0.1068	5.0	0.0171	1.5	0.31	109.1	1.6	103.1	4.9	-34.9	114.5
94TEHA-13	1123	18526	1.3	20.8995	1.2	0.1148	2.0	0.0174	1.6	0.80	111.2	1.7	110.4	2.0	91.7	27.6
94TEHA-14	1242	23902	6.5	20.6889	1.7	0.1142	2.6	0.0171	1.9	0.75	109.6	2.1	109.8	2.7	115.7	40.5
94TEHA-15	571	9974	2.4	21.4022	3.6	0.1084	4.2	0.0168	2.1	0.51	107.5	2.3	104.5	4.2	35.1	86.3
94TEHA-16	451	6651	15.1	21.5529	3.2	0.1015	4.2	0.0159	2.6	0.62	101.5	2.6	98.2	3.9	18.3	78.0
94TEHA-17	204	3314	1.8	23.9008	5.5	0.0966	5.9	0.0167	2.0	0.34	107.1	2.1	93.6	5.3	-236.2	139.9
94TEHA-18	112	1796	2.8	27.0424	11.4	0.0869	11.4	0.0171	1.2	0.11	109.0	1.3	84.6	9.3	-558.0	306.9
94TEHA-20	174	2713	3.6	24.1690	11.6	0.0954	11.7	0.0167	1.3	0.11	106.9	1.4	92.5	10.3	-264.4	295.6
94TEHA-20	242	4071	3.0	22.9049	7.5	0.0989	7.6	0.0164	0.9	0.12	105.0	1.0	95.7	6.9	-129.9	185.8
94TEHA-21	246	5402	4.0	21.2992	6.7	0.1114	6.9	0.0172	1.3	0.19	110.0	1.5	107.3	7.0	46.7	161.3
94TEHA-22	88	1389	3.7	21.9794	17.3	0.1081	17.4	0.0172	1.6	0.09	110.2	1.8	104.2	17.3	-28.9	422.9
94TEHA-23	116	2047	17.8	20.4760	12.5	0.1088	12.6	0.0162	1.2	0.10	103.3	1.2	104.9	12.5	140.1	294.7
94TEHA-24	211	3447	2.1	22.6846	8.3	0.0996	8.6	0.0164	2.0	0.23	104.8	2.1	96.4	7.9	-106.0	205.3
94TEHA-25	502	11251	2.9	21.3073	3.6	0.1078	4.1	0.0167	2.0	0.48	106.5	2.1	103.9	4.0	45.8	85.8
94TEHA-26	212	3301	1.8	23.8344	9.6	0.0972	9.7	0.0168	1.1	0.11	107.4	1.1	94.2	8.7	-229.1	242.3
94TEHA-27	165	2858	3.6	23.0071	13.5	0.1005	14.1	0.0168	4.0	0.29	107.2	4.3	97.2	13.0	-140.9	335.2
94TEHA-28	705	13558	2.3	21.0826	1.9	0.1115	2.2	0.0171	1.1	0.49	109.0	1.2	107.4	2.2	71.1	45.8
94TEHA-29	236	5403	2.6	23.0051	5.7	0.1051	6.1	0.0175	2.3	0.37	112.1	2.5	101.5	5.9	-140.7	140.8
94TEHA-30	156	3332	2.1	23.7773	8.8	0.1011	8.9	0.0174	1.2	0.14	111.4	1.3	97.8	8.3	-223.1	222.6

Table A2.1 (Continued).

Analysis	U	^{206}Pb	U/Th	Isotope ratios							Isotopic ages (Ma)[§]					
				^{206}Pb*	±	^{207}Pb*	±	^{206}Pb*	±	Error	^{206}Pb*	±	^{207}Pb*	±	^{206}Pb*	±
	(ppm)	^{204}Pb		^{207}Pb*	(%)	^{235}U*	(%)	^{238}U	(%)	correlation	^{238}U	(Ma)	^{235}U*	(Ma)	^{207}Pb*	(Ma)
94TEHA-31	1425	22152	3.9	20.7180	1.4	0.1177	2.9	0.0177	2.6	0.88	113.0	2.9	113.0	3.1	112.4	32.1
94TEHA-32	256	4437	1.3	23.3885	7.1	0.0987	7.4	0.0167	1.9	0.26	107.1	2.0	95.6	6.7	-181.8	177.8
94TEHA-33	1171	17383	2.2	21.1459	2.1	0.1094	2.7	0.0168	1.7	0.63	107.2	1.8	105.4	2.7	63.9	50.6
94TEHA-34	144	2849	3.8	22.3648	11.9	0.1131	12.3	0.0183	3.4	0.28	117.2	4.0	108.8	12.7	-71.2	290.5
Sample 08SE450		*San Emigdio gneiss*														
08SE450-1	235	7013	10.3	22.0545	23.0	0.1057	23.1	0.0169	2.5	0.11	108.1	2.6	102.0	22.4	-37.2	564.3
08SE450-3	356	11989	15.1	20.0824	15.5	0.1138	15.6	0.0166	2.3	0.15	106.0	2.4	109.4	16.2	185.4	362.3
08SE450-4	241	6047	8.0	19.0617	11.5	0.1173	11.7	0.0162	2.0	0.17	103.7	2.1	112.7	12.5	305.5	262.7
08SE450-5	232	6026	13.0	22.6181	23.2	0.0985	23.4	0.0162	2.6	0.11	103.3	2.7	95.4	21.3	-98.8	577.0
Sample 08SE674		*Digier Canyon / White Oak diorite gneiss*														
08SE674-1	69	2219	2.8	11.0640	256.4	0.2279	256.5	0.0183	3.3	0.01	116.8	3.9	208.5	525.7	1433.6	854.5
08SE674-2	82	2241	3.4	45.3271	102.6	0.0578	102.6	0.0190	3.1	0.03	121.3	3.7	57.0	57.0	-2226.5	0.0
08SE674-3	50	1617	5.1	18.5116	107.3	0.1318	107.5	0.0177	5.0	0.05	113.1	5.6	125.7	127.7	371.9	807.7
08SE674-4	40	1098	4.0	11.3054	81.5	0.2224	81.7	0.0182	5.9	0.07	116.5	6.8	203.9	152.1	1392.3	2019.8
08SE674-5	70	2803	2.6	12.1203	337.8	0.2102	337.9	0.0185	3.3	0.01	118.0	3.9	193.7	683.2	1257.6	1453.0
08SE674-6	539	14939	3.1	21.6886	12.6	0.1315	12.7	0.0207	1.9	0.15	132.0	2.4	125.4	15.0	3.2	304.1
08SE674-7	73	3000	5.0	20.5444	45.3	0.1293	45.4	0.0193	2.3	0.05	123.0	2.8	123.5	52.8	132.2	1118.2
08SE674-8	71	2830	2.4	25.8696	39.0	0.0979	39.2	0.0184	3.9	0.10	117.4	4.5	94.9	35.5	-440.0	1059.8
08SE674-10	58	2108	2.6	34.0135	65.8	0.0798	66.0	0.0197	4.7	0.07	125.6	5.8	77.9	49.5	-1221.4	2271.7
08SE674-12	65	2227	4.6	18.1738	32.2	0.1468	32.4	0.0194	3.6	0.11	123.6	4.3	139.1	42.1	413.2	736.3
08SE674-13	61	2617	2.4	17.8599	67.1	0.1473	67.3	0.0191	4.6	0.07	121.9	5.5	139.5	87.9	452.0	1696.5
08SE674-14	97	3503	1.9	21.4863	45.1	0.1249	45.2	0.0195	1.4	0.03	124.3	1.7	119.5	51.0	25.7	1135.5
08SE674-16	59	1848	2.6	20.3068	26.8	0.1239	27.2	0.0182	4.5	0.17	116.6	5.2	118.6	30.5	159.5	637.5
08SE674-17	55	2139	2.6	24.6029	36.2	0.1037	36.3	0.0185	3.3	0.09	118.2	3.8	100.2	34.7	-309.8	953.5
08SE674-18	558	18249	3.1	20.2169	5.5	0.1337	6.0	0.0196	2.3	0.39	125.1	2.9	127.4	7.2	169.8	128.8
08SE674-19	88	4462	3.5	26.1089	50.9	0.1030	51.0	0.0195	3.3	0.06	124.5	4.0	99.5	48.4	-464.3	1425.0
08SE674-20	56	2052	2.8	27.8642	66.2	0.0879	66.8	0.0178	8.9	0.13	113.5	10.0	85.5	54.9	-639.4	2025.1
08SE674-22	173	11286	3.8	20.6582	16.9	0.1291	17.1	0.0193	2.6	0.15	123.5	3.1	123.3	19.9	119.2	401.4
08SE674-23	77	2269	3.0	22.0051	48.3	0.1164	48.4	0.0186	2.6	0.05	118.6	3.1	111.8	51.3	-31.8	1238.4
08SE674-24	91	2906	3.1	18.3236	34.8	0.1422	35.0	0.0189	3.3	0.09	120.7	4.0	135.0	44.3	394.8	803.6
08SE674-25	55	2404	4.8	16.7161	130.5	0.1559	130.7	0.0189	5.7	0.04	120.7	6.8	147.1	180.8	597.2	814.6
08SE674-27	53	1709	2.8	25.7656	36.2	0.0983	36.2	0.0184	1.6	0.04	117.4	1.9	95.2	32.9	-429.4	976.4
08SE674-28	61	1912	2.4	16.5883	42.9	0.1559	42.9	0.0188	1.0	0.02	119.8	1.1	147.2	58.9	613.7	970.4
08SE674-29	87	2186	2.9	24.5042	31.3	0.1109	31.3	0.0197	1.3	0.04	125.8	1.6	106.8	31.7	-299.5	816.4
Sample 08SE679		*Digier Canyon / White Oak diorite gneiss*														
08SE679-1	197	7184	2.6	14.8322	88.4	0.1503	88.5	0.0162	5.3	0.06	103.4	5.4	142.2	118.0	850.8	323.3
08SE679-2	91	1339	2.9	14.4713	47.1	0.1647	47.6	0.0173	6.7	0.14	110.5	7.3	154.8	68.4	901.8	1029.5
08SE679-3	70	980	2.9	24.3888	79.9	0.0927	80.0	0.0164	4.1	0.05	104.8	4.3	90.0	69.0	-287.4	2478.8
08SE679-5	86	575	3.0	14.8530	89.7	0.1508	90.2	0.0162	9.3	0.10	103.9	9.6	142.6	120.6	847.9	335.3
08SE679-11	490	8233	1.5	21.8573	30.2	0.1040	31.9	0.0165	10.2	0.32	105.4	10.6	100.4	30.5	-15.4	744.7
Sample 04SE5		*Lebec granodiorite*														
04SE5-1	605	8322	4.0	21.8860	6.9	0.0952	7.2	0.0151	2.0	0.27	96.7	1.9	92.3	6.3	-18.6	167.3
04SE5-2	278	4773	1.8	18.9386	15.3	0.1045	15.6	0.0144	2.9	0.18	91.9	2.6	100.9	15.0	320.3	349.5
04SE5-3	340	9520	2.1	28.6821	22.2	0.0673	22.5	0.0140	3.5	0.15	89.7	3.1	66.2	14.4	-719.4	625.1
04SE5-5	515	11995	3.2	21.1496	10.8	0.0986	11.0	0.0151	1.7	0.15	96.7	1.6	95.4	10.0	63.5	258.7
04SE5-6	166	3916	2.8	35.0469	50.1	0.0543	50.2	0.0138	3.4	0.07	88.4	3.0	53.7	26.3	-1315.7	1681.2
04SE5-7	209	5324	3.1	22.6739	23.0	0.0859	23.0	0.0141	2.0	0.09	90.4	1.8	83.7	18.5	-104.9	571.1
04SE5-8	133	2780	2.5	23.7710	64.0	0.0811	64.0	0.0140	2.6	0.04	89.5	2.3	79.2	48.8	-222.4	1787.3
04SE5-9	189	2348	2.9	23.9632	19.5	0.0829	19.5	0.0144	0.7	0.04	92.2	0.7	80.8	15.2	-242.7	497.4
04SE5-10	191	3345	2.4	27.3170	41.2	0.0691	41.2	0.0137	1.9	0.04	87.6	1.6	67.8	27.1	-585.4	1157.3
04SE5-11	304	8419	3.8	20.4331	15.5	0.0985	15.9	0.0146	3.6	0.22	93.5	3.3	95.4	14.5	144.9	365.0
04SE5-12	140	3610	2.2	18.6085	21.7	0.1065	21.8	0.0144	2.4	0.11	92.0	2.2	102.8	21.3	360.1	494.6
04SE5-13	181	2528	2.3	24.2622	29.8	0.0845	29.9	0.0149	2.9	0.10	95.2	2.7	82.4	23.7	-274.2	771.4
04SE5-14	151	2495	2.8	34.3906	40.8	0.0590	40.8	0.0147	1.3	0.03	94.2	1.2	58.2	23.1	-1255.9	1325.1

Table A2.1 (Continued).

Analysis	U	^{206}Pb	U/Th	Isotope ratios							Isotopic ages (Ma)[§]					
		^{204}Pb		$^{206}Pb^*$	±	$^{207}Pb^*$	±	$^{206}Pb^*$	±	Error	$^{206}Pb^*$	±	$^{207}Pb^*$	±	$^{206}Pb^*$	±
	(ppm)			$^{207}Pb^*$	(%)	$^{235}U^*$	(%)	^{238}U	(%)	correlation	^{238}U	(Ma)	$^{235}U^*$	(Ma)	$^{207}Pb^*$	(Ma)
04SE5-15	179	4504	2.9	21.8174	24.4	0.0902	24.8	0.0143	4.6	0.19	91.4	4.2	87.7	20.8	-11.0	595.8
04SE5-16	160	3109	2.6	24.3913	12.9	0.0801	13.2	0.0142	2.7	0.21	90.8	2.5	78.3	9.9	-287.7	330.4
04SE5-17	226	5990	1.9	20.2734	18.3	0.0991	18.5	0.0146	2.8	0.15	93.3	2.6	96.0	17.0	163.3	431.3
04SE5-18	142	3393	2.2	20.6756	28.1	0.0973	28.3	0.0146	3.1	0.11	93.3	2.9	94.2	25.5	117.2	674.8
04SE5-19	238	4906	2.7	20.6180	26.4	0.0968	26.5	0.0145	2.4	0.09	92.6	2.2	93.8	23.8	123.8	632.1
04SE5-20	174	5608	2.7	27.4217	19.9	0.0708	20.7	0.0141	5.8	0.28	90.1	5.2	69.4	13.9	-595.7	544.9
04SE5-21	179	4652	2.8	24.8690	28.2	0.0786	28.3	0.0142	2.9	0.10	90.7	2.6	76.8	20.9	-337.4	737.0
04SE5-22	183	4319	3.0	22.1465	26.4	0.0974	26.5	0.0156	1.0	0.04	100.0	1.0	94.3	23.8	-47.3	652.7
04SE5-23	296	5626	3.3	21.5268	17.1	0.0910	17.2	0.0142	1.6	0.09	91.0	1.4	88.4	14.5	21.3	413.0
04SE5-24	194	4393	3.1	21.1137	27.2	0.0870	27.6	0.0133	4.6	0.17	85.3	3.9	84.7	22.4	67.6	657.2
04SE5-25	441	8765	2.0	21.9293	16.2	0.0895	16.2	0.0142	1.4	0.09	91.1	1.3	87.0	13.5	-23.4	393.8
04SE5-26	295	9764	2.8	22.5662	26.5	0.0887	26.5	0.0145	1.3	0.05	92.9	1.2	86.3	21.9	-93.2	659.8
04SE5-27	196	4638	2.9	24.5805	15.9	0.0804	16.1	0.0143	2.7	0.17	91.8	2.5	78.5	12.2	-307.4	409.1
04SE5-28	124	3138	3.5	19.6592	30.3	0.0993	30.6	0.0142	4.4	0.14	90.7	4.0	96.2	28.1	234.8	712.8
04SE5-29	225	4076	1.8	26.7039	30.7	0.0708	31.4	0.0137	6.4	0.20	87.7	5.6	69.4	21.1	-524.2	838.8
04SE5-30	269	5708	2.2	23.3959	12.9	0.0828	13.0	0.0140	1.2	0.09	89.9	1.1	80.7	10.1	-182.6	323.8
Sample 06SE19a		*Lebec granodiorite*														
06SE19A-1	883	3926	1.5	21.1983	20.0	0.0917	20.5	0.0141	4.3	0.21	90.2	3.8	89.0	17.5	58.0	482.0
06SE19A-2	1732	3770	4.6	18.5978	12.5	0.1128	13.6	0.0152	5.3	0.39	97.4	5.1	108.6	14.0	361.4	282.4
06SE19A-3	3496	4912	23.4	19.6431	4.7	0.1096	5.4	0.0156	2.8	0.51	99.8	2.7	105.6	5.5	236.7	108.3
06SE19A-4	614	6586	23.6	18.8575	38.6	0.1145	39.1	0.0157	6.6	0.17	100.2	6.5	110.1	40.9	330.0	906.3
06SE19A-5	1613	18852	3.6	19.4661	6.9	0.1152	8.4	0.0163	4.8	0.57	104.0	4.9	110.7	8.8	257.5	159.3
06SE19A-6	949	7410	2.4	21.4205	6.8	0.0956	7.2	0.0149	2.4	0.33	95.0	2.3	92.7	6.4	33.1	163.4
06SE19A-7	4315	11778	1.0	20.1620	3.8	0.0899	10.1	0.0131	9.4	0.93	84.2	7.9	87.4	8.5	176.2	87.9
06SE19A-8	2552	17396	1.0	21.0409	5.6	0.0837	10.8	0.0128	9.3	0.86	81.8	7.6	81.6	8.5	75.7	132.8
06SE19A-9	3376	22355	0.9	21.0788	5.8	0.0896	6.9	0.0137	3.7	0.54	87.7	3.3	87.2	5.7	71.5	137.1
06SE19A-10	542	10275	2.9	21.4603	16.0	0.0954	16.6	0.0148	4.5	0.27	95.0	4.3	92.5	14.7	28.6	384.6
06SE19A-11	2503	10893	0.8	21.9915	10.1	0.0849	13.3	0.0135	8.7	0.66	86.7	7.5	82.7	10.6	-30.3	244.6
06SE19A-12	3338	31694	22.4	20.2957	2.2	0.0999	3.6	0.0147	2.9	0.79	94.1	2.7	96.7	3.3	160.8	51.5
06SE19A-14	4093	37315	55.8	20.8923	2.2	0.0951	3.1	0.0144	2.2	0.69	92.3	2.0	92.3	2.7	92.6	53.3
06SE19A-16	2563	22789	8.5	21.4121	3.0	0.0930	4.8	0.0144	3.7	0.77	92.5	3.4	90.3	4.1	34.0	72.8
06SE19A-17	487	3568	7.6	21.6995	19.0	0.0803	24.6	0.0126	15.6	0.64	80.9	12.6	78.4	18.5	2.0	460.3
06SE19A-18	4329	20721	0.8	20.1539	4.3	0.0877	8.7	0.0128	7.6	0.87	82.1	6.2	85.4	7.2	177.1	100.4
06SE19A-20	553	3220	2.1	27.5170	19.4	0.0715	19.9	0.0143	4.4	0.22	91.4	4.0	70.2	13.5	-605.2	533.1
06SE19A-21	4646	12364	0.7	20.4563	2.4	0.0893	7.6	0.0132	7.2	0.95	84.8	6.1	86.8	6.3	142.3	55.4
06SE19A-23	2273	22443	3.2	19.6163	3.2	0.1166	3.6	0.0166	1.5	0.42	106.1	1.6	112.0	3.8	239.8	74.7
06SE19A-24	1646	20440	1.3	20.7246	6.7	0.0944	7.3	0.0142	2.8	0.39	90.9	2.6	91.6	6.4	111.6	158.7
06SE19A-25	2814	16256	1.5	19.7632	5.9	0.0995	6.8	0.0143	3.3	0.48	91.3	3.0	96.3	6.2	222.6	137.7
06SE19A-27	1362	16978	9.2	20.9951	9.8	0.0908	12.4	0.0138	7.5	0.61	88.5	6.6	88.2	10.4	80.9	232.9
06SE19A-29	3355	23358	0.8	20.9205	5.4	0.0882	6.6	0.0134	3.9	0.59	85.7	3.3	85.8	5.5	89.4	127.1
Sample 08SE256		*Lebec granodiorite*														
262-1	1148	5349	4.5	19.1187	19.1	0.1029	19.1	0.0143	1.0	0.05	91.4	0.9	99.5	18.1	298.7	439.5
262-2	1069	3864	4.7	18.1144	7.7	0.1038	7.7	0.0136	0.5	0.07	87.3	0.4	100.2	7.4	420.5	172.3
262-3	750	8736	15.9	20.4906	5.9	0.0948	6.1	0.0141	1.7	0.27	90.2	1.5	92.0	5.4	138.3	139.0
262-4	142	2235	4.3	24.3979	20.3	0.0747	20.8	0.0132	4.6	0.22	84.7	3.8	73.2	14.7	-288.4	521.8
262-5	207	2589	4.5	22.2951	17.7	0.0845	18.1	0.0137	3.6	0.20	87.5	3.2	82.4	14.3	-63.6	435.2
262-6	80	1134	4.6	23.3179	19.6	0.0815	19.7	0.0138	2.7	0.14	88.2	2.4	79.5	15.1	-174.3	491.4
262-7	500	1629	9.6	10.6396	50.6	0.1872	50.8	0.0144	3.9	0.08	92.5	3.6	174.2	81.5	1507.9	1028.9
262-8	1311	2223	8.3	15.4268	12.8	0.1225	13.0	0.0137	2.6	0.20	87.8	2.2	117.3	14.4	768.6	270.2
262-9	264	2520	2.8	19.4399	16.8	0.1120	16.9	0.0158	1.7	0.10	101.0	1.7	107.8	17.3	260.6	389.2
262-10	196	669	3.1	10.5735	14.1	0.2091	14.2	0.0160	1.1	0.08	102.5	1.1	192.8	24.9	1519.6	268.1
262-11	919	9663	33.8	18.4550	5.9	0.1065	6.1	0.0143	1.4	0.24	91.3	1.3	102.8	5.9	378.8	133.0
262-12	359	3633	3.3	21.4019	7.9	0.0914	8.2	0.0142	2.2	0.27	90.8	2.0	88.8	7.0	35.2	190.1
262-13	390	4530	3.6	21.5755	12.1	0.0888	12.2	0.0139	1.7	0.14	88.9	1.5	86.4	10.1	15.8	291.5
262-14	448	5295	7.3	21.0425	6.9	0.0887	7.4	0.0135	2.7	0.37	86.6	2.3	86.3	6.1	75.6	163.1
262-16	944	4041	6.9	14.2673	35.5	0.1223	36.5	0.0127	8.3	0.23	81.0	6.7	117.1	40.4	931.0	752.5

Table A2.1 (Continued).

Analysis	U	^{206}Pb	U/Th	Isotope ratios							Isotopic ages (Ma)[§]					
				$^{206}Pb^*$	±	$^{207}Pb^*$	±	$^{206}Pb^*$	±	Error	$^{206}Pb^*$	±	$^{207}Pb^*$	±	$^{206}Pb^*$	±
	(ppm)	^{204}Pb		$^{207}Pb^*$	(%)	$^{235}U^*$	(%)	^{238}U	(%)	correlation	^{238}U	(Ma)	$^{235}U^*$	(Ma)	$^{207}Pb^*$	(Ma)
262-18	303	4734	6.3	19.5762	9.6	0.1066	11.5	0.0151	6.4	0.56	96.8	6.2	102.8	11.3	244.5	221.2
262-20	796	2376	4.8	13.9943	32.3	0.1276	32.4	0.0130	2.4	0.08	83.0	2.0	122.0	37.2	970.5	675.3
Sample 10TC5		*Granodiorite of Gato Montes*														
10TC5 - 1	494	8864	4.3	20.2580	12.7	0.0957	13.6	0.0141	4.8	0.36	90.0	4.3	92.8	12.1	165.1	298.7
10TC5 - 2	356	5144	4.1	18.9727	22.7	0.1013	23.1	0.0139	4.4	0.19	89.2	3.9	98.0	21.6	316.2	521.4
10TC5 - 3	942	13731	2.5	19.7740	5.0	0.1114	6.0	0.0160	3.3	0.55	102.2	3.4	107.2	6.1	221.3	116.6
10TC5 - 4	659	15855	2.4	20.4759	11.9	0.0956	12.2	0.0142	2.7	0.22	90.9	2.4	92.7	10.8	140.1	281.4
10TC5 - 5	325	4519	4.4	19.1695	22.5	0.1021	22.6	0.0142	2.6	0.11	90.8	2.3	98.7	21.3	292.7	519.1
10TC5 - 6	998	21164	4.9	21.4015	8.3	0.0937	9.5	0.0145	4.7	0.49	93.0	4.3	90.9	8.3	35.2	199.8
10TC5 - 7	596	9226	4.0	22.3742	19.1	0.0991	19.3	0.0161	2.6	0.13	102.8	2.6	95.9	17.7	-72.3	471.6
10TC5 - 8	1332	16944	6.3	21.7055	5.6	0.0884	5.8	0.0139	1.6	0.28	89.1	1.4	86.0	4.8	1.4	134.6
10TC5 - 9	230	4529	3.5	22.2354	50.6	0.0928	51.2	0.0150	7.7	0.15	95.7	7.3	90.1	44.1	-57.1	1310.3
10TC5 - 10	264	8289	2.2	19.3624	32.0	0.1057	32.9	0.0148	7.7	0.23	95.0	7.2	102.1	32.0	269.8	751.0
10TC5 - 11	580	9175	2.8	20.0433	10.9	0.1037	11.7	0.0151	4.3	0.37	96.5	4.1	100.2	11.2	190.0	253.7
10TC5 - 12	504	29535	3.1	19.5840	15.1	0.1005	15.5	0.0143	3.7	0.24	91.4	3.4	97.2	14.4	243.7	349.0
10TC5 - 13	356	10339	3.2	17.8675	16.9	0.1128	17.9	0.0146	6.0	0.33	93.6	5.5	108.6	18.5	451.1	378.3
10TC5 - 14	690	13478	5.0	21.1244	16.0	0.0931	16.4	0.0143	3.5	0.22	91.3	3.2	90.4	14.2	66.4	382.5
10TC5 - 15	497	9741	3.8	21.6530	16.8	0.1046	17.1	0.0164	3.1	0.18	105.1	3.2	101.1	16.4	7.2	406.1
10TC5 - 16	708	10167	5.3	19.8258	10.7	0.1020	11.0	0.0147	2.7	0.24	93.9	2.5	98.6	10.3	215.3	247.5
10TC5 - 17	300	7308	7.1	21.0040	27.3	0.0945	28.1	0.0144	6.7	0.24	92.2	6.1	91.7	24.7	79.9	659.6
10TC5 - 19	772	20618	5.1	20.3102	7.0	0.1369	9.9	0.0202	7.0	0.70	128.7	8.9	130.3	12.1	159.1	165.0
10TC5 - 20	743	16679	5.6	19.7926	6.3	0.1017	7.3	0.0146	3.8	0.51	93.5	3.5	98.4	6.9	219.2	145.8
10TC5 - 21	1043	43381	4.6	21.4687	9.4	0.0905	10.1	0.0141	3.7	0.37	90.2	3.3	88.0	8.5	27.7	224.8
10TC5 - 22	247	7747	3.6	24.5444	20.6	0.0866	21.8	0.0154	7.2	0.33	98.6	7.1	84.3	17.6	-303.7	530.5
10TC5 - 23	505	8159	3.2	21.4982	18.9	0.0928	20.0	0.0145	6.8	0.34	92.6	6.2	90.1	17.3	24.4	456.2
10TC5 - 24	568	4927	2.6	18.6067	11.7	0.1068	12.6	0.0144	4.5	0.36	92.2	4.1	103.0	12.3	360.3	265.1
10TC5 - 25	798	35726	4.2	21.0033	6.8	0.1068	7.3	0.0163	2.7	0.37	104.1	2.8	103.1	7.2	80.0	161.4
10TC5 - 26	361	5206	3.1	20.2837	16.1	0.1013	16.4	0.0149	2.8	0.17	95.4	2.7	98.0	15.3	162.2	379.4
10TC5 - 27	372	5828	3.0	25.9300	17.8	0.0800	18.3	0.0150	4.0	0.22	96.2	3.8	78.1	13.7	-446.2	472.0
10TC5 - 28	589	12649	3.7	21.4163	10.3	0.0922	11.1	0.0143	4.2	0.38	91.6	3.8	89.5	9.5	33.6	246.8
10TC5 - 29	660	20385	3.1	21.7576	15.5	0.0909	16.2	0.0144	4.7	0.29	91.9	4.3	88.4	13.7	-4.4	376.5
10TC5 - 30	204	2988	4.4	24.1013	62.5	0.0809	63.0	0.0141	8.4	0.13	90.5	7.5	79.0	47.9	-257.3	1745.9
10TC5 - 31	688	12062	4.0	20.8266	10.0	0.1089	10.1	0.0164	1.5	0.15	105.1	1.6	104.9	10.1	100.0	237.6
10TC5 - 33	793	30531	3.7	19.6470	11.7	0.1061	12.0	0.0151	2.6	0.21	96.7	2.5	102.4	11.7	236.2	270.8
10TC5 - 34	369	9179	2.4	24.7933	19.6	0.0826	20.6	0.0149	6.3	0.31	95.1	6.0	80.6	16.0	-329.5	508.4
10TC5 - 35	262	11422	2.8	27.2677	48.6	0.0726	48.8	0.0144	4.7	0.10	92.0	4.3	71.2	33.6	-580.5	1384.7
Sample 08TC27		*Granodiorite of Gamble Spring Canyon*														
TC27-21	223	5619	0.6	21.1522	7.5	0.1483	7.6	0.0228	1.6	0.21	145.1	2.3	140.4	10.0	63.2	178.2
TC27-22	290	8744	0.8	21.4644	5.1	0.1476	5.3	0.0230	1.5	0.28	146.4	2.1	139.7	6.9	28.2	122.6
TC27-24	146	5007	0.8	20.4894	8.2	0.1557	8.3	0.0231	1.5	0.18	147.5	2.2	147.0	11.4	138.5	192.8
TC27-25	168	12780	0.7	20.7719	7.6	0.1532	7.8	0.0231	1.4	0.18	147.1	2.0	144.7	10.5	106.2	180.9
TC27-1	236	8056	0.5	21.6358	4.9	0.1463	4.9	0.0230	0.4	0.08	146.4	0.6	138.7	6.4	9.1	117.8
TC27-2	194	8923	0.6	20.4878	13.9	0.1554	14.2	0.0231	3.1	0.22	147.2	4.6	146.7	19.4	138.7	327.1
TC27-26	140	6463	0.7	23.1799	10.2	0.1370	10.5	0.0230	2.7	0.26	146.8	3.9	130.4	12.9	-159.5	253.5
TC27-3	161	5936	0.7	20.9946	11.3	0.1502	11.5	0.0229	1.9	0.17	145.8	2.8	142.1	15.2	81.0	269.6
TC27-27	196	4362	0.6	21.7356	10.1	0.1467	10.1	0.0231	0.8	0.08	147.4	1.2	139.0	13.1	-2.0	243.1
TC27-4	97	4365	0.9	19.8627	17.0	0.1636	17.0	0.0236	1.5	0.09	150.2	2.2	153.8	24.3	211.0	395.9
TC27-5	180	3901	1.0	22.6203	15.7	0.1406	15.8	0.0231	1.9	0.12	147.0	2.8	133.6	19.8	-99.1	387.9
TC27-29	165	8116	0.8	21.3644	13.0	0.1484	13.2	0.0230	2.1	0.16	146.6	3.0	140.5	17.3	39.4	312.2
TC27-30	153	7988	0.8	21.6583	9.1	0.1474	9.3	0.0231	1.8	0.20	147.5	2.7	139.6	12.1	6.6	219.1
TC27-6	122	4305	1.0	18.8836	11.1	0.1711	11.8	0.0234	3.9	0.33	149.3	5.8	160.4	17.5	326.9	252.3
TC27-7	154	5207	0.9	21.0979	10.4	0.1515	10.4	0.0232	1.2	0.11	147.7	1.7	143.2	13.9	69.4	247.3
TC27	213	11762	1.1	22.4109	9.5	0.1378	9.6	0.0224	1.7	0.17	142.8	2.3	131.1	11.8	-76.3	231.8
TC27-8	134	6476	0.7	22.5889	13.5	0.1411	13.6	0.0231	1.5	0.11	147.3	2.2	134.0	17.1	-95.7	333.6
TC27-32	126	5633	0.9	23.8383	24.7	0.1337	24.9	0.0231	3.1	0.12	147.3	4.5	127.4	29.8	-229.6	629.6
TC27-9	395	9825	1.1	21.3037	6.2	0.1490	7.1	0.0230	3.5	0.49	146.7	5.0	141.0	9.3	46.2	147.6

Table A2.1 (Continued).

Analysis	U	^{206}Pb	U/Th	Isotope ratios							Isotopic ages (Ma)[§]					
				$^{206}Pb^*$	±	$^{207}Pb^*$	±	$^{206}Pb^*$	±	Error	$^{206}Pb^*$	±	$^{207}Pb^*$	±	$^{206}Pb^*$	±
	(ppm)	^{204}Pb		$^{207}Pb^*$	(%)	$^{235}U^*$	(%)	^{238}U	(%)	correlation	^{238}U	(Ma)	$^{235}U^*$	(Ma)	$^{207}Pb^*$	(Ma)
TC27-33	192	8374	0.8	22.9020	10.3	0.1372	10.5	0.0228	2.2	0.21	145.2	3.2	130.5	12.9	-129.6	254.8
TC27-10	211	51988	0.8	20.5493	7.4	0.1550	7.6	0.0231	1.8	0.24	147.3	2.7	146.4	10.4	131.6	174.1
TC27-35	541	26095	1.1	20.6820	3.7	0.1512	4.3	0.0227	2.3	0.52	144.6	3.2	143.0	5.8	116.5	87.4
TC27-11	91	3382	1.3	24.6979	23.1	0.1351	23.2	0.0242	1.8	0.08	154.2	2.8	128.7	28.1	-319.6	600.3
TC27-12	192	13783	0.8	18.6298	8.9	0.1727	9.1	0.0233	1.9	0.21	148.7	2.8	161.8	13.6	357.5	200.9
TC27-13	295	13249	0.6	20.7132	6.5	0.1541	6.7	0.0232	1.7	0.25	147.5	2.5	145.5	9.1	112.9	153.3
TC27-14	209	7064	0.9	22.9552	8.1	0.1387	8.4	0.0231	2.1	0.25	147.2	3.0	131.9	10.4	-135.3	200.8
TC27-15	168	9095	1.2	21.1309	10.6	0.1497	10.8	0.0229	1.9	0.17	146.2	2.7	141.6	14.2	65.6	253.1
TC27-16	145	6532	0.7	20.6545	14.8	0.1530	15.0	0.0229	2.4	0.16	146.1	3.4	144.5	20.2	119.6	350.6
TC27-17	147	3997	0.8	20.9306	7.8	0.1525	8.3	0.0231	2.7	0.33	147.5	4.0	144.1	11.1	88.3	185.1
TC27-18	200	9877	0.5	20.3768	7.5	0.1543	7.7	0.0228	1.8	0.23	145.3	2.6	145.7	10.5	151.4	176.3
TC27-19	192	8388	0.7	20.5194	8.6	0.1549	8.8	0.0230	1.7	0.19	146.9	2.4	146.2	12.0	135.1	202.8
TC27-20	218	6825	0.6	21.0080	9.6	0.1540	9.8	0.0235	2.3	0.23	149.5	3.4	145.5	13.3	79.5	227.2
Sample 08SE596		*Granite of Brush Mountain*														
08SE596-2	1379	7336	3.2	20.8858	3.7	0.1063	4.1	0.0161	1.7	0.42	102.9	1.8	102.5	4.0	93.3	88.3
08SE596-4	2122	4306	3.5	19.7845	9.3	0.1145	9.3	0.0164	1.0	0.11	105.1	1.1	110.1	9.7	220.1	214.7
08SE596-5	1975	13880	3.1	21.1179	3.9	0.1064	4.2	0.0163	1.4	0.34	104.2	1.5	102.6	4.1	67.1	92.9
08SE596-6	2927	8412	2.4	20.6572	1.3	0.1092	2.6	0.0164	2.2	0.85	104.6	2.3	105.2	2.6	119.3	31.3
08SE596-7	2347	21315	3.3	20.2799	2.4	0.1119	2.9	0.0165	1.5	0.52	105.3	1.5	107.7	2.9	162.6	57.2
08SE596-8	3141	3816	4.7	20.4414	3.1	0.0968	4.5	0.0144	3.3	0.73	91.9	3.0	93.9	4.0	144.0	71.8
08SE596-10	2421	15355	3.6	20.8217	2.4	0.1102	3.3	0.0166	2.3	0.70	106.4	2.4	106.1	3.3	100.6	55.7
08SE596-11	2716	21020	2.7	20.7742	1.3	0.1103	2.5	0.0166	2.2	0.86	106.2	2.3	106.2	2.6	106.0	30.5
08SE596-12	2071	14682	3.6	21.1875	1.7	0.1082	3.3	0.0166	2.8	0.85	106.3	2.9	104.3	3.2	59.3	40.7
08SE596-13	3106	21442	2.0	20.7543	1.4	0.1095	2.8	0.0165	2.4	0.86	105.4	2.5	105.5	2.8	108.3	32.8
08SE596-14	3020	26304	2.2	20.8257	1.7	0.1078	3.0	0.0163	2.4	0.83	104.2	2.5	104.0	2.9	100.1	39.4
08SE596-15	1874	12544	3.7	21.1609	2.7	0.1073	3.3	0.0165	1.9	0.58	105.3	2.0	103.5	3.3	62.2	64.2
08SE596-16	2744	16169	4.1	20.8995	1.9	0.1057	2.4	0.0160	1.5	0.63	102.4	1.6	102.0	2.4	91.7	44.5
08SE596-17	1027	7072	1.9	20.9206	4.7	0.1033	5.1	0.0157	2.1	0.40	100.3	2.0	99.8	4.9	89.4	111.5
08SE596-18	2079	17591	4.3	20.8740	1.1	0.1050	1.6	0.0159	1.2	0.75	101.7	1.2	101.4	1.5	94.7	25.1
08SE596-19	1062	3591	5.2	20.7320	5.8	0.1082	6.1	0.0163	1.8	0.30	104.1	1.9	104.3	6.1	110.8	138.1
08SE596-20	2772	12962	3.6	20.5065	3.0	0.1132	4.3	0.0168	3.1	0.73	107.6	3.4	108.8	4.5	136.5	69.3
08SE596-21	2794	30352	2.5	20.9028	1.4	0.1058	2.5	0.0160	2.0	0.82	102.6	2.0	102.1	2.4	91.4	33.6
08SE596-23	2611	25116	2.7	20.7919	1.8	0.1101	3.1	0.0166	2.6	0.83	106.1	2.7	106.0	3.1	104.0	41.6
08SE596-24	2364	6884	4.5	19.6825	8.3	0.1194	8.4	0.0170	1.3	0.15	108.9	1.4	114.5	9.1	232.0	192.0
08SE596-25	1934	21386	2.3	20.9220	2.0	0.1117	3.8	0.0170	3.2	0.84	108.4	3.5	107.5	3.9	89.2	48.4
08SE596-26	2241	26230	4.0	20.9492	2.3	0.1096	3.0	0.0167	2.0	0.65	106.5	2.1	105.6	3.0	86.2	53.7
08SE596-27	2401	16035	4.1	20.5753	1.9	0.1087	3.4	0.0162	2.9	0.83	103.7	2.9	104.8	3.4	128.7	44.5
08SE596-28	2937	28028	2.0	20.7247	2.3	0.1092	3.3	0.0164	2.3	0.71	105.0	2.4	105.3	3.3	111.6	55.1
08SE596-29	2282	23995	2.7	20.6023	3.0	0.1131	3.7	0.0169	2.1	0.56	108.0	2.2	108.8	3.8	125.6	71.7
08SE596-30	2220	10233	3.2	20.6779	1.8	0.1109	3.9	0.0166	3.5	0.89	106.3	3.6	106.8	3.9	117.0	41.7
Sample 09SE23		*White Ridge tonalite*														
08SE582-8	69	1868	3.9	30.9838	45.9	0.1018	45.9	0.0229	2.4	0.05	145.8	3.4	98.4	43.1	-939.8	1402.9
08SE582-13	22	367	7.3	19.9023	134.1	0.1623	134.1	0.0234	3.1	0.02	149.3	4.6	152.7	192.4	206.4	1168.3
08SE582-14	265	3788	2.8	23.0986	9.8	0.1488	10.1	0.0249	2.5	0.24	158.7	3.8	140.9	13.3	-150.7	243.8
08SE582-15	26	595	6.4	14.6670	22.7	0.2048	23.2	0.0218	4.8	0.21	138.9	6.6	189.2	40.0	874.1	475.3
08SE582-19	512	19809	4.0	20.4443	3.9	0.1653	4.9	0.0245	3.1	0.62	156.1	4.7	155.3	7.1	143.7	90.6
08SE582-22	40	1910	7.2	17.7703	101.3	0.1886	101.3	0.0243	2.2	0.02	154.8	3.4	175.4	164.7	463.2	690.5
08SE582-23	54	2141	4.8	21.0116	64.6	0.1576	64.6	0.0240	2.7	0.04	153.0	4.1	148.6	89.5	79.1	1714.0
08SE582-24	24	855	7.7	30.3099	131.4	0.1059	131.5	0.0233	3.5	0.03	148.3	5.2	102.2	128.5	-875.9	0.0
08SE582-25	29	1124	7.9	23.9128	76.6	0.1310	76.9	0.0227	6.7	0.09	144.9	9.6	125.0	90.7	-237.4	2298.5
08SE582-28	69	1313	6.8	29.5484	40.8	0.1041	41.3	0.0223	6.4	0.16	142.3	9.0	100.6	39.5	-803.1	1197.9
08SE582-31	265	6927	4.8	20.0691	11.4	0.1703	11.8	0.0248	3.1	0.26	157.8	4.8	159.6	17.4	186.9	265.1
08SE582-32	77	2040	7.0	19.4769	31.9	0.1676	31.9	0.0237	1.3	0.04	150.8	1.9	157.3	46.5	256.2	749.2
08SE582-33	94	1169	6.0	25.1342	31.1	0.1400	31.1	0.0255	1.2	0.04	162.4	2.0	133.0	38.8	-364.8	821.4
08SE582-34	71	655	6.5	19.8031	105.9	0.1637	106.0	0.0235	2.8	0.03	149.8	4.1	154.0	152.5	218.0	913.9
08SE582-35	545	22997	2.3	20.7238	4.8	0.1673	5.7	0.0251	3.1	0.54	160.1	4.8	157.1	8.2	111.7	112.4

Table A2.1 (Continued).

Analysis	U (ppm)	$^{206}Pb/^{204}Pb$	U/Th	Isotope ratios $^{206}Pb^*/^{207}Pb^*$	± (%)	$^{207}Pb^*/^{235}U^*$	± (%)	$^{206}Pb^*/^{238}U$	± (%)	Error correlation	Isotopic ages (Ma)[§] $^{206}Pb^*/^{238}U$	± (Ma)	$^{207}Pb^*/^{235}U^*$	± (Ma)	$^{206}Pb^*/^{207}Pb^*$	± (Ma)
Sample 07TM10		*Bean Canyon metavolcanic*														
07TM10-2	289	17225	2.9	19.3512	2.3	0.3105	2.8	0.0436	1.6	0.55	274.9	4.2	274.5	6.8	271.1	53.9
07TM10-3	144	8005	2.9	18.2941	27.4	0.3221	27.5	0.0427	1.7	0.06	269.8	4.4	283.5	68.0	398.4	625.0
07TM10-4	517	27825	2.5	19.2844	1.5	0.3136	2.4	0.0439	1.8	0.76	276.7	4.8	277.0	5.7	279.0	35.1
07TM10-5	270	14605	2.7	19.3023	2.3	0.3191	2.9	0.0447	1.7	0.58	281.7	4.6	281.2	7.1	276.9	53.6
07TM10-6	276	15945	2.0	18.8820	2.2	0.3143	3.1	0.0430	2.2	0.72	271.7	6.0	277.5	7.6	327.1	49.2
07TM10-7	337	16260	1.7	19.3228	2.4	0.3004	3.3	0.0421	2.2	0.67	265.9	5.8	266.8	7.7	274.5	55.9
07TM10-8	711	22175	2.1	18.5179	2.7	0.3407	3.1	0.0458	1.5	0.49	288.4	4.3	297.7	8.1	371.1	61.2
07TM10-9	960	58875	2.0	19.2741	3.5	0.3104	3.7	0.0434	1.3	0.34	273.8	3.4	274.5	9.0	280.2	80.6
07TM10-10	241	18065	3.0	19.1973	2.0	0.3142	2.3	0.0437	1.1	0.50	276.0	3.1	277.4	5.5	289.4	44.7
07TM10-11	651	32520	1.6	19.5107	1.2	0.3075	1.9	0.0435	1.4	0.76	274.6	3.8	272.3	4.5	252.2	28.3
07TM10-13	332	20380	2.0	19.8833	2.8	0.3044	5.0	0.0439	4.2	0.84	276.9	11.5	269.8	12.0	208.6	63.9
07TM10-14	210	7840	1.9	19.7845	3.7	0.2917	4.6	0.0419	2.7	0.59	264.3	7.0	259.9	10.5	220.1	85.2
07TM10-15	430	23780	1.4	19.2801	1.7	0.3099	2.1	0.0433	1.2	0.57	273.5	3.2	274.1	5.0	279.5	39.2
07TM10-16	700	44265	1.8	19.4276	1.4	0.3033	2.8	0.0427	2.4	0.85	269.8	6.3	269.0	6.6	262.1	33.1
07TM10-17	295	15445	2.6	17.6708	9.8	0.3476	9.9	0.0445	1.1	0.11	281.0	3.1	302.9	25.9	475.6	218.1
07TM10-18	366	22710	2.4	19.4448	2.9	0.3031	3.1	0.0427	1.2	0.38	269.8	3.1	268.8	7.4	260.0	66.4
07TM10-19	469	26425	1.9	19.1828	2.7	0.3148	2.8	0.0438	1.0	0.35	276.3	2.7	277.9	6.9	291.1	60.7
07TM10-20	413	26735	3.3	19.1188	2.5	0.3076	3.6	0.0426	2.7	0.73	269.2	7.0	272.3	8.6	298.7	56.0
07TM10-21	323	22900	4.7	19.6975	2.3	0.2895	2.7	0.0414	1.4	0.52	261.3	3.6	258.2	6.2	230.3	53.6
07TM10-22	217	13030	2.6	20.0077	1.3	0.2882	2.0	0.0418	1.6	0.78	264.1	4.1	257.1	4.6	194.1	29.7
07TM10-24	158	8700	3.3	19.2689	3.1	0.2978	3.7	0.0416	2.0	0.55	262.8	5.3	264.6	8.6	280.9	70.6
07TM10-25	677	27195	1.8	19.4280	5.0	0.3043	6.0	0.0429	3.4	0.56	270.7	9.0	269.8	14.3	262.0	114.4
07TM10-26	956	52100	3.8	19.4258	1.5	0.3053	2.2	0.0430	1.6	0.72	271.5	4.2	270.5	5.2	262.3	35.1
07TM10-27	405	20860	3.2	19.5424	2.5	0.3097	2.7	0.0439	1.1	0.41	276.9	3.1	273.9	6.6	248.5	57.2
Sample G11		*Guadalupe pluton*														
G11-1-1	461	8344	2.6	20.6261	2.9	0.1589	3.0	0.0238	0.6	0.21	151.5	1.0	149.8	4.2	122.8	69.2
G11-1-3	1088	19860	1.7	20.4275	1.4	0.1613	1.9	0.0239	1.2	0.67	152.2	1.9	151.8	2.6	145.6	32.4
G11-1-4	440	3672	2.1	19.7339	3.4	0.1654	3.5	0.0237	0.8	0.23	150.9	1.2	155.5	5.1	226.0	79.2
G11-1-5	395	6372	2.7	20.7130	3.2	0.1564	3.3	0.0235	0.7	0.23	149.7	1.1	147.6	4.5	112.9	75.1
G11-1-7	441	8940	2.5	20.9174	3.0	0.1564	3.1	0.0237	0.9	0.28	151.2	1.3	147.6	4.3	89.8	70.8
G11-1-9	329	6496	2.2	20.4900	4.1	0.1585	4.2	0.0236	1.1	0.26	150.1	1.6	149.4	5.9	138.5	95.8
G11-1-10	465	7576	2.4	20.0131	2.4	0.1666	2.4	0.0242	0.5	0.21	154.0	0.8	156.5	3.5	193.5	55.0
G11-1-11	344	4590	2.2	20.8246	2.9	0.1566	3.0	0.0237	0.9	0.31	150.7	1.4	147.7	4.1	100.2	67.9
G11-1-12	505	8242	1.6	20.3799	3.7	0.1621	3.9	0.0240	1.1	0.28	152.7	1.6	152.6	5.5	151.1	87.1
G11-1-13	829	14984	1.5	20.5123	1.9	0.1588	2.3	0.0236	1.4	0.60	150.5	2.1	149.7	3.3	135.9	43.9
G11-1-14	479	8934	1.7	20.5928	1.9	0.1613	2.2	0.0241	0.9	0.43	153.4	1.4	151.8	3.0	126.7	45.8
G11-1-15	403	7132	2.4	20.7533	2.0	0.1589	2.3	0.0239	1.0	0.43	152.4	1.5	149.7	3.2	108.4	48.4
G11-1-17	284	1304	1.9	14.7788	19.6	0.2309	19.7	0.0247	2.0	0.10	157.6	3.0	210.9	37.6	858.3	410.9
G11-1-18	764	9620	1.5	20.3448	1.8	0.1656	2.0	0.0244	0.9	0.43	155.6	1.3	155.6	2.9	155.1	42.5
G11-1-19	503	2738	2.4	19.3684	5.0	0.1713	5.3	0.0241	1.8	0.34	153.3	2.7	160.5	7.8	269.1	114.0
G11-1-20	354	7498	3.1	20.8686	4.7	0.1549	4.7	0.0234	0.8	0.16	149.4	1.1	146.3	6.4	95.2	110.6
G11-1-21	382	1308	2.2	16.1242	6.0	0.2084	6.8	0.0244	3.2	0.47	155.2	4.9	192.2	11.9	674.8	128.6
G11-1-22	1426	14790	1.5	20.3539	1.9	0.1631	2.0	0.0241	0.5	0.28	153.4	0.8	153.4	2.8	154.0	44.0
G11-1-23	418	7118	2.1	20.7293	3.9	0.1590	4.0	0.0239	1.0	0.24	152.3	1.5	149.8	5.6	111.1	91.9
G11-1-24	478	7566	2.2	20.7490	3.4	0.1550	3.5	0.0233	0.8	0.21	148.6	1.1	146.3	4.8	108.9	81.4
G11-1-25	463	9720	2.4	20.6427	2.0	0.1571	2.2	0.0235	0.8	0.37	149.8	1.2	148.1	3.0	120.9	47.3
G11-1-26	370	7564	2.3	20.7915	4.0	0.1596	4.1	0.0241	1.0	0.24	153.3	1.5	150.3	5.8	104.0	95.1
G11-1-27	349	6796	2.2	20.1267	3.3	0.1682	3.3	0.0245	0.5	0.15	156.3	0.8	157.8	4.9	180.3	77.0
G11-1-28	608	8952	2.0	20.3410	2.7	0.1601	2.8	0.0236	0.7	0.23	150.5	1.0	150.8	3.9	155.6	63.8
G11-1-29	466	2370	2.0	18.0548	9.6	0.1853	9.7	0.0243	1.2	0.12	154.5	1.8	172.6	15.3	427.9	214.0
G11-1-30	353	5508	2.3	20.7892	2.7	0.1591	2.9	0.0240	1.1	0.39	152.9	1.7	150.0	4.1	104.3	64.0
G11-1-32	407	3200	1.9	19.1550	3.6	0.1664	3.8	0.0231	1.3	0.33	147.3	1.8	156.3	5.5	294.4	81.8
G11-1-33	384	10208	2.2	20.9264	3.8	0.1573	3.9	0.0239	1.1	0.29	152.1	1.7	148.3	5.4	88.7	89.4
G11-1-34	843	8006	1.5	19.2010	10.6	0.1722	10.7	0.0240	1.3	0.12	152.8	1.9	161.3	15.9	288.9	242.9
G11-1-35	374	2298	2.2	18.6344	8.9	0.1757	8.9	0.0237	0.8	0.09	151.3	1.2	164.3	13.5	357.0	201.1

Table A2.1 (Continued).

Analysis	U (ppm)	$^{206}Pb/^{204}Pb$	U/Th	Isotope ratios							Isotopic ages (Ma)§					
				$^{206}Pb^*/^{207}Pb^*$	± (%)	$^{207}Pb^*/^{235}U^*$	± (%)	$^{206}Pb^*/^{238}U$	± (%)	Error correlation	$^{206}Pb^*/^{238}U$	± (Ma)	$^{207}Pb^*/^{235}U^*$	± (Ma)	$^{206}Pb^*/^{207}Pb^*$	± (Ma)
G11-1-36	361	6274	2.3	21.0237	4.4	0.1539	4.5	0.0235	0.8	0.17	149.6	1.1	145.4	6.0	77.7	104.4
G11-1-37	615	8986	1.5	20.5914	2.7	0.1575	2.8	0.0235	0.9	0.31	149.9	1.3	148.5	3.9	126.9	63.6
G11-1-39	455	5184	2.1	20.7522	4.3	0.1544	4.3	0.0232	0.5	0.12	148.1	0.7	145.8	5.8	108.5	100.9
G11-1-40	424	5664	1.8	20.8606	3.5	0.1529	3.7	0.0231	1.1	0.31	147.4	1.6	144.4	5.0	96.2	83.2

* Radiogenic

§ Decay constants used in age calculations: $\lambda^{238}U = 1.55125 \times 10^{-10}$ $\lambda^{235}U = 9.8485 \times 10^{-10}$ (Jaffey *et al*., 1971); $^{238}U/^{235}U = 137.88$ (Chen and Wasserberg, 1981). Uncertainties are given as ± 2σ in last three figures.

Common Pb correction from measured $^{206}Pb/^{204}Pb$, with initial Pb composition from Stacey and Kramers (1975).

Table A2.2. ID-TIMS U-Pb zircon data for plutonic and metavolcanic rocks of the southern Sierra Nevada batholith.

Sample	Fraction (μm)	Amount (mg)	^{238}U (ppm)	$^{206}Pb^*$ (ppm)	Atomic ratios				Isotopic ages (Ma)[§]		
					^{206}Pb / ^{204}Pb	$^{206}Pb^*$ / ^{238}U	$^{207}Pb^*$ / $^{235}U^*$	$^{207}Pb^*$ / $^{206}Pb^*$	$^{206}Pb^*$ / ^{238}U	$^{207}Pb^*$ / $^{235}U^*$	$^{207}Pb^*$ / $^{206}Pb^*$
91TH181	<45μ	1.9	653	8.1	9078	0.01439(09)	0.0959	0.04790(06)	92.1	92.2	94
	45-62μ	2.1	610	7.6	10103	0.01434(10)	0.0948	0.04795(07)	91.8	92.0	97
	62-80μ	2.2	579	7.2	8535	0.01440(12)	0.0958	0.04826(08)	92.2	92.9	112
	80-100μ	1.8	426	5.5	7809	0.01445(13)	0.0968	0.04861(08)	92.5	93.9	129
93TH417	<45μ	1.5	563	7.0	11789	0.01429(13)	0.0942	0.04781(07)	91.5	91.4	90
	45-62μ	1.8	533	6.7	10045	0.01442(12)	0.0952	0.04789(08)	92.3	92.4	94
	62-80μ	1.7	541	6.8	9137	0.01453(13)	0.0977	0.04877(09)	93.0	94.6	137
	80-100μ	1.3	498	6.3	7899	0.01451(12)	0.0969	0.04844(11)	92.9	93.9	121
91TH140	<45μ	0.8	306	4.3	4299	0.01606(12)	0.1065	0.04810(09)	102.8	102.7	104
	80-45μ	0.5	269	3.8	3378	0.01612(14)	0.1073	0.04827(11)	103.1	103.5	113

* Radiogenic; nonradiogenic correction based on 25 picogram blank Pb as determined by periodic measurements and initial Pb detereminations from Saleeby *et al*. (2008) of 1:18.632:15.601:38.735.

§ Decay constants used in age calculations: $\lambda^{238}U = 1.55125 \times 10^{-10}$ $\lambda^{235}U = 9.8485 \times 10^{-10}$ (Jaffey *et al*., 1971); $^{238}U/^{235}U = 137.88$ (Chen and Wasserberg, 1981). Uncertainties in $^{206}Pb^*/^{238}U$ and $^{207}Pb^*/^{206}Pb^*$ are given as ± 2σ in last two figures.
Common Pb correction from measured $^{206}Pb/^{204}Pb$, with initial Pb composition from Stacey and Kramers (1975).

Table A2.3. LA-MC-ICPMS U-Pb detrital zircon data for metamorphic pendant rocks of the southern Sierra Nevada batholith.[†]

Analysis	U (ppm)	$^{206}Pb/^{204}Pb$	U/Th	Isotope ratios $^{206}Pb^*/^{207}Pb^*$	± (%)	$^{207}Pb^*/^{235}U^*$	± (%)	$^{206}Pb^*/^{238}U$	± (%)	Error correlation	Isotopic ages (Ma)[§] $^{206}Pb^*/^{238}U$	± (Ma)	$^{207}Pb^*/^{235}U^*$	± (Ma)	$^{206}Pb^*/^{207}Pb^*$	± (Ma)
Sample 07BC60	*Bean Canyon pendant quartzite*															
08BC60-1	433	101608	2.2	9.0912	0.6	4.5693	1.1	0.3013	0.9	0.84	1697.6	14.0	1743.7	9.3	1799.3	10.9
08BC60-2	261	45856	2.8	11.0421	2.5	2.8781	3.6	0.2305	2.6	0.73	1337.1	31.5	1376.2	27.1	1437.4	47.1
08BC60-3	622	181943	5.3	9.1134	0.4	4.4873	3.0	0.2966	3.0	0.99	1674.4	44.5	1728.6	25.3	1794.9	7.2
08BC60-4	421	135550	6.9	9.1146	0.9	4.5832	1.9	0.3030	1.7	0.89	1706.0	25.8	1746.2	16.0	1794.6	15.7
08BC60-5	511	246994	3.3	9.1523	0.9	4.4190	3.5	0.2933	3.3	0.97	1658.1	48.8	1715.9	28.6	1787.1	16.2
08BC60-6	220	71550	3.2	9.2493	1.4	4.4750	2.5	0.3002	2.0	0.81	1692.3	30.2	1726.4	20.7	1767.9	26.4
08BC60-7	234	104856	5.4	5.6164	0.7	10.7448	2.6	0.4377	2.5	0.97	2340.2	49.6	2501.3	24.3	2634.8	11.1
08BC60-8	149	85338	2.3	9.2390	2.1	4.5515	3.3	0.3050	2.6	0.78	1716.0	39.4	1740.4	27.8	1769.9	38.1
08BC60-9	762	160145	5.6	9.1369	0.6	4.7940	5.0	0.3177	5.0	0.99	1778.4	77.8	1783.8	42.4	1790.2	11.0
08BC60-10	209	44432	2.1	9.1187	1.3	4.3709	3.7	0.2891	3.5	0.94	1636.9	50.3	1706.8	30.7	1793.8	23.6
08BC60-11	459	86756	5.6	9.1299	0.6	4.8694	4.3	0.3224	4.3	0.99	1801.6	67.5	1797.0	36.6	1791.6	11.0
08BC60-12	598	260789	9.0	9.1595	0.8	4.5367	2.5	0.3014	2.4	0.95	1698.2	35.8	1737.7	21.0	1785.7	14.0
08BC60-13	97	39396	1.5	9.1312	1.7	4.6421	3.0	0.3074	2.5	0.83	1728.0	38.2	1756.9	25.4	1791.3	31.1
08BC60-14	94	19783	1.6	8.5879	3.0	5.1574	3.2	0.3212	1.2	0.37	1795.7	18.6	1845.6	27.4	1902.3	53.9
08BC60-16	507	94653	8.0	8.9865	1.0	4.9100	9.0	0.3200	9.0	0.99	1789.8	140.2	1804.0	76.3	1820.4	18.8
08BC60-17	276	57681	4.5	9.2259	1.5	4.5062	3.4	0.3015	3.1	0.90	1698.8	46.1	1732.1	28.4	1772.5	26.8
08BC60-18	308	71488	3.6	9.1615	1.3	4.5499	2.4	0.3023	2.0	0.85	1702.8	30.5	1740.1	20.0	1785.3	23.3
08BC60-19	98	23730	3.0	11.1187	4.0	2.9230	4.5	0.2357	2.0	0.46	1364.4	25.1	1387.9	33.7	1424.2	75.6
08BC60-20	401	145021	6.5	9.1097	0.7	4.6857	2.7	0.3096	2.6	0.97	1738.7	39.6	1764.7	22.5	1795.6	12.8
08BC60-21	188	66895	3.5	8.9906	2.0	4.7396	4.7	0.3091	4.2	0.90	1736.0	64.3	1774.3	39.2	1819.5	36.4
08BC60-22	290	92491	6.7	9.1422	0.7	4.7691	4.1	0.3162	4.1	0.98	1771.2	62.9	1779.5	34.7	1789.1	13.6
08BC60-23	342	170208	3.4	9.0726	0.7	4.5684	2.8	0.3006	2.7	0.97	1694.3	40.6	1743.5	23.3	1803.1	11.8
08BC60-24	439	147481	2.9	9.1210	0.7	4.4757	4.1	0.2961	4.1	0.99	1671.8	60.0	1726.5	34.3	1793.4	12.7
08BC60-25	59	15001	1.9	10.9441	4.6	2.9613	5.1	0.2350	2.2	0.44	1360.9	27.4	1397.7	38.6	1454.4	87.0
08BC60-26	319	75004	2.7	9.2403	0.8	4.6041	2.3	0.3086	2.1	0.93	1733.6	32.1	1750.0	18.9	1769.7	15.0
08BC60-27	790	228418	3.6	9.3419	0.6	3.8586	2.7	0.2614	2.6	0.98	1497.2	35.0	1605.1	21.6	1749.7	10.1
08BC60-28	313	143603	4.8	8.1641	0.6	5.8528	4.2	0.3466	4.1	0.99	1918.1	68.8	1954.3	36.4	1992.8	10.5
08BC60-29	199	60747	2.8	9.2885	1.3	4.4533	3.1	0.3000	2.8	0.90	1691.3	41.1	1722.3	25.5	1760.2	24.6
08BC60-32	236	73027	3.9	9.0634	1.2	4.6636	1.9	0.3066	1.5	0.78	1723.7	22.6	1760.7	16.0	1804.9	21.7
08BC60-33	224	34998	2.2	11.1339	3.3	2.9909	5.8	0.2415	4.8	0.82	1394.6	60.4	1405.3	44.5	1421.6	63.2
08BC60-35	477	141295	9.1	8.7679	0.7	3.9260	6.0	0.2497	6.0	0.99	1436.7	77.1	1619.1	48.8	1865.0	11.9
08BC60-36	79	13176	2.3	9.5739	2.8	3.9518	3.9	0.2744	2.7	0.69	1563.1	36.9	1624.4	31.4	1704.6	52.0
08BC60-37	233	76190	2.1	4.9281	0.6	14.4471	4.1	0.5164	4.1	0.99	2683.8	89.5	2779.5	39.1	2849.8	9.5
08BC60-38	293	97282	3.7	9.2179	1.1	4.2751	1.7	0.2858	1.3	0.76	1620.6	18.4	1688.6	13.8	1774.1	19.8
08BC60-39	734	174670	16.3	9.1238	0.2	4.2914	3.5	0.2840	3.5	1.00	1611.3	49.8	1691.7	28.8	1792.8	4.4
08BC60-40	143	69582	2.2	5.4953	1.1	10.9430	2.7	0.4361	2.5	0.92	2333.3	48.8	2518.3	25.3	2670.9	17.8
08BC60-41	132	36954	2.6	8.7751	1.7	4.4284	3.8	0.2818	3.4	0.89	1600.6	48.4	1717.7	31.7	1863.5	31.0
08BC60-42	239	91937	4.1	8.4833	1.0	5.3000	4.5	0.3261	4.3	0.97	1819.4	68.8	1868.9	38.1	1924.3	17.8
08BC60-43	77	13797	2.4	13.1489	7.1	1.8081	9.5	0.1724	6.3	0.66	1025.5	59.4	1048.4	62.1	1096.4	142.8
08BC60-44	207	39718	3.1	11.1394	1.8	2.8778	2.2	0.2325	1.2	0.55	1347.6	14.6	1376.1	16.4	1420.7	34.7
08BC60-45	59	10864	2.9	11.5016	8.1	2.7933	9.3	0.2330	4.6	0.49	1350.2	55.5	1353.7	69.8	1359.2	157.0
08BC60-46	95	28438	1.1	4.9077	0.7	14.0820	2.7	0.5012	2.6	0.96	2619.1	56.0	2755.2	25.6	2856.6	12.0
08BC60-48	345	50833	3.8	9.1575	0.8	4.5895	3.5	0.3048	3.4	0.97	1715.2	50.7	1747.4	29.0	1786.1	15.3
08BC60-50	354	60842	8.3	9.1469	0.6	4.5526	3.4	0.3020	3.3	0.98	1701.3	49.8	1740.6	28.2	1788.2	11.3
08BC60-51	397	279777	7.8	9.1527	0.7	4.3835	1.9	0.2910	1.8	0.93	1646.4	26.0	1709.2	16.0	1787.1	13.3
08BC60-52	83	22887	1.9	9.9808	2.9	3.7248	4.0	0.2696	2.8	0.70	1538.9	37.8	1576.7	31.8	1627.6	53.0
08BC60-53	307	91849	2.7	9.1799	1.5	4.2397	4.1	0.2823	3.8	0.93	1602.8	54.3	1681.7	33.6	1781.6	26.5
08BC60-54	76	16004	2.3	13.4453	9.9	1.8591	10.2	0.1813	2.5	0.25	1074.0	25.1	1066.7	67.3	1051.7	199.2
08BC60-55	380	107792	4.5	9.1570	0.8	4.8617	4.0	0.3229	4.0	0.98	1803.8	62.3	1795.6	34.0	1786.2	14.4
08BC60-56	79	30801	2.4	9.5514	2.6	4.2919	3.4	0.2973	2.2	0.65	1678.0	32.8	1691.8	28.3	1709.0	48.3
08BC60-57	168	58425	1.4	9.2473	0.9	4.6824	4.3	0.3140	4.2	0.98	1760.6	64.2	1764.1	35.6	1768.3	15.7
08BC60-58	103	34307	1.5	9.2653	1.7	4.7744	4.4	0.3208	4.1	0.92	1793.8	63.5	1780.4	36.9	1764.7	31.1
08BC60-59	211	106526	2.0	9.1541	0.9	4.6580	2.3	0.3093	2.1	0.92	1737.0	32.5	1759.7	19.5	1786.8	17.1
08BC60-60	352	106534	3.2	9.1039	1.1	4.6487	4.1	0.3069	3.9	0.96	1725.7	59.1	1758.1	34.0	1796.8	20.8
08BC60-61	270	126561	2.0	9.0861	0.8	4.8513	3.5	0.3197	3.4	0.97	1788.2	53.3	1793.8	29.5	1800.4	14.8
08BC60-62	281	53418	2.5	9.0712	0.6	4.8560	5.3	0.3195	5.2	0.99	1787.2	81.9	1794.7	44.5	1803.3	10.3
08BC60-63	161	47689	2.0	9.1731	1.4	5.0005	2.8	0.3327	2.4	0.87	1851.4	38.3	1819.4	23.3	1783.0	25.2
08BC60-64	174	31740	2.4	10.9978	2.0	2.9273	3.5	0.2335	2.8	0.81	1352.8	34.2	1389.0	26.2	1445.1	38.6

Table A2.3 (Continued).

Analysis	U	^{206}Pb	U/Th	Isotope ratios							Isotopic ages (Ma)[§]					
				$^{206}Pb^*$	±	$^{207}Pb^*$	±	$^{206}Pb^*$	±	Error	$^{206}Pb^*$	±	$^{207}Pb^*$	±	$^{206}Pb^*$	±
	(ppm)	^{204}Pb		$^{207}Pb^*$	(%)	$^{235}U^*$	(%)	^{238}U	(%)	correlation	^{238}U	(Ma)	$^{235}U^*$	(Ma)	$^{207}Pb^*$	(Ma)
08BC60-65	176	32889	2.6	9.0978	1.4	4.5883	2.9	0.3027	2.6	0.88	1704.9	38.8	1747.1	24.5	1798.0	25.2
08BC60-66	186	36345	7.2	9.4298	2.0	4.3232	4.0	0.2957	3.5	0.87	1669.8	51.6	1697.8	33.2	1732.5	36.0
08BC60-67	134	56430	4.5	9.0071	2.7	4.7390	4.3	0.3096	3.4	0.78	1738.6	51.2	1774.2	36.3	1816.2	49.4
08BC60-68	689	463029	13.9	9.0624	0.4	4.2412	4.3	0.2788	4.3	1.00	1585.1	60.7	1682.0	35.6	1805.1	6.8
08BC60-69	138	44373	4.0	8.9475	2.2	4.5836	3.1	0.2974	2.2	0.70	1678.6	32.6	1746.3	26.2	1828.3	40.4
08BC60-70	116	22947	4.2	8.7264	1.8	5.0276	3.6	0.3182	3.1	0.86	1780.9	48.7	1824.0	30.7	1873.5	32.9
08BC60-71	432	42608	5.8	8.9187	0.8	4.9886	8.2	0.3227	8.1	1.00	1802.8	128.1	1817.4	69.3	1834.1	13.8
08BC60-72	209	37877	2.6	11.2438	2.2	2.7287	3.4	0.2225	2.6	0.76	1295.2	30.1	1336.3	25.1	1402.8	42.2
08BC60-73	147	32446	3.1	9.4838	1.9	4.2521	2.7	0.2925	1.8	0.68	1653.9	26.5	1684.2	21.9	1722.0	35.8
08BC60-74	478	242215	1.1	5.5836	0.4	10.5116	2.4	0.4257	2.4	0.99	2286.2	45.5	2480.9	22.2	2644.5	6.3
08BC60-75	651	118578	6.4	8.9820	0.5	4.8586	2.5	0.3165	2.4	0.98	1772.6	37.2	1795.1	20.7	1821.3	9.5
08BC60-76	228	158461	3.5	9.4642	1.2	3.9582	2.3	0.2717	2.0	0.86	1549.4	27.3	1625.7	18.7	1725.8	21.6
08BC60-77	192	134748	4.8	6.7577	2.8	7.6203	5.2	0.3735	4.4	0.84	2045.8	76.6	2187.3	46.7	2322.7	48.1
08BC60-78	103	18550	2.5	10.6716	3.5	3.0676	4.4	0.2374	2.6	0.59	1373.3	31.6	1424.6	33.4	1502.2	66.8
08BC60-79	210	37684	3.3	10.9144	2.2	3.0650	3.8	0.2426	3.1	0.82	1400.3	39.0	1424.0	29.0	1459.5	41.4
08BC60-80	135	27500	4.2	9.4311	1.5	4.1994	3.0	0.2872	2.6	0.86	1627.7	37.9	1673.9	25.0	1732.3	28.1
08BC60-81	124	51479	1.2	9.0450	1.2	4.7456	2.9	0.3113	2.7	0.92	1747.2	41.3	1775.3	24.7	1808.6	21.4
08BC60-82	72	24485	1.0	5.3239	1.8	12.5278	3.1	0.4837	2.5	0.82	2543.5	52.9	2644.8	29.0	2723.3	29.2
08BC60-83	538	76863	4.7	9.2464	0.7	4.1637	2.5	0.2792	2.4	0.96	1587.5	33.7	1666.9	20.5	1768.5	13.5
08BC60-84	84	45401	0.9	6.2887	1.4	9.6174	3.4	0.4386	3.0	0.91	2344.6	59.8	2398.8	30.9	2445.2	23.9
08BC60-85	434	128105	3.4	8.9880	0.7	4.8149	2.3	0.3139	2.2	0.95	1759.7	33.3	1787.5	19.1	1820.1	12.9
08BC60-86	88	21222	5.0	8.9661	1.8	4.7362	3.3	0.3080	2.8	0.84	1730.8	42.3	1773.7	27.9	1824.5	32.8
08BC60-87	364	148180	2.0	8.7178	1.6	4.6549	2.2	0.2943	1.6	0.70	1663.1	23.0	1759.2	18.6	1875.3	28.5
08BC60-89	379	61283	2.0	9.0956	1.2	4.4586	2.2	0.2941	1.8	0.84	1662.1	26.8	1723.3	18.0	1798.4	21.4
08BC60-90	88	15967	2.8	10.9884	4.1	2.9980	5.0	0.2389	2.9	0.58	1381.1	36.4	1407.1	38.4	1446.7	78.2
08BC60-91	339	154221	2.8	9.1762	1.2	4.6195	3.0	0.3074	2.7	0.91	1728.1	40.9	1752.8	24.8	1782.4	22.4
08BC60-92	238	131455	3.0	4.7462	0.4	14.7037	2.9	0.5061	2.9	0.99	2640.1	63.0	2796.3	27.9	2910.9	6.4
08BC60-93	77	90489	2.1	5.4574	1.2	12.4430	1.8	0.4925	1.4	0.76	2581.5	29.6	2638.4	17.2	2682.4	19.5
08BC60-94	70	31394	1.6	5.1740	1.9	13.4414	3.0	0.5044	2.3	0.77	2632.6	49.3	2711.2	28.1	2770.2	31.3
08BC60-95	289	65780	5.2	9.0627	1.1	4.7545	2.6	0.3125	2.3	0.90	1753.0	35.8	1776.9	21.8	1805.0	20.5
08BC60-96	716	26121	4.3	9.3547	0.5	3.2990	3.1	0.2238	3.1	0.99	1302.1	36.3	1480.8	24.3	1747.2	8.5
08BC60-97	189	87513	2.5	9.4819	0.9	4.1016	2.7	0.2821	2.5	0.94	1601.7	35.7	1654.6	21.9	1722.4	17.4
08BC60-98	140	30270	2.2	10.9808	2.3	2.9183	5.0	0.2324	4.4	0.88	1347.1	53.5	1386.7	37.7	1448.0	44.7
08BC60-99	880	343102	2.1	9.1302	0.4	4.4114	2.7	0.2921	2.6	0.99	1652.1	38.3	1714.5	22.1	1791.5	8.0
08BC60-100	245	42167	3.2	9.5353	1.2	4.2980	2.3	0.2972	2.0	0.87	1677.6	30.0	1693.0	19.3	1712.1	21.4
08BC60-102	184	50681	3.5	9.0926	1.5	4.3918	2.2	0.2896	1.7	0.76	1639.6	24.6	1710.8	18.6	1799.0	26.7
08BC60-103	283	70226	2.4	9.1521	0.8	4.5023	2.4	0.2989	2.3	0.95	1685.6	33.6	1731.4	19.9	1787.2	14.0
08BC60-104	165	32086	1.4	9.4118	1.0	4.0808	3.6	0.2786	3.5	0.96	1584.1	48.7	1650.5	29.4	1736.0	18.5
08BC60-105	83	32580	1.0	9.7072	2.4	3.8530	4.6	0.2713	3.9	0.84	1547.2	53.0	1603.9	36.8	1679.2	45.2
08BC60-106	130	81291	1.9	5.4211	0.9	12.1209	2.5	0.4766	2.3	0.94	2512.3	47.7	2613.8	23.0	2693.4	14.4
08BC60-107	295	76126	4.7	9.2166	0.9	4.4682	3.6	0.2987	3.5	0.97	1684.8	52.0	1725.1	30.1	1774.4	17.2
08BC60-108	74	13845	1.7	11.1038	4.9	2.8975	7.4	0.2333	5.6	0.75	1352.0	67.9	1381.3	56.1	1426.8	93.8
08BC60-109	221	63369	1.9	9.1149	1.0	4.6002	2.6	0.3041	2.4	0.92	1711.7	35.5	1749.3	21.4	1794.6	18.0
08BC60-110	272	61866	2.2	8.7227	1.3	4.8931	3.4	0.3095	3.2	0.92	1738.5	48.2	1801.1	28.9	1874.3	23.8
08BC60-111	81	33310	5.3	8.7041	2.0	4.9641	5.6	0.3134	5.2	0.93	1757.3	80.4	1813.2	47.5	1878.1	36.8
08BC60-112	195	56478	3.0	9.4003	1.8	4.2089	2.5	0.2870	1.7	0.69	1626.3	24.9	1675.8	20.4	1738.3	32.8
08BC60-113	710	166191	9.7	9.1639	0.6	3.9063	5.9	0.2596	5.9	0.99	1487.9	78.0	1615.0	47.8	1784.8	11.0
08BC60-114	374	212273	5.9	9.1292	0.8	4.6021	3.0	0.3047	2.9	0.97	1714.6	43.2	1749.7	24.7	1791.7	13.7
Sample 08SE258 Salt Creek pendant metaturbidite																
08SE258-1	268	21764	1.7	11.0809	1.2	2.5492	2.9	0.2049	2.7	0.90	1201.4	29.0	1286.2	21.4	1430.7	23.8
08SE258-2	49	4946	0.9	11.7987	3.1	2.6105	4.3	0.2234	3.0	0.70	1299.7	35.5	1303.6	31.6	1309.9	59.5
08SE258-6	87	7658	2.8	12.8945	1.9	2.0316	1.9	0.1900	0.5	0.26	1121.3	5.1	1126.1	13.1	1135.4	37.0
08SE258-7	284	35216	4.4	12.7651	1.3	1.8182	1.7	0.1683	1.2	0.67	1002.9	10.8	1052.0	11.4	1155.5	25.8
08SE258-8	132	12658	1.9	11.4320	2.0	2.3544	2.9	0.1952	2.2	0.74	1149.5	22.8	1228.9	20.8	1370.9	37.6
08SE258-10	207	9294	1.6	11.6861	2.8	1.8364	3.5	0.1556	2.0	0.57	932.5	17.2	1058.6	22.7	1328.5	54.8
08SE258-12	251	16398	2.2	12.5497	0.6	2.0252	2.1	0.1843	2.0	0.96	1090.6	20.1	1124.0	14.2	1189.2	11.7
08SE258-14	128	7482	1.2	12.2832	3.1	2.0477	3.6	0.1824	1.8	0.51	1080.2	18.3	1131.5	24.8	1231.4	61.5
08SE258-16	60	4280	2.8	14.4390	3.6	1.5118	3.9	0.1583	1.4	0.37	947.5	12.7	935.2	23.7	906.4	74.1
08SE258-17	104	3630	8.5	13.9376	3.7	0.9388	5.2	0.0949	3.6	0.70	584.5	20.3	672.3	25.7	978.8	76.3

Table A2.3 (Continued).

Analysis	U (ppm)	$^{206}Pb/^{204}Pb$	U/Th	Isotope ratios							Isotopic ages (Ma)[§]					
				$^{206}Pb^*/^{207}Pb^*$	± (%)	$^{207}Pb^*/^{235}U^*$	± (%)	$^{206}Pb^*/^{238}U$	± (%)	Error correlation	$^{206}Pb^*/^{238}U$	± (Ma)	$^{207}Pb^*/^{235}U^*$	± (Ma)	$^{206}Pb^*/^{207}Pb^*$	± (Ma)
08SE258-18	244	20862	3.5	9.4863	1.4	3.7260	2.9	0.2564	2.6	0.88	1471.1	33.9	1577.0	23.4	1721.6	25.1
08SE258-19	58	3292	1.5	13.8593	3.4	1.5843	4.7	0.1593	3.3	0.70	952.6	29.6	964.1	29.6	990.3	68.7
08SE258-20	157	8776	2.2	13.9653	2.0	1.4981	4.5	0.1517	4.0	0.89	910.7	34.1	929.6	27.3	974.8	41.0
08SE258-22	120	15696	1.5	9.8347	1.8	3.7920	3.6	0.2705	3.1	0.87	1543.2	43.1	1591.1	29.1	1655.0	33.4
08SE258-23	199	14062	2.3	12.4518	1.2	2.2924	2.1	0.2070	1.7	0.81	1212.9	18.7	1209.9	14.7	1204.6	23.7
08SE258-24	1140	12760	7.6	8.6124	1.7	0.8591	1.8	0.0537	0.8	0.41	337.0	2.5	629.6	8.6	1897.2	30.0
08SE258-26	968	2264	14.4	19.1252	7.8	0.1027	8.0	0.0142	1.9	0.23	91.2	1.7	99.3	7.6	298.0	178.0
08SE258-27	228	15472	1.2	10.2042	1.8	2.7377	5.5	0.2026	5.2	0.95	1189.3	56.6	1338.8	40.9	1586.4	33.1
08SE258-28	135	8460	2.4	11.1740	1.8	2.1539	5.0	0.1746	4.6	0.94	1037.2	44.5	1166.3	34.4	1414.7	33.5
08SE258-29	282	10044	4.2	13.2570	1.8	0.9981	2.8	0.0960	2.2	0.79	590.7	12.6	702.8	14.4	1080.0	35.1
08SE258-30	53	3376	2.8	14.0305	3.8	1.6010	4.4	0.1629	2.3	0.52	973.0	20.6	970.6	27.5	965.3	76.7
08SE258-31	255	16216	3.8	13.6532	1.5	1.4798	4.2	0.1465	3.9	0.93	881.5	32.5	922.1	25.6	1020.7	31.0
08SE258-33	99	11226	2.3	13.3051	2.6	1.6782	3.7	0.1619	2.6	0.71	967.5	23.2	1000.3	23.3	1072.8	52.1
08SE258-34	115	11842	1.4	11.3817	1.6	2.6084	2.9	0.2153	2.4	0.84	1257.1	27.8	1303.0	21.3	1379.4	30.3
08SE258-36	137	15504	2.5	9.6827	1.8	3.3629	2.3	0.2362	1.4	0.61	1366.7	17.2	1495.8	17.9	1683.8	33.5
08SE258-37	133	12298	2.0	13.6221	2.5	1.6364	3.1	0.1617	1.8	0.58	966.0	15.9	984.3	19.4	1025.3	50.8
08SE258-39	199	8210	2.6	13.5975	4.4	0.8548	4.7	0.0843	1.6	0.35	521.7	8.1	627.3	21.9	1028.9	88.8
08SE258-41	100	7258	1.9	11.6176	1.9	2.1114	6.2	0.1779	5.9	0.95	1055.5	57.3	1152.5	42.6	1339.9	37.1
08SE258-42	160	17888	1.7	9.9873	2.0	3.4628	4.8	0.2508	4.4	0.91	1442.8	56.8	1518.8	38.1	1626.4	37.8
08SE258-43	251	11282	2.8	12.8443	1.9	1.7125	2.0	0.1595	0.5	0.25	954.2	4.4	1013.2	12.7	1143.2	38.1
08SE258-44	77	4916	1.3	11.4509	3.3	2.2441	4.1	0.1864	2.5	0.59	1101.7	24.9	1194.9	29.1	1367.8	64.2
08SE258-45	90	10352	3.5	8.2312	1.4	4.5579	2.4	0.2721	1.9	0.80	1551.5	26.2	1741.6	19.8	1978.2	25.3
08SE258-46	135	6280	3.4	13.7631	2.8	0.9446	2.9	0.0943	0.7	0.23	580.8	3.7	675.3	14.2	1004.4	56.8
08SE258-47	141	16576	2.2	10.8811	0.7	2.6273	2.8	0.2073	2.7	0.97	1214.6	30.0	1308.3	20.6	1465.4	13.7
08SE258-49	278	18638	1.0	13.1149	1.5	1.4717	1.8	0.1400	1.0	0.56	844.6	8.2	918.8	11.2	1101.6	30.5
08SE258-51	115	15134	2.6	13.8899	2.4	1.6051	3.2	0.1617	2.2	0.67	966.2	19.3	972.2	20.0	985.8	48.1
08SE258-53	338	23874	3.0	13.0625	0.9	1.5216	2.2	0.1441	2.0	0.91	868.1	16.0	939.1	13.3	1109.6	18.2
08SE258-54	47	8574	2.4	13.3361	3.1	1.8425	3.7	0.1782	2.0	0.53	1057.2	19.2	1060.7	24.3	1068.1	62.7
08SE258-55	619	12174	3.8	10.2612	1.7	1.2946	4.1	0.0963	3.7	0.91	593.0	21.1	843.4	23.5	1576.0	32.6
08SE258-56	278	19228	2.0	13.0136	2.4	1.7228	3.3	0.1626	2.3	0.70	971.2	21.1	1017.1	21.3	1117.1	47.0
08SE258-57	443	32844	2.2	11.8050	2.3	2.1144	3.8	0.1810	3.1	0.80	1072.6	30.3	1153.5	26.5	1308.9	44.8
08SE258-58	177	26776	3.5	9.4014	0.6	4.3236	0.8	0.2948	0.6	0.69	1665.5	8.4	1697.9	6.8	1738.1	11.1
08SE258-60	204	20436	2.2	10.9353	1.7	2.6617	2.0	0.2111	1.2	0.57	1234.7	13.0	1317.9	14.9	1455.9	31.4
08SE258-62	335	29702	4.0	9.1349	2.1	4.0210	2.4	0.2664	1.1	0.46	1522.5	14.8	1638.4	19.1	1790.6	37.9
08SE258-63	217	15544	2.3	13.4461	1.6	1.6676	1.9	0.1626	1.0	0.53	971.3	8.9	996.3	11.9	1051.6	32.2
08SE258-64	319	32066	4.5	13.0895	1.8	1.5322	2.1	0.1455	1.2	0.55	875.5	9.6	943.4	13.2	1105.5	35.9
08SE258-65	89	10414	2.6	11.5233	2.0	2.5467	2.9	0.2128	2.2	0.74	1244.0	24.8	1285.5	21.5	1355.6	38.0
08SE258-66	53	6744	1.4	10.9537	1.7	2.8138	10.0	0.2235	9.9	0.99	1300.5	116.1	1359.2	75.1	1452.7	32.2
08SE258-67	160	9428	2.0	12.8409	4.6	1.6561	5.4	0.1542	2.7	0.51	924.7	23.6	991.9	34.1	1143.7	92.2
08SE258-68	180	6412	11.8	11.3547	2.9	1.0436	3.6	0.0859	2.2	0.60	531.5	11.0	725.7	18.5	1384.0	54.8
08SE258-70	70	4080	1.5	12.1245	2.4	2.2499	3.2	0.1978	2.1	0.65	1163.7	21.8	1196.8	22.3	1256.9	47.2
08SE258-72	176	10548	2.3	11.6376	2.0	2.2978	3.0	0.1939	2.3	0.76	1142.7	24.1	1211.6	21.5	1336.6	38.3
08SE258-74	72	7086	3.0	11.2651	2.7	2.8418	3.2	0.2322	1.8	0.54	1345.9	21.4	1366.7	24.3	1399.2	52.1
08SE258-75	794	20360	6.7	14.0226	1.7	0.9539	3.3	0.0970	2.8	0.85	596.9	16.2	680.1	16.5	966.4	35.4
08SE258-77	123	16042	2.0	11.1722	4.0	2.9360	4.1	0.2379	0.8	0.20	1375.8	10.0	1391.2	30.8	1415.0	76.2
08SE258-78	165	7582	1.6	13.2823	3.4	1.3148	7.2	0.1267	6.4	0.88	768.8	46.2	852.3	41.7	1076.2	68.3
08SE258-79	283	14836	4.2	13.7996	3.9	1.4289	6.3	0.1430	4.9	0.78	861.6	39.4	901.1	37.5	999.0	79.9
08SE258-81	144	10176	2.0	13.6226	3.5	1.4599	4.2	0.1442	2.3	0.55	868.6	18.8	914.0	25.4	1025.2	71.3
08SE258-83	376	26686	4.3	13.2226	1.7	1.5159	3.9	0.1454	3.5	0.90	875.0	28.4	936.8	23.7	1085.2	34.1
08SE258-86	83	7710	3.5	13.9911	2.2	1.6431	2.3	0.1667	0.7	0.32	994.1	6.6	986.9	14.4	971.0	44.2
08SE258-87	39	4344	2.0	12.9255	2.0	2.0476	2.2	0.1920	0.8	0.36	1131.9	8.2	1131.5	14.9	1130.6	40.7
08SE258-88	412	32162	2.2	13.2269	1.4	1.8049	1.8	0.1731	1.1	0.61	1029.4	10.3	1047.2	11.5	1084.6	27.9
08SE258-89	144	18390	2.8	10.8588	1.0	3.1179	1.1	0.2456	0.5	0.44	1415.5	6.4	1437.1	8.8	1469.2	19.6
08SE258-91	123	10504	3.7	13.5099	2.4	1.7269	3.0	0.1692	1.8	0.60	1007.8	16.6	1018.6	19.1	1042.0	48.0
08SE258-92	467	24924	1.8	13.3458	2.2	1.3544	4.6	0.1311	4.0	0.88	794.1	30.2	869.5	26.9	1066.6	44.7
08SE258-93	308	16912	2.1	12.1116	1.6	1.8614	2.2	0.1635	1.5	0.69	976.2	13.4	1067.5	14.3	1259.0	30.7
08SE258-94	116	17460	2.3	11.3410	4.6	2.5638	9.9	0.2109	8.8	0.89	1233.5	98.6	1290.4	72.5	1386.3	88.2
08SE258-95	83	9408	2.0	12.9937	1.4	1.9672	2.7	0.1854	2.3	0.86	1096.3	23.2	1104.4	18.0	1120.2	27.0
08SE258-97	78	6190	1.7	13.4889	2.1	1.7651	3.0	0.1727	2.1	0.72	1026.9	20.2	1032.7	19.2	1045.2	41.5
08SE258-98	264	18114	2.0	13.4423	1.2	1.5999	2.1	0.1560	1.7	0.81	934.4	15.1	970.2	13.4	1052.1	25.2

Table A2.3 (Continued).

Analysis	U (ppm)	$^{206}Pb/^{204}Pb$	U/Th	Isotope ratios							Isotopic ages (Ma)[§]					
				$^{206}Pb^*/^{207}Pb^*$	± (%)	$^{207}Pb^*/^{235}U^*$	± (%)	$^{206}Pb^*/^{238}U$	± (%)	Error correlation	$^{206}Pb^*/^{238}U$	± (Ma)	$^{207}Pb^*/^{235}U^*$	± (Ma)	$^{206}Pb^*/^{207}Pb^*$	± (Ma)
08SE258-100	134	6870	1.8	13.0608	2.3	1.6753	4.7	0.1587	4.1	0.87	949.5	36.1	999.2	29.7	1109.9	45.2
08SE258-101	76	13320	2.5	13.3619	1.4	1.6836	2.8	0.1632	2.4	0.87	974.3	22.0	1002.3	17.7	1064.2	27.4
08SE258-102	204	25022	3.5	10.9764	1.9	2.9363	2.2	0.2338	1.2	0.55	1354.2	14.8	1391.3	16.8	1448.8	35.4
08SE259-4	100	12056	2.7	13.6229	1.5	1.7410	1.9	0.1720	1.1	0.59	1023.2	10.4	1023.9	12.1	1025.2	30.8
08SE259-18	139	22904	2.6	12.8851	1.7	2.0793	2.6	0.1943	2.0	0.76	1144.7	20.9	1142.0	17.9	1136.9	33.5
08SE259-19	90	23530	2.1	9.6541	1.4	4.0604	3.0	0.2843	2.7	0.89	1613.0	38.1	1646.4	24.6	1689.3	25.8
08SE259-22	135	9560	3.0	13.5090	2.9	1.7839	3.5	0.1748	1.9	0.55	1038.4	18.1	1039.6	22.5	1042.1	58.3
08SE259-24	336	46496	1.0	12.5782	1.3	2.1895	1.4	0.1997	0.5	0.36	1173.9	5.4	1177.7	9.6	1184.7	25.3
08SE259-27	29	11840	1.0	5.3090	1.2	13.2849	1.4	0.5115	0.7	0.51	2663.1	15.9	2700.1	13.6	2727.9	20.5
08SE259-36	1327	13340	5.9	14.8824	1.8	0.4843	1.8	0.0523	0.5	0.27	328.4	1.6	401.0	6.1	843.7	36.6
08SE259-41	686	13862	19.4	6.7169	2.1	0.8071	6.9	0.0393	6.6	0.95	248.6	16.1	600.8	31.4	2333.1	35.8
08SE259-43	893	52338	4.8	13.7240	2.2	0.8806	3.7	0.0877	3.0	0.81	541.6	15.7	641.3	17.6	1010.2	43.6
08SE259-45	109	16270	3.7	12.9742	1.9	2.0296	2.0	0.1910	0.5	0.25	1126.7	5.2	1125.5	13.4	1123.2	38.0
08SE259-48	235	15372	6.7	13.7903	2.6	0.8683	4.3	0.0868	3.4	0.80	536.8	17.6	634.6	20.2	1000.4	52.6
08SE259-52	286	16492	3.8	13.4869	1.4	0.8178	3.8	0.0800	3.5	0.93	496.1	16.8	606.8	17.3	1045.5	29.0
08SE259-55	161	11552	3.7	12.0842	1.5	0.7237	10.0	0.0634	9.9	0.99	396.4	37.9	552.8	42.6	1263.4	29.9
08SE259-56	665	42226	41.4	11.9859	1.4	0.9073	2.8	0.0789	2.4	0.87	489.4	11.4	655.6	13.4	1279.3	26.7
08SE259-60	115	27974	2.0	10.9233	1.2	3.2169	1.6	0.2549	1.1	0.66	1463.5	14.0	1461.2	12.6	1458.0	23.4
08SE259-61	199	4762	7.1	14.8741	2.6	0.4443	3.2	0.0479	1.9	0.58	301.8	5.5	373.3	10.0	844.9	54.2
08SE259-68	1291	10710	5.7	15.0075	1.7	0.3761	1.8	0.0409	0.6	0.35	258.6	1.6	324.2	5.1	826.3	35.7
08SE259-71	53	7574	1.8	13.7503	1.5	1.6376	3.4	0.1633	3.1	0.90	975.2	27.9	984.8	21.5	1006.3	29.6
08SE259-86	98	7490	4.2	13.8498	3.7	0.8261	4.5	0.0830	2.6	0.58	513.9	12.9	611.4	20.8	991.7	75.2
08SE259-87	765	12156	14.9	10.9478	2.9	0.5478	7.9	0.0435	7.4	0.93	274.5	19.8	443.6	28.4	1453.7	55.8
08SE259-91	302	11370	4.6	13.3472	1.7	0.8381	3.4	0.0811	2.9	0.87	502.9	14.2	618.1	15.7	1066.4	33.7
08SE259-93	175	4558	3.8	14.0903	2.7	0.5419	7.4	0.0554	6.9	0.93	347.5	23.2	439.7	26.3	956.6	54.9
08SE259-94	216	7724	2.0	13.5396	2.1	0.8272	6.4	0.0812	6.1	0.95	503.4	29.3	612.0	29.5	1037.6	42.0
08SE259-95	1213	8156	12.7	8.5735	3.6	0.5937	5.4	0.0369	4.1	0.75	233.7	9.3	473.2	20.5	1905.3	64.3
08SE259-96	122	29350	1.3	9.7289	2.0	4.1710	2.1	0.2943	0.5	0.24	1663.0	7.3	1668.3	16.9	1675.0	37.0
08SE259-97	424	30120	4.6	10.6342	2.6	1.1457	7.6	0.0884	7.1	0.94	545.9	37.3	775.2	41.1	1508.8	49.3
08SE259-98	272	9764	6.1	11.0179	3.4	0.6884	5.4	0.0550	4.1	0.77	345.2	13.9	531.9	22.2	1441.6	64.8
08SE259-100	96	14756	3.7	13.5837	1.7	1.7648	2.0	0.1739	1.1	0.56	1033.4	10.7	1032.6	13.0	1031.0	33.5
08SE259-101	191	27982	3.6	13.2337	1.9	1.8603	2.9	0.1786	2.2	0.75	1059.1	21.2	1067.1	19.0	1083.5	37.9
Sample 08TC44		*Tylerhorse Canyon pendant metaturbidite*														
08TC44-1	456	8160	1.1	18.0017	17.3	0.3577	17.3	0.0467	0.5	0.03	294.2	1.4	310.5	46.3	434.4	387.4
08TC44-2	171	6546	0.9	18.2659	1.7	0.5203	1.8	0.0689	0.5	0.28	429.7	2.1	425.3	6.1	401.9	37.8
08TC44-3	219	8428	1.8	12.9641	1.7	1.8155	1.8	0.1707	0.5	0.28	1016.0	4.7	1051.1	11.8	1124.7	34.6
08TC44-5	429	12950	3.0	18.0528	1.6	0.4933	1.6	0.0646	0.5	0.31	403.4	2.0	407.1	5.5	428.1	34.7
08TC44-6	153	22418	2.7	11.2272	1.4	2.9119	1.5	0.2371	0.6	0.37	1371.6	6.9	1385.0	11.5	1405.6	27.0
08TC44-7	210	20748	2.9	13.4397	0.9	1.7736	1.3	0.1729	1.0	0.72	1027.9	9.2	1035.8	8.7	1052.5	18.6
08TC44-11	230	7052	1.4	20.0740	4.4	0.2765	4.6	0.0403	1.0	0.22	254.4	2.5	247.8	10.0	186.4	103.6
08TC44-13	298	12978	1.5	17.7272	1.6	0.5847	1.7	0.0752	0.5	0.30	467.2	2.3	467.5	6.2	468.6	35.2
08TC44-14	98	13732	1.5	10.9931	1.9	3.1290	2.0	0.2495	0.6	0.31	1435.8	7.9	1439.8	15.0	1445.9	35.3
08TC44-16	175	20370	0.9	10.7375	2.0	3.3717	2.8	0.2626	2.0	0.70	1503.0	26.1	1497.8	21.8	1490.6	37.7
08TC44-17	72	11922	1.2	7.9934	1.7	6.2376	1.8	0.3616	0.6	0.32	1989.8	9.8	2009.7	15.6	2030.3	29.9
08TC44-18	464	38288	3.9	12.7815	1.7	1.9976	2.4	0.1852	1.7	0.71	1095.2	17.2	1114.7	16.3	1152.9	33.8
08TC44-20	91	19474	1.5	9.9343	1.3	4.0442	1.8	0.2914	1.3	0.72	1648.5	19.3	1643.1	15.0	1636.3	23.8
08TC44-21	690	73042	3.1	12.1624	2.9	2.2597	3.1	0.1993	1.2	0.39	1171.7	13.0	1199.8	21.9	1250.8	56.2
08TC44-22	80	8276	1.6	13.3230	1.2	1.8648	1.3	0.1802	0.5	0.39	1068.0	4.9	1068.7	8.4	1070.1	23.5
08TC44-23	350	34642	1.3	10.8674	1.8	3.2305	2.1	0.2546	1.0	0.48	1462.2	12.8	1464.5	15.9	1467.7	34.2
08TC44-24	193	37912	1.5	10.4438	0.8	3.5185	1.2	0.2665	0.9	0.75	1523.1	12.3	1531.4	9.6	1542.9	15.2
08TC44-25	349	2192	1.3	15.5034	15.9	0.3696	15.9	0.0416	0.6	0.04	262.5	1.6	319.3	43.6	758.1	337.1
08TC44-26	154	2626	0.9	20.2025	5.0	0.2555	5.0	0.0374	0.8	0.15	236.9	1.7	231.1	10.4	171.5	116.1
08TC44-27	264	9204	1.6	19.0078	2.7	0.3993	2.8	0.0551	1.0	0.34	345.5	3.2	341.2	8.2	312.0	60.7
08TC44-30	163	28836	1.4	9.7486	0.9	3.9547	1.7	0.2796	1.5	0.84	1589.4	20.4	1624.9	13.9	1671.3	17.1
08TC44-31	67	4124	1.1	17.2617	3.6	0.7747	4.7	0.0970	2.9	0.62	596.8	16.5	582.5	20.6	527.2	80.0
08TC44-32	353	58108	5.8	10.0634	1.3	3.7269	1.7	0.2720	1.1	0.64	1551.0	15.4	1577.2	14.0	1612.3	25.0
08TC44-33	497	12644	4.0	18.9669	3.2	0.3159	4.4	0.0435	3.1	0.69	274.2	8.3	278.7	10.8	316.9	72.8
08TC44-34	245	42834	2.7	9.2508	0.8	4.4477	1.7	0.2984	1.5	0.90	1683.4	22.5	1721.3	14.1	1767.6	13.7
08TC44-35	626	57014	2.4	11.9662	0.8	2.4094	1.5	0.2091	1.3	0.85	1224.1	13.9	1245.4	10.5	1282.5	15.0

Analysis	U (ppm)	$^{206}Pb/^{204}Pb$	U/Th	Isotope ratios $^{206}Pb^*/^{207}Pb^*$	± (%)	$^{207}Pb^*/^{235}U^*$	± (%)	$^{206}Pb^*/^{238}U$	± (%)	Error correlation	Isotopic ages (Ma)§ $^{206}Pb^*/^{238}U$	± (Ma)	$^{207}Pb^*/^{235}U^*$	± (Ma)	$^{206}Pb^*/^{207}Pb^*$	± (Ma)
08TC44-36	116	10422	3.4	13.6527	1.0	1.5920	1.1	0.1576	0.5	0.46	943.6	4.4	967.1	6.8	1020.7	19.8
08TC44-37	115	9016	0.8	12.6894	1.3	2.1015	2.7	0.1934	2.3	0.88	1139.8	24.4	1149.3	18.3	1167.2	24.9
08TC44-38	529	7014	0.8	16.7718	5.0	0.5719	5.5	0.0696	2.2	0.40	433.6	9.1	459.3	20.2	590.0	109.1
08TC44-39	630	16816	5.7	16.7460	1.7	0.6009	5.7	0.0730	5.4	0.95	454.1	23.7	477.8	21.6	593.3	36.6
08TC44-40	148	6012	1.5	18.8926	3.2	0.4234	3.4	0.0580	1.3	0.39	363.6	4.7	358.5	10.4	325.8	72.0
08TC44-42	107	31712	1.5	5.9921	0.9	10.9984	1.5	0.4780	1.2	0.81	2518.4	24.6	2523.0	13.5	2526.6	14.3
08TC44-43	128	11686	0.8	11.8593	1.1	2.4106	1.3	0.2073	0.7	0.52	1214.7	7.7	1245.8	9.6	1300.0	22.1
08TC44-44	630	12948	2.5	17.8202	1.3	0.4732	2.7	0.0612	2.4	0.88	382.7	8.8	393.4	8.8	457.0	28.8
08TC44-46	286	8834	1.8	18.8847	2.6	0.4099	2.6	0.0561	0.6	0.22	352.1	2.0	348.8	7.7	326.8	58.1
08TC44-47	307	14710	1.1	17.7691	1.2	0.5866	1.3	0.0756	0.5	0.40	469.8	2.4	468.7	5.0	463.4	26.9
08TC44-50	1029	4034	2.2	16.3418	10.4	0.3921	10.6	0.0465	1.9	0.18	292.8	5.4	335.9	30.4	646.0	225.1
08TC44-52	184	24834	1.0	9.8875	1.0	3.8968	2.2	0.2794	2.0	0.90	1588.6	28.3	1613.0	18.0	1645.1	17.8
08TC44-53	166	6762	1.3	19.0602	3.2	0.4264	3.6	0.0589	1.6	0.45	369.2	5.9	360.6	11.0	305.8	73.8
08TC44-54	141	8818	1.2	16.7529	2.8	0.7245	3.4	0.0880	2.0	0.58	543.9	10.2	553.3	14.4	592.4	59.7
08TC44-55	230	33768	0.6	8.1292	2.1	5.9873	2.6	0.3530	1.5	0.57	1948.9	24.6	1974.0	22.5	2000.4	37.8
08TC44-58	1208	3414	3.9	17.1479	8.1	0.3573	8.1	0.0444	0.8	0.10	280.3	2.2	310.2	21.7	541.7	177.0
08TC44-59	34	2654	1.8	17.7678	5.8	0.6903	5.9	0.0890	1.1	0.19	549.3	6.0	533.0	24.6	463.5	129.1
08TC44-61	122	14072	1.5	9.6015	1.4	4.1708	1.5	0.2904	0.5	0.35	1643.7	7.7	1668.3	12.5	1699.3	26.4
08TC44-62	88	13708	0.8	9.5356	1.2	4.4350	1.3	0.3067	0.5	0.38	1724.5	7.6	1718.9	10.9	1712.0	22.5
08TC44-63	630	7132	3.0	18.5954	3.2	0.3300	3.2	0.0445	0.5	0.16	280.7	1.4	289.6	8.1	361.7	71.9
08TC44-64	154	4746	0.9	19.5440	3.7	0.3608	3.8	0.0511	0.6	0.16	321.5	1.9	312.8	10.2	248.3	85.9
08TC44-65	603	27782	1.2	11.5380	1.5	2.5821	2.2	0.2161	1.6	0.71	1261.1	17.9	1295.6	16.0	1353.2	29.6
08TC44-66	582	12520	1.6	19.4046	0.9	0.2759	1.5	0.0388	1.2	0.80	245.5	2.8	247.4	3.2	264.8	20.5
08TC44-68	389	20170	1.2	16.4929	1.0	0.8383	1.6	0.1003	1.2	0.76	616.0	6.9	618.2	7.2	626.2	22.1
08TC44-69	280	7592	1.6	12.2279	1.2	2.2021	2.3	0.1953	2.0	0.84	1150.0	20.6	1181.7	16.2	1240.2	24.4
08TC44-70	361	6724	1.2	19.7520	2.9	0.2504	3.2	0.0359	1.3	0.40	227.2	2.9	226.9	6.5	223.9	67.9
08TC44-71	300	28550	2.4	12.9816	0.6	1.8636	0.8	0.1755	0.5	0.63	1042.1	4.8	1068.3	5.3	1122.0	12.4
08TC44-72	372	10416	1.1	19.8177	2.8	0.2607	2.9	0.0375	0.8	0.28	237.1	1.8	235.2	6.0	216.3	63.9
08TC44-73	17	1714	0.9	14.4739	3.7	1.5016	3.8	0.1576	1.1	0.29	943.6	9.8	931.0	23.4	901.4	75.8
08TC44-74	525	47462	1.8	13.5325	0.7	1.7025	1.8	0.1671	1.7	0.92	996.1	15.6	1009.5	11.8	1038.6	14.8
08TC44-75	89	13414	1.6	9.5373	0.9	4.2810	1.3	0.2961	0.9	0.67	1672.0	12.5	1689.7	10.5	1711.7	17.5
08TC44-77	301	21776	4.1	8.9699	1.4	4.7896	2.0	0.3116	1.5	0.73	1748.5	22.5	1783.1	16.9	1823.7	24.9
08TC44-80	152	5624	1.0	18.2490	1.6	0.4787	2.7	0.0634	2.2	0.80	396.0	8.3	397.2	8.8	404.0	35.8
08TC44-81	360	26050	1.5	16.3918	1.3	0.8555	1.5	0.1017	0.8	0.50	624.4	4.5	627.7	7.0	639.5	27.7
08TC44-82	245	11400	1.9	17.9895	1.8	0.5339	2.0	0.0697	0.8	0.39	434.1	3.2	434.4	7.1	435.9	41.0
08TC44-83	426	12554	2.1	13.8633	4.1	0.5229	8.1	0.0526	7.0	0.86	330.3	22.5	427.1	28.2	989.7	83.1
08TC44-84	164	21128	3.0	13.4420	1.5	1.8056	1.6	0.1760	0.5	0.31	1045.2	4.8	1047.5	10.4	1052.2	30.5
08TC44-85	189	23262	1.0	9.7413	1.6	4.0203	2.0	0.2840	1.2	0.61	1611.7	17.4	1638.3	16.2	1672.7	29.2
08TC44-86	251	21170	1.1	13.2692	1.3	1.7368	3.0	0.1671	2.7	0.90	996.4	25.2	1022.3	19.6	1078.2	27.0
08TC44-87	302	3880	0.8	17.1121	2.3	0.4964	2.6	0.0616	1.2	0.48	385.4	4.6	409.3	8.7	546.2	49.3
08TC44-88	1503	94156	22.1	9.4471	1.7	4.1039	2.2	0.2812	1.4	0.64	1597.3	19.5	1655.1	17.6	1729.2	30.3
08TC44-89	18	1210	1.2	17.5425	5.4	0.7642	5.6	0.0972	1.3	0.23	598.1	7.5	576.4	24.5	491.7	119.7
08TC44-90	144	4222	0.9	16.1774	15.1	0.6328	15.2	0.0742	1.4	0.09	461.7	6.1	497.8	59.8	667.7	325.4
08TC44-91	127	25256	1.5	9.8261	1.0	3.9023	1.7	0.2781	1.4	0.79	1581.8	19.1	1614.2	13.9	1656.6	19.3
08TC44-92	377	37424	1.5	10.8947	1.2	3.1079	1.5	0.2456	1.0	0.66	1415.6	12.8	1434.7	11.8	1463.0	22.1
08TC44-93	526	16974	1.0	16.8042	0.8	0.7551	1.8	0.0920	1.6	0.89	567.5	8.8	571.2	7.9	585.8	17.8
08TC44-95	329	13928	2.1	17.7944	1.3	0.5633	1.7	0.0727	1.1	0.65	452.4	4.9	453.7	6.3	460.2	29.1
08TC44-96	106	15434	1.1	10.3324	0.8	3.6429	1.3	0.2730	1.0	0.78	1556.0	13.7	1559.0	10.1	1563.0	14.9
08TC44-97	379	32860	2.6	11.6418	1.6	2.5538	1.7	0.2156	0.8	0.44	1258.7	8.7	1287.5	12.6	1335.8	30.0
08TC44-98	140	13654	0.6	10.9136	0.7	2.9730	3.1	0.2353	3.0	0.97	1362.3	37.0	1400.7	23.5	1459.7	13.8
08TC44-99	394	8542	1.3	19.8074	2.2	0.2630	2.3	0.0378	0.6	0.26	239.1	1.4	237.1	4.8	217.4	51.2
08TC44-100	208	5306	3.3	16.8656	13.9	0.5788	13.9	0.0708	1.3	0.09	441.0	5.5	463.7	51.9	577.9	302.5

* Radiogenic

§ Decay constants used in age calculations: $\lambda^{238}U = 1.55125 \times 10^{-10}$ $\lambda^{235}U = 9.8485 \times 10^{-10}$ (Jaffey *et al*., 1971); $^{238}U/^{235}U = 137.88$ (Chen and Wasserberg, 1981). Uncertainties are given as ± 2σ in last three figures.

Common Pb correction from measured $^{206}Pb/^{204}Pb$, with initial Pb composition from Stacey and Kramers (1975).

† Analyses in which epoxy was overlapped and those with greater than 10% uncertainty, 30% discordance, and/or 5% reverse discordance are excluded. Accepted ages calculated using $^{206}Pb/^{238}U$ ages for grains younger than 800 Ma and $^{207}Pb/^{206}Pb$ ages for grains older than 800 Ma.

Table A2.4. Compilation of U-Pb zircon ages from the Sierra Nevada batholith and ophiolitic framework.

Sample	Latitude	Longitude	Age (Ma)	Reference
W34	36.458	-118.872	98	Chen & Moore, 1982
W21	36.758	-119.238	100	Chen & Moore, 1982
W18	36.617	-119.035	101	Chen & Moore, 1982
W19	36.668	-118.980	102	Chen & Moore, 1982
W32	36.440	-118.903	104	Chen & Moore, 1982
W31	36.412	-118.937	108	Chen & Moore, 1982
W22	36.725	-119.292	111	Chen & Moore, 1982
W24	36.708	-119.258	111	Chen & Moore, 1982
W30	36.393	-118.963	112	Chen & Moore, 1982
W26	36.665	-119.218	115	Chen & Moore, 1982
W29	36.405	-119.053	116	Chen & Moore, 1982
W16	36.575	-119.155	119	Chen & Moore, 1982
W6	36.722	-118.970	126	Chen & Moore, 1982
W5	36.748	-119.228	145	Chen & Moore, 1982
KC14	36.780	-118.618	89	Chen & Moore, 1982
K2	36.909	-118.891	90	Chen & Moore, 1982
SQ67	36.718	-118.732	91	Chen & Moore, 1982
KC2	36.805	-118.717	97	Chen & Moore, 1982
K4	36.904	-118.898	97	Chen & Moore, 1982
KC15	36.797	-118.675	97	Chen & Moore, 1982
KC5	36.808	-118.792	99	Chen & Moore, 1982
KC18	36.808	-118.798	99	Chen & Moore, 1982
KC16	36.810	-118.760	108	Chen & Moore, 1982
KC6	36.830	-118.870	110	Chen & Moore, 1982
KC11	36.830	-118.882	110	Chen & Moore, 1982
F11	36.846	-118.930	110	Chen & Moore, 1982
3S37	36.816	-118.838	86	Chen & Moore, 1982
SQ12	36.667	-118.835	98	Chen & Moore, 1982
SQ46	36.730	-118.788	98	Chen & Moore, 1982
SQ48	36.723	-118.807	98	Chen & Moore, 1982
SQ13	36.640	-118.805	97	Chen & Moore, 1982
SQ22	36.605	-118.738	97	Chen & Moore, 1982
SQ57	36.737	-118.893	100	Chen & Moore, 1982
SQ7	36.557	-118.772	102	Chen & Moore, 1982
SQ75	36.582	-118.753	100	Chen & Moore, 1982
SQ9	36.648	-118.825	100	Chen & Moore, 1982
95-10	36.543	-118.767	102	Chen & Moore, 1982
95-11	36.579	-118.742	102	Chen & Moore, 1982

95-12	36.633	-118.792	102	Chen & Moore, 1982
95-13	36.732	-118.898	102	Chen & Moore, 1982
95-14	36.796	-118.867	102	Chen & Moore, 1982
SQ15	36.513	-118.803	99	Chen & Moore, 1982
SQ3	36.502	-118.808	99	Chen & Moore, 1982
SQ5	36.517	-118.787	97	Chen & Moore, 1982
SQ61	36.683	-118.833	100	Chen & Moore, 1982
SQ8	36.603	-118.720	111	Chen & Moore, 1982
A95-10	36.573	-118.254	84	Chen & Moore, 1982
3S36	36.798	-118.582	85	Chen & Moore, 1982
68M15	36.753	-118.613	88	Chen & Moore, 1982
6-124	36.542	-118.477	95	Chen & Moore, 1982
OW34	36.777	-118.332	103	Chen & Moore, 1982
OW4	36.770	-118.348	103	Chen & Moore, 1982
8-38a	36.988	-118.398	153	Chen & Moore, 1982
08_54	36.835	-118.383	156	Chen & Moore, 1982
77-7	36.423	-118.393	159	Chen & Moore, 1982
07_19	36.443	-118.398	160	Chen & Moore, 1982
F1-57	37.603	-117.972	175	Chen & Moore, 1982
OW2	37.380	-118.678	210	Chen & Moore, 1982
MA9	37.650	-118.538	161	Chen & Moore, 1982
02_26	37.273	-117.578	175	Chen & Moore, 1982
MA5	37.860	-118.630	201	Chen & Moore, 1982
MA2	36.893	-118.847	217	Chen & Moore, 1982
OW7	36.793	-118.303	112	Chen & Moore, 1982
E-27-9	36.845	-118.060	152	Chen & Moore, 1982
OW19	36.905	-118.162	163	Chen & Moore, 1982
1S94	37.176	-119.833	112	Bateman, 1992
1S40	37.023	-119.527	114	Bateman, 1992
1S91	37.209	-119.479	114	Bateman, 1992
1S97	37.288	-119.868	114	Bateman, 1992
1S98	37.460	-119.799	114	Bateman, 1992
1S99	37.362	-119.615	114	Bateman, 1992
1S100	37.523	-119.615	114	Bateman, 1992
W1-H	37.509	-119.589	114	Bateman, 1992
W2-H	37.509	-119.589	114	Bateman, 1992
W3-H	37.500	-119.611	114	Bateman, 1992
95-4	37.501	-119.586	114	Bateman, 1992
95-7	37.972	-119.783	114	Bateman, 1992
W4	37.666	-119.611	100	Bateman, 1992
95-9	37.204	-119.233	90	Bateman, 1992
1S84	37.217	-119.152	90	Bateman, 1992

95-18	37.220	-119.244	90	Bateman, 1992
1S67	37.047	-119.075	90	Bateman, 1992
95-1	37.458	-119.542	102	Bateman, 1992
95-2	37.380	-119.434	102	Bateman, 1992
96-24	37.361	-119.418	102	Bateman, 1992
1S90	37.197	-119.420	102	Bateman, 1992
96-19	37.304	-119.379	103	Bateman, 1992
96-21	37.329	-119.415	103	Bateman, 1992
96-2	36.945	-119.014	103	Bateman, 1992
96-3	36.952	-119.012	103	Bateman, 1992
96-4	36.977	-119.006	103	Bateman, 1992
1S125	37.077	-118.353	164	Bateman, 1992
1S126	37.085	-118.337	164	Bateman, 1992
1S122	37.544	-118.691	210	Bateman, 1992
95BR078	37.770	-119.125	210	Bateman, 1992
95BR080	37.764	-119.113	210	Bateman, 1992
95BR029	37.863	-119.195	210	Bateman, 1992
95BR031	37.867	-119.178	210	Bateman, 1992
95BR042	37.820	-118.504	161	Bateman, 1992
95BR048	37.852	-118.841	214	Bateman, 1992
95BR050	37.905	-118.755	214	Bateman, 1992
95BR051	37.852	-118.636	214	Bateman, 1992
95BR041	37.764	-118.457	214	Bateman, 1992
95-15	36.796	-118.959	98	Wenner & Coleman, 2003
1S128	37.135	-118.455	165	Wenner & Coleman, 2003
1S92	37.124	-119.735	115	Stern et al., 1981
1S93	37.194	-119.720	115	Stern et al., 1981
95-6	37.693	-119.622	103	Stern et al., 1981
1S41	37.061	-119.448	93	Stern et al., 1981
1S132	37.287	-118.556	200	Stern et al., 1981
95BR054	37.834	-118.409	90	Stern et al., 1981
95BR055	37.876	-118.394	90	Stern et al., 1981
95BR056	37.895	-118.379	90	Stern et al., 1981
95BR066	37.663	-118.335	90	Stern et al., 1981
95BR067	37.782	-118.410	90	Stern et al., 1981
95BR068	37.768	-118.397	90	Stern et al., 1981
97WM064	37.960	-118.333	90	Stern et al., 1981
97WM065	37.931	-118.332	90	Stern et al., 1981
97WM066	37.898	-118.350	90	Stern et al., 1981
95BR069	37.929	-119.254	96	Schweickert & Lahren, 1999
95BR071	37.946	-119.225	96	Schweickert & Lahren, 1999
95BR036	37.966	-119.153	168	Schweickert & Lahren, 1999

1S106	37.855	-119.484	93.3	Coleman et al., 2004
1S107	37.853	-119.486	93.3	Coleman et al., 2004
1S108	37.853	-119.486	93.3	Coleman et al., 2004
1S119	37.908	-119.265	93.3	Coleman et al., 2004
95-5	37.732	-119.589	93.3	Coleman et al., 2004
1S111	37.856	-119.465	91.9	Coleman et al., 2004
1S118	37.893	-119.263	91.9	Coleman et al., 2004
1S104	37.851	-119.477	91.9	Coleman et al., 2004
1S105	37.855	-119.482	91.9	Coleman et al., 2004
Y2	37.768	-119.488	91.9	Coleman et al., 2004
Y3	37.758	-119.494	91.9	Coleman et al., 2004
Y4	37.757	-119.488	91.9	Coleman et al., 2004
1S109	37.869	-119.457	88.8	Coleman et al., 2004
1S110	37.866	-119.461	88.8	Coleman et al., 2004
1S116	37.878	-119.297	88.8	Coleman et al., 2004
1S101	37.883	-119.345	88.1	Coleman et al., 2004
1S112	37.874	-119.423	88.1	Coleman et al., 2004
1S113	37.875	-119.393	88.1	Coleman et al., 2004
1S117	37.877	-119.305	88.1	Coleman et al., 2004
M95-28	37.992	-119.303	88.1	Coleman et al., 2004
M95-40	37.993	-119.309	88.1	Coleman et al., 2004
M95-79	37.986	-119.325	88.1	Coleman et al., 2004
M95-81	37.987	-119.353	88.1	Coleman et al., 2004
1S114	37.830	-119.356	85.4	Coleman et al., 2004
1S115	37.839	-119.356	85.4	Coleman et al., 2004
L94-7	37.843	-119.369	85.4	Coleman et al., 2004
1S88	37.379	-118.968	92	Coleman & Glazner, 1998
1S130	37.169	-118.567	92	Coleman & Glazner, 1998
1S133	37.754	-119.171	99	Kistler & Swanson, 1981
1S134	37.750	-119.167	99	Kistler & Swanson, 1981
1S66	37.075	-119.182	96	Tobisch & Cruden, 1995
95-16	37.091	-119.242	102	Tobisch & Cruden, 1995
95-17	37.154	-119.269	102	Tobisch & Cruden, 1995
96-5	36.990	-119.014	102	Tobisch & Cruden, 1995
96-6	37.000	-119.044	102	Tobisch & Cruden, 1995
96-7	37.034	-119.073	102	Tobisch & Cruden, 1995
96-8	37.047	-119.098	102	Tobisch & Cruden, 1995
96-9	37.052	-119.136	102	Tobisch & Cruden, 1995
F8	37.093	-118.975	102	Tobisch & Cruden, 1995
F9	37.076	-118.964	102	Tobisch & Cruden, 1995
F9.5	37.055	-118.964	102	Tobisch & Cruden, 1995
1S103	37.853	-119.489	104	Ratajeski et al., 2001

YOS–180	37.729	-119.636	104	Ratajeski et al., 2001
YOS–1	37.728	-119.624	103	Ratajeski et al., 2001
YOS–104	37.731	-119.630	103	Ratajeski et al., 2001
YOS–206	37.723	-119.657	102	Ratajeski et al., 2001
96-10	37.325	-119.317	90	McNulty et al., 2000
96-11	37.322	-119.312	90	McNulty et al., 2000
96-12	37.336	-119.328	90	McNulty et al., 2000
96-13	37.366	-119.343	90	McNulty et al., 2000
96-14	37.388	-119.359	90	McNulty et al., 2000
96-15	37.395	-119.343	90	McNulty et al., 2000
96-16	37.381	-119.384	90	McNulty et al., 2000
96-17	37.363	-119.384	90	McNulty et al., 2000
96-18	37.347	-119.384	90	McNulty et al., 2000
F3	37.481	-119.264	90	McNulty et al., 2000
F4	37.374	-119.159	90	McNulty et al., 2000
F6	37.281	-119.111	90	McNulty et al., 2000
F7f	37.233	-119.117	90	McNulty et al., 2000
1S136	38.309	-119.583	86	Robinson & Kistler, 1986
1S137	38.325	-119.682	86	Robinson & Kistler, 1986
1S138	38.352	-119.851	86	Robinson & Kistler, 1986
1S135	38.324	-119.561	91	Robinson & Kistler, 1986
1S139	38.355	-119.879	91	Robinson & Kistler, 1986
95BR052	37.835	-118.411	74	Hanson et al., 1987
95BR053	37.834	-118.410	74	Hanson et al., 1987
95BR065	37.641	-118.336	147	Hanson et al., 1987
95BR061	37.572	-118.237	165	Ernst et al., 2003
95BR062	37.561	-118.243	165	Ernst et al., 2003
95BR064	37.544	-118.328	165	Ernst et al., 2003
95BR063	37.492	-118.181	175	Coleman et al., 2003
3S28	36.461	-118.634	97	Busby-Spera, 1982
3S29	36.437	-118.734	100	Busby-Spera, 1982
1S86	37.383	-118.961	91.1	Gaschnig et al., 2006
1S87	37.382	-118.964	91.1	Gaschnig et al., 2006
1S131	37.236	-118.668	91.1	Gaschnig et al., 2006
1S121	37.618	-118.955	88.8	Gaschnig et al., 2006
1S123	37.458	-118.734	88.8	Gaschnig et al., 2006
99LV655	37.590	-118.891	88.8	Gaschnig et al., 2006
1S120	37.606	-119.023	87	Gaschnig et al., 2006
1S124	37.083	-118.771	87	Gaschnig et al., 2006
1S127	37.122	-118.498	95	Lackey et al., 2008
1S129	37.111	-118.548	94	Lackey et al., 2008
95BR035	37.932	-119.118	93	Bateman, 1992; Schweickert & Lahren, 1999

95BR073	37.949	-119.192	93	Bateman, 1992; Schweickert & Lahren, 1999
95BR077	37.829	-119.110	93	Bateman, 1992; Schweickert & Lahren, 1999
95BR075	37.933	-119.175	93	Bateman, 1992; Schweickert & Lahren, 1999
95BR037	37.959	-119.125	96	Bateman, 1992; Schweickert & Lahren, 1999
95BR038	37.974	-119.140	96	Bateman, 1992; Schweickert & Lahren, 1999
95BR040	37.997	-119.151	96	Bateman, 1992; Schweickert & Lahren, 1999
95BR032	37.858	-119.074	96	Bateman, 1992; Schweickert & Lahren, 1999
LLC03-01	35.922	-117.942	166	Bartley et al., 2007
SD01-04	36.033	-118.197	147	Bartley et al., 2007
JS035	35.740	-117.910	182	Bartley et al., 2007
JS031	35.856	-117.993	166	Bartley et al., 2007
JS033	35.759	-117.904	176	Bartley et al., 2007
JTRS032	35.837	-117.974	168	Bartley et al., 2007
KOG034	35.739	-117.916	92	Bartley et al., 2007
KMD037	35.634	-117.963	93	Bartley et al., 2007
07_51	36.203	-118.420	170	Chen & Moore, 1982
KGA-1	37.844	-119.489	93	Coleman et al., 2004
HD01-35	37.906	-119.265	94	Coleman et al., 2004
Y01-5	37.867	-119.265	93	Coleman et al., 2004
HD01-49	37.745	-119.571	92	Coleman et al., 2004
HD01-43	37.744	-119.532	91	Coleman et al., 2004
HD02-111	37.743	-119.386	89	Coleman et al., 2004
HD01-2	37.748	-119.544	91	Coleman et al., 2004
HD02-102	37.920	-119.297	89	Coleman et al., 2004
SI-D91-3	36.632	-117.983	163	Dunne & Walker, 2004
IS-D92-3	36.628	-117.980	140	Dunne & Walker, 2004
SI-D53-2	36.528	-117.971	162	Dunne & Walker, 2004
AR-D1-94	36.228	-117.448	176	Dunne & Walker, 2004
Dunne-5	36.151	-117.497	166	Dunne & Walker, 2004
AR-D11-95	36.143	-117.503	188	Dunne & Walker, 2004
DAR-D2-94	36.089	-117.406	174	Dunne & Walker, 2004
Dunne-3	36.046	-117.437	187	Dunne & Walker, 2004
SR-D3-3	35.848	-117.270	100	Dunne & Walker, 2004
SR-D4-3	35.848	-117.270	166	Dunne & Walker, 2004
SR-D1-3	35.837	-117.277	159	Dunne & Walker, 2004
SR-D2-3	35.799	-117.281	185	Dunne & Walker, 2004
HM-D54-2	36.601	-117.496	175	Dunne & Walker, 2004
SR-1	35.596	-117.220	184	Dunne & Walker, 2004
SR-15.1	35.629	-117.158	177	Dunne & Walker, 2004
SR-15.3	35.630	-117.156	145	Dunne & Walker, 2004
SR-35.2	35.611	-117.189	149	Dunne & Walker, 2004
SR-48.11	35.618	-117.242	151	Dunne & Walker, 2004

SR-50.2	35.641	-117.130	148	Dunne & Walker, 2004
SR-50.3	35.643	-117.130	149	Dunne & Walker, 2004
SR-54.6	35.597	-117.220	150	Dunne & Walker, 2004
SR-58.1	35.620	-117.219	152	Dunne & Walker, 2004
SI-D3-94	36.647	-117.989	154	Dunne & Walker, 2004
FP-926	35.184	-117.416	92	Fletcher et al., 2002
B-57	35.102	-117.460	93	Fletcher et al., 2002
126	35.655	-117.448	154	Irwin & Wooden, 2001
127	35.653	-117.412	149	Irwin & Wooden, 2001
125	35.689	-117.394	169	Irwin & Wooden, 2001
124	36.028	-117.432	161	Irwin & Wooden, 2001
121	36.291	-117.592	174	Irwin & Wooden, 2001
122	36.258	-117.579	156	Irwin & Wooden, 2001
123	36.125	-117.458	186	Irwin & Wooden, 2001
155	36.456	-119.193	125	Irwin & Wooden, 2001
168	35.894	-118.928	102	Irwin & Wooden, 2001
167	35.917	-118.904	115	Irwin & Wooden, 2001
166	35.964	-118.946	287	Irwin & Wooden, 2001
165	36.066	-118.937	118	Irwin & Wooden, 2001
164	36.119	-118.991	287	Irwin & Wooden, 2001
163	36.195	-119.002	118	Irwin & Wooden, 2001
162	36.243	-119.000	168	Irwin & Wooden, 2001
158	36.275	-118.961	121	Irwin & Wooden, 2001
161	36.260	-119.028	205	Irwin & Wooden, 2001
157	36.382	-119.028	118	Irwin & Wooden, 2001
203	36.406	-118.922	108	Irwin & Wooden, 2001
204	36.438	-118.913	104	Irwin & Wooden, 2001
156	36.430	-119.137	117	Irwin & Wooden, 2001
154	36.470	-119.166	110	Irwin & Wooden, 2001
153	36.483	-119.143	130	Irwin & Wooden, 2001
152	36.534	-119.210	116	Irwin & Wooden, 2001
151	36.599	-119.291	120	Irwin & Wooden, 2001
196	36.594	-118.711	98	Irwin & Wooden, 2001
200	36.576	-118.330	83	Irwin & Wooden, 2001
201	36.598	-118.249	87	Irwin & Wooden, 2001
159	36.296	-119.096	120	Irwin & Wooden, 2001
160	36.283	-119.093	287	Irwin & Wooden, 2001
195	36.668	-119.226	115	Irwin & Wooden, 2001
179	36.739	-119.282	111	Irwin & Wooden, 2001
178	36.737	-119.312	112	Irwin & Wooden, 2001
177	36.736	-119.353	114	Irwin & Wooden, 2001
150	36.724	-119.351	115	Irwin & Wooden, 2001

180	36.754	-119.126	111	Irwin & Wooden, 2001
181	36.745	-119.070	112	Irwin & Wooden, 2001
182	36.739	-119.018	106	Irwin & Wooden, 2001
183	36.727	-118.944	128	Irwin & Wooden, 2001
198	36.685	-118.851	100	Irwin & Wooden, 2001
197	36.668	-118.841	98	Irwin & Wooden, 2001
199	36.735	-118.714	91	Irwin & Wooden, 2001
187	36.799	-118.785	99	Irwin & Wooden, 2001
188	36.805	-118.759	108	Irwin & Wooden, 2001
189	36.807	-118.723	97	Irwin & Wooden, 2001
190	36.814	-118.682	97	Irwin & Wooden, 2001
191	36.756	-118.352	103	Irwin & Wooden, 2001
116	36.755	-118.322	103	Irwin & Wooden, 2001
117	36.765	-118.301	164	Irwin & Wooden, 2001
118	36.776	-118.270	181	Irwin & Wooden, 2001
194	36.794	-118.280	112	Irwin & Wooden, 2001
193	36.796	-118.314	165	Irwin & Wooden, 2001
192	36.794	-118.358	103	Irwin & Wooden, 2001
115	36.923	-118.153	163	Irwin & Wooden, 2001
112	37.088	-118.272	155	Irwin & Wooden, 2001
111	37.187	-118.337	167	Irwin & Wooden, 2001
110	37.266	-118.386	95	Irwin & Wooden, 2001
97	37.145	-118.557	90	Irwin & Wooden, 2001
114	37.136	-118.741	158	Irwin & Wooden, 2001
96	37.079	-118.955	88	Irwin & Wooden, 2001
184	36.825	-118.902	110	Irwin & Wooden, 2001
185	36.833	-118.882	110	Irwin & Wooden, 2001
186	36.844	-118.861	86	Irwin & Wooden, 2001
93	37.095	-119.270	104	Irwin & Wooden, 2001
88	37.171	-119.301	102	Irwin & Wooden, 2001
87	37.226	-119.326	113	Irwin & Wooden, 2001
85	37.276	-119.441	103	Irwin & Wooden, 2001
92	37.336	-119.011	93	Irwin & Wooden, 2001
67	37.331	-120.071	123	Irwin & Wooden, 2001
75	37.314	-119.642	108	Irwin & Wooden, 2001
76	37.222	-119.803	111	Irwin & Wooden, 2001
82	37.216	-119.723	115	Irwin & Wooden, 2001
81	37.194	-119.625	114	Irwin & Wooden, 2001
77	37.138	-119.900	111	Irwin & Wooden, 2001
78	37.115	-119.674	115	Irwin & Wooden, 2001
83	37.058	-119.727	124	Irwin & Wooden, 2001
84	37.062	-119.692	110	Irwin & Wooden, 2001

137	37.025	-119.688	132	Irwin & Wooden, 2001
89	37.018	-119.525	112	Irwin & Wooden, 2001
91	37.047	-119.409	93	Irwin & Wooden, 2001
90	37.091	-119.357	116	Irwin & Wooden, 2001
138	36.877	-119.501	120	Irwin & Wooden, 2001
139	36.860	-119.457	114	Irwin & Wooden, 2001
140	36.838	-119.476	121	Irwin & Wooden, 2001
149	36.805	-119.397	170	Irwin & Wooden, 2001
148	36.820	-119.388	207	Irwin & Wooden, 2001
147	36.837	-119.388	250	Irwin & Wooden, 2001
141	36.858	-119.409	154	Irwin & Wooden, 2001
146	36.834	-119.356	157	Irwin & Wooden, 2001
142	36.863	-119.354	125	Irwin & Wooden, 2001
143	36.870	-119.304	98	Irwin & Wooden, 2001
144	36.843	-119.320	169	Irwin & Wooden, 2001
145	36.802	-119.299	170	Irwin & Wooden, 2001
98	36.765	-119.257	199	Irwin & Wooden, 2001
63	37.446	-119.947	118	Irwin & Wooden, 2001
37	37.948	-120.535	280	Irwin & Wooden, 2001
40	37.890	-120.460	190	Irwin & Wooden, 2001
41	37.879	-120.441	199	Irwin & Wooden, 2001
42	37.853	-120.398	198	Irwin & Wooden, 2001
47	37.743	-120.333	182	Irwin & Wooden, 2001
48	37.730	-120.328	200	Irwin & Wooden, 2001
49	37.694	-120.266	196	Irwin & Wooden, 2001
45	37.797	-120.258	162	Irwin & Wooden, 2001
43	37.880	-120.380	148	Irwin & Wooden, 2001
39	37.930	-120.327	164	Irwin & Wooden, 2001
38	37.985	-120.323	173	Irwin & Wooden, 2001
130	37.750	-119.884	116	Irwin & Wooden, 2001
52	37.511	-120.225	150	Irwin & Wooden, 2001
53	37.453	-120.257	147	Irwin & Wooden, 2001
54	37.496	-120.280	149	Irwin & Wooden, 2001
58	37.416	-120.264	146	Irwin & Wooden, 2001
62	37.433	-120.112	151	Irwin & Wooden, 2001
64	37.395	-120.026	151	Irwin & Wooden, 2001
128	37.964	-119.785	108	Irwin & Wooden, 2001
129	37.919	-119.803	113	Irwin & Wooden, 2001
44	37.975	-119.985	151	Irwin & Wooden, 2001
46	37.874	-119.987	166	Irwin & Wooden, 2001
50	37.834	-119.927	116	Irwin & Wooden, 2001
51	37.810	-119.906	163	Irwin & Wooden, 2001

131	37.773	-119.771	119	Irwin & Wooden, 2001
132	37.739	-119.721	102	Irwin & Wooden, 2001
57	37.702	-119.711	103	Irwin & Wooden, 2001
61	37.640	-119.716	117	Irwin & Wooden, 2001
60	37.697	-119.607	96	Irwin & Wooden, 2001
66	37.564	-119.632	97	Irwin & Wooden, 2001
70	37.638	-119.428	100	Irwin & Wooden, 2001
210	37.625	-119.430	97	Irwin & Wooden, 2001
65	37.613	-119.535	112	Irwin & Wooden, 2001
68	37.594	-119.398	98	Irwin & Wooden, 2001
212	37.541	-119.323	94	Irwin & Wooden, 2001
72	37.688	-119.375	98	Irwin & Wooden, 2001
69	37.672	-119.379	100	Irwin & Wooden, 2001
71	37.662	-119.363	93	Irwin & Wooden, 2001
208	37.615	-119.369	86	Irwin & Wooden, 2001
211	37.583	-119.296	97	Irwin & Wooden, 2001
209	37.670	-119.280	98	Irwin & Wooden, 2001
55	37.850	-119.484	88	Irwin & Wooden, 2001
58	37.885	-119.348	86	Irwin & Wooden, 2001
73	37.722	-119.162	91	Irwin & Wooden, 2001
136	37.636	-118.528	160	Irwin & Wooden, 2001
100	37.798	-118.552	161	Irwin & Wooden, 2001
135	37.862	-118.621	201	Irwin & Wooden, 2001
99	37.904	-118.823	214	Irwin & Wooden, 2001
133	37.961	-119.225	210	Irwin & Wooden, 2001
134	37.760	-119.120	210	Irwin & Wooden, 2001
79	37.643	-119.064	76	Irwin & Wooden, 2001
80	37.533	-119.031	99	Irwin & Wooden, 2001
74	37.370	-119.603	105	Irwin & Wooden, 2001
86	37.427	-119.068	90	Irwin & Wooden, 2001
103	37.396	-118.736	169	Irwin & Wooden, 2001
95	37.371	-118.737	93	Irwin & Wooden, 2001
113	37.373	-118.667	198	Irwin & Wooden, 2001
105	37.361	-118.687	202	Irwin & Wooden, 2001
104	37.389	-118.681	207	Irwin & Wooden, 2001
94	37.471	-118.760	88	Irwin & Wooden, 2001
102	37.499	-118.726	89	Irwin & Wooden, 2001
101	37.781	-118.401	90	Irwin & Wooden, 2001
106	37.581	-118.216	161	Irwin & Wooden, 2001
107	37.540	-118.145	172	Irwin & Wooden, 2001
108	37.454	-117.935	168	Irwin & Wooden, 2001
109	37.416	-117.970	167	Irwin & Wooden, 2001

120	36.619	-117.978	174	Irwin & Wooden, 2001
202	36.582	-118.108	85	Irwin & Wooden, 2001
119	36.657	-118.112	148	Irwin & Wooden, 2001
1	40.165	-121.026	378	Irwin & Wooden, 2001
2	40.012	-121.167	314	Irwin & Wooden, 2001
8	39.787	-121.064	193	Irwin & Wooden, 2001
231	39.770	-121.299	142	Irwin & Wooden, 2001
236	39.794	-121.329	142	Irwin & Wooden, 2001
3	39.962	-121.286	140	Irwin & Wooden, 2001
4	39.883	-121.361	140	Irwin & Wooden, 2001
230	39.777	-121.506	141	Irwin & Wooden, 2001
5	39.786	-121.453	204	Irwin & Wooden, 2001
16	39.725	-120.731	423	Irwin & Wooden, 2001
229	39.522	-120.541	166	Irwin & Wooden, 2001
20	39.458	-120.609	368	Irwin & Wooden, 2001
18	39.487	-120.694	409	Irwin & Wooden, 2001
21	39.471	-120.710	385	Irwin & Wooden, 2001
19	39.449	-120.647	385	Irwin & Wooden, 2001
22	39.358	-120.667	385	Irwin & Wooden, 2001
23	39.311	-120.608	164	Irwin & Wooden, 2001
24	39.298	-120.608	163	Irwin & Wooden, 2001
26	39.310	-120.507	120	Irwin & Wooden, 2001
17	39.467	-120.862	388	Irwin & Wooden, 2001
14	39.397	-121.074	159	Irwin & Wooden, 2001
219	39.489	-121.109	159	Irwin & Wooden, 2001
11	39.509	-121.049	205	Irwin & Wooden, 2001
10	39.596	-120.993	168	Irwin & Wooden, 2001
218	39.613	-121.006	168	Irwin & Wooden, 2001
217	39.654	-121.043	209	Irwin & Wooden, 2001
216	39.672	-121.045	207	Irwin & Wooden, 2001
237	39.745	-121.375	142	Irwin & Wooden, 2001
6	39.721	-121.503	196	Irwin & Wooden, 2001
7	39.659	-121.469	164	Irwin & Wooden, 2001
9	39.563	-121.379	140	Irwin & Wooden, 2001
232	39.483	-121.456	128	Irwin & Wooden, 2001
230	39.411	-121.370	159	Irwin & Wooden, 2001
13	39.380	-121.278	162	Irwin & Wooden, 2001
12	39.367	-121.303	162	Irwin & Wooden, 2001
234	39.310	-121.148	159	Irwin & Wooden, 2001
220	39.342	-121.110	161	Irwin & Wooden, 2001
15	39.302	-121.075	159	Irwin & Wooden, 2001
222	39.244	-121.109	163	Irwin & Wooden, 2001

221	39.262	-121.016	158	Irwin & Wooden, 2001
235	39.213	-121.064	159	Irwin & Wooden, 2001
25	39.067	-121.309	162	Irwin & Wooden, 2001
27	38.901	-121.107	163	Irwin & Wooden, 2001
206	38.905	-120.612	170	Irwin & Wooden, 2001
214	38.746	-120.863	143	Irwin & Wooden, 2001
28	38.838	-121.063	165	Irwin & Wooden, 2001
223	38.784	-121.157	142	Irwin & Wooden, 2001
29	38.757	-121.003	162	Irwin & Wooden, 2001
30	38.659	-120.982	166	Irwin & Wooden, 2001
32	38.577	-120.959	286	Irwin & Wooden, 2001
31	38.589	-120.899	304	Irwin & Wooden, 2001
215	38.578	-120.878	150	Irwin & Wooden, 2001
225	38.557	-120.772	170	Irwin & Wooden, 2001
224	38.660	-120.699	133	Irwin & Wooden, 2001
205	38.590	-120.567	152	Irwin & Wooden, 2001
207	38.396	-120.651	125	Irwin & Wooden, 2001
227	38.334	-120.638	165	Irwin & Wooden, 2001
228	38.293	-120.610	160	Irwin & Wooden, 2001
226	38.302	-120.717	175	Irwin & Wooden, 2001
33	38.173	-120.622	177	Irwin & Wooden, 2001
31	38.153	-120.367	216	Irwin & Wooden, 2001
35	38.045	-120.446	170	Irwin & Wooden, 2001
36	38.038	-120.262	162	Irwin & Wooden, 2001
ERP 10.30.1*	34.942	-119.212	155	James, 1986a
ERP 10.30.2*	34.945	-119.221	160	James, 1986a
ERP 90*	34.931	-119.217	155	James, 1986a
Gold Hill 1*	35.833	-120.350	143	James, 1986a
2*	37.129	-122.152	99	James, 1986a
1*	37.082	-122.142	99	James, 1986a
10*	37.025	-122.084	93	James, 1986a
3*	37.570	-122.508	103	James, 1986a
Logan1*	36.875	-121.574	161	James, 1986a
noname*	34.869	-119.148	98	James, 1986b
granite*	34.681	-119.047	76	Kellogg, 1999
630-5	36.004	-121.495	92	Kidder et al., 2003
701-4	36.026	-121.476	86	Kidder et al., 2003
706-4	36.042	-121.478	81	Kidder et al., 2003
BH5-88*	38.305	-123.054	97	Kistler & Champion, 2001
PR5-88*	38.186	-122.958	104	Kistler & Champion, 2001
FAIS1-88*	37.699	-122.999	95	Kistler & Champion, 2001
COBA2-92*	37.751	-123.072	100	Kistler & Champion, 2001

MON6-88*	37.560	-122.508	102	Kistler & Champion, 2001
BL10-89*	36.990	-122.133	92	Kistler & Champion, 2001
K1A-87*	37.138	-122.192	99	Kistler & Champion, 2001
SANLU5-90*	36.463	-121.926	92	Kistler & Champion, 2001
SANLU10-91*	36.208	-121.741	99	Kistler & Champion, 2001
24*	36.559	-121.243	83	Kistler & Champion, 2001
27*	36.268	-121.070	85	Kistler & Champion, 2001
29*	36.289	-120.997	84	Kistler & Champion, 2001
23*	36.499	-121.295	91	Kistler & Champion, 2001
26*	36.289	-121.052	80	Kistler & Champion, 2001
14*	36.672	-121.535	105	Kistler & Champion, 2001
31*	35.447	-120.545	80	Kistler & Champion, 2001
32*	35.605	-120.269	82	Kistler & Champion, 2001
KM-11b	36.885	-118.345	95	Mahan et al., 2003
KMR	36.882	-118.359	94	Mahan et al., 2003
KM-10a	36.883	-118.349	98	Mahan et al., 2003
WLT94-9	36.901	-118.413	165	Mahan et al., 2003
KM-1	36.886	-118.356	164	Mahan et al., 2003
SH-2.27.3	34.726	-117.616	148	Martin et al., 2002
AL-26	35.084	-116.611	149	Miller & Walker, 2002
AL27	35.062	-116.642	75	Miller & Walker, 2002
EPM-1	35.422	-117.808	259	Miller et al., 1995
EPM-2	35.407	-117.867	246	Miller et al., 1995
EPM-3	35.483	-117.688	171	Miller et al., 1995
TC27	35.218	-118.461	90	Saleeby et al., 1987
CM620	35.124	-118.739	95	Saleeby et al., 1987
BM684	35.313	-118.656	100	Saleeby et al., 1987
TC15	35.230	-118.491	97	Saleeby et al., 1987
TC42	35.228	-118.496	98	Saleeby et al., 1987
TC40	35.224	-118.483	97	Saleeby et al., 1987
CM25	35.211	-118.663	101	Saleeby et al., 1987
CM26	35.140	-118.618	100	Saleeby et al., 1987
CM9	35.041	-118.568	100	Saleeby et al., 1987
CM22b	35.184	-118.646	100	Saleeby et al., 1987
TL197	34.991	-118.538	102	Saleeby et al., 1987
WR84a	34.983	-118.721	102	Saleeby et al., 1987
WR86	34.974	-118.729	102	Saleeby et al., 1987
CM630	35.125	-118.723	115	Saleeby et al., 1987
WR643	35.024	-118.707	117	Saleeby et al., 1987
WR171	34.992	-118.729	115	Saleeby et al., 1987
WR30/2	34.984	-118.725	115	Saleeby et al., 1987
WR39	34.944	-118.663	113	Saleeby et al., 1987

PC35	34.919	-118.796	110	Saleeby et al., 1987
PC31	34.941	-118.826	114	Saleeby et al., 1987
PC32	34.937	-118.819	113	Saleeby et al., 1987
PC34	34.928	-118.801	117	Saleeby et al., 1987
PC36	34.916	-118.794	112	Saleeby et al., 1987
PC37	34.908	-118.788	115	Saleeby et al., 1987
PC129	34.925	-118.912	115	Saleeby et al., 1987
WR91a	34.958	-118.719	113	Saleeby et al., 1987
WR40	34.946	-118.678	117	Saleeby et al., 1987
TC12a	35.227	-118.488	117	Saleeby et al., 1987
GV1	34.891	-118.912	105	Saleeby et al., 2007
GV2	34.917	-118.922	101	Saleeby et al., 2007
GC46	34.916	-118.858	102	Saleeby et al., 2007
PC107	34.914	-118.823	110	Saleeby et al., 2007
GC33	34.922	-118.827	112	Saleeby et al., 2007
CM657	35.005	-118.758	111	Saleeby et al., 2007
WR643	35.010	-118.707	115	Saleeby et al., 2007
TC2a	34.981	-118.722	102	Saleeby et al., 2007
GC16	35.013	-118.643	112	Saleeby et al., 2007
WR27A	34.946	-118.671	110	Saleeby et al., 2007
GC1	34.981	-118.580	101	Saleeby et al., 2007
CM13b	35.212	-118.551	99	Saleeby et al., 2007
K1	35.875	-118.456	105	Saleeby et al., 2008
K2	35.770	-118.485	104	Saleeby et al., 2008
K3	35.682	-118.443	104	Saleeby et al., 2008
K4	35.615	-118.436	104	Saleeby et al., 2008
K5	35.787	-118.570	103	Saleeby et al., 2008
K6	35.527	-118.425	103	Saleeby et al., 2008
K7	35.498	-118.399	103	Saleeby et al., 2008
K8	35.825	-118.462	103	Saleeby et al., 2008
B1	35.478	-118.733	102	Saleeby et al., 2008
B2	35.507	-118.687	101	Saleeby et al., 2008
B3	35.351	-118.571	100	Saleeby et al., 2008
B4	35.395	-118.435	102	Saleeby et al., 2008
B5	35.750	-118.585	103	Saleeby et al., 2008
B6	35.436	-118.517	109	Saleeby et al., 2008
B7	35.451	-118.589	113	Saleeby et al., 2008
B8	35.454	-118.734	98	Saleeby et al., 2008
B9	35.575	-118.566	100	Saleeby et al., 2008
B10	35.603	-118.648	100	Saleeby et al., 2008
N1	35.666	-118.588	101	Saleeby et al., 2008
N2	35.975	-118.473	101	Saleeby et al., 2008

N3	35.826	-118.600	99	Saleeby et al., 2008
N4	35.852	-118.626	98	Saleeby et al., 2008
N5	35.669	-118.486	98	Saleeby et al., 2008
N6	35.976	-118.569	97	Saleeby et al., 2008
N7	36.095	-118.463	97	Saleeby et al., 2008
N8	35.105	-118.487	96	Saleeby et al., 2008
N9	35.676	-118.464	96	Saleeby et al., 2008
N10	35.426	-118.420	96	Saleeby et al., 2008
S1	35.717	-118.406	100	Saleeby et al., 2008
S2	35.982	-118.359	99	Saleeby et al., 2008
S3	35.673	-118.353	99	Saleeby et al., 2008
S4	35.615	-118.249	98	Saleeby et al., 2008
S5	35.578	-118.393	97	Saleeby et al., 2008
S6	35.563	-118.147	95	Saleeby et al., 2008
S7	35.729	-118.376	94	Saleeby et al., 2008
D1	35.848	-118.349	95	Saleeby et al., 2008
D2	35.709	-118.416	95	Saleeby et al., 2008
D3	35.701	-118.235	93	Saleeby et al., 2008
D4	35.462	-118.281	93	Saleeby et al., 2008
D5	35.380	-118.342	92	Saleeby et al., 2008
D6	35.741	-118.143	91	Saleeby et al., 2008
D7	35.791	-118.050	90	Saleeby et al., 2008
D8	35.483	-118.227	89	Saleeby et al., 2008
D9	35.986	-118.443	89	Saleeby et al., 2008
D10	35.744	-118.309	89	Saleeby et al., 2008
D11	35.857	-118.407	87	Saleeby et al., 2008
D12	35.444	-118.370	86	Saleeby et al., 2008
D13	35.801	-118.416	86	Saleeby et al., 2008
D14	35.736	-118.077	84	Saleeby et al., 2008
Plate III*	35.273	-117.847	87	Silver & Nourse, 1991
08SE596	34.878	-119.219	105	this study
09SE23	34.925	-119.282	155	this study
08SE582	34.867	-119.128	135	this study
08SE451	34.875	-119.111	136	this study
08SE450	34.872	-119.110	105	this study
08SE262	34.896	-119.094	136	this study
04SE5	34.852	-119.065	92	this study
06SE19A	34.857	-119.068	91	this study
07SE94	34.899	-119.029	106	this study
08SE46	34.908	-118.976	136	this study
08SE256	34.869	-119.047	88	this study
08SE675	34.896	-118.921	136	this study

08SE679	34.885	-118.909	105	this study
08SE674	34.885	-118.920	121	this study
08TC27A	34.971	-118.447	147	this study
91TH181	35.053	-118.411	92	this study
93TH417	35.040	-118.440	92	this study
10TC5	34.803	-118.787	92	this study
G11	37.436	-120.119	151	this study
02339	36.552	-121.250	88	Barth et al., 2003
02340	36.364	-121.555	86	Barth et al., 2003
02341	36.464	-121.712	82	Barth et al., 2003
WBK129	36.589	119.202	120	Clemens-Knott & Saleeby, 1999
WBK131	36.539	-119.111	123	Clemens-Knott & Saleeby, 1999
MK-550*	36.500	-118.550	107	Busby-Spera, 1982
MK-510*	36.450	-118.650	99	Busby-Spera, 1982
MK-560*	36.400	-118.525	97	Busby-Spera, 1982
K-D1-0	35.829	-118.112	148	Saleeby and Dunne, in preparation
K-D2-0	35.882	-118.121	225	Saleeby and Dunne, in preparation
K-D1-1	35.944	-118.080	185	Saleeby and Dunne, in preparation
K-D2-1	35.944	-118.081	156	Saleeby and Dunne, in preparation
K-D18-1	35.939	-118.073	158	Saleeby and Dunne, in preparation
B-D2-0	36.020	-118.291	215	Saleeby and Dunne, in preparation
B-D3-0	36.002	-118.336	229	Saleeby and Dunne, in preparation
B-D21-2	36.019	-118.324	85	Saleeby and Dunne, in preparation
B-D23-2	35.986	-118.367	95	Saleeby and Dunne, in preparation
I-D91-0	35.667	-117.949	248	Saleeby and Dunne, in preparation
I-D94-0	35.664	-118.024	248	Saleeby and Dunne, in preparation
04SS39	35.856	-117.992	171	Saleeby and Dunne, in preparation

* Location approximate

Table A2.5. Compilation of Sr_i ratios from the Sierra Nevada batholith and ophiolitic framework.[§]

Sample	Latitude	Longitude	Sr_i	Reference
BL-7	37.320	-119.670	0.70473	Kistler et al., 1986
BL-19	37.450	-119.642	0.70539	Kistler et al., 1986
BL-10	37.340	-119.660	0.70560	Kistler et al., 1986
BL-8	37.330	-119.660	0.70563	Kistler et al., 1986
BL-4	37.300	-119.660	0.70567	Kistler et al., 1986
BL-15	37.390	-119.648	0.70596	Kistler et al., 1986
BL-17	37.400	-119.640	0.70600	Kistler et al., 1986
Z-54	37.855	-119.484	0.70580	Kistler et al., 1986
Z-52	37.857	-119.486	0.70580	Kistler et al., 1986
Z-51	37.854	-119.439	0.70590	Kistler et al., 1986
Z-46	37.906	-119.265	0.70590	Kistler et al., 1986
Z-47	37.909	-119.264	0.70590	Kistler et al., 1986
Z-64	37.854	-119.486	0.70600	Kistler et al., 1986
Z-44	37.904	-119.268	0.70600	Kistler et al., 1986
Z-57	37.851	-119.477	0.70610	Kistler et al., 1986
Z-56	37.854	-119.480	0.70610	Kistler et al., 1986
Z-55	37.855	-119.482	0.70610	Kistler et al., 1986
Z-43	37.892	-119.280	0.70610	Kistler et al., 1986
Z-16	37.894	-119.265	0.70610	Kistler et al., 1986
Z-45	37.905	-119.266	0.70610	Kistler et al., 1986
Z-23	37.812	-119.485	0.70620	Kistler et al., 1986
Z-6	37.813	-119.482	0.70620	Kistler et al., 1986
Z-25	37.821	-119.478	0.70620	Kistler et al., 1986
Z-7	37.827	-119.469	0.70620	Kistler et al., 1986
Z-5	37.814	-119.493	0.70630	Kistler et al., 1986
Z-24	37.817	-119.480	0.70630	Kistler et al., 1986
Z-26	37.825	-119.474	0.70630	Kistler et al., 1986
Z-27	37.831	-119.467	0.70630	Kistler et al., 1986
Z-28	37.834	-119.460	0.70630	Kistler et al., 1986
Z-8	37.835	-119.456	0.70630	Kistler et al., 1986
Z-59	37.860	-119.472	0.70630	Kistler et al., 1986
Z-60	37.864	-119.461	0.70630	Kistler et al., 1986
Z-37	37.875	-119.388	0.70630	Kistler et al., 1986
Z-13	37.878	-119.345	0.70630	Kistler et al., 1986
Z-36	37.881	-119.401	0.70630	Kistler et al., 1986
Z-14	37.881	-119.318	0.70630	Kistler et al., 1986
Z-30	37.840	-119.450	0.70640	Kistler et al., 1986
Z-32	37.846	-119.445	0.70640	Kistler et al., 1986

Z-9	37.850	-119.441	0.70640	Kistler et al., 1986
Z-34	37.854	-119.439	0.70640	Kistler et al., 1986
Z-61	37.866	-119.456	0.70640	Kistler et al., 1986
Z-62	37.868	-119.448	0.70640	Kistler et al., 1986
Z-11	37.877	-119.393	0.70640	Kistler et al., 1986
Z-12	37.878	-119.355	0.70640	Kistler et al., 1986
Z-40	37.878	-119.349	0.70640	Kistler et al., 1986
Z-42	37.879	-119.303	0.70640	Kistler et al., 1986
Z-29	37.837	-119.454	0.70650	Kistler et al., 1986
Z-31	37.844	-119.447	0.70650	Kistler et al., 1986
Z-33	37.848	-119.443	0.70650	Kistler et al., 1986
Z-20	37.865	-119.431	0.70650	Kistler et al., 1986
Z-35	37.874	-119.423	0.70650	Kistler et al., 1986
Z-38	37.874	-119.377	0.70650	Kistler et al., 1986
Z-41	37.881	-119.301	0.70650	Kistler et al., 1986
Z-19	37.873	-119.368	0.70660	Kistler et al., 1986
Z-39	37.874	-119.374	0.70660	Kistler et al., 1986
Z-53	37.855	-119.485	0.70590	Kistler et al., 1986
Z-58	37.852	-119.474	0.70630	Kistler et al., 1986
Z-10	37.877	-119.413	0.70640	Kistler et al., 1986
Z-10	37.877	-119.413	0.70640	Kistler et al., 1986
Z-10	37.877	-119.413	0.70640	Kistler et al., 1986
Z-63	37.870	-119.440	0.70650	Kistler et al., 1986
Z-18	37.873	-119.368	0.70660	Kistler et al., 1986
W10	36.718	-119.357	0.70367	Chen & Tilton, 1991; Chen & Moore, 1982
W29	36.405	-119.053	0.70370	Chen & Tilton, 1991; Chen & Moore, 1982
W22	36.725	-119.292	0.70404	Chen & Tilton, 1991; Chen & Moore, 1982
W30	36.393	-118.963	0.70412	Chen & Tilton, 1991; Chen & Moore, 1982
W12A	36.722	-119.307	0.70413	Chen & Tilton, 1991; Chen & Moore, 1982
W31	36.412	-118.937	0.70494	Chen & Tilton, 1991; Chen & Moore, 1982
W3	36.747	-119.060	0.70524	Chen & Tilton, 1991; Chen & Moore, 1982
W6	36.722	-118.970	0.70530	Chen & Tilton, 1991; Chen & Moore, 1982
W4	36.770	-119.120	0.70565	Chen & Tilton, 1991; Chen & Moore, 1982
W5	36.748	-119.228	0.70580	Chen & Tilton, 1991; Chen & Moore, 1982
OW4	36.770	-118.348	0.70641	Chen & Tilton, 1991; Chen & Moore, 1982
SQ48A	36.723	-118.807	0.70681	Chen & Tilton, 1991; Chen & Moore, 1982
KC14	36.780	-118.618	0.70698	Chen & Tilton, 1991; Chen & Moore, 1982
SQ13A	36.640	-118.805	0.70707	Chen & Tilton, 1991; Chen & Moore, 1982
OW6	36.785	-118.315	0.70708	Chen & Tilton, 1991; Chen & Moore, 1982
SQ7	36.561	-118.772	0.70722	Chen & Tilton, 1991; Chen & Moore, 1982
E27-9	36.845	-118.060	0.70722	Chen & Tilton, 1991; Chen & Moore, 1982
SQ67	36.718	-118.717	0.70724	Chen & Tilton, 1991; Chen & Moore, 1982

KC15	36.797	-118.675	0.70726	Chen & Tilton, 1991; Chen & Moore, 1982
KC6	36.830	-118.870	0.70728	Chen & Tilton, 1991; Chen & Moore, 1982
OW19	36.905	-118.162	0.70730	Chen & Tilton, 1991; Chen & Moore, 1982
KC16	36.810	-118.760	0.70739	Chen & Tilton, 1991; Chen & Moore, 1982
SQ75	36.582	-118.753	0.70751	Chen & Tilton, 1991; Chen & Moore, 1982
SQ8A	36.603	-118.720	0.70784	Chen & Tilton, 1991; Chen & Moore, 1982
KC13	36.798	-118.572	0.70788	Chen & Tilton, 1991; Chen & Moore, 1982
OW40	36.562	-118.292	0.70797	Chen & Tilton, 1991; Chen & Moore, 1982
UB-1a	36.984	-118.407	0.70619	Frost & Mahood, 1987
80FL	37.146	-118.583	0.70636	Frost & Mahood, 1987
6a	37.210	-118.644	0.70639	Frost & Mahood, 1987
76a	37.143	-118.581	0.70652	Frost & Mahood, 1987
20a	37.172	-118.564	0.70658	Frost & Mahood, 1987
15a	37.234	-118.659	0.70679	Frost & Mahood, 1987
CR-5	37.200	-119.117	0.70899	Hill et al., 1988
CR-29	37.217	-119.150	0.70811	Hill et al., 1988
CR-3	37.233	-119.161	0.70869	Hill et al., 1988
KPc-42	37.353	-119.133	0.70874	Hill et al., 1988
KPb-59	37.414	-119.100	0.70897	Hill et al., 1988
EP-10	37.085	-119.010	0.70945	Hill et al., 1988
KPa-66	37.425	-119.181	0.70925	Hill et al., 1988
KPd-72	37.306	-119.022	0.70878	Hill et al., 1988
E83	37.108	-119.044	0.70872	Hill et al., 1988
C1	37.085	-119.017	0.70908	Hill et al., 1988
BC	35.327	-120.260	0.70790	Kistler & Champion, 2001
MP-2	36.622	-121.909	0.70812	Kistler & Champion, 2001
LP-1	35.409	-120.567	0.70840	Kistler & Champion, 2001
CC-3	34.544	-118.535	0.70920	Kistler & Champion, 2001
AC-8	35.299	-120.261	0.71280	Kistler & Champion, 2001
WS	34.500	-118.500	0.71360	Kistler & Champion, 2001
GR-129	36.338	-117.475	0.70610	Kistler & Lee, 1989
GR-130	36.340	-117.481	0.70630	Kistler & Lee, 1989
GR-131	36.324	-117.686	0.70760	Kistler & Lee, 1989
GR-132	36.317	-117.676	0.70780	Kistler & Lee, 1989
GR-133	36.039	-116.676	0.70700	Kistler & Lee, 1989
GR-134	36.044	-116.674	0.70860	Kistler & Lee, 1989
GR-135	36.115	-116.542	0.70840	Kistler & Lee, 1989
GR-136	36.103	-116.558	0.70960	Kistler & Lee, 1989
GR-137	35.790	-116.333	0.71030	Kistler & Lee, 1989
GR-138	35.788	-116.325	0.71090	Kistler & Lee, 1989
GR-143	35.300	-115.539	0.71070	Kistler & Lee, 1989
GR-144	35.314	-115.814	0.70990	Kistler & Lee, 1989

GR-145	35.408	-115.786	0.70980	Kistler & Lee, 1989
GR-146	35.411	-115.139	0.70990	Kistler & Lee, 1989
GR-147	35.186	-116.161	0.75400	Kistler & Lee, 1989
GR-148	35.196	-116.683	0.75400	Kistler & Lee, 1989
GR-149	35.542	-117.676	0.70800	Kistler & Lee, 1989
GR-150	35.521	-117.906	0.70800	Kistler & Lee, 1989
GR-151	35.372	-117.926	0.70360	Kistler & Lee, 1989
GR-152	35.368	-117.056	0.70340	Kistler & Lee, 1989
GR-153	34.458	-117.076	0.70790	Kistler & Lee, 1989
GR-154	34.468	-117.282	0.70690	Kistler & Lee, 1989
GR-155	34.543	-117.293	0.70910	Kistler & Lee, 1989
GR-156	34.546	-117.904	0.70910	Kistler & Lee, 1989
GR-157	34.557	-116.908	0.71855	Kistler & Lee, 1989
GR-158	34.551	-116.824	0.71938	Kistler & Lee, 1989
GR-159	34.575	-116.817	0.70960	Kistler & Lee, 1989
GR-160	34.574	-116.510	0.70890	Kistler & Lee, 1989
GR-167	33.456	-115.117	0.70830	Kistler & Lee, 1989
GR-168	33.476	-115.804	0.70880	Kistler & Lee, 1989
GR-169	33.711	-115.822	0.71870	Kistler & Lee, 1989
GR-170	33.728	-115.657	0.71380	Kistler & Lee, 1989
GR-171	34.065	-114.671	0.70650	Kistler & Lee, 1989
GR-172	34.079	-114.183	0.70650	Kistler & Lee, 1989
GR-173	34.081	-115.201	0.71040	Kistler & Lee, 1989
GR-174	34.040	-115.415	0.71040	Kistler & Lee, 1989
GR-175	34.094	-115.460	0.70990	Kistler & Lee, 1989
GR-176	34.108	-115.693	0.71350	Kistler & Lee, 1989
SCC-25	38.780	-120.740	0.70320	Kistler & Fleck, 1994
Scc-1	38.860	-120.580	0.70340	Kistler & Fleck, 1994
BR8	39.570	-121.200	0.70360	Kistler & Fleck, 1994
BR1	39.570	-121.340	0.70360	Kistler & Fleck, 1994
BR13	39.640	-121.270	0.70360	Kistler & Fleck, 1994
CL-1	36.860	-119.470	0.70380	Kistler & Fleck, 1994
BR3	39.740	-121.130	0.70380	Kistler & Fleck, 1994
SCC-29	38.730	-120.680	0.70400	Kistler & Fleck, 1994
FD-20	37.190	-119.860	0.70420	Kistler & Fleck, 1994
WV-1	36.940	-119.460	0.70430	Kistler & Fleck, 1994
SCC-5	38.570	-120.610	0.70470	Kistler & Fleck, 1994
SCC-33	38.820	-120.400	0.70500	Kistler & Fleck, 1994
SCD-6	38.930	-120.060	0.70530	Kistler & Fleck, 1994
K46-64	37.740	-119.490	0.70564	Kistler & Fleck, 1994
SCD-11	38.830	-120.110	0.70580	Kistler & Fleck, 1994
FD-2	36.840	-117.960	0.70590	Kistler & Fleck, 1994

Kpv-1	37.940	-119.840	0.70600	Kistler & Fleck, 1994
SCD-14	38.730	-120.250	0.70600	Kistler & Fleck, 1994
12	37.832	-119.583	0.70604	Kistler & Fleck, 1994
13	37.805	-119.558	0.70607	Kistler & Fleck, 1994
MT-1	37.440	-118.670	0.70610	Kistler & Fleck, 1994
JB-1	37.100	-119.320	0.70650	Kistler & Fleck, 1994
Kmg41a	37.180	-118.920	0.70650	Kistler & Fleck, 1994
SSr-T1	37.740	-119.490	0.70650	Kistler & Fleck, 1994
K5-64	37.860	-119.690	0.70658	Kistler & Fleck, 1994
78-17	35.420	-117.580	0.70660	Kistler & Fleck, 1994
78-4	35.730	-118.570	0.70660	Kistler & Fleck, 1994
PapFla	37.000	-117.980	0.70660	Kistler & Fleck, 1994
MG-1	37.060	-118.570	0.70660	Kistler & Fleck, 1994
K37-67	37.770	-119.550	0.70668	Kistler & Fleck, 1994
SCH-8	38.090	-120.080	0.70670	Kistler & Fleck, 1994
FD-3	36.760	-117.980	0.70690	Kistler & Fleck, 1994
SLB-93X3	37.090	-119.190	0.70750	Kistler & Fleck, 1994
Kdc20a	37.090	-119.190	0.70750	Kistler & Fleck, 1994
EAGPK91	37.210	-119.030	0.70750	Kistler & Fleck, 1994
BNPK-1	37.740	-118.370	0.70770	Kistler & Fleck, 1994
EAGPK54	37.210	-119.030	0.70790	Kistler & Fleck, 1994
EAGPK97	37.210	-119.030	0.70810	Kistler & Fleck, 1994
R-99	37.030	-118.620	0.70930	Kistler & Fleck, 1994
PF98	36.980	-118.090	0.71030	Kistler & Fleck, 1994
BC-C-24	37.320	-118.110	0.71210	Kistler & Fleck, 1994
6	38.720	-120.500	0.70320	Kistler & Peterman, 1973
4	39.100	-119.970	0.70490	Kistler & Peterman, 1973
11	38.090	-119.530	0.70540	Kistler & Peterman, 1973
7	38.350	-119.750	0.70560	Kistler & Peterman, 1973
17	37.210	-119.260	0.70570	Kistler & Peterman, 1973
12	37.970	-119.650	0.70600	Kistler & Peterman, 1973
13	37.960	-119.540	0.70610	Kistler & Peterman, 1973
8	38.280	-119.830	0.70620	Kistler & Peterman, 1973
23	36.090	-118.450	0.70640	Kistler & Peterman, 1973
10	37.910	-119.220	0.70650	Kistler & Peterman, 1973
19	37.030	-117.970	0.70660	Kistler & Peterman, 1973
22	36.420	-118.120	0.70680	Kistler & Peterman, 1973
21	36.470	-118.620	0.70700	Kistler & Peterman, 1973
20	36.770	-117.890	0.70700	Kistler & Peterman, 1973
18	37.230	-119.030	0.70710	Kistler & Peterman, 1973
24	35.800	-118.380	0.70810	Kistler & Peterman, 1973
27	36.440	-121.950	0.70820	Kistler & Peterman, 1973

31	36.590	-121.480	0.70820	Kistler & Peterman, 1973
30	36.750	-118.010	0.70940	Kistler & Peterman, 1973
28	37.140	-120.200	0.70320	Kistler & Peterman, 1973; DePaolo, 1981
2	40.520	-120.800	0.70370	Kistler & Peterman, 1973; DePaolo, 1981
5	38.950	-119.980	0.70430	Kistler & Peterman, 1973; DePaolo, 1981
29	37.040	-119.700	0.70440	Kistler & Peterman, 1973; DePaolo, 1981
15	37.850	-119.920	0.70470	Kistler & Peterman, 1973; DePaolo, 1981
3	39.750	-120.180	0.70480	Kistler & Peterman, 1973; DePaolo, 1981
26	35.600	-117.910	0.70490	Kistler & Peterman, 1973; DePaolo, 1981
9	37.910	-118.830	0.70520	Kistler & Peterman, 1973; DePaolo, 1981
14	37.970	-119.430	0.70650	Kistler & Peterman, 1973; DePaolo, 1981
A6	35.373	-117.262	0.70410	Kistler & Peterman, 1973; DePaolo, 1981
Sr19-73	35.539	-117.557	0.70410	Kistler & Peterman, 1978
COS10-2	36.045	-117.848	0.70410	Kistler & Peterman, 1978
Sr14-73	35.050	-118.420	0.70485	Kistler & Peterman, 1978
COS13-42-2	35.986	-117.818	0.70600	Kistler & Peterman, 1978
A3	35.308	-117.334	0.70640	Kistler & Peterman, 1978
Sr17-73	35.348	-117.646	0.70660	Kistler & Peterman, 1978
Sr11-73	35.034	-117.957	0.70770	Kistler & Peterman, 1978
Sr18-73	35.516	-117.552	0.70810	Kistler & Peterman, 1978
Sr3-73	35.681	-118.695	0.70325	Kistler & Peterman, 1978
Sr1-73	35.688	-118.913	0.70382	Kistler & Peterman, 1978
Sr2-73	35.700	-118.800	0.70434	Kistler & Peterman, 1978
Sr5-73	35.706	-118.548	0.70530	Kistler & Peterman, 1978
Sr4-73	35.710	-118.625	0.70656	Kistler & Peterman, 1978
TC-40	35.206	-118.476	0.70704	Kistler & Ross, 1990
TC-27	35.206	-118.476	0.70730	Kistler & Ross, 1990
GR-152	35.343	-117.931	0.70362	Kistler & Ross, 1990
GR-151	35.357	-117.919	0.70362	Kistler & Ross, 1990
S31-84	35.418	-117.849	0.70362	Kistler & Ross, 1990
S28-84	35.426	-117.865	0.70362	Kistler & Ross, 1990
DR-6391	35.607	-117.958	0.70362	Kistler & Ross, 1990
DR-6179	35.663	-117.952	0.70362	Kistler & Ross, 1990
DR-6226	35.714	-118.045	0.70362	Kistler & Ross, 1990
DR-6123	35.981	-118.952	0.70366	Kistler & Ross, 1990
DR-5980	35.765	-118.715	0.70382	Kistler & Ross, 1990
DR-6061	35.874	-118.874	0.70382	Kistler & Ross, 1990
DR-6079A	35.808	-118.784	0.70390	Kistler & Ross, 1990
DR-6024	35.869	-118.806	0.70390	Kistler & Ross, 1990
DR-6106	35.904	-118.923	0.70390	Kistler & Ross, 1990
DR-6096	35.767	-118.859	0.70391	Kistler & Ross, 1990
DR-6220	35.745	-118.030	0.70396	Kistler & Ross, 1990

DR-6176A	35.692	-117.968	0.70398	Kistler & Ross, 1990
DR-6174D	35.660	-117.951	0.70400	Kistler & Ross, 1990
DR-6093	35.781	-118.765	0.70403	Kistler & Ross, 1990
DR-6400	35.687	-117.981	0.70407	Kistler & Ross, 1990
DR-6030	35.892	-118.739	0.70408	Kistler & Ross, 1990
DR-6117	35.977	-118.872	0.70411	Kistler & Ross, 1990
DR-6314-1	35.752	-118.830	0.70414	Kistler & Ross, 1990
DR-6088	35.812	-118.834	0.70417	Kistler & Ross, 1990
DR-6321	35.690	-118.898	0.70421	Kistler & Ross, 1990
DR-6356	35.671	-118.915	0.70424	Kistler & Ross, 1990
DR-3631	35.270	-118.734	0.70427	Kistler & Ross, 1990
DR-6385A	35.623	-117.921	0.70428	Kistler & Ross, 1990
DR-6438A	35.632	-117.904	0.70428	Kistler & Ross, 1990
DR-6439	35.632	-117.904	0.70428	Kistler & Ross, 1990
DR-4184	35.445	-118.813	0.70430	Kistler & Ross, 1990
DR-3635	35.258	-118.700	0.70443	Kistler & Ross, 1990
DR-6297	35.628	-118.819	0.70459	Kistler & Ross, 1990
DR-6300	35.622	-118.865	0.70471	Kistler & Ross, 1990
DR-6373	35.537	-118.656	0.70478	Kistler & Ross, 1990
DR-6336	35.593	-118.838	0.70480	Kistler & Ross, 1990
DR-6292	35.618	-118.677	0.70490	Kistler & Ross, 1990
DR-3791	35.038	-118.591	0.70497	Kistler & Ross, 1990
DR-6359	35.627	-118.630	0.70503	Kistler & Ross, 1990
DR-3858	35.317	-118.559	0.70512	Kistler & Ross, 1990
DR-6509A	35.831	-118.115	0.70512	Kistler & Ross, 1990
DR-3837	35.137	-118.678	0.70591	Kistler & Ross, 1990
DR-4281	35.397	-118.470	0.70593	Kistler & Ross, 1990
DR-5421	35.613	-118.380	0.70593	Kistler & Ross, 1990
DR-3575	35.059	-118.627	0.70600	Kistler & Ross, 1990
DR-5153	35.492	-118.395	0.70608	Kistler & Ross, 1990
DR-5423	35.746	-118.551	0.70616	Kistler & Ross, 1990
DR-5852	35.925	-118.545	0.70616	Kistler & Ross, 1990
DR-4995	35.976	-118.548	0.70616	Kistler & Ross, 1990
DR-5034	35.982	-118.464	0.70616	Kistler & Ross, 1990
DR-5974	35.797	-118.691	0.70618	Kistler & Ross, 1990
DR-5946	35.807	-118.647	0.70618	Kistler & Ross, 1990
DR-5965	35.836	-118.652	0.70618	Kistler & Ross, 1990
DR-5285	35.836	-118.528	0.70618	Kistler & Ross, 1990
DR-5922	35.863	-118.606	0.70618	Kistler & Ross, 1990
DR-5801R	35.875	-118.650	0.70618	Kistler & Ross, 1990
DR-5887	35.908	-118.655	0.70618	Kistler & Ross, 1990
DR-5871	35.925	-118.658	0.70618	Kistler & Ross, 1990

DR-4692	36.104	-118.467	0.70623	Kistler & Ross, 1990
DR-5062	35.788	-118.562	0.70628	Kistler & Ross, 1990
DR-5017	35.808	-118.577	0.70628	Kistler & Ross, 1990
DR-6245	35.722	-118.603	0.70638	Kistler & Ross, 1990
DR-6269	35.736	-118.653	0.70644	Kistler & Ross, 1990
DR-5407	35.767	-118.268	0.70645	Kistler & Ross, 1990
DR-5425	35.739	-118.565	0.70653	Kistler & Ross, 1990
DR-5089	35.498	-118.422	0.70671	Kistler & Ross, 1990
DR-5261	35.598	-118.583	0.70675	Kistler & Ross, 1990
DR-6208	35.655	-117.888	0.70675	Kistler & Ross, 1990
DR-6535	35.729	-117.981	0.70679	Kistler & Ross, 1990
DR-4294	35.435	-118.423	0.70680	Kistler & Ross, 1990
DR-5865A	35.952	-118.634	0.70681	Kistler & Ross, 1990
DR-6415	35.685	-117.883	0.70682	Kistler & Ross, 1990
DR-5403	35.834	-118.269	0.70687	Kistler & Ross, 1990
S67-84	35.884	-118.019	0.70718	Kistler & Ross, 1990
DR-6472A	35.891	-117.921	0.70718	Kistler & Ross, 1990
DR-3401	34.805	-118.868	0.70727	Kistler & Ross, 1990
DR-3466	34.852	-118.750	0.70727	Kistler & Ross, 1990
DR-3752	35.038	-118.360	0.70727	Kistler & Ross, 1990
DR-6539	35.778	-117.950	0.70731	Kistler & Ross, 1990
DR-3088	34.857	-118.932	0.70741	Kistler & Ross, 1990
DR-4102A	35.201	-118.446	0.70746	Kistler & Ross, 1990
DR-5133R	35.990	-118.405	0.70762	Kistler & Ross, 1990
DR-4314	35.337	-118.376	0.70766	Kistler & Ross, 1990
DR-5006	35.883	-118.535	0.70767	Kistler & Ross, 1990
DR-4763	35.669	-118.441	0.70773	Kistler & Ross, 1990
DR-3737	35.032	-118.440	0.70777	Kistler & Ross, 1990
DR-4354	35.417	-118.357	0.70782	Kistler & Ross, 1990
DR-3534B	34.955	-118.535	0.70786	Kistler & Ross, 1990
DR-3818	34.979	-118.366	0.70786	Kistler & Ross, 1990
DR-3733A	34.995	-118.454	0.70786	Kistler & Ross, 1990
DR-3745	35.014	-118.420	0.70786	Kistler & Ross, 1990
DR-3740	35.023	-118.407	0.70786	Kistler & Ross, 1990
DR-3746	35.032	-118.397	0.70786	Kistler & Ross, 1990
DR-3747A	35.040	-118.382	0.70786	Kistler & Ross, 1990
DR-5191A	35.593	-118.231	0.70790	Kistler & Ross, 1990
DR-4402	35.376	-118.120	0.70793	Kistler & Ross, 1990
DR-4341	35.471	-118.247	0.70800	Kistler & Ross, 1990
DR-4528	35.305	-118.102	0.70813	Kistler & Ross, 1990
DR-4093	35.213	-118.113	0.70818	Kistler & Ross, 1990
DR-3221	34.826	-118.936	0.70846	Kistler & Ross, 1990

DR-3005	34.882	-119.297	0.70846	Kistler & Ross, 1990
DR-3756A	35.008	-118.345	0.70850	Kistler & Ross, 1990
DR-3829A	34.993	-118.395	0.70855	Kistler & Ross, 1990
NM-30	35.808	-117.917	0.70880	Kistler & Ross, 1990
NM-31	35.808	-117.917	0.70880	Kistler & Ross, 1990
NM-4A	35.814	-117.934	0.70880	Kistler & Ross, 1990
NM-4B	35.814	-117.934	0.70880	Kistler & Ross, 1990
DR-5071	35.591	-118.417	0.70896	Kistler & Ross, 1990
DR-3427B	35.038	-118.639	0.70562	Kistler & Ross, 1990
DR-4181	35.477	-118.653	0.70425	Kistler & Ross, 1990
DR-4189	35.461	-118.790	0.70449	Kistler & Ross, 1990
TC-15	35.217	-118.528	0.70583	Kistler & Ross, 1990
CM-25	35.206	-118.674	0.70591	Kistler & Ross, 1990
DR-3670	35.182	-118.676	0.70601	Kistler & Ross, 1990
DR-5008	35.856	-118.538	0.70618	Kistler & Ross, 1990
DR-4796-1	35.611	-118.497	0.70619	Kistler & Ross, 1990
DR-5031	35.956	-118.470	0.70625	Kistler & Ross, 1990
DR-4789A	35.650	-118.476	0.70626	Kistler & Ross, 1990
CM-26	35.131	-118.644	0.70637	Kistler & Ross, 1990
DR-4848	35.670	-118.357	0.70639	Kistler & Ross, 1990
DR-5236	35.667	-118.594	0.70677	Kistler & Ross, 1990
DR-3181	34.840	-119.060	0.70742	Kistler & Ross, 1990
DR-4819A	35.649	-118.448	0.70767	Kistler & Ross, 1990
DR-3356	34.907	-118.688	0.70786	Kistler & Ross, 1990
DR-4472	35.396	-118.093	0.70852	Kistler & Ross, 1990
Sr16-73	35.355	-117.909	0.70420	Kistler & Peterman, 1978
Sr6-73	35.547	-118.249	0.70582	Kistler & Peterman, 1978
Sr20-73	35.870	-117.891	0.70610	Kistler & Peterman, 1978
Sr10-73	35.326	-118.109	0.70708	Kistler & Peterman, 1978
Sr8-73	35.507	-118.137	0.70751	Kistler & Peterman, 1978
Sr9-73	35.344	-118.176	0.70746	Kistler & Peterman, 1978
TC42	35.217	-118.513	0.70570	Kistler & Peterman, 1978
Z-54	37.855	-119.484	0.70580	Kistler et al., 1986
151	35.372	-117.910	0.70360	Kistler & Lee, 1989
131	36.324	-117.686	0.70760	Kistler & Lee, 1989
149	35.542	-117.693	0.70800	Kistler & Lee, 1989
1	40.598	-120.699	0.70370	Masi et al., 1981
2	40.218	-120.611	0.70389	Masi et al., 1981
3	39.993	-120.184	0.70390	Masi et al., 1981
4	39.835	-120.146	0.70436	Masi et al., 1981
5	39.940	-121.277	0.70370	Masi et al., 1981
6	39.749	-120.123	0.70480	Masi et al., 1981

7	39.658	-120.458	0.70445	Masi et al., 1981
8	39.393	-121.045	0.70410	Masi et al., 1981
9	39.361	-120.372	0.70610	Masi et al., 1981
10	39.178	-120.935	0.70430	Masi et al., 1981
11	39.139	-119.923	0.70450	Masi et al., 1981
12	39.016	-119.919	0.70450	Masi et al., 1981
13	38.862	-120.006	0.70583	Masi et al., 1981
14	38.649	-119.659	0.70549	Masi et al., 1981
15	38.752	-120.843	0.70370	Masi et al., 1981
16	38.620	-120.621	0.70470	Masi et al., 1981
18	38.324	-119.915	0.70620	Masi et al., 1981
19	38.327	-119.819	0.70560	Masi et al., 1981
20	37.972	-120.284	0.70460	Masi et al., 1981
21	37.798	-119.435	0.70600	Masi et al., 1981
22	37.870	-119.407	0.70650	Masi et al., 1981
23	37.825	-119.139	0.70620	Masi et al., 1981
24	37.883	-119.170	0.70620	Masi et al., 1981
25	37.940	-119.170	0.70620	Masi et al., 1981
26	37.835	-118.640	0.70520	Masi et al., 1981
27	37.747	-119.186	0.70480	Masi et al., 1981
28	37.747	-119.186	0.70480	Masi et al., 1981
29	37.747	-119.186	0.70480	Masi et al., 1981
30	37.747	-119.186	0.70480	Masi et al., 1981
31	37.643	-119.784	0.70650	Masi et al., 1981
32	37.680	-119.711	0.70650	Masi et al., 1981
33	37.813	-119.698	0.70650	Masi et al., 1981
34	37.876	-119.514	0.70650	Masi et al., 1981
35	37.843	-119.509	0.70650	Masi et al., 1981
36	37.801	-119.514	0.70650	Masi et al., 1981
38	37.421	-117.767	0.70679	Masi et al., 1981
39	37.434	-119.844	0.70470	Masi et al., 1981
41	37.320	-119.580	0.70589	Masi et al., 1981
42	37.414	-119.617	0.70448	Masi et al., 1981
43	37.235	-119.910	0.70450	Masi et al., 1981
45	37.128	-119.882	0.70480	Masi et al., 1981
46	37.357	-119.437	0.70750	Masi et al., 1981
47	37.154	-120.101	0.70320	Masi et al., 1981
48	36.969	-118.054	0.70660	Masi et al., 1981
49	36.942	-119.485	0.70419	Masi et al., 1981
50	36.564	-118.234	0.70680	Masi et al., 1981
51	36.457	-119.168	0.70380	Masi et al., 1981
54	36.115	-118.483	0.70640	Masi et al., 1981

55	36.155	-117.870	0.70410	Masi et al., 1981
56	36.059	-117.834	0.70600	Masi et al., 1981
57	35.912	-117.877	0.70600	Masi et al., 1981
58	35.768	-118.336	0.70810	Masi et al., 1981
59	35.758	-118.630	0.70610	Masi et al., 1981
60	35.694	-118.565	0.70530	Masi et al., 1981
61	35.800	-118.771	0.70430	Masi et al., 1981
62	35.761	-118.862	0.70380	Masi et al., 1981
63	35.684	-118.734	0.70320	Masi et al., 1981
64	35.711	-118.193	0.70820	Masi et al., 1981
65	35.625	-118.080	0.70490	Masi et al., 1981
66	35.544	-118.236	0.70580	Masi et al., 1981
67	35.626	-117.606	0.70410	Masi et al., 1981
68	35.487	-118.144	0.70750	Masi et al., 1981
69	35.548	-117.558	0.70810	Masi et al., 1981
70	35.434	-118.158	0.70800	Masi et al., 1981
71	35.409	-117.876	0.70420	Masi et al., 1981
72	35.359	-118.092	0.70700	Masi et al., 1981
73	35.170	-118.521	0.70550	Masi et al., 1981
75	34.928	-119.162	0.70380	Masi et al., 1981
76	34.936	-119.111	0.70310	Masi et al., 1981
77	34.913	-118.850	0.70780	Masi et al., 1981
SN-42	36.300	-120.000	0.70450	Masi et al., 1981
SN-66	35.200	-118.700	0.70580	Masi et al., 1981
I-66	34.770	-117.150	0.70767	Miller & Glazner, 1995
SH-4-20-12	34.670	-117.450	0.70891	Miller & Glazner, 1995
EPM-2	35.407	-117.867	0.70386	Miller et al., 1995
EPM-1	35.422	-117.808	0.70407	Miller et al., 1995
Opal-2	35.125	-117.104	0.70413	Miller et al., 1995
EPM-3	35.483	-117.688	0.70805	Miller et al., 1995
CM9	35.041	-118.568	0.70721	Pickett & Saleeby, 1994
GC-8	35.004	-118.759	0.70507	Pickett & Saleeby, 1994
GC-11	34.979	-118.724	0.70499	Pickett & Saleeby, 1994
GC-17	34.998	-118.633	0.70537	Pickett & Saleeby, 1994
GC-53	34.912	-118.859	0.70433	Pickett & Saleeby, 1994
GV-1a	34.890	-118.915	0.70501	Pickett & Saleeby, 1994
GV-3	34.909	-118.921	0.70502	Pickett & Saleeby, 1994
PC175	34.925	-118.785	0.70446	Pickett & Saleeby, 1994
PTC-42	34.950	-118.775	0.70504	Pickett & Saleeby, 1994
TC-45b	34.949	-118.756	0.70476	Pickett & Saleeby, 1994
TC-47	34.966	-118.775	0.70482	Pickett & Saleeby, 1994
TC-49b	34.965	-118.765	0.70546	Pickett & Saleeby, 1994

TC-83	34.984	-118.723	0.70491	Pickett & Saleeby, 1994
GC-1	35.122	-118.726	0.70496	Pickett & Saleeby, 1994
GC-14	35.021	-118.705	0.70549	Pickett & Saleeby, 1994
GC-32	34.920	-118.833	0.70517	Pickett & Saleeby, 1994
GC-55	34.925	-118.801	0.70540	Pickett & Saleeby, 1994
GC-60	34.914	-118.791	0.70412	Pickett & Saleeby, 1994
TC-6	34.993	-118.728	0.70639	Pickett & Saleeby, 1994
TC-34	34.985	-118.769	0.70505	Pickett & Saleeby, 1994
GC-2	35.066	-118.691	0.70666	Pickett & Saleeby, 1994
GV-14	34.880	-118.897	0.70850	Pickett & Saleeby, 1994
TC42	35.230	-118.505	0.70612	Pickett & Saleeby, 1994
CM-9	35.034	-118.590	0.70677	Kistler & Ross, 1990
OC3	36.823	-118.407	0.70560	Saleeby et al., 1990
BM684	35.315	-118.645	0.70440	Kistler & Ross, 1990
BM-684	35.315	-118.645	0.70440	Kistler & Ross, 1990
TC27	35.218	-118.461	0.70731	Saleeby et al., 1987
CM620	35.124	-118.739	0.70576	Saleeby et al., 1987
TC15	35.230	-118.491	0.70583	Saleeby et al., 1987
TC42	35.228	-118.496	0.70570	Saleeby et al., 1987
TC40	35.224	-118.483	0.70703	Saleeby et al., 1987
CM25	35.211	-118.663	0.70591	Saleeby et al., 1987
CM26	35.140	-118.618	0.70637	Saleeby et al., 1987
CM9	35.041	-118.568	0.70677	Saleeby et al., 1987
CM22b	35.184	-118.646	0.70605	Saleeby et al., 1987
TL197	34.991	-118.538	0.70496	Saleeby et al., 1987
WR84a	34.983	-118.721	0.70499	Saleeby et al., 1987
WR86	34.974	-118.729	0.70504	Saleeby et al., 1987
WR190	34.978	-118.762	0.70499	Saleeby et al., 1987
PC227	34.971	-118.778	0.70493	Saleeby et al., 1987
CM630	35.125	-118.723	0.70472	Saleeby et al., 1987
WR643	35.024	-118.707	0.70518	Saleeby et al., 1987
WR171	34.992	-118.729	0.70467	Saleeby et al., 1987
WR30/2	34.984	-118.725	0.70478	Saleeby et al., 1987
WR39	34.944	-118.663	0.70499	Saleeby et al., 1987
PC35	34.919	-118.796	0.70776	Saleeby et al., 1987
PC31	34.941	-118.826	0.70519	Saleeby et al., 1987
PC32	34.937	-118.819	0.70510	Saleeby et al., 1987
PC34	34.928	-118.801	0.70469	Saleeby et al., 1987
PC36	34.916	-118.794	0.70500	Saleeby et al., 1987
PC37	34.908	-118.788	0.70469	Saleeby et al., 1987
PC129	34.925	-118.912	0.70594	Saleeby et al., 1987
WR91a	34.958	-118.719	0.70536	Saleeby et al., 1987

WR40	34.946	-118.678	0.70480	Saleeby et al., 1987
TC12a	35.228	-118.488	0.70682	Saleeby et al., 1987
6	37.072	-118.370	0.70651	Sawka et al., 1990
7	37.072	-118.366	0.70651	Sawka et al., 1990
21	37.084	-118.421	0.70651	Sawka et al., 1990
22	37.084	-118.419	0.70651	Sawka et al., 1990
2	37.092	-118.388	0.70651	Sawka et al., 1990
56	37.063	-118.417	0.70719	Sawka et al., 1990
58	37.067	-118.418	0.70719	Sawka et al., 1990
55	37.070	-118.420	0.70719	Sawka et al., 1990
5	37.071	-118.446	0.70719	Sawka et al., 1990
57	37.075	-118.423	0.70719	Sawka et al., 1990
67	37.088	-118.461	0.70719	Sawka et al., 1990
65	37.094	-118.475	0.70719	Sawka et al., 1990
70	37.094	-118.473	0.70719	Sawka et al., 1990
63	37.094	-118.469	0.70719	Sawka et al., 1990
72	37.075	-118.425	0.70651	Sawka et al., 1990; Kistler & Fleck, 1994
30	37.081	-118.421	0.70651	Sawka et al., 1990; Kistler & Fleck, 1994
8	37.061	-118.420	0.70719	Sawka et al., 1990; Kistler & Fleck, 1994
61	37.086	-118.451	0.70719	Sawka et al., 1990; Kistler & Fleck, 1994
DR570	36.284	-120.979	0.70880	Kistler & Champion, 2001
DR566A	36.547	-121.250	0.70830	Kistler & Champion, 2001
DR584	36.704	-121.543	0.70860	Kistler & Champion, 2001
G1A	36.270	-121.060	0.70830	Kistler & Champion, 2001
DR576	36.323	-121.171	0.70860	Kistler & Champion, 2001
BR-6-3	36.793	-121.503	0.70810	Kistler & Champion, 2001
BH6-88	38.304	-123.052	0.70671	Kistler & Champion, 2001
BH8-88	38.311	-123.061	0.70676	Kistler & Champion, 2001
BH1-88	38.302	-123.055	0.70600	Kistler & Champion, 2001
PR7-88	38.186	-122.960	0.70662	Kistler & Champion, 2001
PR8-88	38.191	-122.959	0.70662	Kistler & Champion, 2001
PR14-88	38.000	-122.974	0.70775	Kistler & Champion, 2001
PR1-88	38.101	-122.869	0.70863	Kistler & Champion, 2001
3Ketal73	37.700	-122.999	0.70613	Kistler & Champion, 2001
MON1-87	37.492	-122.380	0.70702	Kistler & Champion, 2001
MON9-87	37.493	-122.387	0.70640	Kistler & Champion, 2001
MON11-87	37.510	-122.402	0.70640	Kistler & Champion, 2001
MON13-87	37.517	-122.479	0.70640	Kistler & Champion, 2001
4Ketal73	37.518	-122.425	0.70640	Kistler & Champion, 2001
MON5-88	37.558	-122.508	0.70550	Kistler & Champion, 2001
MON12-88	37.547	-122.432	0.70580	Kistler & Champion, 2001
K2-87	37.104	-122.141	0.70565	Kistler & Champion, 2001

5Ketal73	37.101	-122.148	0.70565	Kistler & Champion, 2001
K8-87	37.033	-122.109	0.70565	Kistler & Champion, 2001
BL7-89	37.033	-122.024	0.70638	Kistler & Champion, 2001
BL14-89	37.030	-122.075	0.70638	Kistler & Champion, 2001
BL9-89	36.991	-122.091	0.71472	Kistler & Champion, 2001
SANLU1-90	36.499	-121.936	0.70787	Kistler & Champion, 2001
SANLU14-90	36.579	-121.947	0.70787	Kistler & Champion, 2001
SANLU7-90	36.383	-121.852	0.70787	Kistler & Champion, 2001
SANLU20-90	36.433	-121.789	0.70787	Kistler & Champion, 2001
SANLU25-90	36.369	-121.577	0.70824	Kistler & Champion, 2001
SANLU16-90	36.515	-121.759	0.70824	Kistler & Champion, 2001
SANLU18-90	36.467	-121.711	0.70913	Kistler & Champion, 2001
SANLU10-91	36.210	-121.745	0.71010	Kistler & Champion, 2001
SANLU11-91	36.200	-121.725	0.70660	Kistler & Champion, 2001
SANLU12-91	36.187	-121.707	0.70660	Kistler & Champion, 2001
DR145C	35.832	-120.350	0.70760	Kistler & Champion, 2001
DR109	35.602	-120.267	0.70950	Kistler & Champion, 2001
DR745	34.819	-119.089	0.71640	Kistler & Champion, 2001
813.1	36.049	-121.492	0.70740	Dickinson et al., 2005

§ These data are an extension of an earlier compilation by Nadin (2007).

Table A2.6. Compilation of pressures calculated from aluminum-in-hornblende barometry and conventional thermobarometry from the Sierra Nevada batholith.[§]

Sample	Longitude	Latitude	P (kbar)	Reference
1	-118.911	36.817	4.1	Ague & Brimhall, 1988
3	-119.162	36.762	3.8	Ague & Brimhall, 1988
4	-119.116	36.764	2.9	Ague & Brimhall, 1988
5	-119.074	36.748	2.8	Ague & Brimhall, 1988
6	-119.048	36.743	2.9	Ague & Brimhall, 1988
11	-118.893	36.820	3.8	Ague & Brimhall, 1988
13	-118.864	36.804	2.9	Ague & Brimhall, 1988
14	-118.777	36.802	2.7	Ague & Brimhall, 1988
15	-118.587	36.778	1.3	Ague & Brimhall, 1988
16	-118.605	36.780	1.5	Ague & Brimhall, 1988
18	-118.710	36.790	2.4	Ague & Brimhall, 1988
19	-118.737	36.789	2.6	Ague & Brimhall, 1988
21	-118.997	36.405	2.7	Ague & Brimhall, 1988
23	-118.929	36.386	3.8	Ague & Brimhall, 1988
24	-118.900	36.434	3.6	Ague & Brimhall, 1988
25	-118.820	36.453	3.9	Ague & Brimhall, 1988
26	-118.795	36.442	3.7	Ague & Brimhall, 1988
28	-118.814	36.095	3.4	Ague & Brimhall, 1988
35	-118.560	36.129	2.3	Ague & Brimhall, 1988
36	-118.551	36.109	3.3	Ague & Brimhall, 1988
38	-118.515	35.968	3.2	Ague & Brimhall, 1988
42	-118.576	35.743	1.8	Ague & Brimhall, 1988
43	-118.600	35.742	1.9	Ague & Brimhall, 1988
44	-118.657	35.734	2.5	Ague & Brimhall, 1988
45	-118.728	35.709	2.9	Ague & Brimhall, 1988
47	-118.829	35.707	3.1	Ague & Brimhall, 1988
48	-118.705	35.277	4	Ague & Brimhall, 1988
49	-118.673	35.269	5.4	Ague & Brimhall, 1988
50	-118.591	35.244	5.3	Ague & Brimhall, 1988
51	-118.056	35.672	5.1	Ague & Brimhall, 1988
56	-119.160	37.931	0.7	Ague & Brimhall, 1988
59	-119.583	37.827	2.3	Ague & Brimhall, 1988
60	-119.222	37.929	0.5	Ague & Brimhall, 1988
61	-119.355	37.874	2	Ague & Brimhall, 1988
62	-119.373	37.878	0.4	Ague & Brimhall, 1988
63	-119.393	37.854	3.3	Ague & Brimhall, 1988
64	-119.465	37.828	2.5	Ague & Brimhall, 1988
65	-119.596	37.841	1.9	Ague & Brimhall, 1988

66	-119.713	37.817	3.3	Ague & Brimhall, 1988
67	-119.767	37.765	3.8	Ague & Brimhall, 1988
68	-119.875	37.766	2.5	Ague & Brimhall, 1988
69	-119.998	37.833	0.7	Ague & Brimhall, 1988
73	-120.585	38.771	3.7	Ague & Brimhall, 1988
74	-120.570	38.782	3.7	Ague & Brimhall, 1988
76	-120.462	38.779	2.7	Ague & Brimhall, 1988
77	-120.462	38.779	2.6	Ague & Brimhall, 1988
78	-120.438	38.789	1.1	Ague & Brimhall, 1988
79	-120.407	38.787	3.7	Ague & Brimhall, 1988
80	-120.317	38.793	2.5	Ague & Brimhall, 1988
81	-120.192	38.795	1.7	Ague & Brimhall, 1988
82	-120.148	38.821	1.8	Ague & Brimhall, 1988
83	-120.071	38.827	2.9	Ague & Brimhall, 1988
84	-120.020	38.810	1.8	Ague & Brimhall, 1988
85	-119.939	38.791	1.8	Ague & Brimhall, 1988
89	-119.553	38.653	2.1	Ague & Brimhall, 1988
97	-118.250	37.558	2.1	Ague & Brimhall, 1988
99	-118.250	37.558	2.2	Ague & Brimhall, 1988
103	-118.046	37.338	1.6	Ague & Brimhall, 1988
105	-117.928	37.420	2.9	Ague & Brimhall, 1988
108	-118.349	37.102	2.5	Ague & Brimhall, 1988
109	-118.312	36.776	0.2	Ague & Brimhall, 1988
111	-118.208	36.573	2.3	Ague & Brimhall, 1988
112	-118.230	36.572	2.7	Ague & Brimhall, 1988
116	-118.614	37.206	2.7	Ague & Brimhall, 1988
117	-118.621	37.194	2.7	Ague & Brimhall, 1988
118	-118.564	37.159	2.8	Ague & Brimhall, 1988
120	-118.568	37.149	3.2	Ague & Brimhall, 1988
123	-118.547	37.321	2.3	Ague & Brimhall, 1988
124	-118.530	37.321	2.3	Ague & Brimhall, 1988
128	-120.332	39.345	0.6	Ague & Brimhall, 1988
129	-120.427	39.351	0.1	Ague & Brimhall, 1988
130	-120.625	39.342	0.9	Ague & Brimhall, 1988
132	-121.126	39.421	2.2	Ague & Brimhall, 1988
133	-121.007	39.510	3.4	Ague & Brimhall, 1988
138	-118.071	36.415	0.2	Ague & Brimhall, 1988
139	-118.110	36.432	3.5	Ague & Brimhall, 1988
142	-118.472	37.750	2.5	Ague & Brimhall, 1988
145	-118.632	37.856	4.2	Ague & Brimhall, 1988
147	-118.816	37.884	4.4	Ague & Brimhall, 1988
149	-118.882	37.891	2.5	Ague & Brimhall, 1988

151	-119.197	38.038	1.2	Ague & Brimhall, 1988
154	-118.056	36.819	0.5	Ague & Brimhall, 1988
155	-118.115	36.845	1	Ague & Brimhall, 1988
253	-119.568	38.333	2	Ague & Brimhall, 1988
254	-119.590	38.319	2.2	Ague & Brimhall, 1988
255	-119.611	38.326	1	Ague & Brimhall, 1988
256	-119.686	38.336	0.2	Ague & Brimhall, 1988
257	-119.764	38.338	2	Ague & Brimhall, 1988
258	-119.784	38.345	2.1	Ague & Brimhall, 1988
259	-119.836	38.354	2.1	Ague & Brimhall, 1988
260	-119.904	38.364	2.2	Ague & Brimhall, 1988
261	-119.959	38.311	4.4	Ague & Brimhall, 1988
262	-120.013	38.218	3.3	Ague & Brimhall, 1988
267	-119.232	38.039	3.5	Ague & Brimhall, 1988
268	-118.739	37.452	2.5	Ague & Brimhall, 1988
269	-118.726	37.496	2.6	Ague & Brimhall, 1988
271	-118.695	37.546	3.9	Ague & Brimhall, 1988
278	-118.913	36.817	3.8	Ague & Brimhall, 1988
279	-118.901	36.818	3.2	Ague & Brimhall, 1988
281	-119.159	37.051	3.7	Ague & Brimhall, 1988
282	-119.160	37.035	3.3	Ague & Brimhall, 1988
283	-119.176	36.992	3.1	Ague & Brimhall, 1988
284	-119.181	36.942	3.3	Ague & Brimhall, 1988
287	-119.181	36.942	1.8	Ague & Brimhall, 1988
288	-119.194	36.927	4.4	Ague & Brimhall, 1988
289	-119.117	37.026	3.7	Ague & Brimhall, 1988
293	-119.306	37.134	4.5	Ague & Brimhall, 1988
294	-119.296	37.151	3.6	Ague & Brimhall, 1988
295	-119.249	37.142	3	Ague & Brimhall, 1988
296	-119.199	37.161	2.9	Ague & Brimhall, 1988
297	-119.212	37.195	3.4	Ague & Brimhall, 1988
298	-119.158	37.226	3.5	Ague & Brimhall, 1988
299	-119.106	37.282	3	Ague & Brimhall, 1988
300	-119.075	37.309	2.7	Ague & Brimhall, 1988
301	-119.109	37.311	4	Ague & Brimhall, 1988
305	-119.380	37.061	3.8	Ague & Brimhall, 1988
310	-119.482	37.078	3.3	Ague & Brimhall, 1988
311	-119.502	37.133	4.5	Ague & Brimhall, 1988
312	-119.492	37.147	3.4	Ague & Brimhall, 1988
315	-119.625	37.481	2.7	Ague & Brimhall, 1988
316	-119.628	37.395	1.9	Ague & Brimhall, 1988
317	-119.634	37.363	3.4	Ague & Brimhall, 1988

319	-119.506	37.288	2.4	Ague & Brimhall, 1988
320	-119.504	37.304	2.9	Ague & Brimhall, 1988
322	-119.492	37.337	3	Ague & Brimhall, 1988
323	-119.473	37.357	2.9	Ague & Brimhall, 1988
329	-119.458	37.454	3	Ague & Brimhall, 1988
330	-119.440	37.469	2.1	Ague & Brimhall, 1988
331	-119.427	37.481	2.6	Ague & Brimhall, 1988
332	-119.415	37.484	3.3	Ague & Brimhall, 1988
337	-119.351	37.211	3.2	Ague & Brimhall, 1988
338	-119.338	37.218	2.5	Ague & Brimhall, 1988
339	-119.357	37.238	3.6	Ague & Brimhall, 1988
340	-119.351	37.250	2.7	Ague & Brimhall, 1988
341	-119.349	37.264	2	Ague & Brimhall, 1988
343	-119.363	37.332	2.4	Ague & Brimhall, 1988
344	-119.392	37.370	3.5	Ague & Brimhall, 1988
348	-119.267	37.542	2.5	Ague & Brimhall, 1988
349	-119.289	37.553	3.3	Ague & Brimhall, 1988
353	-119.289	37.553	4.1	Ague & Brimhall, 1988
365	-118.798	36.505	3.5	Ague & Brimhall, 1988
367	-118.776	36.544	3.6	Ague & Brimhall, 1988
368	-118.770	36.561	3.7	Ague & Brimhall, 1988
369	-118.751	36.589	2.8	Ague & Brimhall, 1988
370	-118.800	36.585	2.1	Ague & Brimhall, 1988
371	-118.809	36.599	2.9	Ague & Brimhall, 1988
372	-118.825	36.629	3.2	Ague & Brimhall, 1988
373	-118.839	36.651	3.2	Ague & Brimhall, 1988
374	-118.873	36.685	3	Ague & Brimhall, 1988
375	-118.938	36.702	2.5	Ague & Brimhall, 1988
376	-118.905	36.720	2.6	Ague & Brimhall, 1988
377	-118.904	36.741	2.9	Ague & Brimhall, 1988
378	-118.893	36.749	2.8	Ague & Brimhall, 1988
379	-118.893	36.749	3	Ague & Brimhall, 1988
380	-118.902	36.791	3.4	Ague & Brimhall, 1988
381	-118.899	36.240	3.7	Ague & Brimhall, 1988
384	-118.795	36.175	3.4	Ague & Brimhall, 1988
385	-118.755	36.191	2.8	Ague & Brimhall, 1988
386	-118.729	36.189	2.7	Ague & Brimhall, 1988
387	-118.685	36.191	3	Ague & Brimhall, 1988
389	-118.756	35.450	3.1	Ague & Brimhall, 1988
390	-118.739	35.465	4.4	Ague & Brimhall, 1988
391	-118.705	35.462	3.3	Ague & Brimhall, 1988
393	-118.621	35.523	3.6	Ague & Brimhall, 1988

394	-118.584	35.539	4	Ague & Brimhall, 1988
395	-118.531	35.563	3.4	Ague & Brimhall, 1988
397	-118.470	35.669	4.4	Ague & Brimhall, 1988
398	-118.619	35.725	2	Ague & Brimhall, 1988
401	-118.627	35.767	0.3	Ague & Brimhall, 1988
402	-118.667	35.795	2.9	Ague & Brimhall, 1988
404	-118.594	35.808	3.6	Ague & Brimhall, 1988
409	-118.467	35.393	4.1	Ague & Brimhall, 1988
410	-118.414	35.410	5.3	Ague & Brimhall, 1988
413	-118.376	35.437	6	Ague & Brimhall, 1988
420	-118.241	35.354	5.7	Ague & Brimhall, 1988
422	-119.115	37.598	2.7	Ague & Brimhall, 1988
RB020601	-118.399	35.092	4.1	Brady et al., 2006
RB030304	-118.385	35.445	4.4	Brady et al., 2006
50	-118.600	35.250	5.7	"Brady (Ague redo)" in Nadin, 2007
49	-118.675	35.267	5.8	"Brady (Ague redo)" in Nadin, 2007
48	-118.705	35.279	4.5	"Brady (Ague redo)" in Nadin, 2007
420	-118.233	35.358	6.1	"Brady (Ague redo)" in Nadin, 2007
409	-118.470	35.396	4.6	"Brady (Ague redo)" in Nadin, 2007
410	-118.413	35.417	5.7	"Brady (Ague redo)" in Nadin, 2007
413	-118.367	35.446	6.4	"Brady (Ague redo)" in Nadin, 2007
389	-118.767	35.450	3.7	"Brady (Ague redo)" in Nadin, 2007
414	-118.358	35.450	5.3	"Brady (Ague redo)" in Nadin, 2007
391	-118.713	35.465	3.8	"Brady (Ague redo)" in Nadin, 2007
390	-118.750	35.467	4.9	"Brady (Ague redo)" in Nadin, 2007
393	-118.625	35.525	4.1	"Brady (Ague redo)" in Nadin, 2007
394	-118.583	35.546	4.5	"Brady (Ague redo)" in Nadin, 2007
395	-118.529	35.567	3.9	"Brady (Ague redo)" in Nadin, 2007
397	-118.458	35.671	4.9	"Brady (Ague redo)" in Nadin, 2007
51	-118.042	35.675	5.5	"Brady (Ague redo)" in Nadin, 2007
47	-118.829	35.708	3.7	"Brady (Ague redo)" in Nadin, 2007
45	-118.725	35.717	3.4	"Brady (Ague redo)" in Nadin, 2007
398	-118.613	35.733	2.6	"Brady (Ague redo)" in Nadin, 2007
44	-118.650	35.742	3.1	"Brady (Ague redo)" in Nadin, 2007
42	-118.567	35.746	2.4	"Brady (Ague redo)" in Nadin, 2007
43	-118.592	35.750	2.5	"Brady (Ague redo)" in Nadin, 2007
401	-118.617	35.767	1	"Brady (Ague redo)" in Nadin, 2007
402	-118.658	35.800	3.4	"Brady (Ague redo)" in Nadin, 2007
404	-118.579	35.813	4.1	"Brady (Ague redo)" in Nadin, 2007
38	-118.508	35.967	3.8	"Brady (Ague redo)" in Nadin, 2007
28	-118.817	36.104	3.9	"Brady (Ague redo)" in Nadin, 2007
36	-118.550	36.125	3.8	"Brady (Ague redo)" in Nadin, 2007

35	-118.558	36.146	2.8	"Brady (Ague redo)" in Nadin, 2007
384	-118.796	36.183	3.9	"Brady (Ague redo)" in Nadin, 2007
386	-118.725	36.200	3.3	"Brady (Ague redo)" in Nadin, 2007
385	-118.758	36.204	3.4	"Brady (Ague redo)" in Nadin, 2007
387	-118.683	36.204	3.6	"Brady (Ague redo)" in Nadin, 2007
381	-118.904	36.246	4.2	"Brady (Ague redo)" in Nadin, 2007
23	-118.933	36.392	4.3	"Brady (Ague redo)" in Nadin, 2007
21	-119.000	36.408	3.2	"Brady (Ague redo)" in Nadin, 2007
138	-118.104	36.429	0.9	"Brady (Ague redo)" in Nadin, 2007
24	-118.896	36.442	4.1	"Brady (Ague redo)" in Nadin, 2007
139	-118.058	36.442	4.1	"Brady (Ague redo)" in Nadin, 2007
26	-118.796	36.454	4.2	"Brady (Ague redo)" in Nadin, 2007
25	-118.817	36.458	4.4	"Brady (Ague redo)" in Nadin, 2007
365	-118.796	36.513	4	"Brady (Ague redo)" in Nadin, 2007
367	-118.775	36.550	4.1	"Brady (Ague redo)" in Nadin, 2007
368	-118.767	36.567	4.2	"Brady (Ague redo)" in Nadin, 2007
111	-118.208	36.592	2.9	"Brady (Ague redo)" in Nadin, 2007
112	-118.217	36.592	3.3	"Brady (Ague redo)" in Nadin, 2007
369	-118.746	36.600	3.3	"Brady (Ague redo)" in Nadin, 2007
370	-118.804	36.600	2.7	"Brady (Ague redo)" in Nadin, 2007
371	-118.808	36.604	3.4	"Brady (Ague redo)" in Nadin, 2007
372	-118.821	36.638	3.7	"Brady (Ague redo)" in Nadin, 2007
373	-118.838	36.658	3.8	"Brady (Ague redo)" in Nadin, 2007
374	-118.875	36.692	3.6	"Brady (Ague redo)" in Nadin, 2007
375	-118.938	36.708	3.1	"Brady (Ague redo)" in Nadin, 2007
1	-119.350	36.717	4.6	"Brady (Ague redo)" in Nadin, 2007
376	-118.904	36.725	3.1	"Brady (Ague redo)" in Nadin, 2007
6	-119.050	36.746	3.4	"Brady (Ague redo)" in Nadin, 2007
5	-119.075	36.750	3.3	"Brady (Ague redo)" in Nadin, 2007
377	-118.900	36.750	3.4	"Brady (Ague redo)" in Nadin, 2007
378	-118.888	36.750	3.3	"Brady (Ague redo)" in Nadin, 2007
379	-118.888	36.750	3.5	"Brady (Ague redo)" in Nadin, 2007
3	-119.163	36.765	4.3	"Brady (Ague redo)" in Nadin, 2007
4	-119.117	36.767	3.5	"Brady (Ague redo)" in Nadin, 2007
109	-118.308	36.788	0.9	"Brady (Ague redo)" in Nadin, 2007
15	-118.583	36.792	1.9	"Brady (Ague redo)" in Nadin, 2007
16	-118.600	36.792	2.1	"Brady (Ague redo)" in Nadin, 2007
18	-118.708	36.800	2.9	"Brady (Ague redo)" in Nadin, 2007
19	-118.738	36.800	3.2	"Brady (Ague redo)" in Nadin, 2007
380	-118.904	36.800	3.9	"Brady (Ague redo)" in Nadin, 2007
14	-118.775	36.808	3.3	"Brady (Ague redo)" in Nadin, 2007
278	-118.913	36.817	4.3	"Brady (Ague redo)" in Nadin, 2007

13	-118.875	36.825	3.5	"Brady (Ague redo)" in Nadin, 2007
279	-118.892	36.825	3.7	"Brady (Ague redo)" in Nadin, 2007
11	-118.892	36.833	4.3	"Brady (Ague redo)" in Nadin, 2007
154	-118.054	36.838	1.1	"Brady (Ague redo)" in Nadin, 2007
155	-118.113	36.850	1.6	"Brady (Ague redo)" in Nadin, 2007
288	-119.196	36.933	4.9	"Brady (Ague redo)" in Nadin, 2007
284	-119.183	36.942	3.8	"Brady (Ague redo)" in Nadin, 2007
287	-119.183	36.942	2.4	"Brady (Ague redo)" in Nadin, 2007
283	-119.175	36.992	3.6	"Brady (Ague redo)" in Nadin, 2007
289	-119.121	37.042	4.2	"Brady (Ague redo)" in Nadin, 2007
282	-119.167	37.050	3.9	"Brady (Ague redo)" in Nadin, 2007
281	-119.167	37.063	4.2	"Brady (Ague redo)" in Nadin, 2007
305	-119.388	37.063	4.3	"Brady (Ague redo)" in Nadin, 2007
310	-119.483	37.079	3.8	"Brady (Ague redo)" in Nadin, 2007
108	-118.329	37.133	3.1	"Brady (Ague redo)" in Nadin, 2007
311	-119.508	37.138	5	"Brady (Ague redo)" in Nadin, 2007
293	-119.304	37.146	5	"Brady (Ague redo)" in Nadin, 2007
312	-119.500	37.146	3.9	"Brady (Ague redo)" in Nadin, 2007
295	-119.250	37.150	3.5	"Brady (Ague redo)" in Nadin, 2007
294	-119.300	37.154	4.1	"Brady (Ague redo)" in Nadin, 2007
296	-119.204	37.171	3.5	"Brady (Ague redo)" in Nadin, 2007
118	-118.563	37.175	3.3	"Brady (Ague redo)" in Nadin, 2007
120	-118.558	37.192	3.7	"Brady (Ague redo)" in Nadin, 2007
297	-119.213	37.204	3.9	"Brady (Ague redo)" in Nadin, 2007
117	-118.617	37.217	3.3	"Brady (Ague redo)" in Nadin, 2007
337	-119.354	37.217	3.7	"Brady (Ague redo)" in Nadin, 2007
338	-119.350	37.221	3	"Brady (Ague redo)" in Nadin, 2007
116	-118.608	37.225	3.2	"Brady (Ague redo)" in Nadin, 2007
298	-119.158	37.238	4	"Brady (Ague redo)" in Nadin, 2007
339	-119.363	37.242	4.1	"Brady (Ague redo)" in Nadin, 2007
340	-119.354	37.248	3.3	"Brady (Ague redo)" in Nadin, 2007
341	-119.354	37.263	2.6	"Brady (Ague redo)" in Nadin, 2007
299	-119.104	37.292	3.5	"Brady (Ague redo)" in Nadin, 2007
319	-119.508	37.292	3	"Brady (Ague redo)" in Nadin, 2007
320	-119.508	37.308	3.5	"Brady (Ague redo)" in Nadin, 2007
301	-119.108	37.317	4.5	"Brady (Ague redo)" in Nadin, 2007
300	-119.071	37.321	3.3	"Brady (Ague redo)" in Nadin, 2007
322	-119.496	37.333	3.5	"Brady (Ague redo)" in Nadin, 2007
343	-119.367	37.333	3	"Brady (Ague redo)" in Nadin, 2007
123	-118.538	37.342	2.9	"Brady (Ague redo)" in Nadin, 2007
124	-118.533	37.342	2.9	"Brady (Ague redo)" in Nadin, 2007
103	-118.053	37.350	2.3	"Brady (Ague redo)" in Nadin, 2007

323	-119.475	37.358	3.4	"Brady (Ague redo)" in Nadin, 2007
317	-119.642	37.363	3.9	"Brady (Ague redo)" in Nadin, 2007
344	-119.392	37.371	4.1	"Brady (Ague redo)" in Nadin, 2007
316	-119.633	37.392	2.5	"Brady (Ague redo)" in Nadin, 2007
105	-117.938	37.446	3.5	"Brady (Ague redo)" in Nadin, 2007
329	-119.458	37.454	3.6	"Brady (Ague redo)" in Nadin, 2007
268	-118.738	37.458	3.1	"Brady (Ague redo)" in Nadin, 2007
330	-119.442	37.471	2.6	"Brady (Ague redo)" in Nadin, 2007
315	-119.633	37.479	3.2	"Brady (Ague redo)" in Nadin, 2007
331	-119.429	37.479	3.2	"Brady (Ague redo)" in Nadin, 2007
332	-119.417	37.483	3.8	"Brady (Ague redo)" in Nadin, 2007
269	-118.738	37.504	3.1	"Brady (Ague redo)" in Nadin, 2007
348	-119.271	37.546	3	"Brady (Ague redo)" in Nadin, 2007
271	-118.700	37.550	4.4	"Brady (Ague redo)" in Nadin, 2007
349	-119.292	37.554	3.8	"Brady (Ague redo)" in Nadin, 2007
351	-119.292	37.554	4.3	"Brady (Ague redo)" in Nadin, 2007
353	-119.292	37.554	4.6	"Brady (Ague redo)" in Nadin, 2007
99	-118.239	37.559	2.8	"Brady (Ague redo)" in Nadin, 2007
97	-118.240	37.561	2.7	"Brady (Ague redo)" in Nadin, 2007
96	-118.241	37.563	3.4	"Brady (Ague redo)" in Nadin, 2007
422	-119.100	37.600	3.3	"Brady (Ague redo)" in Nadin, 2007
67	-119.771	37.758	4.3	"Brady (Ague redo)" in Nadin, 2007
68	-119.875	37.763	3.1	"Brady (Ague redo)" in Nadin, 2007
142	-118.475	37.767	3.1	"Brady (Ague redo)" in Nadin, 2007
63	-119.550	37.800	3.8	"Brady (Ague redo)" in Nadin, 2007
62	-119.475	37.817	1.1	"Brady (Ague redo)" in Nadin, 2007
66	-119.708	37.817	3.8	"Brady (Ague redo)" in Nadin, 2007
61	-119.467	37.825	2.6	"Brady (Ague redo)" in Nadin, 2007
64	-119.583	37.825	3.1	"Brady (Ague redo)" in Nadin, 2007
65	-119.588	37.833	2.5	"Brady (Ague redo)" in Nadin, 2007
69	-120.000	37.833	1.3	"Brady (Ague redo)" in Nadin, 2007
60	-119.388	37.850	1.1	"Brady (Ague redo)" in Nadin, 2007
59	-119.367	37.875	2.9	"Brady (Ague redo)" in Nadin, 2007
145	-118.633	37.875	4.6	"Brady (Ague redo)" in Nadin, 2007
147	-118.825	37.892	4.8	"Brady (Ague redo)" in Nadin, 2007
149	-118.871	37.900	3	"Brady (Ague redo)" in Nadin, 2007
56	-119.163	37.933	1.4	"Brady (Ague redo)" in Nadin, 2007
267	-119.258	38.029	4	"Brady (Ague redo)" in Nadin, 2007
151	-119.186	38.042	1.8	"Brady (Ague redo)" in Nadin, 2007
262	-120.004	38.204	3.8	"Brady (Ague redo)" in Nadin, 2007
263	-119.333	38.217	0.6	"Brady (Ague redo)" in Nadin, 2007
261	-119.950	38.300	4.9	"Brady (Ague redo)" in Nadin, 2007

254	-119.583	38.313	2.8	"Brady (Ague redo)" in Nadin, 2007
255	-119.600	38.317	1.6	"Brady (Ague redo)" in Nadin, 2007
253	-119.558	38.325	2.6	"Brady (Ague redo)" in Nadin, 2007
256	-119.679	38.329	0.9	"Brady (Ague redo)" in Nadin, 2007
257	-119.753	38.329	2.6	"Brady (Ague redo)" in Nadin, 2007
258	-119.771	38.338	2.7	"Brady (Ague redo)" in Nadin, 2007
259	-119.825	38.346	2.7	"Brady (Ague redo)" in Nadin, 2007
260	-119.892	38.354	2.7	"Brady (Ague redo)" in Nadin, 2007
90	-119.483	38.517	0.6	"Brady (Ague redo)" in Nadin, 2007
89	-119.538	38.646	2.7	"Brady (Ague redo)" in Nadin, 2007
73	-120.550	38.763	4.2	"Brady (Ague redo)" in Nadin, 2007
74	-120.546	38.764	4.2	"Brady (Ague redo)" in Nadin, 2007
76	-120.433	38.767	3.3	"Brady (Ague redo)" in Nadin, 2007
77	-120.433	38.767	3.1	"Brady (Ague redo)" in Nadin, 2007
79	-120.375	38.771	4.2	"Brady (Ague redo)" in Nadin, 2007
78	-120.413	38.775	1.7	"Brady (Ague redo)" in Nadin, 2007
80	-120.292	38.779	3.1	"Brady (Ague redo)" in Nadin, 2007
85	-119.917	38.779	2.4	"Brady (Ague redo)" in Nadin, 2007
81	-120.167	38.783	2.4	"Brady (Ague redo)" in Nadin, 2007
84	-119.992	38.800	2.4	"Brady (Ague redo)" in Nadin, 2007
82	-120.121	38.813	2.4	"Brady (Ague redo)" in Nadin, 2007
83	-120.033	38.817	3.5	"Brady (Ague redo)" in Nadin, 2007
128	-120.317	39.321	1.3	"Brady (Ague redo)" in Nadin, 2007
130	-120.600	39.325	1.5	"Brady (Ague redo)" in Nadin, 2007
129	-120.392	39.329	0.8	"Brady (Ague redo)" in Nadin, 2007
133	-121.079	39.400	3.9	"Brady (Ague redo)" in Nadin, 2007
132	-120.985	39.517	2.8	"Brady (Ague redo)" in Nadin, 2007
22*	-118.327	35.673	5.3	Dixon, 1995
29*	-118.489	35.306	3.5	Dixon, 1995
36.5*	-118.529	35.232	4.8	Dixon, 1995
45*	-118.583	35.304	4	Dixon, 1995
49*	-118.438	35.042	5.1	Dixon, 1995
51*	-118.475	35.303	5.1	Dixon, 1995
52*	-118.409	35.428	4.8	Dixon, 1995
58*	-118.481	35.070	7.2	Dixon, 1995
Th275*	-118.457	35.075	6.5	Dixon, 1995
18*	-118.352	35.610	5.7	Dixon, 1995
49*	-118.361	35.331	6	Dixon, 1995
45*	-118.583	35.304	4.3	Dixon, 1995
04SS34	-118.217	35.477	6.1	Nadin, 2007
04SS37	-118.277	35.456	5.7	Nadin, 2007
04SS39	-118.361	35.453	5	Nadin, 2007

04SS42	-118.419	35.424	5	Nadin, 2007
03SS1	-118.081	35.740	4.1	Nadin, 2007
02SS16	-118.337	35.681	4.1	Nadin, 2007
02SS13	-118.327	35.673	4.5	Nadin, 2007
03SS5	-118.464	35.676	4.6	Nadin, 2007
03SS27	-118.585	35.750	2.2	Nadin, 2007
04SS43	-118.414	35.405	5.5	Nadin, 2007
04SS45	-118.445	35.304	5.1	Nadin, 2007
04SS44	-118.584	35.304	3.8	Nadin, 2007
04SS31	-118.142	35.558	4.2	Nadin, 2007
04SS27	-118.644	35.223	3.7	Nadin, 2007
04SS28	-118.658	35.209	4.6	Nadin, 2007
BM149	-118.554	35.362	3.2	Pickett & Saleeby, 1993
CM13b	-118.553	35.210	6.9	Pickett & Saleeby, 1993
WR27a	-118.673	34.947	8	Pickett & Saleeby, 1993
TC-12a	-118.754	35.002	7.8	Pickett & Saleeby, 1993
GC-16	-118.647	35.014	8.3	Pickett & Saleeby, 1993
CM657	-118.748	35.008	8.8	Pickett & Saleeby, 1993
GC-33	-118.826	34.920	9.3	Pickett & Saleeby, 1993
04SE1a	-119.072	34.883	8.3	Chapman et al., 2011
08SE270	-119.087	34.875	8.4	Chapman et al., 2011
08SE202	-118.945	34.896	7.1	Chapman et al., 2011
No name	-118.883	34.889	7.5	Chapman et al., 2011
04SE5	-119.064	34.852	3.1	this study
08SE463	-119.102	34.872	5.7	this study
08SE429	-119.129	34.865	5.8	this study
K16b-87	-121.526	36.803	5.2	this study
08SE674	-118.920	34.885	10.7	this study
08SE451	-119.111	34.874	10.2	this study
08TC27a	-118.446	34.971	2.8	this study
08TC29	-118.458	34.969	2.4	this study
10SE1	-119.222	34.884	4	this study
94KK27	-118.605	36.226	4.2	this study
10SE41	-118.943	34.869	3.7	this study
31001-5	-121.647	36.277	3.4	this study
91TH181	-118.411	35.053	4.4	this study
93TH417	-118.440	35.040	3.8	this study
Coast Ridge	-121.479	36.023	7.5	Kidder et al., 2003
No name*	-122.050	37.000	5	DeCristoforo & Cameron, 1977
78-DJ-22*	-121.516	36.747	3.6	John, 1981
78-DJ-24*	-121.519	36.747	3	John, 1981
78-DJ-26*	-121.517	36.751	4.4	John, 1981

FM-16*	-121.488	36.764	3.8	John, 1981
FM-130*	-121.474	36.761	2.7	John, 1981

* Location approximate

§ These data are an extension of an earlier compilation by Nadin (2007).

Table A2.7. Detailed (U-Th)/He replicates data.

	Concentrations			Grain dimensions			Ages (Ma)	
Sample replicate	U (ppm)	Th (ppm)	He (nmol/g)	Radius (μm)	Length (μm)	F_T factor[§]	Raw age	Corr age[†]
Sample 04SS27								
04SS27-4:fai	671	238	257.9	68.28	399.92	0.86	64.9	75.8
04SS27-3:fai	489	127	147.9	56.325	294.95	0.82	52.2	63.2
04SS27-2:las	407	114	160.2	82.035	313.94	0.87	67.5	77.5
04SS27-5:las	149	20	89.6	53.36	303.69	0.82	106.3	129.6
Sample 04SS28								
04SS28-1:las	431	121	168.9	64.74	292.89	0.84	67.2	79.8
04SS28-3:las	379	102	141.9	78.815	335.74	0.87	64.4	74.1
04SS28-2:fai	365	131	150.0	72.27	305.22	0.86	69.3	80.9
04SS28-5:las	337	114	170.5	71.505	359.78	0.86	85.4	99.3
Sample 04SS30								
04SS30-2:las	489	218	146.5	43.5	194.2	0.77	49.6	64.5
04SS30-4:las	288	96	86.3	36.45	150.6	0.72	50.8	69.9
04SS30-3:las	943	296	294.3	34.99	116.58	0.70	53.2	75.5
Sample 04SS32								
04SS32-1:las	22	6	6.9	55.835	284.51	0.82	54.8	66.6
04SS32-2:las	191	26	79.5	46.265	250.78	0.79	73.5	92.9
04SS32-4:las	218	85	83.9	39.175	233.75	0.76	64.5	85.0
04SS32-6:las	194	57	58.2	45.72	291.82	0.79	51.4	64.8
Sample 04SS33								
04SS33-1:las	363	193	132.2	39.5	233.7	0.76	59.1	78.0
04SS33-2:las	240	90	83.4	50	202.2	0.79	58.3	73.4
04SS33-3:las	326	131	128.0	49.75	262.5	0.80	65.7	81.9
04SS33-4:las	250	104	85.2	41.3	245.2	0.77	56.8	73.8
Sample 04SS35								
04SS35-1:las	355	98	128.3	47.885	286.03	0.80	62.1	77.6
04SS35-3:las	113	29	39.0	66.95	330.75	0.85	59.7	70.2
04SS35-5:las	319	92	133.7	59.01	291.12	0.83	71.7	86.3
04SS35-6:fai	283	88	143.2	51.185	256.62	0.81	86.0	106.5
04SS35-7:las	228	74	113.7	75.88	360.24	0.86	84.7	97.8
04SS35-8:las	454	140	155.3	60.34	355.83	0.84	58.4	69.6
Sample 04SS36								
04SS36-3:las	373	97	110.8	52.5	234.9	0.81	51.3	63.4
04SS36-4:las	370	90	123.5	48.8	216.4	0.79	57.7	72.6
04SS36-1:las	585	99	173.6	38.13	240.31	0.75	52.3	69.3
04SS36-2:las	401	77	129.6	48.475	204.24	0.79	56.6	71.5
Sample 04SS38								
04SS38-1:las	269	59	80.1	58.35	337.6	0.83	51.8	62.2
04SS38-7:las	196	42	83.1	47.54	268.83	0.80	73.9	92.6
04SS38-5:las	473	96	249.5	36.185	242.86	0.74	91.8	123.1
04SS38-6:las	367	111	157.1	49.495	212.11	0.79	73.0	91.8
04SS38-9:las	355	64	112.1	61.515	286.25	0.84	55.4	66.3
Sample 04SS39								
04SS39-4:las	636	226	227.7	49.75	320.9	0.81	60.4	74.8
04SS39-2:las	520	126	135.5	34.65	164	0.72	45.2	62.7
04SS39-5:las	275	65	96.6	60.005	311.81	0.83	60.8	72.8
04SS39-6:las	208	61	85.3	57.885	282.41	0.83	70.1	84.7
Sample 04SS40								
04SS40-2:las	155	28	66.2	57.35	273.9	0.82	74.9	90.6
04SS40-3:las	108	33	33.8	72.27	305.22	0.86	53.3	62.2

Table A2.7 (Continued). Detailed (U-Th)/He replicates data.

	Concentrations			Grain dimensions			Ages (Ma)	
Sample replicate	U (ppm)	Th (ppm)	He (nmol/g)	Radius (μm)	Length (μm)	F_T factor[§]	Raw age	Corr age[†]
04SS40-5:las	179	60	70.6	58.69	324.55	0.83	66.8	80.2
04SS40-6:las	158	43	54.3	49.055	270.34	0.80	59.2	73.8
Sample 04SS41								
04SS41-3:las	657	140	215.8	51.755	272.06	0.81	57.2	70.6
04SS41-4:las	359	65	129.9	47.885	286.03	0.80	63.4	79.2
04SS41-2:las	379	81	134.3	30.45	154.69	0.69	61.7	89.4
04SS41-1:las	453	73	194.8	56.315	237.88	0.82	75.6	92.3
04SS41-5:las	185	52	79.3	64.74	247.59	0.84	73.6	87.7
Sample 04SS43								
04SS43-1:las	115	37	47.2	66.97	327.48	0.85	69.8	82.2
04SS43-5:las	332	114	130.3	53.635	299.74	0.82	66.4	81.1
04SS43-6:las	50	22	24.4	47.755	298.98	0.80	80.3	100.3
04SS43-7:las	58	14	32.0	84.5	289.86	0.87	95.2	109.1
04SS43-8:las	183	35	46.0	54.135	258.94	0.81	44.2	54.2
04SS43-9:las	310	53	78.7	47.49	259.82	0.80	44.8	56.2
04SS43-11:la	94	29	36.8	45.665	297.53	0.79	66.9	84.3
Sample 04SS44								
04SS44-1:las	441	116	168.2	71.65	340.9	0.86	65.7	76.5
04SS44-3:las	420	109	133.4	66.95	252.8	0.84	54.8	65.1
04SS44-5:las	518	152	238.7	57.145	317.4	0.83	78.7	95.0
04SS44-7:las	347	104	149.5	96.88	426.14	0.89	73.6	82.4
04SS44-4:las	270	84	183.0	51.005	224.05	0.80	114.9	143.0
Sample 04SS45								
04SS45-2:las	233	87	33.4	67.55	322.5	0.85	24.2	28.4
04SS45-3:las	193	77	23.6	75.05	355.8	0.86	20.6	23.8
04SS45-1:las	246	80	26.0	35.215	207.48	0.73	18.1	24.7
04SS45-5:las	402	115	44.8	53.645	335.3	0.82	19.2	23.3

§ α-ejection correction factor as described by Farley (2002). Measured age must be divided to by this factor to obtain the α-ejection-corrected age.
† α-ejection-corrected age.

Table A2.8. Representative mineral analyses used in thermobarometric calculations.[§]

Sample	*31001-5*	*08TC29*	*10SE41*		*31001-5*	*08TC29*	*10SE41*
Mineral	grt	grt	grt		bt	bt	bt
SiO_2	37.71	37.56	37.36		35.12	34.86	34.34
TiO_2	0.04	0.00	0.02		3.57	2.36	2.73
Al_2O_3	20.74	20.50	20.66		18.52	19.96	19.25
Cr_2O_3	0.06	0.00	0.02		0.00	0.02	0.00
Fe_2O_3	0.12	0.00	0.42		0.00	0.00	0.00
FeO	31.60	33.76	35.81		18.61	22.24	22.31
MnO	2.87	6.56	2.71		0.11	0.14	0.08
MgO	4.84	1.58	2.66		9.04	6.57	6.90
CaO	1.52	1.26	1.05		0.01	0.06	0.01
Na_2O	0.00	0.00	0.01		0.24	0.20	0.25
K_2O	0.00	0.00	0.00		8.98	8.56	8.84
Total	99.49	101.22	100.71		94.20	94.97	94.71
	O units				8 cations		
Si	3.02	3.03	3.01	Si	2.79	2.79	2.75
				Al^{iv}	1.21	1.21	1.25
Al	1.96	1.95	1.96	ΣT	4.00	4.00	4.00
Fe^{3+}	0.01	0.00	0.03				
ΣM2	1.96	1.95	1.99	Al^{vi}	0.52	0.67	0.57
				Ti	0.21	0.14	0.16
Fe^{2+}	2.12	2.28	2.41	Mg	1.07	0.78	0.82
Mn	0.19	0.45	0.18	Fe^{3+}	0.00	0.00	0.00
Mg	0.58	0.19	0.32	Fe^{2+}	1.24	1.49	1.49
Ca	0.13	0.11	0.09	Mn	0.01	0.01	0.01
ΣM1	3.02	3.02	3.01	Ca	0.00	0.01	0.00
				ΣM	3.05	3.10	3.06
Total	8.00	8.00	8.00				
				Na	0.04	0.03	0.04
X_{alm}	0.70	0.75	0.80	K	0.91	0.87	0.90
X_{grs}	0.04	0.04	0.03	ΣA	0.95	0.90	0.94
X_{prp}	0.19	0.06	0.11				
X_{sps}	0.06	0.15	0.06	Total	8.00	8.00	8.00

Table A2.8 (Continued). Representative mineral analyses used in thermobarometric calculations.[§]

Sample	*31001-5*	*08TC29*	*10SE41*		*31001-5*	*08TC29*
Mineral	plag	plag	plag		crd	crd
SiO_2	60.46	60.23	60.11		48.53	48.48
TiO_2	0.00	0.00	0.00		0.01	0.04
Al_2O_3	24.55	25.36	24.81		32.29	33.13
Cr_2O_3	0.00	0.00	0.00		0.00	0.00
Fe_2O_3	0.17	0.00	0.34		0.51	0.00
FeO	0.00	0.00	0.00		7.61	10.67
MnO	0.00	0.00	0.00		0.33	0.52
MgO	0.00	0.00	0.00		8.05	6.24
CaO	5.78	6.86	6.56		0.02	0.02
Na_2O	8.09	7.93	8.07		0.24	0.18
K_2O	0.16	0.05	0.11		0.00	0.00
Total	99.21	100.43	100.00		97.59	99.28
	O units				O units	
Si	2.71	2.67	2.69	Si	5.01	5.00
Al	1.30	1.33	1.31	Al^{iv}	0.99	1.00
Fe^{3+}	0.01	0.00	0.01	ΣT	6.00	6.00
ΣT	4.01	4.00	4.00			
				Al^{vi}	2.95	3.03
Ca	0.28	0.33	0.31	Fe^{3+}	0.04	0.00
Na	0.70	0.68	0.70	ΣM2	2.99	3.03
K	0.01	0.00	0.01			
ΣM	0.99	1.01	1.02	Fe^{2+}	0.66	0.92
				Mn	0.03	0.05
Total	5.00	5.01	5.02	Mg	1.24	0.96
				ΣM1	1.93	1.93
X_{an}	0.28	0.32	0.31			
X_{ab}	0.72	0.68	0.69	Total	9.93	9.96

§ Garnet normalized to 12O, biotite normalized to eight cations, plagioclase normalized to 8O, cordierite normalized to 18O. Ferric iron calculated using the program AX (Holland and Powell, 1998). Mineral abbreviations: ab, albite; an, anorthite; alm, almandine; bt, biotite; crd, cordierite; grs, grossular; grt, garnet; plag, plagioclase; prp, pyrope; sps, spessartine.

Table A2.9. Representative hornblende analyses used in aluminum-in-hornblende pressure calculations.

Sample	*K16b-87*	*91TH181*	*93TH417*	*94KK27*	*04SE5*	*08SE429*
Unit	South tonalite of Vergeles	Claraville granodiorite	Claraville granodiorite	Granodiorite of Jacobsen Meadow	Lebec granodiorite	Unnamed tonalite
SiO_2	44.08	43.01	44.83	44.55	46.54	43.45
TiO_2	1.55	1.59	1.44	1.26	0.35	1.04
Al_2O_3	9.77	8.55	8.03	8.55	7.23	10.36
Fe_2O_3*	3.43	4.75	3.07	4.22	2.38	2.31
FeO	16.99	19.64	19.03	13.44	17.68	16.48
MnO	0.50	0.68	0.44	0.47	0.57	0.42
MgO	8.36	6.54	7.85	10.79	9.10	8.90
CaO	11.52	11.21	11.62	11.83	11.94	11.87
Na_2O	1.21	1.42	1.08	1.13	0.91	1.12
K_2O	1.06	1.06	0.95	0.98	0.73	1.29
Total	98.48	98.45	98.33	97.22	97.43	97.24
Si	6.63	6.61	6.80	6.70	7.04	6.60
Al^{iv}	1.37	1.39	1.20	1.30	0.96	1.40
ΣT	8.00	8.00	8.00	8.00	8.00	8.00
Al^{vi}	0.36	0.16	0.24	0.21	0.33	0.45
Ti	0.18	0.18	0.16	0.14	0.04	0.12
Fe^{3+}	0.39	0.55	0.35	0.48	0.27	0.26
Fe^{2+}	2.14	2.52	2.41	1.69	2.24	2.09
Mn	0.06	0.09	0.06	0.06	0.07	0.05
Mg	1.87	1.50	1.78	2.42	2.05	2.02
ΣM1-M3	5.00	5.00	5.00	5.00	5.00	5.00
Ca	1.86	1.84	1.89	1.91	1.94	1.93
Na	0.35	0.42	0.32	0.33	0.27	0.33
Na^{M4}	0.14	0.16	0.11	0.09	0.06	0.07
ΣM4	2.00	2.00	2.00	2.00	2.00	2.00
Na^{A}	0.21	0.27	0.21	0.23	0.20	0.26
K	0.20	0.21	0.18	0.19	0.14	0.25
ΣA	0.41	0.47	0.39	0.42	0.34	0.51
Total	15.41	15.47	15.39	15.42	15.34	15.51
Amphibole name*	ferro-hornblende	ferro-hornblende	ferro-hornblende	magnesio-hornblende	ferro-hornblende	ferro-edenitic hornblende

Table A2.9 (Continued).

Sample	*08SE451*	*08SE463*	*08SE674*	*08TC27a*	*10SE1*
Unit	Antimony Peak tonalite	Unnamed tonalite	White Oak diorite gneiss	Granodiorite of Gamble Spring Canyon	Granite of Brush Mountain
SiO_2	42.69	42.99	42.45	47.43	47.57
TiO_2	0.31	1.33	0.20	0.45	1.10
Al_2O_3	16.13	10.17	16.69	6.94	8.59
Fe_2O_3*	7.18	2.76	5.78	3.32	6.37
FeO	8.58	16.91	10.41	15.80	8.20
MnO	0.49	0.41	0.29	0.51	0.23
MgO	9.64	8.67	8.69	10.26	13.02
CaO	10.79	11.90	10.89	11.83	11.17
Na_2O	1.89	1.14	1.68	1.08	1.03
K_2O	0.25	1.35	0.30	0.61	0.37
Total	97.95	97.10	97.10	97.10	97.10
Si	6.21	6.54	6.23	7.06	6.89
Al^{iv}	1.79	1.46	1.77	0.94	1.11
ΣT	8.00	8.00	8.00	8.00	8.00
Al^{vi}	0.98	0.36	1.12	0.27	0.35
Ti	0.03	0.15	0.02	0.05	0.12
Fe^{3+}	0.79	0.32	0.64	0.37	0.69
Fe^{2+}	1.04	2.15	1.28	1.97	0.99
Mn	0.06	0.05	0.04	0.06	0.03
Mg	2.09	1.97	1.90	2.28	2.81
ΣM1-M3	5.00	5.00	5.00	5.00	5.00
Ca	1.68	1.94	1.71	1.89	1.73
Na	0.53	0.34	0.48	0.31	0.29
Na^{M4}	0.32	0.06	0.29	0.11	0.27
ΣM4	2.00	2.00	2.00	2.00	2.00
Na^{A}	0.22	0.28	0.19	0.20	0.02
K	0.05	0.26	0.06	0.12	0.07
ΣA	0.26	0.54	0.25	0.31	0.09
Total	15.26	15.54	15.25	15.31	15.09
Amphibole name*	ferrian-tschermakite	potassian-ferro-edenitic hornblende	alumino-tschermakite	magnesio-hornblende	magnesio-hornblende

* determined using Probe-AMPH (Tindle and Webb, 1994).

Table A2.10. Representative plagioclase analyses used in hornblende-plagioclase temperature calculations.

Sample	*K16b-87*	*91TH181*	*93TH417*	*94KK27*	*04SE5*	*08SE429*	*08SE451*	*08SE463*	*08SE674*	*08TC27a*	*10SE1*
Unit	South tonalite of Vergeles	Claraville granodiorite	Claraville granodiorite	Granodiorite of Jacobsen Meadow	Lebec granodiorite	Unnamed tonalite	Antimony Peak tonalite	Unnamed tonalite	White Oak diorite gneiss	Granodiorite of Gamble Spring Canyon	Granite of Brush Mountain
SiO_2	59.98	61.79	62.16	60.26	61.23	58.03	59.54	59.47	61.66	63.20	47.98
Al_2O_3	26.22	24.05	24.08	24.80	24.64	26.18	26.20	25.88	24.43	23.16	32.90
Fe_2O_3*	0.09	0.10	0.02	0.16	0.06	0.10	0.20	0.15	0.07	0.13	0.12
FeO	0.00	0.00	0.00	0.00	0.00	0.00	0.00	0.00	0.00	0.00	0.00
CaO	7.06	5.50	5.47	6.48	6.14	7.70	7.26	7.50	5.55	4.37	16.22
Na_2O	7.76	8.62	8.56	7.98	8.10	7.37	7.23	7.42	8.60	9.40	2.32
K_2O	0.14	0.21	0.20	0.20	0.15	0.21	0.28	0.24	0.09	0.11	0.03
Total	101.24	100.26	100.49	99.87	100.32	99.59	100.71	100.66	100.39	100.37	99.59
Si	2.64	2.74	2.74	2.69	2.71	2.61	2.64	2.64	2.73	2.79	2.21
Al	1.36	1.26	1.25	1.30	1.29	1.39	1.37	1.36	1.27	1.21	1.79
Fe^{3+}	0.00	0.00	0.00	0.01	0.00	0.00	0.01	0.01	0.00	0.00	0.00
ΣT	4.01	4.00	4.00	4.00	4.00	4.00	4.02	4.00	4.00	4.00	4.00
Ca	0.33	0.26	0.26	0.31	0.29	0.37	0.35	0.36	0.26	0.21	0.80
Na	0.66	0.74	0.73	0.69	0.70	0.64	0.62	0.64	0.74	0.80	0.21
K	0.01	0.01	0.01	0.01	0.01	0.01	0.02	0.01	0.00	0.01	0.00
ΣM	1.00	1.01	1.00	1.01	1.00	1.03	0.98	1.01	1.01	1.02	1.01
Total	5.01	5.01	5.00	5.01	5.00	5.03	5.00	5.01	5.01	5.02	5.01
X_{an}	0.33	0.26	0.26	0.31	0.30	0.37	0.36	0.36	0.26	0.20	0.79
X_{ab}	0.67	0.74	0.74	0.69	0.70	0.63	0.64	0.64	0.74	0.80	0.21
Feldspar name	Andesine	Oligoclase	Oligoclase	Andesine	Oligoclase	Andesine	Andesine	Andesine	Oligoclase	Oligoclase	Bytownite

* Ferric iron calculated using the program AX (Holland and Powell, 1998).

Table A2.11. Summary of sample locations, rock units, major and trace element geochemistry, and isotopic data from the western San Emigdio mafic complex and the Bean Canyon pendant.

Sample	*09SE21A*	*09SE21B*	*09SE32B*	*07TM9*	*07TM10*
UTM easting[§]	295364	295364	295451	374356	374329
UTM northing[§]	3869181	3869181	3869123	3872473	3872628
Unit[#]	WSEMC	WSEMC	WSEMC	BC	BC
			Major elements (Wt. %)		
SiO_2	49.45	48.71	49.70	65.29	67.08
TiO_2	1.32	1.04	1.33	0.55	0.34
Al_2O_3	14.91	17.47	14.85	16.31	17.04
FeO*	9.75	8.24	9.75	4.03	2.76
MnO	0.20	0.14	0.16	0.11	0.06
MgO	7.28	6.35	7.75	1.41	0.97
CaO	12.87	13.77	12.88	1.87	3.35
Na_2O	2.44	2.84	2.35	5.26	5.16
K_2O	0.13	0.10	0.11	3.37	1.26
P_2O_5	0.11	0.09	0.11	0.18	0.10
Sum	98.47	98.74	99.00	98.37	98.14
LOI	0.76	0.81	0.93	0.55	0.81
			XRF trace element data (ppm):		
Ni	70	79	49	5	3
Cr	325	316	274	6	4
Sc	47	38	46	13	5
V	284	229	294	59	52
Ba	26	12	27	1073	479
Rb	1	1	0	133	49
Sr	137	147	141	370	197
Zr	77	61	76	166	140
Y	29	23	30	29	14
Nb	3.7	3.0	3.6	13.0	10.2
Ga	16	16	16	16	15
Cu	69	86	73	18	11
Zn	78	64	77	76	53
Pb	0	1	0	10	8
La	4	4	3	32	22
Ce	12	7	18	63	39
Th	0	0	0	11	9
Nd	10	7	10	28	14
U	1	1	0	3	3

Table A2.11 (Continued).

Sample	*09SE21A*	*09SE21B*	*09SE32B*	*07TM9*	*07TM10*
ICP-MS trace element data (ppm)					
La	3.24	2.72	3.44	32.63	21.26
Ce	9.56	7.87	9.84	63.22	39.36
Pr	1.61	1.32	1.65	7.43	4.27
Nd	8.71	6.91	8.80	27.72	14.98
Sm	3.12	2.47	3.09	5.69	2.76
Eu	1.22	1.00	1.18	1.49	1.05
Gd	4.18	3.49	4.15	5.14	2.31
Tb	0.78	0.63	0.78	0.82	0.36
Dy	5.21	4.06	5.20	4.95	2.22
Ho	1.10	0.89	1.11	1.03	0.46
Er	3.06	2.40	3.06	2.88	1.38
Tm	0.44	0.35	0.44	0.43	0.22
Yb	2.70	2.18	2.70	2.72	1.55
Lu	0.43	0.34	0.43	0.44	0.26
Ba	29.17	11.82	24.83	1078.65	480.83
Th	0.18	0.20	0.18	10.35	8.14
Nb	2.24	2.36	2.52	11.99	9.46
Y	27.85	22.01	27.88	26.63	12.50
Hf	2.13	1.72	2.12	4.36	3.47
Ta	0.17	0.17	0.18	0.75	0.75
U	0.09	0.07	0.23	3.26	2.87
Pb	0.47	0.37	0.37	9.67	6.68
Rb	1.17	1.00	0.98	127.82	47.20
Cs	0.03	0.11	0.05	2.98	4.24
Sr	138.32	148.24	141.20	360.87	191.88
Sc	43.23	35.79	41.99	12.11	4.92
Zr	76.02	59.65	74.75	164.72	139.78

* total Fe as FeO.

§ UTM coordinates are WGS datum, zone 11N.

WSEMC, Western San Emigdio mafic complex basaltic sheeted dikes and pillows; BC, Bean Canyon pendant silicic metavolcanics.

Table A2.11 (Continued).

Sample	*09SE21A*	*09SE32B*
	TIMS Sr and Nd data	
Sm (ppm)	2.669	2.932
Nd (ppm)	7.47716	8.751
$^{147}Sm/^{144}Nd$	0.215831	0.202589
$^{143}Nd/^{144}Nd(0)$	0.513289	0.513064
$\varepsilon_{Nd}(160)^{\dagger}$	+13.77	+9.30
$\varepsilon_{Nd}(484)^{\dagger\dagger}$	+15.91	+11.31
Rb (ppm)	2.811	1.49
Sr (ppm)	170.336	133.984
$^{87}Rb/^{86}Sr$	0.04775875	0.031965
$^{87}Sr/^{86}Sr$ (0)	0.703635	0.703393
$^{87}Sr/^{86}Sr$ (160)†	0.703526	0.703320
$^{87}Sr/^{86}Sr$ (484)††	0.703307	0.703173

† Age-corrected for 160 Ma, the intrusion age of tonalite and gabbro of the WSEMC (James, 1986a; this study).
†† Age-corrected for 484 Ma, the age of basalt-gabbro blocks of the Kings-Kaweah ophiolite belt (Saleeby, 2011).

REFERENCES

Ague, J. J., and Brimhall, G. H., 1988, Magmatic arc asymmetry and distribution of anomalous plutonic belts in the batholiths of California; effects of assimilation, crustal thickness, and depth of crystallization: *Geological Society of America Bulletin*, **100**(6), 912-927.

Anderson, J. L., and Smith, D. R., 1995, The effects of temperature and fO2 on the Al-in-hornblende barometer: *American Mineralogist*, **80**(5-6), 549-559.

Barth, A. P., Wooden, J. L., Grove, M., Jacobson, C. E., and Pedrick, J. N., 2003, U-Pb zircon geochronology of rocks in the Salinas Valley region of California; a reevaluation of the crustal structure and origin of the Salinian Block: *Geology*, **31**(6), 517-520.

Bartley, J.M., Glazner, A. F., Coleman, D. S., Kylander-Clark, A.R.C., and Friedrich, A.M., 2007, Large Laramide dextral offset across Owens Valley, California, and its possible relation to tectonic unroofing of the southern Sierra Nevada, in Till, A. B., Roeske, S. M., Foster, D. A. and Sample, J. C., eds., Exhumation Processes Along Major Continental Strike-slip Fault Systems: *Geological Society of America Special Paper*, **434**, 129-148.

Bateman, P. C., 1992, Plutonism in the central part of the Sierra Nevada Batholith, California: *U.S. Geological Survey Professional Paper* 1483, 186 pp.

Borg, I., and Groenen, P. J. F., 1997, Modern multidimensional scaling: Theory and applications, New York, Springer, 471 pp.

Brady, R., Ducea, M., Kidder, S., and Saleeby, J., 2006, The distribution of radiogenic heat production as a function of depth in the Sierra Nevada Batholith, California: *Lithos*, **86**, 229-244.

Busby-Spera, S. C. J., 1982, Paleogeographic reconstruction of a submarine volcanic center: geochronology, volcanology and sedimentology of the Mineral King roof pendant, Sierra Nevada, California. PhD thesis, Princeton University, 290 pp.

Chapman, A. D., Luffi, P., Saleeby, J., and Petersen, S., 2011, Metamorphic evolution, partial melting, and rapid exhumation above an ancient flat slab: Insights from the San Emigdio Schist, southern California: *Journal of Metamorphic Geology*, **29**, 601-626, doi: 10.1111/j.1525-1314.2011.00932.x.

Chen, J.H., and Moore, J.G., 1982, Uranium-lead isotopic ages from the Sierra Nevada batholith: *Journal of Geophysical Research*, **87**, 4761-4784.

Chen, J. H., and Tilton, G. R., 1991, Applications of lead and strontium isotopic relationships to the petrogenesis of granitoid rocks, central Sierra Nevada batholith, California: *Geological Society of America Bulletin*, **103**, 439–447.

Chen, J. H., and Wasserburg, G. J., 1981, Isotopic determination of uranium in picomole and subpicomole quantities: *Analytical Chemistry*, **53**(13), 2060-2067.

Clemens-Knott, D., and Saleeby, J.B., 1999, Impinging ring dike complexes in the Sierra Nevada batholith, California: Roots of the Early Cretaceous volcanic arc: *Geological Society of America Bulletin*, **111**, 484–496, doi: 10.1130/0016-7606(1999)111<0484:IRDCIT>2.3.CO;2.

Coleman, D. S. and Glazner, A. F. (1998) The Sierra Crest magmatic event: rapid formation of juvenile crust during the Late Cretaceous in California. In: Ernst, W. G. and Nelson, C. A. (eds.) *Integrated Earth and environmental evolution of the Southwestern United States: the Clarence A. Hall, Jr. volume.* Columbia, MD: Bellwether Publishing. 253-272.

Coleman, D. S., Briggs, S., Glazner, A. F. and Northrup, C. J., 2003, Timing of plutonism and deformation in the White Mountains of eastern California. *Geological Society of America Bulletin*, **115**, 48-57.

Coleman, D. S., Gray, W. and Glazner, A. F., 2004, Rethinking the emplacement and evolution of zoned plutons: geochronologic evidence for incremental assembly of the Tuolumne Intrusive Suite, California. *Geology*, **32**, 433-436.

DeCrisoforo, D. T., and Cameron, K. L., 1977, Petrology of sillimanite-K-spar zone metapelites from Ben Lomond Mountain, central Coast Ranges, California: *Abstracts with Programs Geological Society of America*, **9**, 411.

DePaolo, D. J., 1981, A neodymium and strontium isotopic study of the Mesozoic calc-alkaline granitic batholiths of the Sierra Nevada and Peninsular Ranges, California. *Journal of Geophysical Research*(B 86), 10470-10488.

Dickinson, W.R., Ducea, M., Rosenberg, L.I., Greene, H.G., Graham, S.A., Clark, J.C., Weber, G.E., Kidder, S., Ernst, G.W., and Brabb, E.E., 2005, Net dextral slip, Neogene San Gregorio-Hosgri fault zone, coastal California; geologic evidence and tectonic implications: *Geological Society of America Special Paper*, **391**, 43 pp.

Dixon, E. T., 1995, $^{40}Ar/^{39}Ar$ hornblende geochronology and evaluation of garnet and hornblende barometry, Lake Isabella and the Tehachapi area, southern Sierra Nevada, California: M.S. thesis, University of Michigan, 63 pp.

Dunne, G. C., Walker, J. D., 2004, Structure and evolution of the east Sierran thrust system, east-central California, *Tectonics*, **23**, doi:10.1029/2002TC001478.

Ernst, W. G., Coleman, D. S. and Van de Ven, C. M., 2003, Petrochemistry of granitic rocks in the Mount Barcroft area: implications for arc evolution, central White

Mountains, easternmost California. *Geological Society of America Bulletin*, **115**, 499-512.

Farley, K. A., 2002, (U-Th)/He Dating: Techniques, Calibrations, and Applications, *Reviews in Mineralogy and Geochemistry*, **47**, 819-844.

Fletcher, J. M., J. S. Miller, M. W. Martin, S. S. Boettcher, A. F. Glazner, and J. M. Bartley (2002), Cretaceous arc tectonism in the Mojave Block: Pro- found crustal modification that controlled subse- quent tectonic regimes, in Geologic Evolution of the Mojave Desert and Southwestern Basin and Range, edited by A. F. Glazner, J. D. Walker, and J. M. Bartley, *Geological Society of America Memoir*, **195**, 131–149, doi:10.1130/0-8137-1195-9.131.

Frost, T. P., and Mahood, C. A., 1987, Field, chemical, and physical constraints on mafic–felsic magma interaction in the Lamarck Granodiorite, Sierra Nevada, California: *Geololgical Society of America Bulletin*, **99**, 272–291.

Gaschnig, R. M., Coleman, D. S. and Glazner, A. F., 2006, Twin of the Tuolumne: new geochronology from the Mono Pass intrusive suite. *Geological Society of America Abstracts with Programs*, **38**, 559.

Gehrels, G., Valencia, V., and Pullen, A., 2006, Detrital zircon geochronology by laser-ablation multicollector ICPMS at the Arizona Laserchron Center: *The Paleontological Society Papers*, **12**, 67-76.

Hammarstrom, J. M., and Zen, E. a., 1986, Aluminum in hornblende; an empirical igneous geobarometer: *American Mineralogist*, **71**(11-12), 1297-1313.

Hanson, R. B., Saleeby, J. B. and Fates, D. G., 1987, Age and tectonic setting of Mesozoic metavolcanic and metasedimentary rocks, northern White Mountains, California.

Geology, **15**, 1074-1078.

Hill, M., O'Neil, J. R., Noyes, H., Frey, F. A. and Wones, D. R. (1988). Sr, Nd, and O isotope variations in compsitionally zoned and unzoned plutons in the central Sierra Nevada batholith: *American Journal of Science*, **288-A**, 213-214.

Hollister, L. S., Grissom, G. C., Peters, E. K., Stowell, H. H., and Sisson, V. B., 1987, Confirmation of the empirical correlation of Al in hornblende with pressure of solidification of calc-alkaline plutons: *American Mineralogist*, **72**(3-4), 231-239.

Holland, T., and Blundy, J., 1994, Non-ideal interactions in calcite amphiboles and their bearing on amphibole-plagioclase thermometry: *Contributions to Mineralogy and Petrology*, **116**(4), 433-447.

Holland, T. J. B., and Powell, R., 1998, An internally consistent thermodynamic data set for phases of petrological interest: *Journal of Metamorphic Geology*, **16**(3), 309-343.

Irwin, W. P., and Wooden, J. L., 2001, Map Showing Plutons and Accreted Terranes of the Sierra Nevada, California with a Tabulation of U/Pb Isotopic Ages, *U.S. Geological Survey Open-File Report* 01-229.

Jaffey, A. H., Flynn, K. F., Glendenin, L. E., Bentley, W. C., and Essling, A. M., 1971, Precision Measurement of Half-Lives and Specific Activities of ^{235}U and ^{238}U: *Physical Review*, **C4**(5), 1889-1906.

James, E. W., 1986a Geochronology, isotopic characteristics, and paleogeography of parts of the Salinian Block of California. Ph.D. thesis, University of California, 176 pp.

James, E. W., 1986b, U/Pb age of the Antimony Peak tonalite and its relation to Rand Schist in the San Emigdio Mountains, California: *Geological Society of America Abstracts with Programs*, **18**(2), 121.

John, D., 1981, Structure and petrology of pelitic schist in the Fremont Peak Pendant, northern Gabilan Range, California: *Geological Society of America Bulletin*, **92**(5), 237-246.

Johnson, D. M., Hooper, P. R., and Conrey, R. M., 1999, XRF Analysis of Rocks and Minerals for Major and Trace Elements on a Single Low Dilution Li-tetraborate Fused Bead: *Advances in X-Ray Analysis*, **41**, 843-867.

Johnson, M. C., and Rutherford, M. J., 1989, Experimental calibration of the aluminum-in-hornblende geobarometer with application to Long Valley Caldera (California) volcanic rocks: *Geology*, **17**(9), 837-841.

Kellogg, K.S., 1999, Geologic map of the Lockwood Valley quadrangle, Ventura County, California: *U.S. Geological Survey Open-File Report* 99–130, scale 1:24,000.

Kidder, S., Ducea, M., Gehrels, G. E., Patchett, P. J., and Vervoort, J., 2003, Tectonic and magmatic development of the Salinian Coast Ridge Belt, California: *Tectonics*, **22**, doi:10.1029/2002TC001409.

Kistler, R. W., and Champion, D. E., 2001, Rb-Sr whole-rock and mineral ages, K-Ar, 40Ar/39Ar, and U-Pb mineral ages, and strontium, lead, neodymium, and oxygen isotopic compositions for granitic rocks from the Salinian Composite Terrane, California: *U.S. Geological Survey Open-File Report*, 01-453, 84 pp.

Kistler, R. W. and Fleck, R. J. (1994). Field guide for a transect of the central Sierra Nevada, California: geochronology and isotope geology. *U.S. Geological Survey, Open-File Report* 94-0267, 50 pp.

Kistler, R. W. and Lee, D. E., 1989, Rubidium and strontium isotopic data for a suite of granitoid rocks from the Basin and Range Province, Arizona, California, Nevada, and

Utah: *U.S. Geological Survey Open-File Report* 89-199, 13pp.

Kistler, R. W., and Peterman, Z., 1973, Variations in Sr, Rb, K, Na and initial $^{87}Sr/^{86}Sr$ in Mesozoic granitic rocks and intruded wall rocks in central California: *Geological Society of America Bulletin*, **84**, 3489-3512.

Kistler, R. W. and Peterman, Z. E., 1978, Reconstruction of crustal blocks of California on the basis of initial strontium isotopic com- positions of Mesozoic granitic rocks. *U.S. Geological Survey Professional Paper* 1071, 17 pp.

Kistler, R. W., and Ross, D. C., 1990, A strontium isotopic study of plutons and associated rocks of the southern Sierra Nevada and vicinity, California: *U. S. Geological Survey Bulletin* 1920, 20 pp.

Kistler, R. W. and Swanson, S. E., 1981, Petrology and geochronology of metamorphosed volcanic rocks and a Middle Cretaceous volcanic neck in the east-central Sierra Nevada, California. *Journal of Geophysical Research*, **B 86**, 10489-10501.

Kistler, R. W., Chappell, B. W., Peck, D. L., and Bateman, P. C., 1986, Isotopic variation in the Tuolumne Intrusive Suite, central Sierra Nevada, California: *Contributions to Mineralogy and Petrology*, **94**, 205–220.

Krogh, T. E., 1973, A low-contamination method for hydrothermal decomposition of zircon and extraction of U and Pb for isotopic age determinations: *Geochimica et Cosmochimica Acta*, **37**(3), 485-494.

Lackey, J. S., Valley, J. W., Chen, J. H., and Stockli, D. F., 2008, Dynamic Magma Systems, Crustal Recycling, and Alteration in the Central Sierra Nevada Batholith: the Oxygen Isotope Record: *Journal of Petrology*, **49**(7), 1397-1426.

Ludwig, K. R., 2003, Mathematical-statistical treatment of data and errors for $^{230}Th/U$

geochronology: *Reviews in Mineralogy and Geochemistry*, **52**, 631-656.

Mahan, K.H., Bartley, J.M., Coleman, D.S., Glazner, A.F., and Carl, B.S., 2003, Sheeted intrusion of the syn- kinematic McDoogle Pluton, Sierra Nevada, California: *Geological Society of America Bulletin*, **115**, 1570–1582, doi: 10.1130/B22083.1.

Mahéo, G., Saleeby, J., Saleeby, Z., and Farley, K. A., 2009, Tectonic control on southern Sierra Nevada topography, California: *Tectonics*, **28**(6), TC6006.

Martin, M. W., Walker, J. D., and Fletcher, J. M., 2002, Timing of Middle to Late Jurassic ductile deformation and implications for paleotectonic setting, Shadow Mountains, western Mojave Desert, *California Geological Society of America Memoirs,* **195**, 43-58.

Masi, U., O'Neil, J. R. and Kistler, R. W., 1981, Stable isotope systema- tics in Mesozoic granites of central and northern California and southwestern Oregon. *Contributions to Mineralogy and Petrology*, **76**, 116-126.

McNulty, B. A., Tobisch, O. T., Cruden, A. R. and Gilder, S., 2000, Multistage emplacement of the Mount Givens Pluton, central Sierra Nevada Batholith, California. *Geological Society of America Bulletin*, **112**, 119-135.

Miller, J.S., Glazner, A.F., Walker, J.D., and Martin, M.W., 1995, Geochronologic and isotopic evidence for Triassic-Jurassic emplacement of the eugeoclinal allochthon in the Mojave Desert region, California: *Geological Society of America Bulletin*, **107**, 1441–1457, doi: 10.1130/0016–7606(1995)1072.3.CO;2.

Miller, J.S. and Glazner, A.F., 1995, Jurassic plutonism and crustal evolution in the central Mojave Desert, California: *Contributions to Mineralogy and Petrology*, **118**, 379-395.

Nadin, E. S., 2007, Structure and history of the Kern Canyon fault system, southern Sierra

Nevada, California: Ph.D. thesis, California Institute of Technology, 296 pp.

Pickett, D. A., and Saleeby, J. B., 1993, Thermobarometric constraints on the depth of exposure and conditions of plutonism and metamorphism at deep levels of the Sierra Nevada Batholith, Tehachapi Mountains, California: *Journal of Geophysical Research*, **98**(B1), 609-629.

Pickett, D. A., and Saleeby, J. B., 1994, Nd, Sr, and Pb isotopic characteristics of Cretaceous intrusive rocks from deep levels of the Sierra Nevada Batholith, Tehachapi Mountains, California: *Contributions to Mineralogy and Petrology*, **118**(2), 198-215, doi: 110.1007/BF01052869.

Powell, R., and Holland, T., 1994, Optimal geothermometry and geobarometry: *American Mineralogist*, **79**(1-2), 120-133.

Ratajeski, K., Glazner, A. F. and Miller, B. V., 2001, Geology and geochemistry of mafic to felsic plutonic rocks in the Cretaceous intrusive suite of Yosemite Valley, California. *Geological Society of America Bulletin*, **113**, 1486-1502.

Robinson, A. C. and Kistler, R. W. (1986) Maps showing isotopic dating in the Walker Lake 1 degrees by 2 degrees Quadrangle, California and Nevada. *U. S. Geological Survey Miscellaneous Field Studies Map* MF-1382-N, **49**, 3 sheets, 1:250,000.

Saleeby, J., 2011, Geochemical mapping of the Kings-Kaweah ophiolite belt, California - evidence for progressive melange formation in a large offset transform-subduction initiation environment: *Geological Society of America Special Paper* (in press).

Saleeby, J., and Dunne, G. C., in preparation, Temporal and Structural Relations of Early Mesozoic Arc Plutonism, southern Sierra Nevada, California: *Geological Society of America Bulletin*.

Saleeby, J. B., Ducea, M. N., Busby, C. J., Nadin, E. S., and Wetmore, P. H., 2008, Chronology of pluton emplacement and regional deformation in the southern Sierra Nevada Batholith, California: *Geological Society of America Special Paper*, **438**, 397-427.

Saleeby, J., Farley, K. A., Kistler, R. W., and Fleck, R. J., 2007, Thermal evolution and exhumation of deep-level batholithic exposures, southernmost Sierra Nevada, California: *Geological Society of America Special Paper*, **419**, 39-66.

Saleeby, J. B., Sams, D. B., and Kistler, R. W., 1987, U/Pb zircon, strontium, and oxygen isotopic and geochronological study of the southernmost Sierra Nevada Batholith, California: *Journal of Geophysical Research*, **92**(B10), 10,443-10,466.

Saleeby, J. B., Geary, E. E., Paterson, S. R., and Tobisch, O. T., 1989, Isotopic systematics of Pb/U (zircon) and $^{40}Ar/^{39}Ar$ (biotite-hornblende) from rocks of the central Foothills terrane, Sierra Nevada, California: *Geological Society of America Bulletin*, **101**(11), 1481-1492.

Saleeby, J. B., 1990, Progress in tectonic and petrogenetic studies in an exposed cross–section of young (~100 Ma) continental crust, southern Sierra Nevada, California, *in*, Salisbury, M. H., ed.: *Exposed Cross Sections of the Continental Crust*, D. Reidel Publishing Co., Dordrecht, Holland, 137–158.

Sawka, W. N., Chappell, B. W., and Kistler, R. W., 1990, Granitoid compositional zoning by side-wall boundary layer differentiation: Evidence from the Palisade Crest intrusive suite, central Sierra Nevada, California, *Journal of Petrology*, **31**, 519-553.

Schmidt, M. W., 1992, Amphibole composition in tonalite as a function of pressure; an experimental calibration of the Al-in-hornblende barometer: *Contributions to*

Mineralogy and Petrology, **110**(2-3), 304-310.

Schweickert, R. A. and Lahren, M. M., 1999, Triassic caldera at Tioga Pass, Yosemite National Park, California: structural relationships and significance. *Geological Society of America Bulletin*, **111**, 1714-1722.

Silver, L. T., and Nourse, J. A., 1991, Timing of the Rand thrust and its implications for Late Cretaceous tectonics in southern California: *Geological Society of America Abstracts with Programs*, **23**(5), A480.

Spear, F. S., 1993, Metamorphic phase equilibria and pressure-temperature-time paths, Washington, D.C., Mineralogical Society of America, 799 p.

Stacey, J. S., and J. D. Kramers, 1975, Approximation of terrestrial lead isotope evolution by a two-stage model, *Earth and Planetary Science Letters*, **26**, 207–221.

Stern, T. W., Bateman, P. C., Morgan, B. A., Newell, M. F., and Peck, D. L., 1981, Isotopic U-Pb ages of zircon from the granitoids of the central Sierra Nevada, California: *U. S. Geological Survey Professional Paper* 1185, 19 pp.

Tindle, A. G., and Webb, P. C., 1994, PROBE-AMPH; a spreadsheet program to classify microprobe-derived amphibole analysis: *Computers & Geosciences*, **20**, 7-8.

Tobisch, O. T. and Cruden, A. R., 1995, Fracture-controlled magma conduits in an obliquely convergent continental magmatic arc: *Geology*, **23**, 941-944.

Wenner, J. M. and Coleman, D. S., 2004, Magma mixing and Cretaceous crustal growth: geology and geochemistry of granites in the central Sierra Nevada batholith, California. *International Geology Review*, **46**, 880-903.

APPENDIX 3

Supporting information and data repository for:

Slab flattening trigger for isotopic disturbance and magmatic flare-up in the southernmost Sierra Nevada batholith, California

1. SAMPLE LOCATIONS, PETROGRAPHY, AND ZIRCON MORPHOLOGY

Figure A3.1 is a geologic map of the San Emigdio and Tehachapi mountains showing the locations of studied samples. Descriptions of analyzed zircon grains and the samples from which they were extracted are given below.

1.1. Plutonic rocks

08SE46 (UTM zone 11 S, 319551 3864823)

San Emigdio tonalite (Chapman and Saleeby, in review). Gray, medium- to coarse-grained, weakly foliated biotite tonalite. Alteration is minor. See Chapman *et al*. (in review) for U-Pb zircon geochronologic data.

08SE451 (UTM zone 11 S, 307028 3861038)

Antomony Peak tonalite (Chapman and Saleeby, in review). Light gray, medium- to coarse-grained, porphyritic, massive to penetratively foliated, hornblende-biotite tonalite containing mainly plagioclase, quartz, hornblende, and K-feldspar, with minor amounts of garnet, biotite, epidote, apatite, sphene, and ilmenite. Where hypidiomorphic granular (igneous)

Figure A3.1. Simplified geologic map showing sample locations in the San Emigdio and Tehachapi mountains. Geology from Crowell (1952), Dibblee and Nilsen (1973), Sharry (1981), Ross (1989), Wood (1997), Saleeby *et al*. (2007), and Chapman and Saleeby (in review).

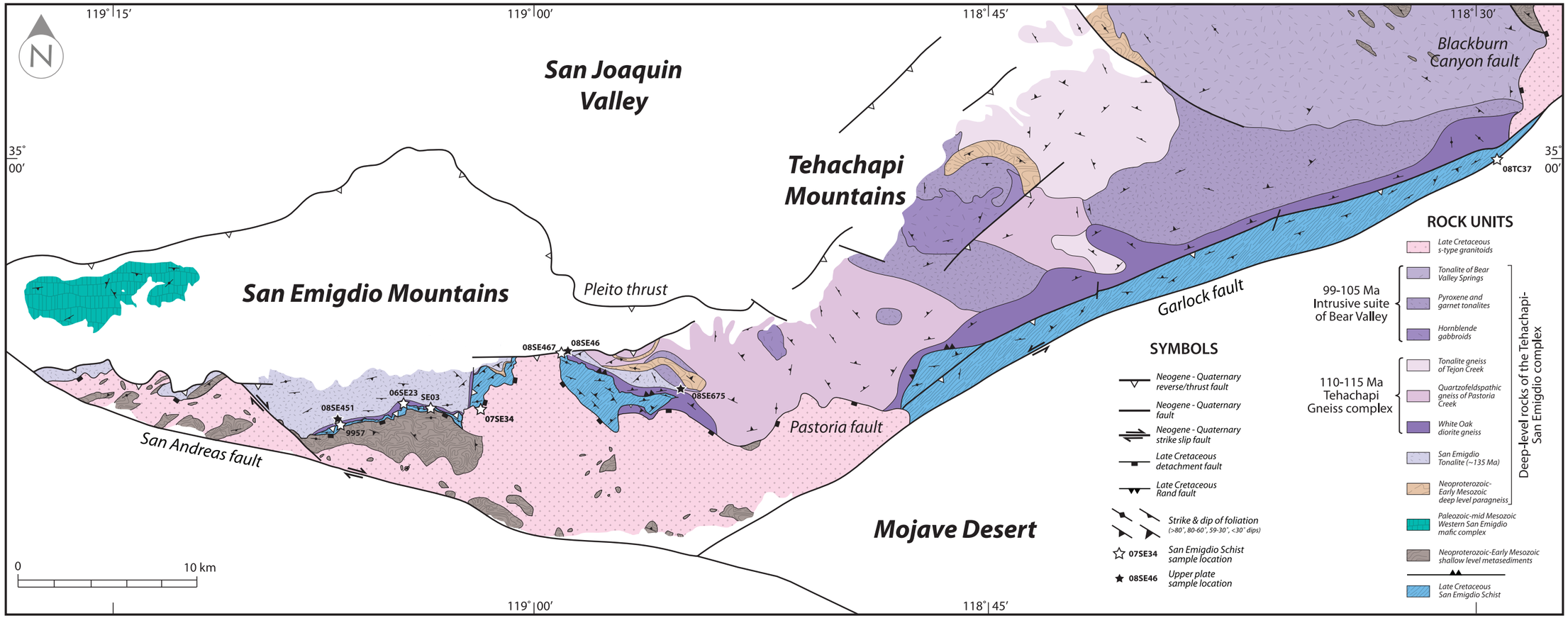
119° 15′
119° 00′
118° 45′
118° 30′
35° 00′
N
San Joaquin Valley
Tehachapi Mountains
Blackburn Canyon fault
San Emigdio Mountains
Pleito thrust
Garlock fault
08TC37
08SE467
08SE46
08SE675
06SE23
SE03
08SE451
9957
07SE34
San Andreas fault
Pastoria fault
Mojave Desert
0
10 km
ROCK UNITS
Late Cretaceous s-type granitoids
99-105 Ma Intrusive suite of Bear Valley
Tonalite of Bear Valley Springs
Pyroxene and garnet tonalites
Hornblende gabbroids
110-115 Ma Tehachapi Gneiss complex
Tonalite gneiss of Tejon Creek
Quartzofeldspathic gneiss of Pastoria Creek
White Oak diorite gneiss
San Emigdio Tonalite (~135 Ma)
Neoproterozoic-Early Mesozoic deep level paragneiss
Deep-level rocks of the Tehachapi-San Emigdio complex
Paleozoic-mid Mesozoic Western San Emigdio mafic complex
Neoproterozoic-Early Mesozoic shallow level metasediments
Late Cretaceous San Emigdio Schist
SYMBOLS
Neogene - Quaternary reverse/thrust fault
Neogene - Quaternary fault
Neogene - Quaternary strike slip fault
Late Cretaceous detachment fault
Late Cretaceous Rand fault
Strike & dip of foliation (>80°, 80-60°, 59-30°, <30° dips)
07SE34 San Emigdio Schist sample location
08SE46 Upper plate sample location

textures are not overprinted by metamorphic foliation, the epidote occurs as subhedral replacement products of embayed hornblende and retains distinct core and rim regions, consistent with a magmatic origin. Original petrographic relationships are locally obscured by extensive seritization and chloritization. Hornblende-rich mafic schlieren are found in the same outcrop as 08SE451. See Chapman *et al*. (in review) for U-Pb zircon geochronologic data.

08SE675 (UTM zone 11 S, 324340 3863296)

San Emigdio tonalite (Chapman and Saleeby, in review). Foliated garnet-biotite leucotonalite. Similar in appearance to the 101 Ma "Garnet-biotite tonalite of Grapevine" of Pickett and Saleeby (1993, 1994). Epidote phenocrysts embayed in biotite. Garnet is 0.5-1 mm in diameter with blebby quartz inclusions. Accessory minerals include zircon, apatite, and opaques. Very little alteration. Radiation-damage halos surrounding zircon inclusions in biotite are common. See Chapman *et al*. (in review) for U-Pb zircon geochronologic data.

Zircon grains in samples 08SE46, 08SE451, and 08SE675 are generally subhedral, ~ 50 – 350 μm in length, inclusion-poor, and exhibit simple oscillatory zoning patterns in CL images that we interpret as magmatic features (Figure A3.2). CL-dark cores are commonly overgrown by CL-bright rims up to ~35 μm wide. *In situ* LA-MC-ICPMS analyses of core and rim regions are concordant with weighted mean ages of ca. 134 to 136 Ma and 98.1 ± 4.9 Ma, respectively (Chapman *et al*., in review). These ages are interpreted to reflect the

Figure A3.2. Representative cathodoluminescence images of selected zircon grains from upper plate samples 08SE46 (a and b), 08SE451 (c), and 08SE675 (d), and schist samples 06SE23 (e), 07SE34 (f), 08SE467 (g), and 08TC37 (h). Yellow circles indicate LA-MC-ICPMS analyzed areas labeled with $^{206}Pb/^{238}U$ ages. Analysis 06SE23-3b (966.0 ± 32.7 Ma) was included (e) despite being > 30% discordant to illustrate a core-rim age difference. Red ellipses indicate SIMS analyzed areas labeled with $\delta^{18}O$. All uncertainties are 2σ.

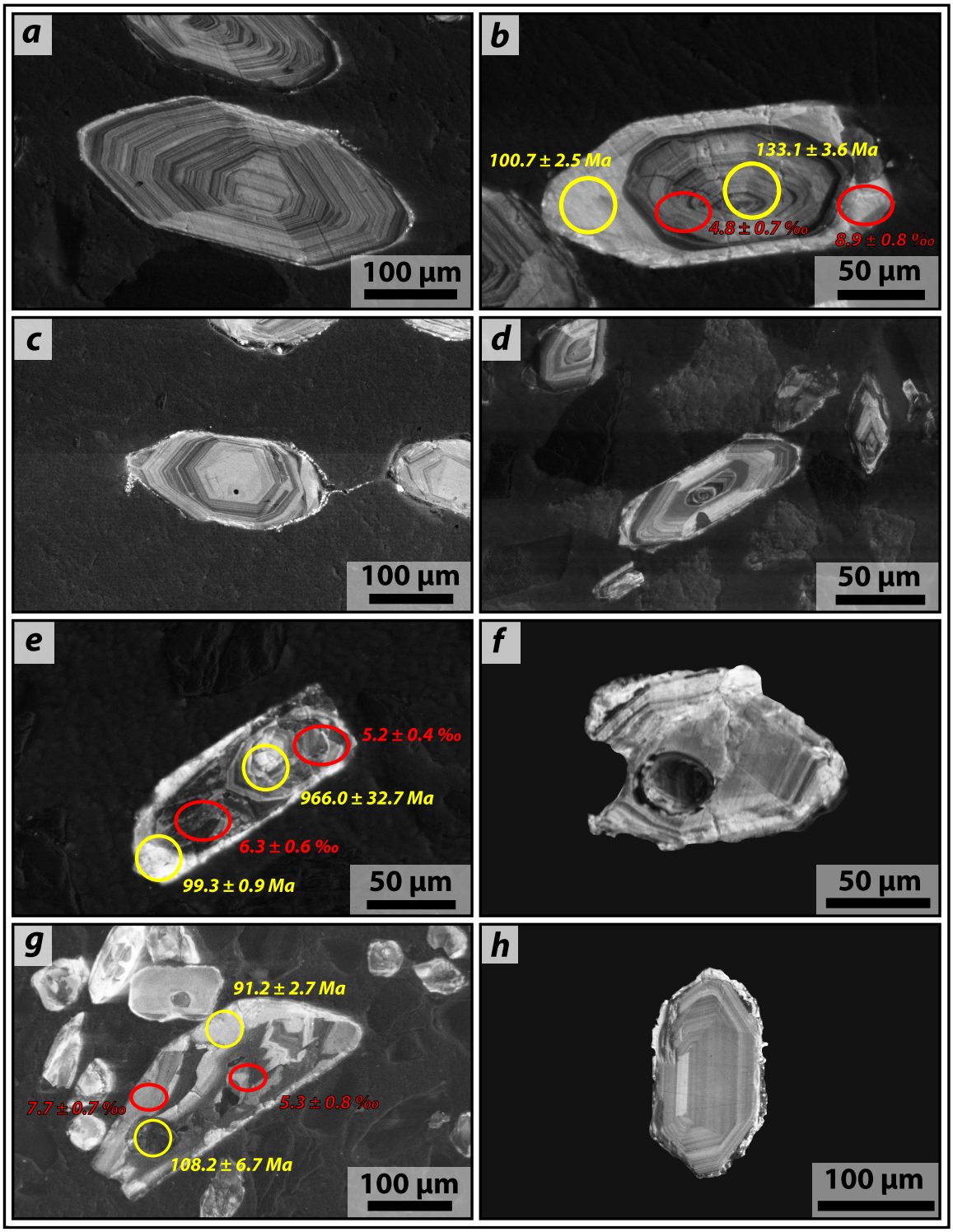
a
100 µm
b
100.7 ± 2.5 Ma
133.1 ± 3.6 Ma
4.8 ± 0.7 ‰
8.9 ± 0.8 ‰
50 µm
c
100 µm
d
50 µm
e
5.2 ± 0.4 ‰
966.0 ± 32.7 Ma
6.3 ± 0.6 ‰
99.3 ± 0.9 Ma
50 µm
f
50 µm
g
91.2 ± 2.7 Ma
7.7 ± 0.7 ‰
5.3 ± 0.8 ‰
108.2 ± 6.7 Ma
100 µm
h
100 µm

timing of crystallization (cores) and deep crustal overgrowth (rims). A single aberrant grain in sample 08SE675, yielding an age of 485.0 ± 34.0 Ma, is interpreted as related to source inheritance and/or entrainment of a Paleozoic or older zircon.

1.2. San Emigdio Schist

06SE23 (UTM zone 11 S, 310593 3861943)

San Emigdio Schist metasandstone (San Emigdio Mountains locality) collected from 30 m below the Rand fault. Medium- to coarse-grained garnet + plagioclase + biotite + quartz + rutile blastomylonitic schist. Garnet grains are idioblastic and 0.5 to 2 mm in diameter with well-defined growth zonation and blebby inclusions of exclusively quartz confined to individual zones (Chapman *et al*., 2011), suggesting epitaxial growth of quartz. Some porphyroblasts have pressure shadows composed of fine quartz, plagioclase, and chlorite. Some garnet grains are torn completely apart or frictionally displaced up to 2 mm along fractured surfaces with no systematic orientation. Plagioclase is poikiloblastic with blebby quartz inclusions and finely disseminated graphite and/or carbonaceous material. Some grains exhibit polysynthetic twinning. Quartz grains lack undulatory extinction and display 120˚ grain boundaries, indicative of high-temperature annealing. Secondary alteration is mainly restricted to mm-scale shear bands that truncate the peak mineral assemblage and contain retrograde clinozoisite, chlorite, celadonitic muscovite, and tourmaline. Sample contains minor tschermakitic hornblende. Calculated temperatures and pressures for this sample are 665 ± 29 °C and 10.0 ± 0.9 kbar (Chapman *et al*., 2011).

07SE34 (UTM zone 11 S, 314729 3862117)

San Emigdio Schist metasandstone (San Emigdio Mountains locality) collected from 425 m below the Rand fault. Fine- to medium-grained plagioclase + biotite + chlorite + muscovite + clinozoisite + quartz granular schist. A faint shape-preferred orientation of biotite defines the schistosity. Plagioclase is poikiloblastic, lacks twinning, and contains blebby quartz inclusions and finely disseminated graphite and/or carbonaceous material. Garnet porphyroblasts are sparse, with a single ~ 1 mm skeletal grain in thin section. Biotite is closely associated with ilmenite, tourmaline, and calcite. This sample was not suitable for thermobarometric work since garnet was not in textural equilibrium with plagioclase, biotite, or muscovite. However, phase relations suggest that peak temperatures did not exceed 600 ˚C (Chapman *et al*., 2011).

08SE467 (UTM zone 11 S, 319332 3864641)

San Emigdio Schist metasandstone (San Emigdio Mountains locality) collected adjacent to the Rand fault. Outcrop contains abundant deformed quartzofeldspathic (milky quartz + plagioclase ± garnet ± muscovite) veins and stromatic leucosomes and melanosomes, interpreted to result from fluid-saturated partial melting (Chapman *et al*., 2011). Sample is a coarse-grained garnet + plagioclase + biotite + quartz + ilmenite blastomylonitic schist. Garnet porphyroblasts are typically 2 to 4 mm in diameter and subhedral, with inclusions of plagioclase, biotite, and quartz. Diffusive relaxation of major and trace element growth zonation is common in garnet porphyroblasts from this sample. Plagioclase porphyroblasts are twinned, contain little to no graphite and/or carbonaceous material, and exhibit distinct

core and rim regions. Quartz grains lack undulatory extinction and display 120˚ grain boundaries. Minor minerals include apatite, zircon, and rutile. Secondary minerals, including clinozoisite, celadonitic muscovite, and fibrolitic sillimanite, usually occur within or adjacent to biotite. Radiation-damage halos surrounding zircon inclusions in biotite are common. Phase relations suggest that peak temperatures exceeded 700˚ C at 10 kbar (Chapman *et al*., 2011).

08TC37 (UTM zone 11 S, 366051 3873180)

San Emigdio Schist metasandstone (Tehachapi Mountains locality) collected from 520 m below the Rand fault. Fine- to medium-grained plagioclase + biotite + chlorite + muscovite + clinozoisite + quartz mylonitic schist. Quartz and feldspar are commonly pinned by elongate biotite grains, evidence for deformation by solution-precipitation creep. No garnet porphyroblasts were found in this sample.

Zircon grains from all structural levels in the schist share similar morphologies. Most grains are subhedral to anhedral, ~ 10 – 150 μm in length, inclusion-poor, with abundant fractures. CL imaging indicates a clear relationship between zircon zoning patters and structural depth (Figure A3.2). At the deepest levels of exposure (> 100 m; e.g., samples 07SE34 and 08TC37), zircons typically exhibit simple oscillatory zoning patterns that we interpret as magmatic features. At shallow structural levels (< 100 m), oscillatory zoning is still generally present; however, metamorphic domains truncate older magmatic zoning in several grains and narrow (5 -35 μm) rims of CL-bright zircon commonly crosscut zoning in zircon cores. Adjacent to the Rand fault (e.g., samples 06SE23 and 08SE467) , little to no

oscillatory zoning is present in zircons; instead, zircons lack cores and display complex metamorphic zoning patterns characterized by multiple crosscutting domains.

2. ANALYTICAL METHODS

2.1. LA-MC-ICPMS

U-Pb geochronology of igneous and detrital zircons was conducted by laser ablation multicollector inductively coupled mass spectrometry (LA-MC-ICPMS) at the Arizona LaserChron Center (ALC) following the methods outlined in Gehrels *et al*. (2006). Zircon grains were extracted from plutonic and metamorphic samples using standard mineral separation techniques of crushing, sieveing, magnetic separation, processing through heavy liquids, and hand picking. Separates were then mounted in epoxy, polished, and imaged on the Caltech Zeiss 1550 VP field emission scanning electron microscope before analysis. Representative cathodoluminescence (CL) images are shown in Figure A3.2. Zircons were ablated using a 193 nm ArF laser with a pit depth of ~12 μm and spot diameters of 25-30 μm depending on grain size. SL2 (564 Ma ± 4 Ma; Gehrels, personal communication, 2011) and R33 (419 ± 1 Ma; Black *et al*., 2004) zircon standards were used. Data reduction was done using in-house ALC Microsoft Excel programs and ISOPLOT/Ex Version 3 (Ludwig, 2003). U-Pb isotopic data is presented in Table A3.1. Plots of U-content and Th/U versus U-Pb age are shown in Figure A3.3.

2.2. SIMS

Oxygen isotope analyses were conducted with a CAMECA IMS 7f-GEO magnetic sector type secondary ion mass spectrometry (SIMS) instrument at the Caltech Center for

Figure A3.3. Plots of zircon trace element chemistry versus U-Pb age for the San Emigdio Schist (A and C) and upper plate batholithic rocks (B and D). Data from Grove *et al*. (2003) (sample 9957), Jacobson *et al*. (2011) (samples SE1b and SE03), Chapman *et al*. (in review), and this study. Note that metamorphic domains generally exhibit high U-content and low Th/U.

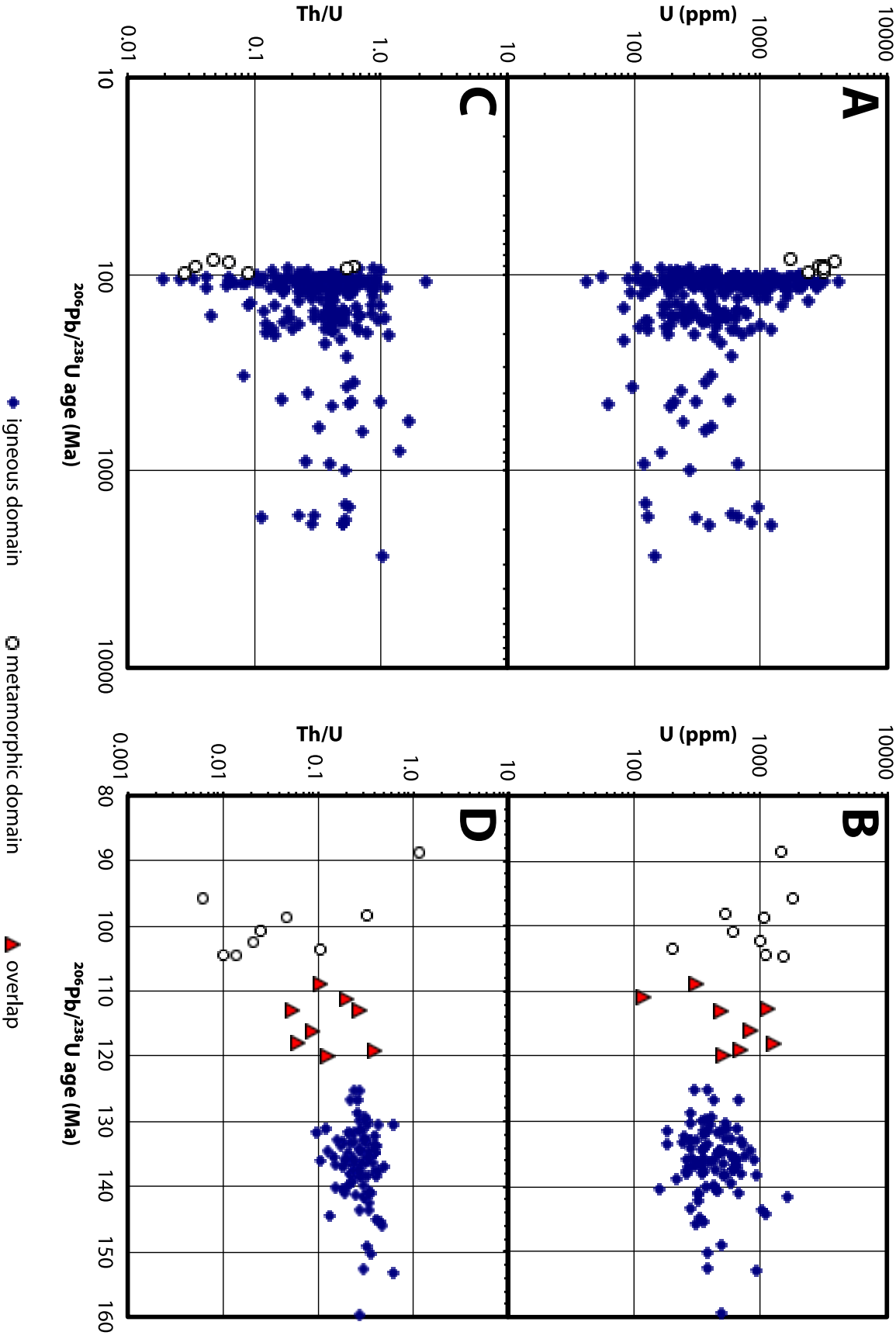
A
B
C
D
U (ppm)
Th/U
$^{206}Pb/^{238}U$ age (Ma)
igneous domain
metamorphic domain
overlap

Table A3.1. LA-MC-ICPMS U-Pb detrital zircon data for the San Emigdio Schist[†].

Analysis	CL notes[#]	U (ppm)	$^{206}Pb/^{204}Pb$	U/Th	Isotope ratios							Isotopic ages (Ma)[§]					
					$^{206}Pb^*/^{207}Pb^*$	± (%)	$^{207}Pb^*/^{235}U^*$	± (%)	$^{206}Pb^*/^{238}U$	± (%)	Error correlation	$^{206}Pb^*/^{238}U$	± (Ma)	$^{207}Pb^*/^{235}U^*$	± (Ma)	$^{206}Pb^*/^{207}Pb^*$	± (Ma)
06SE23	*San Emigdio Schist - San Emigdio Mountains*																
06SE23-1	IG	322	2642	2.3	22.9228	11.0	0.1033	11.3	0.0172	2.3	0.20	109.7	2.5	99.8	10.7	-131.8	273.5
06SE23-3	IG	996	6326	2.6	21.0267	2.3	0.1111	2.6	0.0169	1.3	0.49	108.3	1.4	107.0	2.6	77.3	54.1
06SE23-4	IG	585	2044	11.3	17.7175	24.7	0.1253	24.7	0.0161	0.8	0.03	102.9	0.8	119.8	28.0	469.8	554.7
06SE23-5	IG	413	960	2.1	19.6723	13.7	0.1123	13.9	0.0160	2.6	0.19	102.4	2.7	108.0	14.3	233.3	317.2
06SE23-6	IG	551	4198	2.0	21.6204	4.6	0.1061	5.1	0.0166	2.3	0.45	106.4	2.4	102.4	5.0	10.8	110.4
06SE23-7	IG	1158	7110	2.3	20.9772	2.1	0.1071	2.5	0.0163	1.4	0.55	104.2	1.4	103.3	2.4	82.9	48.9
06SE23-8	IG	1258	5710	2.2	20.9401	1.7	0.1046	2.1	0.0159	1.1	0.55	101.6	1.1	101.0	2.0	87.2	40.6
06SE23-9	IG	298	2122	2.1	20.9322	9.1	0.1179	9.2	0.0179	1.3	0.15	114.4	1.5	113.2	9.9	88.1	216.6
06SE23-10	IG	471	5806	2.1	20.4895	2.5	0.1827	2.6	0.0272	0.6	0.21	172.7	0.9	170.4	4.0	138.5	58.7
06SE23-11	IG	207	2188	2.5	22.6562	10.5	0.1099	11.4	0.0181	4.3	0.38	115.4	5.0	105.9	11.4	-103.0	259.4
06SE23-12	IG	1008	7544	2.3	20.9942	3.0	0.1110	3.5	0.0169	1.8	0.50	108.0	1.9	106.9	3.6	81.0	72.1
06SE23-13	IG	288	2720	2.9	22.3426	8.6	0.1005	8.7	0.0163	1.0	0.11	104.1	1.0	97.2	8.0	-68.8	211.0
06SE23-14	IG	631	1648	2.2	16.6561	19.8	0.1416	19.9	0.0171	2.5	0.12	109.3	2.7	134.5	25.1	604.9	431.2
06SE23-15	IG	662	3096	3.1	20.1821	3.1	0.1116	3.3	0.0163	1.2	0.35	104.5	1.2	107.4	3.4	173.9	72.6
06SE23-16	IG	551	5742	1.5	20.6434	5.4	0.1725	6.0	0.0258	2.7	0.45	164.4	4.4	161.6	9.0	120.9	127.2
06SE23-17	IG	834	3888	1.8	21.0603	3.0	0.1087	3.0	0.0166	0.6	0.20	106.2	0.6	104.8	3.0	73.6	70.4
06SE23-19	IG	189	1124	2.8	22.5703	12.2	0.1050	12.4	0.0172	1.8	0.14	109.9	1.9	101.4	11.9	-93.6	301.1
06SE23-20	IG	439	4536	1.7	21.8650	6.1	0.1013	7.6	0.0161	4.5	0.60	102.8	4.6	98.0	7.1	-16.3	147.0
06SE23-21	IG	665	5698	2.9	21.0225	2.9	0.1049	3.7	0.0160	2.3	0.62	102.3	2.3	101.3	3.6	77.8	68.9
06SE23-22	IG	182	1780	2.1	23.6294	13.0	0.1061	13.2	0.0182	2.4	0.18	116.2	2.8	102.4	12.9	-207.4	326.9
06SE23-1b	MM	3121	12100	36.1	20.3951	3.4	0.1049	3.5	0.0155	1.0	0.27	99.3	0.9	101.3	3.4	149.3	80.1
06SE23-4b	IG	119	1353	1.6	14.8844	133.1	0.1621	133.2	0.0175	4.6	0.03	111.8	5.1	152.6	190.8	843.5	641.7
06SE23-5b	IG	1161	6730	2.4	20.5962	14.0	0.1100	14.1	0.0164	1.7	0.12	105.0	1.8	105.9	14.2	126.3	331.4
06SE23-6b	IG	566	2940	2.2	26.6713	31.2	0.0844	31.3	0.0163	2.1	0.07	104.4	2.2	82.2	24.7	-521.0	852.4
07SE34	*San Emigdio Schist - San Emigdio Mountains*																
07SE34-2	IG	276	4431	2.2	20.9852	6.4	0.1148	6.6	0.0175	1.5	0.23	111.6	1.7	110.3	6.9	82.0	152.2
07SE34-1	IG	728	9498	2.2	21.0746	3.4	0.1130	3.7	0.0173	1.4	0.39	110.4	1.6	108.7	3.8	71.9	80.9
07SE34-3	IG	3123	14724	2.2	20.5700	2.6	0.1134	3.1	0.0169	1.7	0.55	108.2	1.8	109.1	3.2	129.3	60.3
07SE34-4	IG	237	1200	2.6	17.5042	18.0	0.1222	18.0	0.0155	0.7	0.04	99.2	0.7	117.0	19.9	496.5	398.4
07SE34-5	IG	551	5355	2.1	20.7458	3.6	0.1063	4.5	0.0160	2.8	0.61	102.3	2.8	102.6	4.4	109.2	84.9
07SE34-6	IG	306	76191	1.9	9.3456	1.7	4.6608	2.0	0.3159	1.0	0.52	1769.7	15.8	1760.2	16.4	1749.0	30.8
07SE34-7	IG	118	813	3.0	19.0897	11.0	0.1200	11.2	0.0166	2.0	0.18	106.2	2.1	115.1	12.2	302.2	251.5
07SE34-8	IG	146	9960	2.8	13.1960	2.7	1.5150	3.2	0.1450	1.8	0.56	872.9	14.9	936.5	19.8	1089.3	53.6
07SE34-9	IG	268	31269	1.9	9.7414	2.0	3.3767	8.3	0.2386	8.0	0.97	1379.3	99.5	1499.0	64.7	1672.6	36.8
07SE34-10	IG	1215	16287	2.8	20.5994	2.7	0.1075	3.0	0.0161	1.3	0.42	102.7	1.3	103.7	2.9	125.9	64.0
07SE34-11	IG	420	9189	2.4	20.6232	5.2	0.1776	5.4	0.0266	1.7	0.30	169.0	2.8	166.0	8.3	123.2	122.2
07SE34-12	IG	568	7245	2.6	20.9255	4.0	0.1100	4.2	0.0167	1.3	0.30	106.8	1.3	106.0	4.3	88.8	95.8
07SE34-13	IG	1768	1998	4.8	12.3930	5.6	0.5182	6.4	0.0466	3.0	0.47	293.5	8.5	423.9	22.1	1213.9	111.1
07SE34-14	IG	372	6039	1.5	22.2197	10.0	0.1069	10.2	0.0172	2.0	0.19	110.1	2.1	103.1	10.0	-55.4	244.8
07SE34-15	IG	787	7014	1.8	19.9600	2.8	0.1202	3.1	0.0174	1.4	0.46	111.2	1.6	115.2	3.4	199.6	64.0
07SE34-16	IG	740	10149	2.5	20.8734	2.6	0.1163	3.6	0.0176	2.5	0.70	112.5	2.8	111.7	3.8	94.7	60.9
07SE34-17	IG	519	6612	2.5	20.8777	5.1	0.1695	5.3	0.0257	1.5	0.28	163.4	2.4	159.0	7.8	94.2	120.8
07SE34-19	IG	243	12192	1.3	13.3065	1.1	1.6655	1.9	0.1607	1.5	0.79	960.9	13.2	995.5	11.8	1072.6	22.8
07SE34-20	IG	310	4482	6.9	21.3885	6.1	0.1046	6.2	0.0162	1.0	0.17	103.8	1.1	101.0	6.0	36.7	146.6
07SE34-21	IG	480	6117	2.3	21.3551	5.1	0.1100	5.2	0.0170	1.3	0.24	108.9	1.4	106.0	5.3	40.5	121.9
07SE34-22	IG	259	3741	2.9	20.6896	7.1	0.1744	7.3	0.0262	1.4	0.19	166.5	2.2	163.2	10.9	115.6	168.3
07SE34-23	IG	283	5745	3.9	21.6891	9.7	0.1036	10.6	0.0163	4.3	0.40	104.3	4.4	100.1	10.1	3.2	233.3
07SE34-24	IG	94	1521	3.4	20.1872	19.6	0.1308	19.7	0.0192	2.1	0.11	122.3	2.6	124.8	23.1	173.3	460.2
07SE34-25	IG	693	8955	1.9	20.7260	3.5	0.1156	3.9	0.0174	1.7	0.43	111.0	1.8	111.1	4.1	111.5	82.3
07SE34-26	IG	272	1974	3.9	21.1680	10.2	0.1095	10.3	0.0168	1.0	0.10	107.4	1.1	105.5	10.3	61.4	244.4
07SE34-27	IG	558	20424	6.1	18.2572	2.5	0.5228	3.6	0.0692	2.6	0.72	431.5	10.9	427.0	12.6	402.9	56.4
07SE34-28	IG	1699	30210	2.3	21.1152	3.8	0.1070	4.4	0.0164	2.2	0.50	104.8	2.3	103.2	4.3	67.4	90.3
07SE34-29	IG	444	5244	2.5	20.5106	3.2	0.1073	3.3	0.0160	1.0	0.29	102.1	1.0	103.5	3.3	136.1	74.3
07SE34-30	IG	1244	30027	4.1	14.1216	2.1	0.6423	4.8	0.0658	4.3	0.90	410.7	17.2	503.7	19.1	952.0	43.2
07SE34-31	IG	592	10155	1.8	19.2593	1.7	0.2985	2.2	0.0417	1.4	0.62	263.4	3.5	265.3	5.2	282.0	40.0
07SE34-32	IG	285	3573	2.7	20.7048	5.0	0.1098	5.5	0.0165	2.3	0.42	105.5	2.4	105.8	5.5	113.9	118.0
07SE34-33	IG	1299	24888	1.9	20.8026	2.1	0.1101	2.4	0.0166	1.2	0.49	106.2	1.2	106.0	2.4	102.8	50.3
07SE34-35	IG	740	8850	4.8	20.8668	7.3	0.1115	7.4	0.0169	0.8	0.11	107.9	0.9	107.3	7.5	95.5	173.4
07SE34-37	IG	404	5757	2.5	20.8111	6.7	0.1140	7.1	0.0172	2.4	0.34	110.0	2.7	109.7	7.4	101.8	158.9
07SE34-38	IG	200	2202	1.8	21.5126	11.0	0.1129	11.1	0.0176	1.4	0.13	112.6	1.6	108.6	11.4	22.8	263.7

Table A3.1 (Continued). LA-MC-ICPMS U-Pb detrital zircon data for the San Emigdio Schist[†].

Analysis	CL notes[#]	U (ppm)	$^{206}Pb/^{204}Pb$	U/Th	Isotope ratios							Isotopic ages (Ma)[§]					
					$^{206}Pb^*/^{207}Pb^*$	± (%)	$^{207}Pb^*/^{235}U^*$	± (%)	$^{206}Pb^*/^{238}U$	± (%)	Error correlation	$^{206}Pb^*/^{238}U$	± (Ma)	$^{207}Pb^*/^{235}U^*$	± (Ma)	$^{206}Pb^*/^{207}Pb^*$	± (Ma)
07SE34-39	IG	699	4788	3.1	20.2620	2.2	0.1135	2.7	0.0167	1.5	0.56	106.7	1.6	109.2	2.8	164.6	51.6
07SE34-40	IG	385	4581	4.2	20.7274	5.2	0.1123	5.4	0.0169	1.7	0.32	107.9	1.9	108.1	5.6	111.3	121.7
07SE34-41	IG	381	2475	1.9	13.6054	36.4	0.1691	36.4	0.0167	0.8	0.02	106.7	0.8	158.6	53.5	1027.8	760.3
07SE34-42	IG	2375	3060	4.5	15.9218	3.6	0.1843	3.6	0.0213	0.7	0.20	135.7	1.0	171.7	5.7	701.7	75.8
07SE34-43	IG	665	8898	3.8	19.7412	9.6	0.1239	9.9	0.0177	2.3	0.23	113.4	2.5	118.6	11.1	225.2	222.6
07SE34-44	IG	193	42399	2.7	9.5642	1.8	3.3284	4.5	0.2309	4.1	0.92	1339.1	49.7	1487.7	35.1	1706.5	33.3
07SE34-45	IG	204	6129	1.7	18.0605	2.9	0.5482	4.3	0.0718	3.2	0.74	447.0	13.9	443.8	15.6	427.1	64.6
07SE34-46	IG	1002	5802	2.9	20.4525	3.9	0.1050	4.0	0.0156	0.6	0.14	99.7	0.6	101.4	3.8	142.7	92.3
07SE34-47	IG	1180	3024	1.1	18.1216	13.3	0.1264	13.4	0.0166	0.9	0.07	106.2	1.0	120.9	15.2	419.6	298.8
07SE34-48	IG	213	4797	2.9	20.8290	5.6	0.1707	5.9	0.0258	1.8	0.30	164.2	2.9	160.1	8.7	99.7	132.9
07SE34-49	IG	1183	9561	2.6	20.6427	2.8	0.1104	3.0	0.0165	0.9	0.32	105.7	1.0	106.3	3.0	120.9	66.0
07SE34-50	IG	128	54291	3.4	9.6346	1.4	4.3072	1.5	0.3010	0.6	0.40	1696.1	9.1	1694.7	12.5	1693.0	25.6
07SE34-51	IG	632	7179	2.2	20.5504	5.2	0.1163	5.4	0.0173	1.5	0.28	110.7	1.6	111.7	5.7	131.5	121.3
07SE34-52	IG	800	9462	2.7	20.8686	2.4	0.1083	2.8	0.0164	1.3	0.48	104.8	1.4	104.4	2.7	95.2	57.6
07SE34-53	IG	1685	16896	3.4	20.6693	2.0	0.1072	2.9	0.0161	2.2	0.74	102.8	2.2	103.4	2.9	117.9	46.3
07SE34-54	IG	495	28407	3.1	13.2980	1.6	1.3854	3.1	0.1336	2.7	0.86	808.4	20.5	882.7	18.6	1073.9	32.6
07SE34-55	IG	190	3459	2.7	20.0288	13.3	0.1131	13.6	0.0164	2.7	0.20	105.1	2.8	108.8	14.0	191.7	310.5
07SE34-56	IG	204	1161	3.1	24.6418	19.8	0.0933	19.9	0.0167	1.8	0.09	106.6	1.9	90.6	17.3	-313.8	512.6
07SE34-57	IG	247	13851	0.6	16.9924	1.8	0.7388	3.4	0.0911	2.9	0.86	561.8	15.8	561.7	14.7	561.5	38.2
07SE34-58	IG	731	21207	2.9	21.1294	3.1	0.1081	4.0	0.0166	2.6	0.64	105.9	2.7	104.3	4.0	65.8	73.3
07SE34-59	IG	1211	12345	2.9	20.7170	2.9	0.1134	3.0	0.0170	0.9	0.31	108.9	1.0	109.1	3.1	112.5	67.5
07SE34-60	IG	803	8469	2.8	20.5818	3.2	0.1144	3.3	0.0171	1.0	0.30	109.2	1.1	110.0	3.4	128.0	74.2
07SE34-61	IG	369	3969	2.0	21.0505	6.3	0.1095	6.6	0.0167	1.7	0.26	106.9	1.8	105.5	6.6	74.7	150.9
07SE34-62	IG	411	5517	3.5	20.9441	5.9	0.1182	6.2	0.0180	1.9	0.31	114.7	2.1	113.4	6.6	86.7	139.0
07SE34-63	IG	836	2862	3.2	19.9238	2.8	0.1217	3.1	0.0176	1.4	0.45	112.4	1.6	116.6	3.4	203.8	64.4
07SE34-64	IG	108	4785	2.6	21.7939	12.7	0.1875	12.7	0.0296	1.2	0.10	188.2	2.3	174.5	20.4	-8.4	307.0
07SE34-65	IG	248	44925	4.4	12.9481	3.6	1.6441	9.4	0.1544	8.7	0.92	925.5	75.1	987.3	59.6	1127.2	72.4
07SE34-66	IG	443	8019	2.6	21.1285	6.0	0.1124	6.0	0.0172	0.6	0.10	110.1	0.6	108.2	6.1	65.9	141.9
07SE34-67	IG	123	32241	2.0	10.8198	1.7	3.3389	1.8	0.2620	0.6	0.35	1500.1	8.4	1490.2	14.1	1476.1	32.1
07SE34-68	IG	292	6381	2.1	22.5319	10.8	0.1015	10.9	0.0166	0.9	0.08	106.0	1.0	98.1	10.2	-89.5	266.2
07SE34-69	IG	1555	17739	2.0	20.6458	1.3	0.1157	2.0	0.0173	1.5	0.75	110.7	1.6	111.2	2.1	120.6	30.9
07SE34-70	IG	353	104184	2.0	10.9486	0.7	3.1799	1.6	0.2525	1.5	0.89	1451.4	19.1	1452.3	12.7	1453.6	14.1
07SE34-71	IG	185	3123	2.5	21.3291	7.8	0.1141	7.9	0.0176	1.3	0.17	112.8	1.5	109.7	8.2	43.3	186.4
07SE34-72	IG	273	6522	3.2	20.7578	5.7	0.1116	6.2	0.0168	2.4	0.38	107.4	2.5	107.4	6.3	107.9	135.2
07SE34-73	IG	800	12681	2.9	21.1801	3.5	0.1102	3.6	0.0169	0.5	0.14	108.2	0.5	106.1	3.6	60.1	83.9
07SE34-74	IG	555	8835	1.8	20.6995	3.0	0.1187	3.7	0.0178	2.1	0.57	113.9	2.4	113.9	4.0	114.5	71.4
07SE34-75	IG	169	2550	2.8	20.9426	7.6	0.1124	7.7	0.0171	1.2	0.16	109.1	1.3	108.1	7.9	86.9	181.2
07SE34-76	IG	216	2985	1.7	20.7796	6.7	0.1130	6.8	0.0170	1.2	0.17	108.9	1.3	108.7	7.0	105.4	158.3
07SE34-77	IG	586	5784	3.1	20.6925	2.3	0.1091	2.5	0.0164	1.1	0.42	104.7	1.1	105.2	2.5	115.3	54.3
07SE34-78	IG	761	7290	3.4	20.2841	2.1	0.1659	5.2	0.0244	4.7	0.91	155.4	7.2	155.8	7.5	162.1	49.0
07SE34-79	IG	956	13368	3.1	20.6134	2.2	0.1159	3.0	0.0173	2.1	0.68	110.7	2.3	111.3	3.2	124.3	51.9
07SE34-80	IG	1266	17070	2.7	20.9474	2.5	0.1108	3.0	0.0168	1.6	0.54	107.6	1.7	106.7	3.0	86.4	59.1
07SE34-81	IG	1521	14847	2.1	20.6535	1.6	0.1154	2.1	0.0173	1.3	0.64	110.5	1.4	110.9	2.2	119.8	37.6
07SE34-82	IG	672	8784	3.2	20.7386	32.8	0.1090	32.9	0.0164	1.8	0.05	104.8	1.8	105.0	32.8	110.0	794.4
07SE34-83	IG	863	4230	3.0	21.1085	5.4	0.1090	5.9	0.0167	2.4	0.40	106.7	2.5	105.0	5.9	68.1	128.7
07SE34-84	IG	197	1950	2.2	21.5076	12.4	0.1081	12.5	0.0169	1.7	0.14	107.8	1.8	104.2	12.4	23.4	298.4
07SE34-85	IG	538	5511	3.0	20.7713	3.7	0.1225	3.9	0.0185	1.2	0.31	117.9	1.4	117.4	4.4	106.3	88.4
07SE34-86	IG	233	3360	2.5	20.8147	12.2	0.1141	12.2	0.0172	0.6	0.05	110.1	0.7	109.7	12.7	101.4	289.3
07SE34-87	IG	177	60066	1.4	9.4484	1.1	4.4501	1.6	0.3049	1.2	0.74	1715.8	17.6	1721.7	13.2	1728.9	19.7
07SE34-88	IG	828	11844	2.9	20.9120	2.4	0.1162	2.5	0.0176	0.5	0.20	112.6	0.6	111.6	2.6	90.3	57.6
07SE34-89	IG	197	5928	2.4	20.4490	5.2	0.1748	5.5	0.0259	1.7	0.32	165.0	2.8	163.5	8.3	143.2	122.8
07SE34-90	IG	923	7164	2.8	21.1420	4.5	0.1054	4.8	0.0162	1.6	0.33	103.4	1.6	101.8	4.6	64.4	107.3
07SE34-91	IG	376	2985	1.7	20.5461	5.3	0.1317	5.6	0.0196	1.9	0.34	125.3	2.3	125.6	6.6	132.0	124.2
07SE34-92	IG	356	5109	2.2	19.9447	4.5	0.1840	4.7	0.0266	1.2	0.26	169.3	2.0	171.5	7.4	201.4	104.6
07SE34-93	IG	458	1716	5.3	20.1108	6.3	0.1085	6.4	0.0158	1.2	0.19	101.2	1.2	104.6	6.4	182.1	146.5
07SE34-94	IG	356	5625	2.4	20.7492	4.9	0.1202	5.0	0.0181	0.9	0.18	115.6	1.1	115.3	5.5	108.8	116.6
07SE34-95	IG	778	13818	3.3	20.9239	4.1	0.1081	4.3	0.0164	1.5	0.35	104.9	1.6	104.2	4.3	89.0	96.1
07SE34-97	IG	522	2865	1.8	20.5125	13.6	0.1332	13.6	0.0198	0.5	0.04	126.5	0.6	127.0	16.2	135.8	320.0
07SE34-98	IG	430	6429	2.4	21.1490	4.6	0.1103	4.8	0.0169	1.3	0.27	108.1	1.4	106.2	4.9	63.6	110.7
07SE34-99	IG	581	11643	2.8	20.7697	5.2	0.1115	5.8	0.0168	2.4	0.42	107.4	2.6	107.4	5.9	106.5	123.9
07SE34-100	IG	709	19890	6.8	19.7216	1.5	0.2219	1.9	0.0317	1.2	0.62	201.4	2.3	203.5	3.5	227.5	33.9

Table A3.1 (Continued). LA-MC-ICPMS U-Pb detrital zircon data for the San Emigdio Schist[†].

Analysis	CL notes[#]	U (ppm)	$^{206}Pb/^{204}Pb$	U/Th	Isotope ratios							Isotopic ages (Ma)[§]					
					$^{206}Pb^*/^{207}Pb^*$	± (%)	$^{207}Pb^*/^{235}U^*$	± (%)	$^{206}Pb^*/^{238}U$	± (%)	Error correlation	$^{206}Pb^*/^{238}U$	± (Ma)	$^{207}Pb^*/^{235}U^*$	± (Ma)	$^{206}Pb^*/^{207}Pb^*$	± (Ma)
08SE467	*San Emigdio Schist - San Emigdio Mountains*																
08SE467-1	IG	965	7478	3.5	21.0049	3.8	0.1363	4.1	0.0208	1.7	0.40	132.5	2.2	129.8	5.0	79.8	89.8
08SE467-2	IG	280	3718	2.2	21.3644	6.9	0.1592	7.0	0.0247	1.2	0.17	157.1	1.9	150.0	9.7	39.4	164.5
08SE467-3	IG	1534	11970	2.6	21.2329	2.7	0.1198	2.9	0.0185	1.1	0.37	117.9	1.3	114.9	3.2	54.1	64.3
08SE467-4	IG	1919	12452	2.3	21.1723	3.2	0.1203	3.9	0.0185	2.2	0.57	118.0	2.6	115.4	4.2	61.0	75.4
08SE467-5	IG	761	8394	3.5	20.6891	1.7	0.1246	2.9	0.0187	2.3	0.80	119.4	2.7	119.3	3.3	115.7	41.0
08SE467-6	IG	1146	9276	3.9	20.2810	4.1	0.1225	5.5	0.0180	3.6	0.66	115.1	4.1	117.3	6.1	162.5	97.1
08SE467-8	MM	3111	4658	1.8	19.4550	6.8	0.1032	9.3	0.0146	6.3	0.68	93.2	5.8	99.7	8.8	258.9	155.9
08SE467-9	IG	904	9838	3.2	19.8595	7.3	0.1280	7.4	0.0184	1.3	0.18	117.8	1.5	122.3	8.5	211.4	168.9
08SE467-10	IG	886	5244	3.5	20.8937	3.6	0.1211	4.1	0.0184	1.9	0.48	117.3	2.3	116.1	4.5	92.4	84.8
08SE467-11	IG	1060	9172	5.8	20.5317	4.8	0.1303	5.0	0.0194	1.4	0.27	123.9	1.7	124.4	5.9	133.7	113.5
08SE467-13	IG	2073	16396	7.4	20.8950	2.2	0.1220	2.3	0.0185	0.8	0.36	118.1	1.0	116.9	2.5	92.3	51.0
08SE467-14	IG	1676	9654	1.7	21.0473	2.0	0.1226	2.5	0.0187	1.6	0.63	119.6	1.9	117.5	2.8	75.0	46.9
08SE467-15	IG	184	4390	8.1	18.4773	6.0	0.2355	7.2	0.0316	3.9	0.55	200.3	7.8	214.7	13.9	376.0	134.7
08SE467-16	MM	3197	11290	1.6	20.7194	2.2	0.0957	5.8	0.0144	5.4	0.93	92.0	4.9	92.8	5.2	112.2	51.7
08SE467-17	IG	642	7842	1.9	20.6723	4.3	0.1614	4.4	0.0242	0.8	0.18	154.1	1.2	151.9	6.2	117.6	102.2
08SE467-18	IG	1495	9252	2.0	20.0775	4.9	0.1143	6.1	0.0166	3.6	0.60	106.4	3.8	109.9	6.3	186.0	113.2
08SE467-19	IG	1282	10900	14.3	20.9012	2.6	0.1153	3.1	0.0175	1.8	0.56	111.7	1.9	110.8	3.3	91.5	60.6
08SE467-20	IG	814	6022	30.1	20.1643	4.2	0.1121	9.0	0.0164	8.0	0.88	104.8	8.3	107.9	9.2	175.9	97.6
08SE467-21	IG	172	2226	2.4	20.2952	24.3	0.1088	24.4	0.0160	2.2	0.09	102.4	2.2	104.8	24.3	160.9	576.5
08SE467-23	IG	782	8354	38.3	20.9580	5.9	0.1105	5.9	0.0168	0.5	0.08	107.4	0.5	106.4	6.0	85.2	140.6
08SE467-24	IG	899	8076	5.6	21.3893	3.4	0.1054	5.6	0.0164	4.5	0.80	104.6	4.6	101.8	5.4	36.6	80.4
08SE467-27	IG	2584	8750	4.6	20.5799	2.4	0.1156	2.7	0.0173	1.3	0.49	110.3	1.5	111.1	2.9	128.2	56.0
08SE467-28	IG	1955	2756	16.0	16.2838	19.3	0.1383	19.4	0.0163	1.8	0.10	104.4	1.9	131.5	23.9	653.7	417.2
08SE467-29	IG	243	2148	3.4	20.4504	17.1	0.1123	17.1	0.0167	1.3	0.07	106.5	1.4	108.1	17.6	143.0	403.2
08SE467-30	IG	881	7666	3.2	21.1334	3.5	0.1224	3.7	0.0188	1.4	0.37	119.9	1.6	117.3	4.1	65.3	82.5
08SE467-31	IG	284	1944	1.2	21.5657	5.4	0.1438	5.5	0.0225	1.1	0.20	143.4	1.5	136.4	7.0	16.9	128.9
08SE467-32	IG	2085	8416	2.6	20.3486	2.8	0.1163	3.8	0.0172	2.5	0.67	109.7	2.7	111.7	4.0	154.7	65.7
08SE467-33	IG	591	9114	6.0	21.2713	3.5	0.1197	4.0	0.0185	2.0	0.49	118.0	2.3	114.8	4.4	49.8	83.2
08SE467-34	IG	1092	9906	9.4	20.6130	2.8	0.1067	5.4	0.0159	4.6	0.86	102.0	4.7	102.9	5.3	124.3	65.5
08SE467-35	IG	357	7976	1.6	18.1155	1.8	0.4314	3.8	0.0567	3.3	0.88	355.4	11.4	364.2	11.5	420.4	40.7
08SE467-36	IG	2115	13476	2.0	20.7693	1.4	0.1143	2.9	0.0172	2.5	0.87	110.0	2.7	109.9	3.0	106.5	33.6
08SE467-37	IG	2320	7436	6.3	20.3727	2.3	0.1131	7.0	0.0167	6.6	0.95	106.8	7.0	108.8	7.2	151.9	53.5
08SE467-39	IG	2173	11298	1.7	21.2314	2.5	0.1144	3.0	0.0176	1.7	0.56	112.6	1.9	110.0	3.1	54.3	59.3
08SE467-38	IG	408	11934	11.9	18.9591	2.4	0.3799	2.6	0.0522	1.1	0.42	328.3	3.5	327.0	7.3	317.8	53.9
08SE467-42	IG	62	4056	1.8	17.8849	9.0	0.5663	9.2	0.0735	1.8	0.20	457.0	8.1	455.6	33.8	448.9	201.1
08SE467-43	IG	1481	10362	2.1	20.8274	2.4	0.1186	2.7	0.0179	1.1	0.42	114.5	1.3	113.8	2.9	99.9	57.3
08SE467-44	IG	647	6272	24.0	20.8390	3.6	0.1062	3.7	0.0160	1.1	0.31	102.6	1.2	102.5	3.6	98.6	84.2
08SE467-45	IG	1175	9090	3.7	20.8822	1.7	0.1143	3.1	0.0173	2.6	0.84	110.7	2.8	109.9	3.2	93.7	39.5
08SE467-46	IG	903	6758	3.1	20.9220	2.3	0.1211	2.4	0.0184	0.5	0.21	117.3	0.6	116.0	2.6	89.2	55.2
08SE467-47	IG	1138	7490	3.9	20.6873	1.3	0.1276	1.6	0.0191	0.9	0.57	122.2	1.1	121.9	1.8	115.9	30.7
08SE467-48	IG	1087	7534	2.6	21.0042	4.3	0.1234	4.7	0.0188	1.9	0.40	120.1	2.2	118.2	5.2	79.9	102.1
08SE467-49	IG	935	5584	6.5	20.6227	3.1	0.1153	3.3	0.0172	1.3	0.38	110.2	1.4	110.8	3.5	123.2	72.9
08SE467-50	IG	205	1878	15.1	23.3931	11.9	0.0996	12.0	0.0169	0.7	0.06	108.0	0.7	96.4	11.0	-182.3	299.2
08SE467-51	IG	1952	14714	4.5	20.4508	2.8	0.1080	4.9	0.0160	4.0	0.81	102.5	4.0	104.2	4.8	143.0	66.4
08SE467-52	MM	2411	4148	11.3	18.9007	8.4	0.1113	8.4	0.0153	1.3	0.15	97.6	1.2	107.2	8.6	324.9	189.9
08SE467-53	IG	2886	10868	9.5	18.6062	8.0	0.1274	8.5	0.0172	2.7	0.32	109.9	3.0	121.8	9.7	360.4	181.7
08SE467-54	IG	1995	13986	6.5	20.8500	2.2	0.1178	2.5	0.0178	1.1	0.44	113.8	1.2	113.1	2.6	97.4	52.0
08SE467-55	IG	2005	10568	2.5	20.7271	5.9	0.1053	8.1	0.0158	5.5	0.68	101.3	5.5	101.7	7.8	111.4	139.2
08SE467-56	IG	1576	10104	2.8	20.7695	2.8	0.1195	3.4	0.0180	1.9	0.57	115.0	2.2	114.6	3.7	106.5	65.5
08SE467-57	IG	2476	6228	53.2	20.0714	3.5	0.1133	3.6	0.0165	1.2	0.32	105.4	1.2	108.9	3.8	186.7	80.5
08SE467-58	IG	219	2280	10.6	21.4431	4.7	0.1404	8.2	0.0218	6.7	0.82	139.2	9.2	133.4	10.2	30.6	113.9
08SE467-59	IG	2802	13994	24.1	20.4315	1.3	0.1250	1.5	0.0185	0.9	0.57	118.3	1.0	119.6	1.7	145.1	29.7
08SE467-60	IG	183	1862	11.0	18.1111	24.7	0.1709	25.0	0.0224	4.0	0.16	143.1	5.7	160.2	37.0	420.9	558.0
08SE467-61	IG	1566	10430	6.4	20.6625	1.3	0.1195	2.4	0.0179	2.0	0.83	114.4	2.3	114.6	2.6	118.7	31.7
08SE467-62	IG	927	6398	6.0	20.6886	3.2	0.1264	3.4	0.0190	0.9	0.26	121.1	1.0	120.8	3.8	115.8	76.5
08SE467-63	IG	2790	10196	2.5	20.3865	2.1	0.1200	3.4	0.0177	2.7	0.79	113.4	3.0	115.1	3.7	150.3	48.8
08SE467-65	IG	992	16270	8.0	19.7121	1.7	0.1981	2.5	0.0283	1.8	0.74	180.1	3.3	183.6	4.2	228.6	39.0
08SE467-66	IG	1103	7526	11.7	21.0548	3.8	0.1144	4.6	0.0175	2.6	0.55	111.7	2.8	110.0	4.8	74.2	91.2
08SE467-67	IG	190	1380	2.7	24.5385	16.0	0.0934	16.1	0.0166	1.8	0.11	106.3	1.9	90.6	14.0	-303.0	411.5
08SE467-68	IG	922	6984	5.6	20.4619	3.5	0.1238	5.7	0.0184	4.5	0.79	117.4	5.2	118.5	6.4	141.7	82.7
08SE467-69	IG	1562	2478	3.9	18.7951	6.1	0.1326	6.1	0.0181	0.7	0.11	115.5	0.8	126.5	7.3	337.6	138.3

Table A3.1 (Continued). LA-MC-ICPMS U-Pb detrital zircon data for the San Emigdio Schist[†].

Analysis	CL notes[#]	U (ppm)	$^{206}Pb/^{204}Pb$	U/Th	Isotope ratios							Isotopic ages (Ma)[§]					
					$^{206}Pb^*/^{207}Pb^*$	± (%)	$^{207}Pb^*/^{235}U^*$	± (%)	$^{206}Pb^*/^{238}U$	± (%)	Error correlation	$^{206}Pb^*/^{238}U$	± (Ma)	$^{207}Pb^*/^{235}U^*$	± (Ma)	$^{206}Pb^*/^{207}Pb^*$	± (Ma)
08SE467-70	IG	410	2286	2.0	21.7687	6.6	0.1141	6.7	0.0180	0.6	0.09	115.1	0.7	109.7	6.9	-5.6	160.2
08SE467-71	IG	1139	9142	16.2	20.9853	1.6	0.1109	3.0	0.0169	2.6	0.85	107.9	2.7	106.8	3.0	82.0	36.9
08SE467-72	IG	1497	3326	6.9	17.3723	12.5	0.1790	13.2	0.0226	4.3	0.33	143.8	6.1	167.2	20.3	513.1	274.8
08SE467-73	IG	1521	8862	4.2	20.6971	1.5	0.1148	4.0	0.0172	3.7	0.93	110.1	4.1	110.4	4.2	114.7	35.0
08SE467-74	IG	1947	10910	4.4	20.3079	3.9	0.1191	4.1	0.0175	1.3	0.31	112.1	1.4	114.3	4.5	159.4	91.9
08SE467-75	IG	2661	1470	12.6	17.1410	8.9	0.1400	8.9	0.0174	0.9	0.10	111.2	0.9	133.0	11.1	542.5	194.8
08SE467-1b	IG	1351	3806	3.9	23.6818	13.4	0.0963	17.3	0.0165	10.9	0.63	105.8	11.4	93.4	15.4	-213.0	337.6
08SE467-3b	MM	2944	3951	28.9	21.0166	6.2	0.0935	6.9	0.0142	3.0	0.44	91.2	2.7	90.7	6.0	78.5	146.6
08SE467-4b	IG	471	1198	2.9	23.5797	18.0	0.0990	19.0	0.0169	6.3	0.33	108.2	6.7	95.9	17.4	-202.1	454.0
08TC37	*San Emigdio Schist - Tehachapi Mountains*																
08TC37-1	IG	625	11047	0.9	21.1954	5.3	0.1708	6.4	0.0263	3.5	0.54	167.0	5.7	160.1	9.4	58.4	127.5
08TC37-2	IG	773	10980	2.0	20.9789	9.4	0.1046	10.4	0.0159	4.4	0.42	101.8	4.5	101.0	10.0	82.8	223.7
08TC37-3	IG	295	5843	1.1	22.3059	33.7	0.1135	34.0	0.0184	4.2	0.12	117.3	4.8	109.2	35.2	-64.8	843.7
08TC37-4	IG	323	11308	1.6	18.6106	17.1	0.1272	18.2	0.0172	6.2	0.34	109.7	6.8	121.6	20.8	359.8	387.3
08TC37-5	IG	143	61448	1.0	5.3064	1.0	13.8034	2.6	0.5312	2.4	0.92	2746.6	53.6	2736.3	24.7	2728.7	16.9
08TC37-6	IG	339	10600	1.1	19.0822	12.7	0.1928	13.2	0.0267	3.5	0.26	169.7	5.8	179.0	21.6	303.1	290.5
08TC37-7	IG	441	23677	1.6	19.7302	9.5	0.2046	9.5	0.0293	1.2	0.12	186.0	2.2	189.0	16.4	226.5	219.1
08TC37-8	IG	84	2244	2.3	23.0457	129.1	0.1399	129.1	0.0234	2.6	0.02	149.1	3.9	133.0	162.3	-145.0	1441.1
08TC37-10	IG	420	13518	1.0	20.6417	14.3	0.1331	14.4	0.0199	1.4	0.10	127.2	1.8	126.9	17.1	121.1	337.9
08TC37-12	IG	105	4732	1.8	15.4158	26.8	0.2001	26.8	0.0224	1.4	0.05	142.7	1.9	185.2	45.4	770.1	573.6
08TC37-13	IG	487	11793	2.0	21.4394	19.4	0.0946	19.5	0.0147	2.7	0.14	94.2	2.5	91.8	17.2	31.0	467.5
08TC37-14	IG	196	8510	2.5	19.5358	27.2	0.1825	27.3	0.0259	1.5	0.06	164.6	2.5	170.2	42.8	249.3	637.2
08TC37-15	IG	670	79277	8.8	17.3267	2.4	0.6044	4.9	0.0760	4.2	0.87	471.9	19.3	480.0	18.6	518.9	53.0
08TC37-16	IG	240	161531	1.5	9.5291	1.5	4.3856	2.5	0.3031	1.9	0.79	1706.6	29.2	1709.6	20.4	1713.3	27.8
08TC37-17	IG	311	9677	1.0	19.6938	20.0	0.1782	20.3	0.0255	3.4	0.17	162.0	5.4	166.5	31.1	230.7	465.8
08TC37-18	IG	436	22722	5.4	16.5948	6.7	0.5897	7.1	0.0710	2.3	0.33	442.0	10.0	470.7	26.7	612.9	144.4
08TC37-19	IG	807	5316	1.2	22.0355	15.1	0.0926	15.3	0.0148	2.4	0.16	94.7	2.3	89.9	13.2	-35.1	368.1
08TC37-20	IG	1197	29824	3.5	20.8740	5.1	0.1236	7.6	0.0187	5.6	0.74	119.5	6.6	118.3	8.5	94.7	121.4
08TC37-22	IG	165	77761	1.2	8.7422	1.9	5.5227	5.7	0.3502	5.4	0.94	1935.4	89.6	1904.1	49.0	1870.3	34.7
08TC37-24	IG	1080	24097	0.9	20.2104	13.3	0.0991	13.6	0.0145	2.8	0.21	93.0	2.6	96.0	12.5	170.6	312.1
08TC37-25	IG	128	3615	2.1	16.9583	44.0	0.1495	44.1	0.0184	2.8	0.06	117.4	3.2	141.5	58.3	565.9	1004.7
08TC37-26	IG	296	7927	1.3	21.0323	24.4	0.1789	24.8	0.0273	4.4	0.18	173.6	7.5	167.1	38.2	76.7	587.7
08TC37-27	IG	274	14142	1.5	20.5465	21.1	0.2120	21.2	0.0316	2.2	0.10	200.5	4.3	195.3	37.7	132.0	501.1
08TC37-28	IG	949	24931	1.8	21.8711	8.9	0.0923	9.5	0.0146	3.4	0.35	93.7	3.1	89.6	8.2	-17.0	215.4
08TC37-29	IG	85	25015	3.1	10.5101	3.7	3.1986	5.4	0.2438	4.0	0.74	1406.5	51.0	1456.8	42.2	1531.0	68.9
08TC37-30	IG	1090	18981	2.3	22.2230	10.9	0.0877	11.0	0.0141	1.8	0.16	90.5	1.6	85.3	9.0	-55.7	265.8
08TC37-32	IG	659	26131	2.4	19.4098	8.5	0.1499	8.7	0.0211	1.9	0.22	134.7	2.5	141.9	11.5	264.2	194.3
08TC37-33	IG	431	12305	1.8	19.2737	17.7	0.1495	18.1	0.0209	3.8	0.21	133.3	5.0	141.4	23.9	280.3	407.5
08TC37-34	IG	497	17445	1.9	23.5408	12.7	0.0880	13.3	0.0150	3.9	0.30	96.1	3.7	85.6	10.9	-198.0	318.2
08TC37-35	IG	4100	7766	0.4	19.7323	3.7	0.1749	4.0	0.0250	1.4	0.35	159.4	2.2	163.7	6.0	226.2	85.7
08TC37-36	IG	104	2314	2.7	19.7843	114.1	0.1192	114.2	0.0171	5.1	0.04	109.3	5.5	114.4	124.1	220.1	982.9
08TC37-37	IG	303	6718	2.4	21.9557	21.4	0.1030	22.2	0.0164	5.6	0.25	104.9	5.8	99.6	21.0	-26.3	524.7
08TC37-38	IG	1079	18536	1.8	20.4104	5.2	0.0926	5.5	0.0137	1.7	0.31	87.8	1.5	89.9	4.7	147.6	122.1
08TC37-39	IG	130	3322	3.3	20.3238	34.7	0.1295	37.7	0.0191	14.8	0.39	121.9	17.9	123.6	43.9	157.5	834.7
08TC37-40	IG	556	7739	2.3	21.2015	25.1	0.1072	25.5	0.0165	4.7	0.18	105.4	4.9	103.4	25.1	57.6	606.6
08TC37-41	IG	669	10939	2.0	23.0075	10.6	0.0860	11.6	0.0144	4.7	0.40	91.9	4.2	83.8	9.3	-140.9	264.0
08TC37-42	IG	846	33991	2.0	20.3345	7.6	0.1603	9.1	0.0236	5.1	0.55	150.7	7.5	151.0	12.8	156.3	178.1
08TC37-43	IG	167	52464	2.5	8.8235	0.8	4.8203	5.2	0.3085	5.2	0.99	1733.2	78.3	1788.4	43.9	1853.5	14.7
08TC37-45	IG	56	1445	2.2	27.9897	95.3	0.1124	95.4	0.0228	3.8	0.04	145.4	5.5	108.1	98.1	-651.7	1524.0
08TC37-46	IG	841	25926	2.4	19.8730	6.0	0.1113	7.1	0.0160	3.9	0.55	102.6	4.0	107.2	7.2	209.8	138.2
08TC37-47	IG	2218	42412	1.2	20.2778	2.7	0.1163	3.7	0.0171	2.5	0.68	109.4	2.7	111.8	3.9	162.8	64.0
08TC37-48	IG	131	2607	2.5	12.9427	105.2	0.1758	105.4	0.0165	5.6	0.05	105.5	5.8	164.4	161.3	1128.0	254.9
08TC37-50	IG	123	6808	2.3	28.5034	30.2	0.1466	30.6	0.0303	4.4	0.14	192.4	8.4	138.9	39.7	-702.0	856.0
08TC37-51	IG	196	8043	1.2	22.3790	14.8	0.1669	15.8	0.0271	5.4	0.34	172.3	9.2	156.8	22.9	-72.8	363.4
08TC37-52	IG	297	14148	2.9	19.0832	15.9	0.1454	16.5	0.0201	4.1	0.25	128.4	5.2	137.8	21.2	303.0	365.6
08TC37-53	IG	196	5461	2.5	36.0481	42.7	0.0620	42.8	0.0162	3.1	0.07	103.6	3.2	61.0	25.4	-1406.3	1439.7
08TC37-54	IG	41	1258	2.4	10.0223	115.8	0.2320	115.8	0.0169	1.9	0.02	107.8	2.0	211.8	225.0	1619.9	5.1
08TC37-55	IG	591	14176	2.3	22.0513	20.2	0.1054	21.1	0.0169	6.0	0.29	107.7	6.4	101.7	20.4	-36.9	494.3
08TC37-56	IG	170	14018	2.4	25.7058	27.1	0.1634	27.2	0.0305	2.2	0.08	193.4	4.1	153.7	38.9	-423.4	722.4
08TC37-57	IG	346	12044	2.5	22.4625	27.4	0.0884	27.6	0.0144	3.5	0.13	92.2	3.2	86.0	22.8	-81.9	682.6
08TC37-58	IG	245	10648	2.5	21.1696	12.4	0.1839	12.7	0.0282	2.4	0.19	179.5	4.3	171.4	20.0	61.2	297.2
08TC37-59	IG	840	14134	1.5	21.3232	13.8	0.0987	14.2	0.0153	3.3	0.23	97.6	3.2	95.5	12.9	44.0	330.5

Table A3.1 (Continued). LA-MC-ICPMS U-Pb detrital zircon data for the San Emigdio Schist†.

Analysis	CL notes#	U (ppm)	$^{206}Pb/^{204}Pb$	U/Th	Isotope ratios							Isotopic ages (Ma)§					
					$^{206}Pb^*/^{207}Pb^*$	± (%)	$^{207}Pb^*/^{235}U^*$	± (%)	$^{206}Pb^*/^{238}U$	± (%)	Error correlation	$^{206}Pb^*/^{238}U$	± (Ma)	$^{207}Pb^*/^{235}U^*$	± (Ma)	$^{206}Pb^*/^{207}Pb^*$	± (Ma)
08TC37-60	IG	228	16233	1.9	22.5537	28.2	0.1844	28.5	0.0302	3.6	0.13	191.6	6.8	171.9	45.0	-91.8	704.4
08TC37-61	IG	395	4627	2.6	20.0055	22.5	0.1066	22.8	0.0155	3.2	0.14	98.9	3.2	102.8	22.3	194.4	530.0
08TC37-62	IG	255	3224	1.9	16.9904	27.2	0.1428	27.2	0.0176	1.7	0.06	112.5	1.9	135.6	34.5	561.8	601.9
08TC37-63	IG	248	16553	1.7	23.1470	21.4	0.1659	21.5	0.0279	1.1	0.05	177.1	2.0	155.9	31.0	-155.9	537.7
08TC37-64	IG	90	2648	2.9	12.7553	74.9	0.2165	75.1	0.0200	5.2	0.07	127.9	6.5	199.0	136.5	1157.0	1799.4
08TC37-65	IG	405	10156	3.0	20.7621	17.4	0.1104	17.6	0.0166	2.5	0.14	106.2	2.7	106.3	17.8	107.4	414.6
08TC37-66	IG	127	3754	1.4	17.5994	205.4	0.1637	205.4	0.0209	3.6	0.02	133.3	4.7	154.0	302.0	484.6	1482.9
08TC37-67	IG	1184	17749	1.8	21.9923	7.8	0.1013	7.9	0.0162	1.1	0.14	103.3	1.2	98.0	7.4	-30.4	189.0
08TC37-68	IG	97	1744	1.8	20.2710	55.5	0.1166	55.7	0.0171	4.7	0.09	109.6	5.2	112.0	59.1	163.6	1401.9
08TC37-69	IG	167	9801	2.6	21.5585	18.9	0.3778	19.4	0.0591	4.0	0.21	370.0	14.6	325.4	54.0	17.7	458.4
08TC37-70	IG	197	8247	2.1	19.7961	18.0	0.1750	18.1	0.0251	2.4	0.13	160.0	3.9	163.8	27.5	218.8	419.1
08TC37-71	IG	1806	118191	1.8	20.8138	4.8	0.1709	5.3	0.0258	2.4	0.45	164.2	3.8	160.2	7.9	101.5	112.6
08TC37-72	IG	472	20360	2.8	25.1098	23.7	0.0889	23.8	0.0162	2.3	0.10	103.5	2.4	86.5	19.8	-362.3	621.3
08TC37-73	IG	242	35306	1.6	15.4368	18.6	0.3146	22.5	0.0352	12.7	0.56	223.1	27.9	277.7	54.8	767.2	394.6
08TC37-74	IG	194	12910	1.0	22.3642	38.5	0.1433	38.6	0.0232	2.4	0.06	148.1	3.5	136.0	49.2	-71.2	973.7
08TC37-75	IG	234	1160	2.0	15.9090	34.9	0.1304	35.0	0.0150	3.0	0.09	96.3	2.9	124.5	41.0	703.4	764.0
08TC37-76	IG	179	3571	2.7	28.2700	67.6	0.0695	67.7	0.0142	3.4	0.05	91.2	3.1	68.2	44.7	-679.2	2096.9
08TC37-77	IG	267	15883	2.4	20.4651	11.1	0.1996	11.4	0.0296	2.5	0.22	188.2	4.6	184.8	19.2	141.3	260.7
08TC37-78	IG	1605	58940	2.5	20.5508	9.9	0.1058	10.3	0.0158	2.7	0.26	100.9	2.7	102.2	10.0	131.5	234.1
08TC37-79	IG	1201	65991	4.9	21.3243	6.3	0.1338	6.5	0.0207	1.1	0.18	132.1	1.5	127.5	7.7	43.9	151.9
08TC37-80	IG	230	7045	4.0	26.4700	29.8	0.1562	30.1	0.0300	4.0	0.13	190.5	7.5	147.4	41.3	-500.7	808.6
08TC37-81	IG	764	13511	4.5	20.1509	12.4	0.1061	12.6	0.0155	2.1	0.17	99.2	2.1	102.4	12.3	177.5	291.0
08TC37-82	IG	475	15989	4.3	22.2909	20.2	0.1194	20.5	0.0193	3.5	0.17	123.2	4.2	114.5	22.2	-63.2	497.6
08TC37-83	IG	217	7407	7.2	17.0423	29.8	0.1534	30.1	0.0190	4.1	0.14	121.1	5.0	144.9	40.6	555.1	663.1
08TC37-84	IG	382	32118	4.6	19.1652	25.2	0.1078	25.4	0.0150	3.0	0.12	95.9	2.8	103.9	25.1	293.2	584.2
08TC37-85	IG	440	12062	2.6	21.1306	14.7	0.1105	15.6	0.0169	5.1	0.33	108.2	5.4	106.4	15.7	65.6	351.7
08TC37-86	IG	287	9299	2.5	20.7417	13.1	0.1607	13.3	0.0242	2.1	0.16	154.0	3.2	151.3	18.6	109.7	310.2
08TC37-87	IG	315	10266	8.3	22.4174	28.9	0.1594	29.1	0.0259	3.1	0.11	164.9	5.0	150.1	40.6	-77.0	720.2
08TC37-88	IG	347	5355	4.5	17.7000	16.0	0.1901	16.3	0.0244	2.9	0.18	155.4	4.5	176.7	26.4	472.0	356.5
08TC37-90	IG	620	17742	4.2	22.0656	16.9	0.0961	17.0	0.0154	1.7	0.10	98.4	1.6	93.2	15.2	-38.4	414.0
08TC37-91	IG	324	5925	5.2	28.9017	28.1	0.0761	28.2	0.0159	1.5	0.05	102.0	1.5	74.4	20.2	-740.7	800.8
08TC37-92	IG	377	9627	3.8	19.7375	19.3	0.1118	19.8	0.0160	4.6	0.23	102.4	4.7	107.6	20.3	225.6	449.8
08TC37-93	IG	629	15655	7.1	24.4308	17.9	0.0843	18.0	0.0149	2.2	0.12	95.6	2.1	82.2	14.2	-291.8	459.8
08TC37-94	IG	132	8739	5.9	24.9940	47.7	0.1660	47.8	0.0301	2.3	0.05	191.1	4.3	155.9	69.2	-350.3	1297.2
08TC37-95	IG	189	8914	4.5	18.8275	34.6	0.1249	35.1	0.0171	5.5	0.16	109.1	5.9	119.5	39.6	333.7	807.3
08TC37-96	IG	130	939	3.5	20.0176	22.2	0.1955	22.7	0.0284	4.8	0.21	180.4	8.5	181.3	37.7	193.0	521.5
08TC37-97	IG	386	3120	5.9	25.6609	21.8	0.1028	21.9	0.0191	2.6	0.12	122.1	3.2	99.3	20.7	-418.8	575.4
08TC37-98	IG	539	8758	5.1	20.9484	10.3	0.1791	10.8	0.0272	3.0	0.28	173.1	5.2	167.3	16.6	86.2	245.4
08TC37-99	IG	389	92596	2.6	19.1899	15.4	0.1868	15.6	0.0260	2.7	0.17	165.4	4.3	173.9	24.9	290.3	353.2
08TC37-100	IG	245	10432	4.9	18.4095	24.1	0.1697	24.4	0.0227	4.1	0.17	144.4	5.9	159.2	36.0	384.3	548.4

* Radiogenic.

§ Decay constants used in age calculations: $\lambda^{238}U = 1.55125 \times 10^{-10}$ $\lambda^{235}U = 9.8485 \times 10^{-10}$ (Jaffey *et al*., 1971); $^{238}U/^{235}U = 137.88$ (Chen and Wasserberg, 1981). Uncertainties are given as ± 2σ in last three figures.

Common Pb correction from measured $^{206}Pb/^{204}Pb$, with initial Pb composition from Stacey and Kramers (1975).

CL: Cathodoluminescence; IG: Oscillatory zoned zircon, interpreted to be detrital igneous grain; MM: Convolute zoning domain, interpreted to be metamorphic zircon.

† Analyses in which epoxy was overlapped and those with greater than 10% uncertainty, 30% discordance, and/or 5% reverse discordance are excluded. Accepted ages calculated using $^{206}Pb/^{238}U$ ages for grains younger than 800 Ma and $^{207}Pb/^{206}Pb$ ages for grains older than 800 Ma.

Microanalysis. Grain mounts used in U-Pb analysis were polished with 0.25 μm colloidal silica and gold coated prior to SIMS analysis. Zircons were sputtered using a 2 nA $^{133}Cs^{+}$ primary ion beam with 20x30 μm diameter, secondary ions were extracted at 10 kV, and $^{16}O^{-}$ and $^{18}O^{-}$ were measured simultaneously using electron multiplier detectors and $^{18}O/^{16}O$ isotope ratios were derived. Each analysis involved 10 to 60 seconds of pre-sputtering, followed by 10 to 20 cycles of data collection, resulting in a total analysis time of 2 to 5 minutes per spot. Instrumental mass fractionation (IMF) was corrected for, using raw isotopic ratios, by bracketing sample and R33 standard (5.55 ± 0.04‰; Valley, 2003) analyses every 5 to 10 measurements. Finally, $\delta^{18}O_{VSMOW}$ values were calculated using IMF-corrected isotopic ratios. The internal precision on each standard analysis based on counting statistics was typically between ±0.25‰ and ±0.8‰ (2σ) and spot-to-spot reproducibility was typically better than 0.6‰. Oxygen isotope data is presented in Table A3.2 and Figure A3.4.

Figure A3.4. Probability density plots for schist (a) and upper plate (b) zircon $\delta^{18}O$ measurements showing weighted mean values and 2σ uncertainties. Bins of analyses from igneous and metamorphic domains are white and gray, respectively. Probability density curves for igneous and metamorphic domains are black and gray, respectively.

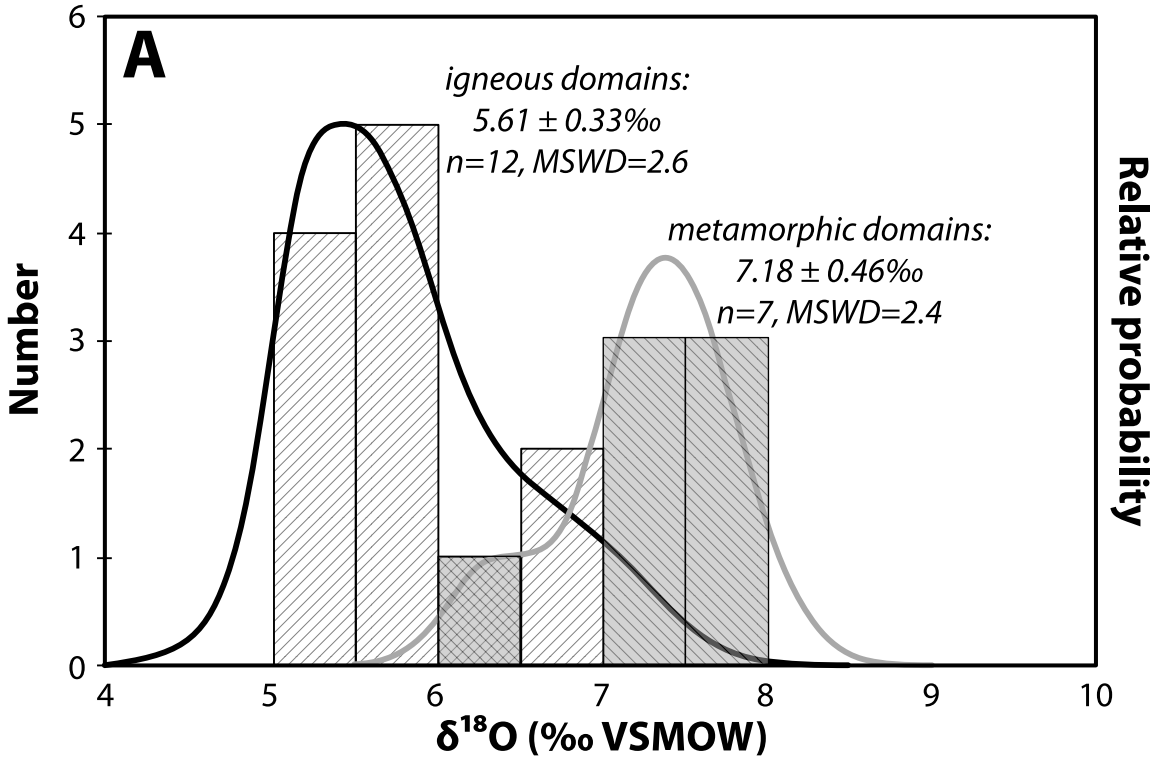
A
igneous domains:
5.61 ± 0.33‰
n=12, MSWD=2.6
metamorphic domains:
7.18 ± 0.46‰
n=7, MSWD=2.4
Number
Relative probability
δ18O (‰ VSMOW)

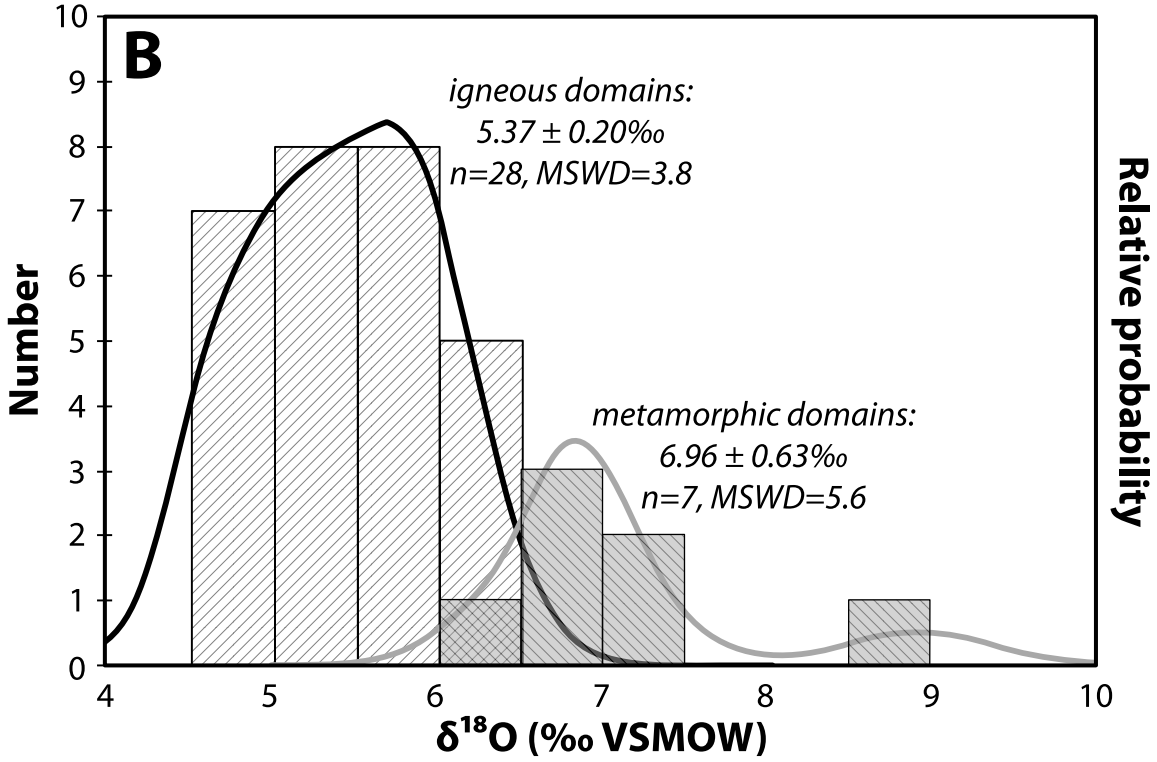
B
igneous domains:
5.37 ± 0.20‰
n=28, MSWD=3.8
metamorphic domains:
6.96 ± 0.63‰
n=7, MSWD=5.6
Number
Relative probability
δ18O (‰ VSMOW)

Table A3.2. SIMS zircon oxygen isotope data.

Analysis	CL notes[§]	Measured $^{18}O/^{16}O$ ($x10^{-3}$)	± ($x10^{-3}$)*	$\delta^{18}O_{VSMOW}$ (‰)	± (‰)*
06SE23	*San Emigdio Schist - San Emigdio Mountains*				
06SE23_det1IG.asc	IG	2.0099	0.000428	5.2	0.4
06SE23_det1b.asc	IG	2.0112	0.000817	5.5	0.5
06SE23_det1MM2.asc	MM	2.0136	0.000900	6.3	0.5
06SE23_2.asc	MM	2.0162	0.001026	7.3	0.6
08SE467	*San Emigdio Schist - San Emigdio Mountains*				
08SE467_1.asc	IG	2.0230	0.000785	6.3	0.8
08SE467_2.asc	IG	2.0214	0.000750	5.6	0.8
08SE467_8.asc	IG	2.0237	0.001382	6.8	1.0
08SE467_9.asc	IG	2.0236	0.000921	6.9	0.8
08SE467_9.asc	IG	2.0212	0.000461	5.8	0.7
08SE467_9b.asc	IG	2.0213	0.000576	5.9	0.7
08SE467_12.asc	IG	2.0209	0.000590	5.8	0.7
08SE467_12b.asc	IG	2.0195	0.000583	5.2	0.7
08SE467_14.asc	IG	2.0194	0.000920	5.3	0.8
08SE467_14.asc	IG	2.0194	0.000836	5.4	0.7
08SE467_14MM.asc	MM	2.0238	0.000738	7.7	0.7
08SE467_14MM2.asc	MM	2.0233	0.001028	7.5	0.8
08SE467_15.asc	MM	2.0222	0.000635	7.1	0.6
08SE467_23.asc	OL	2.0212	0.000900	6.7	0.7
08SE467_25.asc	OL	2.0204	0.001128	6.4	0.8
08SE467_31.asc	MM	2.0226	0.001040	7.6	0.7
08SE467_32.asc	MM	2.0218	0.000910	7.3	0.7
08SE46	*San Emigdio tonalite - San Emigdio Mountains*				
08SE46_1.asc	IG	2.0203	0.001275	4.8	0.7
08SE46_1b.asc	MM	2.0287	0.001408	9.0	0.8
08SE46_1c.asc	MM	2.0252	0.001473	7.2	0.8
08SE46_1d.asc	IG	2.0232	0.000995	6.2	0.6
08SE46_2.asc	IG	2.0230	0.001921	6.1	1.0
08SE46_3.asc	IG	2.0209	0.000775	5.1	0.5
08SE46_3b.asc	MM	2.0251	0.000887	7.1	0.6
08SE46_4.asc	IG	2.0204	0.000750	4.8	0.5
08SE46_4b.asc	MM	2.0246	0.000731	6.9	0.5
08SE46_5.asc	IG	2.0198	0.000978	4.5	0.6

Table A3.2 (Continued). SIMS zircon oxygen isotope data.

Analysis	CL notes§	Measured $^{18}O/^{16}O$ ($x10^{-3}$)	± ($x10^{-3}$)*	$\delta^{18}O_{VSMOW}$ (‰)	± (‰)*
08SE46_5b.asc	MM	2.0233	0.000815	6.3	0.6
08SE46_19.asc	IG	2.0155	0.000705	6.0	0.5
08SE46_20.asc	IG	2.0160	0.000546	6.3	0.5
08SE46_21.asc	IG	2.0146	0.000676	5.6	0.5
08SE46_21b.asc	IG	2.0151	0.000778	5.9	0.6
08SE46_22.asc	IG	2.0138	0.000765	5.2	0.6
08SE46_23.asc	IG	2.0143	0.000636	5.4	0.5
08SE46_24.asc	IG	2.0150	0.000770	5.8	0.6
08SE46_25.asc	IG	2.0132	0.001239	4.9	0.7
08SE46_26.asc	IG	2.0148	0.000851	5.7	0.6
08SE46_27.asc	IG	2.0151	0.000616	5.8	0.5
08SE46_28.asc	IG	2.0135	0.000469	5.0	0.5
08SE46_29.asc	IG	2.0148	0.000758	5.7	0.6
08SE46_30.asc	IG	2.0145	0.000877	5.5	0.6
08SE46_31.asc	IG	2.0144	0.000690	5.5	0.5
08SE675	*San Emigdio tonalite - San Emigdio Mountains*				
08SE675_det1a.asc	IG	2.0159	0.000424	5.8	0.5
08SE675_det1b.asc	IG	2.0161	0.000750	6.1	0.6
08SE675_det2a.asc	IG	2.0142	0.000636	5.2	0.5
08SE675_det2b.asc	MM	2.0171	0.000713	6.8	0.5
08SE675_det3a.asc	IG	2.0128	0.000641	4.7	0.5
08SE675_det3b@1.asc	OL	2.0146	0.000742	5.6	0.5
08SE675_det4a.asc	IG	2.0123	0.000715	5.1	0.5
08SE675_det4c.asc	MM	2.0135	0.000500	6.7	0.5
08SE675_5.asc	IG	2.0168	0.000494	4.7	0.5
08SE675_6.asc	IG	2.0151	0.000667	4.5	0.4
08SE675_7.asc	IG	2.0148	0.000507	5.3	0.5

§ CL: Cathodoluminescence; IG: Oscillatory zoned zircon, interpreted to be detrital igneous grain; MM: Convolute zoning domain, interpreted to be metamorphic zircon; OL: beam overlapped igneous and metamorphic domains.

* Uncertainties given at 2σ.

REFERENCES

Black, L. P., Kamo, S. L., Allen, C. M., Davis, D. W., Aleinikoff, J. N., Valley, J. W., Mundil, R., Campbell, I. H., Korsch, R. J., Williams, I. S., and Foudoulis, C., 2004, Improved $^{206}Pb/^{238}U$ microprobe geochronology by the monitoring of a trace-element-related matrix effect; SHRIMP, ID-TIMS, ELA-ICP-MS and oxygen isotope documentation for a series of zircon standards: *Chemical Geology*, **205**, 115-140.

Chapman, A. D. and Saleeby, J., in review, Geologic map of the San Emigdio Mountains, *Geological Society of America digital map and chart series*.

Chapman, A. D., Luffi, P., Saleeby, J., and Petersen, S., 2011, Metamorphic evolution, partial melting, and rapid exhumation above an ancient flat slab: Insights from the San Emigdio Schist, southern California: *Journal of Metamorphic Geology*, **29**, 601-626, doi: 10.1111/j.1525-1314.2011.00932.x.

Chapman, A. D., Saleeby, J. B., Wood, D. J., Piasecki, A, Farley, K. A., Kidder, S., and Ducea, M. N., in review, Late Cretaceous gravitational collapse of the southern Sierra Nevada batholith, California, submitted to *Geosphere*.

Crowell, J. C., 1952, Geology of the Lebec Quadrangle, California: *California Division of Mines and Geology Special Report*, **24**, 1-24.

Dibblee, T. W., Jr., and Nilsen, T. H., 1973, Geologic map of San Emigdio and western Tehachapi Mountains, *in* Vedder, J. G., ed., Sedimentary facies changes in Tertiary rocks-California Transverse and southern Coast Ranges, *Society of Economic Paleontologists and Mineralogists guidebook to field trip 2*: Anaheim, California.

Gehrels, G., Valencia, V., and Pullen, A., 2006, Detrital zircon geochronology by laser-ablation multicollector ICPMS at the Arizona Laserchron Center: *The Paleontological*

Society Papers, **12**, 67-76.

Grove, M., Jacobson, C. E., Barth, A. P., and Vucic, A., 2003, Temporal and spatial trends of Late Cretaceous-early Tertiary underplating Pelona and related schist beneath Southern California and southwestern Arizona: *Geological Society of America Special Paper*, **374**, 381-406.

Jacobson, C. E., Grove, M., Pedrick, J. N., Barth, A. P., Marsaglia, K. M., Gehrels, G. E., and Nourse, J. A., 2011, Late Cretaceous - early Cenozoic tectonic evolution of the southern California margin inferred from provenance of trench and forearc sediments: *Geological Society of America Bulletin*, **123**(3-4), 485-506.

Ludwig, K. R., 2003, Mathematical-statistical treatment of data and errors for ^{230}Th/U geochronology: *Reviews in Mineralogy and Geochemistry*, **52**, 631-656.

Pickett, D. A., and Saleeby, J. B., 1993, Thermobarometric constraints on the depth of exposure and conditions of plutonism and metamorphism at deep levels of the Sierra Nevada Batholith, Tehachapi Mountains, California: *Journal of Geophysical Research*, **98**(B1), 609-629.

Pickett, D. A., and Saleeby, J. B., 1994, Nd, Sr, and Pb isotopic characteristics of Cretaceous intrusive rocks from deep levels of the Sierra Nevada Batholith, Tehachapi Mountains, California: *Contributions to Mineralogy and Petrology*, **118**(2), 198-215, doi: 110.1007/BF01052869.

Ross, D. C., 1989, The metamorphic and plutonic rocks of the southernmost Sierra Nevada, California, and their tectonic framework: *U.S. Geological Survey Professional Paper* 1381, 159 pp.

Saleeby, J., Farley, K. A., Kistler, R. W., and Fleck, R. J., 2007, Thermal evolution and

exhumation of deep-level batholithic exposures, southernmost Sierra Nevada, California: *Geological Society of America Special Paper*, **419**, 39-66.

Sharry, J., 1981, The geology of the western Tehachapi Mountains, California. Ph.D. thesis, Massachusetts Institute of Technology, 215 pp.

Valley, J. W., 2003, Oxygen isotopes in zircon: *Reviews in Mineralogy and Geochemistry*, **53**, 343-385.

Wood, D. J., 1997, Geology of the eastern Tehachapi Mountains and Late Cretaceous-early Cenozoic tectonics of the southern Sierra Nevada region, Kern County, California. Ph.D. thesis, California Institute of Technology, 287 pp.